

**From some obscurity to clarity in Boom Clay behavior:  
Analysis of its coupled hydro-mechanical response  
in the presence of strain localization**

*by:*

**Fatemeh (Elnaz) SALEHNIA**

*A thesis submitted in fulfillment of the requirements  
for the degree of Doctor of Philosophy*

*in the*

*Faculty of Applied Science*

*Architecture, Geology, Environment, and Construction Department (ArGEnCo)*

JURY members:

Frédéric Nguyen, Associate professor at Université de Liège, President of jury

Robert Charlier, Professor at Université de Liège, Supervisor

Frédéric Collin, Associate professor at Université de Liège

Behrouz Gatmiri, Professor at University of Tehran

Xavier Sillen, Ir., Long-term RD&D, ONDRAF/NIRAS

Jean Vaumat, Professor at Universitat Politècnica de Catalunya

Henry Wong, Professor at Ecole Nationale des Travaux Publics de l'Etat



UNIVERSITÉ DE LIÈGE

September, 2015





*To my dear parents*

*To my lovely brother and sister*



## Acknowledgments

Behind every achievement is passion, many efforts, and the path of overcoming failures. Although, these do not ever make an overall sense of success for one in a solitude. I would like to share the credit of my thesis with who have contributed to its accomplishment by their scientific, financial, or spiritual support.

It is with immense gratitude that I thank, first and foremost, Professor Robert Charlier, the supervisor of this thesis. I would like to thank Robert firstly for trusting me, and giving me the opportunity of working in his group. I am also grateful to Robert for allowing me to work with an independence while his very constructive and insightful comments and questions, in the course of evolution of this work, could truly help me to better conduct my researches path and to then make the progress.

This thesis would not have been possible without the financial and scientific support of ONDRAF/NIRAS. It gives me great pleasure in acknowledging Ir. Xavier Sillen for his active participation in the annual meetings of this thesis, his very useful comments, and for accepting to evaluate this work by being a member of its jury. I consider it an honor to equally have collaborated with EIG EURIDICE. I am truly indebted to Dr. XiangLing Li for her enlightened comments in our annual meetings with regard to her extensive knowledge on Boom Clay behavior, and for providing me with an invaluable data library taken at the HADES URL. I would like to also thank Dr. Arnaud Dizier for furnishing me with those data and participating in the annual meetings concerning this thesis.

I owe my deep gratitude to Professor Frédéric Collin for his comprehensive comments and point of view, which have been always helpful. I would like to equally thank Frédéric for reading most of the manuscript of this thesis, providing me his thoughtful comments, and being part of its jury.

I am sincerely indebted to four other members of the jury for accepting to evaluate this thesis. I owe my earnest thankfulness to Professor Frédéric Nguyen as the president of the jury. I would like to show my gratitude to Professor Behrouz Gatmiri for his acceptance to participate in evaluation of this thesis. It is also many thanks to him that I have met Robert 5 years ago. My sincere thanks also go to Professor Jean Vaunat and Professor Henry Wong. I consider it an honor to have them in my jury.

The positive impact of conviviality in the group where this research has been carried out on its evolution is doubtless. I would like to thank all the team of Geomechanics during the last four years for the sake of stimulating environment provided. It gives me great pleasure in acknowledging Ir. Jean-Pol Radu for his very generous help. I am very much thankful to Jean-Pol for his patience to always listen the questions, and to always have a clue to the answer. Thank you also to Anne-Catherine, Benjamin, Benoît, Bram, François, Georgia, Gwendal, Julien, Marc, Noémie, Pierre, Séverine, Simon for the good humor provided in the team.

I cannot find the words to express my deepest gratitude to my dear parents for all their heartfelt and kind support during these years and indeed for their perennial help. This thesis would have remained a dream had it not been for the spiritual support of my family; my parents, my brother and my sister which I have dedicated to them, the fruit of their constant love every day.



Although the work presented herein has been performed with the financial support of ONDRAF/NIRAS, the views expressed in the paper do not necessarily correspond to those of ONDRAF/NIRAS.

The in-situ measurements performed around and within the HADES underground research facility presented herein have been collected by EIG EURIDICE as part of the Belgian RD& D program on geological disposal that is carried out by ONDRAF/NIRAS. Scientists wishing to use these measurements for further research are kindly encouraged to contact ONDRAF/NIRAS and/or EURIDICE that can provide up-to-date information, references and the latest available experimental data.



## Abstract

Deep disposal of the high-level and high-lived radioactive wastes in the potential geological formations is envisaged as a possible solution in the framework of long-term management of these wastes. The argillaceous materials, namely Boom Clay, are potential to constitute the natural barrier aimed at confining the nuclear waste and protecting the biosphere from it. Around galleries excavated at depth in these media, the creation of a damaged zone with significant irreversible deformation is generally unavoidable. A considerable change in the host rock properties could be likely resulted in this zone, which may potentially be important with respect to the long-term evolution and the performance of the system. In this context, a paramount interest addresses characterization of the so-called Excavation Damaged Zone (EDZ), predicting its extent, and development of localized fracturing during and after the underground excavation in the host rock. This constitutes the foundation of this work, focusing on the Boom Clay formation as the reference potential host rock in Belgium.

Dealing with this purpose, providing a state of knowledge on the hydro-mechanical behavior of Boom Clay, and validating a set of parameters which could realistically reproduce its response through the numerical modelings are firstly addressed as the requisites. Moreover, a special focus is made on the dilatation factor of the rock, commonly described through the dilatancy angle parameter. Correct estimation of the dilatant behavior of a rock has an essential role in a realistic simulation of its volumetric behavior, fracturing threshold during the rock deformation process and its post-failure response. Therefore, a new formula is developed for consideration of the variable dilatancy angle, incorporated into an internal frictional elasto-plastic hardening/softening model, within the LAGAMINE finite element code. This development overcomes the inconveniences associated to using a constant dilatancy angle, for instance encountered in our numerical simulations of some laboratory small-scale tests as well as a large-scale excavation.

This study then focuses more particularly on simulation of EDZ extension at the large scale excavation, around the Connecting gallery (in the HADES URL, Mol, Belgium), through analyzing the evolution of strain localization in shear bands mode. The modeling takes into account of the initial anisotropic stresses, mechanical cross-anisotropy, anisotropic permeabilities, and gravity effects. As a result, an eye-shape extension of EDZ accompanied by an anisotropic convergence of the rock is predicted. A coupled analysis addresses the pore water pressure distribution during the excavation period and in long-term while no more evolution of the localized shear bands is predicted. To assess the reliability of the numerical results, some available in-situ measurements and observations, within the clay, during the gallery's construction and afterwards are precisely analyzed, and then compared with the corresponding numerical predictions. As a result, a good agreement is found between the in-situ data and simulated results.

Moreover, the above study is integrated with a particular analysis of the contact mechanism on the interface between the clay and the gallery's lining. Thence, the coupled interface element is introduced to deal with the contact phenomenon. The obtained results reveal some interesting features regarding the development of contact pressure on the interface linked to the evolution pattern of strain localization within the clay around the gallery. Furthermore, with regard to the own lining behavior, a development of the modeling with the aim of consideration of a discontinuous lining (made of the segments as the real case) is performed. We propose an approach to realistically reproduce the response of the lining's segments and their contact phenomena in the course of a long-term simulation. Defining the interface elements between the neighboring segments, with respect to the real installation procedure of the lining during the gallery construction, this process is aimed to be simulated through some evolution of the contact pressure on the segments' interfaces. As a result, a considerable improvement is achieved in reproducing the in-situ measurements provided in the lining. The numerical and measured evolution of strain and displacement are in a good agreement.

**Keywords:** Radioactive waste disposal, Boom Clay, Numerical modeling, Dilatancy angle, Strain localization, Excavation, Connecting gallery, Lining, EDZ, Pore water pressure, Interfaces, Contact pressure



## Résumé

Le stockage profond de déchets radioactifs de haute activité et de longue durée de vie dans les formations géologiques adaptées est considéré comme une solution possible dans le cadre de la gestion à long terme de ces déchets. Les couches argileuses, et spécifiquement l'Argile de Boom, ont le potentiel de constituer une barrière naturelle permettant de confiner les déchets nucléaires et de protéger la biosphère. La création d'une zone endommagée, suite à des déformations irréversibles significatives, est généralement inévitable autour des galeries creusées en profondeur dans ces formations, et peut entraîner un changement considérable des propriétés de la roche hôte. Ceci peut avoir un impact important sur la performance à long terme du système. Dans ce contexte, il est d'un intérêt primordial de caractériser cette zone endommagée (EDZ) et de prédire son extension et le développement de la fracturation pendant et après l'excavation. Cela constitue la base de ce travail, qui se concentre sur l'Argile de Boom, considérée comme la roche hôte de référence en Belgique.

Dans cette perspective, il est en premier lieu nécessaire de faire l'état des connaissances sur le comportement hydromécanique de l'Argile de Boom, et de valider un ensemble de paramètres permettant de reproduire de façon réaliste sa réponse dans le cadre de modélisations numériques. Une attention particulière est portée à l'angle de dilataance. L'estimation correcte du comportement dilatant d'une roche a un rôle essentiel dans une simulation réaliste de son comportement volumétrique, de son seuil de fracturation au cours du processus de déformation, et de sa réponse postcritique. A cet effet, une nouvelle loi est développée pour tenir compte d'un angle de dilataance variable. Elle est introduite dans un modèle élastoplastique à frottement interne avec écrouissage/adoucissement dans le code d'éléments finis LAGAMINE. Ce développement lève les limitations associées à l'utilisation d'un angle de dilataance constant, rencontrées par exemple dans les simulations de certains tests à petite échelle et d'excavation souterraine à grande échelle.

Cette étude se concentre ensuite plus particulièrement sur la simulation de l'extension de l'EDZ lié à l'excavation à grande échelle de la galerie de liaison du laboratoire de Mol, par l'analyse de l'évolution de la localisation des déformations en bandes de cisaillement. La modélisation prend en compte des contraintes anisotropes initiales, les propriétés mécaniques isotropes transverses, les perméabilités anisotropes et les effets de la gravité. On observe une extension de l'EDZ en forme « d'œil », accompagnée d'une convergence anisotrope de la roche. L'analyse couplée fournit l'évolution des pressions d'eau pendant la période d'excavation et à long terme lorsqu'aucune évolution des bandes de cisaillement localisées n'est plus prédite. Pour évaluer la fiabilité des résultats numériques, certaines observations et mesures in situ, effectuées pendant et après la construction de la galerie, sont analysées, puis comparées avec les prédictions numériques correspondantes. Un bon accord est trouvé entre les données in-situ et les simulations.

En outre, cette étude est enrichie d'une analyse du mécanisme de contact à l'interface entre l'argile et le soutènement de la galerie. Un élément d'interface couplé est introduit pour modéliser les phénomènes de contact. Les résultats obtenus permettent de relier la pression de contact dans l'interface et l'évolution de la localisation des déformations au sein de l'argile. D'autre part, un développement de la modélisation est effectué, et le comportement du soutènement prend en compte les voussoirs, donc le caractère discontinu. Nous proposons une approche permettant de reproduire de façon réaliste la réponse du soutènement dans le cadre d'une simulation à long terme. En définissant des éléments d'interfaces entre les voussoirs, la procédure d'installation réelle peut être simulée, et donne l'évolution de la pression de contact. La concordance des résultats numériques avec les mesures in situ effectuées dans les voussoirs est ainsi considérablement améliorée, notamment en ce qui concerne l'évolution des déformations et du déplacement.

**Keywords:** Stockage de déchets radioactifs, Argile de Boom, Modélisation numérique, Angle de dilataance, Localisation des déformations, Excavation, Galerie de Liaison, Revêtement, EDZ, Pression d'eau, Interfaces, Pression de contact



# Contents

<b>1</b>	<b>Introduction</b>	<b>1</b>
1.1	General context and objectives . . . . .	2
1.2	Layout of the thesis . . . . .	4
<b>2</b>	<b>Boom Clay characteristics: a potential geomaterial for radioactive waste disposal</b>	<b>7</b>
2.1	Introduction . . . . .	8
2.2	Boom Clay in the framework of nuclear waste disposal . . . . .	10
2.2.1	Concept of deep disposal of radioactive waste . . . . .	10
2.2.2	Potentiality of clay materials . . . . .	10
2.2.3	Boom Clay as the reference host formation in Belgium . . . . .	11
2.3	Hydro-mechanical properties of Boom Clay . . . . .	13
2.3.1	Boom Clay formation at depth . . . . .	13
2.3.2	Mineralogy and Microstructures . . . . .	16
2.3.2.1	Mineral composition . . . . .	16
2.3.2.2	Orientations of clay minerals . . . . .	16
2.3.2.3	Microstructures observations of the deformation mechanism . . . . .	17
2.3.3	On the coupled hydro-mechanical analysis . . . . .	20
2.3.4	Basic geotechnical features . . . . .	23
2.3.5	Extended geomechanical properties for numerical simulations . . . . .	25
2.4	Intermediate conclusions . . . . .	25
<b>3</b>	<b>Classical numerical framework</b>	<b>27</b>
3.1	Introduction . . . . .	28
3.2	General configuration of the problem . . . . .	29
3.2.1	Stress and strain description for mechanical analysis . . . . .	29
3.2.2	Mechanical equilibrium conditions . . . . .	31
3.2.2.1	Description of the problem . . . . .	31
3.2.2.2	Equilibrium statement in the framework of the principle of virtual work . . . . .	33
3.2.3	Description of porous media for a coupled hydro-mechanical analysis . . . . .	34
3.2.3.1	On the definition of porous medium . . . . .	34
3.2.3.2	Kinematics of porous medium . . . . .	37
3.2.3.3	Constitutive relations . . . . .	38
3.2.4	On the coupled analysis of the mixture . . . . .	39
3.2.5	Hydraulic equilibrium conditions . . . . .	41
3.2.6	Discretization of the domain . . . . .	42
3.2.7	LAGAMINE resolution algorithm . . . . .	45
3.3	Elasto-plasticity . . . . .	47
3.3.1	General concept . . . . .	47

3.3.2	Yield surface . . . . .	48
3.3.3	Flow rule and potential surface . . . . .	49
3.3.4	Consistency conditions . . . . .	50
3.3.5	Hardening/softening response and hardening rule . . . . .	50
3.4	Internal frictional behavior models for geomaterials . . . . .	53
3.4.1	Stress conventions . . . . .	53
3.4.2	Representation of the yield surfaces for an internal frictional constitutive law . . . . .	54
3.4.2.1	Drucker-Prager yield criterion . . . . .	56
3.4.2.2	Van Eekelen yield criterion . . . . .	60
3.4.3	Review of some other yield criteria . . . . .	62
3.4.4	Choice of the yield criterion for the elasto-plastic analysis . . . . .	66
3.4.5	Return mapping algorithm . . . . .	67
3.4.6	Sub-stepping approach . . . . .	70
3.5	Simulations of the triaxial tests on Boom Clay . . . . .	71
3.5.1	Stress-strain mechanical response: deviatoric stress development . . . . .	72
3.5.2	Description of the triaxial tests . . . . .	73
3.5.2.1	Hydro-mechanical simulation of the triaxial tests performed at ULg . . . . .	74
3.5.2.2	Hydro-mechanical simulation of the triaxial test performed at ENPC . . . . .	79
3.5.2.3	Hydro-mechanical simulation of the triaxial tests performed at IRSM . . . . .	82
3.5.2.4	Simulation of the drained triaxial tests . . . . .	89
3.5.3	Discussion on the influence of dilatancy angle on the numerical results . . . . .	91
3.6	Intermediate conclusions . . . . .	94
<b>4</b>	<b>Development of a method for considering the variable dilatancy angle</b>	<b>97</b>
4.1	Introduction . . . . .	98
4.2	Change of the dilatancy angle . . . . .	99
4.2.1	Overview of the dilatancy angle interest and encountered difficulty . . . . .	99
4.2.2	Proposed formula implemented in LAGAMINE . . . . .	101
4.2.3	Validation of the solution . . . . .	104
4.2.3.1	Drained triaxial tests: Presentation of the capability of the model to simulate observed volumetric responses . . . . .	104
4.2.3.2	Undrained triaxial tests performed at ULg: Studying the influence of the model's parameters . . . . .	107
4.2.3.3	Undrained triaxial tests performed at IRSM . . . . .	116
4.3	Intermediate conclusions . . . . .	121
<b>5</b>	<b>Numerical simulation of strain localization</b>	<b>123</b>
5.1	Introduction . . . . .	124
5.2	Fracturing mechanism and strain localization . . . . .	125
5.2.1	Definition of shearing bands and failure process . . . . .	125
5.2.2	Experimental evidences of strain localization . . . . .	127
5.2.3	In-situ observations of fractures at depth . . . . .	136
5.3	Local second gradient model . . . . .	140
5.3.1	Computational modeling of strain localization . . . . .	140
5.3.2	Continua with microstructures . . . . .	144
5.3.3	Framework of the coupled local second gradient model for microstructured continuum . . . . .	145

5.4	Numerical examples: Definition of the corresponding parameters for modeling of strain localization and analysis of their impact . . . . .	154
5.4.1	Simulation of biaxial compression test . . . . .	154
5.4.1.1	General description . . . . .	155
5.4.1.2	Analysis of the results . . . . .	155
5.4.2	Simulation of the excavation of Praclay gallery . . . . .	162
5.4.2.1	Description of the Praclay experience . . . . .	167
5.4.2.2	Definition of the numerical model . . . . .	167
5.4.2.3	Parametric study . . . . .	170
5.4.2.4	On the application of variable dilatancy angle . . . . .	178
5.5	Intermediate conclusions . . . . .	184
<b>6</b>	<b>Analysis of the hydro-mechanical behavior of Boom Clay associated with the construction of underground galleries: Application to the Connecting gallery</b>	<b>185</b>
6.1	Introduction . . . . .	186
6.2	Description of the Connecting gallery . . . . .	186
6.2.1	Construction objective and the applied technique . . . . .	186
6.2.2	Relative projects . . . . .	187
6.3	Definition of the numerical model . . . . .	189
6.3.1	Geometry, initial and boundary conditions . . . . .	189
6.3.2	Hydro-mechanical properties of the model . . . . .	190
6.3.2.1	Mechanical part . . . . .	190
6.3.2.2	Hydraulic part . . . . .	191
6.3.3	Simulation of the development of strain localization around the gallery . . . . .	192
6.4	An analysis of in-situ measurements and research programs . . . . .	197
6.4.1	Pore water pressure measurements . . . . .	197
6.4.1.1	CLIPLEX program . . . . .	197
6.4.1.2	Boreholes R55 and R13 . . . . .	202
6.4.2	Permeability measurements . . . . .	205
6.4.3	Strain measurements in the lining . . . . .	205
6.4.4	Convergence measurements in the lining . . . . .	207
6.5	Comparison of the extended numerical predictions and in-situ measurements . . . . .	210
6.5.1	Development of the numerical simulation . . . . .	210
6.5.1.1	Cross-anisotropy of the mechanical properties . . . . .	211
6.5.1.2	Definition of the zones of anisotropic permeability . . . . .	213
6.5.1.3	Gravity effects . . . . .	214
6.5.1.4	Results of the modeling . . . . .	215
6.5.2	Fracture characterization . . . . .	224
6.5.3	Convergence of the rock . . . . .	226
6.5.4	Numerical results of pore water pressure compared to the in-situ measurements: R55 and R13 boreholes . . . . .	227
6.5.5	Numerical results of pore water pressure compared to the in-situ measurements: CLIPLEX program . . . . .	230
6.5.6	Numerical results of strain and convergence in the lining compared to the in-situ measurements . . . . .	235
6.6	Intermediate conclusions . . . . .	236

<b>7</b>	<b>Interface features</b>	<b>239</b>
7.1	Introduction . . . . .	240
7.2	General overview of the contact mechanism . . . . .	242
7.2.1	An introduction to the contact problem . . . . .	242
7.2.2	Local kinematical relations of the contact . . . . .	243
7.2.2.1	Normal contact . . . . .	245
7.2.2.2	Tangential contact . . . . .	246
7.3	Constitutive laws for interface element . . . . .	247
7.3.1	Mechanical part . . . . .	247
7.3.2	Hydraulic part . . . . .	249
7.3.3	Description of the interface finite element . . . . .	250
7.3.4	Contact contribution to the global formulation . . . . .	251
7.4	Application of the interface element to the Connecting gallery . . . . .	253
7.4.1	Interface description . . . . .	253
7.4.2	Role of the concrete lining . . . . .	254
7.4.3	Contact phenomena between the lining and Boom Clay . . . . .	257
7.4.3.1	Analysis of the oscillations . . . . .	259
7.4.3.2	The oscillations: Relation between the contact pressure and strain localization . . . . .	262
7.5	Application of the interface element to the gallery's lining . . . . .	264
7.5.1	Description of the numerical model . . . . .	264
7.5.2	Analysis of the contact pressure on the interfaces . . . . .	268
7.5.3	Comparison of the numerical predictions and in-situ measurements in the lining . . . . .	271
7.5.3.1	Analysis of strain . . . . .	271
7.5.3.2	Analysis of convergence . . . . .	273
7.6	Intermediate conclusions . . . . .	275
<b>8</b>	<b>Conclusions and perspectives</b>	<b>277</b>
8.1	General conclusions . . . . .	278
8.2	Perspectives . . . . .	282
	<b>Bibliography</b>	<b>285</b>
<b>A</b>	<b>Convergence criteria</b>	<b>297</b>
A.1	Convergence criterion for the displacement . . . . .	297
A.2	Convergence criterion for the force . . . . .	298
<b>B</b>	<b>Accomplishment to the coupled second gradient formulation</b>	<b>299</b>
<b>C</b>	<b>On the fluid flow along the interface</b>	<b>303</b>

# List of symbols

## Roman symbols

<i>Symbol</i>	<i>Description</i>	<i>Units</i>
$b$	Biot's coefficient	—
$B_\varphi, B_c, B_\Psi$	The value of equivalent plastic strain from which hardening/softening on friction angle/cohesion, and the change in dilatanacy angle is started	—
$c_i, c_f$	Initial and final cohesions	$Pa$
$\mathbf{C}, \mathbf{C}_{ijkl}$	Constitutive tangent matrix	$Pa$
$\mathbf{C}^e, \mathbf{C}_{ijkl}^e$	Elastic constitutive matrix/elasticity tensor	$Pa$
$\mathbf{C}^p, \mathbf{C}_{ijkl}^p$	Plastic constitutive matrix	$Pa$
$D$	Second gradient elastic modulus	$N$
$D_\varphi, D_c, D_\Psi$	The value of equivalent plastic strain for which half of the hardening/softening on friction angle/cohesion, and the change in dilatanacy angle is achieved	—
$\mathbf{D}, \mathbf{D}_{ijkl}$	Constitutive tangent matrix for the second gradient law	$Pa$
$e$	Void ratio	—
$E$	Young's modulus	$Pa$
$f$	Yield criterion	$Pa$
$f_{sl}$	Coulomb yield criterion governing the slipping state on the interface	$Pa$
$\mathcal{F}_I^{el}, \mathcal{F}_E^{el}$	Energetically equivalent internal and external nodal forces vector of the element	$N$
$\mathcal{F}_{\text{OBF}}^{el}, \mathbf{F}_{\text{OBF}}$	Element and global out of balance forces	$N$
$F_i^{s/w}$	True force applied on water by the skeleton	$Pa \cdot m^{-1}$
$\mathbf{F}$	Transformation tensor	—
$g, \mathfrak{g}$	Potential surface	$Pa$
$g = g(x_i n_i)$	An arbitrary vector described with respect to the direction and intensity of the position transverses the band	—
$g_N, \dot{g}_N$	Gap function	$m$
$g_T, \dot{g}_T$	Tangential displacement on the contact interface	$m$
$g_i$	Gravity acceleration	$m/s^2$
$\mathbf{G}, G_i$	Volume body force/gravity volume force vector	$Pa \cdot m^{-1}$
$G$	Shear modulus	$Pa$
$\mathbf{G}$	Lagrangian natural strain tensor	—
$h_{ijk}^*$	Virtual micro second gradient field	$m^{-1}$
$I_\sigma$	First stress tensor invariant	$Pa$
$II_{\hat{\sigma}}$	Second deviatoric stress tensor invariant	$Pa$

$III_{\hat{\sigma}}$	Third deviatoric stress tensor invariant	$Pa^3$
$\mathbf{J}$	Jacobian matrix	–
$k$	Intrinsic permeability	$m^2$
$k_{ij}$	Intrinsic permeability matrix for anisotropic case	$m^2$
$k_{xx}/k_h, k_{yy}/k_v$	Horizontal and vertical intrinsic permeabilities	$m^2$
$k_l$	Longitudinal permeability	$m^2$
$K$	Hydraulic conductivity	$m/s$
$K_h, K_v$	Horizontal and vertical hydraulic conductivities	$m/s$
$K$	Bulk modulus	$Pa$
$K_N, K_T$	Normal and tangential penalty coefficients	$Pa.m^{-1}$
$\mathcal{K}^{el}, \mathbf{K}$	Element and global stiffness matrices	[...]
$LL$	Liquid index	%
$m$	Van Genuchten parameter of the water retention curve	–
$\mathbf{m}, m_i$	Water mass flow	$Kg.m^{-2}.s^{-1}$
$n$	Van Genuchten parameter of the water retention curve	–
$n$	Porosity	%
$n_0$	Initial porosity	%
$n^p$	Plastic porosity	%
$\mathbf{n}, n_i$	Normal vector	–
$\hat{n}_{ij}$	Normal unit vector	–
$N_{en}$	Shape function associated to the $en^{th}$ node	–
$p_w, p_a$	Pore water and air pressures	$Pa$
$p_w^*$	Kinematically admissible virtual pore water pressure field	$Pa$
$p_N$	Normal contact pressure/normal component of contact stress vector	$Pa$
$p_i, p_e$	Internal and external pressures in the thick-walled cylinder/tube	$Pa$
$p, p'$	Total and effective mean stresses	$Pa$
$p_0, P_0$	Preconsolidation stress, for the null suction state and for the suction $s$	$Pa$
$P^c$	Reference preconsolidation stress	$Pa$
$PI$	Plastic index	%
$PL$	Plastic limit	%
$q$	Deviatoric stress	$Pa$
$\bar{q}$	Prescribed water mass per unit area	$Kg.m^{-2}.s^{-1}$
$Q$	Water sink term	$Kg.m^{-3}.s^{-1}$
$r_i, r_e$	Internal and external radii in the thick-walled cylinder/tube	$m$
$Rat_{\Psi}$	Ratio between the peak of dilatancy angle and its initial value	–
$\mathbf{R}$	Orthogonal rotation tensor	–
$s$	Suction	$Pa$
$S$	Water mass content	$Kg/m^3$
$S_r$	Natural degree of saturation	%
$S_{r,res}, S_{r,s}$	Residual and saturated values of degree of saturation	%
$t$	Time	$s$
$\Delta t, \delta t$	Time step, and its corresponding subdivided time increment	$s$
$\bar{t}_i$	Classical external traction force	$Pa$
$\bar{T}_i, \bar{T}_{ij}$	Additional external double surface force	$Pa.m$
$T_w$	Transverse transmissivity	$m.Pa^{-1}.s^{-1}$
$\mathbf{u}, u_i$	Displacement vector	$m$

$\mathbf{u}^*, u_i^*$	Kinematically admissible virtual displacement vector	$m$
$\mathbf{U}_{en}, U_{en,i}$	Nodal displacement vector	$m$
$\mathbf{U}^*, U_{en,i}^*$	Nodal virtual displacement vector	$m$
$d\mathbf{u}$	Corrections on the generalized coordinates vector (consisting of the mechanical displacements, pore pressure variations and the change in second gradient terms (in Chapter 5))	$m, Pa, -$
$\mathbf{u}^*$	Generalized virtual coordinates vector	$m, Pa, -$
$d\mathbf{u}_{en}$	Corrections on the generalized coordinates vector corresponding to the nodal degree of freedom	$m, Pa, -$
$\delta\mathbf{u}_{en}$	Global vector of corrections on the generalized coordinates/Generalized displacements corresponding to the nodal degree of freedom	$m, Pa, -$
$\mathbf{u}_{en}^*$	Generalized virtual coordinates vector corresponding to the nodal degree of freedom	$m, Pa, -$
$\mathbf{U}, \mathbf{V}$	Right and left symmetric stretch tensors	$-$
$\mathbf{V}^d, V_i^d$	Darcy water velocity	$m/s$
$\mathbf{V}^{w/s}, V_i^{w/s}$	True water velocity with respect to solid phase	$m/s$
$w$	Natural water content	$\%$
$\mathcal{W}_I^*, \mathcal{W}_E^*$	Internal and external virtual works	$J (Kg.m^2.s^{-2})$
$W_{IP}$	Gauss weight corresponding to the integration point $IP$	$-$
$\mathbf{x}$	Coordinates corresponding to a solid volume in its current position	$m$
$\mathbf{X}$	Coordinates corresponding to a solid volume in its reference position	$m$

## Greek symbols

<i>Symbol</i>	<i>Description</i>	<i>Units</i>
$\alpha$	Van Genuchten parameter of the water retention curve	$Pa^{-1}$
$\beta$	Lode angle	$^\circ$
$\Gamma_\sigma, \Gamma_u$	Boundary portions of the domain $\Omega$ on which the force(s), and displacement/microkinematic gradient are prescribed	$-$
$\Gamma_q, \Gamma_{p_w}$	Boundary portions of the domain $\Omega$ on which the water mass, and pore pressure are prescribed	$-$
$\Gamma_c$	Boundary portions of the domain $\Omega$ on which the contact occurs with another body	$-$
$\delta_{ij}$	Kronecker delta	$-$
$\boldsymbol{\varepsilon}, \varepsilon_{ij}$	Strain tensor	$-$
$\dot{\boldsymbol{\varepsilon}}, \dot{\varepsilon}_{ij}$	Strain rate tensor	$s^{-1}$
$\boldsymbol{\varepsilon}^e, \varepsilon_{ij}^e$	Elastic component of strain tensor	$-$
$\dot{\boldsymbol{\varepsilon}}^e, \dot{\varepsilon}_{ij}^e$	Elastic component of strain tensor rate	$s^{-1}$
$\boldsymbol{\varepsilon}^p, \varepsilon_{ij}^p$	Plastic component of strain tensor	$-$
$\dot{\boldsymbol{\varepsilon}}^p, \dot{\varepsilon}_{ij}^p$	Plastic component of strain tensor rate	$s^{-1}$
$\varepsilon_v$	Volumetric strain	$-$
$\varepsilon_v^p$	Volumetric plastic strain	$-$
$\dot{\varepsilon}_v^p$	Volumetric plastic strain rate	$s^{-1}$
$\varepsilon_a, \varepsilon_1$	Axial strain	$-$

$\dot{\varepsilon}_1^p, \dot{\varepsilon}_3^p$	Major (axial) and minor principle plastic strain rate	$s^{-1}$
$\varepsilon_s^p$	Volumetric plastic (permanent) strain of the matrix	—
$\varepsilon_{eq}^p$	Von Mises equivalent plastic strain	—
$\dot{\varepsilon}_{eq}^p$	Von Mises equivalent plastic strain rate	$s^{-1}$
$\varepsilon_{ij}^*$	Kinematically admissible virtual strain field	—
$\lambda(0), \lambda(s)$	Plastic slope parameter related to the variations in stress, for the null suction state and for the suction $s$	—
$\dot{\lambda}$	Plastic multiplier	$s^{-1}$
$\lambda_{ij}$	Field of Lagrange multipliers	$Pa$
$\lambda_{ij}^*$	Virtual field of Lagrange multipliers	$Pa$
$\mu$	Coulomb friction coefficient	—
$\mu_w$	Water dynamic viscosity	$Pa \cdot s$
$\nu$	Poisson ratio	—
$\rho$	Bulk (saturated) density/specific mass	$Kg/m^3$
$\rho_d$	Bulk dry density	$Kg/m^3$
$\rho_s$	Bulk solid density/specific mass of the grains	$Kg/m^3$
$\rho_w, \rho_a$	Specific masses of the water and air	$Kg/m^3$
$\boldsymbol{\sigma}, \sigma_{ij}$	Stress tensor	$Pa$
$\dot{\boldsymbol{\sigma}}, \dot{\sigma}_{ij}$	Stress rate tensor	$Pa \cdot s^{-1}$
$\tilde{\boldsymbol{\sigma}}, \tilde{\sigma}_{ij}$	Jaumann stress rate tensor	$Pa \cdot s^{-1}$
$\boldsymbol{\sigma}', \sigma'_{ij}$	Effective stress tensor	$Pa$
$\tilde{\boldsymbol{\sigma}}', \tilde{\sigma}'_{ij}$	Jaumann effective stress rate tensor	$Pa \cdot s^{-1}$
$\hat{\boldsymbol{\sigma}}', \hat{\sigma}'_{ij}$	Deviatoric stress tensor	$Pa$
$\sigma_1, \sigma_2, \sigma_3$	Principle stresses	$Pa$
$\sigma'_{t,i}$	Isotropic traction resistance limit	$Pa$
$\boldsymbol{\sigma}_c$	Contact stress vector	$Pa$
$\sigma^H$	Circumferential (Hoop) stress in the thick-walled cylinder/tube	$Pa$
$\Sigma_{ijk}$	Double stress, dual of the virtual (micro) second gradient field	$Pa \cdot m$
$\dot{\Sigma}_{ijk}$	Double stress rate tensor	$Pa \cdot m \cdot s^{-1}$
$\tilde{\Sigma}_{ijk}$	Jaumann double stress rate tensor	$Pa \cdot m \cdot s^{-1}$
$\tau$	Shear stress	$Pa$
$\tau_{ij}$	Microstress tensor	$Pa$
$\tau_T$	Tangential component of contact stress vector	$Pa$
$v_{ij}$	Microkinematic gradient field	—
$\dot{v}_{ij}$	Time derivative of microkinematic gradient field	$s^{-1}$
$v_{ij}^*$	Virtual microkinematic gradient field	—
$\varphi_{C0}, \varphi_{Cf}$	Initial and final compression friction angles	$^\circ$
$\varphi_{E0}, \varphi_{Ef}$	Initial and final extension friction angles	$^\circ$
$\varphi_{cv}$	Friction angle at constant volume, (no dilatation)	$^\circ$
$1/\chi_w$	Water compressibility	$Pa^{-1}$
$\Psi$	Dilatancy angle	$^\circ$
$\Psi_{peak}$	Peak of dilatancy angle	$^\circ$
$\Psi_{lim}$	Limit value of dilatancy angle	$^\circ$
$\boldsymbol{\omega}, \omega_{ij}$	Spin tensor	$s^{-1}$
$\Omega$	Domain	—

# Chapter 1

## Introduction

### Contents

---

1.1	General context and objectives . . . . .	2
1.2	Layout of the thesis . . . . .	4

---

*The science of today is the technology of tomorrow.*

Edward Teller

## 1.1 General context and objectives

In all countries equipped with nuclear power plants, producing some amount of long-lived high-level radioactive waste is an unavoidable outcome of the contribution of this energy to the global electricity production. This contribution is currently about 50 % in Belgium. With regard to the harmfulness that arises from radioactivity of nuclear waste to man and the environment, they need to be carefully managed.

In the framework of the long-term management of these high-level radioactive wastes, storing them in deep stable geological formations is internationally considered as a possible solution. Geological disposal facilities (GDFs) combine a suitable system of engineered barriers with an host rock (natural barrier) with favorable confinement properties at a depth that ensures adequate isolation from man and the environment. Geomaterials are commonly involved in this confinement process in terms of the natural and/or engineered barriers. In that matter, geomechanics comes through the complex process in order to understand the behavior of these barriers around the system of underground galleries surrounding the radioactive wastes. The argillaceous formations, in a number of European countries, are considered to constitute the natural barrier (host rock) aimed at confining the nuclear waste and protecting the biosphere from it, with respect to their natural advantageous properties among which there is a very low hydraulic conductivity. Within this framework, *Boom Clay* is being studied as the considered reference host formation in Belgium [ONDRAF/NIRAS, 2001] given its various favorable properties such as its good sorption capacity for many radioelements and its self-sealing capacity, in addition to its very low hydraulic conductivity. Taking into account of the aforesaid introduction, the paramount interest in characterizing and understanding the coupled<sup>1</sup> behavior of the clay barrier in the course of construction of the disposal galleries system, and its long-term life is obvious.

Thence, the Underground Research Laboratories (URLs) have been constructed in different countries, including HADES URL (within Boom Clay formation) in Belgium. They allow overall for studying the feasibility of deep disposal of high-level radioactive waste in potential geological formation, namely Boom Clay. As a result, the appropriate technology for construction of the real repositories and the upcoming effect of the applied technique and construction procedure in the surrounding host rock could be studied. Additionally, the URLs' construction is aimed at execution of some large-scale experiments and projects for a better understanding of the overall concept of deep storage and coupled response of the host formation to this disposal. The obtained information and data through these experiments and research projects, nevertheless invaluable, could be senseless without a subsequent precise analysis, though.

However, limiting to the in-situ experiments with regard to the large-scale of the problem, complex coupling features, the cost of each project, and specially the time period must be addressed is not practical. The latter issue concerns the long-time analysis that the safety aspect of the problem needs. Thence, understanding and characterization of the whole phenomena would be chiefly based on the simulations and predictions. Problem of scale and complexity could be nowadays resolved through the use of computers and computational methods, which are by definition built based on the mathematical description of the physical process. Therefore, numerical modeling comes to help the in-situ experiments in firstly a better comprehension of the performed measurements and field observations, and then accomplishing a more complete and utter analysis of the whole phenomena.

Hence, this thesis is mainly *motivated* by the coupled hydro-mechanical numerical analysis

---

<sup>1</sup>Thermo-hydro-chemo-mechanical in a general sense, and hydro-mechanical with regard to the concern of this work.

of the Boom Clay host rock behavior, with a particular focus on strain localization phenomenon, around an underground gallery in the HADES URL. Within the aforesaid framework, the numerical modelings give the possibility of focusing on some aspects of the material behavior which may not be possible to be analyzed and understood to a desirable level only through the performed site experiments and field observations. Or, they additionally need the help of computations to fulfill the gap between those in-situ observations and experiments, and, theoretical perception of the problem to ultimately clarify some remained obscurities of the material response. Moreover, these modelings are flexible to the parametric studies and they could be a very useful complement to our coupled analysis. As the fundamental step in characterizing the whole process of deep disposal, the *basis* of this research is the simulation of hydro-mechanical behavior of the host rock within the damaged zone, with localization of deformation, resulted from the underground excavations. The latter is supposed to induce a significant stress redistribution within a perturbed clay zone around the opening which leads to trigger the damage propagation. An Excavation Damaged Zone (EDZ) is therefore expected to be created resulting to the important irreversible (localized) deformations, macro and micro-fracturing and likely modification of the favorable original flow properties of the rock. Characterization of this zone and its extension in time is then of the foremost issues in the framework of long-term evolution and performance management of repositories.

This thesis has been granted by ONDRAF/NIRAS (Organisme National des Déchets RAdioactifs et des matières Fissiles enrichies), and it has been developed in collaboration with ONDRAF/NIRAS as well as EIG EURIDICE (European Underground Research Infrastructure for Disposal of nuclear waste in a Clay Environment).

Dealing with the aforesaid ambitious purposes, the main **objectives** of this thesis are summarized as follows:

- To provide an overall knowledge on the hydro-mechanical behavior of Boom Clay with respect to the literature and the laboratory experiments performed in the past under a similar conditions as in-situ. Consistently, the corresponding hydro-mechanical parameters for a realistic modeling of the material behavior are aimed to be identified with a particular focus on the most disregarded parameter in the previous studies, namely dilatancy angle, for which a new formula is developed to fulfill our numerical need.
- To analyze the possible mechanisms controlling the creation of the EDZ and its extension within the clay due to the underground excavation as well as its evolution during a longer time, taking into account of the aforementioned essential importance of this task. An analysis of this zone is proposed in the framework of a strain localization approach in shear band mode, with respect to the field observations. This study is not only in terms of the development of localized fracturing around the opening, but also with regard to the overall hydro-mechanical response of the clay, and in interaction with the gallery's lining.
- To integrate the above numerical simulations with a particular examination of the available in-situ measurements and evidences. It consists in firstly a precise coupled analysis to give those invaluable data, on the individual processes, a practical sense. Afterwards, they are used to validate our numerical simulations as to be in the best agreement possible with the in-situ data.
- To develop the model to address realistically the behavior of the gallery's discontinuous lining<sup>2</sup> (in interaction with the host rock). Consequently, the contact phenomenon on the

---

<sup>2</sup>Consisting of the jointed segments, with respect to the used technique for the lining of our studied gallery: Wedge-block technique [Bastiaens et al., 2003].

interfaces between the lining's segments is aimed to be numerically analyzed and illustrated. In addition, the response of different segments can be studied in comparison with some available in-situ measurements.

It is finally noteworthy that in spite of the fact that the above objectives addressed in this thesis basically originate in the framework of the industrial interest in long-term management of deep disposal of the nuclear waste, they could still provide a useful insight on a wider range of geomechanical and geotechnical problems. For instance, tunneling in its broad sense, the fracturing and localization of deformation in foundation design and in many applications of rock engineering, and equally the failure mechanism in geomaterials which is frequently preceded by the localization of strains in narrow so-called shear bands; in addition to their resulting volumetric behavior.

## 1.2 Layout of the thesis

The layout of this thesis is given as follows:

**Chapter 2** provides a state of knowledge on Boom Clay characteristics, and its role in the framework of high-level radioactive waste disposal, based on a literature analysis. An overview on different types of the nuclear waste, the concept of deep disposal and potentiality of Boom Clay as a natural barrier for this purpose is given. Subsequently, the mineral composition and some microstructures observation of the material deformation mechanism are represented following by a bibliographical collection of its main hydraulical and mechanical properties.

**Chapter 3** introduces firstly the basic numerical framework applied in this work. The coupled equilibrium conditions and the general resolution algorithm in the finite element code LAGAMINE (used in this study) are described. After a brief overview on the general concept of elasto-plasticity, the frictional elasto-plastic constitutive laws are summarized, consisting in a description on our reference Drucker-Prager yield criterion. Secondly, the introduced theoretical formulation is applied for numerical modeling of some drained and undrained triaxial compression tests, performed in the past on natural Boom Clay. After an analysis of each of those experiments, the relative numerical simulation is presented. This part of the Chapter is principally aimed at validation of one set of the material's main parameters which could represent as realistic as possible its hydro-mechanical response based on the reference experiments. This set of parameters will be then mainly referred in the rest of thesis. In addition, this study highlights the need to focus more particularly on the dilatancy angle parameter, which will be then the objective of the next Chapter.

**Chapter 4** proposes a new formula for considering the variable dilatancy angle in rock, which has been implemented in the LAGAMINE code. This parameter and basically the variable volumetric behavior of the soils and rocks has been poorly treated in most of the former numerical studies, an overview of the literature declares. Therefore, this Chapter is devoted to more particularly address this aspect to fulfill the existing numerical gap affecting our analysis. The capability of our model of variable dilatancy angle, and its preference to considering a constant parameter value, is illustrated through some numerical modelings of the described triaxial tests in Chapter 3.

**Chapter 5** is devoted to numerical analysis of strain localization. The general concept of shear banding, localization phenomenon and its corresponding conditions are firstly described. An overview on the laboratory and in-situ observations of strain localization is given. The classical

numerical framework, presented in Chapter 3, is then developed based on application of the coupled second gradient method, for a proper simulation of localization phenomenon and post-peak behavior of the material. Subsequently, the numerical analysis of strain localization and the relative essential features are better illustrated through the simulation of a drained biaxial compression test. Afterwards, a large-scale numerical modeling of a gallery excavation is addressed through which a parametric study is performed with regard to the influential parameters in terms of numerical analysis of strain localization. Lastly, the model proposed in Chapter 4 is applied to this large-scale tunneling and the influence of using the variable dilatancy angle is discussed in contrast with a constant value.

**Chapter 6** presents an analysis of the coupled hydro-mechanical phenomena that take place in the Boom Clay formation during the excavation of Connecting gallery and afterwards. The numerical modeling of strain localization and EDZ extension within the rock in the gallery's proximity is presented, in comparison with the in-situ observations. This Chapter thence equally aimed at coupled analysis of an invaluable data library provided during and after the gallery's construction. Subsequently, this in-situ data are compared to the obtained numerical results while the latter could help the field data to fulfill our hydro-mechanical perception of the whole processes. Additionally, the limitation of the current model for truly reproducing the gallery's lining behavior is discussed, which will be then addressed in the next Chapter.

**Chapter 7** focuses on analysis of the interfaces behavior integrated in our hydro-mechanical modeling. It consists in the interface of the clay with the gallery's lining, and the interfaces between the lining's segments. The general concept of the contact mechanism and the governing equations of the interface problem are therefore firstly described. We propose the application of the coupled interface finite element to address the aforesaid interfaces behavior, which is thence described. Highlighting the role of the concrete lining of the gallery, its contact mechanism with the rock in the course of excavation phase and afterwards, simultaneously with the development of localized shear bands in the gallery's proximity, is then presented. Subsequently, the numerical model is developed to take into consideration of the discontinuous lining with the jointed segments and definition of the interface elements between them. Consequently, the contact phenomenon between the segments during the time could be presented. In addition, the numerical response of the segments is analyzed in comparison with some corresponding available measurements, described in Chapter 6.

**Chapter 8** contains a synthesis and the main conclusions of the present work, and it proposes some perspectives for the further researches in the field.



# Chapter 2

## Boom Clay characteristics: a potential geomaterial for radioactive waste disposal

### Contents

---

<b>2.1</b>	<b>Introduction</b>	<b>8</b>
<b>2.2</b>	<b>Boom Clay in the framework of nuclear waste disposal</b>	<b>10</b>
2.2.1	Concept of deep disposal of radioactive waste	10
2.2.2	Potentiality of clay materials	10
2.2.3	Boom Clay as the reference host formation in Belgium	11
<b>2.3</b>	<b>Hydro-mechanical properties of Boom Clay</b>	<b>13</b>
2.3.1	Boom Clay formation at depth	13
2.3.2	Mineralogy and Microstructures	16
2.3.3	On the coupled hydro-mechanical analysis	20
2.3.4	Basic geotechnical features	23
2.3.5	Extended geomechanical properties for numerical simulations	25
<b>2.4</b>	<b>Intermediate conclusions</b>	<b>25</b>

---

*Although Nature needs thousands or millions of years to create a new species, man needs only a few dozen years to destroy one.*

Victor Scheffer

## 2.1 Introduction

Boom Clay as a deep tertiary formation located beneath the Mol-Dessel nuclear zone (north-east of Belgium) is of particular interest since mid-1970s when it has been considered for studying the feasibility of deep disposal of high-level nuclear waste in Belgium. This importance has been highlighted since Boom Clay was selected as a reference host formation in Belgium [ON-DRAF/NIRAS, 2001]. The latter is supposed to play the most essential role as a natural barrier in protecting the biosphere by retardation of the radionuclides's migration towards it. Hence, studying the behavior and characteristics of this host formation is significant to better understand its response in the framework of a natural barrier.

The general scope of this Chapter is to provide a basic preview of some of the most important behavior features and properties of Boom Clay as an introduction to the *geotechnical/geomechanical* modelings and analyses addressed in the framework of the present thesis on this material. Before going through the properties and structure of Boom Clay, it is primitive that one comes to realize the definition of the high-level radioactive waste, the concept of their deep storage and the role of Boom Clay with regard to this task. In this way, an introduction to the definition of these wastes and their source is given in the following.

Nuclear energy is strategically and quantitatively an important contributor to diversified fields like the world global electricity generation. Nuclear power plants provides over 12 percent of the world's electricity production today. Figure 2.1 shows the nuclear share in electricity production for different countries in 2014 and 2013. As it is observed, nuclear power is an essential source of the electricity generation in Belgium. Consequently, as an inevitable outcome of this energy, it has been producing some amount of potentially highly hazardous radioactive wastes which have to be carefully managed.

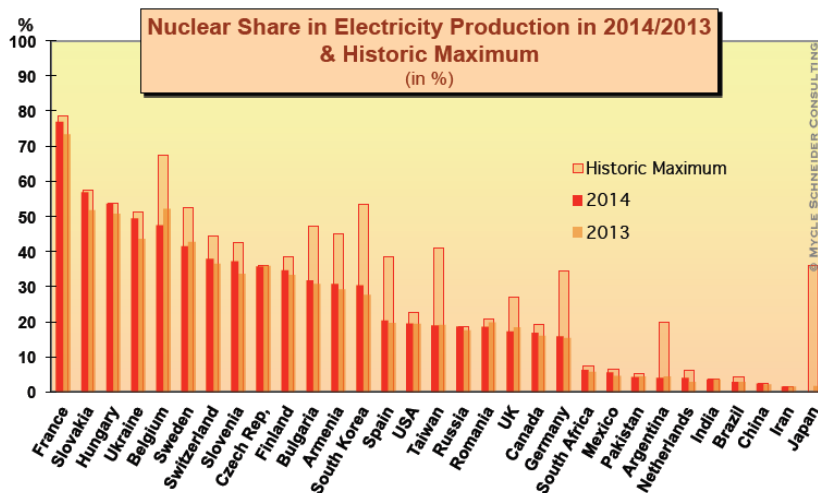


Figure 2.1: Nuclear share in electricity production in different countries [IAEA, 2015].

Generally, radioactive waste is the waste containing any material with a concentration of the radionuclides greater than those deemed safe by national authorities and for which no use is foreseen. This radioactive waste comes from various origins : the nuclear power generation activities in the framework of the power plant operation, reprocessing of the spent fuel, uranium and MOX fuel fabrication, and decommissioning (about 70% in Belgium); as well as nuclear research, production of radioisotopes and their usage in medicine and private laboratories, and food sterilization (about 30% in Belgium) [Belgium Profile, 2013]. More particularly, with regard

to the high application of nuclear power to the electricity generation in some countries including Belgium, and since High-Level Waste (HLW) accounts for over 95 percent of the total radioactivity produced in the process of nuclear electricity generation, this is an important task to ensure the long-term management of these HLW. The reason is associated to their level of the activities and half-life. Radioactive waste are classified in three categories based on Belgium Profile [2013]:

- **Category A: Low- and medium-level short-lived waste** The category A waste contains small amounts of mainly beta and gamma emitters with half-lives shorter than 30 years and traces of longer-lived emitters. This waste has sort of radionuclides with such a low enough and half-lived short enough activities which permit their surface disposal. It is mostly derived from the nuclear power plants operation, reprocessing, nuclear research, production of radioisotopes and their usage in nuclear medicine and industry. The total volume of 74% of the category A waste is estimated to be produced by the decommissioning of nuclear facilities. The approximate total volume of the conditioned waste in this category is  $69900 \text{ m}^3$ .
- **Category B: Low- and medium-level long-lived waste** The category B waste contains predominantly alpha emitters with half-lives exceeding 30 years and in some cases, together with intermediate amounts of beta and gamma emitters. This waste does not meet the criterion to be classified neither as the category A nor the category C waste. It is mostly derived from the fabrication of nuclear fuels, nuclear research and the reprocessing of spent nuclear fuel. The approximate total volume of the conditioned waste in this category is  $10430 \text{ m}^3$  in the non-reprocessing scenario and  $11100 \text{ m}^3$  in the full reprocessing scenario.
- **Category C: Long-lived high-level waste** The category C waste contains important amounts of beta and gamma emitters with short and medium half-lives, together with longer-lived alpha emitters. This waste has a high level of heat generation (over  $20 \text{ W.m}^{-3}$ ) which makes it to be distinguished from the category B waste. It is mostly derived from the reprocessing of spent nuclear fuel, and nuclear research. The total volume of the conditioned waste in this category is estimated to be  $4500 \text{ m}^3$  in the non-reprocessing scenario and  $600 \text{ m}^3$  in the full processing scenario.

With reference to ONDRAF/NIRAS (Organisme National des Déchets RAdioactifs et des matières Fissiles enrichies), the above estimation of the total volume of waste in each category is based on the continuous operation of nuclear power plants (shut down after 40 years of operation), reprocessing of all spent fuel, and nuclear facility decommissioning by 2050.

The radioactivity of nuclear wastes naturally decays in time. However, these wastes should be carefully managed while their level of radioactivity could still be harmful for man and the environment. That is to say, to confine the radioanuclides and keep eventual releases from a repository at a low enough level so that its consequences remain acceptable in terms of the protection of man and environment. In this framework, near-surface disposal (at the ground level; or in caverns below ground level, at depths of tens of meters) is considered principally for the short-lived waste (category A waste). In addition, the concept of deep geological disposal of nuclear waste (at depths of several hundred meters) is considered internationally a possible solution which is being studied in many countries for the categories B and C wastes.

In this way, this Chapter is firstly focused more on the concept of the deep geological disposal of nuclear waste. Following the importance of deep disposal of radioactive waste in the geological stable formations as a promising option in the framework of long-term management of high-level radioactive waste, studying the potentially suitable host rocks is significant. With this objective, Boom Clay characteristics as one of these potential geological formations is presented

in this Chapter. That is to say, it is considered to be a natural barrier which has the favorable properties for deep disposal of the categories B and C wastes. Hence, the formation of Boom Clay in Belgium, its mineralogy, some geological aspects and microstructures are briefly presented. Moreover, a bibliographical review is given on the main geotechnical properties of Boom Clay, followed by an introduction to some extended geomechanical parameters for the subsequent modelings.

## 2.2 Boom Clay in the framework of nuclear waste disposal

### 2.2.1 Concept of deep disposal of radioactive waste

Considering the long timescales over which the categories B and C wastes remain radioactive led to the idea of underground deep disposal in stable geological formations with the large retention (sorption) capacities for the radionuclides. This has to guarantee the confinement of the wastes so that it retards the migration of the radionuclides towards the biosphere during the timescale which is necessary for enough decay of their radioactivity. The waste isolation is provided by a combination of engineered and natural barriers (rock, salt, clay); it is often termed a multi-barrier concept. This contains the waste packaging, the engineered repository, and the natural geological barrier. Hence, a repository is comprised of the underground galleries where the packaged waste are placed. In a superior level, the waste container is then surrounded by a material such as bentonite which provides another barrier namely buffer and/or backfill. In the last level, there is the natural geological barrier. Figure 2.2 shows schematically a multi-barrier system.

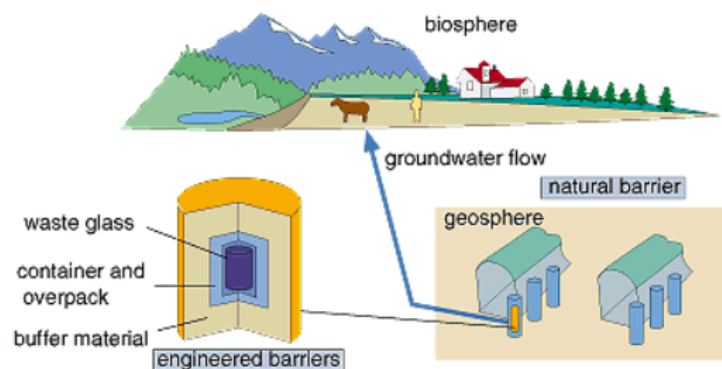


Figure 2.2: Multi-barrier system for geological disposal of radioactive waste [JAEA, 1995].

### 2.2.2 Potentiality of clay materials

The role of the geological barrier concerns limitation and retardation of the radionuclides' migration towards the biosphere in the event that a loss of containment due to the degradation of the engineered barrier occurs. Since the underground water flow is an essential likely factor which questions the transfer of the released radionuclides, the first and important criterion that defines a potential formation is its low permeability. Besides, these formations should be geologically and tectonically stable, and they have to be initially in a good quality to host the radioactive waste. Several geological materials which are considered to meet these requirements include [WNA, 2013]: Clays (Belgium, Switzerland, France), Volcanic tuff rock (USA), Salt bed (New Mexico), Salt dome (Germany), and Crystalline rocks, granite (Sweden, Finland).

Clay formations in their natural state have favorable properties for the disposal of radioactive waste among which there is a very low hydraulic conductivity. Moreover, they exhibit good retention (sorption) capacity for retardation of the radionuclides' migration. Additionally, based on their degree of plasticity, they present the (self-)sealing capacities (sealing is defined [Bernier et al., 2007a] as the reduction of fracture permeability by any of hydro-mechanical, hydro-chemical or hydro-biochemical process). Therefore, they are considered to be potentially suitable to host the radioactive waste repositories in a number of European countries.

The behavior of the clay formations in this framework is being investigated in France, Switzerland, and Belgium thanks to some Underground Research Laboratories (URLs). In France, the Callovo-Oxfordian argillite and Toarian argillite are studied in the URLs of Bure and Tournemire, respectively. In Switzerland, the Opalinus clay is studied in the Mont Terri URL. In Belgium, the plastic Boom Clay (beneath the nuclear zone of Mol-Dessel) is studied in the HADES (High Activity Disposal Experimental Site) URL as the reference host formation. As an alternative host formation, the Ypresian clay (beneath the nuclear zone of Doel) is also under research.

### 2.2.3 Boom Clay as the reference host formation in Belgium

Belgian Nuclear Research Center, SCK-CEN, launched the study of the categories B and C wastes' deep disposal in the mid-1970s. Boom Clay formation beneath the Mol-Dessel nuclear zone (north-east of Belgium) has been considered so far for this purpose although there were not enough knowledge of its properties at depth at the time. The interesting preliminary results of its lithology and containment capacity encouraged SCK-CEN, and ONDRAF to research more accentuated into this formation. In 1990, SAFIR (Safety Assessment and Feasibility Interim Report) Evaluation Commission justified this decision [ONDRAF/NIRAS, 2001].

Following the safety criterion in the concept of deep disposal of radioactive waste, the initial qualities of the host rock should not be degraded by the storage and during the time. Thus, the fact that the rock is able to regain its favorable properties, and the self-sealing capacities could be interesting. Therefore, the plastic rock formations are so privileged; this is one of the main and essential characteristics of Boom Clay. Moreover, Boom Clay has very low hydraulic permeability, and large retention capacity of the radionuclides. These important features in the framework of safe long-term disposal of the high-level nuclear waste as well as the geochemical and geological stability make Boom Clay to be the reference host formation considered for examining the solution of the deep disposal of categories B and C wastes in Belgium. This formation is present in a region with no volcanic activity and only low seismic activity in Belgium.

The HADES (High-Activity Disposal Experimental Site) underground research laboratory was then constructed in 1980, close to the city of Mol, Belgium, to study the feasibility of deep disposal of high-level radioactive waste in Belgium. This URL (Figure 2.3) is located at a depth of 225 meters, in the core of the Boom Clay formation which is present between 190 and 290 meters depth under the terrain of SCK-CEN.

The ONDRAF developed the supercontainer concept for the deep disposal of the vitrified HLW canisters or the spent fuel assemblies. In this framework, they are enclosed by some various envelopes at different levels in order to be protected in the maximum possible degree. Figure 2.4 shows the supercontainer system at the depth of repository in Boom Clay. Firstly, a 30 mm of the carbon-steel overpack wraps the waste canister. It is aimed to prevent the contact of the waste with the water coming from the host formation at least during the thermal phase (hundreds of years for vitrified waste and thousands of years for the spent fuel). Next, this overpack is covered

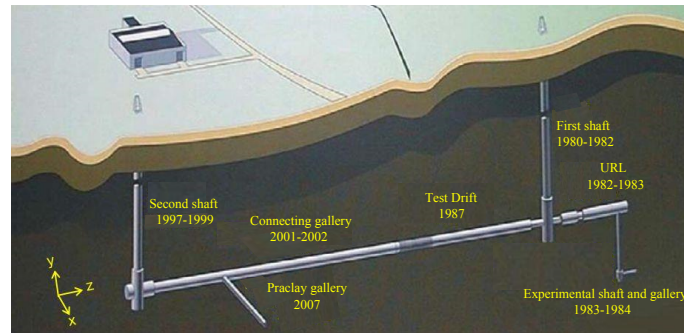


Figure 2.3: Sketch of different galleries in HADES URL and their construction history; after [Bastiaens et al., 2003].

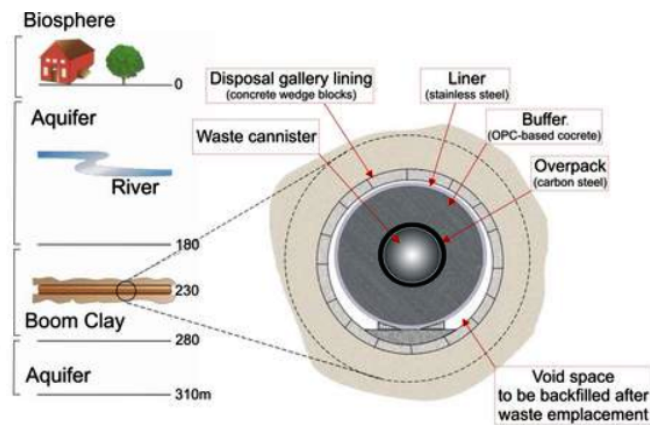


Figure 2.4: Schematic representation of the supercontainer system at depth with an illustration of its surrounding environment [SCK-CEN, 2009].

by the (high alkaline) concrete buffer which provides kind of radiological protection for the case of transport of the supercontainers as well as ensuring the workers' conditions. It could provide a favorable chemical environment in which overpack corrosion is very slow because of passivation of carbon steel. Then, this buffer may be enfolded by a stainless steel cylindrical envelope (also called liner) [Craeye et al., 2009]. Stainless steel envelope would limit exchanges between buffer and host formation, to slow physico-chemical degradation of the buffer.

The supercontainer with the described different envelopes is then emplaced in a disposal gallery. The remaining space between the gallery's lining and the supercontainer is finally back-filled by grouting. The backfill should be able to highly fill the remaining space so that it prevents the creep of the clay to the void spaces if ever the gallery wall loses its coherence and thus, to protect the supercontainer. Figure 2.5 shows a supercontainer emplaced in a disposal gallery in Boom Clay.

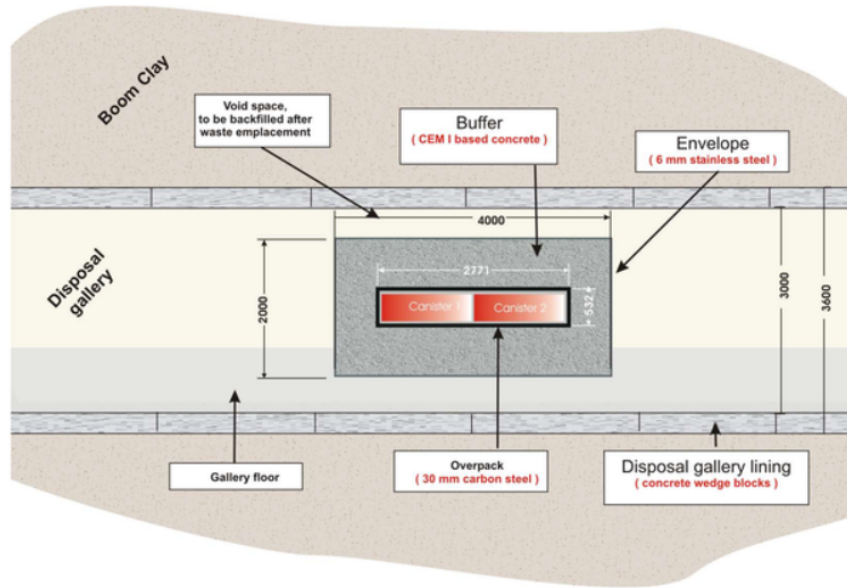


Figure 2.5: Schematic representation of a longitudinal section through a disposal gallery containing a supercontainer with vitrified HLW [SCK-CEN, 2014].

## 2.3 Hydro-mechanical properties of Boom Clay

### 2.3.1 Boom Clay formation at depth

Boom Clay is present mainly in the north-east of Belgium, Campine region. This formation belongs to the Rupelian, the geological part of the Tertiary Period which lasted from 36 to 30 million years ago, according to ONDRAF/NIRAS [2001]. Boom Clay forms a belt of 5 to 15 *km* wide. The eastern outcrop is situated in the north of the Leuven-Tongeren line, and it is extended to the Waasland region (to the north of the Durme, the Rupel, and the Dyle rivers) as it is observed in Figure 2.6. However, the top layers of this outcrop were eroded during the continental episode (i.e. an interruption of sedimentation) lasting some 9 million years after their deposition. The detailed information on the geological history can be found in the report of ONDRAF/NIRAS [2001] upon interest.

As it is observed in Figure 2.6, the thickness of Boom Clay is about 100 *m* in the Mol area where the HADES URL is located. In fact, the Boom formation exhibits a slight dipping of 1 to 2% towards the north - north-east direction along which it is thickened. Boom Clay at the HADES site, is at a depth of about 190 *m* at its top layer with reference to which it has a thickness of about 100 *m*. In addition, this formation overlies two aquifers of Lower Rupelian and Lede-Brussel, and it is protected by the sandy layers of the Neogene aquifer at its top (Figure 2.7).

The composition of Boom formation is neither constant with location nor with depth. Boom Clay can be subdivided in its thickness from bottom to top respectively as: Belsele-Waas member, Terhagen member, Putte member, and Transition zone [ONDRAF/NIRAS, 2001; Wemaere et al., 2008]. The first member at the lowest level, Belsele-Waas, contains lower contents of fine particles and higher contents of coarser particles; it is considered as the siltiest part of Boom Clay. The Putte and Terhagen members have quite similar characteristics, and they are presented as the least pervious unit of Boom Clay consisting of the lowest proportion of coarsest particles (silt or sand). However, Terhagen member appears to contain a bit less sand particles than the

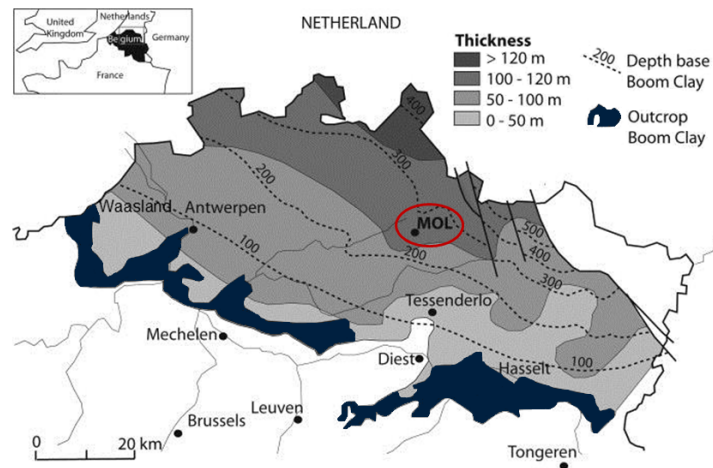


Figure 2.6: The extension of Boom Clay, and the formation's depth by location; after [ONDRAF/NIRAS, 2001].

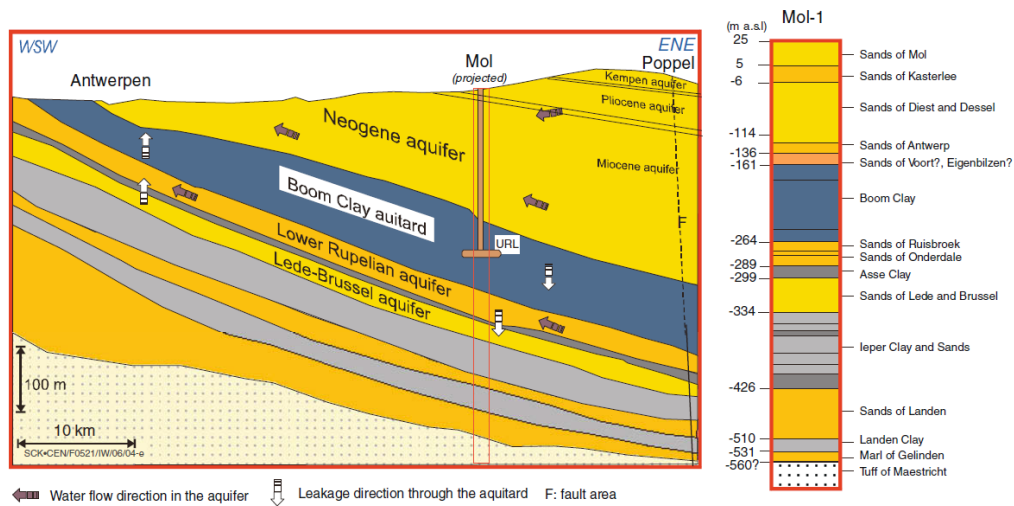


Figure 2.7: Hydro-geological cross-section intersected in Mol-1<sup>1</sup> borehole (a.s.l.: above sea level) [SCK-CEN, 1997].

<sup>1</sup>The borehole Mol-1 was drilled in 1996 by ONDRAF to provide samples of the Boom formation.

Putte member. The Putte unit is also characterized as a rich member in the organic matter. The transition zone at the top of Putte unit is represented as a granulometric transition zone between the Belsele-Waas member, and the Terhagen and Putte units (Figure 2.8).

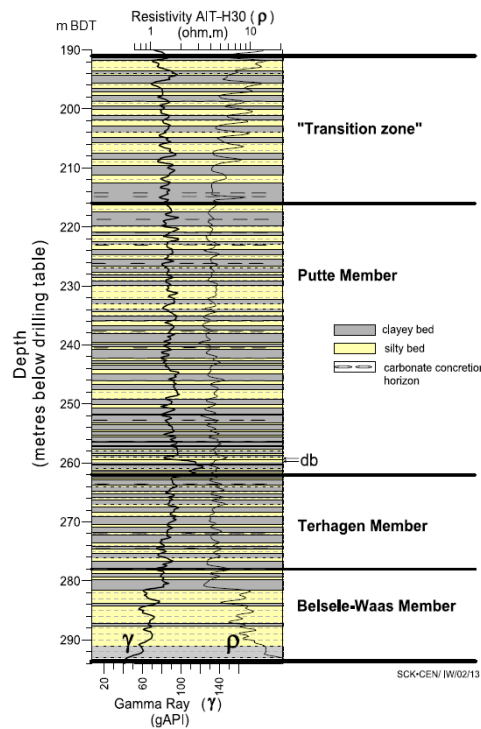


Figure 2.8: Lithostratigraphic profile of Boom Clay in Mol-1 borehole<sup>2</sup>(BDT: below drilling table) [Aertsens et al., 2004].

Boom Clay at a depth of more than 200 m has been fundamentally the subject of numerous experimental studies since more than 30 years, such as [Horseman et al., 1987; Baldi et al., 1991; Bernier et al., 1997; Sultan, 1997; Coll, 2005]. They were mainly aimed to characterize the geological, and geotechnical properties of Boom Clay, and to better understand its thermo-hydro-mechanical behavior. One essential objective of many of this sort of studies was defined in the framework of the significant importance of this formation for the deep disposal of high-level radioactive waste in Belgium. Based on the rich data and results obtained by those studies in the last decades, Boom Clay is considered as a plastic clay, moderately over-consolidated ( $OCR=2.17-2.4$  with regard to Coll [2005]-Horseman et al. [1987]), and with very low hydraulic permeability and limited swelling potential. Moreover, the Boom Clay formation at the URL depth is characterized by a vertical total stress component of 4.5 MPa, and an earth pressure's coefficient at rest of 0.83-0.88 (with reference to total stress) based on the in-situ stress measurements performed at the HADES URL [Cornet, 2009; Li et al., 2010].

<sup>2</sup>Lithostratigraphic log of the Mol-1 borehole, based on the macroscopic description of cores and FMI log of Schlumberger (Fullbore Formation MicroImager, a multiple micro-resistivity measurement) interpreted by [Mertens, 2002] and shifted by 0.5 m to correspond to the cores (db: "double band"), according to [Aertsens et al., 2004].

## 2.3.2 Mineralogy and Microstructures

### 2.3.2.1 Mineral composition

The mineral composition of Boom Clay differs considerably from one study to another. Table 2.1 summarizes a literature review of the proportions of different mineral fractions present in this argillaceous formation. These studies show an important variability regarding the clay minerals. These variations appear to result from the lithological and stratigraphic differences of the various geotechnical units identified for the Boom Clay formation [Romero Morales, 1999]. The study of Horseman et al. [1987] has highlighted this clay spatial variability, where the clay mineralogy of a sample from a depth of 247 *m* was analyzed compared to data that had been reported for another depth in the same site. It can be stated that the proportions of the various minerals vary from one unit to another, as these are related to the grain-size variations: clay-rich members comprise relatively more clay-minerals whereas silt-rich layers comprise relatively more non-clay minerals [Yu et al., 2013]. Furthermore, as it is observed in Table 2.1, the Illite and Smectite have a total important proportion in clay minerals, which can promote the swelling potentiality of the clay upon the presence of water [Coll, 2005].

Table 2.1: Literature review of Boom Clay mineralogy

Composition*	Decler et al. [1983]	Horseman et al. [1987]	OECD/NEA [1996]	Laenen [1998]	ONDRAF/NIRAS [2001]
Clay minerals	37 – 71	≈ 70	60	≈ 76	30 – 70 (averagely 55)
<i>Illite</i>	3 – 23	19	20 – 30	21.5	50
<i>Smectite</i>	19 – 42	22	10 – 20	29.3	30
<i>Kaolinite</i>	1 – 9	29	20 – 30	22	10
<i>Chlorite</i>			5 – 20	3.22	≈ 5
<i>Glauconite</i>					≈ 3
Quartz	23.8 – 58.3	30	20		20
Feldspars			5 – 10		1 – 5
<i>Microcline</i>	6.5 – 11.3				
<i>Plagioclase</i>	3.2 – 6.2				
Pyrite	0.7 – 2.5		1 – 5		1 – 5
Carbonates	0 – 4.3		1 – 5		1 – 5
Organic matter			1 – 5		1 – 3

\* All values are in % weight of the total solids.

The porosity of Boom Clay is generally of the order of 30 to 40% by volume [ONDRAF/NIRAS, 2001], however, connected porosity of Boom Clay has been reported as 28% by Dehandschutter et al. [2004], and 33.5% by Coll [2005] using the mercury porosimetry. The latter is lower than the total porosity of Boom Clay (can be considered around 39% based on Bernier et al. [2007c]). This can result from the existence of some small and isolated pores which might not be accessible by the inserted mercury. Concerning the water content in this formation, free water is only present in the Belsele-Waas member, and in the upper part of transition zone [ONDRAF/NIRAS, 2001]. In fact, most of the water in the argillaceous units are not free, and they are bounded by the clay minerals. Hence, there is an increase in the water content where the formation has more clay minerals.

### 2.3.2.2 Orientations of clay minerals

The microstructure of Boom Clay has been studied by Dehandschutter et al. [2004] sampling the material during the construction of Connecting gallery (83 *m* long N-S oriented gallery, Figure 2.3). The sampling was performed both from the gallery's sidewalls and from the collapsed blocks

at the open gallery front.

The preferred alignment of the clay minerals of these samples was analyzed using the SEM (Scanning Electron Microscope) imaging of the samples. This study has shown an open-structure of the clay with a high porosity nature, and a well-rounded preferred orientation of the particles parallel to the bedding plane (Figure 2.9). With regard to the moderately over-consolidated nature of Boom Clay, the compaction could be captured by imaging the tendency of the clay particles to be wrapped around the silt grains (Figure 2.9c). In addition, the same study demonstrated that this material is naturally fine-grained and uncemented. The latter has been already illustrated in Table 2.1 where the carbonate proportion is indicated to be less than 5%. Therefore, the structure of Boom Clay is not homogeneous so that it is strictly induced by the material's stratification, and not by the cementation [Coop et al., 1995]. With respect to the uncemented fine-grained structure of Boom Clay, the contact particles will dislocate under water and external force action and easy to break, and the material will likely tend to swell and soften in macro, according to Yu et al. [2012].

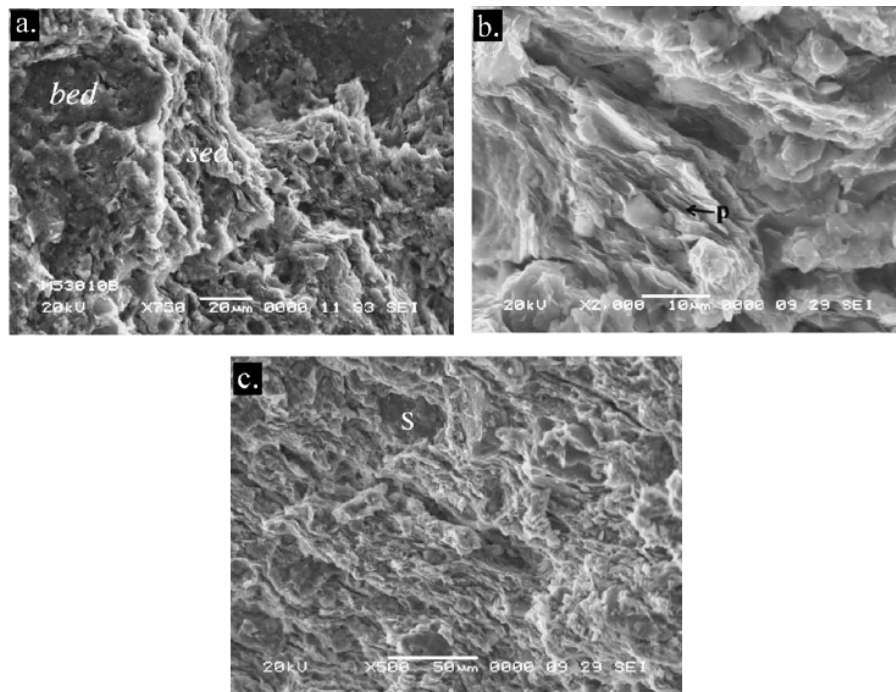


Figure 2.9: SEM imaging of the Boom Clay microstructure with a view on: (a) Bedding plane (bed) and a perpendicular section (sec). (b) Perpendicular section to the bedding. (c) Perpendicular section to the bedding showing clay particles which are wrapped around the silt grain [Dehandschutter et al., 2004].

### 2.3.2.3 Microstructures observations of the deformation mechanism

Microstructure analysis supplies a better understanding of the clay behavior and the fracturing mechanism, which is primitive in the analysis of the formation's response, as well as the influence of fracturing on the origin favorable properties of the clay (i.e. hydraulic conductivity) in the framework of long-term management of high-level radioactive waste. Therefore, this issue is briefly focused in this Section with respect to the literature, mostly in the geological point of view.

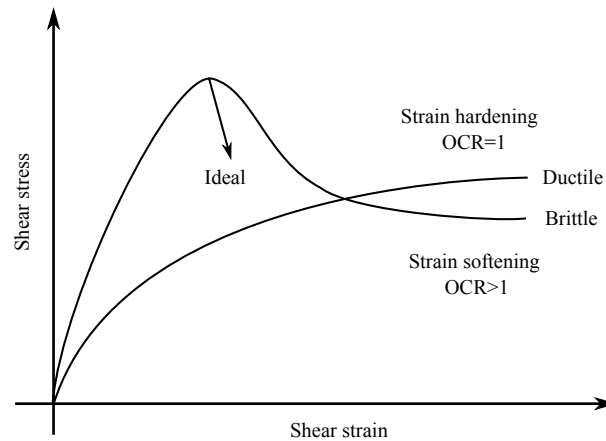


Figure 2.10: Ductile and brittle failure mechanism.

Argillaceous material exhibits mechanically a transitional behavior upon deformation. In general, clay is physically behaving between rock and soil and, it has a transitional behavior that can be important in terms of its geomechanical response during the time, which can affect its resistance. A transitional brittle-ductile response has been illustrated for Boom Clay, following the geological studies of Dehandschutter et al. [2004, 2005].

Ductile behavior is identified by a weak elasticity state (low Young modulus), and a large inelastic deformation by plastic hardening (i.e. increase of shear resistance with increasing deformation), where the peak strength is quite undefined. Brittle behavior is established by a basically elastic material at a distinguishable peak strength followed by strong softening (i.e. decrease of shear resistance with increasing deformation) and loss of cohesion (failure) (Figure 2.10). Ductile plastic deformation occurs normally with a relatively low strain (such micrometric displacements) that in this case, there is a particle reorientation, and the pore space is decreased within the sheared zone. In fact, shearing at a high confining pressure induces a ductile behavior. On the other hand, the same material tends to show a brittle pattern of deformation at a relatively low confining pressure; likely with higher concentrated strain. This may be possibly induced by larger strain rates, which result in a brittle, dilatant response. With a focus on the deformation prior to the failure in brittle or ductile mode, Paterson and Wong [2005] distinguishes these two types by definition of brittle mode as a discrete failure without significant preceding deformation and without warning, and ductile mode as a rupture with a previous large plastic deformation. Moreover, an over-consolidated material ( $\frac{p^I_{max}}{p^I_{actual}} > 1$ ) has generally a brittle deformation, whereas a normally consolidated material deforms in a compacted ductile manner. Furthermore, the water content also influences the dominant behavior so that the material exhibits more ductility by increasing the water content [Dehandschutter et al., 2004].

Figure 2.11 shows an example of two types of deformation observed in Boom Clay. There were a few zones at the HADES URL where the clay particles were reoriented to reduce their porosity, evidencing the ductile deformation (micrometer scale) as it is observed in Figure 2.11a. Figure 2.11b presents a type of brittle dilatant deformation where fracture porosity (centimeters scale) is created by activation and dilatancy of the bedding plane oblique to the fault plane. This has been identified in several fault blocks coming from the gallery excavation front at different levels. In that case, there could be a secondary type of shear bands (micrometer scale) connecting the main fault plane to those fractures [Dehandschutter et al., 2004]. Another example of the brittle tendency in deformation can be observed is Figure 2.12b which shows the microstructure of a Boom Clay sample after an undrained triaxial shearing under the in-situ confining pressure; the clay specimen was extracted from a gallery's sidewalls (at tens of meters deep) at the HADES

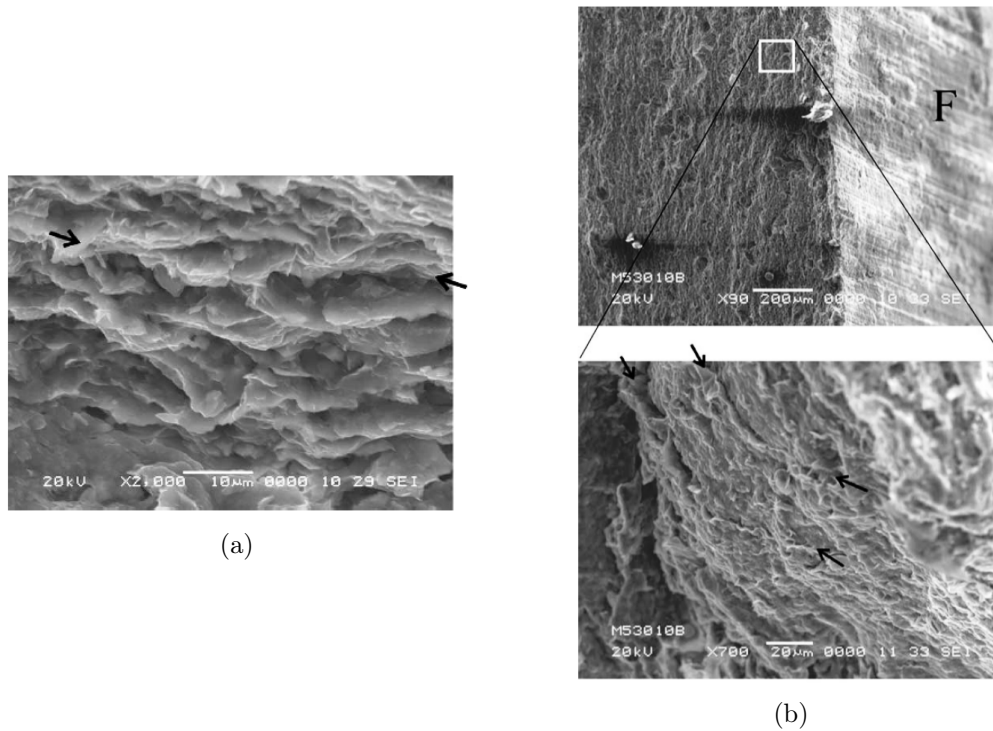


Figure 2.11: SEM images of the Boom Clay samples. Example of the shear bands in Boom Clay. (a) Ductile manner. (b) Brittle manner [Dehandschutter et al., 2004].

URL [Yu et al., 2012]. From these images, an (undisturbed) open-structure of the clay with big pores and edge-to-face or face-to-face particles' contact can be concluded before the test (see Figure 2.12a). After the shearing test, the particles seem to be oriented parallel to the direction of shearing while they made a flaky structure (see Figure 2.12b). A similar reorientation of the clay particles, under a relatively low/intermediate confining pressure, parallel to the shearing direction with increasing strain was also reported by Bishop et al. [1965] who did the triaxial tests on natural stiff London clay.

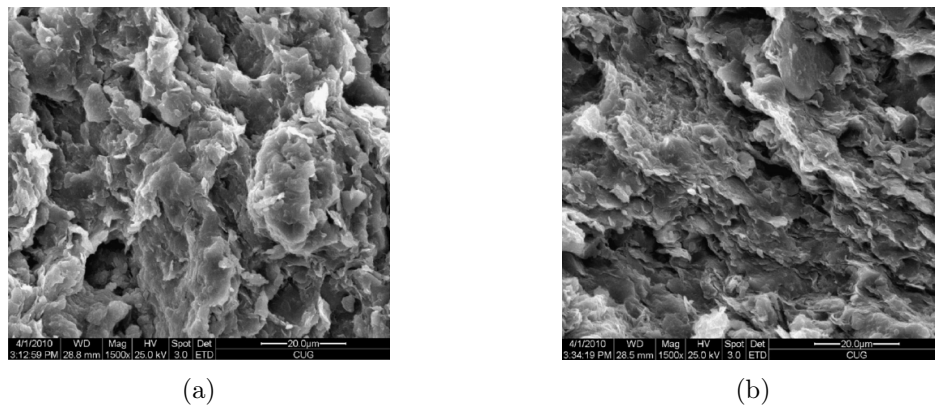


Figure 2.12: SEM images of the microstructure of Boom Clay sample. (a) Before an undrained triaxial test. (b) After the test. [Yu et al., 2012].

In fact, the ductile (non-dilatant) type of deformation which appears in a diffused/distributed [Dehandschutter et al., 2005] pattern in material was rarely observed in the URL's level, according to the geological study of Dehandschutter et al. [2004]. The brittle (dilatant) shear induced discontinuities were mostly identified which could establish a localized type of deformation. How-

ever, some experimental results of the triaxial compression tests performed on the Boom Clay samples extracted from Mol site showed a quite ductile type of response [TIMODAZ, 2010b]. In fact, in a geomechanical point of view, as stated by Desrues [1998], rocks cannot be generally said "brittle" or "ductile" whatever the circumstances are: pressure, OCR, temperature and strain rate. That is to say that the failure mode may vary upon conditions.

Dehandschutter et al. [2004] also indicates that there is not such an evidence that the natural through-going fractures has been existed at the level of URL in Boom Clay, which could provide the potential fluid pathways. Indeed, most of the fractures faced during the excavation resulted from the excavation process. That has been confirmed by their symmetric geometry around the gallery axis, and stress concentration (i.e. local stress state) caused by removal of the clay during the tunneling, which could provoke the fracturing [Dehandschutter et al., 2002]. Nevertheless, Mertens et al. [2003] indicated the existence of a system of natural, vertical fractures: tensional jointing system, within the outcropping clay-pit faces. These joints has been shown to be independent from the excavation process, and they are rather of regional importance. However, this study declared that these tensional joints cannot occur below a maximal depth (for instance, around 40-50 *m* for Boom Clay in Antwerp area) because of a relative high cohesion, and the fact of having a certain level of vertical stress above which tensional failure would be impossible (i.e. lack of negative horizontal stress<sup>3</sup>: tensional forces), and shear failure will occur. Therefore, there is generally no evidence of these natural fractures at depth, and they are almost limited to near surface. These fractures, which are considered as the most apparent natural discontinuity observed in Boom Clay formation, have not been then observed during the tunnel excavation at the HADES URL in Mol; only in the first few meters within the clay in Mol area, such as these joints could be developed based on the geological history of the region. This absence of the natural discontinuities at depth has been also confirmed by the observation made thanks to the cored boreholes drilled during the auscultation program in the HADES URL [Bastiaens et al., 2003]<sup>4</sup>.

The artificial origin of the fractures encountered during the gallery excavation has been briefly described to give an introduction for the coming numerical simulations and analysis of the localized shear bands resulted from the gallery excavation in HADES URL (will be discussed more particularly in Chapters 5 and 6). In fact, dilatancy of the clay held by the shear strains is considered to be responsible for the fracture porosity. This response is launched during the excavation and the resulting stress redistribution, under sufficient differential stress and at a certain strain level. It is then possibly linked to the large macroscopic dilatant shear fractures (faults), the micro-cracking prior to the macroscopic failure (brittle dilatant deformation) (Figure 2.11b) [Dehandschutter et al., 2004].

### 2.3.3 On the coupled hydro-mechanical analysis

Boom Clay formation beneath the Mol nuclear zone is a saturated porous medium: solid phase (i.e. argillaceous skeleton) and fluid phase (i.e. water) [ONDRAF/NIRAS, 2001]. Therefore, the coupled hydro-mechanical mechanics can be applied to analyze its behavior. That is to say, the coupled effects between the phases as well as the mechanics of each of those phases. However, from a more general point of view, the behavior of argillaceous formations may be expressed in the framework of coupling thermo-hydro-chemo-mechanical phenomena, which signifies the multi-physical nature of these rocks. On the whole, taking into account that the argillaceous formations have generally an intermediate behavior between rocks and soils as it has been already

<sup>3</sup>With regard to the Mohr-Coulomb representation of failure criterion in tensional domain.

<sup>4</sup>See Section 5.2.2 for a more detailed discussion on the fracturing pattern in the URL depth.

mentioned, coupled analysis of their behavior (e.g. Boom Clay) may be quite complicated in the realistic point of view. From now on, the term *coupled behavior* in this thesis links to the *Hydro-Mechanical coupling* with regard to the objectives of the current study. This coupled behavior can be affected by many factors such as: structure, discontinuities, mineralogy, stress history and OCR, porosity (different scales), and water-clay interactions.

Besides microstructure and mineralogy, it has to be considered that stress history is also a significant factor to determine the behavior of the argillaceous formations since the geomaterials generally retain their loading history. Hence, the compressibility as a mechanical property in their behavior is dependent on their loading history as well as their stress state and the level of consolidation, and it is finally expected to be ranged between the rocks' and soils' based on their nature. The influence of this stress history could be evident for Boom Clay with regard to its preconsolidation stress reported in the literature. Horseman et al. [1987] performed some oedometric compression tests on the samples of Boom Clay from the depth of 247 m based on which the most probable value for the (vertical) effective preconsolidation stress has been indicated as 6 MPa, with an OCR of 2.4 taking into account in-situ vertical effective stress of 2.5 MPa. This preconsolidation stress might declare a high degree of compaction for Boom Clay because it states that the rock seems to have experienced a higher value of vertical effective stress in the past even though the vertical effective stress is of the order of 2.25 MPa at the level of URL now (considering vertical stress component of 4.5 MPa, and in-situ water pressure of 2.25 MPa [Bernier et al., 2007c]). However, in a geological point of view, the over-consolidation may not be attributed to the erosion of the strata overlaid on the Boom Clay formation, i.e. the removal of overburden. They could be instead ascribed to a secondary compression and diagenetic process, according to Horseman et al. [1987].

The mineral composition influences the volumetric deformation and compressibility of material as well. The Smectite minerals can affect the fluid concentration and swelling potentiality of the clay [Di Maio, 2004]. Moreover, Coll [2005] performed some isotropic compression tests on Boom Clay, and she showed that the volume of the samples is increased under the low stress ( $= 1 \text{ MPa}^5$ ), and there is a volume reduction afterwards indicating the consolidation process. In addition, the compressibility is illustrated to be increased with the isotropic stress (particularly for stress higher than 8 MPa). The same study demonstrated a preconsolidation stress of about 5 MPa with an OCR of 2.17 for Boom Clay.

The behavior of material is dependent on the OCR value, such as its response under the deviatoric stress. As it has been already described in Section 2.3.2.3, Boom Clay can show a transitional brittle-ductile behavior. The brittle behavior is normally characterized by an OCR higher than 1, which indicates that the clay is overconsolidated. The latter could describe the Boom Clay at the level of HADES URL. This behavior may likely induce a pretty brittle failure which is being accompanied by the shear bands in the localized mode. In the volumetric change's point of view, the clay has firstly a contracting behavior followed by a dilatant brittle behavior. On the contrary, a normally consolidated clay has a continuous contracting behavior. It has basically more resistance than an overconsolidated clay, and it could establish a ductile failure with diffused deformation. Coll [2005] indicates that the stiffness of the argillaceous clays (defined by Young modulus) is generally dependent on their stress level and water content level; the stiffness increases as the stress level does, considering a constant level of water content.

The water-clay interactions is also a significant feature in an hydro-mechanical analysis since it can characterize the free water within the clay, which is related to permeability. In fact, the water mobilized during a permeability test in Boom Clay (as an argillaceous clay) is the free

---

<sup>5</sup>This stresses is about 2.85 MPa based on [Horseman et al., 1987], with a swelling pressure of about 0.8-0.9 MPa; swelling pressure is defined as the consolidation pressure for which the volume change is null.

water [Delage et al., 2000]. This could be of particular importance when one takes into account the role of permeability in definition of a suitable host rock for deep disposal of radioactive waste.

The permeability of an argillaceous clay depends generally on the porosity, the particle size distribution, interconnected pores, the proportions of clay minerals (i.e. mineralogy), and any other parameter which could modify them by a mechanical or physico-chemical process<sup>6</sup>. For instance, the variations of the effective stress can affect the pores' arrangement and thence, permeability [Romero Morales, 1999; Coll, 2005]. The permeability measurements coming from the isotropic compression test in Bésuelle et al. [2014] showed that permeability decreases with increasing effective stress. The mineral composition (the nature and proportion of the clay minerals) is an essential factors in terms of permeability. The swelling tendency of the clay in the presence of water with respect to its mineral composition, can decrease the permeability inside the clay formation.

Generally, the swelling tendency due to the physico-chemical process could reflect as the inter-particle swelling, or intra-particle swelling. The terms inter-particles and intra-particles come from the classification of the pores. In the largest scale, there are the aggregates (grains, the scale of some micrometers), which are constituted from the particles themselves. In the smaller scale, these particles could also have many layers. Hence, the pores can be categorized as: inter-aggregate, intra-aggregate (or, inter-particles), and intra-particles. The latter is the most responsible for the adsorbed water and the swelling capability, while the first (and possibly the second) type of pores have the flow potentiality. In fact, in the inter-particle swelling, the water does not enter within the clay layers and it affects the whole clay particles in a general diffusive manner but by a limited level. However, the intra-particle swelling is concerning the phenomena at the particles level. The water can penetrate within the layers of different clay minerals. This is the case of the smectites which consist of layers among which the basal spacing is highly variable, and this process then results in a notable level of swelling. These minerals have normally large surfaces which adsorb water and then, the amount of free water and permeability become low [Coll, 2005].

Moreover, the permeability is supposed to be affected by the microstructural change due to the development of discontinuities. This may generally induce important modifications of the hydro-mechanical properties of the rock including its resistance, and permeability. The latter becomes dominant when the argillaceous clay gets more compacted since it is reformed to be more brittle, and this promotes the presence of (micro-)fractures which make a suitable bed for the water flow [Coll, 2005]. In this case, the pores dimension become very small and the water tend to be absorbed by the clay particles, and the permeability is quite limited to the fracture induced permeability. Although in the less compacted material, water tend to flow inside the inter-aggregate pores. Boom Clay in its natural state possesses a fairly compacted structure, with a moderate swelling potentiality with respect to its clay minerals (see Section 2.3.2.1), and a low permeability. Compacted Boom Clay was also the subject of some studies [Romero Morales, 1999; Romero et al., 1999], but it is out of scope of this work. Figure 2.13 visualizes an example of the inter-aggregate and intra-aggregate in a compacted Boom Clay sample. The inter-connected porosity is entrapped by the constricted porosity arises from the clayey bridges (resulted from the low distance between the aggregates) and irregularity of the aggregates.

---

<sup>6</sup>This process can be explained in the framework of the diffuse double layer theory which describes the water-clay particle interactions at the vicinity of the particle [Gaombalet, 2004; Coll, 2005; François, 2008], although it is out of scope of the current study

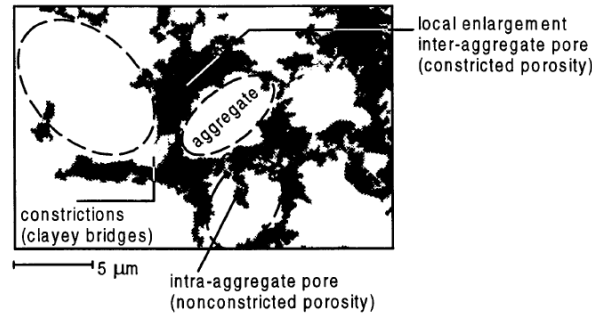


Figure 2.13: Image analysis of SEM photomicrographs for a compacted Boom Clay sample; the pores are in black and the particles are in white [Romero et al., 1999].

### 2.3.4 Basic geotechnical features

Regarding the hydro-mechanical characteristics of Boom Clay, many studies have been done based on various experimental works. These studies are not generally easy to be compared since their conditions are somehow different. That is to include the tests on the samples taken from different sites, intact or reconstituted samples, saturated or partially saturated samples, under triaxial or oedometric test, drained or undrained conditions, etc. Hence, one ought to consider the initial state of each experiment. The results of some important studies on the main geotechnical properties of natural Boom Clay are collected from various sources in Table 2.2.

This argillaceous formation has a fraction of 80% of particles smaller than  $20 \mu m$ , and 54% of particles smaller than  $2 \mu m$  [Schittekat et al., 1983; Mertens et al., 2003]. Apart from this, Bernier et al. [2007c] indicated that laboratory tests have shown an obvious tendency of stiffness variation in Boom Clay by strain level, which declares its non-linear stress-strain behavior response. Moreover, Boom Clay at the Mol site is characterized by a high porosity ( $n \simeq 39\%$ ), and a Biot's coefficient equal to one which could be responsible for a strong hydro-mechanical coupling [Barnichon and Volckaert, 2000].

One of the main properties in the framework of a coupled hydro-mechanical analysis is the hydraulic conductivity of Boom Clay, which is being of particular interest in many studies. Previously, the different units of Boom Clay has been described (Section 2.3.1). The hydraulic conductivity of Boom Clay is varied at the member scale although one can consider it as homogeneous. Through a more detailed study, the Putte (where the HADES URL at the Mol site is located) and Terhagen units are the most homogeneous and least pervious part of Boom Clay [Wemaere et al., 2008]. Although, the permeability in these two units with similar characteristics can be also unified with the transition zone, and upper part of Belsele-Waas member (see Figure 2.8), representing a single value of vertical hydraulic conductivity as  $K_v = 2.3 \times 10^{-12} m/s$  [Aertsens et al., 2004]. The (lower part of) Belsele-Waas unit - as the siltiest part of Boom Clay - has the highest hydraulic conductivity, and higher variations with regard to depth and stratigraphy, with a mean value of  $K_v = 1.6 \times 10^{-11} m/s$  [Wemaere et al., 2008] -  $K_v = 4 \times 10^{-11} m/s$  [Aertsens et al., 2004]. Hence, these variations could be obviously related to the variations of grain size in different layers in Boom Clay formation [Aertsens et al., 2004]. This factor then influences the variation of conduction properties of Boom Clay at different sites (with regard to Figure 2.6). In addition to the grain size, the degree of compaction of the clay, which is related to the actual depth of the sediment and the geological history that the sediment has undergone, is also effective in the observed variations of permeability by location. Boom Clay at the Mol site was shown to be the least pervious one [Wemaere et al., 2008].

Table 2.2: Literature review of the geotechnical properties of Boom Clay

Parameter	Symbol	Unit	Bésuelle et al. [2014]	Bernier et al. [2007c]	Dehandschutter et al. [2005]	Mertens et al. [2004]	Mertens et al. [2003]	ONDRAF/NIRAS	SCK-CEN [1997]	OECD/NEA [1996]	Horseman et al. [1987]	Schittekat et al. [1983]
								[2001] and Bastiaens et al. [1991]				
Bulk density (saturated)	$\rho$	$Kg/m^3$				1900 – 2100	1968		1900 – 2100		2050	1968
Dry density	$\rho_d$	$Kg/m^3$			1900		1519				1660	1498
Solid density	$\rho_s$	$Kg/m^3$					2702					2704
Porosity	$n$	%	36.5	39	35	36 – 40		39	33 – 40	36 – 40	39	
Natural water content	$w$	%	20 – 25		25 – 30	19 – 24	28	30 – 40	22 – 27		23.9	28.89
Natural degree of saturation	$S_r$	%							95 – 100			
Poisson ratio	$\nu$	–		0.125	0.4	0.4	0.4	0.4 – 0.45				0.468
Young's modulus	$E$	$MPa$	500/150	300	150 – 200	200 – 400	300	200 – 400		200 – 400	197	735
Unconfined (uniaxial) compressive strength	$USC$	$MPa$	2.5	2		2.2 – 2.8		2				
Internal friction angle	$\varphi$	$^\circ$	18	18	18	11		4	4 – 8			20.4
Cohesion	$c$	$kPa$	80	300	175 – 300	396		500 – 1000	600 – 1200			40
Dilatancy angle	$\Psi$	$^\circ$	4 – 11	0 – 10								
Liquid limit	$LL$	%	60		70			55 – 80	70 – 83		66	64.7
Plastic limit	$PL$	%	26		25			23 – 29	25 – 28		19	
Plastic index	$PI$	%	33		45		40	32 – 51	42 – 58	32 – 51	47	38.45
Note			<i>At the level of HADES URL; based on drained triaxial compression test</i>	<i>At the level of HADES URL; based on drained triaxial compression test</i>	<i>Undrained properties at the outcropping clay-pit</i>	<i>At the level of HADES URL</i>		<i>Undrained properties at the level of HADES URL</i>	<i>Undrained properties at the level of HADES URL</i>	<i>At the level of HADES URL</i>	<i>At the depth of 247 m; based on undrained triaxial compression test</i>	<i>Geometrical average on the corresponding values of different units at depth of Boom formation in the Antwerp zone; based on undrained triaxial compression test</i>

Table 2.3: Literature review of the parameter of hydraulic conductivity for Boom Clay at around the level of HADES URL

Parameter	Symbol	Unit	Bésuelle et al. [2014]	Wemaere et al. [2008]	Bernier et al. [2007c]	Aertsens et al. [2004]	Delage et al. [2000]	SCK-CEN [1997]	OECD/NEA [1996]	Volckaert et al. [1994]	Horseman et al. [1987]
Hydraulic conductivity	$K$	$m/s$	$3 \times 10^{-12}$		$2 - 4 \times 10^{-12}$		$2.5 - 3.5 \times 10^{-12}$		$2 \times 10^{-12}$		
<i>Vertical hydraulic conductivity</i>	$K_v$	$m/s$	$1.2 - 1.6 \times 10^{-12}$	$2.3 \times 10^{-12} *$		$2 \times 10^{-12} **$		$2 \times 10^{-12}$		$2.3 \times 10^{-12}$	$2 - 3.5 \times 10^{-12} ***$
<i>Horizontal hydraulic conductivity</i>	$K_h$	$m/s$		$5 \times 10^{-12} *$		$4 \times 10^{-12} **$		$4 \times 10^{-12}$		$5.2 \times 10^{-12}$	$5.5 \times 10^{-12} ***$

\* At the scale of the formation thickness, the mean values determined as  $K_v = 2.8 \times 10^{-12}$  and  $K_h = 1.3 \times 10^{-11}$  at the Mol site.

\*\* At the scale of the formation thickness (except the lower part of Belsele-Waas member), the mean values determined as  $K_v = 2.3 \times 10^{-12}$  and  $K_h = 4.6 \times 10^{-12}$  at the Mol site.

\*\*\* At the depth of 247 m.

Considering the Boom Clay at the level of HADES URL in Mol (corresponds to the characteristics of Putte/Terhagen units), Table 2.3 presents a literature review of the parameter of hydraulic conductivity. As it is given, most of the studies indicate an anisotropy of hydraulic conductivity (i.e.  $K_h/K_v$ ) of about 2. This ratio could be increased to 5 at the scale of the entire formation (about 100 m thickness) because of the contrasting nature of some sub-units (particularly Belsele-Waas unit), according to Wemaere et al. [2008].

### 2.3.5 Extended geomechanical properties for numerical simulations

The characteristics discussed in the last Section are the main geotechnical properties of Boom Clay involved in an hydro-mechanical analysis. However, with respect to the response type of material during the deformation (see Figure 2.10), some extended parameters may be considered in order to characterize the hardening/softening mode of material behavior as well as the dilatant type of deformation. Thence, some new parameters will be presented which can provide the possibility of consideration of a variable dilatation factor in a numerical analysis (see Chapter 4). Furthermore, the material softening parameters will be defined (as discussed in Chapters 5 and 6) following basically an essential objective of this thesis regarding the numerical modeling of evolution of shearing bands, *predominantly in the localized mode*, during a large-scale excavation in Boom Clay host formation. These parameters are regarded taking into account the formation of these shear bands, with a quite brittle behavior as the dominant mode of failure at the proximity of the gallery wall during its construction (see Section 2.3.2.3).

Moreover, a specific approach will be introduced into our simulations to correctly characterize the post-peak behavior (softening response after the peak), i.e. the creation of *localized* shear bands. To do this, the geomechanical properties will be elaborated to include a new parameter corresponds to the numerical simulation of strain localization in shear band mode (as discussed in Chapter 5).

## 2.4 Intermediate conclusions

This Chapter consisted in a review of the significant characteristics of Boom Clay considering its particular importance in the framework of deep disposal of high-level and long-lived radioactive waste in the geological stable formations in Belgium. Firstly, the origin of these wastes was briefly described introducing the concept of deep disposal of nuclear waste. Then, the application of argillaceous clays, namely Boom Clay, was declared considering their favorable properties. Boom Clay is regarded as the reference host formation in Belgium, due to which it has been under study during the last three decades in the HADES URL close to the city of Mol, Belgium. Hence, there is a particular interest in studying the different behavior aspects of this argillaceous clay to better understand its response as a host formation, which is the basis of the current thesis.

Some geological microstructure analyses recognized the evidences of quite brittle (dilatant) deformation response, induced by shear, in Boom Clay at the level of HADES URL, that it could establish a localized type of deformation. However, the origin of the fracturing has been fundamentally associated to the excavation process with no related natural phenomena behind it. A more detailed discussion on the in-situ observation of the fracturing network and the localized deformation due to the excavation will be given in Chapter 5. The fracturing and stress history are of principle factors which influence the hydro-mechanical response of clay; the intrinsic permeability and stiffness are likely to be affected by those. Moreover, the mineral composition of Boom Clay identifies a considerable proportion of clay minerals, which confirms

the potentiality of this argillaceous formation to be very low permeable with respect to the water-clay interactions mechanism. The bibliographical review of the hydro-mechanical properties of Boom Clay also confirms a very low hydraulic conductivity of this argillaceous formation.

# Chapter 3

## Classical numerical framework

### Contents

---

<b>3.1</b>	<b>Introduction</b>	<b>28</b>
<b>3.2</b>	<b>General configuration of the problem</b>	<b>29</b>
3.2.1	Stress and strain description for mechanical analysis	29
3.2.2	Mechanical equilibrium conditions	31
3.2.3	Description of porous media for a coupled hydro-mechanical analysis	34
3.2.4	On the coupled analysis of the mixture	39
3.2.5	Hydraulic equilibrium conditions	41
3.2.6	Discretization of the domain	42
3.2.7	LAGAMINE resolution algorithm	45
<b>3.3</b>	<b>Elasto-plasticity</b>	<b>47</b>
3.3.1	General concept	47
3.3.2	Yield surface	48
3.3.3	Flow rule and potential surface	49
3.3.4	Consistency conditions	50
3.3.5	Hardening/softening response and hardening rule	50
<b>3.4</b>	<b>Internal frictional behavior models for geomaterials</b>	<b>53</b>
3.4.1	Stress conventions	53
3.4.2	Representation of the yield surfaces for an internal frictional constitutive law	54
3.4.3	Review of some other yield criteria	62
3.4.4	Choice of the yield criterion for the elasto-plastic analysis	66
3.4.5	Return mapping algorithm	67
3.4.6	Sub-stepping approach	70
<b>3.5</b>	<b>Simulations of the triaxial tests on Boom Clay</b>	<b>71</b>
3.5.1	Stress-strain mechanical response: deviatoric stress development	72
3.5.2	Description of the triaxial tests	73
3.5.3	Discussion on the influence of dilatancy angle on the numerical results	91
<b>3.6</b>	<b>Intermediate conclusions</b>	<b>94</b>

---

*If you wish to make an apple pie from scratch, you must first invent the universe.*

Carl Sagan

### 3.1 Introduction

"If you wish to make an apple pie from scratch, you must first invent the universe," Carl Sagan states. Before going through the complex numerical modelings and analyses, an introductory description of the general numerical framework is needed. Hence, the basics of finite element configuration of the LAGAMINE code<sup>1</sup>, used in this study, are addressed in this Chapter. However, for a more detailed description of the implemented formulations, the interested reader may refer to [Charlier, 1987; Barnichon, 1998; Collin, 2003]. The stress-strain relationship and the chosen referential system are firstly introduced followed by giving the classical mechanical equilibrium conditions. The numerical layout is then extended to briefly describe the kinematics of porous medium so that the coupled equilibrium conditions and the general resolution algorithm are represented.

The main concepts of the elasto-plasticity are recalled in the second part of this Chapter. Next, the frictional elasto-plastic constitutive laws, existing in the LAGAMINE library, for the geomaterials are presented. A comparison of the different yield surfaces is then given with a discussion on the choice made for this work.

Finally, some experimental triaxial tests on Boom Clay are analyzed based on the literature, accompanied by their numerical simulations. The triaxial tests have been already performed and analyzed in many studies focusing on different materials including Boom Clay. Although, a correct comparison of these studies in general seems very complicated even if all are about the same material since they could be performed under different conditions and assumptions. That is to say, the experimental samples as to be intact or reconstituted, saturated or unsaturated, under different initial and boundary conditions, various loading rates, the drained or undrained tests, and etc. We don't aim to gather all the available data on Boom Clay, and to repeat their analysis and comparison here which of course neither is it being within our main objectives. In preference to that, a literature analysis of some experimental results of the drained and undrained triaxial tests on natural Boom Clay, which have been performed within the similar frameworks, is conducted such that some interesting features of the response of our considered material could be addressed through studying them. These tests consist of the undrained triaxial tests performed at the Université de Liège and École Nationale des Ponts et Chaussées, in the framework of TIMODAZ (Thermal Impact on the Damaged Zone Around a Radioactive Waste Disposal in Clay Host Rocks) project [TIMODAZ, 2010b], the undrained triaxial tests performed at the Institute of Rock and Soil Mechanics, Chinese Academy of sciences [Yu et al., 2012], and the drained triaxial tests performed by Coll [2005]; Lenoir et al. [2008]. Then, these experiments are modeled numerically while the numerical results are discussed in comparison with the experimental results. The objective is not verification of the computational framework, nor the validation of the numerical model, but rather the validation of main numerical parameters applied to the model further on. The latter is a subdivision of the model's validation, though. One should keep in mind the difference between the terms verification and validation. *Verification* replies to "Are we building the model right? Are the computer representation of the model and input parameters correctly produce the conceptual model?" *Validation* replies to "Are we building the right model? Are the model and its relative parameters accurately represent the real problem?" The latter is usually attained through the calibration of the model. This process is focused here to validate the model's parameters, with the objective of ensuring *one* set of the material's main parameters which could represent realistically its hydro-mechanical response.

---

<sup>1</sup>This code has been basically developed by Charlier [1987] and Habraken [1989] at the Université de Liège.

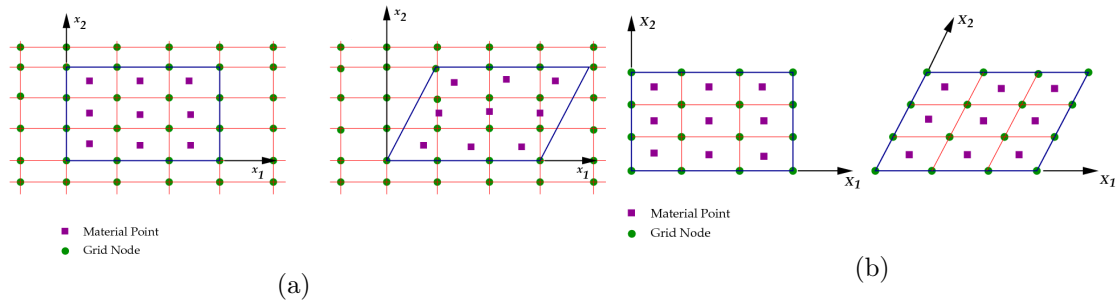


Figure 3.1: Schematic representation of: (a) Eulerian mesh. (b) Lagrangian mesh<sup>2</sup>.

## 3.2 General configuration of the problem

### 3.2.1 Stress and strain description for mechanical analysis

Considering the similar initial and final configurations is practicable as long as the infinitesimal deformations are taken into account. Going through the large deformation, the initial and final configurations become different. In this case, for which the LAGAMINE code has been developed, the large deformation, large rotation, and translation of body are simulated. It is necessary to declare the problem's configuration based on which the numerical framework is extended further on. However, whatever our choice is, the body's equilibrium has to be achieved in its current state. Possible configurations can mainly be subdivided as:

- **Eulerian description** The problem is stated with regard to the deformed configuration while the motion of material through a stationary control volume is considered, i.e. this is described with reference to a fixed referential basis. Moreover, the Eulerian grid nodes are fixed in space, and the material points move through it (Figure 3.1a).
- **Lagrangian description** The problem is stated with regard to the reference configuration while we track the movement of all particles of the body, i.e. this is described with reference to a referential basis attached to the body. In addition, the Lagrangian grid nodes are tied to the material points (Figure 3.1b).

The Lagrangian formulation is typically used to deal with the problems with large deformations in solid mechanics. In this work, an updated Lagrangian description is applied which considers the Lagrangian mesh. In addition, the stress and strain are measured in the current configuration, with respect to an (updated) reference configuration. That is to say that the reference configuration evolves at each step in the finite element point of view. In LAGAMINE, the equilibrium formulation is stated based on the orthonormal basis which is linked to the spatial movement of system, although, the direction of the unit vectors remains constant (see Figure 3.2).

The deformation gradient for the current configuration with respect to the reference configuration is characterized through the definition of transformation tensor  $\mathbf{F}$ ; in fact, it links the tangent vectors<sup>3</sup> in initial and deformed configuration.

$$\mathbf{F} = \frac{\partial \mathbf{x}}{\partial \mathbf{X}}, \quad (3.1)$$

<sup>2</sup>Source: Wikiversity.

<sup>3</sup>In the mathematical point of view, vectors and tensors are expressed in bold characters.

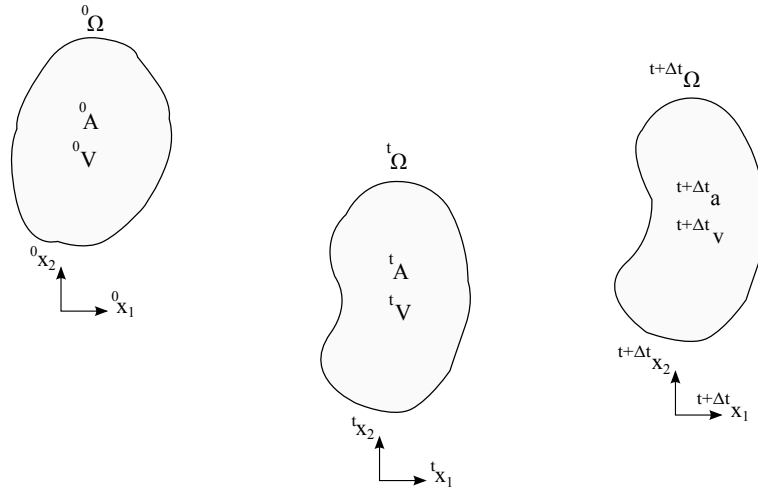


Figure 3.2: Updated lagrangian approach; the superscript  $0$  refers to the initial configuration,  $t$  refers to the updated reference configuration, and  $t+\Delta t$  refers to the current configuration.

This could be denoted as the line transformation. Similarly, the areas in the deformed configuration are related to those in the reference configuration by the Nanson's relation [Goriely, 2013] as:

$$\mathbf{n}da = J\mathbf{F}^{-T}\mathbf{N}dA \iff da = J\mathbf{F}^{-T}d\mathbf{A}, \quad (3.2)$$

where Jacobian determinant  $J = \det\mathbf{F}$ , and  $\mathbf{n}$  is the outward normal to the area element in the current configuration while  $\mathbf{N}$  is the outward normal to the equivalent area element in the reference configuration. The corresponding relation between the volume elements is expressed as:

$$dv = JdV, \quad (3.3)$$

We have assumed  $\mathbf{F}$  is a bijection, therefore,  $J = \det\mathbf{F} > 0$ , so that  $\mathbf{F}^{-1}$  is well defined.

An important kinematic quantity is the velocity gradient tensor. The velocity of a material point  $\mathbf{x}$  in the current configuration, and its gradient tensor are defined respectively as:

$$\mathbf{v} = \frac{d\mathbf{x}}{dt}, \quad (3.4)$$

$$\mathbf{L} = \text{grad}\mathbf{v} = \frac{\partial\mathbf{v}}{\partial\mathbf{x}} = \frac{\partial\mathbf{v}}{\partial\mathbf{X}} \frac{\partial\mathbf{X}}{\partial\mathbf{x}}, \quad (3.5)$$

The velocity gradient can be decomposed into a symmetrical part and an anti-symmetrical part as follows:

$$\mathbf{L} = \frac{1}{2}(\mathbf{L} + \mathbf{L}^T) + \frac{1}{2}(\mathbf{L} - \mathbf{L}^T), \quad (3.6)$$

where the first term, the symmetrical part of the velocity gradient, corresponds to the rate of deformation tensor ( $\dot{\boldsymbol{\epsilon}}$  or  $\mathbf{D}$ <sup>4</sup>; see Equation 3.7), and the second term, the anti-symmetrical part, is called the spin tensor that it is directly related to the rate of rotation of an object, (see Equation 3.8).

$$\dot{\boldsymbol{\epsilon}} = \frac{1}{2}(\mathbf{L} + \mathbf{L}^T), \quad (3.7)$$

<sup>4</sup>The symmetrical part of the velocity gradient is some times called  $\mathbf{D}$  in the literature while dealing with the large deformations. In a general point of view of the infinitesimal or large deformations domains, the basic notation of  $\dot{\boldsymbol{\epsilon}}$  is used for the rate of deformation (or, strain rate) all through this thesis for the matter of consistency with the former numerical works presented based on the theoretical framework of the LAGAMINE finite element code.

$$\boldsymbol{\omega} = \frac{1}{2}(\mathbf{L} - \mathbf{L}^T), \quad (3.8)$$

Definition of a notion of strain is necessary. A strain tensor is a tensor that is identically zero if there is no stretch in any direction of the body [Goriely, 2013]. As a consequence of decomposition operation, a separated strain rate is supposed to be established which is not affected by body rotation (Equation 3.7). Although, definition of its integration does not have generally a physical meaning in the domain of large rotations and deformations. Hence, to define a notion of strain, the Polar decomposition theorem may be applied [Goriely, 2013] to the transformation tensor considering that it is under the influence of the rigid body rotation.

The action of the transformation tensor is to rotate a vector along a direction  $R_1$  to a direction  $R_2$ , then stretch it to a size  $\lambda(R_1)$ . This split between stretch and rotation is contained in the polar decomposition theorem as:

$$\mathbf{F} = \mathbf{R}\mathbf{U} = \mathbf{V}\mathbf{R}, \quad (3.9)$$

where  $\mathbf{R}$  is the orthogonal rotation tensor, and  $\mathbf{U}$  and  $\mathbf{V}$  are respectively, right and left symmetric stretch tensors. Thence, the Lagrangian natural strain tensor,  $\mathbf{G}$ , is defined as:

$$\mathbf{G} = \ln \mathbf{U}, \quad (3.10)$$

In addition, the Cauchy stress rate tensor  $\dot{\boldsymbol{\sigma}}$  may be defined to be associated to  $\dot{\boldsymbol{\epsilon}}$ . Although, through an incremental formulation, the definition of an objective derivative of stress (invariant to rigid spin) is required if deformation or rotation in the solid is large. The Jaumann stress rate is then applied as a common objective stress rates in continuum mechanics, which imposes the rotation-independency:

$$\tilde{\boldsymbol{\sigma}} = \dot{\boldsymbol{\sigma}} - \boldsymbol{\omega}\boldsymbol{\sigma} - \boldsymbol{\sigma}\boldsymbol{\omega}^T, \quad (3.11)$$

The stress and strain rate are connected generally through the definition of a constitutive relation which is dependent on some internal variables. The formulation of the appropriate elasto-plastic constitutive relations for geomaterials, which are considered in this work are brought in Section 3.4.

### 3.2.2 Mechanical equilibrium conditions

Let consider a deformable body  $\Omega$  for which we aim to describe the equilibrium conditions for mechanical analysis. The statement of the boundary conditions is firstly necessary. Thence, the equilibrium conditions can be defined locally for all the points of volume  $\Omega$  with respect to those boundary conditions. This is then extended for the whole mechanical system.

#### 3.2.2.1 Description of the problem

Figure 3.3a shows a deformable body  $\Omega$ , and we assume that it is delineated by boundary portions  $\overline{AB}$ ,  $\overline{BCDE}$ ,  $\overline{EF}$ , and  $\overline{FA}$ . The body is fixed along the  $\overline{AB}$  and  $\overline{EF}$ . Figure 3.3b details the prescribed displacements and forces after the body is deformed. This deformation is attained in two ways: a known displacement is applied on the boundary portion  $\overline{EF}$  as  $d$ , and a known force  $\bar{t}$  is applied along the portion  $\overline{CD}$ . Regardless of the loading, the displacements are prescribed along  $\overline{AB}$  and  $\overline{EF}$ , i.e.  $d$  along  $\overline{EF}$  and zero along  $\overline{AB}$ . On the contrary, the displacement is not prescribed in other portions ( $\overline{BCDE}$  and  $\overline{FA}$ ); it is initially zero in the undeformed state, and it could be built upon deformation. On the other hand, forces are prescribed along the boundaries

$\overline{BCDE}$  and  $\overline{FA}$ , i.e. equal to  $t$  along the portion  $\overline{CD}$ , and always zero along  $\overline{BC}$ ,  $\overline{DE}$ , and  $\overline{FA}$ . The forces are not contrarily prescribed along the portions  $\overline{EF}$  and  $\overline{AB}$  since they have zero forces initially (in the undeformed and unstressed state), and could build it up depending on the final configuration of the system.

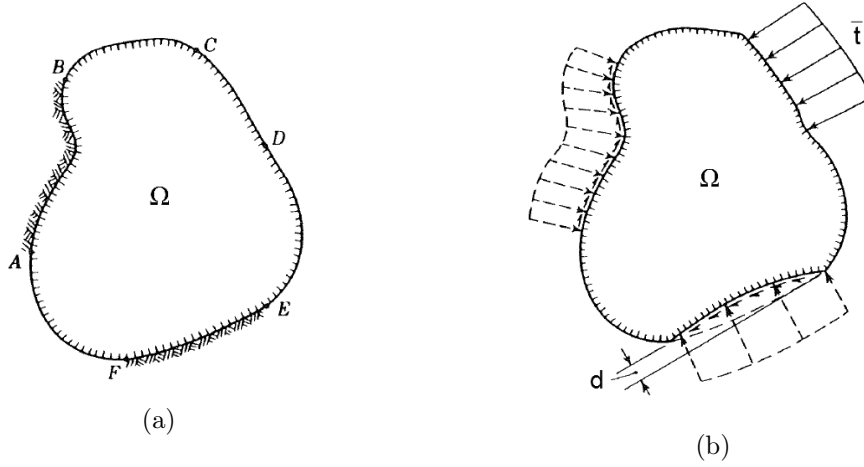


Figure 3.3: Deformable system. (a) Representation of the problem domain  $\Omega$  and its boundary portions. (b) Definition of the prescribed displacements and forces; after [Oden and Ripperger, 1967].

Consequently, the body's boundary is supposed to be decomposed in two non-overlapping parts: the part where the forces (traction loads) are prescribed and displacements are not prescribed (Neumann boundary,  $\Gamma_\sigma$ ), and the part where the displacements are prescribed and the forces are not prescribed (Dirichlet boundary,  $\Gamma_u$ ), such that:

$$\Gamma_\sigma \cup \Gamma_u = \Gamma \quad \text{and} \quad \Gamma_\sigma \cap \Gamma_u = \emptyset \quad (3.12)$$

A simple representation of the total boundary surface of a deformable body is also shown in Figure 3.4.

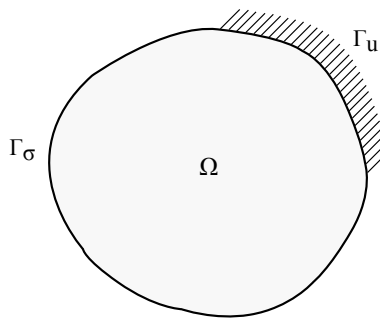


Figure 3.4: Definition of the boundaries  $\Gamma_u$  and  $\Gamma_\sigma$  for the domain  $\Omega$ .

Therefore, for any  $\mathbf{x} \in \Omega$ , displacement field  $\mathbf{u}$  is obtained in the framework of strong form of the initial boundary-value problem for an elementary volume  $\Omega$ , under quasi-static condition, such that:

$$\operatorname{div} \boldsymbol{\sigma} + \mathbf{G} = 0 \quad \text{in } \Omega \quad (3.13)$$

and,

$$\mathbf{u} = \mathbf{d} \quad \text{on } \Gamma_u \quad (3.14)$$

$$\boldsymbol{\sigma} \cdot \mathbf{n} = \bar{\mathbf{t}} \quad \text{on } \Gamma_\sigma \quad (3.15)$$

where  $\mathbf{G}$  is the volume body force (e.g. the gravity force), and  $\mathbf{n}$  is outward unit normal vector to  $\Gamma_\sigma$ .

### 3.2.2.2 Equilibrium statement in the framework of the principle of virtual work

The equations described in the last section characterize the local equilibrium in the strong form. The strong form requires strong continuity on the dependent field variables and then, the exact solution for a strong form of the system's governing equation is usually very difficult for practical engineering problems [Quek and Liu, 2003]. The finite element equations could be established from the weak form of the problem stated previously [Borja, 2013]; the finite element code LAGAMINE is also derived from the weak form of the governing equations. The principle of virtual work is then used for this extension.

#### *Principle of virtual work:*

The principle of virtual work can also lead up to the principle of virtual power. The latter can be considered as a consequence of the principle of virtual work [Grossetie, 1981], and its system of governing equations is derived from the definition of the virtual velocity field [Germain, 1973b]. However, the principle of virtual work could signify the definition of virtual, or imaginary, displacements field based on which its governing equations are derived.

Let firstly assume a system of particles that each has independent virtual displacements along each of their degree of freedom. The necessary and sufficient condition for equilibrium [Oden and Ripperger, 1967] is stated as: *A system of particles is in equilibrium if the total virtual work is zero for every independent virtual displacement.* Now, let consider a rigid body which is not only a collection of particles, but also under constraints to ensure its rigidity (constant distance among the particles is then assumed). Thence, the principle of virtual work to assure the equilibrium is rewritten as: *A mechanical system (i.e. rigid body and particles) is in equilibrium if the total virtual work done is zero for every virtual displacement consistent with the constraints.* Consequently, the virtual work done during the all virtual displacements is zero. In fact, each point with an independent virtual displacement, isolated from the other points and virtual displacements, is linked to a unique movement of the rigid body. This establishes the restatement of the theory of virtual work for a rigid body as: *The virtual work of all internal forces is null if the virtual displacement of all particles supplies a unique movement of the rigid body* [Germain, 1973b; Grossetie, 1981].

Next, we aim to develop the above concept for a deformable body which is the case in this work. The difference with the solid body is that points within a body may move relative to one another without violating conditions of constraint. Therefore, both internal and external forces could do virtual work. It is noteworthy to recall that external forces are generally independent of the material properties, and they are represented by the volume body forces which act within the body and surface forces (traction loads) which act on the body's boundary. On the other hand, internal forces are identified as the stresses that are developed within the body. Hence, internal virtual work is interpreted by the produced stress within a deformable body due to its deformation while the body was initially unstressed and subjected to self-equilibrating external forces [Oden and Ripperger, 1967].

The principle of virtual work is defined for an *admissible* virtual displacement field,  $u_i^*$ . That is to say that this field should firstly satisfy the kinematical boundary conditions. Considering the concept explained for a deformable body with regard to Figure 3.3, since the prescribed

displacements of a point can be signified as constraining that point, we must consider such virtual displacement (while applying the principle of virtual displacement) that satisfies those kinematic boundary conditions. Secondly, the virtual displacement field should verify the solid continuity; the material is supposed to be distributed continuously within the system. Upon this conditions, the general principle of virtual work for a deformable body is stated as:

*A deformable system is in equilibrium if the total external virtual work is equal to the total internal virtual work for every virtual displacement consistent with the constraints.*

This condition is then expressed in Equation 3.16 where the left-hand side denotes the internal virtual work, and the right-hand side signifies the external virtual work. The Einstein (or, indicial) notation is adopted in the following to provide more readability.

$$\int_{\Omega} \sigma_{ij} \varepsilon_{ij}^* d\Omega = \int_{\Omega} G_i u_i^* d\Omega + \int_{\Gamma_{\sigma}} \bar{t}_i u_i^* d\Gamma \quad (3.16)$$

where  $\varepsilon_{ij}^*$  is the kinematically admissible virtual strain field which can be defined as  $\varepsilon_{ij}^* = \frac{1}{2} \left( (\partial u_i^* / \partial x_j) + (\partial u_j^* / \partial x_i) \right)$  taking into account the symmetry of the stress tensor (shayad in jomle akhre taking ro bardaram ..).

### 3.2.3 Description of porous media for a coupled hydro-mechanical analysis

#### 3.2.3.1 On the definition of porous medium

To pass through the coupled analysis, the one should consider the existence of the other phase(s) than solid, which is mostly the case in dealing with the problems in the field of soil mechanics. This leads to the theory of the porous media. Let consider an elementary volume  $\Omega$ , surrounding a geometrical point, as observed in Figure 3.5. A saturated porous medium is represented as the superposition, in time and space, of two continuous media [Coussy and Ulm, 1995]. These two coincide with one at the same geometrical point.

- **Skeleton** The skeleton portion constituted of the so-called "matrix", comprised the solid part and occluded inter-aggregate [Romero et al., 2014] porosity, and the connected porous space of the elementary volume. These two porosity indicate the void medium in the elementary volume  $\Omega$ . The volume of the solid part is denoted as  $\Omega_s$ , and its specific mass is noted as  $\rho_s$ .
- **Fluid phase** The fluid saturates the void medium, primarily the connected porosity. The term *saturated* refers to the void volume filled by one fluid, e.g. water. In this case, the specific mass of the fluid phase (i.e. water) is noted as  $\rho_w$ .

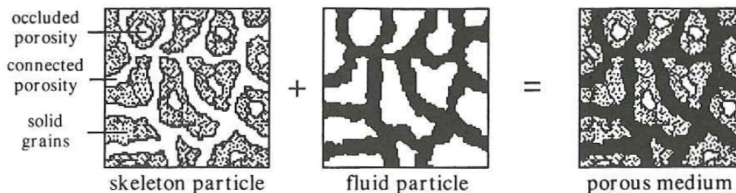


Figure 3.5: Microscopic representation of a saturated porous medium [Coussy and Ulm, 1995].

The void volume generally can be filled by a combination of fluids. Thence, the soil state is called unsaturated or partially saturated. These fluids could commonly be water and air.

Furthermore, there is a particular behavior state in which the soil<sup>5</sup> sustains a negative pore water pressure (i.e. pressure lower than atmospheric pressure), which may generally signify an unsaturated state, but it still remains in the fully-saturated state. The latter will be also addressed in this thesis as well as the normal state of a saturated medium. To clarify the former state, the concept of negative pore water pressure is firstly explained. To do this, the notion of surface tension is recalled.

At the interface of water and air (gas) phases, there is a specific property named surface tension which is resulted from the molecular forces acted on the molecules of water. In fact, a molecule in the interior of the water is under equilibrium since it experiences forces in all directions. However, a molecule at the interface is under the unbalanced forces towards the water interior. The mechanical effect of this phenomenon resulted in a tensile pull generated along the interface to acquire the equilibrium [Fredlund and Rahardjo, 1993]. Figure 3.6a shows this mechanism while an example of this phenomenon in the real world is brought in Figure 3.6b.

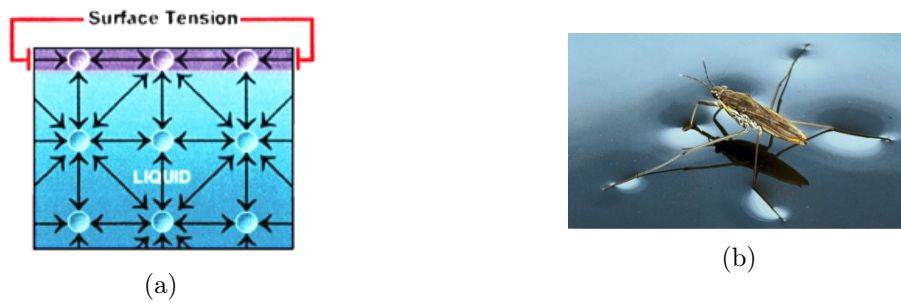


Figure 3.6: Surface tension. (a) Molecular forces on a water particle. (b) An example of the surface tension.

The concept of surface tension leads to the definition of capillary action and negative pore water pressure. Figure 3.7 represents a physical modeling of the capillarity. This indicates that the rise of water within a thin capillary tube is given by the Jurin's law, based on the vertical equilibrium, such that:

$$p_c = p_a - p_w = \rho_w g h_c = \frac{2T_s \cos \alpha}{r} = \frac{2T_s}{R_s} \quad (3.17)$$

where  $p_c$  is the capillary pressure,  $p_a$  is the pore air pressure,  $p_w$  is the pore water pressure,  $h_c$  is the rise of water within the capillary tube,  $T_s$  is the surface tension, and  $R_s$  is called the meniscus radius, and as this radius is lower, the rise of water within the capillary tube is higher.

This concept declares the capillary effects observed in an unsaturated soil - that is to say the negative pore water pressure with respect to the pore air pressure - following the creation of meniscus radius, i.e. the void space within the skeleton, and establishment of capillary pressure. This capillary pressure is termed as suction in soil mechanics. However, in an argillaceous clay - generally fine-grained soils - there is another mechanism beside the capillary actions, that they can characterize the total suction of medium<sup>6</sup>. This mechanism is not uniquely occurred in unsaturated soils like the former mechanism (i.e. capillarity), but rather it may be observed in both saturated and unsaturated media. It is regarded to the adsorption of water by solid particles and physico-chemical effects as already mentioned in Section 2.3.3. These two mechanisms (i.e.

<sup>5</sup>By soil, we mean the both soils and rocks in this section.

<sup>6</sup>There is in fact a third mechanism named "osmotic effects" which is usually negligible compared to two other aspects.

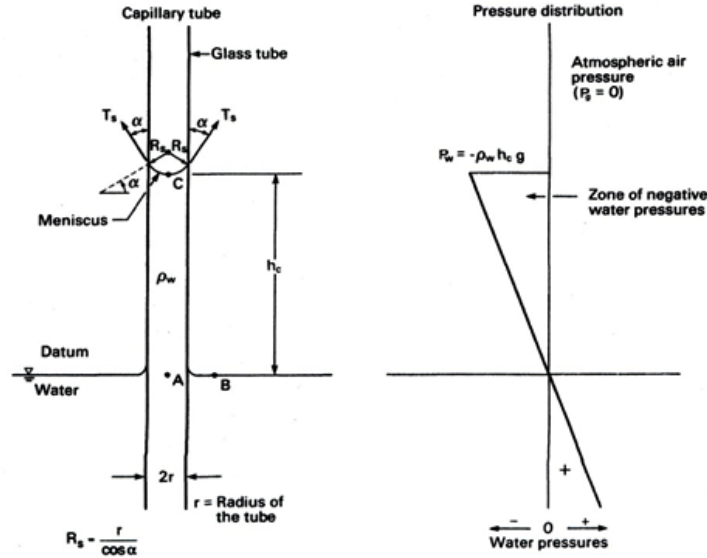


Figure 3.7: Capillary phenomenon [Fredlund and Rahardjo, 1993].

capillarity and water absorption) are usually called as matric suction. On the whole, the total suction is described as the potential of soil pore water relative to a reference potential of free water, which implies the capability of drawing water from the soil pores [Lu and Likos, 2004].

The Water Retention Curve (WRC) of a soil relates its suction and degree of saturation<sup>7</sup> (or, water content<sup>8</sup>). Figure 6.5 shows a typical water retention curve. There are three aspects observed in a WRC. Air entry value (AEV),  $s_b$ , is the suction from which the soil is getting desaturated during drying. Residual degree of saturation characterizes the water content which remains ultimately within the soil no matter the increase of suction. Finally, the difference occurred under (re-)wetting path compared to the drying path; this is called hysteresis effect. This signifies that at the same suction, the degree of saturation is lower on the wetting path than on a drying path; it is out of scope of this work, though.

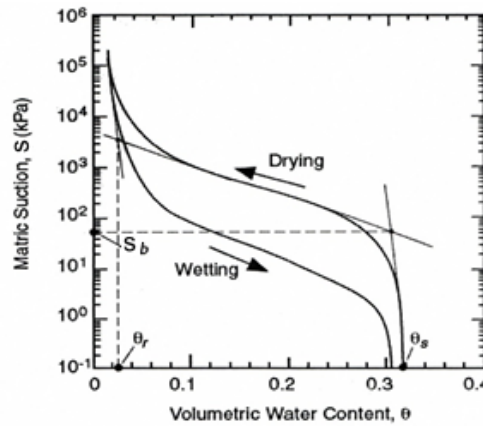


Figure 3.8: Water retention curve [Lu and Likos, 2004].

<sup>7</sup>  $S_{r,w} = \frac{\Omega_w}{\Omega_v}$ , where  $\Omega_w$  is the water volume, and  $\Omega_v$  is the void volume.

<sup>8</sup>  $\theta_w = \frac{W_w}{W_s}$ , where  $W_w$  is the mass of water, and  $W_s$  is the solid mass.

As it has been already mentioned, we stay in the saturated domain in this work, although there will be some cases where a negative pore water pressure is observed but the medium still remains in the fully-saturated state (see Chapter 6). With regard to the description given for the water retention curve's elements, the latter state can be then simply explained by a suction state which is lower than the air entry value. Therefore, we are generally dealing with the *saturated* porous medium further on, and the numerical framework is extended by then.

Therefore, the specific mass of a saturated porous medium, where the void volume is filled by one fluid (water, in this work<sup>9</sup>), is defined as:

$$\rho = (1 - n)\rho_s + n\rho_w \quad (3.18)$$

and  $n$  is the porosity, such that:

$$n = \frac{\Omega_v}{\Omega} = \frac{\Omega_v}{\Omega_s + \Omega_v} \quad (3.19)$$

where  $\Omega_v$  is the void volume, and  $\Omega_s$  is the solid volume.

### 3.2.3.2 Kinematics of porous medium

Regarding the two phases nature of the porous medium, the kinematics of both phases should be considered taking into account the coupling effects between them. Skeleton kinematics can be expressed similarly to a monophasic continuum (as described in Section 3.2.1); hence, the updated lagrangian formulation is assigned to the solid part. However, this approach can not be equivalently applied to the fluid phase. The reason is related to the fact that there is an essential difference between a monophasic and porous continua. Unlikely to the former continuum which is closed, any elementary volume  $\Omega$  in a porous continuum may exchange some fluid with the outer environment in the course of system evolution. Thence, the fluid phase is referred as an open continuum [Coussy and Ulm, 1995]. In the following, the Eulerian and Lagrangian descriptions of the fluid kinematics are stated:

- **Eulerian description** The fluid properties are expressed as functions of space and time. The flow is then determined by analyzing the behavior of these functions. Let consider an infinitesimal surface  $da$  with an outer normal  $\mathbf{n}$ . With respect to Coussy and Ulm [1995], the transformation of the fluid can be expressed by the Eulerian relative flow of fluid mass vector  $\mathbf{m}$  (Equation 3.21) so that the water mass (fluid mass) which flows through  $da$  at time  $t$  and per unit of time is defined by Equation 3.20.

$$J_w^m = \mathbf{m} \cdot \mathbf{n} da \quad (3.20)$$

$$\mathbf{m} = \rho_w n \mathbf{V}^{\mathbf{w}/\mathbf{s}} = \rho_w \mathbf{V}^{\mathbf{d}} \quad (3.21)$$

where  $\mathbf{V}^{\mathbf{w}/\mathbf{s}}$  is the true water velocity with respect to solid phase, and it is linked to Darcy velocity  $\mathbf{V}^{\mathbf{d}}$ .

- **Lagrangian description** Pieces of the fluid are *tagged*. The fluid flow properties are then determined by tracking the motion, and properties of the particles as they move in time. The fluid mass flows through an infinitesimal surface  $dA$  in reference configuration, with an outer normal  $\mathbf{N}$  is expressed as:

$$J_w^m = \mathbf{M} \cdot \mathbf{N} dA \quad (3.22)$$

---

<sup>9</sup>The fluid phase in this thesis refers to water, and vice-versa.

where  $\mathbf{M}$  is the Lagrangian relative flow of fluid mass vector.

It is generally more common to use Eulerian approach for fluid flows. In LAGAMINE code, we may apply the hybrid description; the grid nodes are tied to the solid skeleton points which deform while the fluid flows follow the Eulerian formulation.

### 3.2.3.3 Constitutive relations

The description of the hydro-mechanical behavior needs to specify the relative constitutive equations.

First, the compressibility of the water is assumed to be obtained through the linearized water state equation [Lewis and Schrefler, 1998] as:

$${}^{t+\Delta t}\rho_w - {}^t\rho_w = \frac{{}^t\rho_w}{\chi_w} ({}^{t+\Delta t}p_w - {}^tp_w) \quad (3.23)$$

where  $\chi_w$  is the water bulk modulus, and  $1/\chi_w$  characterizes the water compressibility. As it has been already mentioned, the superscripts  ${}^{t+\Delta t}$  and  ${}^t$  refer to the deformed and reference configurations, respectively. This statement predicts an increase of water density as a function of pore water pressure.

Second, the water motion is governed by the generalized Darcy's law which is valid for low Reynolds numbers. The Darcy water velocity  $V^d$  in an isotropic porous medium is defined as:

$$\mathbf{V}^d = -\frac{K}{\rho_w g} \cdot (\nabla p_w + \rho_w g \nabla z) \quad (3.24)$$

where  $K$  [m/s] is the isotropic hydraulic conductivity (also called, permeability coefficient), such that:

$$k = K \frac{\mu_w}{\rho_w g} \quad (3.25)$$

where  $k$  [m<sup>2</sup>] is the intrinsic permeability. Unlikely to the hydraulic conductivity, the intrinsic permeability is a property of the porous media, and not related to the considered fluid.  $\mu_w$  is the water dynamic viscosity; it is equal to  $10^{-3}$  Pa.s for water at 20°C. Therefore, Equation 3.24 can be reexpressed as:

$$\mathbf{V}^d = -\frac{k}{\mu_w} \cdot (\nabla p_w + \rho_w g \nabla z) \quad (3.26)$$

Considering an anisotropic porous medium, a second rank tensor of intrinsic permeability (or, hydraulic conductivity) is defined in Equations 3.24 and 3.26. Hence, Equation 3.27 gives the Darcy law for an anisotropic porous medium using the indicial notation:

$$V_i^d = -\frac{k_{ij}}{\mu_w} \left( \frac{\partial p_w}{\partial x_j} + \rho_w g \frac{\partial z}{\partial x_j} \right); \quad i, j = 1, 2, 3, \quad (3.27)$$

Third, the Terzaghi's postulate is assumed to define the effective stress  $\boldsymbol{\sigma}'$ , which engenders the deformation of solid skeleton, relatively to total stress on the bulk material  $\boldsymbol{\sigma}$  and the water pressure field  $p_w$ .

$$\boldsymbol{\sigma}' = \boldsymbol{\sigma} + p_w \mathbf{I}, \quad (3.28)$$

where  $\mathbf{I}$  is the identity matrix.

This definition supposes that the solid grains are incompressible, and the contact among the

grains is punctual. However, in the framework of linear poroelasticity, the effective stress can be generally defined as [Biot, 1973]:

$$\boldsymbol{\sigma}' = \boldsymbol{\sigma} + b p_w \mathbf{I}, \quad (3.29)$$

where  $b$  is the Biot's coefficient, and it allows considering the compressibility of solid part. In fact, when the fluid and the solid are chemically inert, this coefficient  $b$  is equal to  $1 - K_0/K_s$  where  $K_0$  is the modulus of drained bulk modulus (modulus of drained rigidity) in the isothermal condition of skeleton, and  $K_s$  is the isotropic bulk modulus of solid grains. Thence, when the grains rigidity is very high (or, infinite) compared to the skeleton rigidity,  $b \approx 1$ .

It may be noteworthy that, in the LAGAMINE code, the Biot's coefficient is considered similarly either the material is in the elastic state or in the plastic state<sup>10</sup>.

As it has been already mentioned in Section 2.3.4, the Biot's coefficient for Boom Clay at the Mol site is equal to one which imposes a strong hydro-mechanical coupling effect [Barnichon and Volckaert, 2000]. Thus, the unit value is considered in this work for the Biot's coefficient, and the Terzaghi's effective stress tensor (Equation 3.28) governs the behavior of solid skeleton.

The mechanical constitutive relation for representation of stress-strain characteristics is particularly discussed in Section 3.4.

### 3.2.4 On the coupled analysis of the mixture

Following the poromechanical framework explained in the previous section, the incremental<sup>11</sup> stress-strain relation can be expressed by Equation 3.35, which relates the Jaumann derivative (see Section 3.2.1) of the effective stress rate tensor to the strain rate tensor [Barnichon, 1998; Barnichon and Volckaert, 2000], such that:

$$\tilde{\boldsymbol{\sigma}}' = \tilde{\boldsymbol{\sigma}} + \dot{p}_w \mathbf{I} = \mathbf{C}^e : (\dot{\boldsymbol{\varepsilon}} - \dot{\boldsymbol{\varepsilon}}^P), \quad (3.35)$$

<sup>10</sup>However, in the general point of view, the effective stress can be defined in poroplasticity, i.e. when the skeleton deformation is permanent (irreversible) [Coussy and Ulm, 1995], such that:

$$\boldsymbol{\sigma}'^P = \boldsymbol{\sigma} + \beta p_w \mathbf{I}, \quad (3.30)$$

where  $\beta$  characterizes the Biot's coefficient for an isotropic case in plastic state. This is related to the permanent volumetric strain of skeleton by Equation 3.31, and this permanent strain is expressed by Equation 3.32.

$$n^P = \beta \varepsilon_v^P, \quad (3.31)$$

$$\varepsilon_v^P = n^P + (1 - n_0) \varepsilon_s^P, \quad (3.32)$$

where  $n^P$  is the plastic porosity,  $n_0$  is the initial porosity, and  $\varepsilon_s^P$  is the permanent volumetric strain of the matrix (it corresponds to the volume change in solid part based on the definition of matrix in Section 3.2.3.1). Therefore, the permanent change of volume has two microscopic origins. The first part is the plastic porosity and it corresponds to irreversible change in volume of the connected porous space. The second part is related to the solid part, grain volume change.

Therefore, in the particular case that the matrix undergoes no permanent change in volume, i.e. the solid part is plastically incompressible ( $\varepsilon_s^P = 0$ ), Equation 3.32 is simplified to:

$$\varepsilon_v^P = n^P, \quad (3.33)$$

That is to say that the permanent volumetric strain corresponds to the change in plastic porosity and then,  $\beta = 1$  following Equation 3.31.

On the whole, when the solid part (or, grains) is elastically and plastically incompressible, i.e. the Biot's coefficients  $b$  and  $\beta$  are equal to one, the Biot elastic and plastic effective stress tensor coincide and they represent the Terzaghi's postulate:

$$\boldsymbol{\sigma}'^e = \boldsymbol{\sigma}'^P = \boldsymbol{\sigma} + p_w \mathbf{I}, \quad (3.34)$$

<sup>11</sup>Due to the non-linear behavior of solid matrix.

In which,  $\mathbf{C}^e$  is the (effective) elastic constitutive matrix, considering a linear elastic law. Thence, this matrix is obtained from the drained elastic parameters<sup>12</sup>.  $\dot{\boldsymbol{\varepsilon}}^P$  is the plastic component of strain. The *dot* notation is regarded to the variation between the deformed state and reference one ( ${}^{t+\Delta t}$  and  ${}^t$ ). Additionally,  $\dot{p}_w$  is defined as:

$$\dot{p}_w = \frac{\chi_w}{n} \left( -tr(\dot{\boldsymbol{\varepsilon}}) + \frac{\dot{S}}{\rho_w} - \dot{n}^P \right), \quad (3.36)$$

where  $n$  is the porosity and the superscript  ${}^P$  refers to the plastic part. The term of plastic porosity, i.e.  $\dot{n}^P$  - the void volume change due to the mechanical process - is neglected.  $S$  is the water mass content.

Indeed, these relations express the Hydro-Mechanical coupling: the  $H \xrightarrow{on} M$  is represented by the pore water pressure term in the effective stress formulation, and the  $M \xrightarrow{on} H$  is obtained through the role of volumetric strain in the statement of pore water pressure variation.

**Balance of momentum for the mixture:** In the weak form relation presented in Equation 3.16, the term  $G_i$  corresponds to the gravity volume force  $\rho g_i$  where  $g_i$  is the gravity acceleration. Considering a mixture of fluid and solid part in a coupled hydro-mechanical analysis, the specific mass in the force term  $\rho g_i$  follows Equation 3.18 to give the balance of momentum for the mixture as:

$$\int_{\Omega} \sigma_{ij} \varepsilon_{ij}^* d\Omega = \int_{\Omega} ((1-n)\rho_s + n\rho_w) g_i u_i^* d\Omega + \int_{\Gamma_{\sigma}} \bar{t}_i u_i^* d\Gamma \quad (3.37)$$

Since this relation is computed in the deformed state, the term  $(1-n)\rho_s + n\rho_w$ , mixture apparent specific mass (it may be denoted as  $\rho_m$  hereafter), should be obtained for the deformed configuration  ${}^{t+\Delta t}$ , which needs the porosity to be then updated for the deformed state. We recall that  $\rho_s$  is constant in Equation 3.37 assuming the incompressibility of the solid part, and the fluid compressibility, i.e. change of  $\rho_w$  is obtained through the Equation 3.23. Therefore, the porosity gets updated for the deformed configuration as the following.

**Mass balance equation for the solid phase:** Since we considered the updated Lagrangian formulation for the solid phase in which the current configuration is supposed to track the skeleton movement, the mass balance equation for solid skeleton is necessarily met. Thence, for a given mixture volume  $\Omega$ , its strong form is given by:

$$\frac{\partial (\rho_s (1-n)\Omega)}{\partial t} = 0 \quad (3.38)$$

Consequently, we can extend Equation 3.38 as:

$$\frac{\partial \rho_s}{\partial t} (1-n)\Omega - \frac{\partial n}{\partial t} \rho_s \Omega + \rho_s (1-n) \frac{\partial \Omega}{\partial t} = 0 \quad (3.39)$$

Then, considering the incompressibility of the solid part, it gives the variation of porosity as:

$$\frac{\partial n}{\partial t} = (1-n) \frac{\partial \Omega}{\partial t} \quad (3.40)$$

Hence, the updated porosity in the deformed configuration can be obtained as:

$${}^{t+\Delta t}n = {}^t n + (1-{}^t n) ({}^{t+\Delta t}\varepsilon_v - {}^t\varepsilon_v) \quad (3.41)$$

<sup>12</sup>For the Boom Clay at Mol site, they are taken as:  $E = 300$  and  $\nu = 0.125$ ; see Table 2.2. The drained properties may be also noted with the superscript  $'$ . However, in this thesis, we use the standard symbols *without any special indication by the superscript  $'$*  for all the properties such as  $E$ , and  $\nu$  as well as the cohesion  $c$  and friction angle  $\varphi$  hereafter, which are generally considered to be drained properties.

where  $\varepsilon_v$  is the volumetric strain.

### 3.2.5 Hydraulic equilibrium conditions

To accomplish the coupled hydro-mechanical analysis, we need to develop the boundary conditions and to define particularly the equilibrium statement for the fluid phase. Let consider a deformable body  $\Omega$  for which we aim to describe the hydraulic equilibrium conditions for a coupled analysis. A simple representation of the boundary surface is then shown in Figure 3.9 with respect to which the following conditions are true:

$$\Gamma_q \cup \Gamma_{p_w} = \Gamma \quad \text{and} \quad \Gamma_q \cap \Gamma_{p_w} = \emptyset \quad (3.42)$$

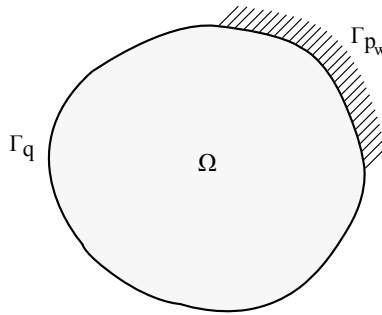


Figure 3.9: Definition of the boundaries  $\Gamma_{p_w}$  and  $\Gamma_q$  for the domain  $\Omega$ .

Hence, for any  $\mathbf{x} \in \Omega$ , the field of pore water pressure  $p_w$  is obtained in the framework of strong form of the initial boundary-value problem for an elementary volume  $\Omega$ , such that:

$$\dot{S} + \text{div } \mathbf{m} = Q \quad \text{in } \Omega \quad (3.43)$$

and,

$$p_w = \mathfrak{p}_w \quad \text{on } \Gamma_{p_w} \quad (3.44)$$

$$\mathbf{m}^T \cdot \mathbf{n} = \bar{q} \quad \text{on } \Gamma_q \quad (3.45)$$

where  $\dot{S}$  is the variation of water (fluid) mass content,  $\mathbf{m}$  is the water mass flow,  $Q$  is the water sink term,  $\mathfrak{p}_w$  is the water pressure prescribed on the boundary portion  $\Gamma_{p_w}$ ,  $\mathbf{n}$  is outward unit normal vector to  $\Gamma_q$ , and  $\bar{q}$  is the prescribed water mass per unit area on the boundary portion  $\Gamma_q$ .

**Mass balance equation for the fluid phase:** The Equations 3.43-3.45 are then expressed in the weak form following the principle of virtual work explained in Section 3.2.2.2. Thence, for an admissible virtual pore water pressure field  $p_w^*$ , the weak form of the balance equation for the fluid phase is stated for the current configuration as:

$$\int_{\Omega} \left( \dot{S} p_w^* - m_i \frac{\partial p_w^*}{\partial x_i} \right) d\Omega = \int_{\Omega} Q p_w^* d\Omega - \int_{\Gamma_q} \bar{q} p_w^* d\Gamma \quad (3.46)$$

where the left-hand side denotes the internal virtual work, and the right-hand side indicates the external virtual work.

The water mass in a volume  $\Omega$  is defined by:

$$S_\Omega = \rho_w n \Omega \quad (3.47)$$

To compute the variation of the water mass content, the water compressibility and volume change of skeleton is needed. The latter is given by Equation 3.40 assuming the incompressibility of solid grain part. In addition, water compressibility follows Equation 3.23 which can be reexpressed in the derivative form as:

$$\dot{\rho}_w = \frac{\rho_w}{\chi_w} \dot{p}_w \quad (3.48)$$

Thence, the time derivative of water mass (Equation 3.47) is obtained using Equations 3.40 and 3.48, such that:

$$\dot{S} = \rho_w \left( \frac{\dot{p}_w}{\chi_w} n + \frac{\dot{\Omega}}{\Omega} \right) \quad (3.49)$$

Indeed, this relation, as already explained (see Equation 3.36), represents the coupling effects between the skeleton and fluid phase by the simultaneous influence of the terms related to water and skeleton behavior.

Next, the water mass flow is described in the following.

**Balance of momentum for the fluid phase:** In addition to the balance of momentum for the mixture (Equation 3.37), the balance of momentum for the fluid phase is given by:

$$\frac{\partial p_w}{\partial x_j} + F_j^{s/w} + \rho_w g_j = 0 \quad (3.50)$$

where  $nF_j^{s/w}$  is the true drag force applied on water (fluid) by the skeleton for the current volume of the mixture, and  $F_j^{s/w}$  can be reexpressed through the restatement of Darcy's law (Equation 3.27) taking into account  $nV_i^{w/s} = V_i^d$  as brought in Equation 3.21; thence:

$$F_j^{s/w} = \frac{\mu_w n}{k_{ij}} V_i^{w/s} \quad (3.51)$$

The water mass flow  $m_i$  in Equation 3.46 can be hence obtained through Equation 3.21, with respect to Equations 3.51 and 3.50, such that:

$$m_i = -\rho_w \frac{k_{ij}}{\mu_w} \left( \frac{\partial p_w}{\partial x_j} + \rho_w g_j \right) \quad (3.52)$$

### 3.2.6 Discretization of the domain

In order to resolve the global non-linear problem, it is necessary to discretize the domain of problem over time and space. In fact, we aim to find the displacement and pressure so that they satisfy the skeleton and fluid constitutive equations and boundary conditions (weak form Equations 3.37 and 3.46) at any time  $t$ . In order to solve numerically this non-linear problem, we assume an algorithmic approximation to the exact solution at the times  $t + \Delta t$  and  $t$ , and we define the algorithmic approximations between these times via the interpolation formula [Simo and Hughes, 1998]. In fact, the loading process is assumed to be discretized (i.e. time discretization) into finite time steps  $\Delta t$ , and the system of equations is then solved for the sequential times  $0, \Delta t, 2\Delta t, 3\Delta t, \text{etc.}$ , and the variables are found so that in each time step, for

instance, the displacement and pressure are defined as follows:

$$u_i = (1 - \beta) u_i^t + \beta u_i^{t+\Delta t} \quad (3.53)$$

$$p_w = (1 - \beta) p_w^t + \beta p_w^{t+\Delta t} \quad (3.54)$$

The choice of  $\beta$  is made between 0 and 1 so that:

$\beta = 0$  refers to fully explicit, forward Euler interpolation scheme; it is explicit since all the variables required to be computed are known at the beginning of the time step;

On the contrary,

$\beta = 1$  refers to fully implicit, backward Euler interpolation scheme;

And,

$\beta = 0.5$  refers to mid-point rule, linear interpolation scheme (Crank-Nicholson scheme).

The two last methods need iteration process since the variables aimed to be computed are not known. For a linear system, the unconditional stability is obtained by the choice of  $\beta \geq 0.5$  [Zienkiewicz and Taylor, 2000]. Although, we may consider a full implicit scheme, i.e.  $\beta = 1$ , for a highly non-linear system of equations.

Next, the finite element method induces a discretization of the continuum  $\Omega$  (i.e. space discretization) into a finite number of elements,  $n^{el}$  with the volume  $\Omega^{el}$  (see Figure 3.10) such that:

$$\Omega = \bigcup_{el=1}^{n^{el}} \Omega^{el} \quad (3.55)$$

These  $n^{el}$  elements are connected at their nodal points to which the primary unknowns correspond, i.e. coordinates, displacements, velocities and pore water pressures (both mechanical and hydraulic variables). These variables are then expressed for each element by interpolation over their correspondence at the elements' nodal points using the shape functions. In LAGAMINE, the isoparametric elements (from Serendipity family) are used. The term isoparametric means that the same shape functions (i.e. interpolation polynomials) are used to define the geometrical coordinates and displacements over the element. The structure and properties of shape functions, and the concept of isoparametric elements are extensively discussed in many finite element book such as Bathe [1996]; Zienkiewicz and Taylor [2000]; Quek and Liu [2003], and they are not aimed to be detailed in this work. Thence, the following framework is extended assuming a preknowledge on these basic concepts. In addition, the description is given for an example of the special case of two-dimensional analysis in plane strain conditions.<sup>13</sup>

Hence, considering three degrees of freedom for each node belonging to  $\Omega^{el}$  - *two coordinates* ( $\mathbf{x}$ ) and displacements ( $\mathbf{u}$ ) correspond to two global directions, and *a pore water pressure* ( $p_w$ ) and its variations ( $\Delta p_w$ ) - the finite element process seeks the solution over this element in the approximate form of:

$$\mathbf{x}^{el} \approx \hat{\mathbf{x}} = \sum_{en=1}^{n_{en}} N_{en} \mathbf{x}_{en} \quad \text{and} \quad \mathbf{u}^{el} \approx \hat{\mathbf{u}} = \sum_{en=1}^{n_{en}} N_{en} \mathbf{U}_{en} \quad (3.56)$$

<sup>13</sup>Two types of isoparametric elements in LAGAMINE are mainly used in this work: CSOL2, and SGRC2. The both can be applied to a plane strain or axisymmetric analysis. The latter element is associated to a second gradient analysis which will be extensively used in next Chapters. Therefore, the equations and description in this Chapter are being performed to address our general numerical simulations in classical poromechanics, and the extension of the formulation and the used element for a second gradient analysis will be described in Chapter 5.

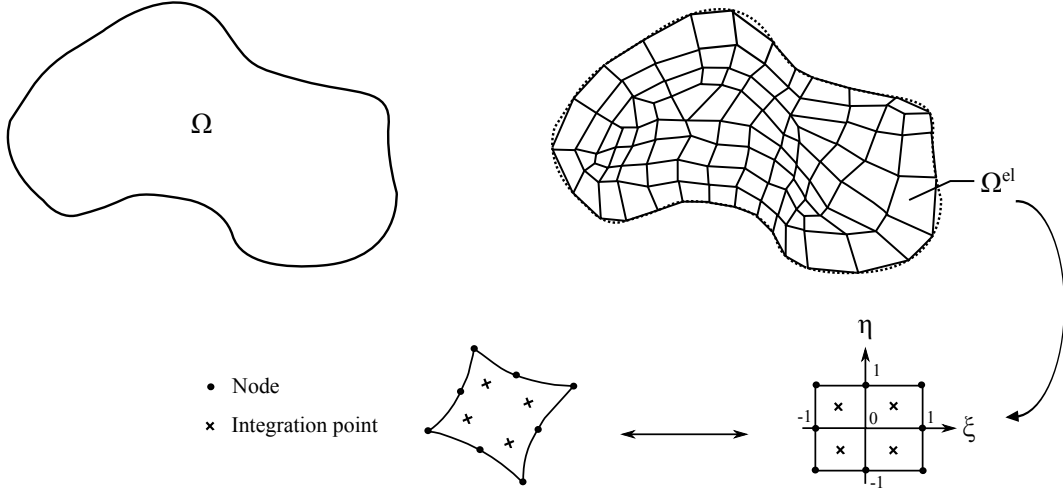


Figure 3.10: Discretization of the domain  $\Omega$  to  $n^{el}$  elements with volume  $\Omega^{el}$ ; at the bottom, quadrilateral element is shown on the left-hand side, and the corresponding parent element in the isoparametric local coordinate of  $(\xi, \eta)$  is shown on the right-hand side.

$$p_w^{el} \approx \hat{p}_w = \sum_{en=1}^{n_{en}} N_{en} P_{w,en} \quad \text{and} \quad \Delta p_w^{el} \approx \Delta \hat{p}_w = \sum_{en=1}^{n_{en}} N_{en} \Delta P_{w,en} \quad (3.57)$$

where the subscript  $en$  refers to the corresponding variable at the  $en^{th}$  node of the element, and  $N$  describes the shape function, for the nodal interpolation, in the local coordinates  $(\xi, \eta)$ .

Let consider the internal virtual work following Equation 3.16 as:

$$\mathcal{W}_I^{*el} = \int_{\Omega^{el}} \sigma_{ij} \frac{1}{2} \left( \left( \frac{\partial u_i^*}{\partial x_j} \right) + \left( \frac{\partial u_j^*}{\partial x_i} \right) \right) d\Omega \quad (3.58)$$

In which, the gradient of the virtual displacement can be defined such as:

$$\frac{\partial u_i^*}{\partial x_j} = \frac{\partial N_{en}}{\partial x_j} U_{en,i}^* \quad (3.59)$$

where  $en$  varies between 1 and the number of the element nodes  $n_{en}$ . The spatial derivative of the shape functions are expressed in the local coordinates as:

$$\frac{\partial N_{en}}{\partial x_j} = \frac{\partial N_{en}}{\partial \xi} \frac{\partial \xi}{\partial x_j} + \frac{\partial N_{en}}{\partial \eta} \frac{\partial \eta}{\partial x_j} \quad (3.60)$$

The Jacobian matrix  $\mathbf{J}$  for mapping from the local coordinates  $(\xi, \eta)$  to the global coordinates  $(x_1, x_2)$  is defined by Equation 3.61 considering which the spatial derivatives with regard to the local coordinates  $(\xi, \eta)$  is evaluated.

$$\mathbf{J} = \begin{bmatrix} \frac{\partial x_1}{\partial \xi} & \frac{\partial x_1}{\partial \eta} \\ \frac{\partial x_2}{\partial \xi} & \frac{\partial x_2}{\partial \eta} \end{bmatrix} \quad (3.61)$$

that  $\det \mathbf{J}$  is identified to be non-zero.

Using the shape functions (i.e. interpolation functions), we apply the Gaussian quadrature to integrate over an element. Indeed, the constitutive responses are tracked and stored in the

Gauss integration point  $IP$ , and the sum of all these integrant gives the evaluated response over an element; e.g. it describes, in sum, the element internal virtual work, such that:

$$\mathscr{W}_I^{\star el} = \sum_{IP=1}^{n_{IP}} \left[ \sigma_{ij} \frac{1}{2} \left( \frac{\partial N_{en}}{\partial x_j} U_{en,i}^{\star} + \frac{\partial N_{en}}{\partial x_i} U_{en,j}^{\star} \right) t \det \mathbf{J} W_{IP} \right] \quad (3.62)$$

where  $n_{IP}$  is the number of integration (quadrature) points,  $t$  is the element thickness (which is equal to unit for the two-dimensional plane elements), and  $W_{IP}$  is the Gauss weight corresponding to the integration point  $IP$ . This relation can be expressed in terms of the so-called energetically equivalent nodal forces, for two mechanical degrees of freedom, along the global axis  $x_1$  and  $x_2$ , such that:

$$\mathscr{W}_I^{\star el} = \mathcal{F}_{I,en,1}^{el} U_{en,1}^{\star} + \mathcal{F}_{I,en,2}^{el} U_{en,2}^{\star} \quad (3.63)$$

and,

$$\mathcal{F}_{I,en,1}^{el} = \sum_{IP=1}^{n_{IP}} \left[ \left( \sigma_{11} \frac{\partial N_{en}}{\partial x_1} + \sigma_{12} \frac{\partial N_{en}}{\partial x_2} \right) \det \mathbf{J} W_{IP} \right] \quad (3.64)$$

$$\mathcal{F}_{I,en,2}^{el} = \sum_{IP=1}^{n_{IP}} \left[ \left( \sigma_{12} \frac{\partial N_{en}}{\partial x_1} + \sigma_{22} \frac{\partial N_{en}}{\partial x_2} \right) \det \mathbf{J} W_{IP} \right] \quad (3.65)$$

The internal equivalent nodal force can be similarly found for the hydraulic part (hydraulic degree of freedom) with respect to Equation 3.46. The hydraulic and mechanical nodal forces are in fact gathered together for  $n_{en}$  nodes of an element to make a generalized equivalent internal nodal force vector of the element  $\mathcal{F}_I^{el}$ . In addition, the energetically equivalent body force vector, and generally the external nodal force vector over an element can be also derived in the similar manner, with respect to Equations 3.46 and 3.37, sampling the corresponding contribution at the quadrature points for  $n_{en}$  nodes of the element. Then, the so-called element out of balance force can be expressed by:

$$\mathcal{F}_{\mathbf{OBF}}^{el} = \mathcal{F}_I^{el} - \mathcal{F}_E \quad (3.66)$$

### 3.2.7 LAGAMINE resolution algorithm

The resolution of the non-linear global problem can be achieved through introducing the global out of balance forces  $\mathbf{F}_{\mathbf{OBF}}$  (Equation 3.67). Hence, if  $\mathbf{F}_{\mathbf{OBF}}^i$  is the out of balance force encountered at the iteration  $i$  of the current time step, it is aimed to be vanished (event though it might not be exactly equal to zero) to get equilibrium.

$$\mathbf{F}_{\mathbf{OBF}} = \mathbf{A} \sum_{el=1}^{n^{el}} \mathcal{F}_{\mathbf{OBF}}^{el} \quad (3.67)$$

where  $\mathbf{A}$  denotes the standard, finite element, assembly operator [Hughes, 1987].

Using the Taylor series, and discarding the terms with the degree higher than one, the out of balance force can be expanded as Equation 3.68. Thence, the Newton-Raphson procedure is followed to predict a new solution corresponding to  $\mathbf{u}^{i+1}$ . Indeed, the non-linear problem is handled through the linearization of the field equations through which the one can take of the error at the iteration  $i + 1$ . Hence, the iterative process is continued until the equilibrium is reached and the error is tended to zero (although it would never be exactly zero).

$$\mathbf{F}_{\mathbf{OBF}}^{i+1} = \mathbf{F}_{\mathbf{OBF}}^i + \frac{\partial \mathbf{F}_{\mathbf{OBF}}^i}{\partial \mathbf{u}_{en}} \delta \mathbf{u}_{en} \quad (3.68)$$

where  $\delta \mathbf{u}_{en}$  refers to the global corrections on the generalized coordinates vector, i.e. both mechanical displacement, and pore pressure variations (both mechanical and hydraulic terms). To get equilibrium at the end of iterative procedure, the out of balance force should be null, i.e.  $\mathbf{F}_{\text{OBF}}^{i+1} \simeq 0$ , such that the corrections are obtained as:

$$\delta \mathbf{u}_{en} = - \left[ \frac{\partial \mathbf{F}_{\text{OBF}}^i}{\partial \mathbf{u}_{en}} \right]^{-1} \cdot \mathbf{F}_{\text{OBF}}^i \quad (3.69)$$

and,

$$\left[ \frac{\partial \mathbf{F}_{\text{OBF}}^i}{\partial \mathbf{u}_{en}} \right] = [\mathbf{K}^i] \quad (3.70)$$

where  $\mathbf{K}^i$  is the stiffness matrix at the iteration  $i$ . The global stiffness matrix can be obtained by assembling the elementary matrices while the latter contains the contribution of the derivation of the nodal forces with respect to the generalized coordinates.

Thence, the corrections on generalized coordinates (both mechanically and hydraulically) are added to their relative current value, in order to predict a new solution, i.e. new configuration and new pore pressure field, closer to the well-balanced configuration.

$$\mathbf{u}_{en}^{i+1} = \mathbf{u}_{en}^i + \delta \mathbf{u}_{en} \quad (3.71)$$

Then, the equilibrium is re-checked, and this procedure may be continued with regard to the obtained out of balance forces and generalized displacements (i.e. global corrections on the generalized coordinates vector). It is noteworthy that in LAGAMINE, the precision of the computed solution can be controlled with respect to which the convergence can be obtained when the norm of out of balance forces (and/or norm of generalized displacements) satisfy the given convergence criterion (see Appendix A).

*The resolution procedure in LAGAMINE is then summarized, for one time step, as the following<sup>14</sup>:*

1. Consider a time step  $\Delta t$ , and the initial configuration at the beginning of the step such as: stresses and pore pressure;
2. The nodal coordinates are updated for the first iteration ( $i = 1$ ) with an assumption on the final configuration and final pressure for the current step;
3. The iterative procedure is launched for the iteration  $i$ ;
4. For each element:
  - ✓ For each integration point:
    - The strain and rotation rates as well as the pore pressure rate are computed;
    - Using the constitutive equations and flow model, the variation of effective stress as well as mass flow are computed;
    - The updated effective stress is obtained by integration over time;
    - The total stress is computed;
    - The compliance matrices are obtained with respect to the perturbation method [Charlier, 1987].
  - ✓ The element out of balance forces are obtained with regard to the energetically equivalent nodal forces;

---

<sup>14</sup>The explained general procedure will be detailed in Section 5.3.3 for an analysis involving second gradient model.

- ✓ The element stiffness matrix is computed;
- 5. The global out of balance forces are computed;
- 6. The global stiffness matrix is assembled and inverted;
- 7. The corrections on the nodal displacement fields and pore pressure field are computed;
- 8. Convergence on a norm of out of balance forces and norm of generalized displacements is checked with respect to a given precision which is prescribed by the user:
  - ✓ If the convergence is reached: go to 9;
  - ✓ If no convergence: the correction is made, and the final configuration and final pore pressure are then updated for a new iteration, go to 3;
- 9. End of the time step.

### 3.3 Elasto-plasticity

#### 3.3.1 General concept

A material in the elastic domain tends to return to its original state after being deformed. Therefore, the strain produced by a given loading is reversible upon unloading and then, no energy is dissipated by the material during loading. In other words, the material remembers always its stress-free configuration [Kolymbas, 1991]. The linear elasticity law is defined by a stress state which is directly related to elastic strain through a linear relation following the Hooke's law [Lemaitre et al., 2009], so that under the definition of effective stress, it gives:

$$\boldsymbol{\sigma}' = \mathbb{C}^e : \boldsymbol{\varepsilon}^e \quad \text{or} \quad \sigma'_{ij} = \mathbb{C}^e_{ijkl} \varepsilon^e_{kl} \quad (3.72)$$

where  $\mathbb{C}^e = \mathbb{C}^e_{ijkl}$ <sup>15</sup> is a fourth order tensor usually called the elasticity tensor. This tensor for an isotropic material can be defined by two elastic parameters which may be: Young modulus ( $E$ ) and Poisson's ratio ( $\nu$ ) as:

$$\mathbb{C}^e_{ijkl} = \frac{E}{1+\nu} \delta_{ik} \delta_{jl} + \frac{E\nu}{(1+\nu)(1-2\nu)} \delta_{ij} \delta_{kl} \quad (3.73)$$

where  $\delta_{ij}$  is the Kronecker delta defined by:

$$\delta_{ij} = \begin{cases} 1 & \text{if } i = j \\ 0 & \text{if } i \neq j \end{cases} \quad (3.74)$$

Thence, Equation 3.73 gives the symmetrical tensor of:

$$\mathbb{C}^e = \frac{E(1-\nu)}{(1+\nu)(1-2\nu)} \begin{bmatrix} 1 & \frac{\nu}{1-\nu} & \frac{\nu}{1-\nu} & 0 & 0 & 0 \\ & 1 & \frac{\nu}{1-\nu} & 0 & 0 & 0 \\ & & 1 & 0 & 0 & 0 \\ & & & \frac{1-2\nu}{2(1-\nu)} & 0 & 0 \\ \text{Sym.} & & & & \frac{1-2\nu}{2(1-\nu)} & 0 \\ & & & & & \frac{1-2\nu}{2(1-\nu)} \end{bmatrix} \quad (3.75)$$

<sup>15</sup>As it has been already mentioned, the indicial notation might be adopted all through this thesis to provide more readability.

Using the definition of bulk modulus ( $K = E/3(1 - 2\nu)$ ) and shear modulus ( $G = E/2(1 + \nu)$ ), the elastic tensor may be also expressed in terms of these two elastic parameters as follows:

$$\mathbb{C}_{ijkl}^e = 2G\delta_{ik}\delta_{jl} + \left(K - \frac{2}{3}G\right)\delta_{ij}\delta_{kl} \quad (3.76)$$

On the contrary to elasticity, plasticity describes the non-reversibility of the original state of a material which is being deformed upon loading, even once the applied forces are removed. Then the current state of the material depends on its deformation path. Hence, there is a quantity of energy which is dissipated by the material upon loading and it is not recoverable thereafter. Consequently, the work done by the stresses on the change of plastic (permanent) strain, i.e. the work expanded on the plastic deformation, should be positive (i.e.  $\sigma'_{ij}\varepsilon^p_{ij} > 0$ ), stated by Prager [1949] as the *condition of irreversibility*.

Then, *elastoplasticity* is a conjunction of elasticity and plasticity [Kolymbas, 1991]. The total strain is then considered as the sum of the reversible *elastic strain* and permanent *plastic strain* [Prager, 1949]<sup>16</sup>, such that:

$$\varepsilon_{ij} = \varepsilon_{ij}^e + \varepsilon_{ij}^p \quad (3.77)$$

Hence, Equation 3.72 can be rewritten as:

$$\sigma'_{ij} = \mathbb{C}_{ijkl}^e (\varepsilon_{kl} - \varepsilon_{kl}^p) \quad (3.78)$$

This statement of elasticity law may not be applied in the domain of large deformation, though. Its description in the rate form for any applied load that produces additional plastic strain, induces using the strain rate (or, rate of deformation) ( $\dot{\sigma}'_{ij} = \mathbb{C}_{ijkl}^e (\dot{\varepsilon}_{kl} - \dot{\varepsilon}_{kl}^p)$ ) [Lemaitre et al., 2009]. As it has been brought in Section 3.2.1, the application of an objective derivative of stress instead of  $\dot{\sigma}'_{ij}$  must be then adopted to define the problem in the zone of large deformation. Thence, the elasticity law takes the form of *hypo-elasticity* as:

$$\tilde{\sigma}'_{ij} = \mathbb{C}_{ijkl}^e (\dot{\varepsilon}_{kl} - \dot{\varepsilon}_{kl}^p) \quad (3.79)$$

Moreover, the decomposition of total deformation is not additive as for finite deformation, but rather multiplicative:

$$F_{ij} = F_{ik}^e F_{kj}^p \quad (3.80)$$

where  $F_{ik}^e$  and  $F_{kj}^p$  denote the gradient of elastic and plastic deformation, respectively. Hence, the transformation of the initial configuration to the current configuration  $dx_i = F_{ij}dX_j$  is supposed to be defined as a plastic pass from the initial state to an intermediate state by  $d\bar{X}_k = F_{kj}^p dX_j$  and then an elastic transformation from the intermediate state to the current configuration by  $dx_i = F_{ik}^e d\bar{X}_k$  [Lemaitre et al., 2009].

### 3.3.2 Yield surface

A distinction between the elastic state of stress and the yield point in the stress space is established by means of a so-called yield surface, or yield criterion. Inside the yield surface, state of stress is elastic, and when the stress state lies on the surface, the material is said to reach to its yield point and it then becomes plastic. On the other words, the yield criterion is a condition which defines the limit of elasticity and the beginning of plastic deformation under any possible

<sup>16</sup>From a physical point of view, this distinction is rather artificial since it can hardly be achieved by experiment [Kolymbas, 1991].

combination of stresses [Burland and Yu, 2007]. Thence, the permanent (irreversible) deformation can occur once the yield condition is reached. Following the classic plasticity theory, the yield criterion can be generally expressed in function of the effective stress  $\sigma'_{ij}$  and one or several internal variables  $\zeta$ , such that:

$$f(\sigma'_{ij}, \zeta) = 0 \quad (3.81)$$

Figure 3.11 represents the different domains defined by a yield surface. Thence, the material behavior is assumed to be elastic inside the yield surface. For any combination of stresses which lies on the yield surface, the material is in the plastic domain, and the stress state outside of the yield surface is not admissible.

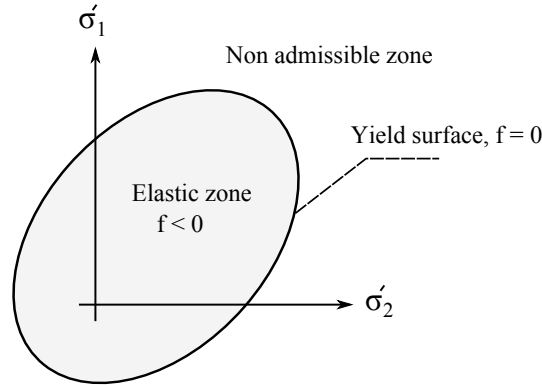


Figure 3.11: Representation of the different domains defined by a yield surface in the stress space.

### 3.3.3 Flow rule and potential surface

Flow rule defines the increment of plastic strain in a material after it hits its yield limit, which is presented in a general form of:

$$\dot{\epsilon}_{ij}^p = \dot{\lambda} \frac{\partial g}{\partial \sigma'_{ij}} \quad (3.82)$$

where  $\dot{\lambda}$  is called plastic multiplier and it characterizes the magnitude of plastic strain rate. It is a non-negative variable which is positive if the stress state is plastic and it is null if the stress state is elastic. In addition,  $\partial g / \partial \sigma'_{ij}$  governs the direction of plastic strain increment where  $g$  is plastic potential function. This function is defined with respect to the current stress state point of the material and its gradient as a function of stresses gives a unique direction with regard to the plastic potential  $g$ .

The plastic potential  $g$  can be the same as the yield function  $f$ , that signifies the plastic flow is determined from the yield function. In this case, the plastic flow rule is called *associated* (Figure 3.12). However, experimental evidence suggests that a *non-associated* plastic flow, where the plastic strain increment is not generated by the gradient of the yield function, may provide a more realistic description of actual material behavior [Borja, 2013].

Combining Equation 3.79, and Equation 3.82 in its incremental form, give the rate form stress-strain relation as:

$$\tilde{\sigma}'_{ij} = \mathbb{C}_{ijkl}^e \left( \dot{\epsilon}_{kl} - \dot{\lambda} \frac{\partial g}{\partial \sigma'_{kl}} \right) \quad (3.83)$$

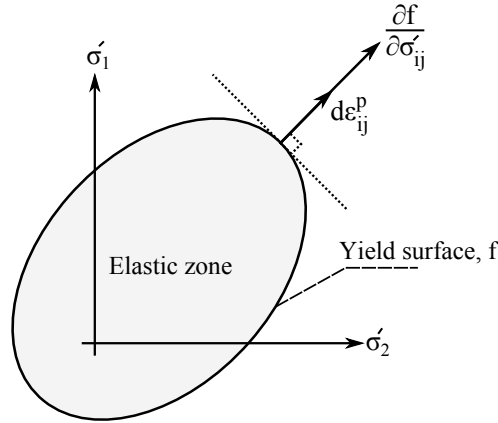


Figure 3.12: Direction of plastic strain increment for an associated plastic flow.

### 3.3.4 Consistency conditions

Considering the stress state of a material, it can behave in two ways: it may deform elastically, then  $\dot{\lambda} = 0$  and  $f(\sigma'_{ij}, \zeta) < 0$ ; or it may deform plastically, then  $\dot{\lambda} > 0$  and  $f(\sigma'_{ij}, \zeta) = 0$ . Therefore, there is generally the restriction of  $\dot{\lambda} \geq 0$  and  $f(\sigma'_{ij}, \zeta) \leq 0$ . Hence, the following expression holds [Kuhn and Tucker, 1951]:

$$\dot{\lambda} f(\sigma'_{ij}, \zeta) = 0 \quad (3.84)$$

These conditions, called Karush-Kuhn-Tucker conditions, must be satisfied in either plastic or elastic domain of a material response. In the plastic state, as a consequence of the condition 3.84, and taking its time derivative, the following expression can be obtained:

$$\dot{\lambda} \dot{f}(\sigma'_{ij}, \zeta) = 0 \quad \xrightarrow{\dot{\lambda} > 0} \quad \dot{f}(\sigma'_{ij}, \zeta) = 0 \quad (3.85)$$

This last condition is called the *consistency condition*. Indeed, this condition simply guarantees that as long as the material is in the plastic state, the yield criterion is satisfied, and the stress state lies on the yield surface. On the other words, loading from a plastic state must again lead to a plastic state as described by Prager [1949].

### 3.3.5 Hardening/softening response and hardening rule

Since the stress state point hits the yield limit ( $f = 0$ ), any infinitesimal change of stress from that given plastic state can be classified as: In the first case, this change may be directed towards the exterior of the yield surface ( $df > 0$ ), which must be lead to another plastic state as the consequence of consistency condition; the change of stress in this sense is said to be *loading*. In the second case, it may lie on the yield limit upon arrival ( $df = 0$ ); which is said to be *neutral*. In the third case, the change of stress leads to an elastic state ( $df < 0$ ); which is said to be *unloading* [Prager, 1949] (see Figure 3.13).

Then, following the condition of consistency and non-admissibility of the exterior of the yield surface, there may be some evolution of the initial yield surface leading to a/several subsequent surface(s). In this sense, the material is said to remain in the elastic state if any infinitesimal change of stress does not leave any permanent strain, and if this condition is not fulfilled, the material is said to be in the plastic state where the elasticity limit evolves to satisfy again the

condition of  $f = 0$  with respect to the consistency condition. Therefore, with the assumption of an infinitesimal change of stress  $d\sigma_{ij}$  which leaves the plastic strain, we would have [Lemaitre et al., 2009]:

$$f(\sigma'_{ij} + d\sigma'_{ij}, \zeta + d\zeta) = 0 \quad (3.86)$$

Figure 3.13 shows a subsequent yield surface in order to satisfy this condition, and to have  $f = 0$  at any time. Hence,  $\dot{f} = 0$ , such that:

$$df = \frac{\partial f}{\partial \sigma'_{ij}} \tilde{\sigma}'_{ij} + \frac{\partial f}{\partial \zeta} \dot{\zeta} = 0 \quad (3.87)$$

Considering the hypothesis that the internal variable is linked to the plastic strain (also called

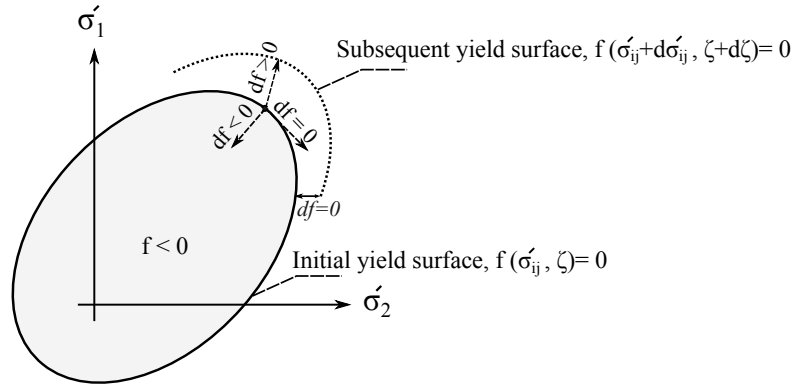


Figure 3.13: The criterion of loading, neutral and unloading; and the evolution of yield surface with respect to the consistency condition .

the strain hardening hypothesis [Desai and Siriwardane, 1984]), Equation 3.87 may be rewritten as:

$$df = \frac{\partial f}{\partial \sigma'_{ij}} \tilde{\sigma}'_{ij} + \frac{\partial f}{\partial \varepsilon_{ij}^p} \frac{\partial \varepsilon_{ij}^p}{\partial \lambda} \dot{\lambda} = 0 \quad (3.88)$$

Combining this relation with Equation 3.83 gives the plastic multiplier increment as:

$$\dot{\lambda} = \frac{\frac{\partial f}{\partial \sigma'_{ij}} \mathbb{C}_{ijkl}^e \dot{\varepsilon}_{kl}}{\frac{\partial f}{\partial \sigma'_{ij}} \mathbb{C}_{ijkl}^e \frac{\partial g}{\partial \sigma'_{kl}} - \frac{\partial f}{\partial \varepsilon_{ij}^p} \frac{\partial \varepsilon_{ij}^p}{\partial \lambda}} \quad (3.89)$$

so that the *hardening modulus*  $\mathcal{H}$  is defined as:

$$\mathcal{H} = \frac{\partial f}{\partial \sigma'_{ij}} \mathbb{C}_{ijkl}^e \frac{\partial g}{\partial \sigma'_{kl}} - \frac{\partial f}{\partial \varepsilon_{ij}^p} \frac{\partial \varepsilon_{ij}^p}{\partial \lambda} \quad (3.90)$$

The parameter  $\mathcal{H}$  may be interpreted as the slope of the stress-strain curve after removing the elastic component of strain [Borja, 2013]. Since the plastic strain occurs, i.e.  $\dot{\lambda} > 0$ , the stress can then increase or decrease with plastic deformation depending on the sign of  $\mathcal{H}$ . If  $\mathcal{H} > 0$ , one speaks of a *strain-hardening* response; if  $\mathcal{H} = 0$ , one speaks of a *perfectly plastic response*; and if  $\mathcal{H} < 0$ , one speaks of a *strain-softening response*<sup>17</sup> [Simo and Hughes, 1998]. Figure 3.14 shows these different elasto-plastic responses for an one-dimensional bar.

<sup>17</sup>There is although some restriction in the lowest acceptable value of  $\mathcal{H}$  below which there may be some snap back; the interested reader may refer to [Borja, 2013].

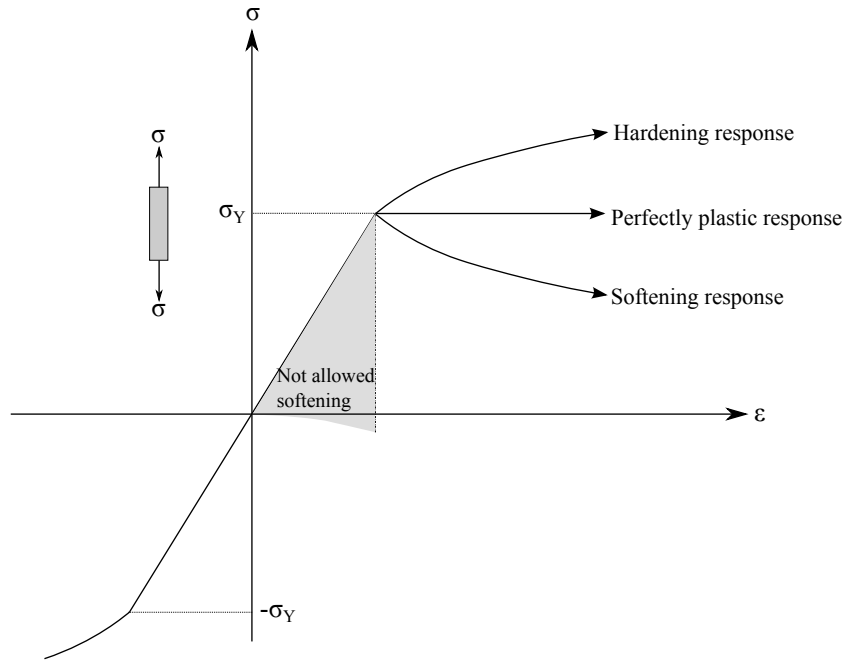


Figure 3.14: The different behavior response for a bar under uniaxial loading,  $\sigma_y$  is the yield stress; after [Simo and Hughes, 1998].

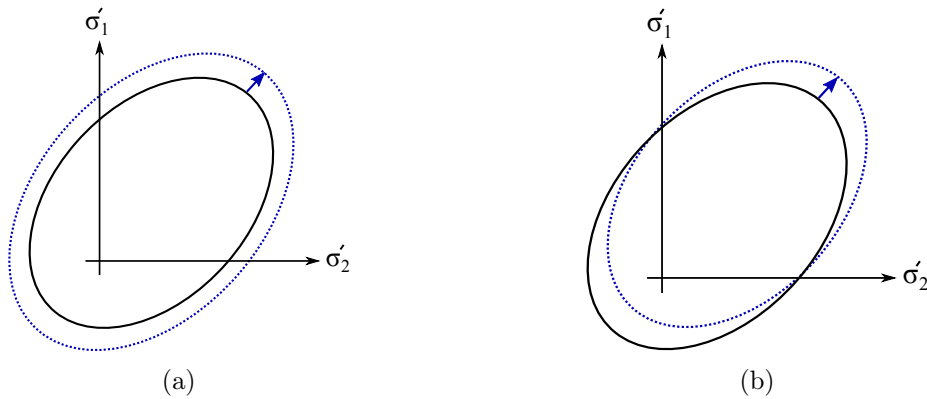


Figure 3.15: (a) Isotropic hardening. (b) kinematic hardening.

*Hardening rule* is then introduced to define the evolution of yield surface, i.e. elasticity limit, with the plastic deformation [Lemaitre et al., 2009]. Thence, besides the above physical interpretation of the response of a material, this response can be described, in the numerical point of view, with respect to how the yield surface evolves. Apart from the *perfect plasticity* where the yield surface remains constant, it may have *isotropic hardening* or/and *kinematic hardening*. In the former, the yield surface may shrink, i.e. *softening response*, or expand, i.e. *hardening response* (Figure 3.15a). In the latter, the yield surface is translated within the stress space, and its size remains unchanged (Figure 3.15b), that this type is common to model the hysteresis formed under cyclic loadings, and we don't deal with it in this thesis. Whatever the hardening approach is, the hardening rule must be applied to describe the evolution of the yield surface.

## 3.4 Internal frictional behavior models for geomaterials

### 3.4.1 Stress conventions

Stress tensor has generally six independent components in three-dimensions, and it can be represented by a symmetrical  $3 \times 3$  tensor as:

$$\sigma_{ij} = \begin{bmatrix} \sigma_{11} & \sigma_{12} & \sigma_{13} \\ & \sigma_{22} & \sigma_{23} \\ Sym. & & \sigma_{33} \end{bmatrix} \quad (3.91)$$

Figure 3.16 illustrates the components of the stress tensor in 3D. These are assumed to be positive in traction and negative in compression, following the sign convention in classical continuum mechanics. Moreover, knowing the stress tensor at a point, it is possible to find a new referential system (by rotating the original coordinate system) where the shear stresses are zero, and then the stress tensor is diagonal (Equation 3.92). The new coordinate's directions are the principle directions, which are perpendicular to the so-called principle planes.

$$\sigma_i = \begin{bmatrix} \sigma_1 & 0 & 0 \\ 0 & \sigma_2 & 0 \\ 0 & 0 & \sigma_3 \end{bmatrix} \quad (3.92)$$

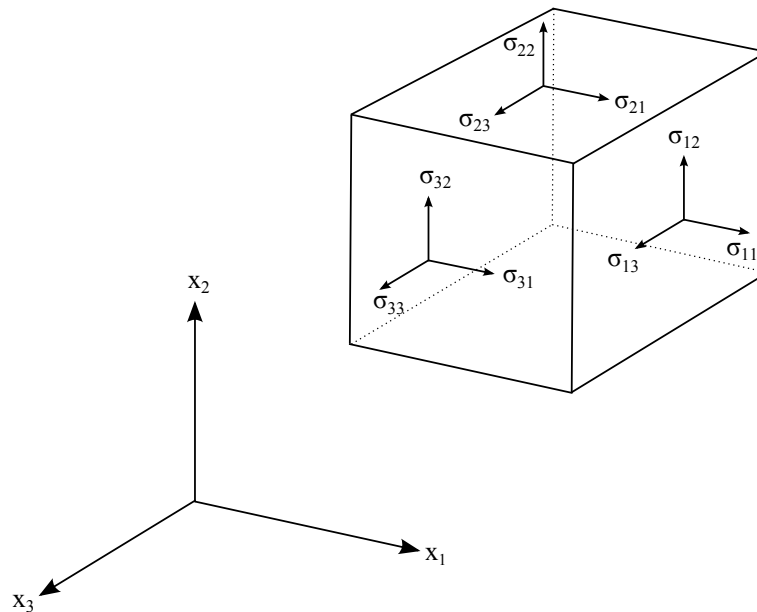


Figure 3.16: Components of the stress tensor in 3D for a representative elementary volume.

The stress tensor can be described by three stress tensor invariants:  $I_\sigma$  (first stress tensor invariant),  $II_{\hat{\sigma}}$  (second deviatoric stress tensor invariant) and  $III_{\hat{\sigma}}$  (third deviatoric stress tensor invariant). The invariants of the deviatoric stress are frequently used in failure criteria. These three invariants, with respect to the effective stresses, are defined in an usual way as:

$$I_\sigma = \sigma'_{ii} \quad (3.93)$$

$$II_{\hat{\sigma}} = \sqrt{\frac{1}{2} \hat{\sigma}'_{ij} \hat{\sigma}'_{ij}}, \quad \text{with} \quad \hat{\sigma}'_{ij} = \sigma'_{ij} - \frac{I_{\sigma}}{3} \delta_{ij} \quad (3.94)$$

$$III_{\hat{\sigma}} = \frac{1}{3} \hat{\sigma}'_{ij} \hat{\sigma}'_{jk} \hat{\sigma}'_{kl} \quad (3.95)$$

The third deviatoric stress tensor invariant is commonly expressed in terms of the Lode angle  $\beta$  in the deviatoric plane, such that:

$$\beta = -\frac{1}{3} \sin^{-1} \left( \frac{3\sqrt{3} III_{\hat{\sigma}}}{2 II_{\hat{\sigma}}^3} \right), \quad \text{and} \quad \beta \in [-30^\circ, +30^\circ] \quad (3.96)$$

Hence, the three components  $I_{\sigma}$ ,  $II_{\hat{\sigma}}$ , and  $\beta$  characterize a cylindrical referential around the  $I_{\sigma}$  axis in the  $\Pi$  plane (deviatoric plane). In this plane as it is shown in Figure 3.17, the second invariant  $II_{\hat{\sigma}}$  describes the distance of stress state  $\sigma'$  from the  $I_{\sigma}$  axis, and the Lode angle  $\beta$  is the direction of the stress state with regard to the pure shear line.

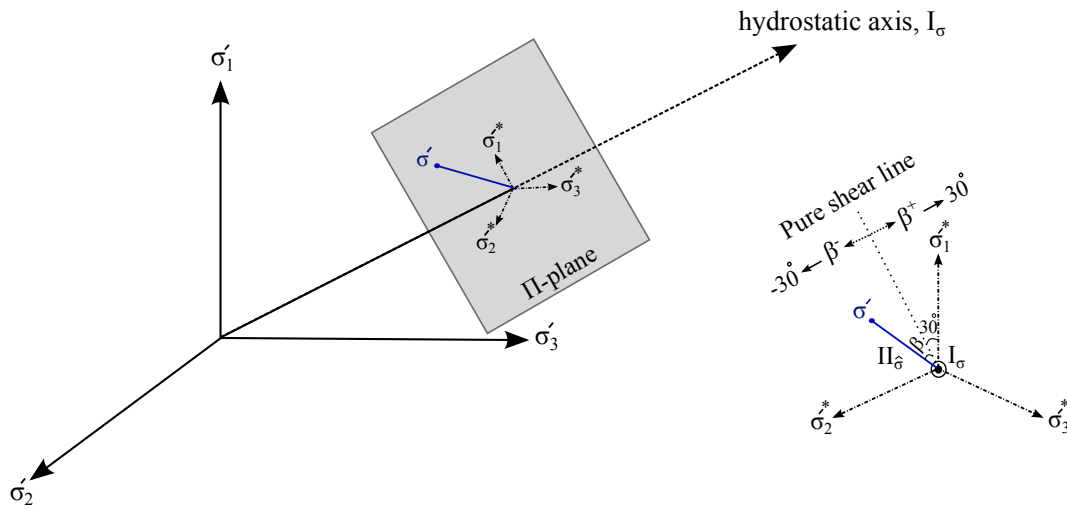


Figure 3.17: Representation of the stress state in the principle stress space (left side), and in the deviatoric plane (right side);  $\sigma_i^*$  is the projection of the principle stress direction on the deviatoric plane.

Another set of quantities  $(p', q)$ , i.e. the mean (or, hydrostatic) stress and deviatoric stress, are also commonly used to describe yield surfaces for cohesive frictional materials such as rocks and soils. They are defined as:

$$p' = \frac{I_{\sigma}}{3} \quad (3.97)$$

$$q = \sqrt{3} II_{\hat{\sigma}} \quad (3.98)$$

### 3.4.2 Representation of the yield surfaces for an internal frictional constitutive law

The most familiar internal-friction criterion is the Mohr-Coulomb failure criterion in which the normal effective stress on a failure plane,  $\sigma'_N$ , is linearly related to the shear stress  $\tau$ , such that:

$$\tau = c - \sigma'_N \tan \varphi \quad (3.99)$$

where  $\sigma'_N$  is the normal effective stress.  $c$ , the cohesion, and  $\varphi$ , the friction angle (determines the slope of the failure envelop) are the drained properties. On the whole, they describe the Mohr-failure relation, commonly used in geotechnical engineering, to define the shear strength of soils and rocks at different effective stresses. Figure 3.18a shows this criterion. Let consider the normal and shear stresses,  $\sigma'_N$  and  $\tau$ , acting on a plane of known orientation, plane  $A - A'$ , in a soil element as shown in Figure 3.18b. Then, these stresses may define a stress state of  $B$ ,  $C$  or  $D$  in Figure 3.18a.  $B$  corresponds to a state where the shear failure does not occurred,  $C$  describes the shear failure along the surface  $A - A'$ , and  $D$  is not admissible (i.e. does not exist).

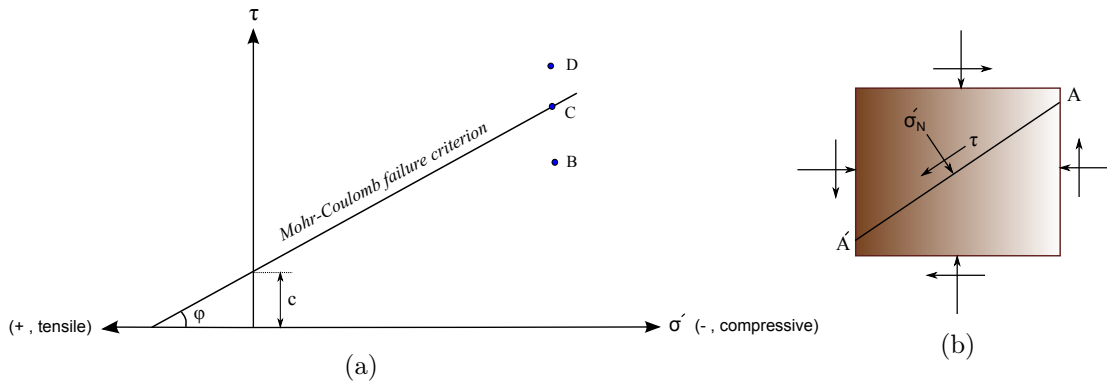


Figure 3.18: (a) Mohr-Coulomb failure criterion. (b) Schematic representation of a soil element with the normal and shear stresses acting on a plane of known orientation.

Considering the principle stresses for a particular stress state at a point within a soil mass, three Mohr's circles with diameters specified by  $\sigma'_1 > \sigma'_2 > \sigma'_3$  may be defined based on which the failure can occur if only one of these circles is tangential to the yield surface (see Figure 3.19).

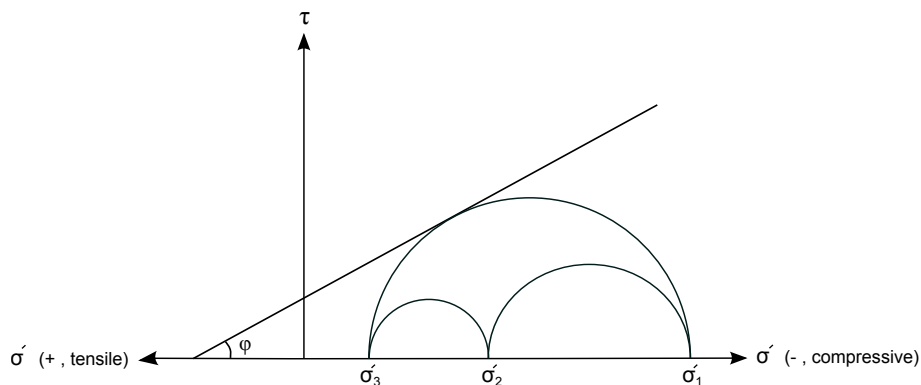


Figure 3.19: Representation of the Mohr circles based on the principal stresses; one of the circles touches the yield locus, and so it is the onset of yielding.

The Mohr-criterion can be expressed in a more fashionable manner as Equation 3.100. It may be noteworthy that this criterion considers the identical friction angles under triaxial compression paths,  $\varphi_c$ , and triaxial extension paths,  $\varphi_E$ . Figure 3.20 represents this criterion in the deviatoric plane.

$$f \equiv \frac{I_\sigma}{3} \sin \varphi + II_{\hat{\sigma}} \cos \beta - \frac{II_{\hat{\sigma}}}{\sqrt{3}} \sin \beta \sin \varphi - c \cos \varphi = 0 \quad (3.100)$$

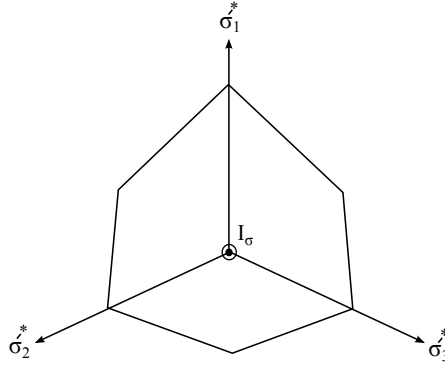


Figure 3.20: Representation of the Mohr-Coulomb yield surface in the deviatoric plane.

Taking into account the hexagon corners of this surface, which makes it straightforward for this criterion to be treated analytically, it is quite problematic to implement and use this model in the framework of a classical plasticity in a FE code. In fact, the constitutive equations are difficult to handle from a numerical point of view because of the sharp corners. Therefore, two more derivable yield surfaces have been implemented in the LAGAMINE code by Barnichon [1998] to constitute an internal frictional law in the code, called *PLASOL*. These two yield criteria are then described in the following.

### 3.4.2.1 Drucker-Prager yield criterion

The yield surface proposed by Drucker and Prager [1952] is a conical surface (in the principle stress space; see Figure 3.21a) defined on the basis of Von Mises yield criterion. It relates the first stress tensor invariant and the second deviatoric stress tensor invariant, such that:

$$f \equiv II_{\hat{\sigma}} + mI_{\sigma} - k = 0 \quad (3.101)$$

Figure 3.21b represents the trace of this regular cone shaped surface in the deviatoric plane, which signifies a circle. Since the Drucker-Prager (DP) yield surface can be considered as a smooth version of the Mohr-Coulomb yield surface (see Figure 3.21c), it is often expressed in terms of the internal friction angle and cohesion (as they are used to describe the Mohr-Coulomb yield surface). Hence, the parameters  $m$  and  $k$  can be defined as a function of internal friction angle in compression ( $\varphi_C$ ) and cohesion, as Equations 3.102-3.103, if we assume that the Drucker-Prager yield surface circumscribes the Mohr-Coulomb yield surface.

$$m = \frac{2 \sin \varphi_C}{\sqrt{3} (3 - \sin \varphi_C)} \quad (3.102)$$

$$k = \frac{6c \cos \varphi_C}{\sqrt{3} (3 - \sin \varphi_C)} \quad (3.103)$$

Therefore, the Drucker-Prager **yield surface** can be reexpressed by:

$$f \equiv II_{\hat{\sigma}} + m \left( I_{\sigma} - \frac{3c}{\tan \varphi_C} \right) = 0 \quad (3.104)$$

With respect to the definition of the reduced radius as  $r = II_{\hat{\sigma}}/I_{\sigma}$ , the relation of this radius for the triaxial paths in compression and extension can be concluded based on the Mohr's circle as given in Equations 3.105-3.106, respectively. These radii must be equal together for the Drucker-

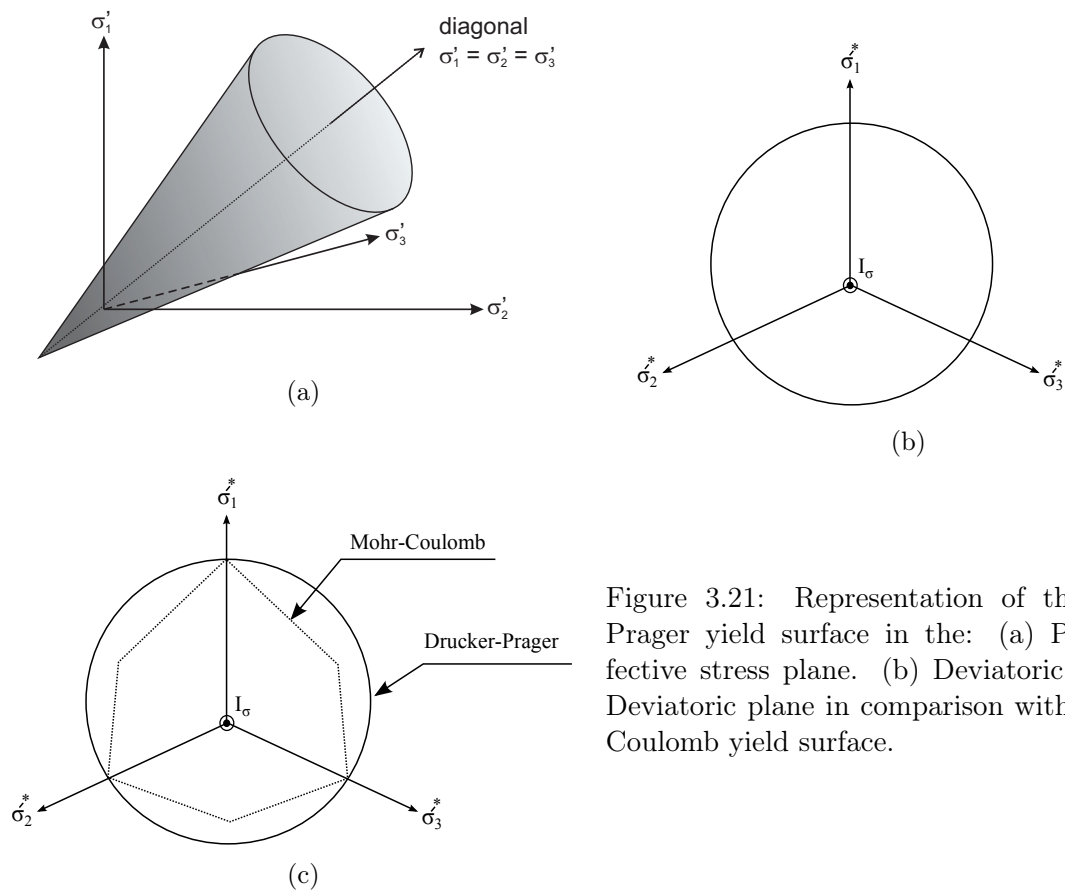


Figure 3.21: Representation of the Drucker-Prager yield surface in the: (a) Principle effective stress plane. (b) Deviatoric plane. (c) Deviatoric plane in comparison with the Mohr-Coulomb yield surface.

Prager model since it has a constant radius. Hence, the internal friction angle in compression  $\varphi_C$  is related to the internal friction angle in extension  $\varphi_E$  as expressed in Equation 3.107.

$$r_C = \frac{1}{\sqrt{3}} \left( \frac{2 \sin \varphi_C}{3 - 3 \sin \varphi_C} \right) \quad (3.105)$$

$$r_E = \frac{1}{\sqrt{3}} \left( \frac{2 \sin \varphi_E}{3 + 3 \sin \varphi_E} \right) \quad (3.106)$$

$$\varphi_E = \sin^{-1} \left( \frac{\frac{3 \sin \varphi_C}{3 - \sin \varphi_C}}{1 - \frac{\sin \varphi_C}{3 - \sin \varphi_C}} \right) \quad (3.107)$$

That is to say the values of  $\varphi_C$  and  $\varphi_E$  during the simulation (and upon the hardening of friction angle as explained in the following) are related to each other in a general non-linear manner. In fact, the variation of  $\varphi_E$  is dependent on the variation of  $\varphi_C$ . This dependency is not crucial for the range of internal friction angle of our studied material (see Section 3.4.4).

Then, hardening/softening of the yield surface in the frictional model are defined generally by the variations of friction angles, and also cohesion. These are the internal variables ( $\zeta$ ) of the model, which are defined in function of the Von Mises equivalent plastic strain  $\varepsilon_{eq}^p$ , through the hyperbolic relations as Equations 3.108-3.110. However, the DP model has only *two independent*

*hardening variables*: internal friction angle in compression  $\varphi_C$  and cohesion  $c$  (see Figure 3.22a).

$$\varphi_C = \varphi_{C0} + \frac{(\varphi_{Cf} - \varphi_{C0}) [\varepsilon_{eq}^p - D_\varphi]}{B_\varphi + [\varepsilon_{eq}^p - D_\varphi]} \quad (3.108)$$

$$\varphi_E = \varphi_{E0} + \frac{(\varphi_{Ef} - \varphi_{E0}) [\varepsilon_{eq}^p - D_\varphi]}{B_\varphi + [\varepsilon_{eq}^p - D_\varphi]} \quad (3.109)$$

$$c = c_0 + \frac{(c_f - c_0) [\varepsilon_{eq}^p - D_c]}{B_c + [\varepsilon_{eq}^p - D_c]} \quad (3.110)$$

where  $\varphi_{C0}/\varphi_{E0}$  are the initial compression/extension friction angles,  $\varphi_{Cf}/\varphi_{Ef}$  are the final compression/extension friction angles,  $c_0$  and  $c_f$  are the initial and final cohesions,  $D_\varphi$  and  $D_c$  are the values of equivalent plastic strain from which hardening/softening on friction angle and/or cohesion starts (it can then induce a delay in the hardening/softening process),  $B_\varphi$  and  $B_c$  are the values of equivalent plastic strain for which half of hardening/softening on friction angle and/or cohesion is achieved. For instance, Figure 3.22b illustrates how the friction angle is varied in function of Von Mises equivalent plastic strain, for three different values of  $B_\varphi$  (the value of  $D_\varphi$  has been chosen equal to zero). Moreover, the Von Mises equivalent plastic strain<sup>18</sup> is expressed by:

$$\varepsilon_{eq}^p = \int_0^t \dot{\varepsilon}_{eq}^p dt \quad (3.111)$$

$$\dot{\varepsilon}_{eq}^p = \sqrt{\frac{2}{3} \left( \dot{\varepsilon}_{ij}^p - \frac{\dot{\varepsilon}_v^p}{3} \delta_{ij} \right) \left( \dot{\varepsilon}_{ij}^p - \frac{\dot{\varepsilon}_v^p}{3} \delta_{ij} \right)} \quad (3.112)$$

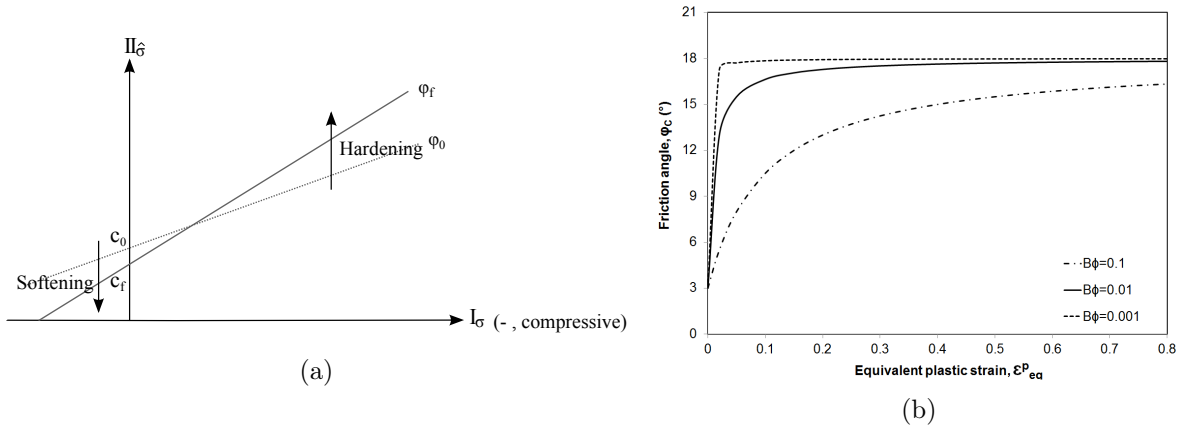


Figure 3.22: (a) Schematic representation of the yield limit, in the  $(I_\sigma, II_{\hat{\sigma}})$  plane, under  $\varphi_C$  hardening and  $c$  softening. (b) Hardening of friction angle from the initial value of  $\varphi_{C0} = 3^\circ$  to the final value of  $\varphi_{Cf} = 18^\circ$ , for three values of  $B_\varphi$ .

A non-associated flow rule (Equation 3.82), is considered taking into account the dependency of the dilatancy to the direction of plastic strain increment  $\partial g / \partial \sigma'_{ij}$ , thence, the dilatant response of the material can better be reproduced not with only one surface (i.e. associated flow rule), but rather through the definition of a non-associated flow rule. The **potential surface** is then given by:

$$g \equiv II_{\hat{\sigma}} + m' I_\sigma = 0 \quad (3.113)$$

<sup>18</sup>Hereafter, equivalent plastic strain signifies the Von Mises equivalent plastic strain.

where  $m'$  is defined similarly to  $m$ , such that:

$$m' = \frac{2 \sin \Psi}{\sqrt{3} (3 - \sin \Psi)} \quad (3.114)$$

where  $\Psi$  is the dilatancy angle.

One originality of this work provides the possibility of modification of the potential surface through the definition of variable dilatancy angle which is also a function of the equivalent plastic strain; this development will be described in Chapter 4.

Moreover, the hardening mechanism must be defined through the definition of a **hardening rule**. Therefore, considering the internal friction angle in compression and cohesion as our hardening variables, this rule can be resulted with respect to the equivalent plastic strain rate (Equation 3.112). The latter relation may be reexpressed based on Equation 3.82, such that:

$$\dot{\varepsilon}_{eq}^p = \sqrt{\frac{2}{3} \left( \frac{\partial g}{\partial \sigma'_{ij}} \frac{\partial g}{\partial \sigma'_{ij}} - \frac{1}{3} \frac{\partial g}{\partial \sigma'_{kk}} \frac{\partial g}{\partial \sigma'_{ll}} \right)} \dot{\lambda} \quad (3.115)$$

Hence, the hardening rule is governed by the derivatives of the internal variables as:

$$\dot{\varphi}_C = \frac{d\varphi_C}{d\varepsilon_{eq}^p} \dot{\varepsilon}_{eq}^p, \quad \dot{c} = \frac{dc}{d\varepsilon_{eq}^p} \dot{\varepsilon}_{eq}^p \quad (3.116)$$

Furthermore, an elasto-plastic constitutive law must always satisfy the **consistency condition** as it has been already explained, which reads:

$$\dot{f} = \frac{\partial f}{\partial \sigma'_{ij}} \dot{\sigma}'_{ij} + \frac{\partial f}{\partial \varphi_C} \dot{\varphi}_C + \frac{\partial f}{\partial c} \dot{c} = 0 \quad (3.117)$$

that is given as the following with respect to Equations 3.115-3.116:

$$\dot{f} = \frac{\partial f}{\partial \sigma'_{ij}} \dot{\sigma}'_{ij} + \sqrt{\frac{2}{3} \left( \frac{\partial g}{\partial \sigma'_{ij}} \frac{\partial g}{\partial \sigma'_{ij}} - \frac{1}{3} \frac{\partial g}{\partial \sigma'_{kk}} \frac{\partial g}{\partial \sigma'_{ll}} \right)} \dot{\lambda} \left( \frac{\partial f}{\partial \varphi_C} \frac{d\varphi_C}{d\varepsilon_{eq}^p} + \frac{\partial f}{\partial c} \frac{dc}{d\varepsilon_{eq}^p} \right) = 0 \quad (3.118)$$

Then, the plastic multiplier increment can be obtained by combining Equations 3.118 and the rate form stress-strain relation, Equation 3.83, such that:

$$\dot{\lambda} = \frac{\frac{\partial f}{\partial \sigma'_{ij}} \mathbb{C}_{ijkl}^e \dot{\varepsilon}_{kl}}{\frac{\partial f}{\partial \sigma'_{ef}} \mathbb{C}_{efgh}^e \frac{\partial g}{\partial \sigma_{gh}} - \sqrt{\frac{2}{3} \left( \frac{\partial g}{\partial \sigma'_{ij}} \frac{\partial g}{\partial \sigma'_{ij}} - \frac{1}{3} \frac{\partial g}{\partial \sigma'_{kk}} \frac{\partial g}{\partial \sigma'_{ll}} \right)} \left( \frac{\partial f}{\partial \varphi_C} \frac{d\varphi_C}{d\varepsilon_{eq}^p} + \frac{\partial f}{\partial c} \frac{dc}{d\varepsilon_{eq}^p} \right)} \quad (3.119)$$

Therefore, the constitutive incremental elasto-plastic relation can be expressed by incorporating Equation 3.119 into Equation 3.83, such that:

$$\dot{\sigma}'_{ij} = \mathbb{C}_{ijkl}^{ep} \dot{\varepsilon}_{kl} = \left( \mathbb{C}_{ijkl}^e - \mathbb{C}_{ijkl}^p \right) \dot{\varepsilon}_{kl} \quad (3.120)$$

where the  $\mathbb{C}_{ijkl}^{ep}$  is the elasto-plastic tensor through which the plastic tensor  $\mathbb{C}_{ijkl}^p$  is defined by:

$$\mathbb{C}_{ijkl}^p = \frac{\frac{\partial f}{\partial \sigma'_{mn}} \mathbb{C}_{mnpq}^e \mathbb{C}_{ijop}^e \frac{\partial g}{\partial \sigma'_{op}}}{\frac{\partial f}{\partial \sigma'_{ef}} \mathbb{C}_{efgh}^e \frac{\partial g}{\partial \sigma'_{gh}} - \sqrt{\frac{2}{3} \left( \frac{\partial g}{\partial \sigma'_{ij}} \frac{\partial g}{\partial \sigma'_{ij}} - \frac{1}{3} \frac{\partial g}{\partial \sigma'_{kk}} \frac{\partial g}{\partial \sigma'_{ll}} \right)} \left( \frac{\partial f}{\partial \varphi_C} \frac{d\varphi_C}{d\varepsilon_{eq}^p} + \frac{\partial f}{\partial c} \frac{dc}{d\varepsilon_{eq}^p} \right)} \quad (3.121)$$

Then, the derivatives of the yield surface  $f$  and potential surface  $g$  should be obtained with respect to the stress  $\sigma'_{ij}$ , thence based on the Equations 3.93, 3.94, 3.101 and 3.113, we have:

$$\frac{\partial f}{\partial \sigma'_{ij}} = \frac{\partial f}{\partial I_\sigma} \frac{I_\sigma}{\partial \sigma'_{ij}} + \frac{\partial f}{\partial III_{\hat{\sigma}}} \frac{\partial III_{\hat{\sigma}}}{\partial \sigma'_{ij}} = m \delta_{ij} + \frac{\hat{\sigma}'_{ij}}{2III_{\hat{\sigma}}} \quad (3.122)$$

$$\frac{\partial g}{\partial \sigma'_{ij}} = \frac{\partial g}{\partial I_\sigma} \frac{I_\sigma}{\partial \sigma'_{ij}} + \frac{\partial g}{\partial III_{\hat{\sigma}}} \frac{\partial III_{\hat{\sigma}}}{\partial \sigma'_{ij}} = m' \delta_{ij} + \frac{\hat{\sigma}'_{ij}}{2III_{\hat{\sigma}}} \quad (3.123)$$

In addition, with respect to Equations 3.104, 3.108 and 3.110, the following derivatives can be obtained:

$$\frac{\partial f}{\partial \varphi_C} = \frac{2I_\sigma}{\sqrt{3}} \left( \frac{\cos \varphi_C}{3 - \sin \varphi_C} + \frac{\cos \varphi_C \sin \varphi_C}{(3 - \sin \varphi_C)^2} \right) - \frac{6c}{\sqrt{3}} \left( \frac{\sin \varphi_C}{3 - \sin \varphi_C} + \frac{\cos^2 \varphi_C}{(3 - \sin \varphi_C)^2} \right) \quad (3.124)$$

$$\frac{d\varphi_C}{d\varepsilon_{eq}^p} = \frac{(\varphi_{Cf} - \varphi_{C0})}{B_\varphi + [\varepsilon_{eq}^p - D_\varphi]} - \frac{[\varepsilon_{eq}^p - D_\varphi](\varphi_{Cf} - \varphi_{C0})}{(B_\varphi + [\varepsilon_{eq}^p - D_\varphi])^2} \quad (3.125)$$

$$\frac{\partial f}{\partial c} = \frac{-3m}{\tan \varphi_C} \quad (3.126)$$

$$\frac{dc}{d\varepsilon_{eq}^p} = \frac{(c_f - c_0)}{B_c + [\varepsilon_{eq}^p - D_c]} - \frac{[\varepsilon_{eq}^p - D_c](c_f - c_0)}{(B_c + [\varepsilon_{eq}^p - D_c])^2} \quad (3.127)$$

Therefore, the constitutive incremental elasto-plastic relation (3.120) can be achieved.

### 3.4.2.2 Van Eekelen yield criterion

The Van Eekelen (VE) yield surface, proposed by Van Eekelen [1980], is defined by introduction of the Lode angle dependency into the model, compared to the DP model. The definition of the **yield surface** is then similar to the DP model (see Equation 3.128), but the coefficient  $m$  is not constant as for the DP yield surface. It is a function of the Lode angle (Equation 3.129). Figure 3.23 shows the trace of the VE yield surface in the deviatoric plane.

$$f \equiv III_{\hat{\sigma}} + m \left( I_\sigma - \frac{3c}{\tan \varphi_C} \right) = 0 \quad (3.128)$$

$$m = a(1 + b \sin 3\beta)^n, \quad \text{with} \quad \sin 3\beta = - \left( \frac{3\sqrt{3} III_{\hat{\sigma}}}{2 III_{\hat{\sigma}}^3} \right) \quad (3.129)$$

where  $a$  and  $b$  are defined as:

$$a = \frac{r_C}{(1+b)^n} \quad (3.130)$$

$$b = \frac{\left(\frac{r_C}{r_E}\right)^{\frac{1}{n}} - 1}{\left(\frac{r_C}{r_E}\right)^{\frac{1}{n}} + 1} \quad (3.131)$$

where  $r_C$  and  $r_E$  can be found with respect to the Equations 3.105-3.106. In addition,  $n$  is a constant which defines the convexity of the yield surface. These three parameters must generally verify that  $a > 0$ ,  $bn > 0$  and  $-1 < b < 1$ . A value of  $n = -0.229$  has been recommended by Van Eekelen [1980] to assure the convexity condition, although there may be necessary to give a special care in some cases to ensure this condition, according to Barnichon [1998].

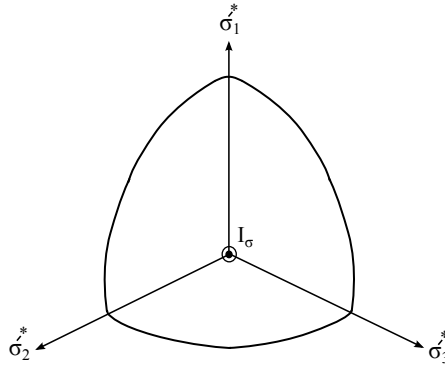


Figure 3.23: Representation of the Van Eekelen yield surface in the deviatoric plane.

The **potential surface** is expressed by Equation 3.132 where the corresponding parameter  $m'$  is defined similarly to Equation 3.129, with respect to Equations 3.130-3.131 and, Equations 3.105-3.106 substituting the friction angles  $\varphi_C$  and  $\varphi_E$  by the dilatancy angles  $\Psi_C$  and  $\Psi_E$ . A new formula is proposed in this thesis to permit the modification of the dilatancy angles with respect to the equivalent plastic strain (see Chapter 4).

$$g \equiv II_{\hat{\sigma}} + m' \left( I_{\sigma} - \frac{3c}{\tan \varphi_C} \right) = 0 \quad (3.132)$$

In addition, considering the three hardening variables  $\varphi_C$ ,  $\varphi_E$ , and  $c$ , the **hardening rule** is governed by Equations 3.115 and 3.116 as well as:

$$\dot{\varphi}_E = \frac{d\varphi_E}{d\varepsilon_{eq}^p} \dot{\varepsilon}_{eq}^p \quad (3.133)$$

Finally, **consistency condition** must be satisfied, which gives:

$$\dot{f} = \frac{\partial f}{\partial \sigma'_{ij}} \dot{\sigma}'_{ij} + \frac{\partial f}{\partial \varphi_C} \dot{\varphi}_C + \frac{\partial f}{\partial \varphi_E} \dot{\varphi}_E + \frac{\partial f}{\partial c} \dot{c} = 0 \quad (3.134)$$

The plastic multiplier increment can be obtained in the similar manner as for the DP model with

respect to Equations 3.115, 3.116, 3.133 and 3.83, such that:

$$\dot{\lambda} = \frac{\frac{\partial f}{\partial \sigma'_{ij}} \mathbb{C}_{ijkl}^e \dot{\epsilon}_{kl}}{\frac{\partial f}{\partial \sigma'_{ef}} \mathbb{C}_{efgh}^e \frac{\partial g}{\partial \sigma_{gh}} - \sqrt{\frac{2}{3} \left( \frac{\partial g}{\partial \sigma'_{ij}} \frac{\partial g}{\partial \sigma'_{ij}} - \frac{1}{3} \frac{\partial g}{\partial \sigma'_{kk}} \frac{\partial g}{\partial \sigma'_{ll}} \right) \left( \frac{\partial f}{\partial \varphi_C} \frac{d\varphi_C}{d\varepsilon_{eq}^p} + \frac{\partial f}{\partial \varphi_E} \frac{d\varphi_E}{d\varepsilon_{eq}^p} + \frac{\partial f}{\partial c} \frac{dc}{d\varepsilon_{eq}^p} \right)}} \quad (3.135)$$

Consequently, the constitutive incremental elasto-plastic relation can be given by incorporating Equation 3.135 into Equation 3.83, such that:

$$\tilde{\sigma}'_{ij} = \mathbb{C}_{ijkl}^{ep} \dot{\epsilon}_{kl} = \left( \mathbb{C}_{ijkl}^e - \mathbb{C}_{ijkl}^p \right) \dot{\epsilon}_{kl} \quad (3.136)$$

where the plastic tensor  $\mathbb{C}_{ijkl}^p$  is given by:

$$\mathbb{C}_{ijkl}^p = \frac{\frac{\partial f}{\partial \sigma'_{mn}} \mathbb{C}_{mnpq}^e \mathbb{C}_{ijop}^e \frac{\partial g}{\partial \sigma'_{op}}}{\frac{\partial f}{\partial \sigma'_{ef}} \mathbb{C}_{efgh}^e \frac{\partial g}{\partial \sigma_{gh}} - \sqrt{\frac{2}{3} \left( \frac{\partial g}{\partial \sigma'_{ij}} \frac{\partial g}{\partial \sigma'_{ij}} - \frac{1}{3} \frac{\partial g}{\partial \sigma'_{kk}} \frac{\partial g}{\partial \sigma'_{ll}} \right) \left( \frac{\partial f}{\partial \varphi_C} \frac{d\varphi_C}{d\varepsilon_{eq}^p} + \frac{\partial f}{\partial \varphi_E} \frac{d\varphi_E}{d\varepsilon_{eq}^p} + \frac{\partial f}{\partial c} \frac{dc}{d\varepsilon_{eq}^p} \right)}} \quad (3.137)$$

### 3.4.3 Review of some other yield criteria

The well-known Cam-Clay model is one of the main criterion which is the basis of a family of the models. The Cam-Clay model was basically developed [Roscoe et al., 1958] to model the response and strength of the (soft) soils, specially normally consolidated soils, under isotropic loading; with the assumption of an isotropic and elasto-plastic soil which deforms as a continuum. The original Cam-Clay model has an almond shaped yield surface. This model has been later modified with an adaptation of its yield limit to an elliptical surface, and it is then known as the Modified Cam-Clay model (MCC) [Roscoe and Burland, 1968; Schofield and Wroth, 1968]. The objective was mainly to overcome the deficiency of the original model which has predicted a deviatoric component of the plastic strain upon the hardening process under the isotropic loading while it must only produce the volumetric strain. In the MCC model with an elliptical yield surface, there is no incremental deviatoric plastic strain takes place for hydrostatic states of stress since the plastic strain increment vector (which is perpendicular to the yield surface, see Figure 3.24) for the largest value of the mean effective stress is horizontal.

One of the important constitutive elasto-plastic laws that belongs to the MCC family is the Barcelona Basic Model (BBM) which is also available in the LAGAMINE library<sup>19</sup>. This model has been developed by Alonso et al. [1990] basically to describe the stress-strain behavior of the partially saturated soils which are slightly/moderately expansive. Hence, it has been aimed to better model the wetting-drying paths considering the fact that suction can stiffen the soil like a hardening parameter to modify the plasticity limit<sup>20</sup>. The description of the BBM yield limit for the saturated conditions represents the modified Cam-Clay yield surface, as it is shown in Figure 3.24 in the  $(I_\sigma, II_\sigma)$  plane, with an illustration of the plastic strain increment vector. Thence,

<sup>19</sup>We are reviewing in this Section some other criteria that are in fact addressed more often in the LAGAMINE code.

<sup>20</sup>We don't go through the different aspects of BBM since it is out of scope of this thesis.

the Cam-Clay **yield surface** may be expressed by:

$$f \equiv II_{\hat{\sigma}}^2 + m^2 \left( I_{\sigma} - \frac{3c}{\tan \varphi_C} \right) (I_{\sigma} + 3p'_0) = 0 \quad (3.138)$$

where  $c$  is the cohesion,  $\varphi_C$  is the friction angle in compression (under triaxial compression

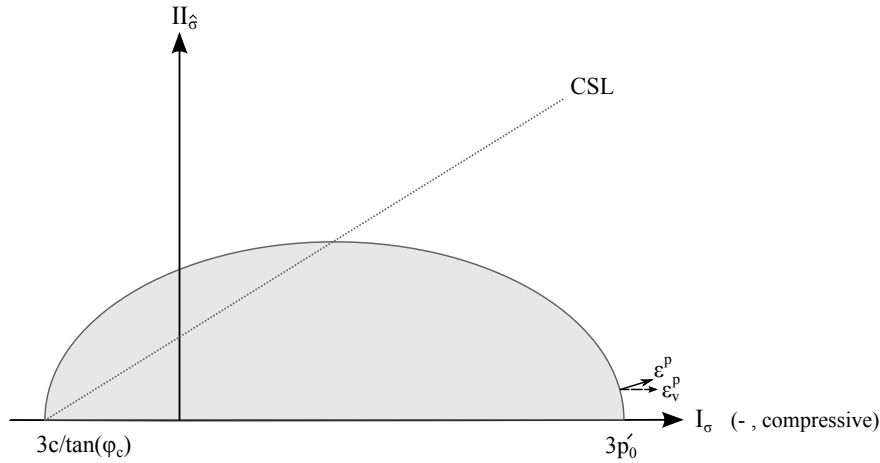


Figure 3.24: Representation of the modified Cam-Clay yield limit in the  $(I_{\sigma}, II_{\hat{\sigma}})$  plane.

paths), and  $p'_0$  is the pre-consolidation stress. In addition, the parameter  $m$ , which is defined by Equation 3.129, introduces the dependency on the third invariant of deviatoric stress that results in a non-circular yield surface in the deviatoric plane<sup>21</sup>. It is noteworthy to recall that CSL (Critical State Line) indicates an eventual state in which further shearing (soil distortion) can occur at constant state of stress with no volume change. One may notice that for a general case concerning the unsaturated state, the cohesion and preconsolidation stress in the relation 3.138 are function of suction.

The internal variable which controls the hardening of the yield surface for the Cam-Clay model is preconsolidation stress. Therefore, the **consistency condition** can be expressed by:

$$\dot{f} = \frac{\partial f}{\partial \sigma'_{ij}} \dot{\sigma}'_{ij} + \frac{\partial f}{\partial p'_0} \dot{p}'_0 = 0 \quad (3.139)$$

Moreover, an associated plastic flow rule has been considered with a **potential surface** defined same as the yield surface. In addition, the **hardening rule**, with respect to its definition, is responsible to define the evolution of the yield surface and the hardening process. It describes (in incremental manner) the relation between the hardening parameter  $p'_0$  and plastic volumetric strain. Hence, the increment of the preconsolidation stress is defined in function of the volumetric plastic strain  $\varepsilon_v^p$ , such that:

$$dp'_0 = -\frac{(1 + e_0)p'_0}{\lambda(0) - \kappa} d\varepsilon_v^p \quad (3.140)$$

where  $\lambda(0)$  is a plastic slope parameter related to the variations in stress; *zero* notation corresponds to a null suction state.  $e_0$  is the initial void ratio, and  $\kappa$  is an elastic slope parameter related to the variations in stress. Therefore, Equation 3.139 can be rewritten as:

$$\dot{f} = \frac{\partial f}{\partial \sigma'_{ij}} \dot{\sigma}'_{ij} + \frac{\partial f}{\partial p'_0} \frac{dp'_0}{d\varepsilon_v^p} \dot{\varepsilon}_v^p = 0 \quad (3.141)$$

<sup>21</sup>This formulation has been incorporated into the LAGAMINE library, see relatively [Li, 2000; Collin, 2003].

where, the rate of volumetric plastic strain is defined by:

$$\dot{\varepsilon}_v^p = \dot{\lambda} \frac{\partial g}{\partial \sigma'_{ii}} \quad (3.142)$$

With respect to Equation 3.140, hardening can occur when the stress point reaches the right side of the Cam-Clay yield surface, which corresponds to the increase of preconsolidation stress following the compression volumetric plastic strain,. On the contrary, softening appears if the stress point hits the left side of the yield surface, which corresponds to the dilative plastic volumetric strain.

In the framework of the review on some other popular yield surfaces in this section<sup>19</sup>, a brief complementary description on the additional yield surfaces defined in the BBM model - which concern the unsaturated state - is given in the following, without going through the details<sup>22</sup>. The objective is solely providing a preview for the discussion handled in the next Section.

The BBM was developed based on two independent sets of state variables, i.e. net mean stress (i.e. excess of mean stress over air pressure) and suction, and it is capable to reproduce certain phenomena of the partially saturated soils' behavior. One essential aspect of the BBM is to model the effect of suction and its variation (the paths of increase and decrease of suction), in modifying the plasticity limit; it deals then with the wetting-drying paths. In fact, upon wetting (i.e. reduction in suction) under sufficiently high level of confining pressure, soil may experience the compression plastic deformation and an ultimate collapse. The yield surface LC (Loading-Collapse) can characterize the collapse which may occur during the suction reduction's path. On the contrary, a partially saturated soil may expand under sufficiently low confining pressure. Moreover, the increase of suction can be interpreted as an effective cohesion, that may non-linearly increase the soil's strength [Fredlund et al., 1978] while the latter increase tends to a maximum at some given high suction ( $s_0$ ) after which irreversible strain can occur. This is the basis of the second yield limit, SI, which corresponds to a transition from the elastic state to the plastic one upon the suction increase. These two yield surfaces are given by Equations 3.143-3.144.

$$P_0 = P^c \left( \frac{p_0}{P^c} \right)^{\frac{\lambda(0)-\kappa}{\lambda(s)-\kappa}} \quad (3.143)$$

where  $P^c$  is a reference preconsolidation,  $p_0$  corresponds to the preconsolidation stress  $P_0$  in the null suction state, and  $\lambda(s)$  is the plastic slope parameter for the suction  $s$  [Alonso et al., 1990] .

$$s = s_0 = cts. \quad (3.144)$$

Figure 3.25a shows these two yield surfaces in the  $(s, p)$  plane, and Figure 3.25b represents the BBM yield surface in three-dimensional  $(p, q, s)$  plane. The BBM on the  $(q, p)$  plane characterizes the Cam-Clay criterion, following the description formerly given for a null suction state. The position of the general BBM yield surface is controlled by the coupled response of two<sup>23</sup> surfaces LC and SI since their hardening is not independent from each other (a discussion on their coupled behavior can be found in [Salehnia, 2010]). For instance, during a loading path with a suction increase, the volumetric response of an unsaturated soil is not uniquely dependent to its initial and final suction, but also to its variation path which affect the hardening procedure of the yield surfaces LC and SI.

<sup>22</sup>Interested readers may refer to Alonso et al. [1990] for a detailed explanation and formulation.

<sup>23</sup>The model may have another extra yield surface SD to model the soil behavior with a strong dilatancy potential.

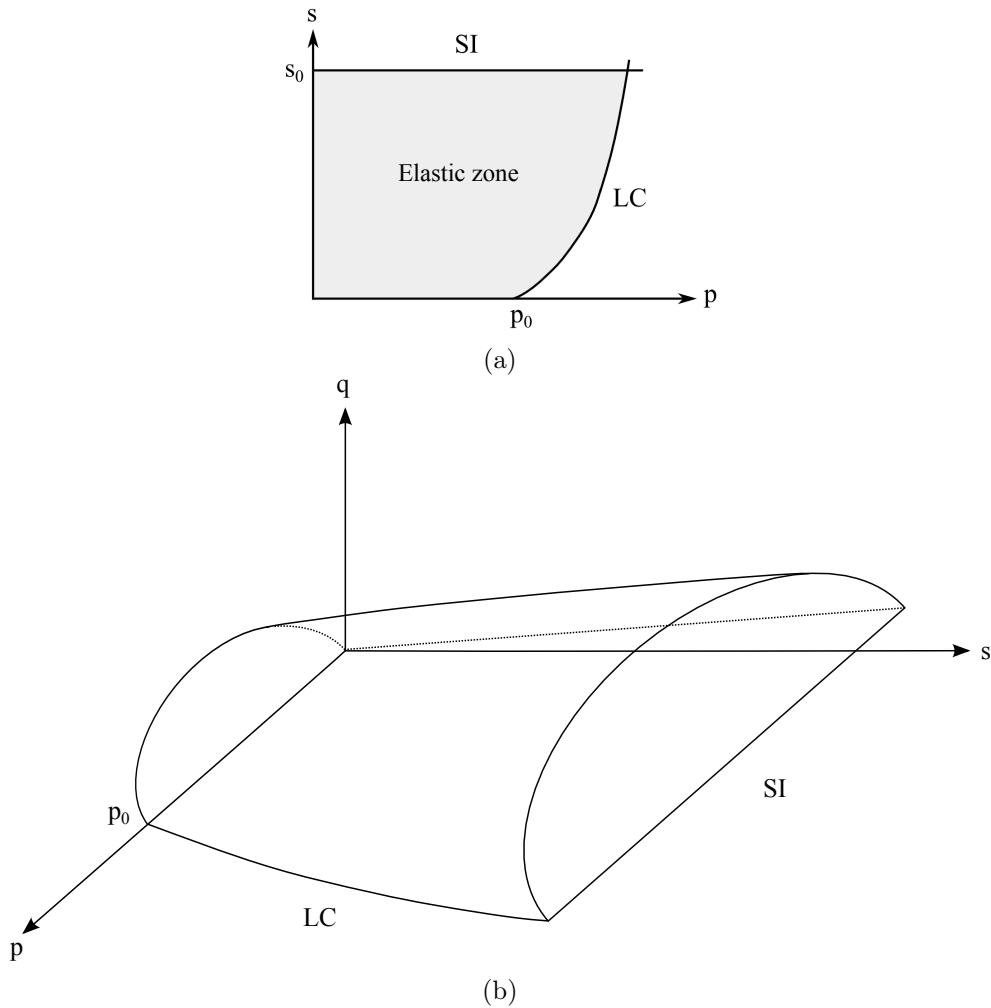


Figure 3.25: (a) The LC and SI yield surfaces in the  $(s, p)$  plane. (b) The BBM yield surface in the  $(p, q, s)$  plane.

### Cap-Model:

The so-called Cap-model was basically incorporated in LAGAMINE by Collin [2003] to model more realistically the chalk behavior. It is a blend of three yield surfaces: the right part (or, humid part) of the MCC criterion, an internal frictional criterion (DP/VE), and a traction failure criterion (see Figure 3.26). The first part of the Cap-model follows the Cam-Clay criterion (Equation 3.138) as described heretofore, which can model the compaction plastic strain. However, the left side of this criterion (dry part) was replaced by an internal frictional criterion (see Section 3.4.2) to better model the shearing mechanism. Indeed, the left side of MCC model overestimates the shearing resistance for the over-consolidated soils. If stress path hit the left side of the MCC yield surface, softening can occur, and yield surface may shrink that this softening may also impose some numerical instabilities. Thence, a frictional yield criterion replaces MCC criterion in its left side.

In addition to the MCC and an internal frictional criteria, which have been already described, the Cap-model includes another criterion in order to deal with the traction failure. The latter is based on some experimental works which have shown such an overestimation of the tensile stresses by an internal fractional model; more particularly for the chalk according to [Collin, 2003]. Hence, an hyperbolic traction yield surface has been considered in the Cap-model, such

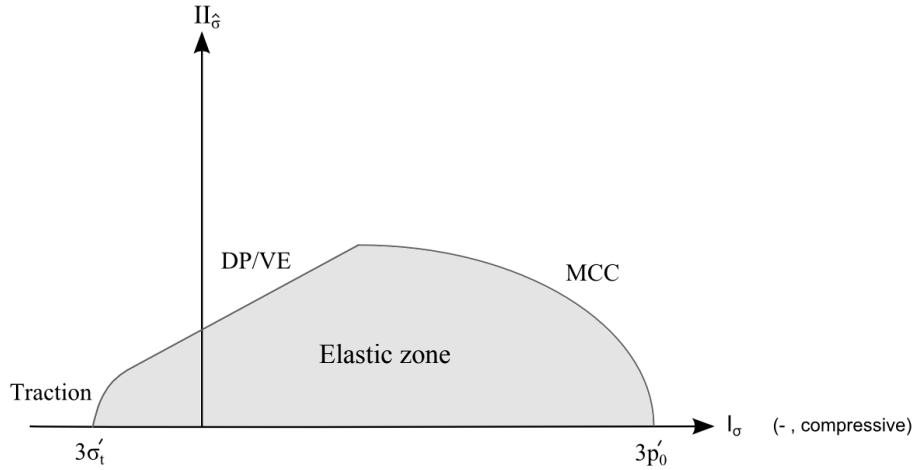


Figure 3.26: Representation of the Cap-model in the  $(I_\sigma, II_\delta)$  plane.

that:

$$f \equiv II_\delta^2 - m^2 (I_\sigma - 3\sigma'_{t,i}) \left( I_\sigma - \left( \frac{3c}{\tan \varphi_C} \right)^2 \frac{1}{3\sigma'_{t,i}} \right) = 0 \quad (3.145)$$

where  $\sigma'_{t,i}$  is isotropic traction resistance limit. This yield criterion is perfectly plastic, and it obeys an associated flow rule.

### 3.4.4 Choice of the yield criterion for the elasto-plastic analysis

This section discusses about the choice of the yield surface applied in this work<sup>24</sup>. First, focusing on the well-known BBM, the one should consider that the most important feature of the BBM, is dealing with the wetting-drying path in the stress-strain description of a partially saturated soil (e.g. see [Gatmiri and Arson, 2008; Salehnia and Gatmiri, 2011]). Consequently to these loading paths, suction can change, and this change may include irreversible volumetric deformation [Alonso et al., 1990]. However, as it has been previously explained in this Chapter, we are dealing principally with the saturated state in this thesis, and even if some low suction might exist, the modeling of the wetting-drying loading paths are not aimed in this work. Instead, a model is needed whose focal point is reproducing the shearing mechanism, and the development of the deviatoric plastic strains.

Second, with regard to the Cam-Clay model, in spite of its considerable features for modeling the reversible and irreversible volume change under isotropic loading and shearing, etc., it has also some important limitations. The latter in the level of this work concerns the overestimation of shearing resistance for the over-consolidated soils. With regard to the dominant deviatoric loading path in most of the problems addressed in this thesis (e.g. tunneling), Cam-clay model is not then an appropriate choice whereas it can be suitable when the volumetric behavior is supreme. Moreover, Cam-Clay criterion does not take into account of the structural and stress-induced anisotropy, which is quite influential in the Boom Clay behavior, as it will be discussed in Chapter 6. Furthermore, the one may notice that the original Cam-Clay has also another deficiency of a sharp transition from the elastic state to the plastic state. In addition, the deviatoric plastic strain is not correctly reproduced; non realistically, the model predicts a deviatoric component of the plastic strain upon the hardening process under the isotropic loading while it must only produce the volumetric strain.

<sup>24</sup>Mainly among the other aforesaid criteria (that are used more frequently in the LAGAMINE code).

Third, in Cap-model, the concern regarding the overestimation of the shearing resistance by the Cam-Clay criterion was addressed by combination of an internal frictional criterion with Cam-Clay. Although, this model could be of particular interest mostly for the materials, with two main plastic mechanism: pore collapse<sup>25</sup> and shearing rupture. The Cam-Clay's part of the model concerns modeling of the pore collapse which appears in the high level of confining pressure. However, with reference to the discussion in Section 2.3.2.3, Boom Clay at the URL level in the Mol site has a dominant shearing failure (traction is not an essential mechanism in our work) and it could show a brittle dilatant response upon shearing (more likely to prevail close to the gallery wall), which corresponds to the deformation pattern of an over-consolidated material at a relatively low confining pressure. That is to say that we are dealing principally with the internal frictional criterion even though using the Cap-model. In fact, the frictional model is capable to reproduce the prevailing mechanisms of the Boom Clay behavior. The role of the deviatoric plastic strain is essential in the frictional family of elasto-plastic constitutive laws that this feature is fundamental in modeling the excavation paths (dominantly deviatoric), the shear bands evolution and strain localization, in this thesis.

Lastly, following the conclusion for application of an internal frictional model, we recall firstly that Mohr-Coloumb model is not convenient to deal with in a numerical point of view since its yield surface has geometric singularities in the principal stress state. Furthermore, the Drucker Prager model has been chosen over the Van Eekelen in this work. In fact, the only difference of these two yield surfaces is the dependency of the latter on the third stress invariant, i.e. on the Lode angle  $\beta$ . This results in a non-circular yield surface in the deviatoric plane for which the internal friction angle in compression and extension are not related to each other on the contrary to the DP criterion, and then the variation of  $\varphi_C$  during the hardening can not influence the variation of  $\varphi_E$ . This feature could be important in the high friction angles ( $\varphi_C$  higher than  $20^\circ$  according to [Barnichon, 1998]), which it may induce a considerable difference between the trace of DP yield surface with the trace of VE and MC yield surfaces. However, for the lower friction angle, as for the range of Boom Clay's, it does not make any distinguished difference and the DP and VE criteria act similarly. Therefore, the choice of DP model over the VE model in this work seems logical. Besides, DP is a simpler model which does not have to deal with the convexity condition of the yield surface (on the contrary to the VE model).

### 3.4.5 Return mapping algorithm

There are different algorithms for integrating unlike rate constitutive relations. Hereafter, a summary of the classical return mapping algorithm with respect to the operator split formulation [Simo and Hughes, 1998] is described which is applied in this work. This method is a two-step algorithm which consist of an elastic *trial* predictor followed by a plastic corrector that projects the trial state onto the yield surface. The objective is defined in the framework of the consistency condition, and it consists in restoring this condition when it is violated. Let consider a notation of the state  $n$  at the beginning of the step,  $^{tr,n+1}$  as the trial state, and  $^{n+1}$  as the corrected state. Then, Figure 3.27 shows a general geometric interpretation of return mapping algorithm. From a given state  $\sigma'_n$ , the *first* step corresponds to computation of an elastic predictor where we consider a purely elastic trial step defined by:

$$\sigma'^{tr,n+1}_{ij} = \sigma^m_{ij} + \mathbb{C}^e_{ijkl} \Delta \varepsilon_{kl} \quad (3.146)$$

$$\varepsilon^p_{eq}{}^{tr,n+1} = \varepsilon^p_{eq}{}^n \quad (3.147)$$

---

<sup>25</sup>Pore collapse signifies an important reduction in the pore space which results ultimately in hardening related to an increase of contact among the grains.

Hence, the trial state is determined in terms of an initial state and a given incremental strain.

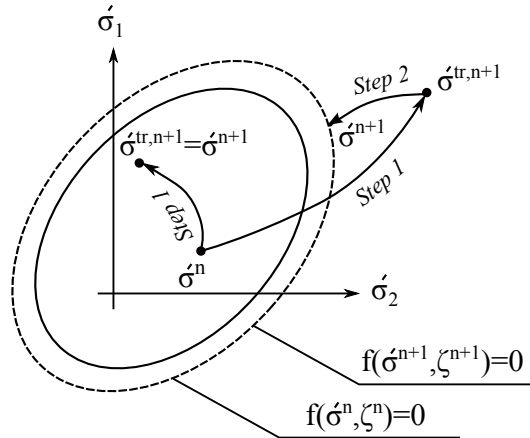


Figure 3.27: Conceptual representation of the elastic predictor (*and*) plastic return mapping algorithm for isotropic hardening.

The trial state may not and *in general will not* belong to any actual, physically admissible state. Indeed, there is two possibilities following Equation 3.146, and evaluation of the yield criterion at the computed trial state:

- This trial state does not violate the yield criterion, i.e.  $f(\sigma_{ij}^{tr,n+1}, \zeta^n) \leq 0$ . Thence, the step is purely elastic, and the final state is the same as this trial state.
- This trial state results in  $f(\sigma_{ij}^{tr,n+1}, \zeta^n) > 0$ , the consistency condition is violated and it must be restored through the return mapping algorithm and then computation of a plastic predictor.

Consequently to violation of the consistency condition, the *second* step of the return mapping algorithm consists in mapping back the part of stress which passed over the yield limit. We recall the generalized rate form of stress-strain relation as:

$$\tilde{\sigma}'_{ij} = \mathbb{C}_{ijkl}^e \left( \dot{\varepsilon}_{kl} - \dot{\lambda} \frac{\partial g}{\partial \sigma'_{kl}} \right) \quad (3.148)$$

where  $\partial g / \partial \sigma'_{kl}$  was described to define the direction of the plastic strain increment in the framework of a non-associated plasticity. Let denote this direction with the normal unit vector as  $\hat{n}_{ij}$ . This normal can be chosen with respect to the stress point at the beginning of the step (fully explicit scheme), middle of the step (semi-implicit, mid-point rule), or end of the step (fully implicit scheme), following Section 3.2.6. Let consider the last scheme, using a backward implicit scheme for integrating the incremental plastic flow, we obtain:

$$\Delta \varepsilon_{ij}^p = \int_{t^n}^{t^{n+1}} \dot{\lambda} \hat{n}_{ij} dt \approx \Delta \lambda \hat{n}_{ij}^{n+1} \quad (3.149)$$

where  $\Delta \lambda$  is the discrete plastic multiplier [Borja, 2013].

Therefore, Equation 3.148 may be rewritten in the incremental form as:

$$\sigma_{ij}^{m+1} - \sigma_{ij}^m = \mathbb{C}_{ijkl}^e \left( \varepsilon_{kl}^{tr,n+1} - \varepsilon_{kl}^n \right) - \mathbb{C}_{ijkl}^e \Delta \lambda \left. \frac{\partial g}{\partial \sigma'_{kl}} \right|_{n+1} \quad (3.150)$$

$$\sigma_{ij}^{m+1} - \cancel{\sigma}_{ij}^{m+1} = \sigma_{ij}^{tr,n+1} - \cancel{\sigma}_{ij}^{m+1} - \mathbb{C}_{ijkl}^e \Delta\lambda \left. \frac{\partial g}{\partial \sigma'_{ij}} \right|_{n+1} \quad (3.151)$$

Thence, the updated stress, i.e.  $\sigma_{ij}^{m+1}$  is obtained as:

$$\sigma_{ij}^{m+1} = \sigma_{ij}^{tr,n+1} - \mathbb{C}_{ijkl}^e \Delta\lambda \left. \frac{\partial g}{\partial \sigma'_{ij}} \right|_{n+1} \quad (3.152)$$

For a given strain increment, integrating the constitutive law then needs obtaining the correction  $\Delta\lambda$ . The solution which has been incorporated into the LAGAMINE code [Barnichon, 1998] uses the Newton-Raphson iterative method. A first order Taylor development of the yield criterion around the trial stress state  $^{tr,n+1}$  reads:

$$f\left(\sigma_{ij}^{tr,n+1} + \Delta\sigma_{ij}^{rp}, \zeta^{tr,n+1} + \Delta\zeta\right) = f\left(\sigma_{ij}^{tr,n+1}, \zeta^{tr,n+1}\right) + \left. \frac{\partial f}{\partial \sigma'_{ij}} \right|_{tr,n+1} \Delta\sigma_{ij}^{rp} + \left. \frac{\partial f}{\partial \zeta} \right|_{tr,n+1} \Delta\zeta \quad (3.153)$$

where with respect to Equations 3.149 and 3.152, we have:

$$\Delta\sigma_{ij}^{rp} = -\mathbb{C}_{ijkl}^e \Delta\lambda \left. \frac{\partial g}{\partial \sigma'_{kl}} \right|_{n+1} \quad (3.154)$$

Also, Equation 3.115 may be simplified as  $\dot{\varepsilon}_{eq}^p = \mathfrak{Val}\dot{\lambda}$  which leads to:

$$\Delta\zeta = \frac{d\zeta}{d\varepsilon_{eq}^p} \mathfrak{Val} \Delta\lambda \quad (3.155)$$

Thence, Equation 3.153 is reexpressed as:

$$f = f\left(\sigma_{ij}^{tr,n+1}, \zeta^{tr,n+1}\right) - \left. \frac{\partial f}{\partial \sigma'_{ij}} \right|_{tr,n+1} \mathbb{C}_{ijkl}^e \Delta\lambda \left. \frac{\partial g}{\partial \sigma'_{kl}} \right|_{n+1} + \left. \frac{\partial f}{\partial \zeta} \right|_{tr,n+1} \frac{d\zeta}{d\varepsilon_{eq}^p} \mathfrak{Val} \Delta\lambda \quad (3.156)$$

Thus, the correction  $\Delta\lambda$  which can restore the consistency condition,  $f = 0$ , is then obtained as:

$$\Delta\lambda = \frac{f\left(\sigma_{ij}^{tr,n+1}, \zeta^{tr,n+1}\right)}{\left. \frac{\partial f}{\partial \sigma'_{ij}} \right|_{tr,n+1} \mathbb{C}_{ijkl}^e \Delta\lambda \left. \frac{\partial g}{\partial \sigma'_{kl}} \right|_{n+1} - \left. \frac{\partial f}{\partial \zeta} \right|_{tr,n+1} \frac{d\zeta}{d\varepsilon_{eq}^p} \mathfrak{Val}} \quad (3.157)$$

It must be pointed out that at the first iteration,  $\zeta^n = \zeta^{tr,n+1}$ . Then, consequently to the obtained correction  $\Delta\lambda$ , the new stress can be found by Equation 3.152. In addition, the new equivalent plastic strain  $\varepsilon_{eq}^p + \mathfrak{Val} \Delta\lambda$ , and then the new hardening/softening parameters can be also found. Thence, the test on the yield surface is conducted to check whether  $f(\sigma_{ij}^{m+1}, \zeta^{n+1}) = 0$ , or not, that in the latter case, more iteration(s) is needed.

On the numerical point of view, the convergence criterion to satisfy  $f(\sigma_{ij}^{m+1}, \zeta^{n+1})$ , has been adopted in terms of the stress increment ratio between the iterations  $i^{th}$  and  $i+1^{th}$  as:

$$1 - \text{precision} < \max \left| \frac{\Delta\sigma_{ij}^{i+1}}{\Delta\sigma_{ij}^i} \right| < 1 + \text{precision} \quad (3.158)$$

where the value of **precision** is chosen by the user. This method of convergence check has an advantage of being independent of the chosen unit system, according to Barnichon [1998]. The latter also indicated that for a perfectly plastic circular criterion (as for the DP model), a coherent stress state for which the condition  $f(\sigma_{ij}^{m+1}, \zeta^{n+1})$  is fulfilled, can be obtained after one iteration (one step of return mapping). Although, some more iterations may be needed in the case that there is hardening/softening in order to integrate  $\zeta^{n+1}$  over the step. However, in a more general case of a non-circular criterion, several iterations are required to obtain a stress state such that  $f(\sigma_{ij}^{m+1}, \zeta^{n+1}) = 0$  even if there is not any hardening/softening.

It is noteworthy that the choice of using a backward implicit scheme, for the  $J_2$  (or, Von mises) type of plasticity, i.e. for the circular yield criterion, leads to the radial return algorithm [Wilkins, 1963]. Thence, the DP yield criterion follows this procedure motivated by the shape of its yield surface. Geometrically, radial return algorithm corresponds to the plastic corrector step which can be interpreted as a simple radial mapping of the elastic predictor stress  $\sigma_{ij}^{tr,n+1}$  onto the yield surface  $f(\sigma_{ij}^{n+1}, \zeta^{n+1}) = 0$  to determine the final corrected stress  $\sigma_{ij}^{n+1}$  (see Figure 3.28).

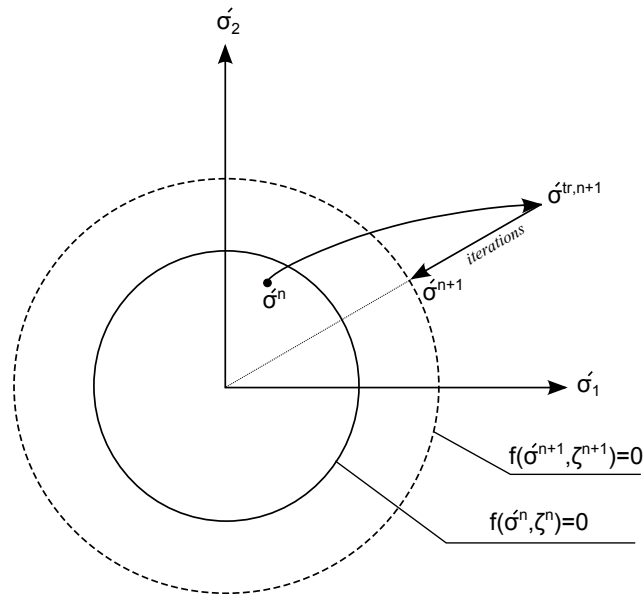


Figure 3.28: Conceptual representation of the radial return algorithm for isotropic hardening.

### 3.4.6 Sub-stepping approach

Following the acquirement of the updated stress, and computation of the local tangent operators, the global stiffness matrix has to be computed and inverted, as it has been already mentioned in the general resolution algorithm brought in Section 3.2.7. The consummation of the time during this procedure is the cost of a numerical simulation. Therefore, the loading step  $\Delta t$  is aimed to be chosen large enough in order to decrease the computation time spent by CPU. However, the accuracy of the results, i.e. the stress integration, must be still guaranteed. Thus, an integration approach by sub-stepping is applied to overcome this concern. Traditionally, in the LAGAMINE code, the subdivided time increment  $\delta t$  over the time step  $\Delta t$  may be obtained by Equation

3.159 through the definition of a given numbers of sub-intervals as **nintv**, such that:

$$\delta t = \frac{\Delta t}{\mathbf{nintv}} \quad (3.159)$$

However, the choice of **nintv** remains a difficulty, specially since it induces a constant number of subdivision during the whole loading time, and over the space for all the integration points.

In this work, we are dealing principally with the localization problems where the deformation is localized within the shear bands and then, a strong non-linearity in the stress path can occur at those zones. Therefore, the number of sub-intervals, parameter **nintv**, is of particular interest in the localized zones in order to increase the precision of the results at the bifurcation<sup>26</sup> time - when there is normally numerical convergence difficulties - and afterwards; the latter means to better simulate the post-localization behavior. However, it is not logical and time efficient if the sub-intervals' number is totally increased over the whole space when it is just necessary in some particular zones. Therefore, a varied number of **nintv** over the space is desirable. In this sense, an adaptive formulation of the sub-intervals' number is applied in this work in which this number is computed at each loading step corresponds to  $\Delta t$ , and for each integration point as a function of strain increment, such that:

$$\mathbf{nintv} = \min \left\{ 1 + \frac{\|\dot{\epsilon}\| \Delta t}{\mathfrak{Div}}, 100 \right\} \quad (3.160)$$

where  $\mathfrak{Div}$  is defined in an arbitrary manner and based on the user's experience.  $\|\dot{\epsilon}\|$  is the norm of strain rate, defined as  $\sqrt{\dot{\epsilon}_{ij}\dot{\epsilon}_{ij}}$ . Consequently to this relation, the higher number of sub-interval can be applied at the *time* and *space (integration points)* with higher strain to result in a better stress accuracy. Although, a maximum number of sub-intervals as 100 has been prescribed in the code [Wang, 1993]. In this work, a default value of  $\mathfrak{Div} = 5 \times 10^{-3}$  has principally been appropriate based on our numerical experience.

### 3.5 Simulations of the triaxial tests on Boom Clay

The triaxial test is frequently used to study the behavior of the soils and soft rocks, and it stands as a reliable method to determine their shear strength parameters. Figure 3.29 shows schematically a triaxial testing machine. In a triaxial cell, the cylindrical sample is surrounded by oil/water as the confining medium which applies the so-called confining pressure. Basically, the principle of the triaxial test is expressed by an applied stress in the vertical direction, i.e. along the axis of the cylindrical sample, which is different from the stresses applied perpendicular to the cylinder sides (i.e. confining pressure). This could be described in terms of the principle stresses as<sup>27</sup>  $\sigma_1 \neq \sigma_2 = \sigma_3$  for a compression test, and as  $\sigma_1 = \sigma_2 \neq \sigma_3$  for a tensile test. Thence, the sample is firstly put under a constant confining pressure (that may correspond to the consolidation phase), with respect to which our desirable isotropic stress can be attained. Then, a vertical (axial) stress induces the shearing. In this work, we are solely dealing with the compression triaxial tests. The triaxial test can be generally performed under the Consolidated-Drained (CD), Consolidated-Undrained (CU), or Unconsolidated-Undrained (UU) conditions.

In the following, the numerical simulation of some experimental triaxial compression tests on Boom Clay samples are performed with application of the theoretical framework explained

<sup>26</sup>These terms will be discussed in Chapter 5.

<sup>27</sup> $\sigma_1$  is the major principle stress.

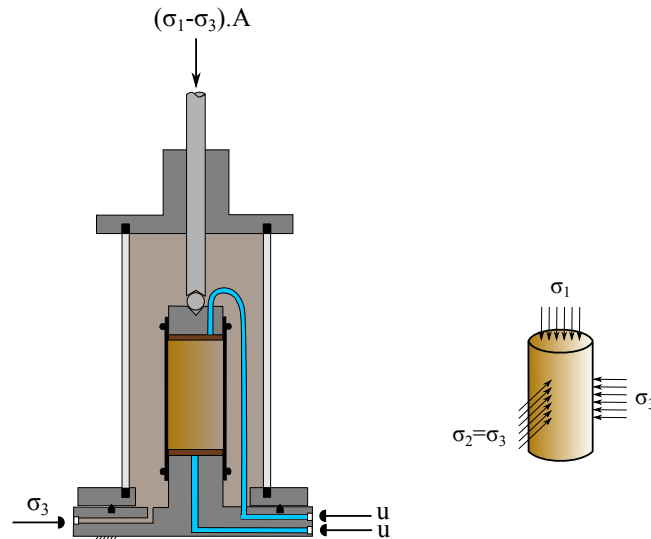


Figure 3.29: Schematic representation of a triaxial testing machine, and a cylindrical sample under compression.

heretofore in this Chapter. The main objective is not validation of the classical numerical framework, it is rather ensuring a set of parameters which could represent realistically the material behavior in order to be used for the more complicated simulations in the next Chapters. A basic set of parameters with respect to the literature is considered as the reference, and significant influence of some of these parameters, or the corresponding modifications applied with respect to the experimental results, are then discussed.

### 3.5.1 Stress-strain mechanical response: deviatoric stress development

Prior to the presentation of the referred triaxial tests and the corresponding numerical results, it is noteworthy to remind that the natural saturated Boom Clay behavior during the compression triaxial tests, and its rupture response are strongly dependent on the initial effective mean stress ( $p'_0$ ), and the drainage conditions [Horseman et al., 1987; Coop et al., 1995].

The force-displacement curves or the deviatoric stress-axial strain curves are commonly used to characterize the mechanical response of a geomaterial. Following the literature with regard to the experimental results of the drained triaxial tests on Boom Clay [Sultan, 1997; Coll, 2005], in the deviatoric plane, the deviatoric stress has a considerable decrease (i.e. softening behavior) until a residual value after a remarkable peak, for the low enough values of the effective mean stress. This response is accompanied by firstly a contracting and then dilatant behavior in the volumetric plane. By increasing the mean effective stress, this peak is less considerable which signifies the tendency to the disappearance of the post-peak dilatant response (see Figure 3.30). The latter response is less remarkable for an undrained triaxial test, according to Coll [2005]. That is to say that a considerable peak could be observed for the higher level of mean effective stress. For instance, with regard to the undrained triaxial tests performed by Horseman et al. [1987] on the Boom Clay samples consolidated at various pressure in the range of 0.89-5.42 MPa, the softening response and a clear peak strength have been observed for all the tests (see Figure 3.31). Although, this may not be always the case as the softening behavior was not marked for instance neither during the undrained triaxial tests performed by [Baldi et al., 1991] with  $p'_0 = 3.77 \text{ MPa}$ , nor in the tests performed at Université de Liège (ULg) in the framework of TIMODAZ project [TIMODAZ, 2010b], with the actual consolidation pressure as

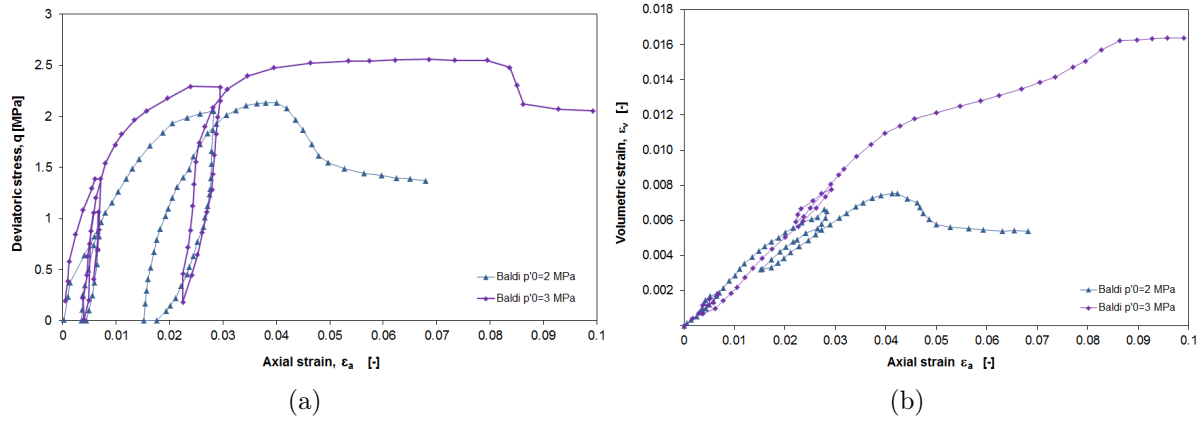


Figure 3.30: Drained triaxial test results [Baldi et al., 1991]: (a) Deviatoric stress versus axial strain. (b) Volumetric strain versus axial strain.

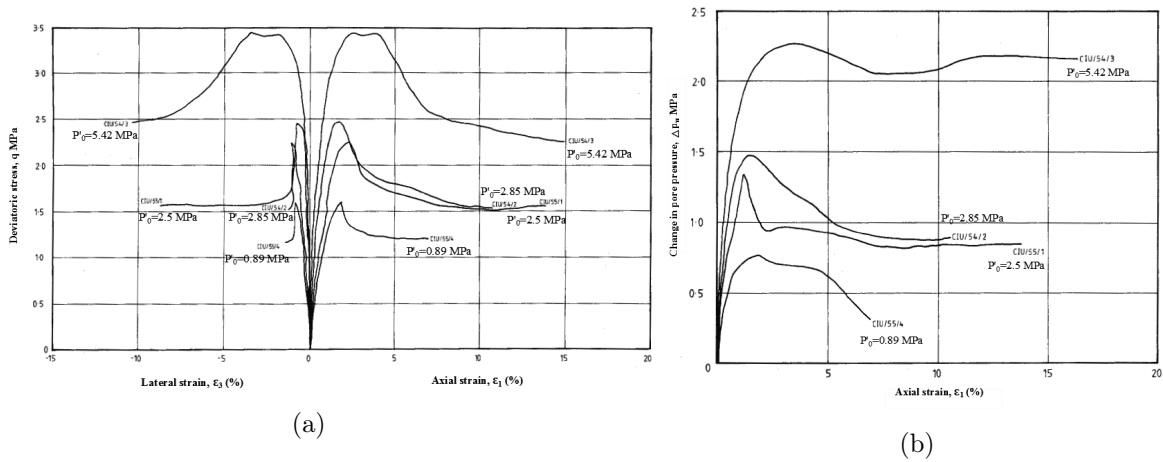


Figure 3.31: Undrained triaxial test results; after [Horseman et al., 1987]: (a) Deviatoric stress versus axial and lateral strain. (b) Change in pore water pressure versus axial strain.

$p'_0 = 3.5 - 4 \text{ MPa}$  (see Section 3.5.2.1).

Indeed, interpretation of the triaxial tests on Boom Clay is not generally an easy job taking into account its characteristics, and it could show quite different behavior with reference to various former studies [Horseman et al., 1987; Baldi et al., 1991; Sultan, 1997; Coll, 2005; TIMODAZ, 2010b; Yu et al., 2012]. One should notice the initial conditions of the test, the properties of the sample (water content, saturation condition, etc.), the site and depth at which the samples have been taken, the intact or reconstituted samples, etc. Thence, it would not likely be possible to conclude one general response of the material in the deviatoric plane even through gathering and studying all the available data from the literature.

### 3.5.2 Description of the triaxial tests

This Section does not aim to gather all various available triaxial tests results since it has been already the objective of some former studies, taking also into account that it may not be a straightforward task as already mentioned. But within the framework of this thesis and as a requisite to the more complicated simulations of the next Chapters, this Section intends for

ensuring a set of parameter to be used hereafter. To do this, four series of the available triaxial tests are discussed in comparison with the numerical simulations: the undrained triaxial tests performed at ULg, and in ENPC in the framework of TIMODAZ project [TIMODAZ, 2010b], the undrained triaxial tests performed by Yu et al. [2012], and the drained triaxial tests performed by Lenoir et al. [2008] and Coll [2005]. Each of these tests are firstly represented followed by an analysis of their results in comparison with the numerical predictions. All the numerical modelings have been performed in the axisymmetric state, and under similar conditions and loading procedure as the corresponding experiments.

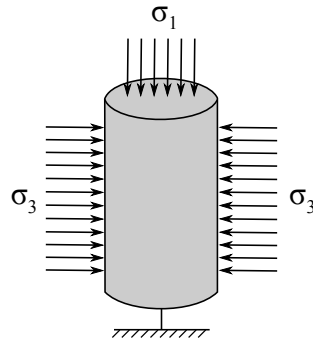
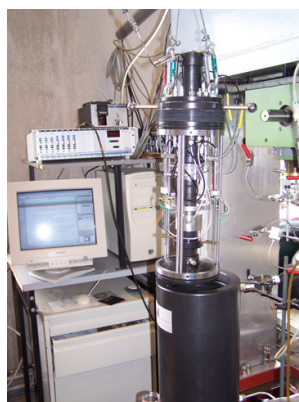


Figure 3.32: The triaxial test simulation; the bottom nodes are restricted in the vertical direction.

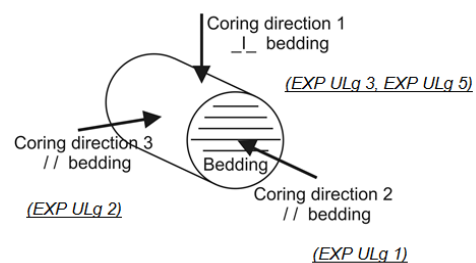
### 3.5.2.1 Hydro-mechanical simulation of the triaxial tests performed at ULg

Four undrained triaxial tests performed at ULg, ArGEnCo, GEO<sup>3</sup>, on the cylindrical samples of Boom Clay cored by SCK.CEN at the URL of Mol, are discussed here. The 36 mm diameter plugs were water cored and after wiping, immediately wrapped in cellophane and brought to the lab where they were dressed and placed in the Viton jacket [TIMODAZ, 2010b]. Two of these samples, namely EXP ULg 1 and EXP ULg 2, has been cored parallel to the bedding, and the other two samples, namely EXP ULg 3 and EXP ULg 5, has been cored perpendicular to the bedding (see Figure 5.23).

The general test procedure includes an isotropic loading, the saturation phase so that the samples are supposed to be saturated by then, and force-controlled shearing with the rate of



(a)



(b)

Figure 3.33: (a) Triaxial cell at ArGEnCo - GEO<sup>3</sup> laboratory, ULg. (b) Coring direction of the samples; after [TIMODAZ, 2010b].

$5 \times 10^{-6} \text{ MPa/s}$  for EXP ULg 5, and  $5 \times 10^{-5} \text{ MPa/s}$  for the others, after increasing of the confining pressure up to  $4.5 \text{ MPa}$ . In reality, EXP ULg 1, EXP ULg 2, and EXP ULg 3 have initially had an effective stress of about  $3 \text{ MPa}$  with the initial pore water pressure of  $1.5 \text{ MPa}$  at the zero axial strain level. Although, EXP ULg 5 could better attain the in-situ effective stress of about  $2.5 \text{ MPa}$ . It must be noted that the conditions of the saturation phase could be important in the obtained results of a triaxial test. The saturation process of the samples under zero stress might result in a swelling of around  $18^\circ$ , following Delage et al. [2008]. On the contrary, saturation of the samples under the in-situ stress lies in a zero suction, and no further swelling is supposed to occur. Thence, based on the latter reference, this point has been taken into account during the triaxial tests performed in the framework of TIMODAZ project (presented in this Section and Section 3.5.2.2).

Figures 3.34a-3.34b show the evolution of the deviatoric stress and pore water pressure in function of the axial strain. As it is observed with reference to the results of EXP ULg 1 and EXP ULg 2, the deviatoric stress consists in a quite remarkable resistance; it is increased drastically at the beginning and then, an slight increase up to the maximum value of about  $3.5 \text{ MPa}$ . The pore water pressure also experiences a quick increase initially, which is in accordance with the deviatoric stress evolution, and then, it tends to a slight decrease (in case of EXP ULg 2) and a general ultimate stabilization afterwards. On the contrary, EXP ULg 3 may not be a good reference for interpretation of the material behavior since it shows an anomaly in the form of a strong drop of pore water pressure (as the deviatoric stress increases), which signifies an increase of effective mean stress (Figure 3.34d). In addition, EXP ULg 5 does also show an irregular drop of the deviatoric stress at the axial strain of about 4%, which is probably due to the sample collapse, and this causes also a drop of pore water pressure.

#### **Simulation of the tests:**

The numerical modeling have been performed with the set of hydro-mechanical parameters as presented in Tables 3.1-3.2. They have been basically chosen through an analysis with reference to the literature as summarized in Tables 2.2-2.3, and they are being validated hereafter; the present choice is consistent with the former numerical studies on the basis of the experimental data gathered during the TIMODAZ project [Dizier, 2011; François et al., 2012].

Considering the fact that the tests had been done with two different rates of the applied force and the *actual* initial effective stresses ( $p'_0 = 2.5 \text{ MPa}$  and  $p'_0 = 3 \text{ MPa}$ ) and pore water pressures as already mentioned, two simulations have been done at the this level, as presented in Figure 3.35. First, with regard to the simulation with  $p'_0 = 2.5 \text{ MPa}$  - and the shearing rate of  $5 \times 10^{-6} \text{ MPa/s}$  - which corresponds to the EXP ULg 5, the general pattern of evolution of pore water pressure in comparison with the experimental result seems good in terms of the maximum value of pressure, although the anomaly of the experimental results does not let a correct interpretation. The latter is more considerable in the deviatoric plane where there is a quite remarkable strength peak in spite of the strong drop faced afterwards, and this feature is also observable in the effective stress path. On the contrary, the total stress path shows a correct representation of the initial condition. On the whole, this test might not be possible to be more focused numerically because of the observed unexpected response of the sample. The similar problem was faced for the EXP ULg 3. Thence, in the following, our numerical simulations focus on the interpretation of the EXP ULg 1 and EXP ULg 2 (with  $p'_0 = 3 \text{ MPa}$ ).

With reference to EXP ULg 1 and EXP ULg 2, the corresponding numerical results could model the first drastic increase of the deviatoric stress accompanied by a quick increase of pore water pressure. However, the experimental results show a longer strengthening process of the sample while the numerical result underestimates the ultimate deviatoric stress (Figure 3.35a). On the contrary, the numerical results stays in a quite good accordance with the experimental

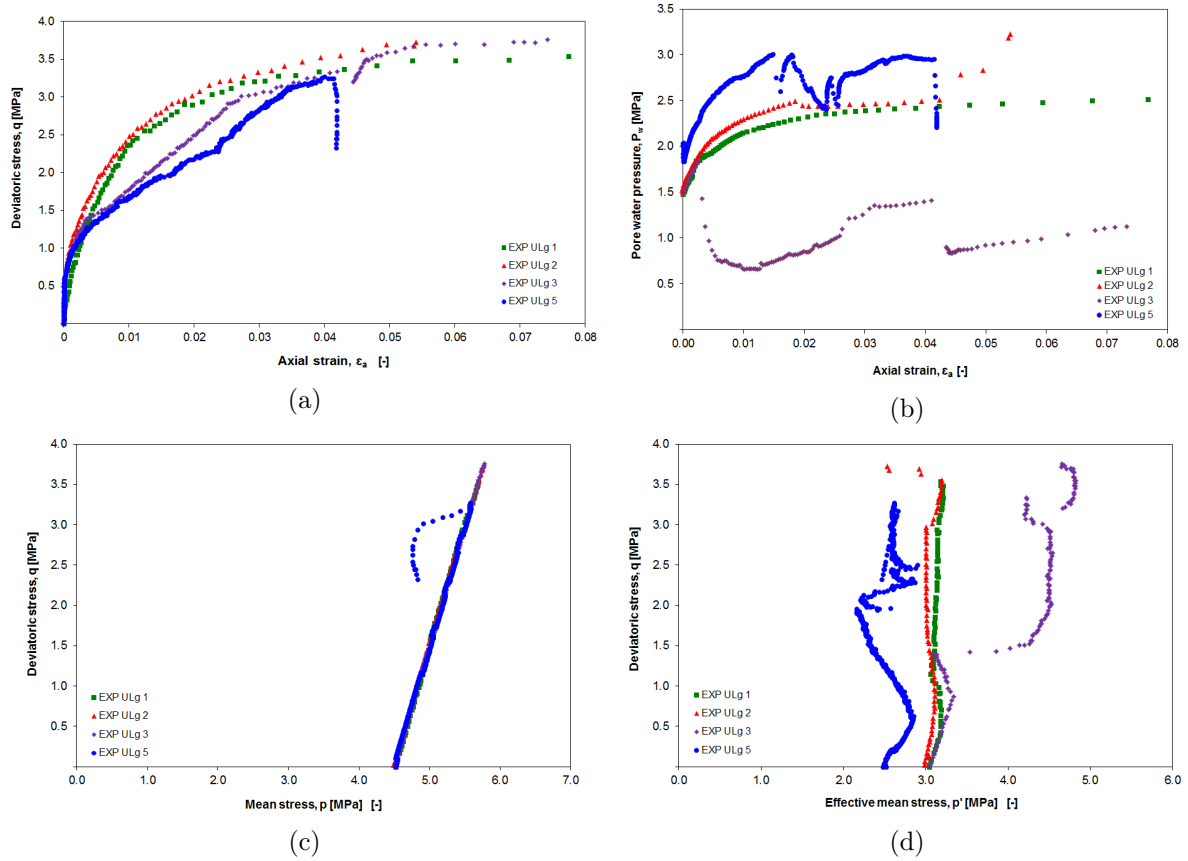


Figure 3.34: Experimental undrained triaxial tests results performed at ULg, ArGEnCo: (a) Deviatoric stress in function of axial strain. (b) Pore water pressure in function of axial strain. (c) Stress path in the  $(p, q)$  plane. (d) Stress path in the  $(p', q)$  plane; after [TIMODAZ, 2010b].

Table 3.1: Mechanical parameters of the model

Parameter	Symbol	Value	Unit
Young elastic modulus	$E$	300	$MPa$
Poisson ratio	$\nu$	0.125	-
Specific mass of the grains	$\rho_s$	2700	$Kg/m^3$
Initial compression friction angle	$\varphi_{C0}$	8	$^\circ$
Final compression friction angle	$\varphi_{Cf}$	18	$^\circ$
Hardening coefficient	$B_\varphi$	0.001	-
Hardening coefficient	$D_\varphi$	0	-
Initial cohesion	$c_0$	300	$kPa$
Final cohesion	$c_f$	300	$kPa$
Softening coefficient	$B_c$	0	-
Softening coefficient	$D_c$	0	-
Dilatancy angle	$\Psi$	0	$^\circ$

Table 3.2: Hydraulic parameters of the model

Parameter	Symbol	Value	Unit
Water permeability	$k$	$3 \times 10^{-19}$	$m^2$
Specific mass of water	$\rho_w$	$1 \times 10^3$	$Kg/m^3$
Porosity	$n$	0.39	-
Water compressibility	$\frac{1}{\chi_w}$	$5 \times 10^{-10}$	$Pa^{-1}$
Water dynamic viscosity	$\mu_w$	$1 \times 10^{-3}$	$Pa.s$

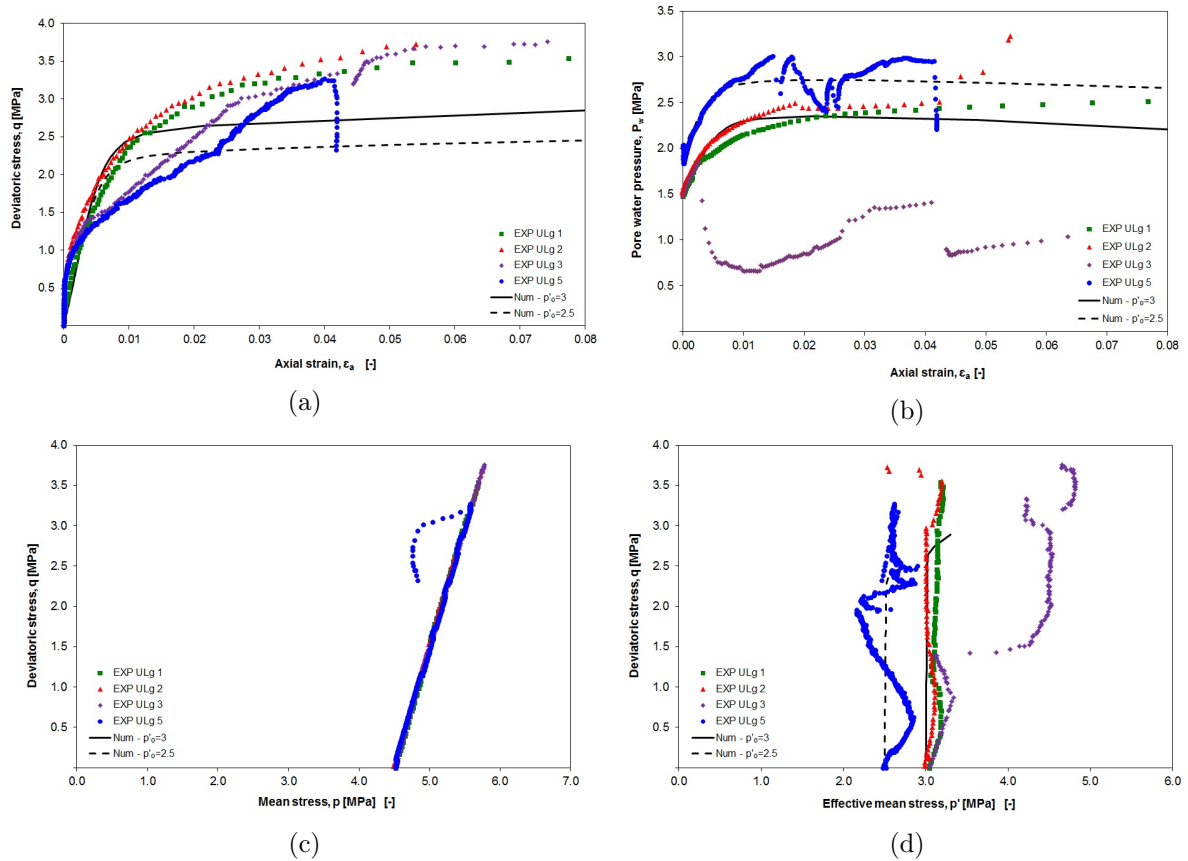


Figure 3.35: Results of the numerical simulations of the tests performed at ULg, ArGENCo, compared to the experimental results: (a) Deviatoric stress in function of axial strain. (b) Pore water pressure in function of axial strain. (c) Stress path in the  $(p, q)$  plane. (d) Stress path in the  $(p', q)$  plane.

ones in the pore water pressure plane. In addition, the numerical underestimation of the deviatoric stress, i.e. strengthening response of the material upon reaching to the plasticity surface, can be also observed in the  $(p', q)$  plane.

Since the chosen hardening parameters might be important in the obtained numerical response of the material, in terms of strengthening process, the sensitivity of the results to the change of the initial friction angle  $\varphi_i$  and hardening parameter  $B_\varphi$  - with reference to the values brought in Tables 3.1-3.2 - is shown in Figures 3.36-3.37. It is observed that a higher value of the initial friction angle than the reference one could fairly delay the entrance to plasticity (see Figure 3.36a). The lower value of friction angle than  $8^\circ$  does not seem to make a considerable change in the results. Moreover, Figure 3.37 shows that increasing the  $B_\varphi$  from the reference value could slow down the strengthening process after the entrance to plasticity (see Figure 3.37a), where by decreasing this parameter, this process gets quicker than the experimental observations. Comparing the results of these three values can justify the chosen value so far.

Furthermore, the model's parameters (consisting in cohesion and friction angle) might be recalibrated in order to better reproduce the experimental results. Considering Figure 3.35d, the Drucker-Prager failure criterion for the reference numerical simulation (i.e. with  $p'_0 = 3 \text{ MPa}$  and the parameters listed in Tables 3.1-3.2<sup>28</sup>), and its regression line for the experimental

<sup>28</sup>These parameters are supposed to be the reference set of parameters hereafter, and any modification will be done with respect to them.

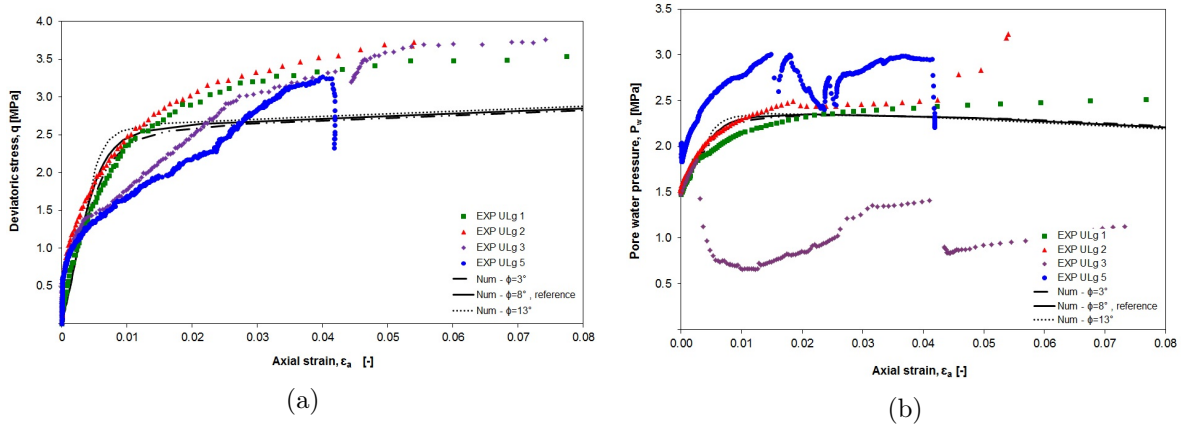


Figure 3.36: Results of the numerical simulations of the tests performed at ULg, ArGENCo, with three values of  $\varphi_i$ , compared to the experimental results:(a) Deviatoric stress in function of axial strain. (b) Pore water pressure in function of axial strain.

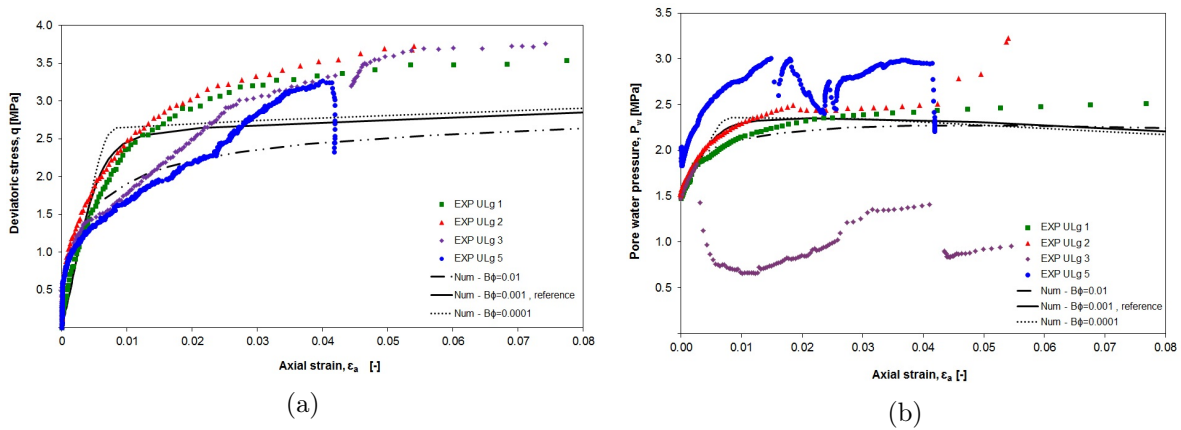


Figure 3.37: Results of the numerical simulations of the tests performed at ULg, ArGENCo, with three values of  $B_\varphi$ , compared to the experimental results:(a) Deviatoric stress in function of axial strain. (b) Pore water pressure in function of axial strain.

results are shown in Figure 3.38. The friction angle and cohesion values which correspond to the experimental failure line are calculated as  $\varphi = 14.59^\circ$  and  $c = 872.65kPa$ .

Table 3.3 presents the parameters correspond to our reference simulation as well as two other sets of parameters. The first set correlates with the modification of cohesion and friction angle based on the experimental failure criterion while the other parameters kept constant. The second set corresponds to the simulation with two other modified parameters of the model ( $\varphi_{C0}$ ,  $B_\varphi$ ), besides the cohesion and friction angle in order to fit in with the experimental results. Figures 3.39 show the comparison of the results of reference simulation and two other ones with the experimental results. As it is observed, the simulation *Num* overestimates the initial radical increase of deviatoric stress and pore water pressure. However, by modification of the initial friction angle  $\varphi_i$  and hardening parameter  $B_\varphi$ , besides the desired cohesion and friction angle, the experimental results could be reproduced quite well by the numerical simulation, i.e. *Num* 2.

Since our objective is to validate *one single* set of main parameters (such as friction angle and cohesion) which could reproduce the Boom Clay behavior satisfactory enough in order to use them in all the coming simulations, this validation of the parameters only with reference to

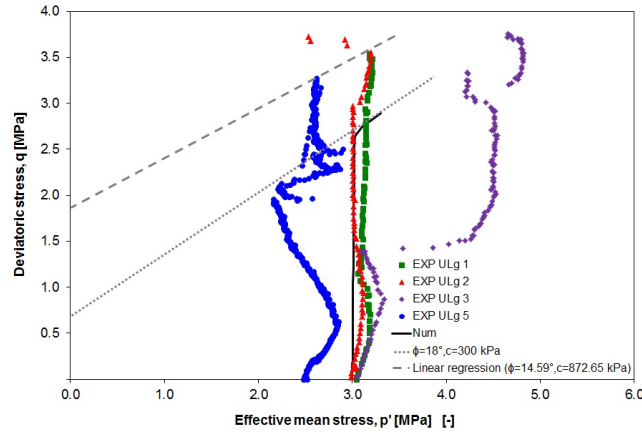
Figure 3.38: Drucker-Prager failure criterion in the  $(p', q)$  plane.

Table 3.3: Sets of mechanical parameters used for the modelings

Parameter	Symbol	Value			Unit
		Num , reference	Num	Num 2	
Young elastic modulus	$E$	300	300	300	$MPa$
Poisson ratio	$\nu$	0.125	0.125	0.125	-
Specific mass of the grains	$\rho_s$	2700	2700	2700	$Kg/m^3$
Initial compression friction angle	$\varphi_0$	8	8	2	$^\circ$
Final compression friction angle	$\varphi_f$	18	15	15	$^\circ$
Hardening coefficient	$B_\varphi$	0.001	0.001	0.01	-
Hardening coefficient	$D_\varphi$	0	0	0	-
Initial cohesion	$c_0$	300	870	870	$kPa$
Final cohesion	$c_f$	300	870	870	$kPa$
Softening coefficient	$B_c$	0	0	0	-
Softening coefficient	$D_c$	0	0	0	-
Dilatancy angle	$\Psi$	0	0	0	$^\circ$

one series of experimental results does not seem realistic. On the whole, it is concluded that the undrained triaxial tests performed at ULg, ArGENCo could be better reproduced *principally* by increasing the cohesion (or, more precisely the set of parameters applied for the simulation Num 2). This is due to the quite high strength peak of deviatoric stress observed during the experiments. However, the latter is not supposed to correspond to a general response of Boom Clay. Therefore, three other series of the triaxial tests are discussed in the following to ensure the final set of main parameters.

### 3.5.2.2 Hydro-mechanical simulation of the triaxial test performed at ENPC

The undrained triaxial test performed - on the Boom Clay sample cored by SCK.CEN - at ENPC, CERMES was not a standard triaxial test. The test has been performed using a developed hollow cylinder cell with an inner diameter of 60mm and an outer diameter of 100mm. The specimen could have an height of 75–80mm (Figure 3.40) (see [TIMODAZ, 2010b] for further information).

The general test procedure consists in a non-conventional thermo-mechanical loading including a consolidation phase, saturation under the in-situ effective mean stress (i.e. 2.25 MPa: applied total mean stress of 3.25 MPa and back pressure of 1 MPa), undrained heating (up to 80°C) and drained cooling, undrained shearing at constant total mean stress (a path close to that followed by material during the gallery excavation), a relaxation from the maximum

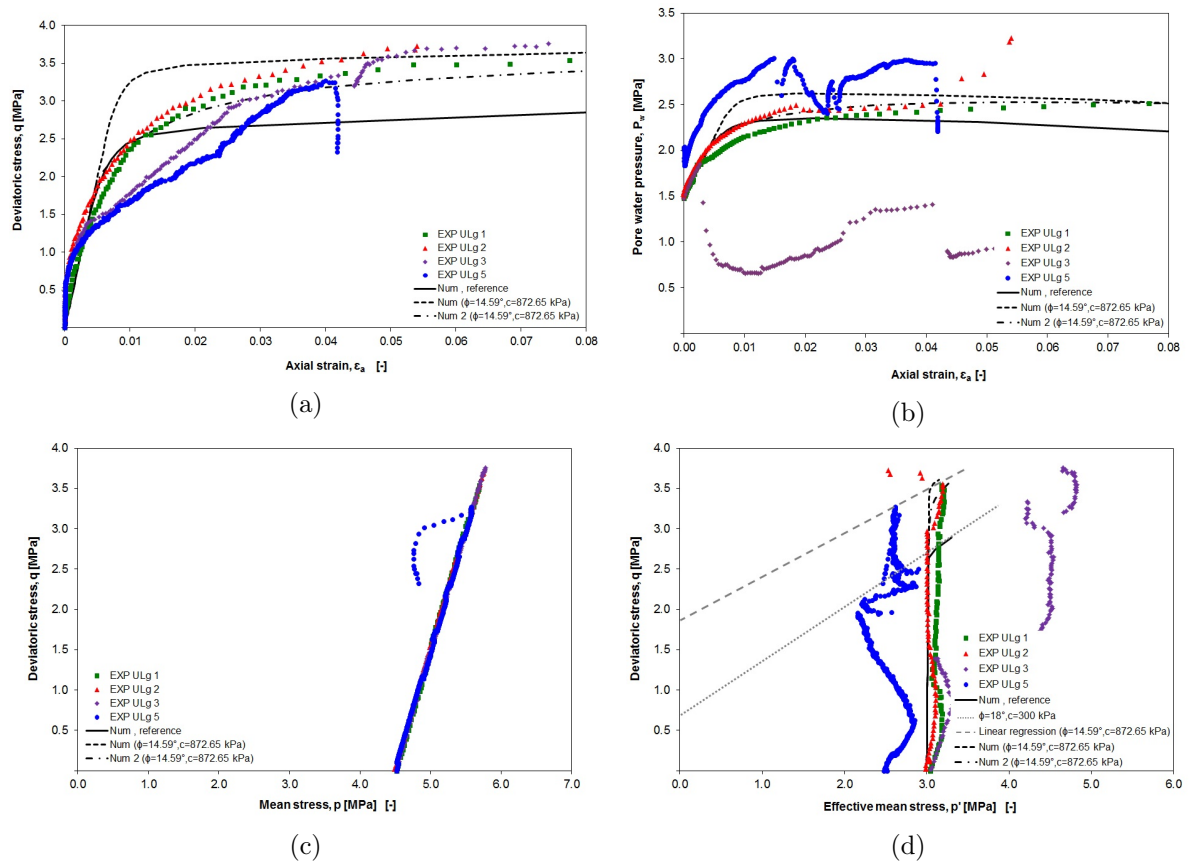


Figure 3.39: Results of the numerical simulations of the tests performed at ULg, ArGenCo, compared to the experimental results: (a) Deviatoric stress in function of axial strain. (b) Pore water pressure in function of axial strain. (c) Stress path in the  $(p, q)$  plane. (d) Stress path in the  $(p', q)$  plane and the failure criteria.



Figure 3.40: (a) Schematic representation of the hollow cylinder triaxial cell. (b) Boom Clay hollow cylinder sample [TIMODAZ, 2010b].

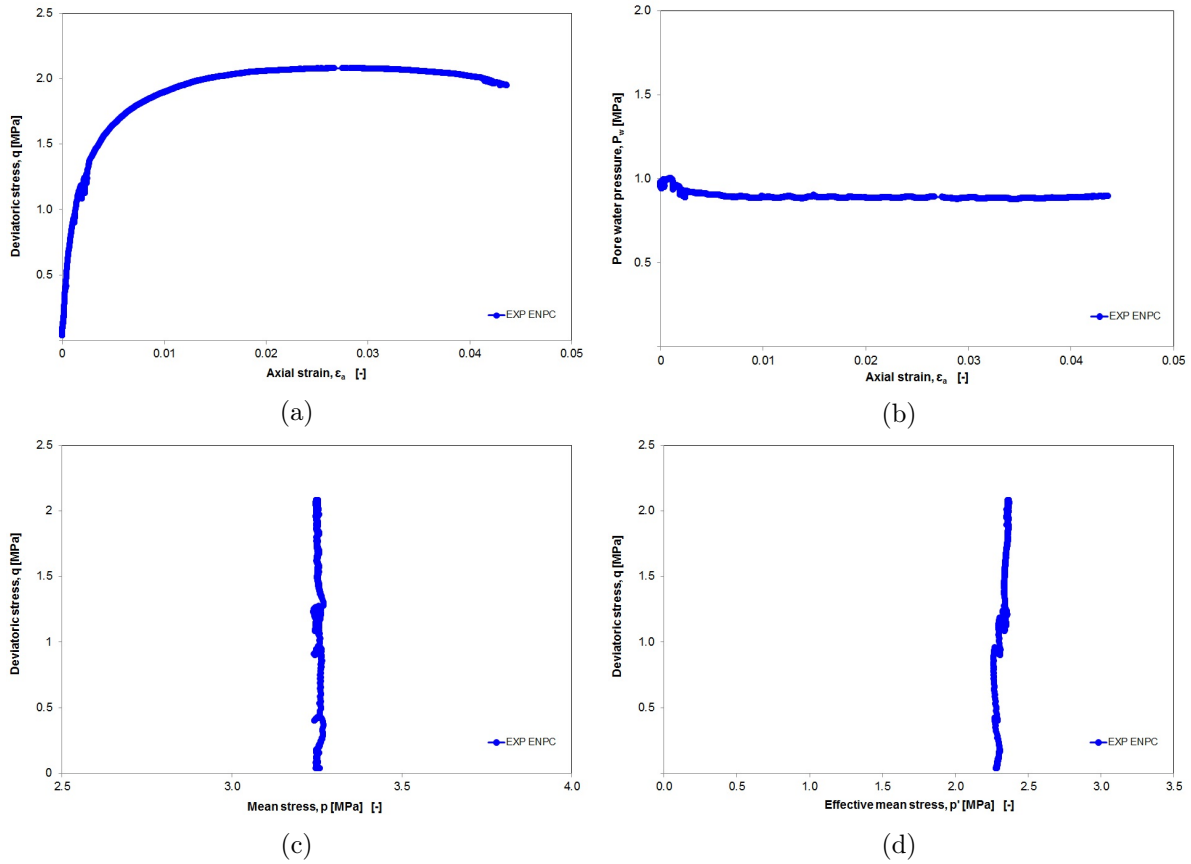


Figure 3.41: Experimental undrained triaxial test results performed at ENPC, CERMES: (a) Deviatoric stress in function of axial strain. (b) Pore water pressure in function of axial strain. (c) Stress path in the  $(p, q)$  plane. (d) Stress path in the  $(p', q)$  plane; after [TIMODAZ, 2010b].

attained shear stress of 2.08 MPa to 1.6 MPa, and finally undrained heating phase up to 80°C [TIMODAZ, 2010b]. What we concern here is the shearing phase, i.e. without modeling the pre-heating and post-heating. Figure 3.41 shows the evolution of the deviatoric stress, and pore water pressure in function of the axial strain, the stress paths in the  $(p, q)$  and  $(p', q)$  planes. It is observed that the deviatoric stress is increased to attain the maximum value of about 2.08 MPa (Figure 3.41a) while total mean stress is constant (Figure 3.41c). It reaches a plateau subsequently to the peak value in the deviatoric plane. Pore water pressure shows also this stationary phase after a very slight decrease of the pressure at the beginning of test (Figure 3.41b). Thence, the effective stress path is quite straight too (Figure 3.41d).

#### Simulation of the test:

With regard to our reference parameters (i.e. Tables 3.1-3.2), Figure 3.42 show the results of the numerical simulation in comparison with the experimental results. A good agreement is observed between the numerical and experimental results. Therefore, the chosen set of parameter is validated by the undrained triaxial test results obtained at ENPC.

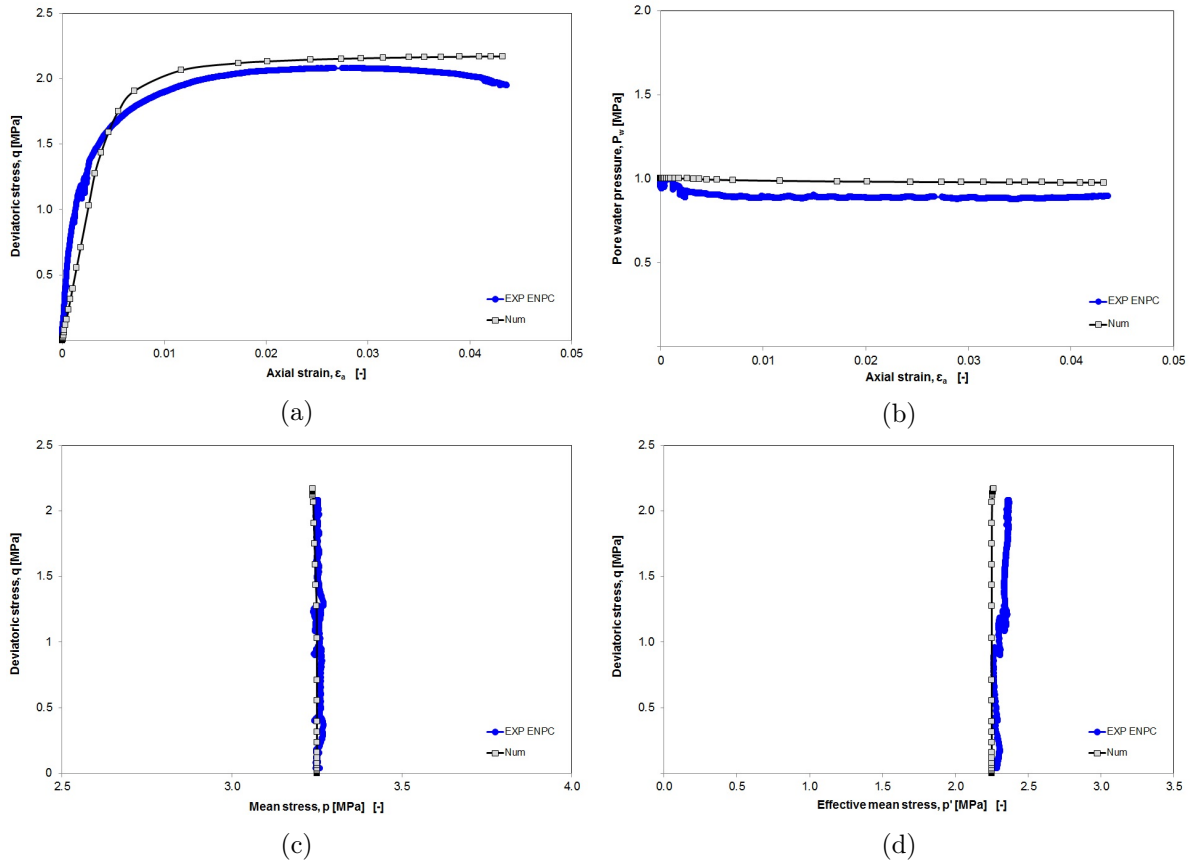


Figure 3.42: Results of the numerical simulations of the test performed at ENPC, CERMES, compared to the experimental results: (a) Deviatoric stress in function of axial strain. (b) Pore water pressure in function of axial strain. (c) Stress path in the  $(p, q)$  plane. (d) Stress path in the  $(p', q)$  plane.

### 3.5.2.3 Hydro-mechanical simulation of the triaxial tests performed at IRSM

Three undrained triaxial tests were performed at IRSM, CAS<sup>29</sup> on the cylindrical samples cored once more by SCK.CEN at the URL's level in Mol<sup>30</sup>. The triaxial tests have been performed by a special designed double linkage triaxial testing machine as shown in Figure 3.43. Its advantage compared to an ordinary triaxial device is that it can execute the simultaneous tests on two samples with the same axial pressure, different confining pressure, and the same water pressure [Yu et al., 2012]. Two tests have been performed with an initial effective stress of 3.5 MPa (IRSM1 and IRSM2) and the other test has been conducted to have an initial effective stress similar to the in-situ one, i.e. 2.5 MPa (IRSM3).

The general test procedure includes an isotropic consolidation loading, saturation phase, and shearing at the rate of  $20\mu\text{m}/\text{min}$ , after reaching an effective stress of 3.5 MPa for the tests IRSM1 and IRSM2 (total mean stress of 4.7 MPa and back pressure of 1.2 MPa) and 2.5 MPa for the test IRSM3 (total mean stress of 3.7 MPa and back pressure of 1.2 MPa). Figure 3.44 represents the evolution of deviatoric stress and pore water pressure in function of the axial strain for three tests. All the tests show an increase of deviatoric stress to a peak

<sup>29</sup>Institute of Rock and Soil Mechanics, Chinese Academy of sciences.

<sup>30</sup>Mol Site / HADES borehole 2007-2 / Connecting gallery / Ring 68-69E / 15.0 m to 17.50 m from the HADES URF (intrados).

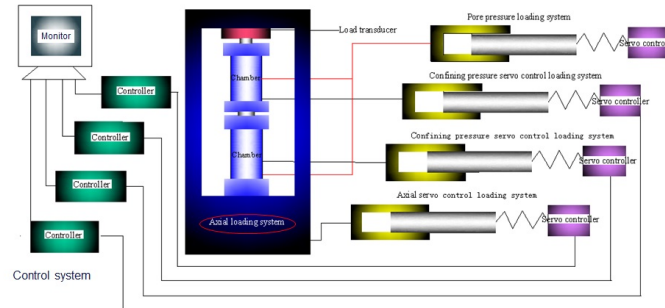


Figure 3.43: Schematic representation of the triaxial testing machine at IRSM, CAS [Chen and Li, 2011].

value ranged from 3-3.5  $MPa$  (Figure 3.44a-3.44c-3.44e). These peak values signifies a quite high mobilized shear strength. In addition, the plastic behavior of Boom Clay can be marked since the tests seem to follow a considerable strengthening process before reaching their peak; specially in the second test IRSM2. Furthermore, the first two tests show a relatively fairly ductile behavior that it can be related to the higher confining pressure under which the tests have been performed. Although, a slight softening behavior is also noticed after the stress peak. This softening response is considerable for the test IRSM3. This behavior could contrast with the results of the undrained tests performed by ULg and ENPC. As it has been already discussed in Section 2.3.2.3, besides the confining pressure, OCR is also important to establish the dominant response of the material; higher value of OCR results in a more brittle response. In the IRSM tests, an OCR of about 2 has been determined, according to Yu et al. [2012].

Pore water pressure variations, are demonstrated in Figures 3.44b-3.44d-3.44f. They show a fairly gradual increasing pattern while a more drastic rise could be expected on the pre-peak state (the deviatoric stress of about 2  $MPa$ , with respect to Figures 3.44a-3.44c-3.44e), which is accompanied by the propagation of micro-fractures based on [Yu et al., 2012]. This can be caused by a partially saturated state of the material, i.e. they possibly have not achieved a fully saturated state before shearing. It might lie in the existence of some air bubbles in the samples. This issue can be also verified by a quite high resistance of the material in the deviatoric plane. In the same sense, considering the stress paths in the  $(p', q)$  plane shown in Figure 3.45b<sup>31</sup>, an un-usuality is observed with reference to a normal undrained stress path. Indeed, the samples have experienced a quite dominant dilatancy tendency. This has been reported in [Yu et al., 2012] as well, based on which a short-time compression tendency and a second dominant swelling tendency have been observed during shearing. However, the latter was reported to be up to 7% of swelling for IRSM1, 4.6% for IRSM2, and 2.8% for IRSM3, which are far from a volumetric strain  $\approx 0\%$ <sup>32</sup> that is normally expected through an undrained triaxial test. On the contrary to these observations, the pore pressure does not drop down, though (see Figures 3.44b-3.44d-3.44f). On the whole, we may conclude that the samples were not fully saturated at the shearing time, and it could prevent an initial quick increase of pore pressure. Then, they might have also experienced some swelling with regard to which a slower evolution of pore pressure was observed and it then tended to get stabilized (although, it could be expected to have more realistically a drop of pore pressure).

#### Simulation of the tests:

<sup>31</sup>It was not possible to plot the stress path in the  $(p', q)$  plane for the test IRSM2, with respect to our available data.

<sup>32</sup>A very slight non-zero volumetric strain could be attributed to the fracturing.

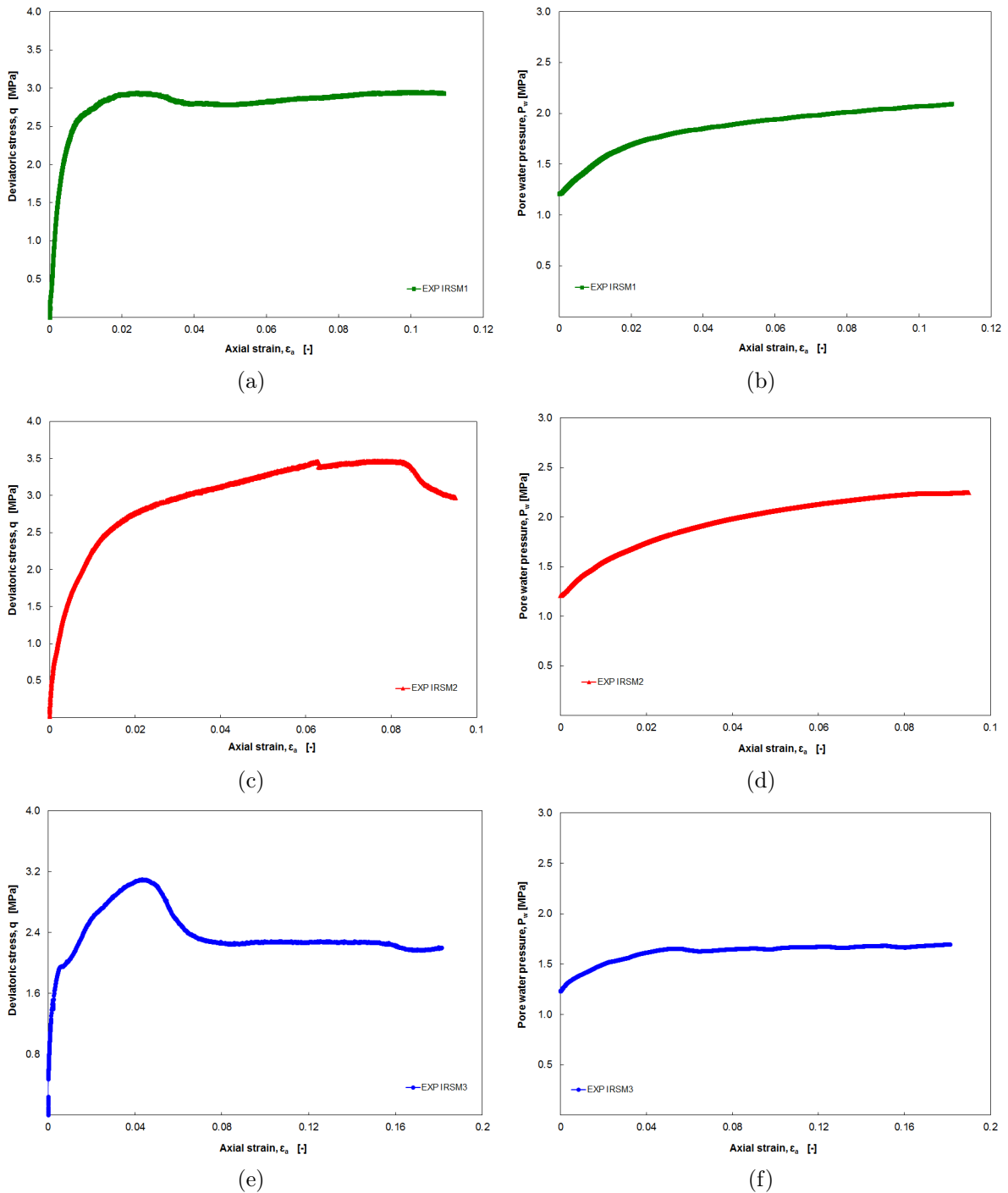


Figure 3.44: Experimental undrained triaxial tests results performed at IRSM, CAS: (a) Deviatoric stress in function of axial strain for the first test. (b) Pore water pressure in function of axial strain for the first test. (c) Deviatoric stress in function of axial strain for the second test. (d) Pore water pressure in function of axial strain for the second test. (e) Deviatoric stress in function of axial strain for the third test. (f) Pore water pressure in function of axial strain for the third test; after [Yu et al., 2012].

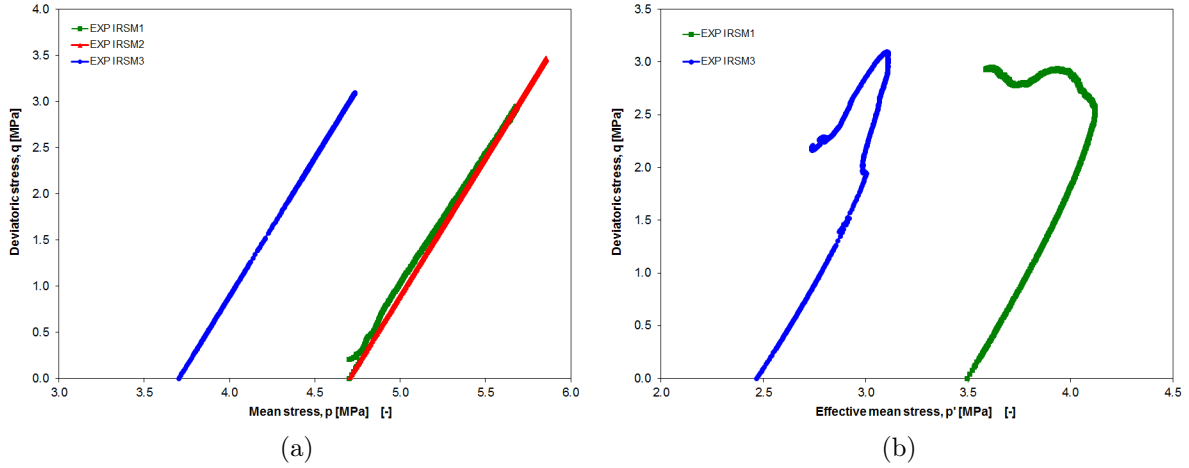


Figure 3.45: Experimental stress paths for the undrained triaxial tests performed at IRSM, CAS: (a) Stress path in the  $(p, q)$  plane. (b) Stress path in the  $(p', q)$  plane.

To simulate the observed softening behavior in the post-peak regime (after peak of deviatoric

Table 3.4: Mechanical parameters used for the modelings

Parameter	Symbol	Value			Unit
		<i>Num IRSM1</i>	<i>Num IRSM2</i>	<i>Num IRSM3</i>	
Young elastic modulus	$E$	300	300	300	MPa
Poisson ratio	$\nu$	0.125	0.125	0.125	-
Specific mass of the grains	$\rho_s$	2700	2700	2700	Kg/m <sup>3</sup>
Initial compression friction angle	$\varphi_{C0}$	8	8	8	°
Final compression friction angle	$\varphi_{Cf}$	18	18	18	°
Hardening coefficient	$B_\varphi$	0.001	<u>0.004</u>	0.001	-
Hardening coefficient	$D_\varphi$	0	0	0	-
Initial cohesion	$c_0$	300	300	300	kPa
Final cohesion	$c_f$	<u>30</u>	<u>3</u>	<u>30</u>	kPa
Softening coefficient	$B_c$	<u>0.01</u>	<u>0.01</u>	<u>0.01</u>	-
Softening coefficient	$D_c$	<u>0.017</u>	<u>0.075</u>	<u>0.037</u>	-
Dilatancy angle	$\Psi$	0	0	0	°

stress, see Figures 3.44a-3.44c-3.44e) of this test series, besides our reference parameters (i.e. Tables 3.1-3.2), the cohesion softening parameters are also defined in the model. The latter have been calibrated here for each test with respect to the observed experimental softening response<sup>33</sup>. Thence, Table 3.4 presents the accomplished mechanical parameters applied to the simulations; slight increase of the hardening parameter  $B_\varphi$  for *Num IRSM2* could help the model to approach better the *delayed* strengthening process up to the stress peak observed in EXP IRSM2, in comparison with two other tests. Figure 3.46 shows the comparison of the experimental and numerical results. In deviatoric plane (Figures 3.46a-3.46c-3.46e), the numerical simulations show a similar general pattern of evolution of deviatoric stress by increasing the axial strain, in comparison with the experimental results. Although, in case of IRSM1, there is a slight underestimation of the ultimate stress. In addition, in IRSM2, and more importantly in IRSM3, the peak of deviatoric stress is underestimated by the numerical modelings. In terms of pore water pressure evolution, on the contrary to the experimental results, the full saturation state of the numerical simulations could realistically produce an initial *quick* increase of pore pressure.

<sup>33</sup>However, a particular discussion will be conducted in Chapter 5 on the parameters associated to softening (i.e.  $c_f$ ,  $B_c$  and  $D_c$ ) to validate them, with a focus on their impact on our analyses involving the strain localization phenomenon.

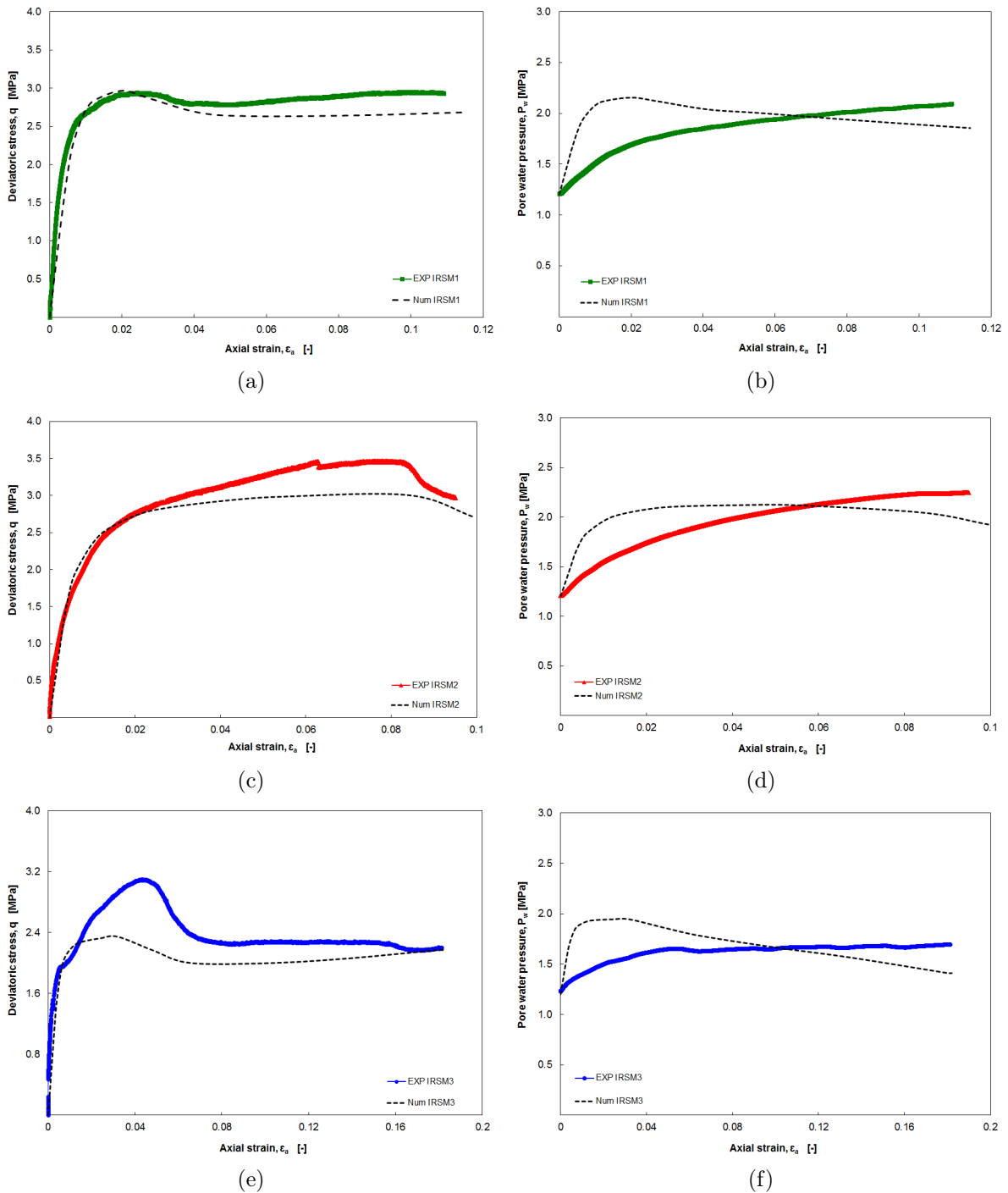


Figure 3.46: Results of the numerical simulations of the tests performed at IRSM, CAS, compared to the experimental results: (a) Deviatoric stress in function of axial strain for the first test. (b) Pore water pressure in function of axial strain for the first test. (c) Deviatoric stress in function of axial strain for the second test. (d) Pore water pressure in function of axial strain for the second test. (e) Deviatoric stress in function of axial strain for the third test. (f) Pore water pressure in function of axial strain for the third test.

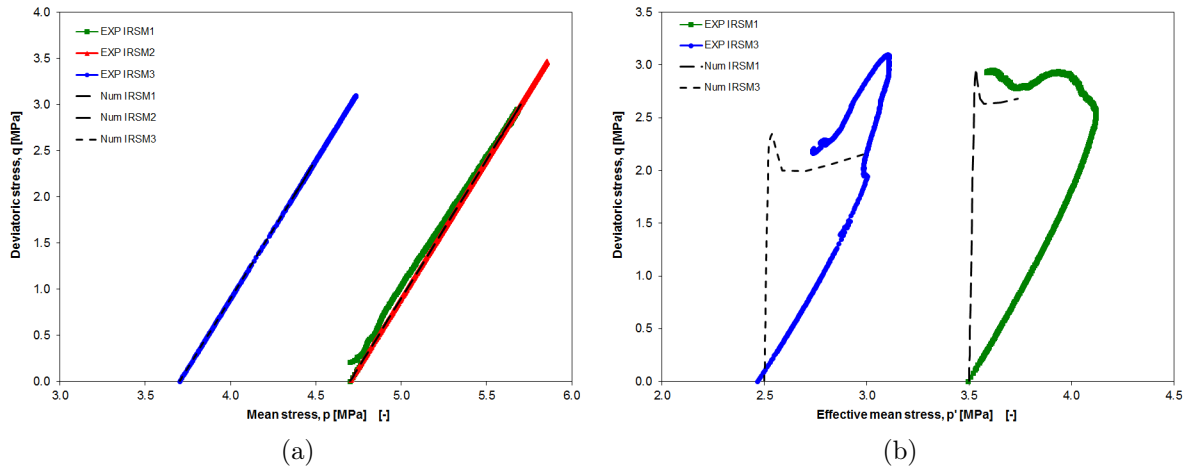


Figure 3.47: Numerical stress paths for the tests performed at IRSM, CAS, compared to the experimental results: (a) Stress path in the  $(p, q)$  plane. (b) Stress path in the  $(p', q)$  plane.

Subsequently to a pore pressure's peak, a slight decrease of the pressure in the post-peak regime is tended. This decrease is not in accordance with the experimental results since the latter still shows a gradual increase of the pore pressure. In fact, a delayed increasing process of pore pressure caused by the possible partially saturated state of the samples in laboratory (otherwise stated, a *gradual* increasing of the pressure during the tests time) seems to have occurred.

Figure 3.47 shows the numerical stress paths in comparison with the experimental results. In the total stress plane (Figure 3.47a), the path followed by the samples are generally reproduced by the numerical results, however, the maximum deviatoric stress is underestimated for the tests IRSM2 and IRSM3 (as already observed in Figures 3.46c and 3.46e). In the effective stress plane (Figure 3.47b), the numerical results show a normal path of an undrained test, which is not the case of the experimental observations with regard to the aforesaid discussion following Figure 3.45.

In order to simulate the *likely* partially saturated state of the samples in the laboratory, one method is defining a higher value of water compressibility,  $1/\chi_w$ , in our modelings. As it was given in Table 3.2, this value has been basically defined as  $5 \times 10^{-10} Pa^{-1}$ . Thence, this parameter is recalibrated here such that the early evolution of the experimental pore pressure could be better reproduced, i.e. the material behavior until it gets to its strength peak. In fact, by enough increasing the value of water compressibility, the material will be less tended to a quick increase of excess pore pressure. Consequently, Figure 3.48 compares the results of the numerical simulations using two different values of the compressibility parameter (i.e. the reference value and a new calibrated value for each test), with the experimental results. With regard to the early evolution of the pore pressure, which is presented in a smaller scale of the axial strain (in right side of Figures 3.48b, 3.48d and 3.48f), an improvement of the numerical results is identified by application of the higher value of  $1/\chi_w$ . Indeed, the water is more compressible, and by increasing the deviatoric stress during shearing, the pore pressure is then slightly increased. That signifies a higher peak strength too (see Figures 3.48a, 3.48c and 3.48e). Moreover, apart from Figure 3.48a, the peak of deviatoric stress then better approaches the corresponding experimental results. On the other hand, the pore pressure is getting farther from the experimental results in the higher values of axial strain; the constant value of water compressibility still plays an important role in inducing the lower values of pore pressure. Regarding the stress paths in the  $(p', q)$  plane (Figure 3.49), the numerical results inclines to the left getting closer to the experimental stress paths, with respect to the change in pore pressure evolution (see Figures 3.48b, 3.48d and 3.48f).

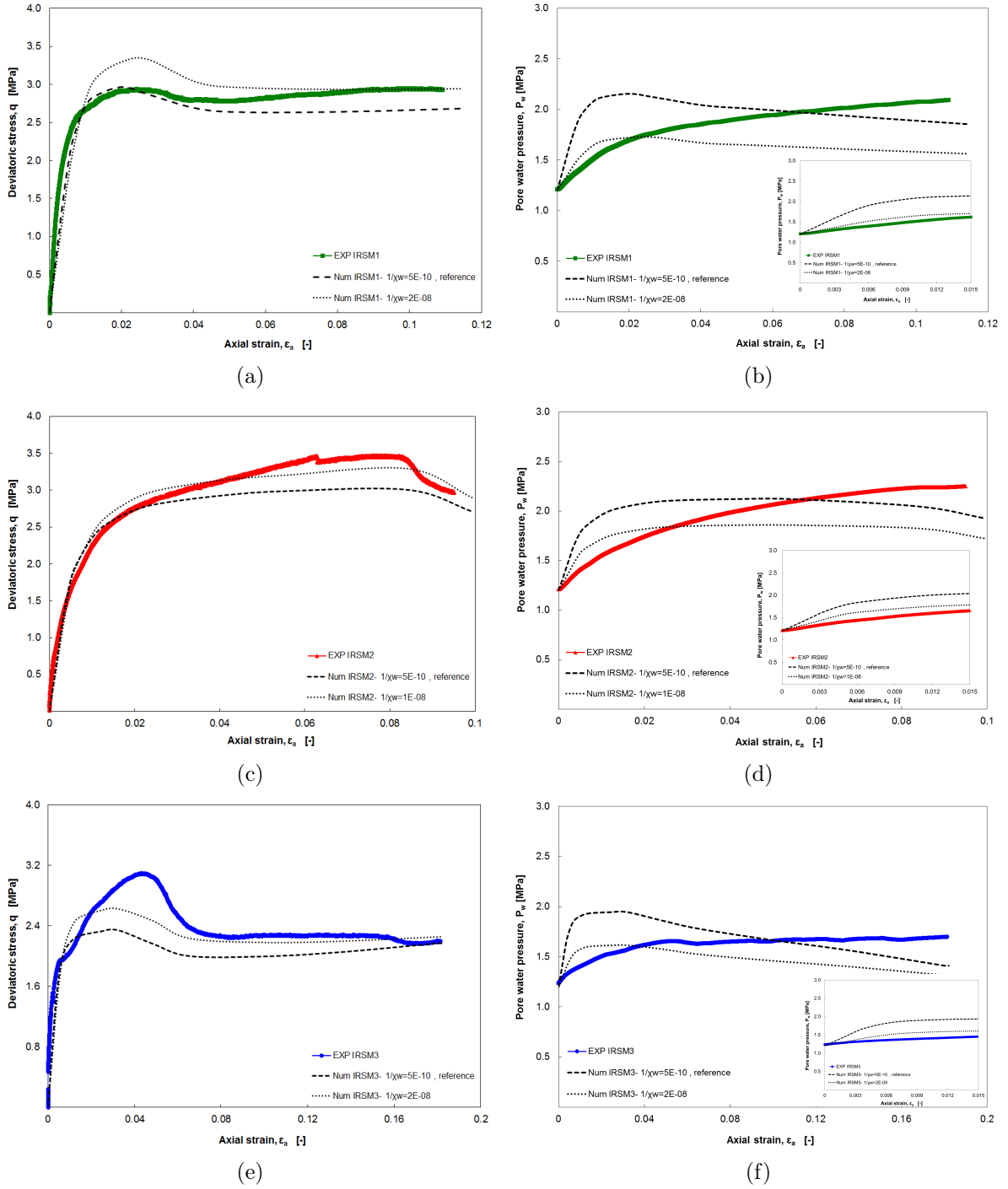


Figure 3.48: Results of the numerical simulations of the tests performed at IRSM, CAS, with two values of  $1/\chi_w$ , compared to the experimental results: (a) Deviatoric stress in function of axial strain for the first test. (b) Pore water pressure in function of axial strain for the first test. (c) Deviatoric stress in function of axial strain for the second test. (d) Pore water pressure in function of axial strain for the second test. (e) Deviatoric stress in function of axial strain for the third test. (f) Pore water pressure in function of axial strain for the third test.

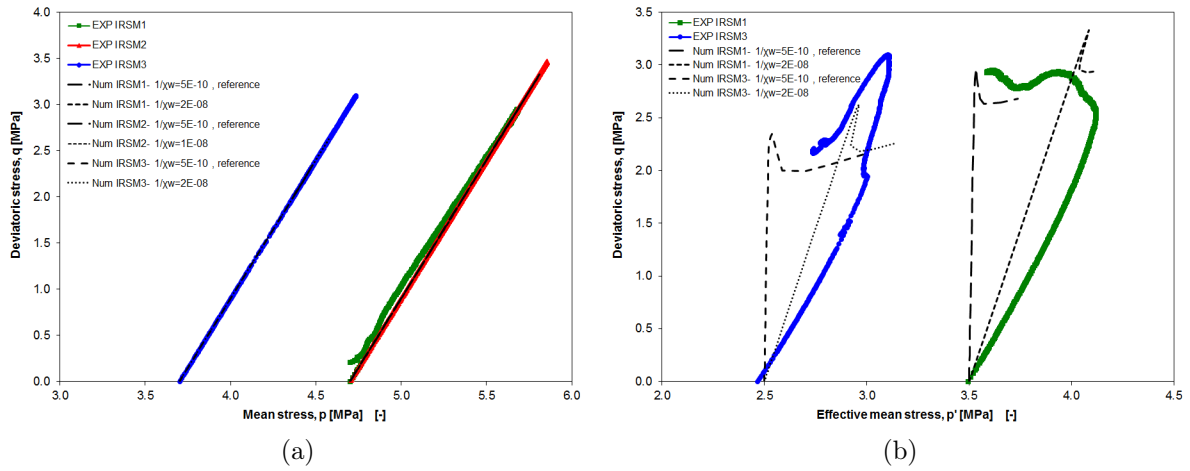


Figure 3.49: Numerical stress paths for the tests performed at IRSM, CAS, with two values of  $1/\chi_w$ , compared to the experimental results: (a) Stress path in the  $(p, q)$  plane. (b) Stress path in the  $(p', q)$  plane.

On the whole, increasing the water compressibility parameter could quite improve the numerical predictions for the current case (IRSM results), *with regard to the samples conditions, but* it is not a realistic choice to be validated for a general set of parameter for Boom Clay, which is supposed to be applied in all the upcoming simulations.

### 3.5.2.4 Simulation of the drained triaxial tests

To address also some drained triaxial tests, three tests are discussed in this Section. One test which has been performed by Lenoir et al. [2008], and two other tests that have been operated by Coll [2005] on the cylindrical samples of Boom Clay extracted at the URL level in Mol during the construction of Connecting gallery. Basically, 20 drained tests have been performed by the latter author, on Boom Clay samples, with different characteristics including various consolidated pressure (0.4-5 MPa); interested readers may refer to [Coll, 2005] for further information. Two of these tests in which the samples were sheared after an isotropic consolidated pressure similar to the in-situ one, i.e. 2.3 MPa, namely EXP Coll 1 and EXP Coll 2<sup>34</sup>, are represented here in addition to the aforementioned other test, namely EXP Lenoir.

The general test procedure consists in an isotropic consolidation phase and saturation of the samples. The (in-situ) effective mean stress of 2.3 MPa (total mean stress of 4.5 MPa and pore pressure of 2.2 MPa) was obtained. Then, the shearing phase has been conducted. It must be noted that in the two tests of EXP Coll 1 and EXP Coll 2, the consolidation phase has not been directed in the same manner; e.g. the rate of isotropic loading in EXP Coll 2 is 100 times of the rate applied for EXP Coll 1, but the shearing rate is the same for the both (0.25  $\mu\text{m}/\text{min}$ ). Figure 3.50 shows the evolution of the volumetric strain and deviatoric stress in function of the axial strain as well as the stress path in the  $(p', q)$  plane, for the three tests. In the deviatoric plane (Figure 3.50a), the material behavior is quite similar for the three tests; there is a stress peak of about 2.4 MPa at the axial strain of about 3% for EXP Coll 1, a stress peak of about 2.2 MPa at the axial strain of about 4% for EXP Coll 2, and a stress peak of about 2.4 MPa at the axial strain of about 2.5% for EXP Lenoir. This behavior is linked to a dominant contracting response in the volumetric plane (Figure 3.50b). At the end of the tests EXP Coll 1 and EXP

<sup>34</sup>They correspond to the tests BC07 and BC20, respectively, in [Coll, 2005].

coll 2, a dilatancy tendency accompanied by a very slight decrease of the deviatoric stress (after the peak) is observed in two planes (Figures 3.50a-3.50b). This response may be attributed to the collapse of the samples and possible creation of the zones with localization of strain (in the case of EXP Coll 2 [Coll, 2005]; see also Figure 5.6b). In addition, EXP Coll 2 demonstrates still a resistance subsequently to that localization of deformation and collapse. Also, comparatively, EXP Coll 2 shows a less contracting behavior in general (see Figure 3.50b). This difference is ascribed *a priori* to the dissimilar conditions under which the corresponding consolidation phase (of each of these tests) has been conducted.

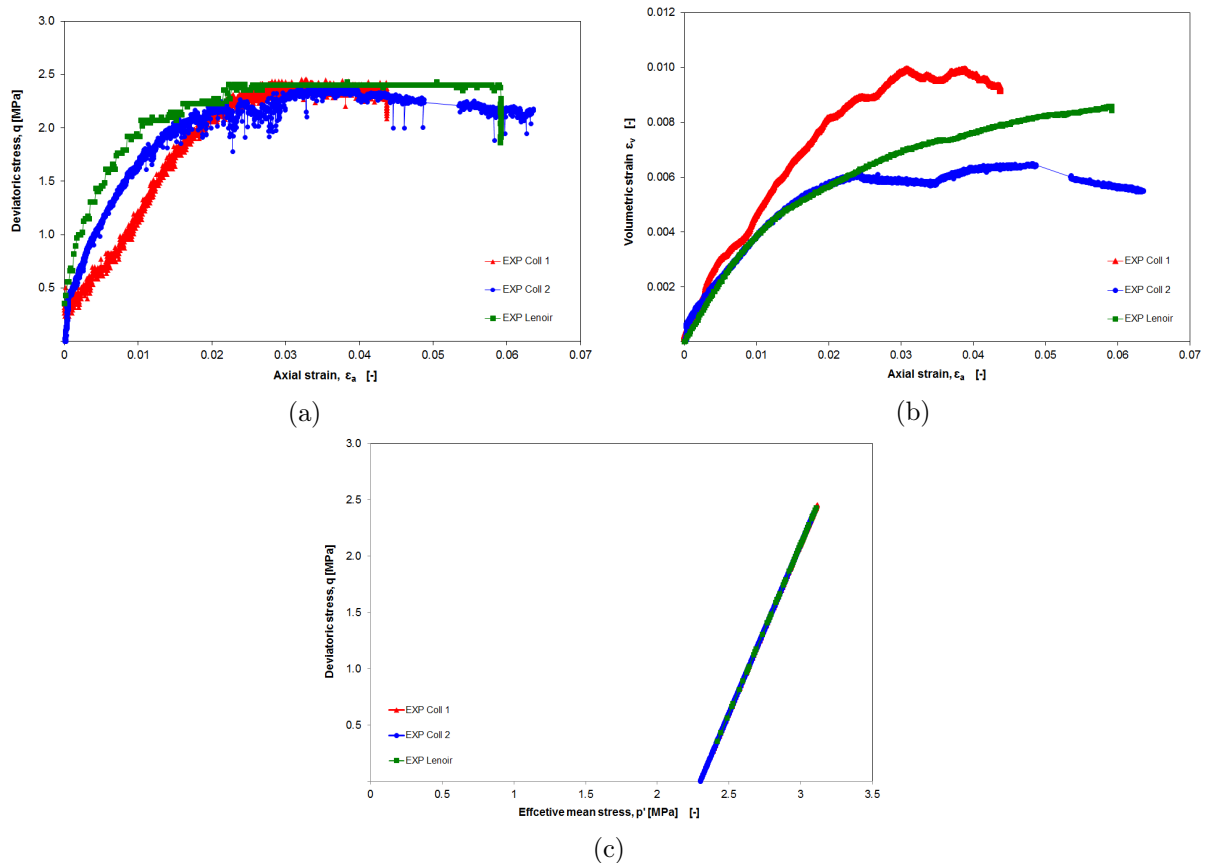


Figure 3.50: Experimental drained triaxial tests results: (a) Deviatoric stress in function of axial strain. (b) Volumetric strain in function of axial strain. (c) Stress path in the  $(p', q)$  plane; after [Coll, 2005; Lenoir et al., 2008].

### Simulation of the tests:

The reference main parameters (i.e. Tables 3.1-3.2) are still used for the numerical simulation of the drained tests; the hardening parameter  $B_\varphi$  is just a bit modified ( $=0.01$ ) to be able to model a slower hardening response (as for instance illustrated in Figure 3.37a) observed in the studied drained tests. Figure 3.51 shows the results of the numerical modeling in comparison with the experimental results. The numerical results in the deviatoric plane and stress path plane (Figures 3.51a-3.51c) are generally consistent with the experimental results, although the very slight decrease of stress at the end of the tests did not be reproduced numerically (Figure 3.51a). With regard to the evolution of volumetric strain (Figure 3.51b), a general contracting response is simulated numerically. This response is closer to the experimental result of the test EXP Coll 2 (the fairly dilatant behavior at the end of the test was not reproduced, though). However, the contracting behavior of the other two tests is underestimated besides that the numerical modeling does not simulate the dilatancy tendency observed in the material's ultimate response of the test

EXP Coll 1 either. In fact, these three tests are presenting pretty different volumetric behaviors in terms of the contracting/dilatant transition response, and the level of the contracting response. This difference of behaviors could not be reproduced by our numerical modeling. The latter will be more discussed in the following Section and the next Chapter.

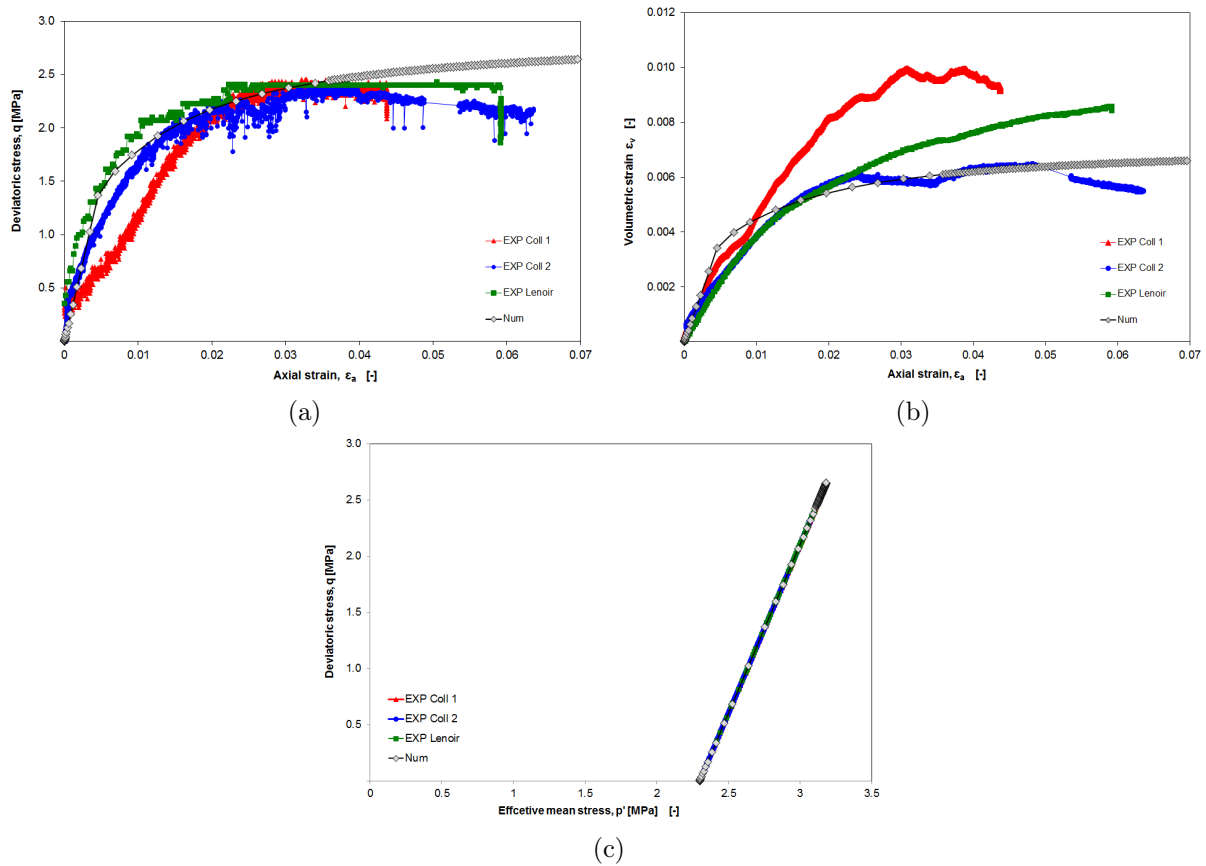


Figure 3.51: Results of the numerical simulations compared to the experimental results: (a) Volumetric strain in function of axial strain. (b) Deviatoric stress in function of axial strain. (c) Stress path in the  $(p', q)$  plane.

### 3.5.3 Discussion on the influence of dilatancy angle on the numerical results

This Section is intended for giving a general overview of the obtained numerical results in the last Sections focusing on how the input dilatancy parameter in the model could influence some weaknesses of the numerical results. In fact, our objective has been being to validate *a single* set of material's *main* parameters such that the best possible fit with all simulated triaxial tests' results is obtained by using this set as the model input parameters. Then, this set could be applied for the more complicated modelings of the next Chapters.

In this sense, considering the simulation of the first test series (Section 3.5.2.1) keeping our reference parameters as listed in Tables 3.1-3.2, an underestimation of the peak of deviatoric stress (Figure 3.35) has been previously predicted. The higher deviatoric stress observed in the experimental results compared to the numerical one is assumed to be attributed to the definition of the zero dilatancy angle in our modeling. Dilatancy tends to increase the shear strength, according to Kirkebo [1994]. Figure 3.52 shows the results of the former simulation ( $Num - p'_0 = 3$  in Figure 3.35) - called here as  $Num - \Psi = 0^\circ$ , *reference* - in comparison with two new

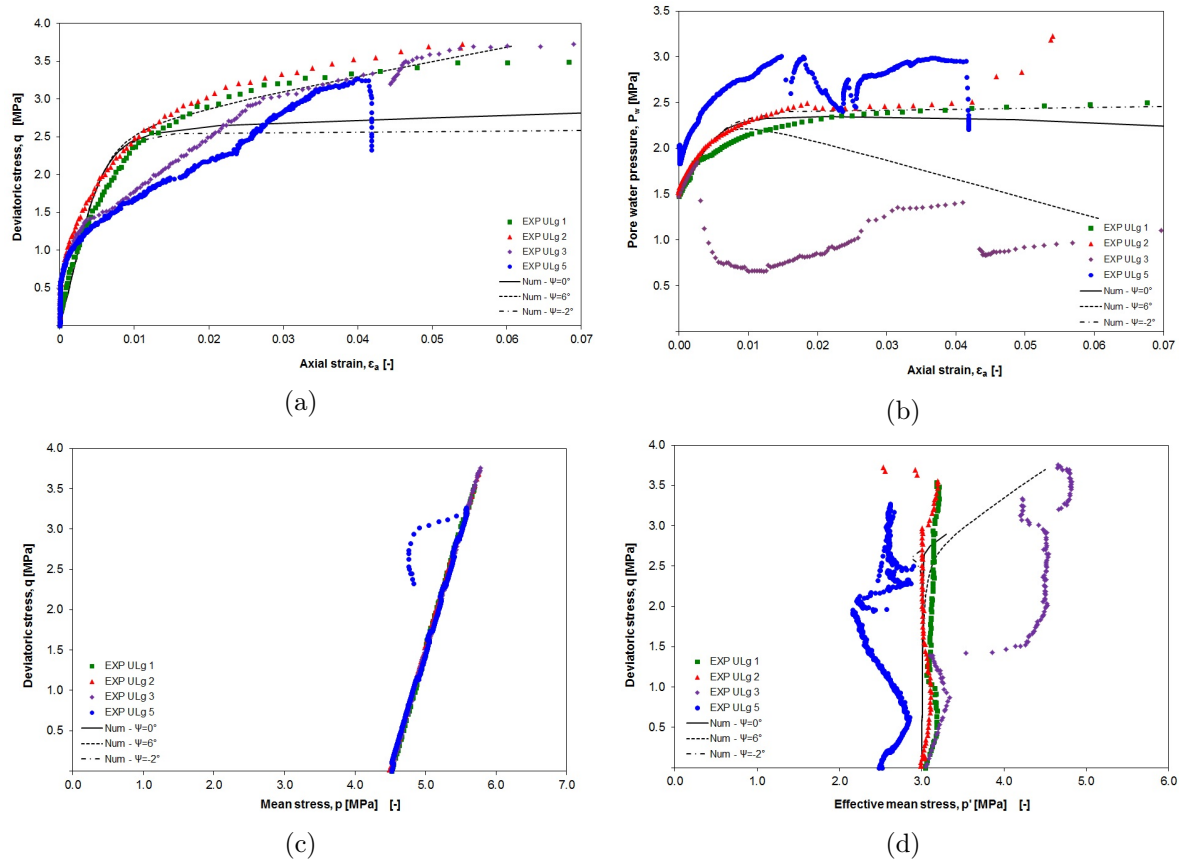


Figure 3.52: Results of the numerical simulations of the tests performed at ULg, ArGENCo, with three values of  $\Psi$ , compared to the experimental results: (a) Deviatoric stress in function of axial strain. (b) Pore water pressure in function of axial strain. (c) Stress path in the  $(p, q)$  plane. (d) Stress path in the  $(p', q)$  plane.

simulations with the same set of parameters and adding a non-zero value of dilatancy angle as  $\Psi = 6^\circ$  and  $\Psi = -2^\circ$ ; i.e.  $Num - \Psi = 6^\circ$  and  $Num - \Psi = -2^\circ$ , respectively. By introducing a large enough value of dilatancy angle into the model (i.e.  $\Psi = 6^\circ$ ), we could reproduce the evolution of the deviatoric stress very well (see Figure 3.52a). However, the fact of having a *constant* dilatancy angle during the whole simulation time induced a drastic drop of pore water pressure after its maximum value (see Figure 3.52b). The latter is reflected by an increase of the mean effective stress by entrance of the material to the plastic domain (see Figure 3.52d). On the contrary, the same simulation with introduction of a slight negative dilatancy angle (i.e.  $\Psi = -2^\circ$ ) could reproduce the best fit with the experimental evolution of pore pressure. Expectedly, the latter worsens the numerical response of the material in the deviatoric plane. The introduction of an appropriate non-zero (positive) dilatancy angle into the model for the tests IRSM2 and IRSM3 presented in Section 3.5.2.3 could also similarly improve the prediction of the deviatoric stress such that it would get closer to the experimental results. Although, the same deficiency would be encountered in the pore pressure plane. That is to say that a constant dilatancy angle will expectedly induce a drop of pore water pressure in the modeling that it was not observed experimentally.

Furthermore, the simulation of the drained triaxial tests (Section 3.5.2.4) have demonstrated two main deficiencies taking into account a quite different volumetric response of the material in the three studied tests: First, the contracting behavior was underestimated for the tests EXP Coll 1 and EXP Lenoir, and second, the ultimate dilatancy tendency observed for the tests

EXP Coll 1 and EXP Coll 2 was not reproduced by the model. To address a more contracting response, defining a negative dilatancy angle in the model will be *a priori* a convenient solution. On the other hand, the dilatancy tendency at the end of the volumetric response may signify the need to introduce a non-zero (positive) dilatancy angle into the model. Figure 3.53 clarifies this issue where the results of the former simulation (as demonstrated in Figure 3.51) is represented besides two new simulations (with a negative dilatancy angle as  $\Psi = -4^\circ$ , and a slight dilatancy angle<sup>35</sup> as  $\Psi = 3^\circ$ ). As it is observed in the volumetric plane, a high enough negative dilatancy angle could allow us to approach the more contracting behavior of the material observed in the test EXP Coll 1. This high contracting volumetric behavior is tended to be strongly continued in the higher axial strains (on the contrary to the corresponding experimental result) with regard to having a constant negative dilatancy angle during the whole simulation, though. On the other hand, the simulation with  $\Psi = 3^\circ$  shows an early dilatant response of the material (positive increment of volumetric strain) which is not realistic with regard to the experiments. This is linked to having this constant value from the beginning of our simulation. The last part of the relative obtained result could although simulate a similar increment rate of the volumetric strain (in function of the axial strain) as observed eventually in the test EXP Coll 2. On the whole, it is not obviously possible to reproduce the initial contracting (at different levels) and ultimate dilatant behavior of the material by introducing of a *constant* dilatancy angle into the model.

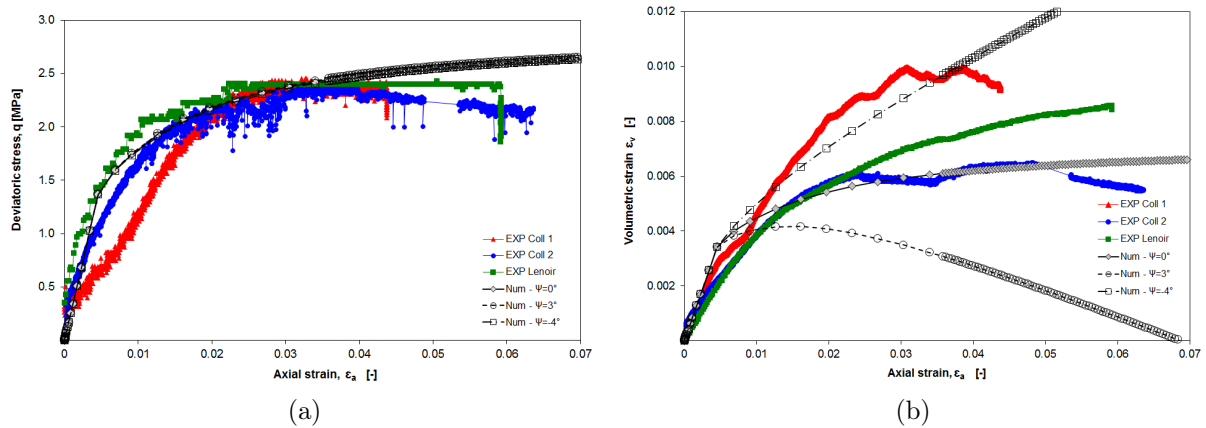


Figure 3.53: Results of the numerical simulations of the drained triaxial tests, with three values of  $\Psi$ , compared to the experimental results: (b) Volumetric strain in function of axial strain. (a) Deviatoric stress in function of axial strain.

Consequently, development of the model to consider a variable dilatancy angle is needed to overcome the discussed problems encountered through application of a constant value of dilatancy angle. By this, our objective - as mentioned at the beginning of this Section - will be achieved such that a final unique set of the main parameters can reproduce to the best possible the experimental tests while some various features relative to each test, which might not be modeled well in the basic simulations, are aimed to be addressed by definition of a variable dilatancy law. Hence, improvement of our numerical simulations, using the reference parameters (Tables 3.1/3.4<sup>36</sup> and 3.2), by focusing on the variable dilatancy angle is the scope of the next Chapter.

<sup>35</sup>Using the term "Dilatancy angle" for a non-zero value is interpreted as a positive value by default in this thesis, except that it is indicated to be a *negative* dilatancy angle; the contracting behavior tendency.

<sup>36</sup>The both present the same main mechanical properties of the material; some slight differences are limited to the hardening and softening parameters which play with the hardening of friction angle/softening of cohesion *numerical processes* that are expected to be defined fairly differently for the tests under different conditions.

### 3.6 Intermediate conclusions

This Chapter focused primarily on the classical numerical framework of this thesis. Introducing the applied numerical configuration, the hydro-mechanical equilibrium equations have been given. To do this, the principle of virtual work and the kinematics of porous media were represented to the necessary extent. Thence, mass balance equations as well as the balance of momentum relations for a coupled hydro-mechanical analysis were defined. Then, the general resolution algorithm was discussed. Moreover, with regard to the capability that an elasto-plastic model could offer to model the soils and rocks behavior, it was noteworthy to firstly recall some fundamental features of elasto-plasticity and thence, to employ them. Thereafter, the family of internal frictional elasto-plastic criteria have been presented followed by a summary on some other yield criteria. Next, the Drucker-Prager model has been introduced as the one applied in this thesis, with a discussion on its preference to the other described models with respect to their different features.

The second main part of this Chapter addressed the validation of one set of the model's input hydro-mechanical parameters to be mainly used throughout this thesis. With this objective, a literature analysis have been done with regard to four series of the available triaxial tests results. The discussion on each test series have been followed by presenting the results of the relative numerical simulations. The performance of the model, with respect to its input parameters, compared to the experimental results were then studied. The sensitivity of the numerical results to the change of some parameters were also discussed upon necessity.

First, regarding the undrained triaxial tests performed at ULg [TIMODAZ, 2010b], it has been noticed that the model with the chosen reference parameters could predict quite well the pore water pressure evolution, although, it underestimated the maximum value of the deviatoric stress. In fact, the experimental result have consisted in a continuous strengthening process while pore pressure does not decrease in general. It has been then shown that an improvement could be numerically obtained by changing the main parameters of cohesion and (final) friction angle as well as hardening parameters:  $\varphi_{Ci}$  (initial friction angle) and  $B_\varphi$ . Second, based on the undrained triaxial tests performed at ENPC [TIMODAZ, 2010b], a good agreement has been observed with the experimental results using our reference parameters (validating those parameters). Third, with regard to the undrained triaxial tests performed at IRSM [Yu et al., 2012], the deviatoric stress variation was generally modeled in a realistic manner; an underestimation of the peak of deviatoric stress have been observed for two of the tests, though. In addition, a quite different pattern of pore pressure evolution and stress path was obtained numerically compared to the experimental results. This has been discussed to be probably caused by the samples conditions at the shearing time: perhaps not fully saturated/existence of some air bubbles, and dilatancy tendency of the samples. It has been then shown that changing the water compressibility parameter could make the numerical results to approach the experimental ones. Finally, regarding the three drained triaxial tests [Coll, 2005; Lenoir et al., 2008], an underestimation of the contracting response has been observed for EXP Coll 1 and EXP Lenoir, as well as an imperfection of the model to reproduce the dilatancy tendency at the end of EXP Coll 1 and EXP Coll 2.

On the whole, the model parameters were quite appropriate for an overall simulation of the main aspects of the material behavior. Nevertheless, some parameters were needed to be adapted in the simulation of some tests in order to better approach the experimental results of the corresponding test. In fact, each of the studied tests involve quite specific features in their performance conditions and/or the obtained results, as already individually explained. However, it might be always possible to calibrate a model for one experiment, and differently (by changing the input parameters) for another one, but this is not what a numerical modeling of an experiment is looking for. Indeed, a laboratory experiment is generally aimed to characterize the behavior

of a material as close to its actual in-situ response as possible, and the obtained results could be somehow different with regard to the experiment conditions. Then, a numerical modeling should be able to reproduce this material's behavior such that it could possibly simulate a realistic response of the material with reference to the one observed in some relative experiments (even) under some probable dissimilar conditions and loading procedure (at least, strictly not only with reference to one experiment). Although, it is obvious that it may not be feasible to calibrate a model with a unique set of parameters which can *perfectly* fit the results of *all* of the experiments performed on the same material. Instead, it is *a priori* possible to have *one single* set of *main* parameters of a model, with respect to the capability of that used model, which could *moderately* fit in (as best as possible) with the results of some experiments which have basically sought similar objective.

In the last section of this Chapter, the influence of introducing a non-zero dilatancy angle into the model as an alternative parameter which might be able to improve the numerical prediction of the material response has been discussed. It has been shown that a high enough (positive) dilatancy angle helped the model to approach the observed strength evolution in the deviatoric plane for some undrained tests. However, keeping this value constant in the model could induce a strong pore pressure's drop which was not realistic. In the drained tests, a negative dilatancy angle could model a higher contracting behavior (more similar to one of the studied experimental results). However, the ultimate numerical response got farther from the less contracting/dilatant behavior observed experimentally at the end of the tests. The reason of all these aforesaid deficiencies can be summarized as the inconvenience involved by using a *constant* dilatancy angle in the modelings. In fact, this parameter might help the model to simulate better some features which were not reproduced satisfactory enough so far. However, it needs to be varied during the simulation with respect to the material progressive response. Therefore, one originality of this thesis consist in developing a new method to consider the variable dilatancy angle, as it will be presented in the next Chapter. On the whole, following our aforementioned objective, we keep our reference parameters as a constant set of input parameters from now on - without changing some main parameters such as cohesion, friction angle, and water compressibility in order to fit in with the results of one special test - and we are aimed to focus on variations of dilatancy angle throughout the simulations and its impact on improvement of the numerical predictions.



# Chapter 4

## Development of a method for considering the variable dilatancy angle

### Contents

---

<b>4.1</b>	<b>Introduction</b>	<b>98</b>
<b>4.2</b>	<b>Change of the dilatancy angle</b>	<b>99</b>
4.2.1	Overview of the dilatancy angle interest and encountered difficulty	99
4.2.2	Proposed formula implemented in LAGAMINE	101
4.2.3	Validation of the solution	104
<b>4.3</b>	<b>Intermediate conclusions</b>	<b>121</b>

---

*Things should be made as simple as possible,  
but no simpler.*

Albert Einstein

## 4.1 Introduction

A short review of the literature regarding the experimental and field observations of the soils and rocks behavior evidences how important is addressing their correct volumetric response in the process of a realistic numerical modeling of their behavior; the rock failure and post-failure processes are frequently associated to its dilatation. Correct evaluation of dilatation is in fact of significant importance in analyzing some post-failure mechanisms in rock mechanics such as fracture development and fluid flow behavior in rocks around the underground galleries. The dilatancy angle as a commonly used parameter for describing the dilatation response of a rock is mostly simplified to be a constant value. Contrarily, a literature review declares the inadequacy of this approach in many rock mechanics applications. In this sense, with regard to our hydro-mechanical coupled modelings in Chapter 3, some inconveniences related to consideration of a constant dilatancy angle (either zero or a non-zero value) in the modelings have been demonstrated. Thence, one important concern is attributed to correctly define our material's dilatancy angle into the model. Introduction of the dilatancy angle could directly influence the obtained volumetric response of the material in the simulation of a drained triaxial test, and it might change the obtained pore pressure evolution in the course of an undrained triaxial test. The latter influences also the strengthening mechanism of the material with respect to a coupled hydro-mechanical analysis. Realistically, the introduced value of dilatancy angle must not be constant - when a material is deformed - in order to be able to address the correct hydro-mechanical response of the material during a gradual loading process. In fact, this may be interpreted in the similar manner as the hardening/softening (numerical) concept that we have applied to the material's friction angle/cohesion so far. The need to consider the variable dilatancy was primitively concluded by Detournay [1986]: *The assumption of a constant dilatancy angle is believed to be unrealistic because the dilatation should be a function of the plastic strain (damage) and the confining stress.*

Therefore, in this Chapter, a new formula for considering the variable dilatancy angle in rock is presented which has been developed in a semi-empirical manner with respect to an analysis of a clay rock (i.e. Boom Clay) response during the triaxial tests experiments and tunnel excavation. It has been intended to be able to characterize an evolution of the dilatant, contracting, dilatant/contracting transitional responses of a material following its loading procedure. The proposed formula has been implemented in the PLASOL and ORTHOPLA laws in LAGAMINE library, which use the frictional elasto-plastic models (with DP/VE yield surfaces) considering the material's isotropy and anisotropy, respectively.

At the beginning of this Chapter, the dilatancy angle definition in the literature point of view and the interest for focusing on this parameter as a non-constant value are overviewed. To the author's knowledge, there are not many available numerical studies on the variable dilatancy in addressing the problems in rock engineering. In fact, this parameter is seldom taken into account and if it is, the used approach is poorly developed. Most of the researchers used the simplistic methods taking into account a constant dilatancy angle, according to [Detournay, 1986; Alejano and Alonso, 2005]; it mostly consisted in considering a zero value for a non-associated flow rule and equal to friction angle for an associated flow rule<sup>1</sup>. Nevertheless, some relevant suggestions among some published studies are firstly summarized. Subsequently, the new formula for considering the variable dilatancy angle is presented introducing its new elements. The model's capability to simulate the different volumetric behavior observed during the discussed drained triaxial test (see Section 3.5.2.4) is then presented through the new simulations with

---

<sup>1</sup>Although, considering an associated flow rule does not undoubtedly reproduce properly the post-failure response of a rock [Vermeer and De Borst, 1984]

application of the variable dilatancy angle. Next, the undrained triaxial tests performed at ULg are re-simulated, and through these simulations, the influence of the proposed model's new parameters is also studied. Finally, the last test series which has needed an improvement of the numerical predictions with respect to the experimental results, i.e. IRSM tests, are modeled with application of the proposed formula. However, the application of this proposition is not limited to the problems hitherto addressed. For instance, with regard to a gallery excavation within a rock, the proposed model can be used to address the likely tendency to dilatancy of the rock within the created localized fractures, and its subsequent variations. The latter application will be presented in Chapter 5.

## 4.2 Change of the dilatancy angle

### 4.2.1 Overview of the dilatancy angle interest and encountered difficulty

Dilatancy may be defined as an inelastic change in volume that is associated to shear distortion of an element in the material. The dilatancy parameter is essential for characterizing the soil and rock behavior when they are deformed. To describe the dilatant behavior of a material, dilatancy angle,  $\Psi$ , is a suitable parameter [Vermeer and De Borst, 1984] that is widely used. Vermeer and De Borst [1984] proposed an estimation of the dilatancy angle for rocks, granular soils and concrete as follows:

$$\Psi = \arcsin \frac{\dot{\varepsilon}_v^p}{-2\dot{\varepsilon}_1^p + \dot{\varepsilon}_v^p} \quad \text{for } \sigma_1 < \sigma_2 < \sigma_3, \text{ and, } \sigma_1 < \sigma_2 = \sigma_3 \quad (4.1)$$

where  $\dot{\varepsilon}_v^p$  is the volumetric plastic strain increment,  $\dot{\varepsilon}_1^p$  is the major (axial) plastic strain increment. The advantage of this formula to the classical notation used for a non-hardening model (Equation 4.2), as the authors indicated, is that the relation 4.1 is also valid for a common triaxial compression case ( $\sigma_1 < \sigma_2 = \sigma_3$ ).

$$\Psi = \arcsin \frac{\dot{\varepsilon}_1^p + \dot{\varepsilon}_3^p}{-\dot{\varepsilon}_1^p + \dot{\varepsilon}_3^p} \quad \text{for } \sigma_1 < \sigma_2 < \sigma_3 \quad (4.2)$$

where  $\dot{\varepsilon}_1^p$  and  $\dot{\varepsilon}_3^p$  are major and minor principle plastic strains. Based on the analysis of the latter authors, the dilatancy angle is at least  $20^\circ$  less than the friction angle.

Generally, it has been very common in soil and rock mechanics that the dilatancy angle is associated to the friction angle. Dealing with dilatancy angle relatively to the friction angle may be more realistic to be considered, for the granular soils and (hard) rocks. One of the first approaches regarding the relation between the dilatancy angle and friction angle was suggested by Taylor [1948]. Basically, this author proposed that the angle of internal friction, in spite of its name, does not depend solely on internal friction, since a portion of the shearing stress on a plane of failure is utilized in overcoming interlocking. Thence, it was concluded that:

$$\tan \varphi = \tan \varphi_{cv} + \tan \Psi \quad (4.3)$$

where  $\varphi_{cv}$  is a constant which is referred to the friction angle at constant volume, i.e. no dilatancy is occurred. The relation of these two parameters may be also defined as Equation 4.4 following the sawtooth model [Houlsby, 1991].

$$\varphi = \varphi_{cv} + \Psi \quad (4.4)$$

That is indeed similar to the previous relation in stating that friction angle term is equal to the sum of a constant and the term of dilatancy. Later, Hoek and Brown [1997] recommended the

use of a constant dilatancy angle value based on the rock mass quality. Thus, with respect to their experience on dilatant behaviour in rock masses, they suggested the value of  $\Psi = \varphi/4$  for very good quality rock masses,  $\Psi = \varphi/8$  for average quality rock masses,  $\Psi = 0$  for very poor quality rock masses.

Considering the dilatancy angle as a constant value in many numerical studies may be ascribed to that generally little is known about how the dilatation of a rock changes, specially in the post-peak regime (or, post failure regime). However, this assumption is not physically realistic, according to the primary study of Detournay [1986]. This author indicates that the dilatancy of a rock is a function of the plastic shear strain. As a common example of the problems encountered by consideration of a constant dilatancy, it was shown that simulation of tunnel closure in a rock is unrealistic using a constant dilatancy since there is no bound on the volume increase that the material can experience. The solution proposed in the latter reference was defining a tangent dilatancy factor  $K_p^*$  that decays from an initial value  $K_p$  (which is a function of the friction angle) according to an exponential function of the plastic shear strain  $\gamma$ , such that:

$$K_p^* = 1 + (K_p - 1) \exp\left(-\frac{\gamma}{\gamma^*}\right) \quad (4.5)$$

where  $\gamma^*$  can most usefully be related to the maximum inelastic volume increase  $\Delta^*$  as:

$$\gamma^* = \frac{\Delta^*}{\ln \frac{(K_p + 1)}{2}} \quad (4.6)$$

This proposition is limited to the definition of a (positive) value for dilatancy which could decay until a (possible) residual value of 1. This is the case for a dilatant behavior which is tended to degrade (a less dilatant response). Although, it cannot cover the possible variety of a material response throughout the evolution of plastic shear strain. For instance, with regard to a drained triaxial test (see Figure 3.50b), the material has had a contracting behavior (negative dilatancy angle) and then after its peak of the volumetric strain, it has shown a dilatancy tendency. As another likely behavior which could not be addressed by the proposed model is the propagation of the fractures and creation of the localized shear bands in a triaxial test experiment or large-scale tunnel excavation, which normally induce a dilatancy tendency in the rock, that could be subsequently vanished (for instance during the consolidation phase). The latter could be *a priori* modeled through an increase of the dilatation parameter (due to fractures opening/macro-crack propagation and localization of deformation in the planar bands) and an ultimate reduction process after the peak of deviatoric stress (possible closure or no more opening mode of the fractures/no more development of the shear bands).

Another proposition was made recently by El Moustapha [2014] which suggests also a decay from an initial value  $\Psi_i$  to a final value  $\Psi_f$  as a function of equivalent plastic strain  $\varepsilon_{eq}^p$ , according to an hyperbolic function (Equation 4.7). This formulation was defined in a similar manner as the one proposed for friction angle and cohesion evolution (see Equations 3.108-3.110). Then,  $DEC_\Psi$  and  $\beta_\Psi$ , as called in the author's thesis, respectively, allows a retardation in the reduction process of dilatancy angle from its initial value, and signifies the value of  $\varepsilon_{eq}^p$  when  $\Psi$  has been half decreased between its initial and final values.

$$\Psi = \Psi_i + \frac{(\Psi_f - \Psi_i) [\varepsilon_{eq}^p - DEC_\Psi]}{\beta_\Psi + [\varepsilon_{eq}^p - DEC_\Psi]} \quad (4.7)$$

The same problem explained for the last proposition is present in this solution too. In fact, the scope of this author was basically limited to reduction of dilatancy angle from its initial to the

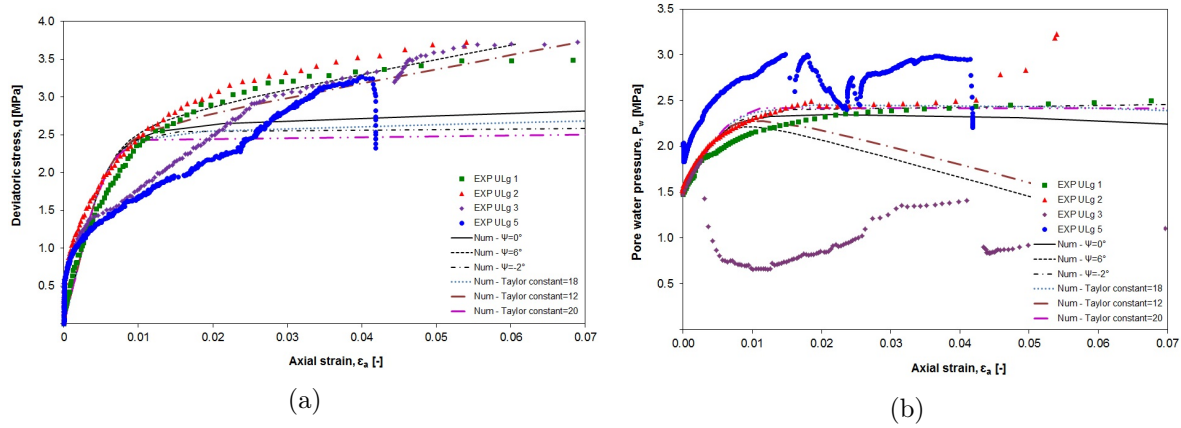


Figure 4.1: Results of the numerical simulations of the tests performed at ULg, ArGEnCo, with three values of  $\Psi$  and three values of Taylor rule's constant, compared to the experimental results: (a) Deviatoric stress in function of axial strain. (b) Pore water pressure in function of axial strain.

final given values;  $\Psi \geq 0$ . However, a more general behavior response is desirably intended to be addressed here (see Section 4.2.2).

Prior to going through the new development to overcome the aforesaid problems, it is interesting to see the response of our numerical model with application of a rule associated to the family which defines a relation between the dilatancy and friction angles. The so-called Taylor rule [Taylor, 1948] has been already existed in LAGAMINE code in the following form (with respect to aforesaid approach) and it could induce the change in dilatancy angle based on the variations in friction angle:

$$\varphi - \Psi = cts. \quad (4.8)$$

This method induces a same evolution process of dilatancy angle as the one that friction angle follows. Considering the same tests series presented in Section 3.5.3 using the null and constant dilatancy angles, Figure 4.1 presents the results of the last simulations with three values of  $\Psi = 6^\circ$ ,  $\Psi = 0^\circ$  and  $\Psi = -2^\circ$ , in comparison with three new simulations using three constant values based on Equation 4.8. Indeed, based on this relation, the dilatancy angle varies by evolution of  $\varphi$  and since the latter follows a hardening process, dilatancy angle is also increased. Thence, it gets to a constant value when the friction angle reaches to its final value (i.e.  $\varphi_f = 18^\circ$ ) that the latter is actually happens fast based on the hardening parameter  $B_\varphi$  given to the model (see Figure 3.22b). Therefore, the dilatancy angle gets constant soon after the entrance to plasticity, and the simulation results are then quite similar to the modelings with constant dilatancy. For instance, given the input constant value in Equation 4.8 as 18, 12 and 20, quite similar results can be predicted as the ones obtained by application of the constant dilatancy angles of  $\Psi = 0^\circ$ ,  $\Psi = 6^\circ$  and  $\Psi = -2^\circ$ , respectively (taking into account the final friction angle as  $18^\circ$  in Equation 4.8). Therefore, the encountered problems (in using a constant dilatancy angle value) are similarly there and a new treatment is interestingly required.

#### 4.2.2 Proposed formula implemented in LAGAMINE

To adjust the encountered difficulties, a new formula is proposed which defines the change in dilatancy angle in function of the equivalent plastic strain based on an introduced initial, peak, and limit value of dilatancy angle. With respect to the former studies [El Moustapha, 2014],

the new model has been developed in a semi-empirical manner with regard to the material response observed during the small scale experiments (i.e. triaxial tests), and the large-scale ones (tunnel excavation; as will be particularly focused in Chapter 5). Besides the former as it has been already discussed, the latter concerns the likely tendency to dilatation of the host rock within the fractures created due to galleries' excavation. This dilatancy tendency is basically concentrated at the localized shear bands, and it is not supposed to remain constant during the time. However, considering a constant dilatancy, spatially and throughout the time, signifies an overall dilatant behavior of the material which is not realistic and it could impose some impractical predictions, as it will be demonstrated in Chapter 5.

In fact, the new formula is aimed to address two main aspects mostly lacked in the existing methods (e.g. with regard to Equations 4.5 and 4.7). First, it is intended to provide the possibility of simulating a multi-mechanism (two-step) volumetric behavior by definition of three (instead of two) main factors of the dilatancy angle. Thence, for instance, a primary contracting behavior and subsequent dilatancy tendency of a material (like the observed response in the discussed drained triaxial tests; see Figure 3.50b) can be desirably reproduced. As another result of this potential, the likely local tendency to dilatancy of a host-rock within the fractures/shear bands and the zone with localization of deformation created due to tunneling, and a degradation of this tendency (because of the possible closure or no more opening mode of the fractures/no more shear dilatation/no more development of the localized bands) could be numerically addressed. Therefore, besides that the dilatation behavior of a material could be simulated spatially differently (with regard to amount of computed plastic strain), it is varying in time following the loading procedure and response of the material. This aspect is in contrast with the unrealistic approach followed by consideration of a constant dilatancy.

Second, those three main parameters of the model are possible to be freely defined, and they can be positive or negative. Hence, for instance, an initial contraction (a negative initial value of dilatancy angle) and subsequent dilatation - e.g. due to the creation of localized bands during a compression triaxial test - could be reproducible (integrated with the first described potentiality of the model).

Equation 4.9 presents the new proposition to vary the dilatancy angle:

$$\Psi = \frac{\Psi_{lim}}{2} + (\Psi_{peak} - \Psi_{lim}) + \frac{[(\Psi_{peak} \times Rat_{\Psi}) - (\Psi_{peak} - \Psi_{lim})][\varepsilon_{eq}^p - D_{\Psi}]}{B_{\Psi} + [\varepsilon_{eq}^p - D_{\Psi}]} \quad \text{for } \varepsilon_{eq}^p > D_{\Psi}$$

$$\Psi = \begin{cases} \Psi_{peak}, & \text{if } Rat_{\Psi} = 0 \\ \Psi_{peak} \times Rat_{\Psi}, & \text{otherwise} \end{cases} \quad \text{for } \varepsilon_{eq}^p \leq D_{\Psi}$$
(4.9)

where  $\Psi_{peak}$  is the peak of dilatancy angle (which could be positive or negative),  $\Psi_{lim}$  is the limit value of the dilatancy angle (positive or negative limit) that it cannot be surpassed,  $\varepsilon_{eq}^p$  is the equivalent plastic strain,  $B_{\Psi}$  is the value of equivalent plastic strain for which half of the change in dilatancy angle is achieved, and  $D_{\Psi}$  is the value of equivalent plastic strain beyond which the change in dilatancy angle starts (thence, the first relation in 4.9 is activated); it could then induce a delay in the variation process.

In addition, the parameter  $Rat_{\Psi}$  is defined as the ratio between the peak of dilatancy angle and its initial value. Then, it can make distinguishable the initial value of the dilatancy angle from its peak value. In fact, with regard to Equation 4.9, the dilatancy angle is initially (under the condition of  $\varepsilon_{eq}^p \leq D_{\Psi}$ ) equal to  $\Psi_{peak} \times Rat_{\Psi}$  if we give a  $Rat_{\Psi}$  value to the model (i.e.  $Rat_{\Psi} \neq 0$ ). Otherwise, it is considered to be the same as  $\Psi_{peak}$  before it starts to vary (if  $\varepsilon_{eq}^p > D_{\Psi}$ ) in an hyperbolic manner. On the other words,  $Rat_{\Psi}$  counts for anything in the latter case. In the former case (i.e.  $Rat_{\Psi} \neq 0$ ), if the condition  $\varepsilon_{eq}^p > D_{\Psi}$  is satisfied, the dilatancy evolves firstly to its peak value and then changes approaching its limit value, with respect to

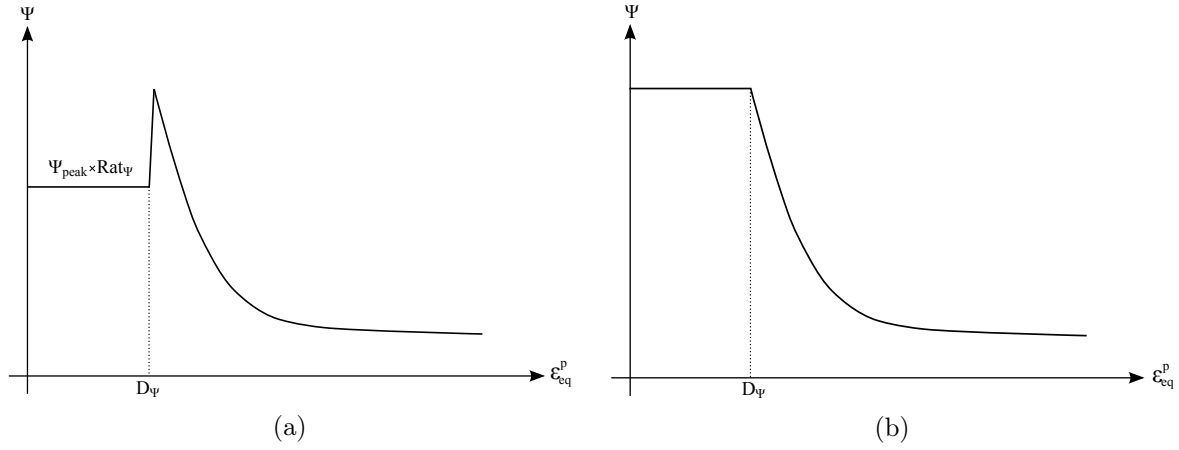


Figure 4.2: An example of the variations of dilatancy angle while: (a)  $Rat_{\Psi} \neq 0$ . (b)  $Rat_{\Psi} = 0$ .

the first relation in 4.9. Through introduction of  $Rat_{\Psi}$  parameter, possibility of modeling of a multi-mechanism volumetric behavior could be realized. For instance, a dilatant behavior with an initial dilatancy value that is increased to a peak value, and it is then reduced towards a limit value; e.g. due to the opening of the fractures's network and a later consolidation phase. Figure 4.2 shows an example of the variations of dilatancy angle when  $Rat_{\Psi} = 0$  or  $Rat_{\Psi} \neq 0$ , assuming a positive value of  $\Psi_{peak}$  and  $\Psi_{lim}$ . It is recalled that there is no restriction in definition of "positive" or "negative" values for the three main factors of dilatancy angle (i.e.  $\Psi_{peak}$ ,  $\Psi_{lim}$ , and  $Rat_{\Psi}$ ) in either case as it will be shown through some applications of the model in Section 4.2.3. Indeed, these values could be calibrated with respect to the material behavior and loading procedure.

It must be noted that the dilatancy angle obtained by the first relation in Equation 4.9 is subsequently checked with regard to the condition 4.10. The latter is aimed to ensure that the obtained  $\Psi$  would not have gone beyond the defined limit value during its process of change.

$$\text{if } |\Psi_{peak} - \Psi| > |\Psi_{peak} - \Psi_{lim}| \quad \Rightarrow \quad \Psi = \Psi_{lim} \quad (4.10)$$

This model has been implemented in the PLASOL and ORTHOPLA laws in LAGAMINE code. These laws use the frictional elasto-plastic models (with DP/VE yield surfaces) considering the material's isotropy and anisotropy, respectively. Therefore, the model could be generally applied in either case. With respect to our used frictional model with DP yield surface (described in Section 3.4.2.1), through which the variable dilatancy rule has been incorporated, a modification of the potential surface can be then induced during the computation. Thence, with regard to Equation 3.113-3.114, it gives:

$$\begin{aligned} \text{With respect to the formulation 4.9} \quad & \xrightarrow{\text{Update of } \Psi \text{ value}} \quad m' = \frac{2 \sin \Psi}{\sqrt{3}(3 - \sin \Psi)} \\ \longrightarrow \quad & g \equiv II_{\hat{\sigma}} + m' I_{\sigma} = 0 \end{aligned} \quad (4.11)$$

Then, the derivative of potential surface with respect to stresses (Equation 4.12) is also updated for each  $\varepsilon_{eq}^p$  during the iteration procedure (with regard to Section 3.4.5).

$$\frac{\partial g}{\partial \sigma'_{ij}} = m' \delta_{ij} + \frac{\hat{\sigma}'_{ij}}{2II_{\hat{\sigma}}} \quad (4.12)$$

Table 4.1: Mechanical parameters for the modelings with variable dilatancy

Parameter	Symbol	Value			Unit
		<i>Num - Variable <math>\Psi</math>, Coll 1</i>	<i>Num - Variable <math>\Psi</math>, Coll 2</i>	<i>Num - Variable <math>\Psi</math>, Lenoir</i>	
Young elastic modulus	$E$	300	300	300	$MPa$
Poisson ratio	$\nu$	0.125	0.125	0.125	-
Specific mass of the grains	$\rho_s$	2700	2700	2700	$Kg/m^3$
Initial compression friction angle	$\varphi_{C0}$	8	8	8	$^\circ$
Final compression friction angle	$\varphi_{Cf}$	18	18	18	$^\circ$
Hardening coefficient	$B_\varphi$	0.01	0.01	0.01	-
Hardening coefficient	$D_\varphi$	0	0	0	-
Initial cohesion	$c_0$	300	300	300	$kPa$
Final cohesion	$c_f$	300	300	300	$kPa$
Softening coefficient	$B_c$	0	0	0	-
Softening coefficient	$D_c$	0	0	0	-
Dilatancy angle	$\Psi$				$^\circ$
Peak of dilatancy angle	$\Psi_{peak}$	<u>-10</u>	<u>-3</u>	<u>-3</u>	$^\circ$
Limit of dilatancy angle	$\Psi_{lim}$	<u>4</u>	<u>1.5</u>	<u>-1.5</u>	$^\circ$
Dilatancy ratio	$Rat_\Psi$	<u>-0.01</u>	<u>-0.5</u>	<u>-0.5</u>	-
Dilatancy coefficient	$B_\Psi$	<u>0.007</u>	<u>0.008</u>	<u>0.008</u>	-
Dilatancy coefficient	$D_\Psi$	<u>0.001</u>	<u>0.005</u>	<u>0.005</u>	-

In the following, the application of the model is presented for the studied triaxial tests in Sections 3.5.2-3.5.3 to validate our proposition for some different experimental observed responses.

### 4.2.3 Validation of the solution

#### 4.2.3.1 Drained triaxial tests: Presentation of the capability of the model to simulate observed volumetric responses

In the following, the previous numerical results using the constant dilatancy angles (zero/non-zero values) as given in Sections 3.5.2.4 and 3.5.3 are presented in contrast with the results of the simulations with application of variable dilatancy angle. As it has been already observed, the three experimental tests have shown quite different volumetric behaviors, likely with respect to the tests' conditions. Thence, the proposed model is firstly tested against these available experimental data. In this framework, this section intends for illustration of the capability of the proposed model to simulate different volumetric responses.

Table 4.1 lists the set of reference mechanical parameters (basically similar as Table 3.1) in addition to new parameters corresponding to our model of variable dilatancy angle. The model's parameters have been then calibrated based on the observed volumetric behavior in EXP Coll 1, EXP Coll 2, and EXP Lenoir. Figure 4.3 shows the experimental results compared to the simulated results with application of variable and constant (presented in Section 3.5.3) dilatancy angles.

As it is observed in Figure 4.3b, the new numerical predictions for all the three tests are in agreement with the corresponding experimental results. Indeed, the model is capable to reproduce the three experimental responses in the volumetric plane, on the contrary to the application of a constant dilatancy angle. With regard to the test EXP Coll 1, the most important contracting behavior could be principally achieved by introducing a pretty high negative value of  $\Psi_{peak}$  and a slight negative value of  $Rat_\Psi$  (i.e. slight initial (positive) dilatancy angle equal to  $\Psi_{peak} \times Rat_\Psi$ ). Therefore, the high contracting tendency of the material during the drained shearing could be obtained through the primitive negative jump of dilatancy angle (see Figure 4.3c). Then, the negative dilatancy angle continues to decline and finally, it is approaching its limit value. Thence, it does not allow the steady contraction obtained by using a negative

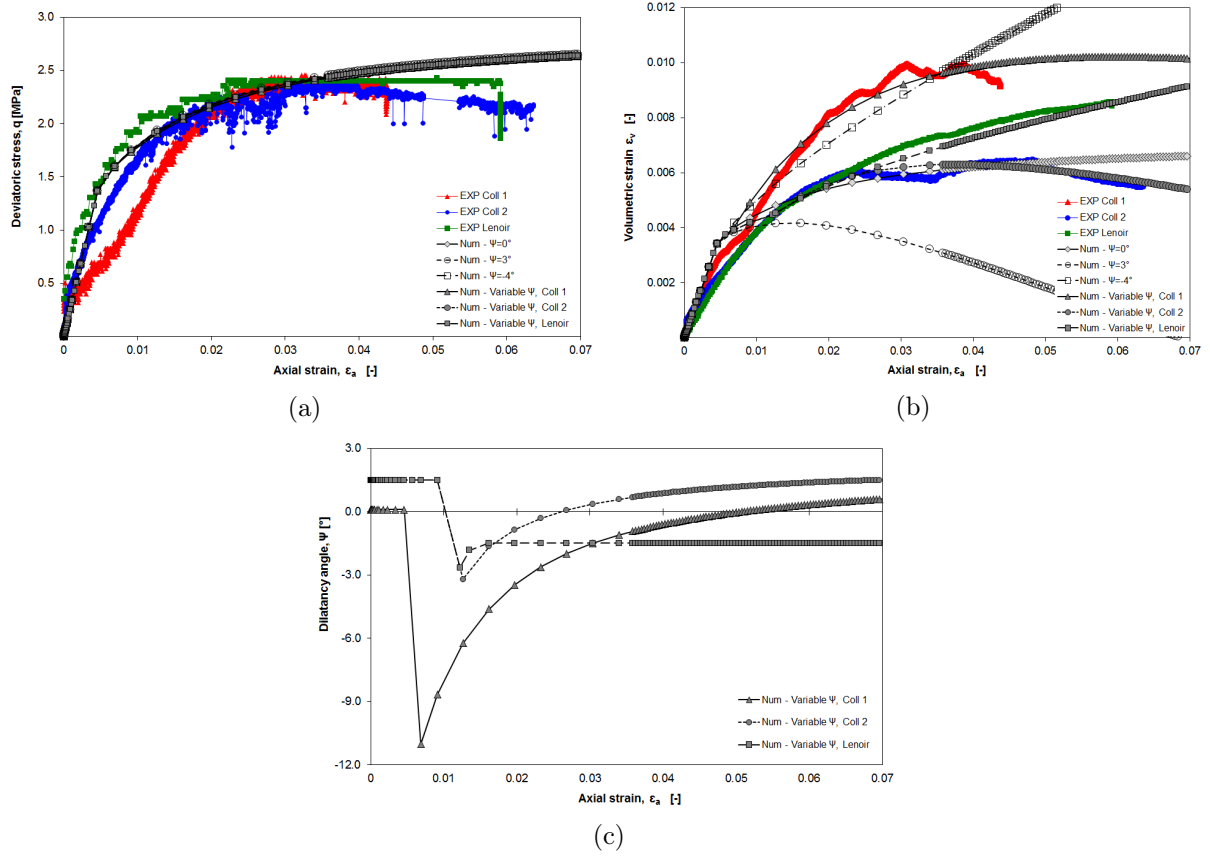


Figure 4.3: Results of the numerical simulations of the drained triaxial tests, with variable dilatancy angle in contrast with the constant values, compared to the experimental results: (a) Volumetric strain in function of axial strain. (b) Deviatoric stress in function of axial strain. (c) Dilatancy angle variations in function of axial strain.

constant dilatancy angle (see the curve of  $\Psi = -4^\circ$ ). A general similar process occurs for the simulation of test EXP Coll 2 with variable dilatancy angle. A moderate contracting response of the material is modeled for which a lower negative peak of dilatancy angle has been introduced into the model. Subsequently, a dilatancy tendency in the material ultimate response could be ideally achieved well through the variations of dilatancy angle towards  $\Psi_{lim} = 1.5^\circ$ . The latter could not be indeed attained through application of neither  $\Psi = 0^\circ$  nor  $\Psi = 3^\circ$ . Regarding the test EXP Lenoir, an average contracting behavior was observed experimentally in comparison with two other studied tests. This behavior is also reproduced well by the relative numerical model with variable dilatancy angle. On the contrary to two other tests, the material does not show any tendency to dilate at the end of the test that this behavior is noticed in the numerical prediction as well. In fact, a slight negative limit value of dilatancy angle has been given to the model for this test, which allows keeping a fairly contraction tendency with respect to the observed material ultimate response (see also Figure 4.3c). This reproduces the difference of the experimental volumetric behavior in the tests EXP Coll 2 and EXP Lenoir.

The peak and limit values of dilatancy angles could determine the variation range of dilatancy angle. Although, it is noteworthy that since the first relation in 4.9 is activated, the first calculated value of the dilatancy angle could surpass a bit the defined peak value, or the ultimate value might not reach to the limit value, with respect to the evolution of equivalent plastic strain and the defined values for other parameters of our model (e.g. see the corresponding curve of *Num - Variable  $\Psi$ , Coll 1* in Figure 4.3c). The three other parameters could influence the

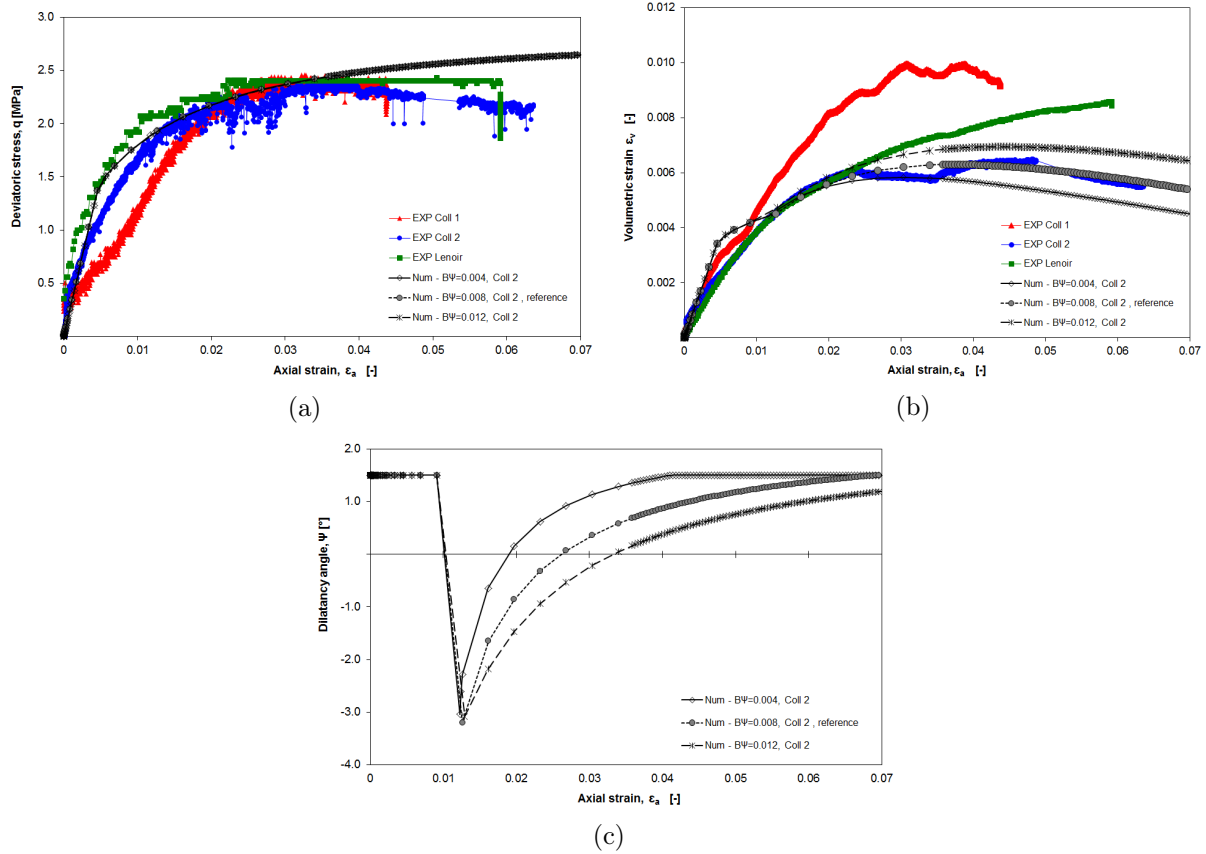


Figure 4.4: Results of the numerical simulations of the drained triaxial test, with three values of  $B_\Psi$  with reference to *Num - Variable  $\Psi$ , Coll 2*, compared to the experimental results: (a) Volumetric strain in function of axial strain. (b) Deviatoric stress in function of axial strain. (c) Dilatancy angle variations in function of axial strain.

variation procedure of dilatancy angle since its peak.  $B_\Psi$  affect the rate of the change, similarly to the role of  $B_\varphi$  and  $B_c$  in the hardening and softening processes of friction angle and cohesion. For instance, with reference to the simulation *Num - Variable  $\Psi$ , Coll 2*, Figure 4.4 demonstrates the influence of this parameter on the obtained results. It is then observed that a lower value of  $B_\Psi$  than the reference chosen value imposes a faster evolution of the  $\Psi_{peak}$  towards its limit value (i.e.  $\Psi_{lim} = 1.5^\circ$ ); see Figure 4.4c. Consequently, the dilatancy tendency is met sooner than it is observed in the corresponding experimental result (see Figure 4.4b). On the contrary, a higher value of  $B_\Psi$  slows down undesirably the dilatancy tendency in the material response. Moreover,  $D_\Psi$  makes a retardation in the diminution of dilatancy angle. The latter could be already noticed in the different points where the dilatancy angles come to vary for the test EXP Coll 1 in contrast with the tests EXP Coll 2 and EXP Lenoir (with different value of  $D_\Psi$  relatively to EXP Coll 1, see Table 4.1). Also, the results of the simulation *Num - Variable  $\Psi$ , Coll 2*, using two other values of  $D_\Psi$  than the corresponding chosen value ( $D_\Psi = 0.005$ ) are compared to the reference simulation in Figure 4.5. The influence of this parameter on delaying the procedure of change in dilatancy angle (see Figure 4.5c) affects the volumetric behavior of the material. With respect to the beginning of the computed curves in Figure 4.5b, considering  $D_\Psi = 0.001$  imposes a contracting behavior shortly with a sooner jump to the negative peak of dilatancy angle. On the contrary, using  $D_\Psi = 0.009$  keeps longer the initial (positive) dilatancy angle (i.e.  $1.5^\circ = \Psi_{peak} \times Rat_\Psi$ ) resulting in an undesirable dilatant volumetric behavior (in contrast with the corresponding experiment EXP Coll 2) before tending to the observed contraction volumetric

response.

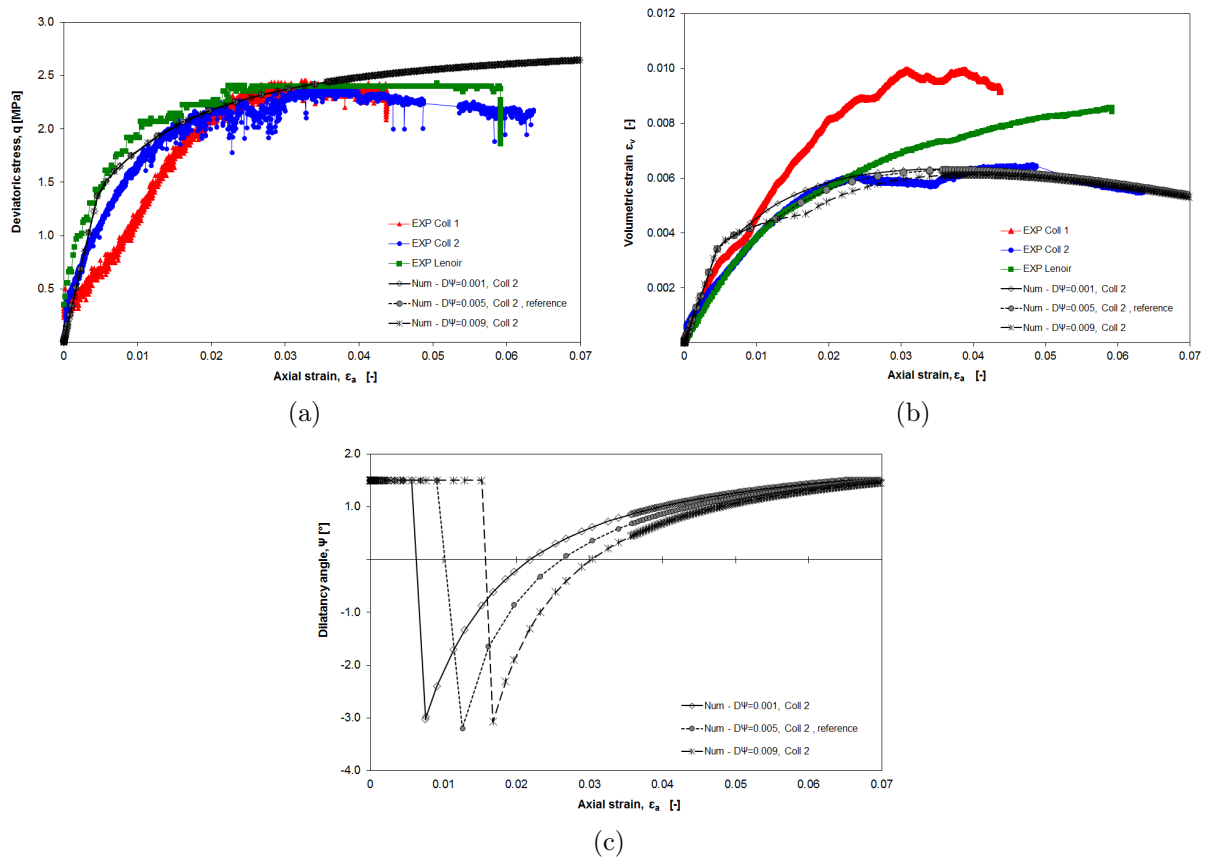


Figure 4.5: Results of the numerical simulations of the drained triaxial test, with three values of  $D\Psi$  with reference to *Num - Variable  $\Psi$ , Coll 2*, compared to the experimental results: (a) Volumetric strain in function of axial strain. (b) Deviatoric stress in function of axial strain. (c) Dilatancy angle variations in function of axial strain.

Finally, it must be noted that the parameter  $Rat_\Psi$  does not only signify the initial statue of  $\Psi$ , and its first evolution to  $\Psi_{peak}$ . In addition, it has also an implicit impact on the variation rate of dilatancy angle, with respect to the third term in the first relation in 4.9. With regard to the simulation *Num - Variable  $\Psi$ , Coll 2*, Figure 4.6 compares the results of that simulation with three different values of  $Rat_\Psi$ . In the first place, the initial value of dilatancy angle induces the primary most contracting volumetric behavior in the case with  $Rat_\Psi = 0$  (i.e. initial value equal to the peak value of  $-3^\circ$ , see the second relation in 4.9), and then  $Rat_\Psi = 0.5$  and  $Rat_\Psi = -0.5$ , respectively. In the second place, the dilatancy angle is declined less rapidly in the simulation with  $Rat_\Psi = 0.5$  than two other ones (see Figure 4.6c). As a result, the case with  $Rat_\Psi = 0.5$  shows ultimately the most contracting response (see Figure 4.6b), furthest from the relative experimental result.

#### 4.2.3.2 Undrained triaxial tests performed at ULg: Studying the influence of the model's parameters

This section is firstly focused on the influence of using the variable dilatancy angle on the numerical results presented in Sections 3.5.2.1 and 3.5.3 with constant dilatancy angles (zero/non-zero values). As it has been already mentioned, the reference parameters are still used, i.e. Table

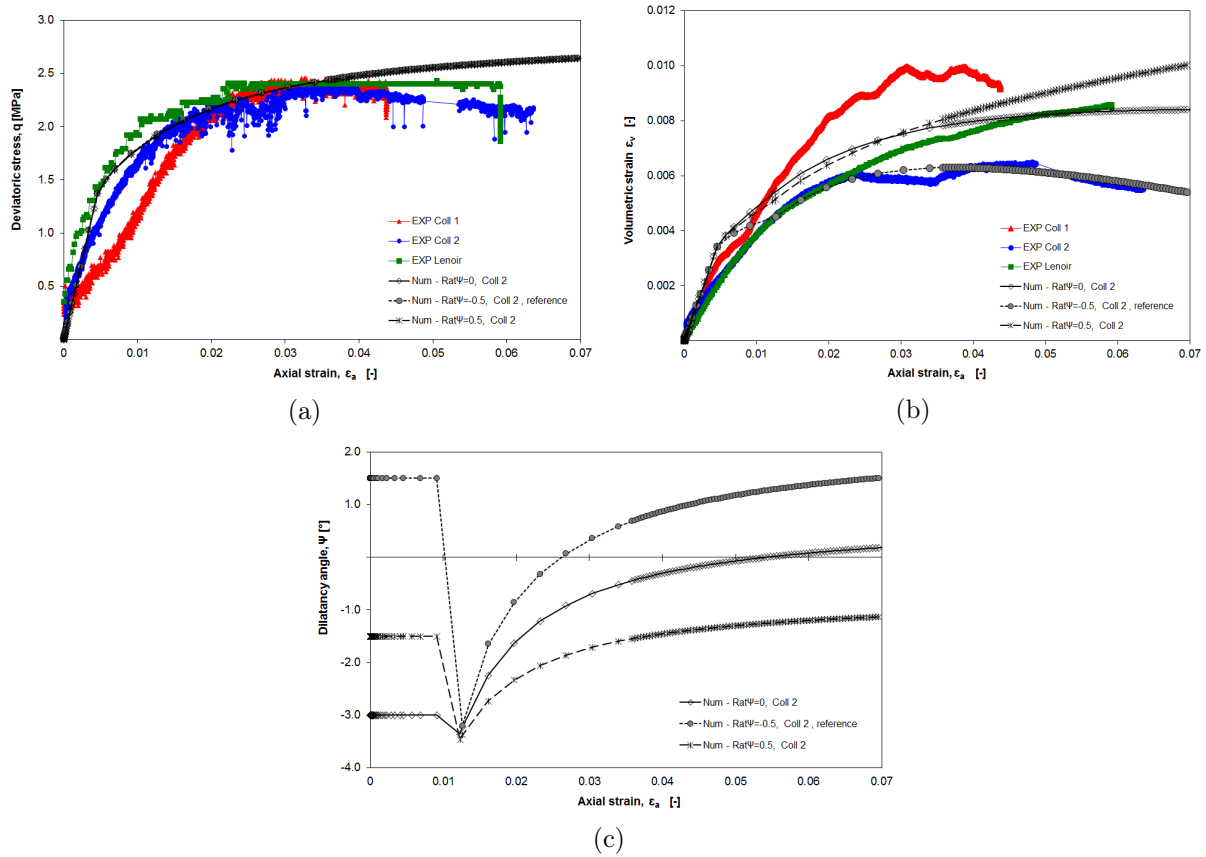


Figure 4.6: Results of the numerical simulations of the drained triaxial test, with three values of  $Rat_\Psi$  with reference to  $Num - Variable \Psi, Coll 2$ , compared to the experimental results : (a) Volumetric strain in function of axial strain. (b) Deviatoric stress in function of axial strain. (c) Dilatancy angle variations in function of axial strain.

3.1. Thence, some encountered difficulties in modeling of the experimental results in the pore pressure and deviatoric planes are addressed here by adding the variable dilatancy angle to the previous modelings (see Table 4.2 for the complementary parameters). However, a perfect numerical response could not be expected (in comparison with the experimental results) only by focusing on the dilatancy angle, particularly considering the pretty inconsistent evolution of pore water pressure *with respect to* the deviatoric stress in function of axial strain, obtained in the laboratory (see Sections 3.5.2.1 and 3.6). Furthermore, a study on the influence of the new parameters, regarding the consideration of variable dilatancy angle, is conducted to better understand the influence of each parameter.

Figure 4.7 presents the results of the new modeling, with variable dilatancy angle, in contrast with the previous simulations using the constant values, compared to the experimental results. It is observed that the modeling with variable dilatancy angle could *generally* simulate a *moderate* response in terms of *both* pore water pressure evolution and in the deviatoric plane. In fact, the primary increase of deviatoric stress touches better the experimental results, compared to the simulations with  $\Psi = 0^\circ$  and  $\Psi = -2^\circ$ . The pore water pressure is pretty underestimated in the plastic zone, though. On the other hand, the deviatoric stress is not modeled as good as for the simulation with  $\Psi = 6^\circ$ . However, the pore water pressure approaches better the experimental results, with reference to the same simulation. This is also evidenced considering the stress path in the  $(p', q)$  plane. Indeed, a high enough peak value of dilatancy angle has been necessary to approach the peak of deviatoric stress while the pore pressure would not experience a sudden

Table 4.2: Mechanical parameters of the model with variable dilatancy

Parameter	Symbol	Value	Unit
<i>Num - Variable <math>\Psi</math></i>			
Young elastic modulus	$E$	300	$MPa$
Poisson ratio	$\nu$	0.125	-
Specific mass of the grains	$\rho_s$	2700	$Kg/m^3$
Initial compression friction angle	$\varphi_{C0}$	8	$^\circ$
Final compression friction angle	$\varphi_{Cf}$	18	$^\circ$
Hardening coefficient	$B_\varphi$	0.001	-
Hardening coefficient	$D_\varphi$	0	-
Initial cohesion	$c_0$	300	$kPa$
Final cohesion	$c_f$	300	$kPa$
Softening coefficient	$B_c$	0	-
Softening coefficient	$D_c$	0	-
Dilatancy angle	$\Psi$		$^\circ$
Peak of dilatancy angle	$\Psi_{peak}$	<u>8</u>	$^\circ$
Limit of dilatancy angle	$\Psi_{lim}$	<u>-1.5</u>	$^\circ$
Dilatancy ratio	$Rat_\Psi$	<u>0</u>	-
Dilatancy coefficient	$B_\Psi$	<u>0.001</u>	-
Dilatancy coefficient	$D_\Psi$	<u>0.007</u>	-

decrease like the one occurred due to the definition of a constant dilatancy angle. Besides, a slight negative limit of dilatancy angle could help getting a plateau in the pore pressure evolution; the dilatancy angle is declined rapidly enough towards a negative limit value of dilatancy angle that this process does not allow the drastic drop of  $p_w$  (see also Figure 4.7e). This reduction of dilatancy angle could generally refer to the material's overall contracting behavior under axial force during the shearing phase of an undrained triaxial test. On the whole, a reasonable response could be predicted in the hydro-mechanical coupled point of view, with application of the model of variable dilatancy angle.

Furthermore, to better understand the impact of each parameter of the model of variable dilatancy angle, a specific study is carried out in the following (in addition to the one conducted in Section 4.2.3.1). Hence, with reference to the calibrated parameters of the variable dilatancy model (as listed in Table 4.2), each of these parameters is changed when the others are kept constant, and the influence of this change on the aforesaid results (shown in Figure 4.7) is then discussed.

#### $\Psi_{lim}$ :

Figure 4.8 shows how the numerical results could be changed following the application of four values of  $\Psi_{lim}$ . It is noticed that for the simulations with  $\Psi_{lim} = -2.5^\circ$  and  $-1.5^\circ$ , the pore pressure evolution is quite the same. Although, the calibrated value, i.e.  $\Psi_{lim} = -1.5^\circ$  could better approach the experimental results in the deviatoric plane. In addition, the simulation with zero limit value of dilatancy angle underestimates more the ultimate pore water pressure, in comparison with the reference simulation. Likewise, the positive value of  $\Psi_{lim} = 3^\circ$  could induce an important underestimation of the pore pressure, even though, the results in the deviatoric plane are improved. In fact, the latter keeps a relatively high dilatancy factor up to the end of simulation (see Figure 4.8d), which prompts a drop of pore pressure. All at once, in the framework of our main objective to have a set of parameters which could reasonably model the experimental results in both hydraulic and mechanical point of view (i.e. deviatoric stress and pore pressure evolution), the calibrated value of  $\Psi_{lim}$  equal to  $-1.5^\circ$  seems appropriate.

#### $\Psi_{peak}$ :

Next, the influence of the peak of dilatancy angle is studied through four simulations using different values of  $\Psi_{peak}$ ; see Figure 4.9. It is observed that the initial increase of deviatoric stress

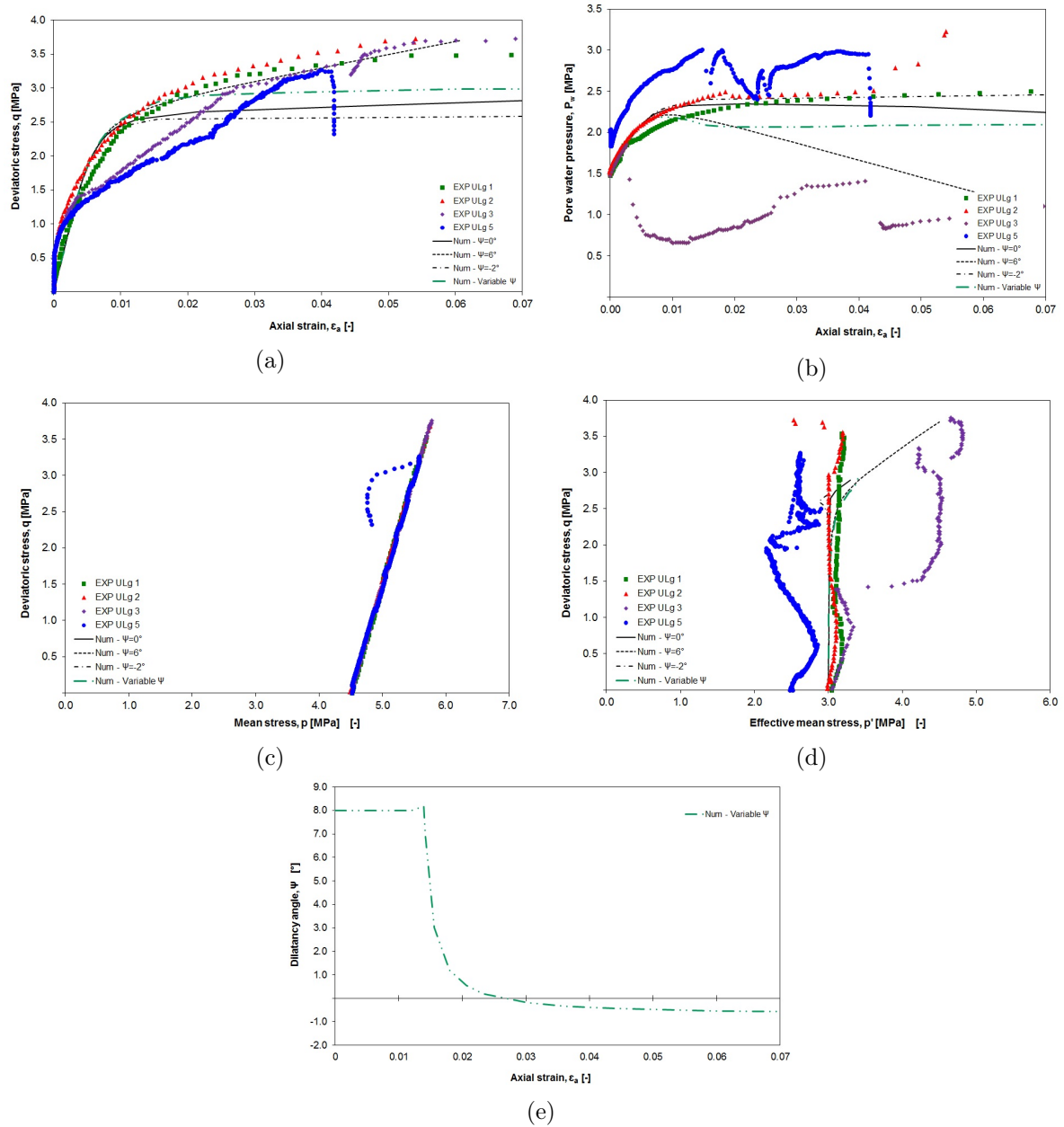


Figure 4.7: Results of the numerical simulations of the tests performed at ULg, ArGENCo, with variable dilatancy angle in contrast with the constant values, compared to the experimental results: (a) Deviatoric stress in function of axial strain. (b) Pore water pressure in function of axial strain. (c) Stress path in the  $(p, q)$  plane. (d) Stress path in the  $(p', q)$  plane. (e) Dilatancy angle variations in function of axial strain.

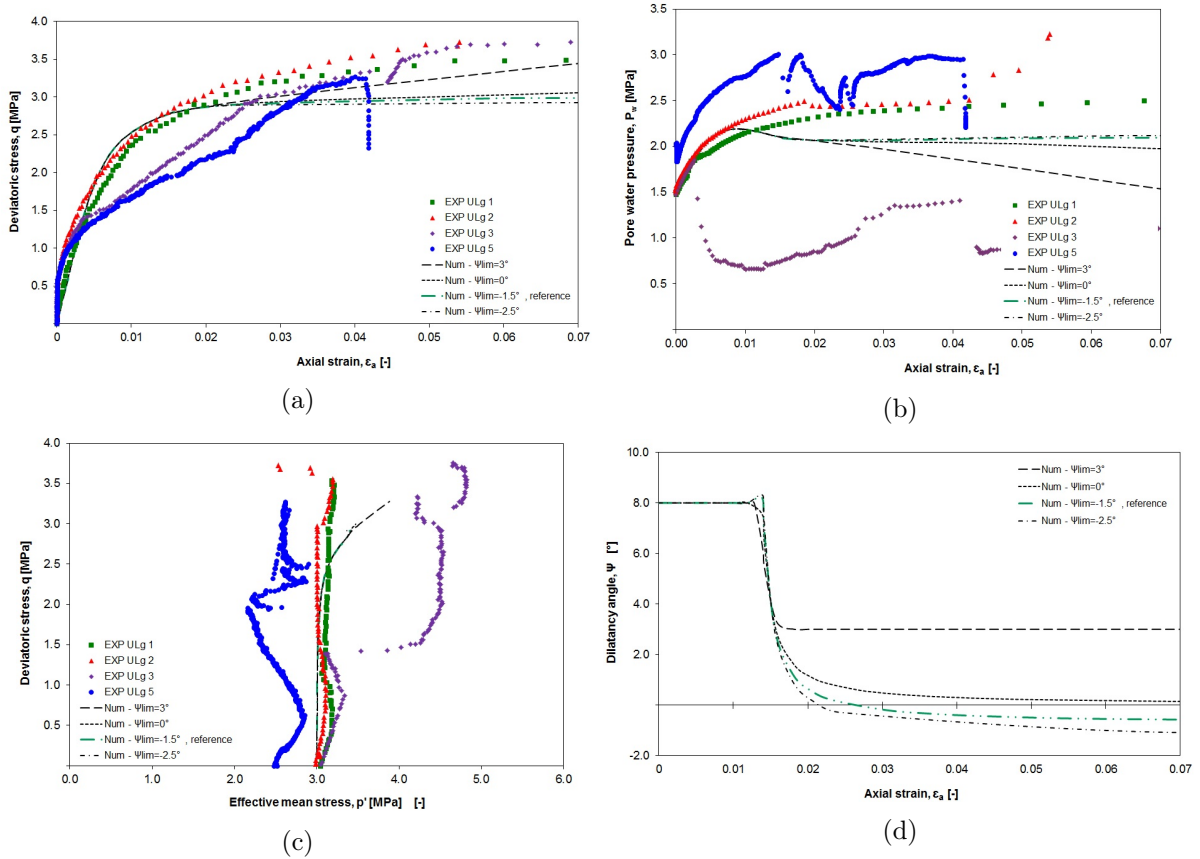


Figure 4.8: Results of the numerical simulations of the tests performed at ULg, ArGENCo, with variable dilatancy angle - *studying the influence of  $\Psi_{lim}$*  - compared to the experimental results: (a) Deviatoric stress in function of axial strain. (b) Pore water pressure in function of axial strain. (c) Stress path in the  $(p', q)$  plane. (d) Dilatancy angle variations in function of axial strain.

(until the axial strain around 0.01) is modeled well with the reference simulation with  $\Psi_{peak} = 8^\circ$  (Figure 4.9a). Through using a higher value, i.e.  $\Psi_{peak} = 14^\circ$ , the result could expectedly get closer to the experimental maximum deviatoric stress; the stress evolves in parallel with the reference simulation, though. The latter can be understood considering the evolution pattern of dilatancy angle in two simulations (see Figure 4.9d). Moreover, the change in the peak of dilatancy angle to  $\Psi_{peak} = 2^\circ$  does not show an interesting improvement if one overviews its coupled impact on the results. Likewise, the simulation with  $\Psi_{peak} = -4^\circ$  underestimates considerably the deviatoric stress (both the initial increase and the subsequent variations), although, it could approach the experimental pore pressure results. The latter case is quite similar to the preceding simulation with a constant negative dilatancy angle. Although, the present case prompts a fairly dilatancy tendency since the initial negative value of  $\Psi = -4^\circ$  evolves to a less absolute value, with respect to  $\Psi_{lim} = -1.5^\circ$  (see Figure 4.9d), that this tendency may not be realistic taking into account a normal response of the material under the axial force during an undrained triaxial test. All together, the modeling with  $\Psi_{peak} = 8^\circ$  could simulate a moderate response (in the both mechanical and hydraulic point of views) as it was aimed for.

#### *Rat $_{\Psi}$* :

The  $Rat_{\Psi}$  parameter is studied to see the influence of definition of a non-zero value on the numerical results. With regard to the difference between  $\Psi_{peak} \times Rat_{\Psi}$  and  $\Psi_{peak}$  (see the relation 4.9 and Figure 4.2), a defined non-zero value may cause a jump in the variation process

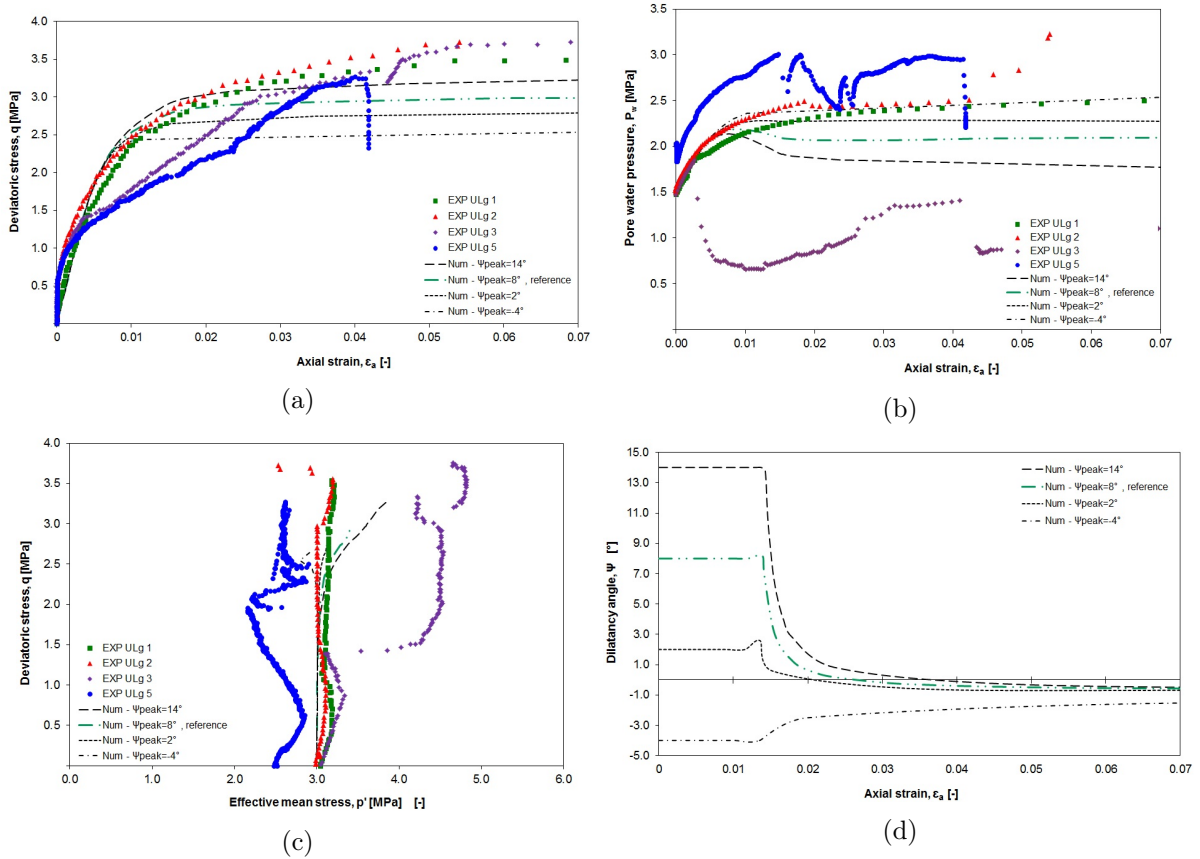


Figure 4.9: Results of the numerical simulations of the tests performed at ULg, ArGENCo, with variable dilatancy angle - *studying the influence of  $\Psi_{peak}$*  - compared to the experimental results: (a) Deviatoric stress in function of axial strain. (b) Pore water pressure in function of axial strain. (c) Stress path in the  $(p', q)$  plane. (d) Dilatancy angle variations in function of axial strain.

of dilatancy angle (increased dilatancy tendency). This behavior is likely to be resulted from fracturing and a softening response in the post-peak regime (after a distinguished stress peak), which it is not actually evidenced by the relative experimental results (with respect to the deviatoric stress evolution). Thence, a dominant (abrupt) dilatancy tendency does not seem realistic during the shearing. As a consequence, a high difference between the initial value and the defined peak of dilatancy angle (i.e.  $\Psi_{peak} = 8^\circ$ ) is not reasonable; e.g. through definition of a negative  $Rat_\Psi$  parameter leading to the negative initial value of  $\Psi$ .

Figure 4.10 shows the results of the simulation with  $Rat_\Psi = 0$  with three other modelings with positive values of  $Rat_\Psi$ . As it is observed in Figure 4.10d, the three simulations with  $Rat_\Psi \neq 0$  have a lower initial dilatancy angle ( $= \Psi_{peak} \times Rat_\Psi$ ) than the reference simulation. The simulation with  $Rat_\Psi = 0.15$  underestimates to the most the (experimental) initial increase of deviatoric stress which has been touched well through definition of a null  $Rat_\Psi$ . The pore pressure gets expectedly pretty closer to the experimental result, at the beginning, with  $Rat_\Psi = 0.15$ , though (because of the less initial  $\Psi$ ). Then, following the variations of the dilatancy angle (Figure 4.10d), there is some strengthening process (Figure 4.10a), and pore pressure has also reduced (Figure 4.10b). The procedure of decline of dilatancy angle after its peak may be affected by  $Rat_\Psi$  parameter, as it has been already mentioned in Section 4.2.3.1. Figure 4.10d illustrates this influence; the simulations with  $Rat_\Psi = 0.45$  exhibits the least decline of dilatancy angle towards the defined limit value, compared to the other simulations. Therefore, the deviatoric

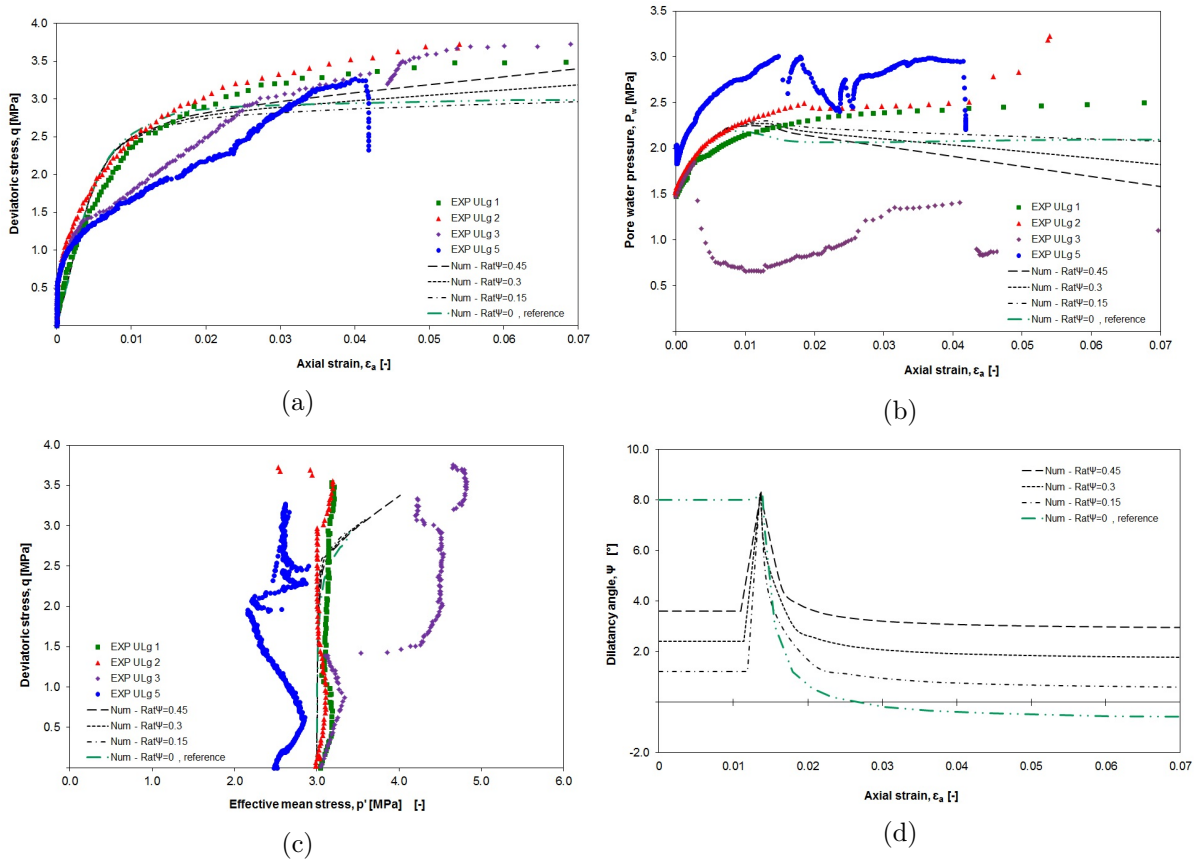


Figure 4.10: Results of the numerical simulations of the tests performed at ULg, ArGENCo, with variable dilatancy angle - *studying the influence of  $Rat_{\Psi}$*  - compared to the experimental results: (a) Deviatoric stress in function of axial strain. (b) Pore water pressure in function of axial strain. (c) Stress path in the  $(p', q)$  plane. (d) Dilatancy angle variations in function of axial strain.

stress lies closer to the experimental results in comparison with the other simulations. However, this improvement does not seem interesting since the simultaneous effect in the pore pressure plane induces negatively a sudden drop of pore pressure. On the whole, taking a non-zero  $Rat_{\Psi}$  worsens the numerical prediction of the initial increase of deviatoric stress. Moreover, the strengthening process in the deviatoric plane is not improved by considering a  $Rat_{\Psi} \neq 0$ , spontaneously with the pore pressure which would not drop.

#### $B_{\Psi}$ :

In the matter of influence of  $B_{\Psi}$ , Figure 4.11 shows the results of simulations with different values of  $B_{\Psi}$ , compared to the experimental results. It is observed in Figure 4.11d that this parameter directly plays with the rate of reduction in dilatancy angle. Indeed, as this parameter is higher, the dilatancy angle declines slower. It means having a higher dilatancy angles for the same axial strain. That is the reason for which the simulation with  $B_{\Psi} = 0.025$  fits in better with the experimental curve of deviatoric stress. However, the pore water pressure suffers from a strong drop, on the contrary to the experimental results. This response is similar to the modeling with a constant (positive) moderate value of dilatancy angle leading to an increase of obtained deviatoric stress and a drop of pore water pressure (see Figure 3.52). Next, the case with  $B_{\Psi} = 0.005$  worsens the pore pressure predictions (relatively to the reference simulation) more than its impact to fairly improve the results in deviatoric plane. On the other hand, the lowest value of  $B_{\Psi}$  ( $= 0.0002$ ) did not make a considerable change in the results with reference

to the simulation with  $B_\Psi = 0.001$ . The deviatoric stress evolution is a bit better modeled using  $B_\Psi = 0.001$ , though. All at once, in a coupled point of view, the value of 0.001 was calibrated for  $B_\Psi$  parameter in order to prevent the non-desirable drop of pore pressure while the material's response in deviatoric plane is also moderately simulated.

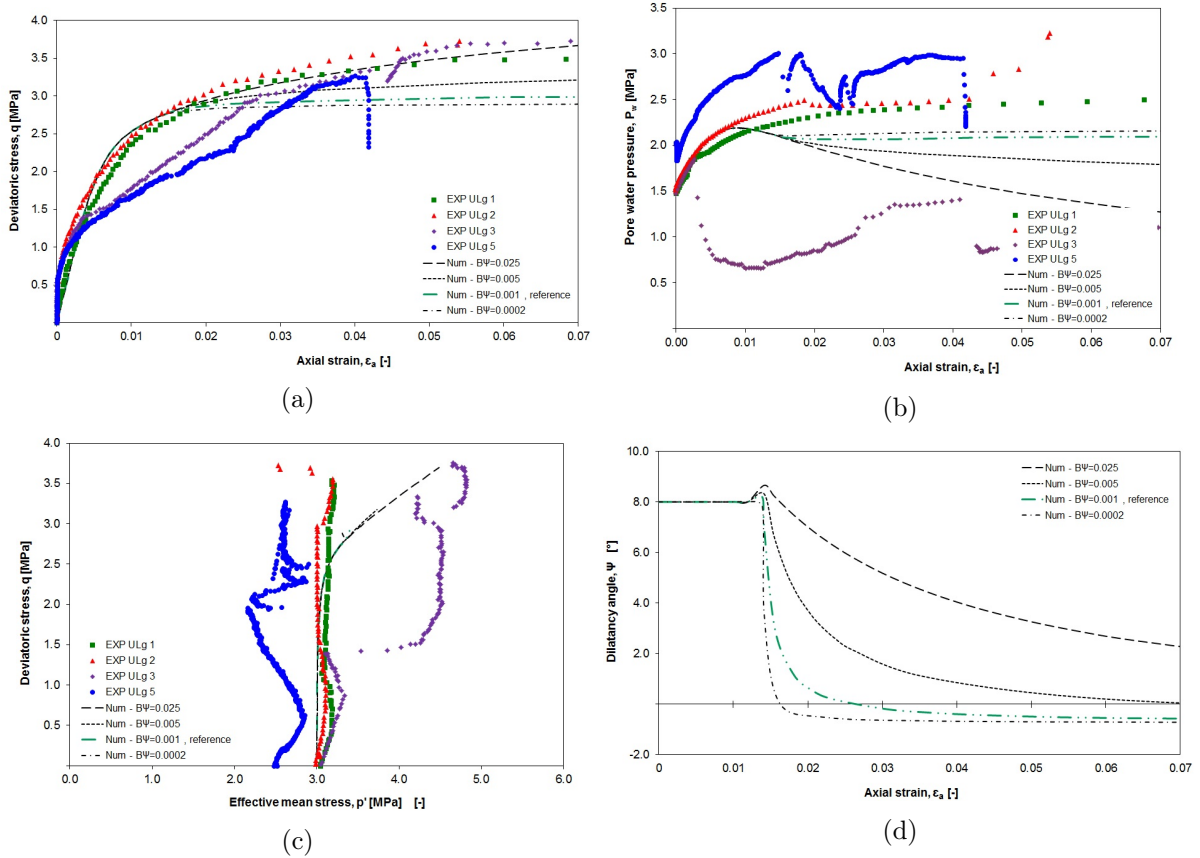


Figure 4.11: Results of the numerical simulations of the tests performed at ULg, ArGENCo, with variable dilatancy angle - *studying the influence of  $B_\Psi$*  - compared to the experimental results: (a) Deviatoric stress in function of axial strain. (b) Pore water pressure in function of axial strain. (c) Stress path in the  $(p', q)$  plane. (d) Dilatancy angle variations in function of axial strain.

### $D_\Psi$ :

With regard to the  $D_\Psi$ , Figure 4.12 displays the influence of this parameter on the numerical results; the results of same simulation with four different values of  $D_\Psi$  are presented. This parameter could induce a retardation in the decline process of dilatancy angle after its peak value (see Figure 4.12d). Consequently, the deviatoric stress evolves in parallel with the experimental results up to a higher axial strain, by increasing  $D_\Psi$  (see Figure 4.12a). That is to say the peak value of dilatancy angle does decline later. This causes a stronger drop in pore water pressure as well (see Figure 4.12b). This drop is significant for the simulations with  $D_\Psi = 0.017$  and  $D_\Psi = 0.012$  with respect to the experimental results. Thus, the reference simulation with  $D_\Psi = 0.007$  has been considered to predict a more realistic coupled response. Moreover, the case with  $D_\Psi = 0.002$  makes a slight improvement in the pore pressure plane, although, the results in deviatoric plane are got worse; the initial increase of deviatoric stress is underestimated, in contrast with the reference simulation.

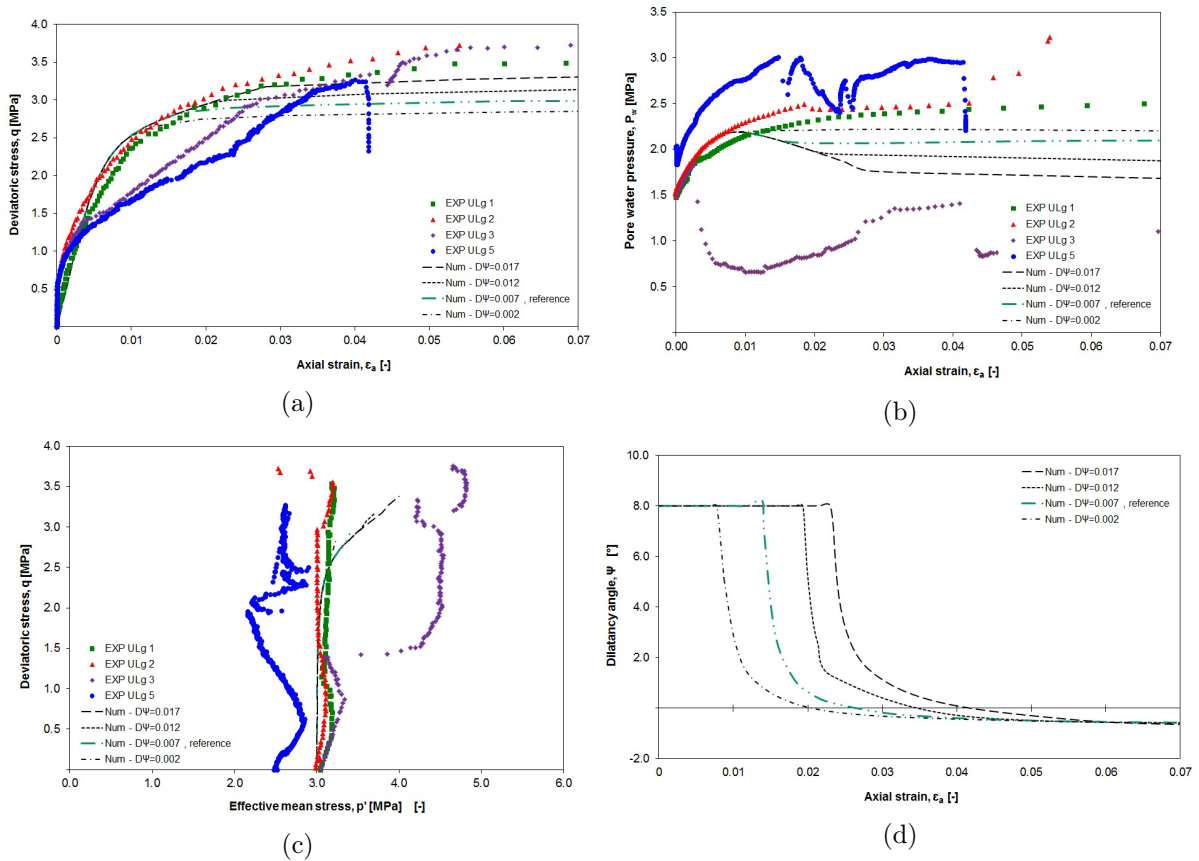


Figure 4.12: Results of the numerical simulations of the tests performed at ULg, ArGENCo, with variable dilatancy angle - *studying the influence of  $D\Psi$*  - compared to the experimental results: (a) Deviatoric stress in function of axial strain. (b) Pore water pressure in function of axial strain. (c) Stress path in the  $(p', q)$  plane. (d) Dilatancy angle variations in function of axial strain.

Table 4.3: Mechanical parameters used for the modelings with variable dilatancy

Parameter	Symbol	Value			Unit
		<i>Num IRSM1 - Variable <math>\Psi</math></i>	<i>Num IRSM2 - Variable <math>\Psi</math></i>	<i>Num IRSM3 - Variable <math>\Psi</math></i>	
Young elastic modulus	$E$	300	300	300	$MPa$
Poisson ratio	$\nu$	0.125	0.125	0.125	-
Specific mass of the grains	$\rho_s$	2700	2700	2700	$Kg/m^3$
Initial compression friction angle	$\varphi_{C0}$	8	8	8	$^\circ$
Final compression friction angle	$\varphi_{Cf}$	18	18	18	$^\circ$
Hardening coefficient	$B_\varphi$	0.001	0.004	0.001	-
Hardening coefficient	$D_\varphi$	0	0	0	-
Initial cohesion	$c_0$	300	300	300	$kPa$
Final cohesion	$c_f$	30	3	30	$kPa$
Softening coefficient	$B_c$	0.01	0.01	0.01	-
Softening coefficient	$D_c$	0.017	0.075	0.037	-
Dilatancy angle	$\Psi$				$^\circ$
Peak of dilatancy angle	$\Psi_{peak}$	<u>8</u>	<u>8</u>	<u>8</u>	$^\circ$
Limit of dilatancy angle	$\Psi_{lim}$	<u>-1.5</u>	<u>-1.5</u>	<u>-1.5</u>	$^\circ$
Dilatancy ratio	$Rat_\Psi$	<u>-0.06</u>	<u>0.06</u>	<u>0</u>	-
Dilatancy coefficient	$B_\Psi$	<u>0.006</u>	<u>0.001</u>	<u>0.001</u>	-
Dilatancy coefficient	$D_\Psi$	<u>0.01</u>	<u>0.028</u>	<u>0.007</u>	-

#### 4.2.3.3 Undrained triaxial tests performed at IRSM

Another application of our model of variable dilatancy angle is presented in this section, with regard to the tests discussed in Section 3.5.2.3. The results of the numerical modeling with application of variable  $\Psi$  are then presented in contrast with the preceding numerical results with  $\Psi = 0$ , in addition to the simulations with a constant dilatancy angle equal to  $4^\circ$ . Table 4.3 gives the parameters applied to the modeling with variable dilatancy; the complementary parameters are then listed with respect to Table 3.4. The peak and limit of dilatancy angle are defined the same as calibrated in the last Section. The test conditions and consequently, the material response is not the same for the present three tests (as discussed in Section 3.5.2.3), and also compared to the tests performed at ULg, in terms of softening behavior. Thus, the three other parameters of the model of dilatancy angle were defined pretty differently for each test in order to control the rate and variation procedure of dilatancy angle, with regard to the relative observed experimental result.

Figure 4.13 shows the deviatoric stress and pore water pressure evolution in function of the axial strain for the all aforesaid simulations, compared to the experimental results. With regard to the test IRSM1, it is observed that the numerical results using the variable dilatancy model could touch well the experimental result in the deviatoric plane. In fact, the underestimation predicted by the former modeling is improved. The defined slight negative value of  $Rat_\Psi$  could help the model to touch the peak of deviatoric stress observed in the laboratory at the quite low axial strain of about 2%. In addition, it is noticed that taking into account a constant middling dilatancy angle ( $\Psi = 4^\circ$ ) deteriorates obviously the numerical results since the fact of having this constant  $\Psi$  could induce an unrealistic strengthening in the post-peak regime. On the contrary, the variable dilatancy angle makes a decline of  $\Psi$  after the peak (see Figure 4.14a), which prompts a better simulation of the experimental results. In terms of pore water pressure, following the discussion given in Section 3.5.2.3, it might not be generally possible to perfectly fit the experimental results (specially at the beginning part), under a full-saturation hypothesis, with regard to the probable initial conditions of the samples. The pore water pressure evolution obtained with the model of variable  $\Psi$  shows a sooner reduction in  $p_w$ , in comparison to the former modeling (i.e.  $\Psi = 0^\circ$ ); see accordingly Figure 4.14. In addition, the ultimate stabilization of pore pressure in the new modeling simulates better the experimental data. On the contrary, the test with  $\Psi = 4^\circ$  shows an unreal drop of pore water pressure. Regarding the test IRSM2, a

similar pattern is observed in the pore pressure plane. The peak of deviatoric stress approaches the experimental results using the variable dilatancy angle. The higher introduced  $D_\Psi$  in *Num IRSM2 - Variable  $\Psi$*  has been intended for the delayed peak of deviatoric stress, followed by some softening behavior, observed experimentally. On the other hand, defining a constant value for  $\Psi$  could impose an overestimation of the observed strengthening process and consequently, the peak of deviatoric stress. Considering the test IRSM3, an improvement of the predicted peak of deviatoric stress, and the post-peak response is obviously obtained by application of our model of variable dilatancy angle, in contrast with the model with  $\Psi = 0^\circ$ . The null  $Rat_\Psi$  value (so initial dilatancy angle equal to  $\Psi_{peak}$ ) has been defined here with respect to a quite high increase of deviatoric stress (in the pre-peak state) in EXP IRSM3 (in spite of the relatively lower confining pressure of the test). On the contrary, it is noticed that there is a significant overestimation of deviatoric stress using a constant  $\Psi$ . The latter is accompanied by a drastic drop of pore water pressure, contrasting the experimental results. The change in dilatancy angle (see Figure 4.14c) could prevent this drop as observed in Figure 4.13f. In fact, the pore pressure variations is better simulated using the variable dilatancy angle, in comparison to two other simulations.

The stress paths of the numerical simulations are presented in Figure 4.15, in comparison with the experimental stress paths. The total stress path (Figure 4.15a) of the simulations with constant dilatancy angle illustrates again the overestimation of the peak strength. The experimental stress paths are better approximated by the simulations with variable dilatancy, with reference to the former modelings with  $\Psi = 0^\circ$ . The stress paths in the  $(p', q)$  plane also confirm the same improvement. However, the probable existence of the air bubbles within the samples (or, their partially saturated state, as discussed in Section 3.5.2.3) made the experimental stress paths to be quite far from the numerical ones, as it could be expected. Furthermore, the stress paths of the simulations with  $\Psi = 4^\circ$  incline drastically to the left, which is not desirable with respect to the experimental results, as the consequence of the strong drop of pore pressure induced by considering a constant dilatancy angle.

To accomplish the debate, the impact of the water compressibility parameter introduced into the model is studied, following the discussion made in Section 3.5.2.3. The results of the simulation of the test IRSM3 has been influenced to the most using the variable dilatancy angle in comparison with the tests IRSM1 and IRSM2 (see Figure 4.13). Thence, these results are represented, by way of example, in contrast with the former modeling with  $\Psi = 0^\circ$  while the parameter  $1/\chi_w$  is changed to the value  $2 \times 10^{-8} Pa^{-1}$  in the both simulations (see Figures 4.16-4.17). Figure 4.16a shows that the peak strength prediction is improved by application of variable  $\Psi$ . In addition, with regard to the pore water pressure evolution, the previous improvement that achieved by definition of  $1/\chi_w = 2 \times 10^{-8} Pa^{-1}$  (see Figure 3.48f) in the basic model with null dilatancy angle, is still upgraded through the application of our model of variable dilatancy angle. That is to say the early response in the lower axial strain as well as the ultimate stabilization of pore pressure. Consequently, the stress paths approach better the experimental results (Figure 4.17). The latter responses could confirm the improvement attained by using our model of variable dilatancy, also for the simulations with modified parameter of water compressibility. However, the main enhancement was basically made through the usage of the variable dilatancy angle (with regard to the Figures 4.13e, 4.13f and 4.15) rather than changing this parameter. Additionally, as it has been already discussed at the end of Section 3.5.2.3, this change of water compressibility parameter is not intended to be considered in the set of parameters which are supposed to be applied in all next simulations.

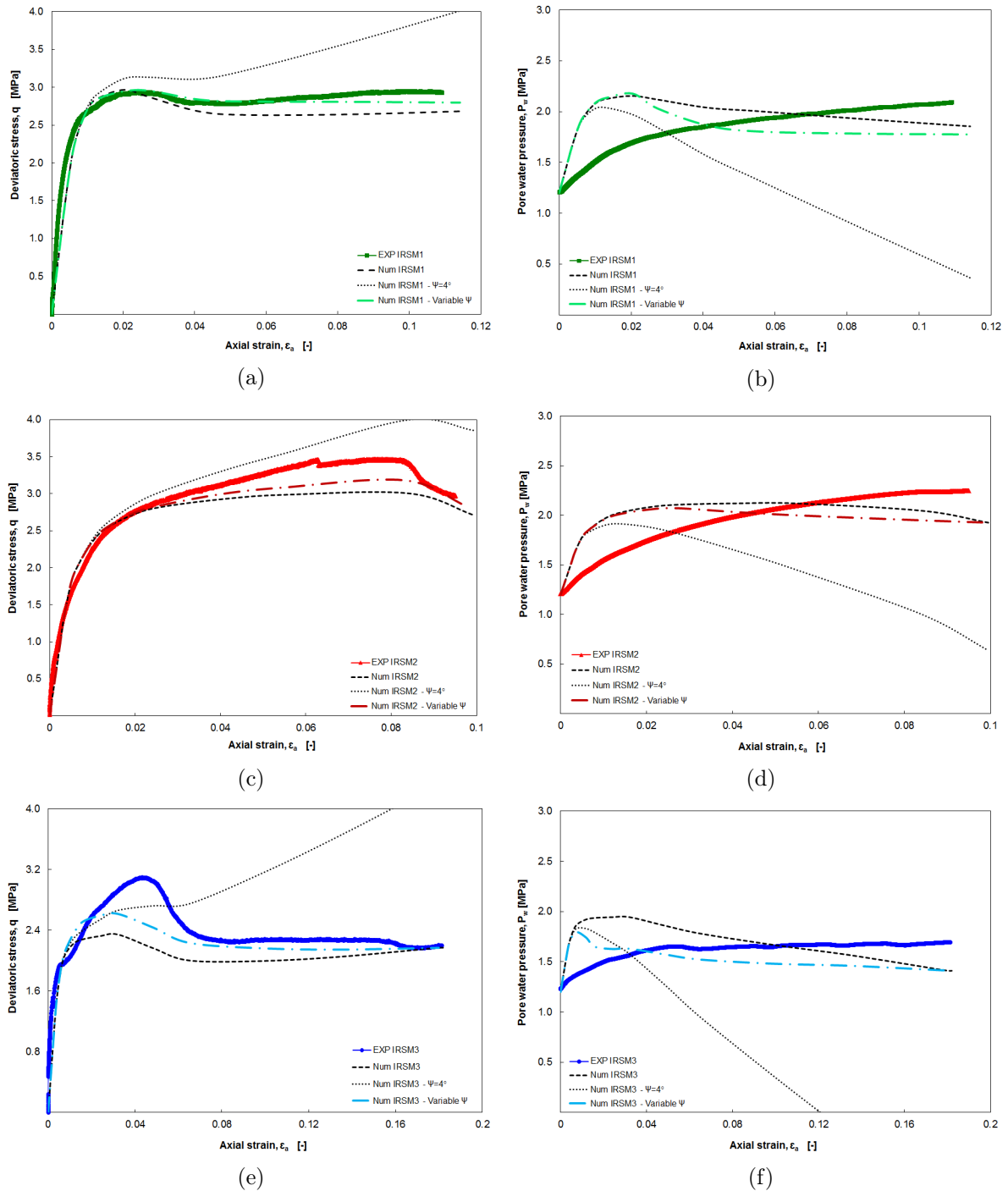


Figure 4.13: Results of the numerical simulations of the tests performed at IRSM, CAS, with variable dilatancy angle in contrast with the constant values, compared to the experimental results: (a) Deviatoric stress in function of axial strain for the first test. (b) Pore water pressure in function of axial strain for the first test. (c) Deviatoric stress in function of axial strain for the second test. (d) Pore water pressure in function of axial strain for the second test. (e) Deviatoric stress in function of axial strain for the third test. (f) Pore water pressure in function of axial strain for the third test.

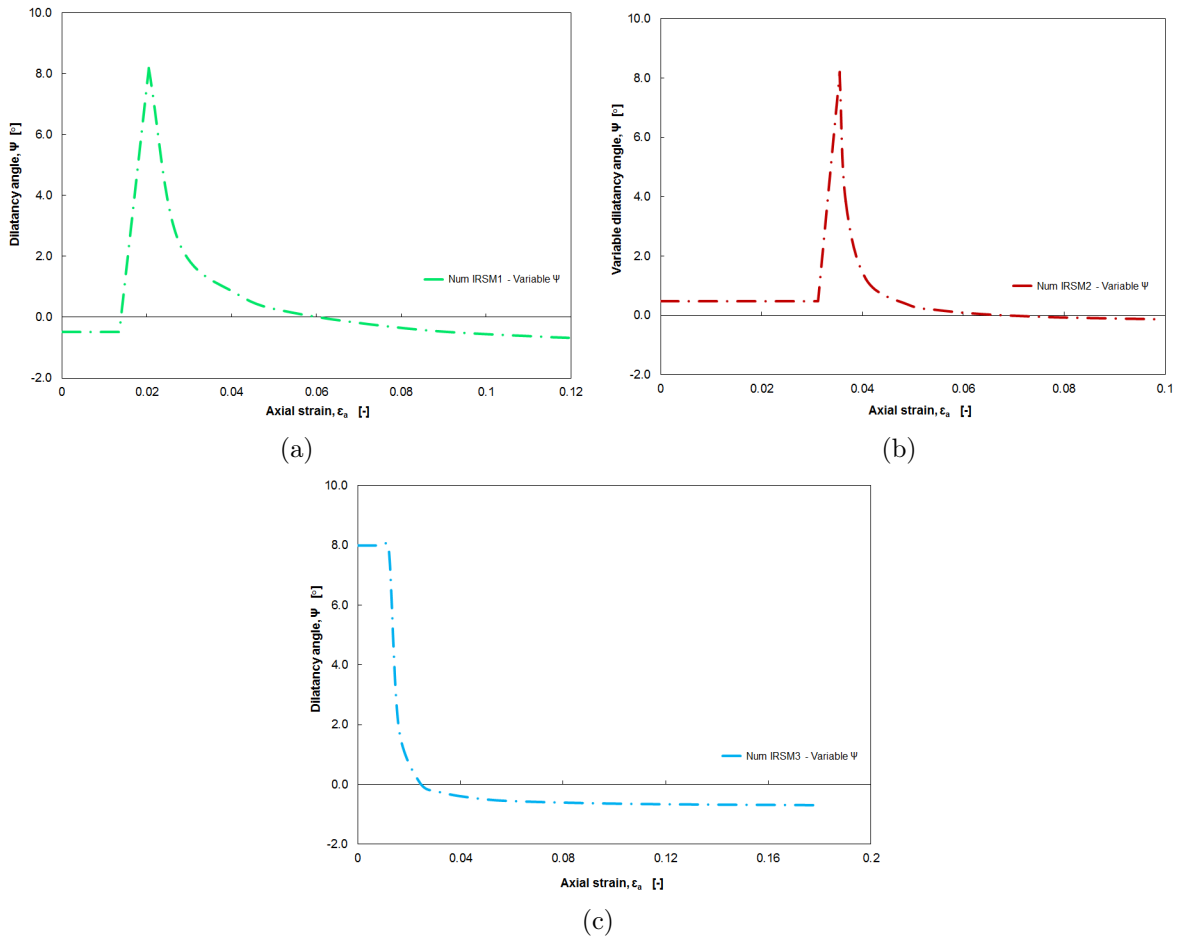


Figure 4.14: Results of the numerical simulations of the tests performed at IRSM, CAS, with variable dilatancy angle in contrast with the constant values, compared to the experimental results: (a) Dilatancy angle in function of axial strain for the first test. (b) Dilatancy angle in function of axial strain for the second test. (c) Dilatancy angle in function of axial strain for the third test.

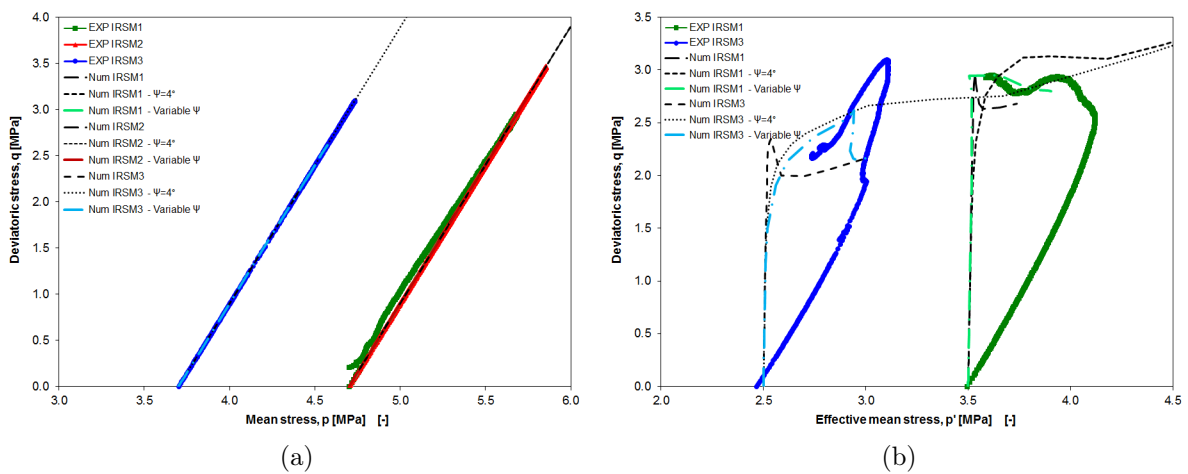


Figure 4.15: Numerical stress paths for the tests performed at IRSM, CAS, with variable dilatancy angle in contrast with the constant values, compared to the experimental results: (a) Stress path in the  $(p, q)$  plane. (b) Stress path in the  $(p', q)$  plane.

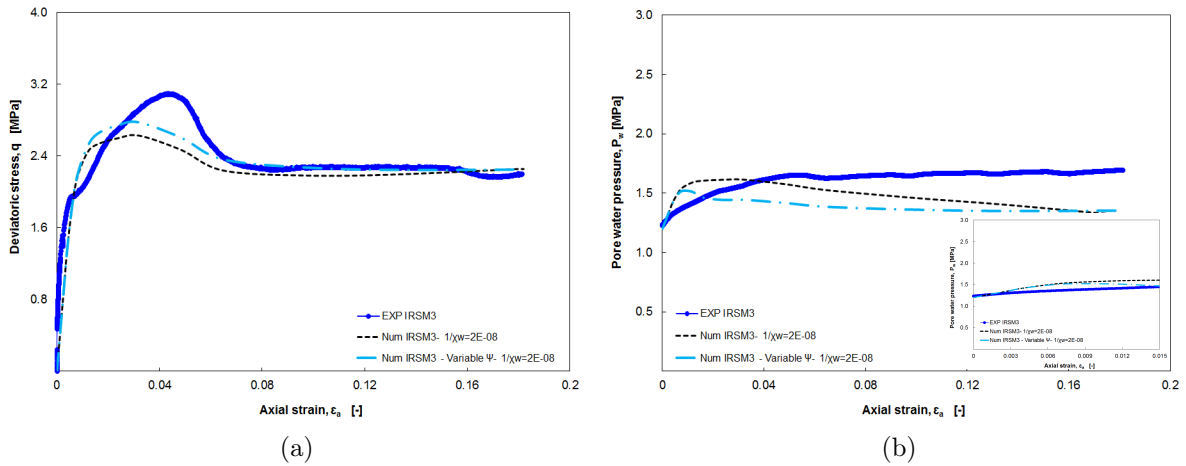


Figure 4.16: Results of the numerical simulations of the test IRSM3 performed at IRSM, CAS, with  $1/\chi_w = 2 \times 10^{-8} Pa^{-1}$  using the variable dilatancy angle in contrast with the zero constant value, compared to the experimental results: (a) Deviatoric stress in function of axial strain. (b) Pore water pressure in function of axial strain.

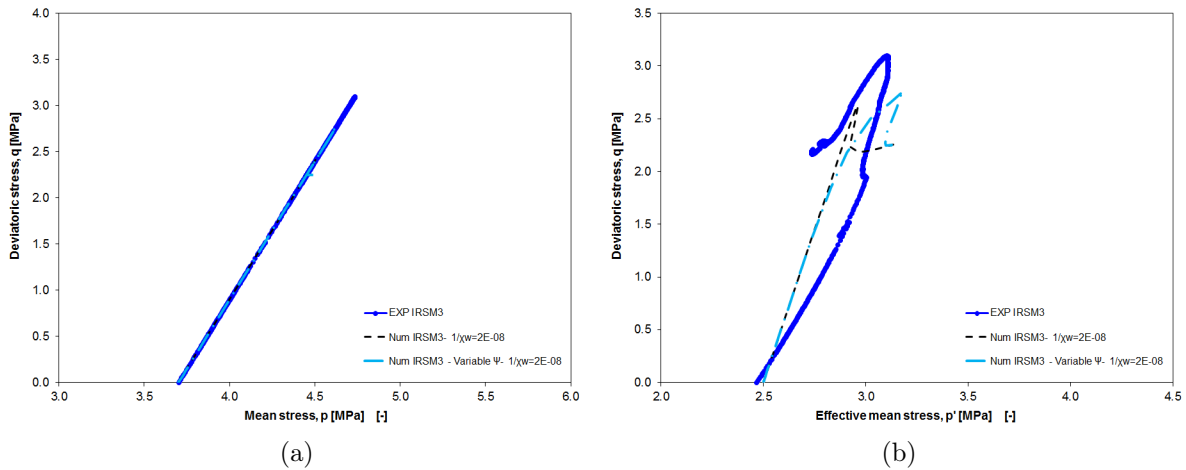


Figure 4.17: Numerical stress paths for the test IRSM3 performed at IRSM, CAS, with  $1/\chi_w = 2 \times 10^{-8} Pa^{-1}$  using the variable dilatancy angle in contrast with the zero constant value, compared to the experimental results: (a) Stress path in the  $(p, q)$  plane. (b) Stress path in the  $(p', q)$  plane.

### 4.3 Intermediate conclusions

A new formula for considering the variable dilatancy angle was presented in this Chapter. Indeed, this proposition is originated at the encountered inconveniences using a constant dilatancy angle, and the lack of available studies which could appropriately address our concern. In this sense, this Chapter was firstly focused on giving a preview on the interest in the variation of dilatancy angle based on the literature. Then, the new model of variable dilatancy angle has been presented introducing its new elements. This model was basically developed and validated based on some available experimental observations. This proposition has been implemented into the finite element code LAGAMINE, integrating with an elasto-plastic frictional hardening/softening model (through the PLASOL and ORTHOPLA laws in LAGAMINE library).

Within the framework of our new formula, three main factors of dilatancy angle are considered for a material consisting in an initial value, a peak value and a limit value, among which the dilatancy angle varies with respect to the plastic strain in the course of a loading process. As a result, a variety of volumetric responses can be realistically reproduced. A dilatant or contracting volumetric behavior of a rock as well as a dilatant/contracting transitional response can be in fact characterized based on the defined model's elements. This capability has been then illustrated through the numerical simulations of some different observed volumetric responses of the studied material in the laboratory (i.e. the tests EXP Coll 1, EXP Coll 2 and EXP Lenoir). Comparison of our numerical predictions with the experimental results have shown a good agreement indicating that different observed responses could be reproduced well using the proposed model. With regard to these drained triaxial tests, the influence of the model's new parameters on the computed results have been also discussed.

Furthermore, the undrained triaxial tests performed at ULg were modeled again using the proposed model of variable dilatancy angle. The new results have been compared with the previous predictions which could confirm the potential of our model to simulate a *moderate* response in the *both* mechanically and hydraulically point of view, with respect to the experimental results. However, these experimental results were not expected to be perfectly modeled only through the application of variable dilatancy angle, particularly with regard to the observed specific variation pattern of pore water pressure besides how the relative deviatoric stress evolves. Next, the sensitivity of the numerical results to each of our model's parameters was studied through some specific simulations. Each parameter was then changed while the other properties kept constant, following by a discussion on the influence of the relative parameter. Thence, the choice of the new parameters regarding the consideration of variable dilatancy angle was validated. Finally, the model has been applied to simulate the undrained triaxial tests performed at IRSM. The numerical results without considering the variable dilatancy angle were then represented in contrast with the modeling results using the proposed model which allows the change in  $\Psi$ . Using the new proposition, the evolution of deviatoric stress was better modeled in comparison with the experimental results. In addition, there was an improvement in modeling of the pore pressure evolution; the stabilization process at the end of the tests could be better reproduced. Furthermore, using our model of variable dilatancy angle, the unrealistic drop of pore water pressure accompanied by a continuous increase of deviatoric stress, as it has been obtained in the simulations of the undrained triaxial tests with application of a constant dilatancy angle, was not observed. On the whole, considering the change in dilatancy angle could improve our coupled hydro-mechanical numerical predictions so that a better simulation of the experimental observations can be achieved.

As the consequence, in order to keep a single set of the parameters for one material (i.e. Boom Clay), the reference main parameters including the mechanical friction angle and cohesion

as well as the (hydraulic) water compressibility will be kept constant, in the next simulations, as they have been primitively given in Tables 3.1-3.2. Some specific aspects of the material response is then attempted to be necessarily addressed through using the variable dilatancy angle, with regard to the dilatancy tendency in the material's behavior.

# Chapter 5

## Numerical simulation of strain localization

### Contents

---

<b>5.1</b>	<b>Introduction</b>	<b>124</b>
<b>5.2</b>	<b>Fracturing mechanism and strain localization</b>	<b>125</b>
5.2.1	Definition of shearing bands and failure process	125
5.2.2	Experimental evidences of strain localization	127
5.2.3	In-situ observations of fractures at depth	136
<b>5.3</b>	<b>Local second gradient model</b>	<b>140</b>
5.3.1	Computational modeling of strain localization	140
5.3.2	Continua with microstructures	144
5.3.3	Framework of the coupled local second gradient model for microstructured continuum	145
<b>5.4</b>	<b>Numerical examples: Definition of the corresponding parameters for modeling of strain localization and analysis of their impact</b>	<b>154</b>
5.4.1	Simulation of biaxial compression test	154
5.4.2	Simulation of the excavation of Praclay gallery	162
<b>5.5</b>	<b>Intermediate conclusions</b>	<b>184</b>

---

*Have patience. All things are difficult before they become easy.*

Saadi Shirazi

## 5.1 Introduction

Localized deformation is a pervasive phenomenon occurs in geomaterials leading up to failure, in the laboratory tests or in the fields. It can appear in various size scales: from one single crack to a much more complex representation of failure, a gouge zone or a fault plane (e.g. Figure 5.1). This mode of deformation is very common in many applications such as the boreholes, tunnels excavation, deep disposal of nuclear waste, and in the broad sense of geotechnical works such as shallow foundations and retaining walls. On the other hand of localized rupture, there is diffuse mode of failure (i.e. homogeneous failure in laboratory tests). However, failure in soil and rock masses frequently occurs under the former mode of deformation, preceded by development of the localization of strains into one or more narrow so-called shear bands. Therefore, in a progressive failure, these shear bands with localized plastic strain are realistically giving rise to the discontinuities, the rupture zones. Hence, modeling and understanding the mechanism of this shear offset within a very narrow zone, strain localization and the post-localization behavior have received particular attention over the past few decades to characterize the failure mechanism in geomaterials. In this framework, this issue has been considered at the core of the present work.



Figure 5.1: An example of the fault planes; located in Tehran-Tabriz free way, Iran.

The mechanism responsible for the formation of shear bands and the process of localization may widely vary. Although, an instability in the inelastic behavior of the material can be considered as a common feature giving rise to these phenomena [Leroy and Ortiz, 1989]. Thence, the localization condition can be analyzed with respect to the onset of instability. The latter is frequently sought through the bifurcation theory. This theory signifies a stress state at which the solution could lose uniqueness [Rice, 1976; Borja, 2013]. The underground openings (which are the principle applications addressed in this thesis) are accompanied by a considerable dilation and high loss of strength in the material constitutive law [Ewy, 1993]. This causes the local inhomogeneties leading to the localization of deformation. These inhomogeneties at the microscopic scale (micro-cracks, fissures, etc.), can be reflected in the material softening which can be accounted through a strain-softening constitutive law. Therefore, the material softening prompts the localization phenomenon; this issue is more clarified in this Chapter. However, the practical implication of the numerical analysis of this process when using a classical finite element is that the response is inherently dependent on the spatial discretization [Wells, 2001]. Therefore, a specific approach, defining an additional parameter of material length, is needed to overcome this problem in order to properly model the localization phenomenon and post-localization behavior. In this sense, the coupled local second gradient model, with an enrichment of the continuum with microstructure effects, is used in this work [Mindlin, 1964; Germain, 1973a; Chambon et al.,

2001a].

Therefore, in the framework of understanding the mechanisms leading to the fractures' network at the proximity of the underground galleries for the deep disposal of nuclear waste, a particular interest has been given to numerical simulation of strain localization in shear band mode, in this thesis. This Chapter then focuses on development of the numerical framework applied hereafter to model the localization of strain. Firstly, the shear bands and failure process are defined taking into account the localization phenomenon. Next, some observations of strain localization in the experimental point of view are reported, with regard to the literature. In addition, since the shear induced fractures with localization of strain have been also evidenced in the field, a description on some in-situ observations is then given. Thence, taking into account the need to use a regularization method to adjust the deficiency of the classical finite element for correctly modeling of strain localization, the coupled local second gradient model is introduced. In this sense, the chosen approach for numerical analysis of strain localization is primarily motivated. Then, the classical numerical framework presented in Section 3.2 is developed based on the local second gradient formulation.

Furthermore, a drained biaxial compression test is simulated numerically in order to simply understand the process of strain localization and some essential relative features, through a small-scale modeling. The role of some model's parameters in term of strain localization analysis, such as the softening parameters, is then clarified. Moreover, a particular parametric study is conducted to analyze the impact of those relative parameters, through a large-scale numerical modeling. The excavation of a gallery defined by analogy with Praclay gallery (Mol, Belgium) is modeled with an analysis of the localized shearing band network around the opening due to the excavation and henceforth. The two-dimensional hydro-mechanical modeling is performed in plane strain condition taking into account the initial anisotropic stress state. Several computations are then carried out in the framework of a parametric study. Consequently, the softening parameters as well as the second gradient modulus are ensured besides the reference set of parameters concluded in Chapters 3-4, in order to provide the final set of parameters for the modelings in which the strain localization is involved (subsequent numerical simulations). In addition, a discussion is handled to show the influence of using the model of variable dilatancy angle (as proposed in Chapter 4) in the numerical simulation of a gallery excavation.

## 5.2 Fracturing mechanism and strain localization

### 5.2.1 Definition of shearing bands and failure process

Shear band has been regarded by Hill [1962] as a very thin layer bounded by two parallel material discontinuity surfaces of incremental displacement gradient, as shown schematically in Figure 5.2. The thickness of a shear band,  $2t$ , is undetermined, in a numerical analysis, without the presence of a material length in the used constitutive model.

The stress redistribution within a perturbed zone in a geomaterial (e.g. around the underground openings) could trigger the damage propagation, which are commonly localized. A shear band (or, more generally, a *strain localization*) signifies the localization of strains into one or more narrow zones of intense shearing. This localized deformation often precedes the failure. The pioneering works performed by Rice [1976] and Vardoulakis [1976] were illustrated a zone of localized deformation where it seemed to be a failure plane. It is why understanding the formation process of shearing bands of localization is essentially useful in understanding the failure mechanism. By then, the response of the material in the post-failure regime (i.e. where there is

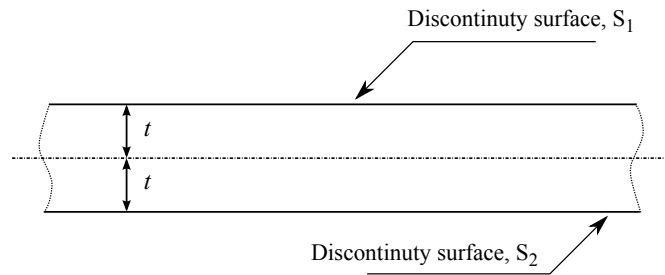


Figure 5.2: Schematic representation of a deforming shear band.

a drop in the material's strength) can also be understandable.

The localization process is seen as an instability that can be predicted from the pre-failure constitutive behavior of the material, according to Sulem [2010]. Thence, in the numerical point of view, it is stated that the necessary condition for the *onset* of localization are established by seeking a possible critical condition for which the constitutive equations of the material (in the pre-localized stage) may allow the existence of a bifurcation point. The deformation mode in this point would be then localized into a shear band [Rice, 1976; Vardoulakis, 1976]. In this framework, one should distinguish the signification of the terms instability and bifurcation. *Stability* for a mechanical system indicates that it is stable (with reference to theory of [Lyapunov, 1992]) if a little perturbation in the initial condition is not increased with time. *Bifurcation* signifies the loss of uniqueness of the solution for a given boundary problem [Rice, 1976; Sulem, 2010]. The latter corresponds to a point (and the relative stress state), for which during the evolution of physical process, there is an *alternative solution* in addition to the *fundamental solution*, for the next loading increment (see Figure 5.3). Hence, spontaneous change of deformation mode, e.g. in the form of localized deformation in a planar band, can occur [Sulem, 2010] (the branch of alternative solution in Figure 5.3). That is to say, loss of uniqueness of the solution, which is attributed to the material instability.

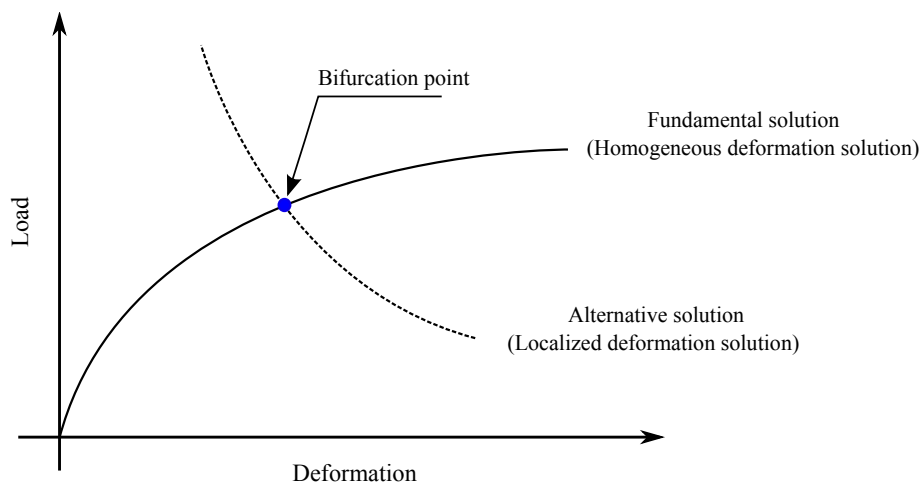


Figure 5.3: Conceptual presentation of bifurcation problem: the fundamental and alternative solutions.

The stress-strain curves could characterize the fundamental aspects of the mechanical response of a geomaterial. The strain localization in shear bands and fracturing process have been frequently observed in a quite brittle mode of deformation in the rocks, i.e. presence of a dis-

tinguishable peak of stress [Desrues, 1998; Bésuelle et al., 2000; Valès, 2008]. However, overall, strain localization in geomaterials can have another aspect: observation of ductile deformation in granular masses [Desrues, 1998]. In addition, as it has been already discussed in Chapter 2, strain localization and deformation mode is not only dependent on the material considered, but on some other features like the loading process. Taking into account a dominant brittle behavior at the presence of strain localization to clarify its concept, Figure 5.4 represents schematically the main phases of deformation during an example of an uniaxial compression test, with respect to [Haied, 1995; Valès, 2008]. These phases can be classified as the following:

- i The very low stress level which corresponds to the primary contraction of the sample. This may result in closing of the pre-existed micro-cracks and pores inside the material. This phase is supposed to be reduced while the confining pressure has been applied in advance.
- ii The elastic zone where the material behaves elastically (either linear or non-linear elasticity). Hence, the strains assign to the elastic deformation of the pores and grains as well as possible slight displacement and relative sliding of the grains (in the case of non-linearity). The sample is not yet tended to the micro-cracking process (neither re-opening of the existed micro-cracks, nor the creation of the new ones). The rock stiffness is supposed to increase upon the application of confining pressure.
- iii The threshold of the micro-cracking is passed by the increment of deviatoric stress, and they initiate, accumulates and propagates (stably). This response can result in a dilatancy tendency. The propagation of these micro-cracks are supposed to be more stable if the confining pressure has been applied.
- iv The unstable propagation of micro-cracks and connection of the fractures occur likely in the pre-peak phase, until the resistance peak. The local inhomogeneity in the material response and the localization of deformation could be initiated at this stage <sup>1</sup>.
- v The post-peak (or, post-localization) phase where the macro-cracks (inter-connected fractures) may come out, and they can initiate a progressive damage leading up to the general collapse of the sample. This process is accompanied by a drop in the material's resistance (or, softening).  
In this sense, for instance during a triaxial compression test, the localization in shear band mode can evolve after the peak, and this behavior may be ended up in failure.

### 5.2.2 Experimental evidences of strain localization

Many experimental small-scale tests devoted to studying the strain localization in geomaterials. They illustrated that a distinguished stress peak in stress-strain curve are usually accompanied by the establishment of localization shear band (as it has been also schematically shown in Figure 5.4, and discussed thereafter), e.g. see [Desrues, 1998; Mokni and Desrues, 1999; Bésuelle et al., 2000]. Figure 5.5a shows an example of the process of shear strain localization during a biaxial compression test on Hostun sand. A drop of resistance beyond the stress peak (i.e. softening response), accompanied by the development of the strain localization within the shear band, can be noticed.

---

<sup>1</sup>It may be interesting to note that if one considers a ductile failure, there will be *stable* development of the cracks before failure; the term *stable* indicates that the cracks will not progress any more if the external force kept constant [Lemaitre et al., 2009].

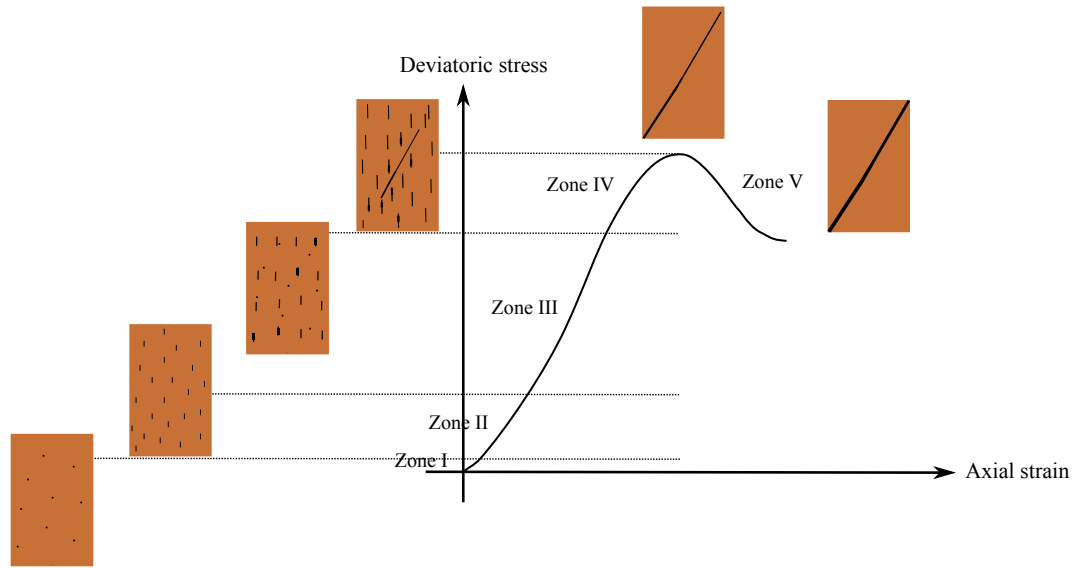


Figure 5.4: Schematic representation of deformation zones and the phenomenon of strain localization during an uniaxial compression test.

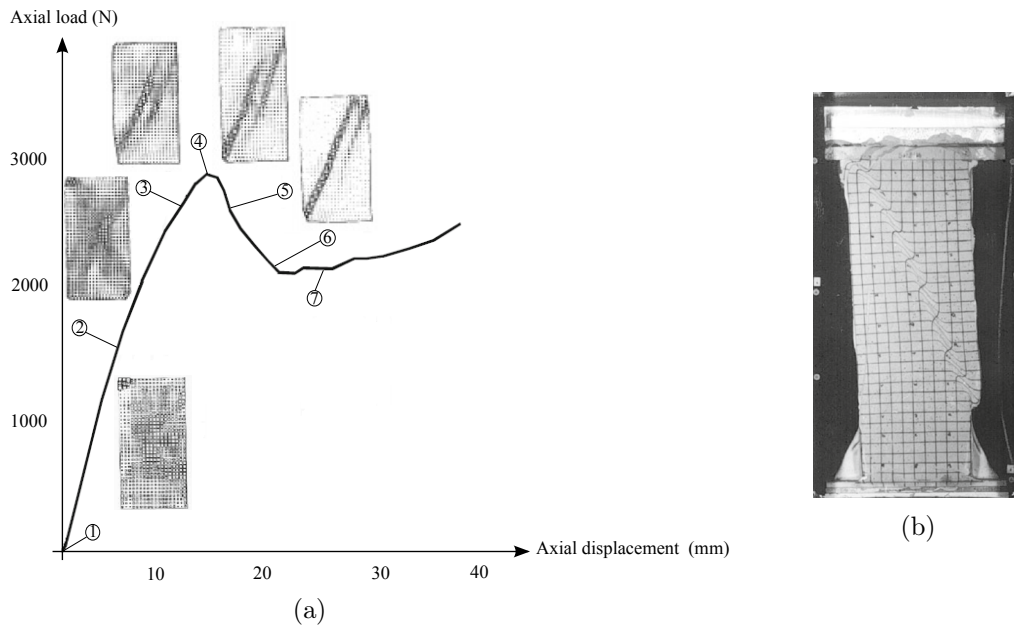


Figure 5.5: The biaxial compression tests on Hostun sand: (a) Development of strain localization in shear band mode during the test, with respect to the different steps in the stress-strain curve. (b) Visualization of a localized shear band during the biaxial compression of a block of sand; after [Mokni and Desrues, 1999].

Most of the experimental works involve some special techniques for a better visualization of strain localization. The experimental methods for analyzing this phenomenon may be generally defined as conventional, or regarded within the so-called non-contact full-field techniques. The conventional methods are basically using the transducers installed at the specimen's boundaries, which could give some information about the overall, averaged response of the material. In fact, their information can be identified as macroscopic with respect to the detailed phases of the material behavior, even though they may also be identified as local measurements taking into account the point-wise data that they give (no information between the measurements points). Therefore, they are more useful when dealing with an homogeneous material with uniform deformation [Viggiani and Hall, 2012]. Indeed, upon localization, the measurements at some specific points at the specimen's boundaries could not obviously represent the material's response within the localized bands, neither could it track the evolution of localization during the loading process. However, there are some experimental studies with regard to the "detection" of the strain localization, during the deviatoric loading, based on this sort of measurements, e.g. in [Bésuelle et al., 2000; Coll, 2005]. The latter study analyzes the appearance of localization on some drained triaxial tests among which there are two tests that were represented in Section 3.5.2.4. The correspondent triaxial cell was instrumented by three axial LVDTs<sup>2</sup> on the specimen's membrane. Then, the homogeneity of deformation was assessed through the comparison of these sensors measurements. Thence, the loading point at which the localized shear bands are formed, i.e. local inhomogeneity, could be detected. With regard to the aforementioned two tests EXP Coll 1 and EXP Coll 2 (see Figure 5.6 for the sheared samples after these tests), no sign of the loss of homogeneity (i.e. localization of deformation) was observed for the first test. On the contrary, Figure 5.7 illustrates how the localization could be detected for the EXP Coll 2. In Figure 5.7c, the differences of the readings of three axial LVDTs with the mean axial strain (average of those three readings) versus the mean axial strain is shown. The threshold of strain localization is considered to be reached when these curves loose the linearity, based on the concept discussed in Bésuelle et al. [2000]. It is then observed that after an initial setup phase, the linear curves continues and they loose their linearity somewhere with the axial strain between 0.03 and 0.04 (see also Figure 5.7a for a noticeable change in the stress-strain response around the same axial strain). Figure 5.7b that compares two readings of radial strain does not clearly show any loss of homogeneity, though.



Figure 5.6: Representation of the sheared samples after the test: (a) EXP Coll 1. (b) EXP Coll 2 [Coll, 2005].

Furthermore, there are the non-contact full-field methods which are being used more frequently during the last three decades. They can provide the desired information (regarding density, deformation, etc.) not only at some specific points, but over the entire specimen. These techniques allow tracking the variations of the requested variables (e.g. incremental strain field) in time and space, and they can give qualitative and quantitative characterization of heterogene-

<sup>2</sup>The Linear Variable Differential Transformer (LVDT) is a type of electrical transformer used for measuring the displacement (position).

ity in material (that are not achieved using the conventional methods) [Viggiani and Hall, 2012]. In the following, some of the most popular full-field techniques in experimental geomechanics that could allow perception of strain localization are summarized, accompanied by a literature review on some practical examples in the framework of this thesis topics. Although, more details on these techniques are beyond the scope of this work; see for instance [Viggiani and Hall, 2012] upon interest.

The False Relief Stereophotogrammetry (FRS) is a technique based on an analysis of the photographs taken from a fixed viewpoint at different times during the loading (deformation) procedure [Desrues, 1998]. It is stated that the deformation can be perceived as a fictitious relief by using a well-known stereoscopic effect on successive pairs of photographs [Desrues and Viggiani, 2004]. Relief conception refers to an interpretation of slight difference noticed while seeing a picture by left or right eye. Since this perception is not due to a 3D nature of the object, and it is resulted from the time difference (and the corresponding plane deformation in that time interval) between two photographs seen by two eyes, it can be called as fictitious. Consequently, a 3D perception of the differences can be obtained. Furthermore, quantitative information could be found by application of a stereophotogrammetric apparatuses that can measure the displacement (by giving the coordinates) in two considered configurations [Desrues, 1998]. An example of the images taken by this technique is represented in Figure 5.8. It corresponds to a plane strain compression test, performed at the laboratory 3SR in Grenoble, on dry Hostun sand in the biaxial apparatus. The shear strain field could illustrate a non-homogeneous deformation from the pre-peak steps. One shear localized band is firstly formed in the upper part of specimen at the step 4-5 (just before the stress peak). Then, another shear band is appeared intersecting the previous one at the subsequent step 5-6. Also, the volumetric strain field could clearly show a concentration of the volumetric strain within the same bands as observed for the shear strain (heterogeneity pattern) [Desrues and Viggiani, 2004].

A development of the aforementioned technique could be achieved by using the simplicity of digital image analysis. Digital Image Correlation (DIC) profits from the computer technology through replacing the analogue photographs by the digital ones. Therefore, the computer programs could assess the displacement field (or, strain field) on the surface of a deformed material by tracking a set of material points in one digital image to the next one (e.g. used in [Hall et al., 2010; Nguyen et al., 2011]).

X-ray Computed Tomography (CT) is another technique which has been basically aimed to overcome the limitations of traditional X-ray imaging by giving more quantitative information on the observed density changes in a specimen and providing 3D imaging. In fact, this technique reveals quantification of density and internal features of an object in 3D by recording the photographs in many angular positions all around the considered object, and subsequent application of back projection principle [Viggiani and Hall, 2012]. Then, in experimental soil and rock mechanics, this method as a practical tool has been commonly used for investigation of strain localization. Figure 5.9 shows the horizontal slices of 3D CT images of dry dense Hostun sand at the end of triaxial compression test while the pattern of localized density is highlighted. Since in a triaxial test, these features might be hidden to a naked eye, these types of techniques are very useful. However, there is one important drawback for this technique that corresponds to the fact that CT images can principally reveal the local density variations. Thence, if the material within the localized bands has some noticeable volumetric change (e.g. dilatancy tendency as it can be expected through the localization in planar band), the local density changes and the CT images can be useful to evidence the localization. On the contrary, if the localization does not induce the volume change, e.g. for closed shear cracks, CT images can not illustrate it. Therefore, this technique has been sometimes combined with the 3D DIC for overcoming this problem and to better analyze the internal phenomena. For instance, Figure 5.10 shows the stress-strain response

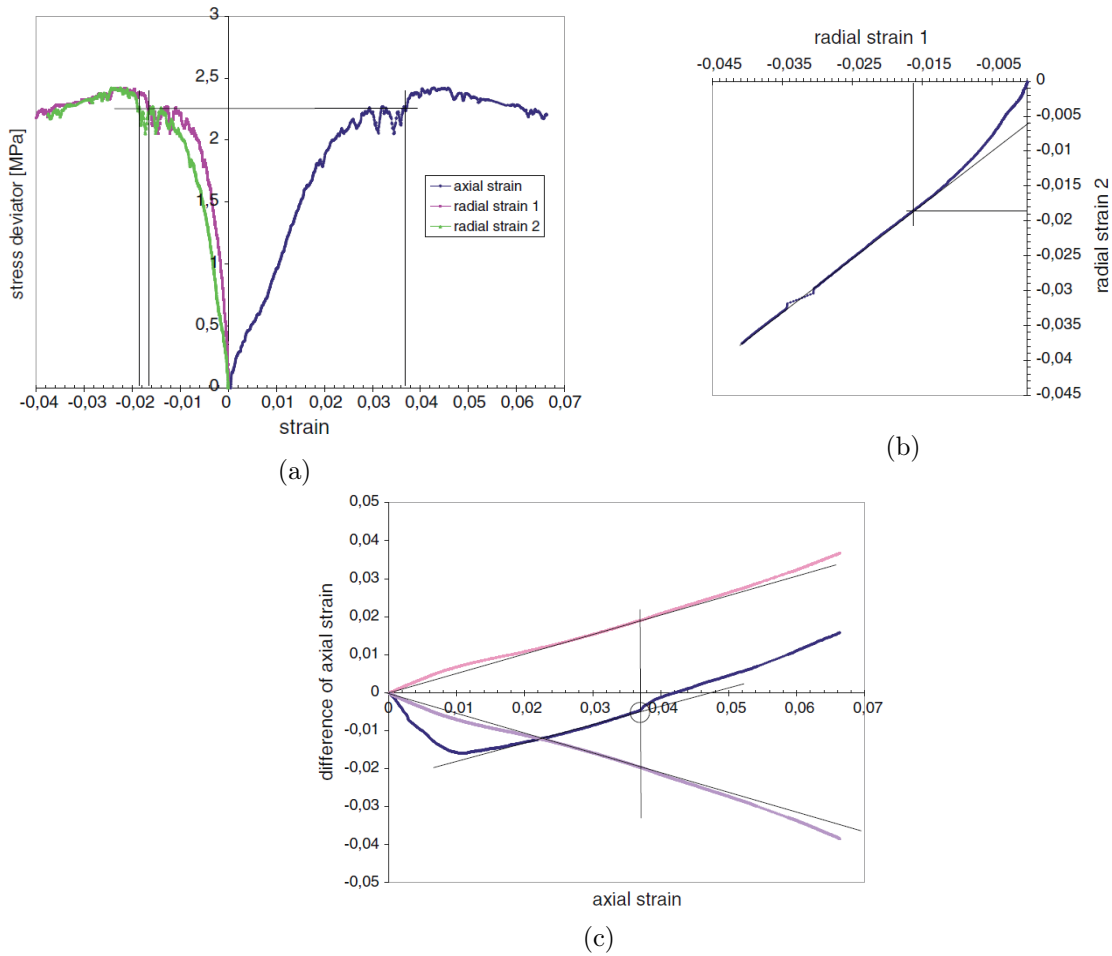


Figure 5.7: Detection of strain localization in the test EXP Coll 2<sup>3</sup>: (a) Deviatoric stress in function of axial strain and radial strains. (b) First radial strain versus the second radial strain. (c) Differences of three axial strains with the mean axial strain in function of the mean axial strain [Bésuelle et al., 2014].

<sup>3</sup>Test BC20 in the corresponding references.

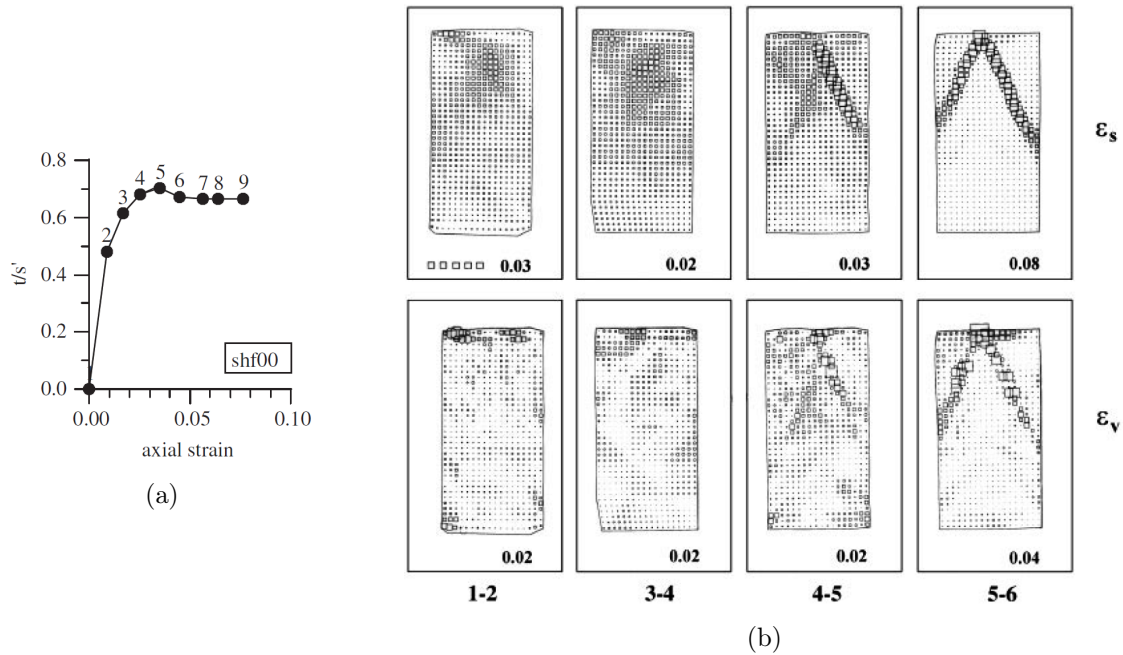


Figure 5.8: The results of experimental plane strain compression test on dry Hostun sand in the biaxial apparatus: (a) Axial load in function of axial strain. (b) FRS-derived incremental fields of shear strain (top row) and volumetric strain (bottom row) [Desrues and Viggiani, 2004].

of Callovo-Oxfordian (the potential host rock for deep disposal of nuclear waste in France) during a triaxial compression tests with  $10\text{MPa}$  of confining pressure, besides the CT images taken at different steps (before and after the stress peak); see [Bésuelle et al., 2006b; Lenoir et al., 2007] for more information about the concept of the applied methods and the detailed discussion on the results. Given the step numbering on the curve, it is observed that two open cracks can be seen at the end of test (let say step 8; after the removal of confining pressure). At the stress peak (step 3), no clear localization can be detected (on the contrary to what was expected), though; a very narrow band in upper left part of the slice could be hardly noticed since step 4 (see for instance step 7). Besides, Figure 5.11 shows the results of an analysis of the same test, using the 3D DIC, for the pre-peak (step 2-3) and post-peak (step 3-4) states. It is observed based on the shear strain maps that the localized shear bands have been already formed in the pre-peak step and they have been fully developed at the step 4. In addition, the circular shape of shear zone in the horizontal cut suggest some impacts of the boundary conditions on the localization pattern. Therefore, the 3D DIC results could help to reveal better some remained hidden internal features upon localization (without significant volume change).

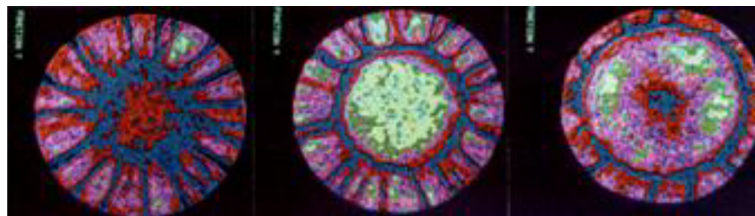


Figure 5.9: Horizontal slices of 3D CT images of dry dense sand Hostun at the end of triaxial compression test; Image courtesy of J. Desrues, according to [Viggiani and Hall, 2012].

In the framework of experimental observations of strain localization and investigation of

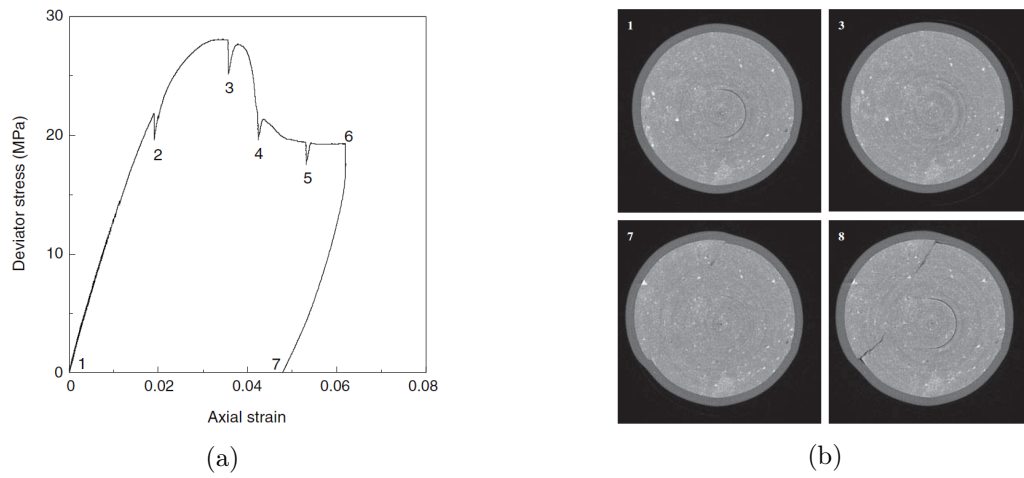


Figure 5.10: The results of triaxial compression test on Callovo-Oxfordian sample ESTSYN01: (a) Deviatoric stress in function of axial strain. (b) Horizontal slices of CT images during the test [Lenoir et al., 2007].

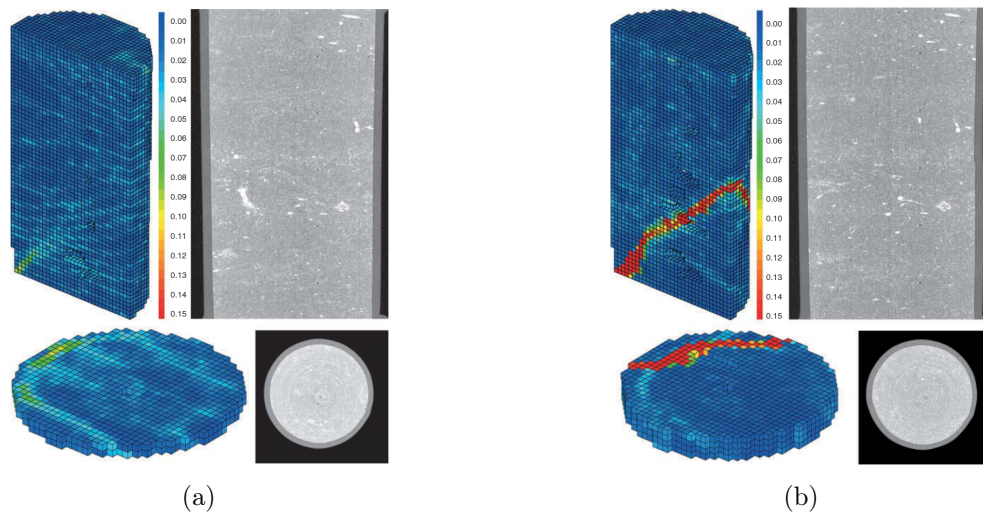


Figure 5.11: The DIC-derived deformation map for the triaxial compression test on Callovo-Oxfordian sample ESTSYN01; vertical cut (along the axis of specimen) and horizontal cut (near to the sample bottom) through the CT images (right), and the radiographic cuts through the incremental shear strain map - using the Von-Mises equivalent strain - (left) for the step: (a) 2-3. (b) 3-4 [Lenoir et al., 2007].

damage mechanism in Boom Clay, some relative published works using the X-ray CT technique are then briefly represented. The hollow cylinder test was performed by the rock mechanics group at EPFL in the framework of TIMODAZ project on the samples cored during the construction of Praclay gallery at Mol. During the test, the in-situ conditions was firstly recovered through a saturation phase and then a loading procedure to achieve the in-situ stress of  $4.5 \text{ MPa}$  and pore water pressure of  $2.2 \text{ MPa}$  [Labieuse et al., 2014]. Next, the mechanical unloading was conducted with the objective of simulating the extension stress path resulted from the gallery excavation, and to induce the emerged damaged zone around the central hole. Finally, there was a drainage phase as well. Therefore, the results may be comparable with a large-scale simulation of the gallery excavation in Boom Clay (we will see some similarities later in the next Chapter). Figure 5.12 shows the X-ray CT scans of the samples N°13B-Bis, cored parallel to the bedding, (according to [Labieuse et al., 2014]) before and after the mechanical unloading. The deformation pattern was obviously revealed by CT imaging. A clear ovalized shape of deformation can be noticed by comparing the scans before and after mechanical unloading. This feature will be also observed in the future large-scale simulations in this thesis (see Chapter 6). The white spots are pyrite inclusions which have also lead up to a quantitative analysis of the occurred phenomenon by tracking these particles. Thence, by comparing their positions before and after the mechanical unloading and the data processing (particle manual tracking; see the latter reference for further details), the displacement profiles could be obtained<sup>4</sup>. Figure 5.13 illustrates the eye-shaped damaged zone around the central hole deduced from the displacement profiles that have been also displayed, themselves, along the sections parallel and perpendicular to bedding.

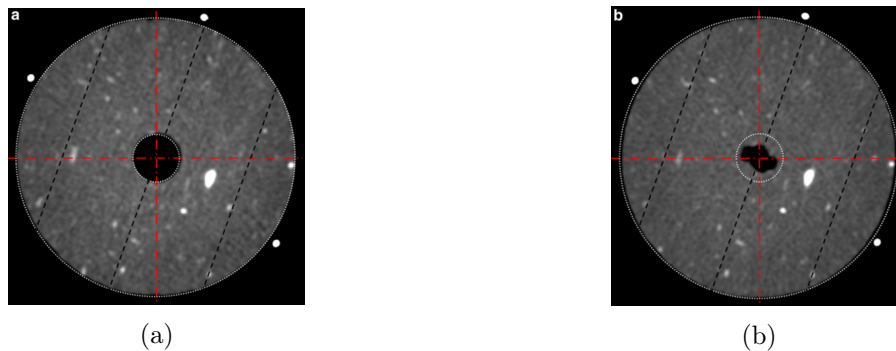


Figure 5.12: The results of hollow cylinder test on Boom Clay sample N°13B-Bis through the X-ray CT images taken: (a) Before the mechanical unloading. (b) After the mechanical unloading. The black dashed line is the schematic representation of bedding plane [Labieuse et al., 2014].

Furthermore, X-ray computed microtomography scan was also similarly used at the 3SR laboratory to study the strain localization phenomenon in Boom Clay. In addition, it was a practical tool to illustrate the probable existence of pre-existing inclusions and even fractures inside the Boom Clay samples before the tests (consisting in the triaxial shear tests performed in the hollow cylinder cell [TIMODAZ, 2010b; Bésuelle et al., 2014]). For instance, Figure 5.14 shows a CT 3D reconstruction of the surface and inside inclusions of the specimen BCTIMODAZ02. Moreover, Figure 5.15 shows the X-ray CT scans of the same specimen before and after the deviatoric loading where the localized band is clearly observed. The pre-existing discontinuity is illustrated in Figure 5.15a that it has had an essential impact on determining the localization pattern of shear fracture during the test (see Figure 5.15b). In this sense, it is observed that the initial cracks, probably resulted from the coring process, could be reactivated and developed during the test. The authors then concluded that this full-field technique could help to disclose some pre-existing

<sup>4</sup>The authors indicated that the DIC method has been also applied for this purpose, which provided the similar results.

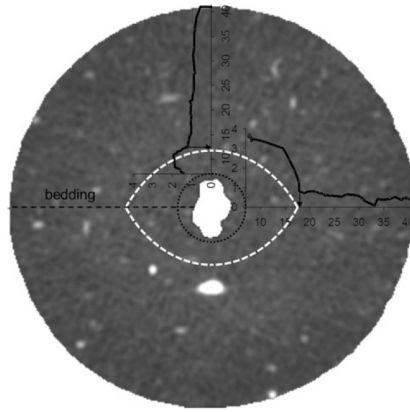


Figure 5.13: The eye-shaped damaged zone around the hole in the hollow cylinder test on Boom Clay sample N°13B-Bis; the black lines are the displacement profiles [Labieuse et al., 2014].

inclusions and fractures in the samples besides the analysis of strain localization, which could affect the mechanical response and the observed pattern of fracturing and localization. This issue and the similar cases are important to be considered before any interpretation of the laboratory experiments for characterizing the material behavior in the field.



Figure 5.14: Illustration of the pre-existed inclusions in Boom Clay sample BCTIMODAZ02 before the test. (a) X-ray CT 3D reconstruction of the surface of specimen. (b) X-ray CT 3D reconstruction of the inclusions inside the specimen [TIMODAZ, 2010b].



Figure 5.15: X-ray CT vertical sections through the specimen BCTIMODAZ02: (a) Before the test. (b) After the test; after [Bésuelle et al., 2014].

Finally, looking at Boom Clay in the smaller scale, i.e. microscopic scale, was also considered by some (e.g. [Yu et al., 2012]) at the laboratory to analyze the microstructures change due to shearing and localization. Given the triaxial tests described in Section 3.5.2.3, Figure 5.16 illustrates the localized shear bands in the deformed samples after the test. Besides, the localization phenomenon made an rearrangement of the particles to be concentrated around the

existed fractures as it could be seen in Figure 5.17. It is observed that the particles' positions are more regular after the test while they have been reoriented around the localized fractures, parallel to the direction of shearing.

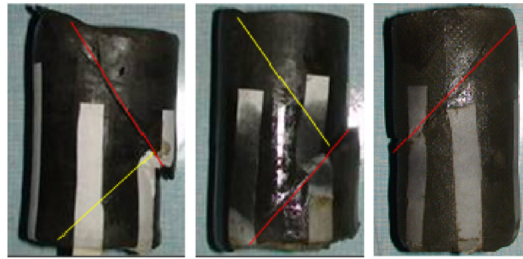


Figure 5.16: Localized shear bands in the damaged samples after the tests [Yu et al., 2012].

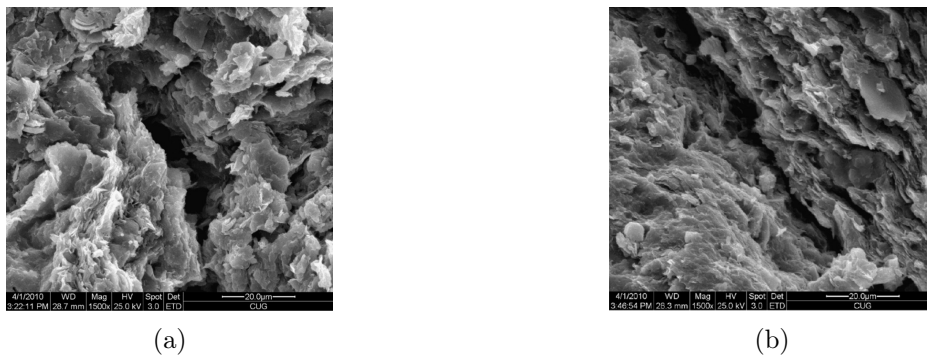


Figure 5.17: SEM images of the microstructure variations of Boom Clay sample, around the fractures, upon shearing. (a) Before the test. (b) After the test [Yu et al., 2012].

### 5.2.3 In-situ observations of fractures at depth

The underground excavation process is expected to induce stress redistribution around the openings. Significant changes in the local stress field are then generated; e.g. in a cylindrical unsupported tunnel, this process leads to the radial stress to vanish and the tangential stress to increase (then the confining stress gets to zero). Consequently, it can trigger the damage propagation around the cavities creating the so-called Excavation disturbed Zone (EdZ) or Excavation Damaged Zone (EDZ). These two zones are defined based on the level of change in their flow and transport properties induced by excavation [Bernier et al., 2007a]. The latter zone which is mostly concerned in the framework of long-term safety of deep disposal of high-level nuclear waste - and in this thesis - characterizes a zone with significant irreversible deformations and important modifications in the hydro-mechanical host rock's properties including influential changes in flow and transport properties (e.g. hydraulic conductivity)<sup>5</sup>. In fact, as the rock is damaged, crack networks are created. They might then constitute preferential flow paths depending on the network connectivity and consequently, they could alter the favorable original flow and transport properties of the rock masses. On the other hand, given the hydro-mechanical coupling processes, the significant deformation, induced by excavation, could impose the change in pore spaces. The latter as well as the (natural) low hydraulic conductivity of the host rock may infer an (immediate) important variations in pore water pressure distribution around the gallery (and in stress

<sup>5</sup>On the contrary, EdZ is without major changes in transport and flow properties, and within this zone, there is not any negative effects on the long-term safety [Bernier et al., 2007a].

state) that can also affect the failure process. Indeed, the extension pattern and characteristics of this damaged zone is managed by local stress state, the anisotropic features of stress and rock properties, the pore pressure distribution, existence of pre-existing fractures, tunnel geometry and supporting technique [Blümling et al., 2007].

Figures 5.18 and 5.19 show the fracturing pattern in two potential host rocks for deep disposal of nuclear waste in France (i.e. Callovo-Oxfordian; COX) and Switzerland (i.e. Opalinus clay; OPA), respectively. In Figure 5.18a, the EDZ pattern with the herringbone structure of fractures around the gallery excavated in COX is schematically shown, and an example of this type of fracturing along a COX borehole core, induced by the drilling process, can be observed in Figure 5.18b [Wileveau and Bernier, 2008]. Furthermore, Figure 5.19a shows schematically the EDZ pattern around a gallery excavated in Opalinus clay. Figure 5.19b displays an inferred EDZ caused by the bedding and bedding parallel fracturing (resulted from the potential material anisotropy; see [Blümling et al., 2007] for further discussion) around a formerly horseshoe tunnel in OPA. In addition, a similar pattern of EDZ can be observed in Figure 5.19d in a smaller scale, at the top of a borehole in OPA. Moreover, Figure 5.19c shows a basic result of stress redistribution in a damaged zone which caused a combined shear-extensional fracturing around a borehole in OPA.

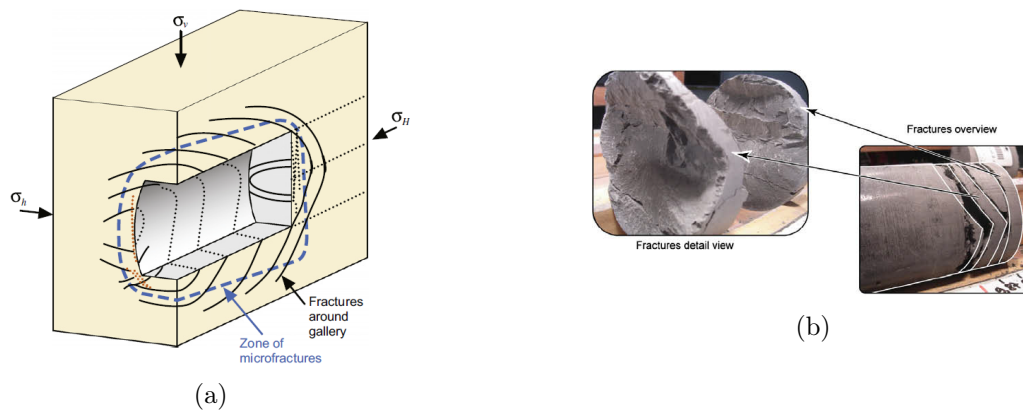


Figure 5.18: (a) Schematic representation of the herringbone pattern of fracturing, observed at the Bure site (France), around the gallery excavated in COX, parallel to  $\sigma_H$ . (b) Fractures pattern along a COX borehole core induced by the drilling process [Wileveau and Bernier, 2008].

Focusing more particularly on our studied material, Boom Clay, the rock is perturbed within a zone around a gallery, excavated through it, due to the differential stresses, and the local stresses ahead of excavation front, generated during the gallery excavation [Bastiaens et al., 2003]. During the construction of Connecting gallery (see Figure 2.3), consequently to this stress redistribution, the shear induced fractures have been observed both in the excavation front and on the gallery sidewalls. Figure 5.20a shows the parallel shear planes in the gallery front photographed during the excavation. The observed fractures on the sidewalls can be also seen in Figure 5.20b. An interesting feature observed during the construction of Praclay gallery (see Figure 2.3), which has been constructed perpendicular to the Connecting gallery, was the fractured zone induced by the latter gallery excavation. Figure 5.21 displays the fractures observed in the first few meters of Praclay gallery excavation that have been fundamentally originated by the construction of Connecting gallery [Van Marcke and Bastiaens, 2010].

During the construction of Connecting gallery, a consistent fracturing pattern was observed in the EDZ, along most of the excavation<sup>6</sup> [Bastiaens et al., 2003], as it is shown schematically

<sup>6</sup>Except in the first and last few meters of the gallery due the impact of the earlier constructions of second

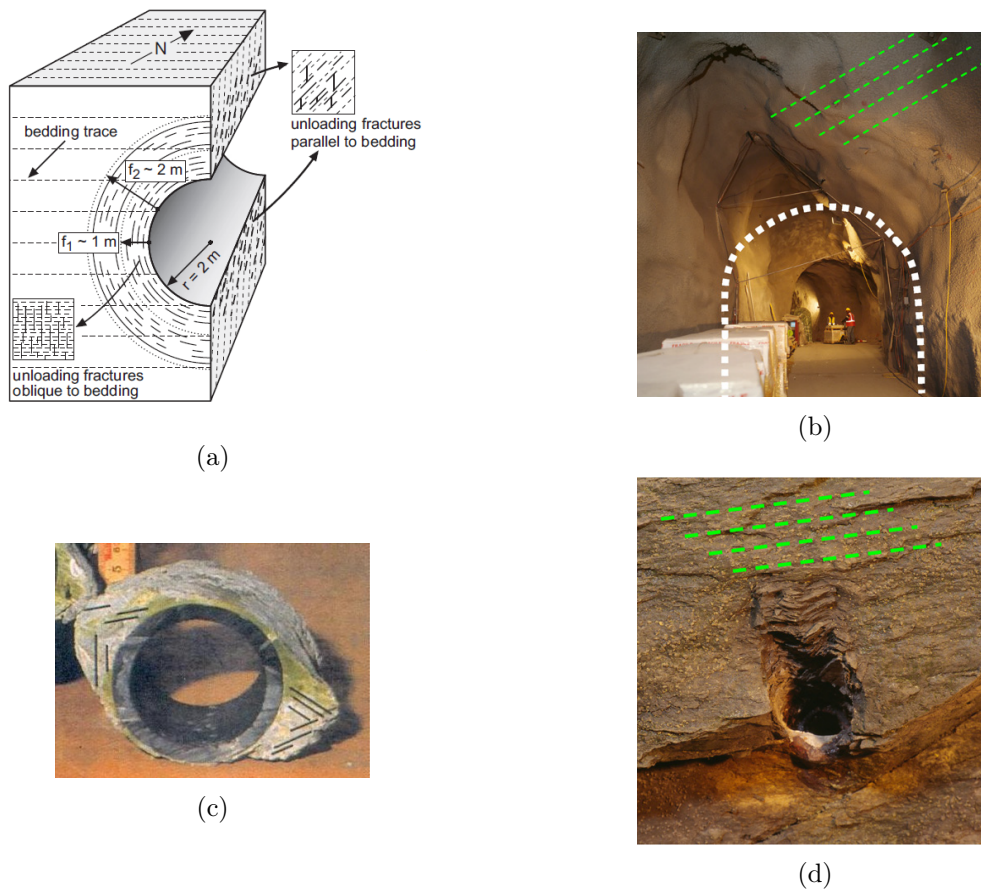


Figure 5.19: (a) Schematic representation of fracturing pattern, observed at Mont Terri (Switzerland), in the damaged zone around a gallery excavated in OPA, normal to bedding strike. (b) EDZ induced by bedding (the green lines denote the bedding orientation) around a formerly horseshoe tunnel (denoted by white dashed line) in OPA. (c) Combined shear-extensional fractures around a borehole in OPA. (d) Fracturing in the damaged zone induced by bedding at the top of a borehole in OPA [Blümling et al., 2007].

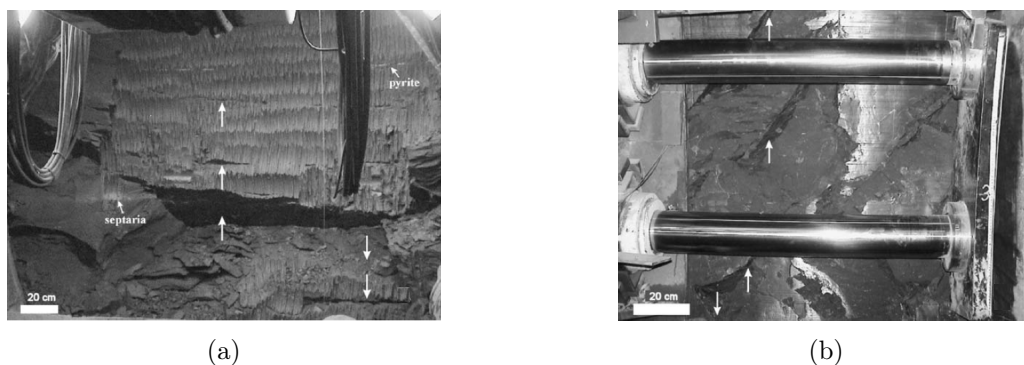


Figure 5.20: Fractures observed during the construction of Connecting gallery. (a) In the gallery front while the cross-section of the parallel shear planes can be observed. (b) On the sidewalls [Mertens et al., 2004].



Figure 5.21: Fractures observed in the excavation front of Praclay gallery. (a) 0.5 m from the Connecting gallery. (b) 4 m from the Connecting gallery [Van Marcke and Bastiaens, 2010].

in Figure 5.22. As it has been previously mentioned in Chapter 2, no pre-existing fractures and discontinuities were evidenced in the clay formation through the site observations in HADES URL, and the excavation induced fractures that have been mainly observed during the excavation process were the shear planes [Bastiaens et al., 2003; Mertens et al., 2004].

The observed pattern consists of two main conjugated localized shear planes [Bastiaens et al., 2003]: one in the upper part which is dipped towards the excavation direction, and the other one in the lower part dipping towards the opposite direction. These fracture planes intersect at the mid-height of the gallery. In addition, they are also curved at their intersection with the vertical and horizontal planes passing through the gallery axis, although this curve was found to be more accentuated vertically than horizontally (because of the anisotropic stresses in the clay: vertical stress is higher than horizontal one). In addition, Figure 5.23 exhibits the fractures observed in the clay core obtained from a borehole drilled out of the gallery, as shown in Figure 5.22. Moreover, taking into account that the lining of the gallery was done almost simultaneously with its excavation, it is observed that the local stress changes (due to excavation process) induced a more accentuated fracturing in the gallery front which has not been secured by the lining (see Figure 5.22).

A similar fractures pattern has been interestingly observed along the last core retrieved from the borehole 2001-2<sup>7</sup> drilled close to the second shaft (see Figure 2.3), as illustrated in Figure 5.24.

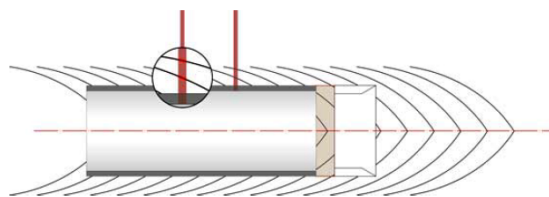


Figure 5.22: Schematic representation of fracturing pattern observed along a vertical cross-section parallel to the Connecting gallery axis [Bastiaens et al., 2003].

Therefore, the simulation of shear induced fracturing pattern, development of strain localization in shear planes, and extension of the EDZ around the large scale's excavation remain such essential issues. These key issues in the framework of long-term safety of deep disposal of high-level nuclear waste, particularly in Boom Clay formation, are then being the foundation of

shaft and Test Drift, respectively.

<sup>7</sup>This borehole is part of the auscultation program; see [Bastiaens et al., 2003] for further information about this program.



Figure 5.23: Fractures observed in the clay core taken from a borehole drilled out of the gallery, as shown in Figure 5.22 [Bastiaens et al., 2003].



Figure 5.24: Fracturing pattern in a core taken from the borehole 2001-2 [Bastiaens et al., 2003].

this work. Thence, the numerical framework applied for treating these phenomena is explained in the following.

## 5.3 Local second gradient model

### 5.3.1 Computational modeling of strain localization

The numerical analysis of strain localization and fracturing process can be generally performed based on two different approaches: within the theory of continuum mechanics (as it has been being done in this thesis), or considering the discontinuous medium. The models in the latter category (e.g. [Armero and Garikipati, 1996; Larsson et al., 1999; Wells, 2001; Callari et al., 2010]) treat the strain localization accounting for the development of jumps in displacement field of a body (see Figure 5.25). In the physical term, this signifies the development of failure surfaces within a body [Wells, 2001]. On the other hand, there is another common modeling approach which is used in this work, that treats the strain localization taking into account a continuous displacement field (e.g. applied in [Leroy and Ortiz, 1989; Chambon et al., 2001a; Collin et al., 2006; Salehnia et al., 2013a, 2015b; Pardoen et al., 2015]). In this case, a jump in strain rate occurs (see Figure 5.25). In the physical point of view, for very brittle material like glass, the displacement jump (i.e. discrete crack) occurs almost spontaneously with reaching to the material's yield strength, and very ductile material exhibits displacement jump just at the last phase of failure (i.e. after the peak stress and prior to the ultimate collapse), according to Wells [2001]. However, the latter study indicated that many engineering materials such as polymers, some metals, concrete, and rocks (thence, Boom Clay) are considered as the *quasi*-brittle materials in the sense that for their response in proximity of the stress-peak (phase iv and partially phase v in Figure 5.4), i.e. development of micro-cracks and connection of fractures in the localized mode, the continuum models can be suitable. Indeed, these responses could be considered as the degradation of continuum, i.e. strain softening. The development of displacement jump may just be critical at the last stage before the catastrophic failure occurs. Therefore, analysis of strain localization assuming the discontinuities in strain rate (i.e. development of shearing band with

finite thickness) seems very useful as the preceding mechanism helping to better understand the failure process.

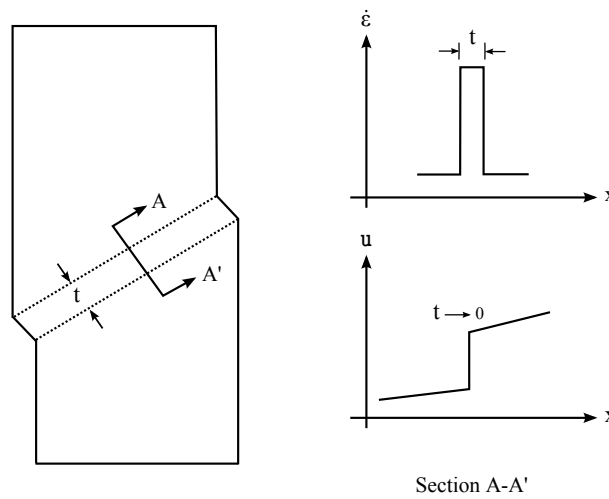


Figure 5.25: Conceptual presentation of two approaches for numerical treatment of the deformation band with thickness  $t$ : jump in strain rate  $\dot{\epsilon}$  considering a finite thickness of  $t > 0$ , and jump in displacement field  $\mathbf{u}$  while  $t \rightarrow 0$ ; after [Wells, 2001; Borja, 2013].

Furthermore, in the fields and in the laboratory tests, the localized shear bands are commonly observed as a phenomenon leading up to failure in geomaterials [Desrues, 1998; Bésuelle et al., 2000; Desrues and Viggiani, 2004; Lenoir et al., 2007; Bésuelle et al., 2014]. In the large-scale point of view, during the construction of Connecting gallery in Boom Clay host rock, the shear induced fractures were observed [Bastiaens et al., 2003; Mertens et al., 2004]. This type of fracturing, or discontinuities as often called, are indeed frequently preceded by development of the localization of strains in narrow so-called shear bands. Therefore, in a progressive failure, these shear zones with localized plastic strain are realistically giving rise to the discontinuities, the rupture zones. Hence, to better understand the mechanisms leading to this fractures' network, we propose to analyze their development around the underground galleries, during the construction phase and afterwards, by numerical modeling, in the framework of a strain localization approach in shear band mode (i.e. considering the jumps in strain rate). As a consequence, the shear bands with finite thickness are modeled, within the theory of continuum mechanics, to simulate the probable surface of the localized failure and discontinuities.

#### **Bifurcation condition:**

Following an introductory explanation given in Section 5.2.1, the bifurcation theory is defined based on the primary works of Rudnicki and Rice [1975]; Rice [1976] resulted in the so-called Rice criterion in which the system has been supposed to be infinite and initially homogeneous. This bifurcation theory seeks conditions that an homogeneous system may going to evolve naturally, for the next loading increment, towards another alternative solution - than an additional homogeneous deformation - corresponding to localized deformation in a planar band (i.e. a non-uniform state). In this case, the onset of localization is connected [Besuelle and Rudnicki, 2003] to this loss of uniqueness of the solution. Figure 5.26 represents this solution alternation in which the superscript <sup>0</sup> indicates the variables outside of the shear band, and <sup>1</sup> denotes the variables inside the band. Seeking an alternative deformation solution in the localized mode in Rice criterion is based on three conditions. These conditions are summarized in the following; more details can be found in [Rudnicki and Rice, 1975; Rice, 1976; Besuelle and Rudnicki, 2003].

The kinematic condition for having a non-homogeneous solution in shear band mode (with

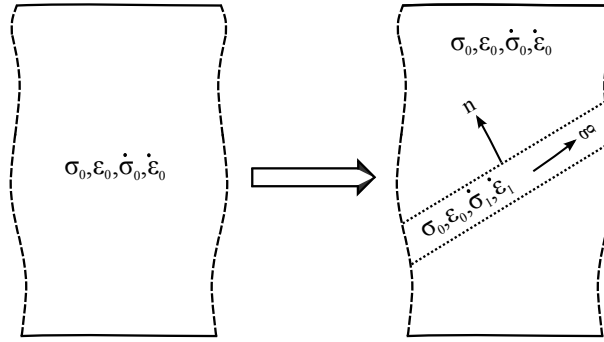


Figure 5.26: Theoretical representation of bifurcation in the localized shear band.

normal vector of  $\mathbf{n}$ ) is expressed by Equation 5.1 if the velocity field remains continuous at the instant of band formation [Rice, 1976]. Thence, the strain jump across the band interface is the superposition of the shear strain jump and the relative volumetric component (i.e. dilatant strain jump).

$$\dot{\epsilon}_{ij}^1 = \dot{\epsilon}_{ij}^0 + \frac{1}{2} (g_i n_j + g_j n_i) \quad (5.1)$$

where  $\dot{\epsilon}_{ij}^1 = \text{sym}(\partial v_i / \partial x_j)$  (see Equation 3.7) is the rate of deformation - which it is recalled that it might be sometimes called by  $D_{ij}$  in the literature in the case of dealing with the large deformations - as described in Section 3.2.1.  $g = g(x_i n_i)$  is an arbitrary vector described with respect to the direction and intensity of the position transverses the band.

Since the stress rate is assumed to be uniform inside the band in addition to outside the band, the second condition imposes the surface equilibrium at the interface of the band, such that:

$$\dot{\sigma}_{ij}^1 n_j = \dot{\sigma}_{ij}^0 n_j \quad (5.2)$$

The third condition is the constitutive law to relate the rate of stress to the rate of strain. Assuming a constitutive tensor which is continuous across the band, and the material state that is uniform at the bifurcation instant (not necessarily afterwards) inside and outside of the band, we have:

$$\tilde{\sigma}'_{ij} = \mathbb{C}_{ijkl} \dot{\epsilon}_{kl} \quad (5.3)$$

where  $\mathbb{C}_{ijkl}$  is the constitutive tangent tensor. The Jaumann derivative of stress is once again used rather than  $\dot{\sigma}_{ij}$  to be invariant to the rigid spin in the domain of large rotations and deformations [Rice and Rudnicki, 1980].

Next, introducing Equation 5.3 into the Equations 5.1 and 5.2 gives the bifurcation condition as:

$$\mathbb{C}_{ijkl} \left( \dot{\epsilon}_{kl}^0 + \frac{1}{2} (g_k n_l + g_l n_k) \right) n_j = \mathbb{C}_{ijkl} (\dot{\epsilon}_{kl}^0) n_j \quad (5.4)$$

The trivial solution of this condition lays on  $g = 0$  which signifies no shear band creation, i.e. continued homogeneous deformation. Non trivial solution needs  $g \neq 0$  and a unit vector  $n$  which satisfies the condition 5.4, and they are met if:

$$\det [\mathbb{C}_{ijkl} n_j n_l] = 0 \quad \text{or} \quad \det [\mathbf{n} \cdot \mathbb{C} \cdot \mathbf{n}] = 0 \quad (5.5)$$

Thence, the null determinant of the so-called acoustic tensor  $\mathbf{n} \cdot \mathbb{C} \cdot \mathbf{n}$  can satisfy the condition of localization, and it corresponds to the loss of ellipticity condition. This criterion can remain

valid in the local level of a finite body. Moreover, it must be kept in mind that this criterion depends clearly on the constitutive relations; this issue has been more detailed in [Besuelle and Rudnicki, 2003; Lemaitre et al., 2009].

Furthermore, with regard to the experimental observations, the constitutive response across the shear band can be commonly discontinuous, i.e. the so-called discontinuous bifurcation [Rice and Rudnicki, 1980]. In this sense, an elastic unloading occurs outside of the shear band while the deformation localizes inside the band with a continued elastic-plastic loading. Thence, the constitutive tensors outside and inside the band are different, i.e.  $\mathbb{C}_{ijkl}^0 \neq \mathbb{C}_{ijkl}^1$  while each of  $\mathbb{C}_{ijkl}^0$  and  $\mathbb{C}_{ijkl}^1$  ( $=\mathbb{C}_{ijkl}$ ) can be respectively equal to  $\mathbb{C}_{ijkl}^e$  and  $\mathbb{C}_{ijkl}^{ep}$  [Besuelle and Rudnicki, 2003]. Therefore, Equation 5.4 yields:

$$\mathbb{C}_{ijkl}^1 n_j n_l g_k = (\mathbb{C}_{ijkl}^0 - \mathbb{C}_{ijkl}^1) \dot{\varepsilon}_{kl}^0 n_j \quad (5.6)$$

Rice and Rudnicki [1980] have shown that the former case (so-called continuous bifurcation) provides the lower limit to the range of deformation for which the discontinuous bifurcation can occur, if the elasto-plastic constitutive law admits a single yield surface and potential surface. That is to say that the discontinuous bifurcation is preceded by the continuous bifurcation. Consequently, the condition 5.5 is only needed to be analyzed providing the necessary condition for bifurcation which correspond to the *first* occurrence of non homogeneous deformation. However, it may not be the sufficient condition for appearance of shear bands. Then, a necessary and sufficient condition for localization of deformation in a shear band can be desirably concluded by [Lemaitre et al., 2009]:

$$\det [\mathbf{n} \cdot \mathbb{C} \cdot \mathbf{n}] \leq 0 \quad (5.7)$$

where there exist a range of possible orientations for the band rather than one predicted orientation.

Moreover, it may be noteworthy that in a particular case of constitutive model, the sign of the determinant 5.5 may be suddenly changed from positive to negative without passing through zero. The bifurcation condition for this case then must be verified by Equation 5.7 (see [Besuelle and Rudnicki, 2003] for more details).

#### The need of a regularization method:

All things considered, the strain localization phenomenon is understood as the appearance of a discontinuity in strain rate (localized shear bands), which can be perceived by the loss of solution uniqueness. This non-uniformity of the responses and the satisfactions of the bifurcation conditions can be caused by some material's behavior characteristics among which the material softening is a principal mechanism [Lemaitre et al., 2009], that can be accounted in the simplest way through a strain-softening constitutive law. Material softening can be considered as the macroscopic reflection of inhomogeneities at the microscopic scale (micro-cracks, fractures, etc.). Indeed, by accumulation of inelastic strain, the load carrying capacity of the material decreases, as stated by Wells [2001]. Thence, the continuum models for failure analysis are generally based on the strain softening, and the the strain localization response could be considered as the degradation of continuum, i.e. strain softening.

However, the governing equations of the classical continuum predicts that the strains will localize within a band of zero width, upon softening [Wells, 2001]. In fact, there is not any intrinsic material length scale, and consequently, it leads to a mathematically ill-posed boundary value problem in the post-bifurcation (post-localization) regime. Thence, the numerical analysis in the framework of classical finite element modeling suffers from a pathological problem of mesh dependency. There is no material length and the discretization sets the length scale. Therefore, the localization zone (the bands thickness) which is associated to the strain softening depends

on the size of the mesh used for spatial discretization. Then, the discontinuities in strain rate at the boundaries of the elements allows strain to localize in finite volume depending on the mesh discretization [Wells, 2001; Sulem, 2010]. Hence, a specific approach introducing a length scale is needed to overcome this problem in order to properly model the localization phenomenon and post-localization behavior. In this sense, the length scale controls the thickness of the localized band.

Different enhanced approaches can be found in the literature for regularization of this problem. One family refers to the models with the non-local continua [Pijaudier-Cabot and Bazant, 1987; Tvergaard and Needleman, 1995]. They are based on the fact that the response of the material at a point is determined not only by the state at that point but also from the deformation of its neighborhood. The latter can be attained through an integral equation over a domain that by the extent of the integral domain, the material length is defined. Thence, the microstructures effect are not directly considered in the formulation. Furthermore, the family of second grade models are often used since the pioneering work of Aifantis [1984] which introduced gradient of internal variables. Gradient plasticity/elasto-plasticity theories [Mühlhaus and Aifantis, 1991; Vardoulakis and Aifantis, 1991; De Borst and Mühlhaus, 1992; Pamin, 1994; Zervos et al., 2001a] have been developed either by considering the yield function to be dependent directly on the Laplacian of the plastic strain, or introduction of second gradient of plastic strain into the plasticity flow rule. With regard to the importance of microstructures effects in most of the enhanced models, next Section focuses more particularly on a last class of enriched models which comes from the continua with microstructures which is also the case of the regularization method applied in this work.

### 5.3.2 Continua with microstructures

The classical continuum mechanics deals with the problem in the macroscopic scale, although, reproducing the material behavior upon localization, in the physical point of view, leads to the non-ignorable phenomena at the scale of the grains (microscopic scale). In fact, to model the proper macroscopic behavior of the material (generally a geomaterial), looking at the problem in microscopic scale and analysis of the micromechanical phenomena are indispensable. Hence, the onset the localized bands could be described identifying the zones with accumulated plastic deformation, due to the movement of the grains and the deformation at the microscopic scale. In addition, upon the onset of the bands, to correctly model the evolution of the bands and the material response in the post-localization regime, the behavior of the material inside the bands is important. Therefore, it seems that the classical continuum models require to be adopted with regard to the microstructures. Moreover, in the numerical point of view, it has been already declared at the end of last Section that a regularization method must be incorporated into a classical continuum models to adjust the problem of mesh dependency. This could be also achieved by employing the theory of continua with microstructures. This theory generally consists in adding an additional cinematic description of the microstructures into the classical continuum model through which the material internal length is introduced.

The continua with microstructures (or, generalized continua) could refer to the higher grade continuum with the higher deformation gradients, or the Cosserat continuum with the additional kinematical degrees of freedom. The latter is the most ancient extended continuum which is tracked back to the work of the brothers Cosserat and Cosserat [1909]. The Cosserat or micropolar continuum consists in a continuum with three additional rotational degrees of freedom besides the usual translational degrees of freedom, for the oriented rigid particles. In a polar continuum, the stress tensor is not necessarily symmetric. The length scale parameter is incor-

porated in this theory by prediction of a size effect, which lays on a relatively stiffer response of a smaller sample of a material compared to a larger sample. This theory was later used in several numerical studies, e.g. [Mindlin, 1963; De Borst and Sluys, 1991] and [Mühlhaus and Vardoulakis, 1987; Vardoulakis, 1989] (applications to geomaterials). However, with reference to the study of Kunin [1982], the utilization of the Cosserat theory remains debatable. There is not any compelling verification for the use of micropolar continuum since the last several decades that it has been applied. One problem of this theory is regarding the prescription of boundary conditions for the microrotations [Papamichos, 2010].

The higher grade continuum theory is not considered to be, generally, preferable to the Cosserat theory, though. In fact, the regularization method must be chosen based on the physics of a problem in addition to consideration of the capabilities of a model. Thence, besides the aforementioned questionable elements of the Cosserat theory, it must be noted that the Cosserat continuum is more suitable for the granular medium where the rotation of the grains are the most important inelastic deformation mode. However, a comparison of the shortcomings and advantages of each class of the enhanced models is out of scope of this work.

In this thesis, the prediction of our material response by the strain softening constitutive law is then regularized in the framework of microstructure continuum theory, using a higher (second) gradient continua. Fundamentally, the theory of second gradient is based on the framework proposed by Toupin [1962]; Mindlin [1964] within the scheme of the second gradient elasticity. A few years later, their work was more generalized by Germain [1973b] through the use of the principle of virtual power. Since then, this theory has been the basis of many numerical works; e.g. [Chambon et al., 1998; Zervos et al., 2001b; Matsushima et al., 2002]. In the second gradient theory, the material response at each point is not only dependent on the first gradient of strain, but also on the second gradient of strain. The *local*<sup>8</sup> *second gradient method* is used in this work based on the model developed by Chambon et al. [1998, 2001a]. The numerical framework of this model is described in the following Section.

### 5.3.3 Framework of the coupled local second gradient model for microstructured continuum

Considering an enriched kinematic description of the continuum - the kinematics includes macrokinematics as well as microkinematics - a microkinematic gradient field  $v_{ij}$  is defined to describe strain and rotation of the grains at the microscale. Hence, with reference to the classical continuum mechanics, additional terms are then added in the internal virtual work of a given body. In fact, in the classical first grade models, the gradient of virtual displacement ( $F_{ij}^* = \partial u_i^* / \partial x_j$ ) is used to establish the internal virtual work. However, in the second grade model, the internal virtual work is a linear form of the virtual displacement gradient (or, virtual macrodeformation gradient) as well as virtual microkinematic gradient  $v_{ij}^*$ , and the virtual (micro) second gradient  $h_{ijk}^* = (\partial v_{ij}^* / \partial x_k)$ . Thence, with respect to Equation 3.37 within the classical numerical framework presented in Section 3.2, an extension of the internal virtual work expression is given as:

$$\mathcal{W}_I^* = \int_{\Omega} \left( \sigma_{ij} \frac{\partial u_i^*}{\partial x_j} + \tau_{ij} (v_{ij}^* - F_{ij}^*) + \Sigma_{ijk} h_{ijk}^* \right) d\Omega \quad (5.8)$$

where  $\tau_{ij}$  is the microstress tensor which is defined here in addition to the classical macrostress  $\sigma_{ij}$  and it is associated to the microstructures, and  $\Sigma_{ijk}$  is the double stress, dual of the virtual (micro) second gradient  $h_{ijk}^*$ . Double stress needs an additional constitutive law and it is defined

<sup>8</sup>The term local consists in the constitutive equations which remain local. One advantage of this issue is that it will be straightforward to formulate a second gradient extension of any classical models.

within an elastic law [Mindlin, 1964] as a function of (micro) second gradient of the virtual displacement.

On the other hand, assuming that a double surface force  $\bar{T}_{ij}$  is acting on the boundary  $\Gamma_\sigma$ , in addition to the (classical) external traction force  $\bar{t}_i$ , the external virtual work expression (with respect to the classical form in Equation 3.37) can be defined as follows:

$$\mathcal{W}_E^* = \int_{\Omega} \rho_m g_i u_i^* d\Omega + \int_{\Gamma_\sigma} (\bar{t}_i u_i^* + \bar{T}_{ij} v_{ij}^*) d\Gamma \quad (5.9)$$

Therefore, similarly to the first grade framework, taking into account a simple representation of the boundary surface as displayed in Figure 3.4 such that the relation 3.12 is satisfied, the strong form of the initial boundary-value problem for an elementary volume  $\Omega$  is extended (with respect to the classical Equations 3.13-3.15) through the following balance equations and boundary conditions:

$$\frac{\partial(\sigma_{ij} - \tau_{ij})}{\partial x_j} + G_i = 0 \quad \text{in } \Omega \quad (5.10)$$

$$\frac{\partial \Sigma_{ijk}}{\partial x_k} - \tau_{ij} = 0 \quad \text{in } \Omega \quad (5.11)$$

and,

$$u_i = d_i \quad \text{on } \Gamma_u \quad (5.12)$$

$$v_{ij} = \mathbf{v}_{ij} \quad \text{on } \Gamma_u \quad (5.13)$$

$$(\sigma_{ij} - \tau_{ij}) n_j = \bar{t}_i \quad \text{on } \Gamma_\sigma \quad (5.14)$$

$$\Sigma_{ijk} n_k = \bar{T}_{ij} \quad \text{on } \Gamma_\sigma \quad (5.15)$$

Furthermore, in the local second gradient model used in this work [Chambon et al., 1998, 2001a], it is assumed that microkinematic gradient is equal to the macrodeformation gradient, i.e.  $v_{ij} = F_{ij} = \partial u_i / \partial x_j$ . As a result, the virtual microkinematic gradient is also equal to the virtual macrodeformation gradient ( $v_{ij}^* = F_{ij}^* = \partial u_i^* / \partial x_j$ ). Consequently, the principle of virtual work in the weak form, with regard to Equations 5.8-5.9 is rewritten as:

$$\int_{\Omega} \left( \sigma_{ij} \frac{\partial u_i^*}{\partial x_j} + \Sigma_{ijk} \frac{\partial^2 u_i^*}{\partial x_j \partial x_k} \right) d\Omega = \int_{\Omega} \rho_m g_i u_i^* d\Omega + \int_{\Gamma_\sigma} (\bar{t}_i u_i^* + \bar{T}_i Du_i^*) d\Gamma \quad (5.16)$$

where  $Du_i^*$  is the normal derivative of  $u_i^*$ , i.e.  $Du_i^* = (\partial u_i^* / \partial x_k) n_k$ .  $\bar{t}_i$  and  $\bar{T}_i$  can be chosen independently [Chambon et al., 2001a].

Following the above assumption, the second derivative of the virtual displacement field is involved in the formulation. Hence, with regard to the  $C^{m-1}$  functions within a finite element approach to treat the problem, where  $m$  is defined here as the highest order of derivation appeared in the virtual work relation, the use of  $C^1$  function is then necessary. To avoid this procedure and its subsequent numerical difficulties, the assumptions  $v_{ij} = F_{ij}$  and  $v_{ij}^* = F_{ij}^*$  are introduced through a field of Lagrange multipliers  $\lambda_{ij}$  [Chambon et al., 1998]. Thence, Equation 5.16 reads:

$$\int_{\Omega} \left( \sigma_{ij} \frac{\partial u_i^*}{\partial x_j} + \Sigma_{ijk} \frac{\partial v_{ij}^*}{\partial x_k} \right) d\Omega - \int_{\Omega} \lambda_{ij} \left( \frac{\partial u_i^*}{\partial x_j} - v_{ij}^* \right) d\Omega = \int_{\Omega} \rho_m g_i u_i^* d\Omega + \int_{\Gamma_\sigma} (\bar{t}_i u_i^* + \bar{T}_i v_{ik}^* n_k) d\Gamma \quad (5.17)$$

$$\int_{\Omega} \lambda_{ij}^* \left( \frac{\partial u_i}{\partial x_j} - v_{ij} \right) d\Omega = 0 \quad (5.18)$$

Moreover, within the framework of our coupled analysis, the above local second gradient formulation is accomplished giving the mass balance expression for the fluid (water) phase as Equation 5.19. In this extension, it has been assumed that the fluid has no influence at the microstructure level, and the double stress  $\Sigma_{ijk}$  has then no link with the pore water pressure [Collin et al., 2006]; thence, the mass balance relation is remained similar to the former Equation 3.46.

$$\int_{\Omega} \left( \dot{S}p_w^* - m_i \frac{\partial p_w^*}{\partial x_i} \right) d\Omega = \int_{\Omega} Qp_w^* d\Omega - \int_{\Gamma_q} \bar{q}p_w^* d\Gamma \quad (5.19)$$

Equations 5.17-5.19 must be met for every kinematically admissible virtual displacement field  $u_i^*$ , virtual microkinematic gradient field  $v_{ij}^*$ , virtual pore water pressure field  $p_w^*$ , and every virtual field  $\lambda_{ij}^*$ . Moreover, it must be noted that these equations are held for any time  $t$ ; the virtual quantities in these equations are dependent on the history of boundary conditions and then on the time  $t$ . This time  $t$ , with regard to the description given in Section 3.2.6, belongs to discretized sequential times  $0, \Delta t, 2\Delta t, 3\Delta t, \text{etc.}$ , while a fully implicit scheme is considered in each time step. The time step problem is then solved on the basis of a full Newton-Raphson method.

#### Iterative procedure:

Following a known solution at time  $t$ , let us assume that an approximation to the solution at the time  $t + \Delta t$  is initially (i.e. at the first iteration of the current time step) guessed. This solution corresponds to the so-called  $\Omega^{(t+\Delta t)_i}$  configuration for which the equilibrium is not yet met. Thence, according to aforementioned set of equations, the following residuals could be found:

$$\begin{aligned} & \int_{\Omega^{(t+\Delta t)_i}} \left( \sigma_{ij}^{(t+\Delta t)_i} \frac{\partial u_i^*}{\partial x_j^{(t+\Delta t)_i}} + \Sigma_{ijk}^{(t+\Delta t)_i} \frac{\partial v_{ij}^*}{\partial x_k^{(t+\Delta t)_i}} \right) d\Omega^{(t+\Delta t)_i} \\ & - \int_{\Omega^{(t+\Delta t)_i}} \lambda_{ij}^{(t+\Delta t)_i} \left( \frac{\partial u_i^*}{\partial x_j^{(t+\Delta t)_i}} - v_{ij}^* \right) d\Omega^{(t+\Delta t)_i} - \int_{\Omega^{(t+\Delta t)_i}} \rho_m^{(t+\Delta t)_i} g_i u_i^* d\Omega^{(t+\Delta t)_i} \\ & - \int_{\Gamma_{\sigma}^{(t+\Delta t)_i}} \left( \bar{t}_i u_i^* + \bar{T}_i v_{ik}^* n_k^{(t+\Delta t)_i} \right) d\Gamma^{(t+\Delta t)_i} = \mathfrak{R}_1^{(t+\Delta t)_i} \end{aligned} \quad (5.20)$$

$$\int_{\Omega^{(t+\Delta t)_i}} \lambda_{ij}^* \left( \frac{\partial u_i}{\partial x_j^{(t+\Delta t)_i}} - v_{ij}^{(t+\Delta t)_i} \right) d\Omega^{(t+\Delta t)_i} = \mathfrak{R}_2^{(t+\Delta t)_i} \quad (5.21)$$

$$\begin{aligned} & \int_{\Omega^{(t+\Delta t)_i}} \left( \dot{S}^{(t+\Delta t)_i} p_w^* - m_i^{(t+\Delta t)_i} \frac{\partial p_w^*}{\partial x_i^{(t+\Delta t)_i}} \right) d\Omega^{(t+\Delta t)_i} - \int_{\Omega^{(t+\Delta t)_i}} Q^{(t+\Delta t)_i} p_w^* d\Omega^{(t+\Delta t)_i} \\ & + \int_{\Gamma_q^{(t+\Delta t)_i}} \bar{q}^{(t+\Delta t)_i} p_w^* d\Gamma^{(t+\Delta t)_i} = \mathfrak{R}_3^{(t+\Delta t)_i} \end{aligned} \quad (5.22)$$

It is recalled that  $\rho_m$  is being the mixture apparent specific mass which reads  $((1 - n^{(t+\Delta t)_i})\rho_s + n^{(t+\Delta t)_i}\rho_w^{(t+\Delta t)_i})$  within Equation 5.20. Hence, we are aimed to find a better (unknown) approximation  $\Omega^{(t+\Delta t)_{i+1}}$ , close to  $\Omega^{(t+\Delta t)_i}$  for which the above residuals vanish. To get the linear auxiliary problem, the field equations corresponding to configuration  $\Omega^{(t+\Delta t)_{i+1}}$  are written in configuration  $\Omega^{(t+\Delta t)_i}$ , and they are then subtracted from the ones corresponding to  $\Omega^{(t+\Delta t)_i}$

(i.e. Equations 5.20-5.22); which reads:

$$\begin{aligned} & \int_{\Omega^{(t+\Delta t)_i}} \frac{\partial u_i^*}{\partial x_l^{(t+\Delta t)_i}} \left( \sigma_{ij}^{(t+\Delta t)_{i+1}} \frac{\partial x_l^{(t+\Delta t)_i}}{\partial x_j^{(t+\Delta t)_{i+1}}} \det \mathbf{F} - \sigma_{il}^{(t+\Delta t)_i} \right) \\ & + \frac{\partial v_{ij}^*}{\partial x_l^{(t+\Delta t)_i}} \left( \Sigma_{ijk}^{(t+\Delta t)_{i+1}} \frac{\partial x_l^{(t+\Delta t)_i}}{\partial x_k^{(t+\Delta t)_{i+1}}} \det \mathbf{F} - \Sigma_{ijl}^{(t+\Delta t)_i} \right) d\Omega^{(t+\Delta t)_i} \\ & - \int_{\Omega^{(t+\Delta t)_i}} \frac{\partial u_i^*}{\partial x_l^{(t+\Delta t)_i}} \left( \lambda_{ij}^{(t+\Delta t)_{i+1}} \frac{\partial x_l^{(t+\Delta t)_i}}{\partial x_j^{(t+\Delta t)_{i+1}}} \det \mathbf{F} - \lambda_{il}^{(t+\Delta t)_i} \right) \end{aligned} \quad (5.23)$$

$$\begin{aligned} & + v_{ij}^* \left( \lambda_{ij}^{(t+\Delta t)_{i+1}} \det \mathbf{F} - \lambda_{ij}^{(t+\Delta t)_i} \right) d\Omega^{(t+\Delta t)_i} \\ & - \int_{\Omega^{(t+\Delta t)_i}} u_i^* \left( \rho_m^{(t+\Delta t)_{i+1}} \det \mathbf{F} - \rho_m^{(t+\Delta t)_i} \right) g_i d\Omega^{(t+\Delta t)_i} = -\mathfrak{R}_1^{(t+\Delta t)_i} \end{aligned}$$

$$\begin{aligned} & \int_{\Omega^{(t+\Delta t)_i}} \lambda_{ij}^* \left[ \left( \frac{\partial u_i^{(t+\Delta t)_{i+1}}}{\partial x_k^{(t+\Delta t)_i}} \frac{\partial x_k^{(t+\Delta t)_i}}{\partial x_j^{(t+\Delta t)_{i+1}}} \det \mathbf{F} - \frac{\partial u_i^{(t+\Delta t)_i}}{\partial x_j^{(t+\Delta t)_i}} \right) - \left( v_{ij}^{(t+\Delta t)_{i+1}} \det \mathbf{F} - v_{ij}^{(t+\Delta t)_i} \right) \right] d\Omega^{(t+\Delta t)_i} \\ & = -\mathfrak{R}_2^{(t+\Delta t)_i} \end{aligned} \quad (5.24)$$

$$\begin{aligned} & \int_{\Omega^{(t+\Delta t)_i}} \left( \dot{S}^{(t+\Delta t)_{i+1}} \det \mathbf{F} - \dot{S}^{(t+\Delta t)_i} \right) p_w^* - \\ & \frac{\partial p_w^*}{\partial x_l^{(t+\Delta t)_i}} \left( m_i^{(t+\Delta t)_{i+1}} \frac{\partial x_l^{(t+\Delta t)_i}}{\partial x_i^{(t+\Delta t)_{i+1}}} \det \mathbf{F} - m_i^{(t+\Delta t)_i} \right) d\Omega^{(t+\Delta t)_i} = -\mathfrak{R}_3^{(t+\Delta t)_i} \end{aligned} \quad (5.25)$$

where  $\det \mathbf{F}$  is the Jacobian of transformation matrix,  $F_{ij} = \partial x_i^{(t+\Delta t)_{i+1}} / \partial x_j^{(t+\Delta t)_i}$  using which, we have  $d\Omega^{(t+\Delta t)_{i+1}} = \det \mathbf{F} d\Omega^{(t+\Delta t)_i}$ . In addition, it is assumed that double force  $\bar{T}_i$  vanishes, and  $g_i$ ,  $\bar{t}_i$ ,  $\bar{q}$  and  $Q$  are position independent.

Next, let us denote the variations between two configuration as the following:

$$du_i^{(t+\Delta t)_i} = x_i^{(t+\Delta t)_{i+1}} - x_i^{(t+\Delta t)_i} \quad (5.26)$$

$$dv_{ij}^{(t+\Delta t)_i} = v_{ij}^{(t+\Delta t)_{i+1}} - v_{ij}^{(t+\Delta t)_i} \quad (5.27)$$

$$d\sigma_{ij}^{(t+\Delta t)_i} = \sigma_{ij}^{(t+\Delta t)_{i+1}} - \sigma_{ij}^{(t+\Delta t)_i} \quad (5.28)$$

$$d\Sigma_{ijk}^{(t+\Delta t)_i} = \Sigma_{ijk}^{(t+\Delta t)_{i+1}} - \Sigma_{ijk}^{(t+\Delta t)_i} \quad (5.29)$$

$$d\lambda_{ij}^{(t+\Delta t)_i} = \lambda_{ij}^{(t+\Delta t)_{i+1}} - \lambda_{ij}^{(t+\Delta t)_i} \quad (5.30)$$

$$dp_w^{(t+\Delta t)_i} = p_w^{(t+\Delta t)_{i+1}} - p_w^{(t+\Delta t)_i} \quad (5.31)$$

$$dn^{(t+\Delta t)_i} = n^{(t+\Delta t)_{i+1}} - n^{(t+\Delta t)_i} \quad (5.32)$$

$$d\rho_w^{(t+\Delta t)_i} = \rho_w^{(t+\Delta t)_{i+1}} - \rho_w^{(t+\Delta t)_i} \quad (5.33)$$

Then, Equations 5.23-5.25 are developed in a Taylor expansion while the terms with degree greater than one are eliminated. Subsequently to some algebra, the linear equations of the Newton-Raphson iterative procedure could be obtained<sup>9</sup>. Consequently, taking into account the relations given in 5.34-5.37, the whole linearized system of equations can be finally expressed as a function of the (unknown) corrections  $du_i$ ,  $dv_{ij}$ ,  $d\lambda_{ij}$ , and  $dp_w$ , which could be obtained and then added to their relative current values in order to give a better approximation to the current configuration.

$$d\sigma_{ij}^{(t+\Delta t)_i} = d\sigma'_{ij}{}^{(t+\Delta t)_i} - dp_w^{(t+\Delta t)_i} \delta_{ij} = \mathbb{C}_{ijkl}^{(t+\Delta t)_i} \frac{\partial du_k^{(t+\Delta t)_i}}{\partial x_i^{(t+\Delta t)_i}} - dp_w^{(t+\Delta t)_i} \delta_{ij} \quad (5.34)$$

$$d\Sigma_{ijk}^{(t+\Delta t)_i} = \mathbb{D}_{ijklmnn}^{(t+\Delta t)_i} \frac{\partial dv_{lm}^{(t+\Delta t)_i}}{\partial x_n^{(t+\Delta t)_i}} \quad (5.35)$$

$$dn^{(t+\Delta t)_i} = \left(1 - n^{(t+\Delta t)_i}\right) \frac{d\Omega^{(t+\Delta t)_i}}{\Omega^{(t+\Delta t)_i}} = \left(1 - n^{(t+\Delta t)_i}\right) \frac{\partial du_i^{(t+\Delta t)_i}}{\partial x_i^{(t+\Delta t)_i}} \quad (5.36)$$

$$d\rho_w^{(t+\Delta t)_i} = \frac{\rho_w^{(t+\Delta t)_i}}{\chi_w} dp_w^{(t+\Delta t)_i} \quad (5.37)$$

where Equations 5.34-5.35 are obtained through a consistent linearization of the used constitutive law integration algorithm for the first and second gradient parts, respectively [Chambon and Moullet, 2004] while the latter one has been considered as a generalization of the ideas of Simo and Taylor [1985] for the first gradient law (regarding the consistent tangent operators) to the second grade part. In addition, Equations 5.36-5.37 are resulted from the linearization of Equations 3.40 and 3.48.

In the framework of the two-dimensional analyses in this thesis, the explained coupled formulation can be rewritten in the matricial form as given in Equation 5.38, with definition of  $[d\mathbf{u}^{(t+\Delta t)_i}]^T$  by Equation 5.39.

$$\int_{\Omega^{(t+\Delta t)_i}} [\mathbf{u}^\star]^T [\mathbf{E}^{(t+\Delta t)_i}] [d\mathbf{u}^{(t+\Delta t)_i}] d\Omega^{(t+\Delta t)_i} = -\mathfrak{R}_1^{(t+\Delta t)_i} - \mathfrak{R}_2^{(t+\Delta t)_i} - \mathfrak{R}_3^{(t+\Delta t)_i} \quad (5.38)$$

$$\begin{aligned} [d\mathbf{u}^{(t+\Delta t)_i}]^T &\equiv \left[ \frac{\partial du_1^{(t+\Delta t)_i}}{\partial x_1^{(t+\Delta t)_i}} \frac{\partial du_1^{(t+\Delta t)_i}}{\partial x_2^{(t+\Delta t)_i}} \frac{\partial du_2^{(t+\Delta t)_i}}{\partial x_1^{(t+\Delta t)_i}} \frac{\partial du_2^{(t+\Delta t)_i}}{\partial x_2^{(t+\Delta t)_i}} du_1^{(t+\Delta t)_i} du_2^{(t+\Delta t)_i} \right. \\ &\frac{\partial dp_w^{(t+\Delta t)_i}}{\partial x_1^{(t+\Delta t)_i}} \frac{\partial dp_w^{(t+\Delta t)_i}}{\partial x_2^{(t+\Delta t)_i}} dp_w^{(t+\Delta t)_i} \frac{\partial dv_{11}^{(t+\Delta t)_i}}{\partial x_1^{(t+\Delta t)_i}} \frac{\partial dv_{11}^{(t+\Delta t)_i}}{\partial x_2^{(t+\Delta t)_i}} \frac{\partial dv_{12}^{(t+\Delta t)_i}}{\partial x_1^{(t+\Delta t)_i}} \cdots \frac{\partial dv_{22}^{(t+\Delta t)_i}}{\partial x_2^{(t+\Delta t)_i}} \\ &\left. dv_{11}^{(t+\Delta t)_i} dv_{12}^{(t+\Delta t)_i} dv_{21}^{(t+\Delta t)_i} dv_{22}^{(t+\Delta t)_i} d\lambda_{11}^{(t+\Delta t)_i} d\lambda_{12}^{(t+\Delta t)_i} d\lambda_{21}^{(t+\Delta t)_i} d\lambda_{22}^{(t+\Delta t)_i} \right] \end{aligned} \quad (5.39)$$

$[\mathbf{u}^\star]$  is also defined by the similar structure as  $[d\mathbf{u}^{(t+\Delta t)_i}]$ , for the corresponding virtual quantities.

<sup>9</sup>Detailed mathematical procedure is beyond the scope of this thesis; more details can be found in [Chambon and Moullet, 2004; Collin et al., 2006], though.

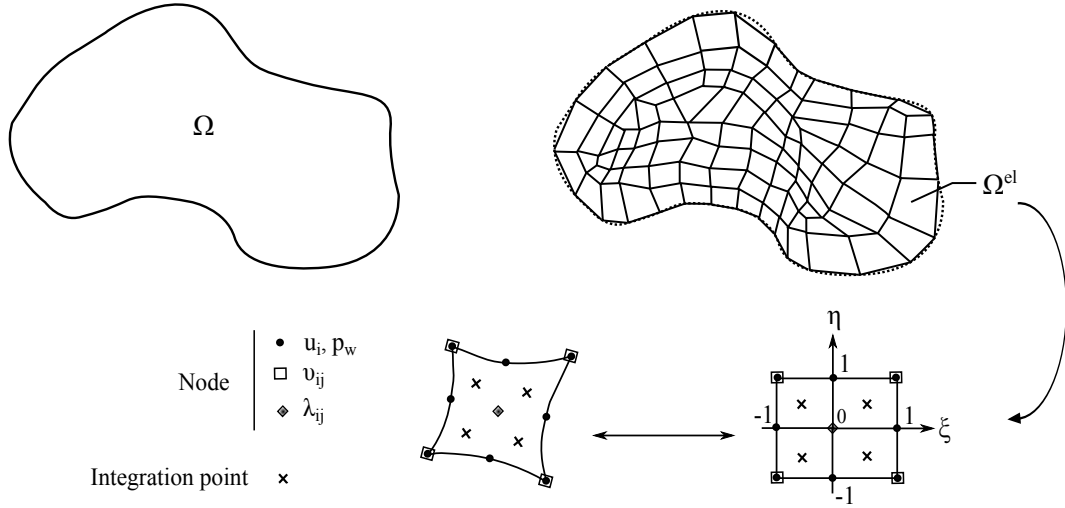


Figure 5.27: Discretization of the domain  $\Omega$ ; at the bottom, quadrilateral 2D second gradient element is shown at the left-hand side, and the corresponding parent element in the isoparametric local coordinate of  $(\xi, \eta)$  is shown at the right-hand side.

Moreover,  $[\mathbf{E}^{(t+\Delta t)_i}]$  is structured as follows:

$$[\mathbf{E}^{(t+\Delta t)_i}]_{(25 \times 25)} = \begin{bmatrix} \mathbf{E}_1^{(t+\Delta t)_i}_{(4 \times 4)} & 0_{(4 \times 2)} & \mathbf{K}_{\mathbf{WM}}^{(t+\Delta t)_i}_{(4 \times 3)} & 0_{(4 \times 8)} & 0_{(4 \times 4)} & -\mathbf{I}_{(4 \times 4)} \\ \mathbf{G}_1^{(t+\Delta t)_i}_{(2 \times 4)} & 0_{(2 \times 2)} & \mathbf{G}_2^{(t+\Delta t)_i}_{(2 \times 3)} & 0_{(2 \times 8)} & 0_{(2 \times 4)} & 0_{(2 \times 4)} \\ \mathbf{K}_{\mathbf{MW}}^{(t+\Delta t)_i}_{(3 \times 4)} & 0_{(3 \times 2)} & \mathbf{K}_{\mathbf{WW}}^{(t+\Delta t)_i}_{(3 \times 3)} & 0_{(3 \times 8)} & 0_{(3 \times 4)} & 0_{(3 \times 4)} \\ \mathbf{E}_2^{(t+\Delta t)_i}_{(8 \times 4)} & 0_{(8 \times 2)} & 0_{(8 \times 3)} & \mathbf{D}^{(t+\Delta t)_i}_{(8 \times 8)} & 0_{(8 \times 4)} & 0_{(8 \times 4)} \\ \mathbf{E}_3^{(t+\Delta t)_i}_{(4 \times 4)} & 0_{(4 \times 2)} & 0_{(4 \times 3)} & 0_{(4 \times 8)} & 0_{(4 \times 4)} & \mathbf{I}_{(4 \times 4)} \\ \mathbf{E}_4^{(t+\Delta t)_i}_{(4 \times 4)} & 0_{(4 \times 2)} & 0_{(4 \times 3)} & 0_{(4 \times 8)} & -\mathbf{I}_{(4 \times 4)} & 0_{(4 \times 4)} \end{bmatrix} \quad (5.40)$$

This matrix contains all the terms corresponding to the mechanical part of the problem, fluid part, and their coupling. The different matrices within the matrix  $[\mathbf{E}^{(t+\Delta t)_i}]_{(25 \times 25)}$  are extended for a coupled hydro-mechanical analysis, in consideration of an anisotropic porous medium, in Appendix B.

**Finite element formulation:** The spatial discretization of the field Equation 5.38 is performed using the finite element method through definition of 2D plane strain isoparametric finite elements (see Figure 5.27). These quadrilateral elements have eight nodes for the displacement and pore pressure fields ( $u_i$  and  $p_w$ ), four nodes for  $v_{ij}$ , and one node for  $\lambda_{ij}$ . The quadratic shape functions [Zienkiewicz and Taylor, 2000] are applied for the  $u_i$  and  $p_w$  interpolation whereas the linear shape functions are used for  $v_{ij}$ , and  $\lambda_{ij}$  is supposed to be constant.

Then, the matrix  $[d\mathbf{u}^{(t+\Delta t)_i}]$  in Equation 5.38 is linked to the nodal variables  $[d\mathbf{u}_{en}^{(t+\Delta t)_i}]$  through the use of the transformation matrices  $[\mathbf{T}^{(t+\Delta t)_i}]$  and  $[\mathbf{B}]$ , such that:

$$[d\mathbf{u}^{(t+\Delta t)_i}] = [\mathbf{T}^{(t+\Delta t)_i}] [d\mathbf{u}_{(\xi, \eta)}^{(t+\Delta t)_i}] \quad (5.41)$$

$$\left[ d\mathbf{u}_{(\xi,\eta)}^{(t+\Delta t)_i} \right] = [\mathbf{B}] \left[ d\mathbf{u}_{en}^{(t+\Delta t)_i} \right] \quad (5.42)$$

where  $\left[ d\mathbf{u}_{(\xi,\eta)}^{(t+\Delta t)_i} \right]^T$  is given by:

$$\begin{aligned} \left[ d\mathbf{u}_{(\xi,\eta)}^{(t+\Delta t)_i} \right]^T \equiv & \left[ \frac{\partial du_1^{(t+\Delta t)_i}}{\partial \xi} \frac{\partial du_1^{(t+\Delta t)_i}}{\partial \eta} \frac{\partial du_2^{(t+\Delta t)_i}}{\partial \xi} \frac{\partial du_2^{(t+\Delta t)_i}}{\partial \eta} du_1^{(t+\Delta t)_i} du_2^{(t+\Delta t)_i} \right. \\ & \frac{\partial dp_w^{(t+\Delta t)_i}}{\partial \xi} \frac{\partial dp_w^{(t+\Delta t)_i}}{\partial \eta} dp_w^{(t+\Delta t)_i} \frac{\partial dv_{11}^{(t+\Delta t)_i}}{\partial \xi} \frac{\partial dv_{11}^{(t+\Delta t)_i}}{\partial \eta} \frac{\partial dv_{12}^{(t+\Delta t)_i}}{\partial \xi} \dots \frac{\partial dv_{22}^{(t+\Delta t)_i}}{\partial \eta} \\ & \left. dv_{11}^{(t+\Delta t)_i} dv_{12}^{(t+\Delta t)_i} dv_{21}^{(t+\Delta t)_i} dv_{22}^{(t+\Delta t)_i} d\lambda_{11}^{(t+\Delta t)_i} d\lambda_{12}^{(t+\Delta t)_i} d\lambda_{21}^{(t+\Delta t)_i} d\lambda_{22}^{(t+\Delta t)_i} \right] \end{aligned} \quad (5.43)$$

and, the nodal matrix  $\left[ d\mathbf{u}_{en}^{(t+\Delta t)_i} \right]^T$  is expressed by:

$$\begin{aligned} \left[ d\mathbf{u}_{en}^{(t+\Delta t)_i} \right]^T \equiv & \left[ du_{1(-1,-1)}^{(t+\Delta t)_i} du_{2(-1,-1)}^{(t+\Delta t)_i} dp_{w(-1,-1)}^{(t+\Delta t)_i} dv_{11(-1,-1)}^{(t+\Delta t)_i} dv_{12(-1,-1)}^{(t+\Delta t)_i} dv_{21(-1,-1)}^{(t+\Delta t)_i} dv_{22(-1,-1)}^{(t+\Delta t)_i} \right. \\ & du_{1(-1,0)}^{(t+\Delta t)_i} du_{2(-1,0)}^{(t+\Delta t)_i} dp_{w(-1,0)}^{(t+\Delta t)_i} du_{1(-1,1)}^{(t+\Delta t)_i} du_{2(-1,1)}^{(t+\Delta t)_i} dp_{w(-1,1)}^{(t+\Delta t)_i} dv_{11(-1,1)}^{(t+\Delta t)_i} dv_{12(-1,1)}^{(t+\Delta t)_i} dv_{21(-1,1)}^{(t+\Delta t)_i} dv_{22(-1,1)}^{(t+\Delta t)_i} \\ & du_{1(0,-1)}^{(t+\Delta t)_i} du_{2(0,-1)}^{(t+\Delta t)_i} dp_{w(0,-1)}^{(t+\Delta t)_i} d\lambda_{11(0,0)}^{(t+\Delta t)_i} d\lambda_{12(0,0)}^{(t+\Delta t)_i} d\lambda_{21(0,0)}^{(t+\Delta t)_i} d\lambda_{22(0,0)}^{(t+\Delta t)_i} du_{1(0,1)}^{(t+\Delta t)_i} du_{2(0,1)}^{(t+\Delta t)_i} \\ & dp_{w(0,1)}^{(t+\Delta t)_i} du_{1(1,-1)}^{(t+\Delta t)_i} du_{2(1,-1)}^{(t+\Delta t)_i} dp_{w(1,-1)}^{(t+\Delta t)_i} dv_{11(1,-1)}^{(t+\Delta t)_i} dv_{12(1,-1)}^{(t+\Delta t)_i} dv_{21(1,-1)}^{(t+\Delta t)_i} dv_{22(1,-1)}^{(t+\Delta t)_i} du_{1(1,0)}^{(t+\Delta t)_i} \\ & \left. du_{2(1,0)}^{(t+\Delta t)_i} dp_{w(1,0)}^{(t+\Delta t)_i} du_{1(1,1)}^{(t+\Delta t)_i} du_{2(1,1)}^{(t+\Delta t)_i} dp_{w(1,1)}^{(t+\Delta t)_i} dv_{11(1,1)}^{(t+\Delta t)_i} dv_{12(1,1)}^{(t+\Delta t)_i} dv_{21(1,1)}^{(t+\Delta t)_i} dv_{22(1,1)}^{(t+\Delta t)_i} \right] \end{aligned} \quad (5.44)$$

Then, the relation 5.38 for one finite element reads:

$$\begin{aligned} & \int_{\Omega^{(t+\Delta t)_i}^{el}} [\mathbf{u}^*]^T \left[ \mathbf{E}^{(t+\Delta t)_i} \right] \left[ d\mathbf{u}^{(t+\Delta t)_i} \right] d\Omega^{(t+\Delta t)_i} \\ & = [\mathbf{u}_{en}^*]^T \int_{-1}^1 \int_{-1}^1 [\mathbf{B}]^T \left[ \mathbf{T}^{(t+\Delta t)_i} \right]^T \left[ \mathbf{E}^{(t+\Delta t)_i} \right] \left[ \mathbf{T}^{(t+\Delta t)_i} \right] [\mathbf{B}] \det \mathbf{J}^{(t+\Delta t)_i} d\xi d\eta \left[ d\mathbf{u}_{en}^{(t+\Delta t)_i} \right] \\ & \equiv [\mathbf{u}_{en}^*]^T \left[ \mathfrak{K}^{(t+\Delta t)_i, el} \right] \left[ d\mathbf{u}_{en}^{(t+\Delta t)_i} \right] \end{aligned} \quad (5.45)$$

where  $\left[ \mathfrak{K}^{(t+\Delta t)_i, el} \right]$  is the element stiffness matrix, and  $\mathbf{J}^{(t+\Delta t)_i}$  is the Jacobian matrix for mapping from the local coordinates  $(\xi, \eta)$  to the global coordinates  $(x_1, x_2)$  (see Equation 3.61).

Thence, the residual terms  $\mathfrak{R}_1^{(t+\Delta t)_i}$ ,  $\mathfrak{R}_2^{(t+\Delta t)_i}$ , and  $\mathfrak{R}_3^{(t+\Delta t)_i}$  can be computed for one element

through Equation 5.46 while the element out of balance forces is expressed by  $\left[ \mathcal{F}_{\mathbf{OBF}}^{(t+\Delta t)_i \text{el}} \right]$ .

$$\begin{aligned} & - \mathfrak{R}_1^{(t+\Delta t)_i} - \mathfrak{R}_2^{(t+\Delta t)_i} - \mathfrak{R}_3^{(t+\Delta t)_i} \\ & = \mathcal{W}_E^{\star(t+\Delta t)_i} - [\mathbf{u}_{en}^{\star}]^T \int_{-1}^1 \int_{-1}^1 [\mathbf{B}]^T [\mathbf{T}^{(t+\Delta t)_i}]^T [\boldsymbol{\sigma}^{(t+\Delta t)_i}] \det \mathbf{J}^{(t+\Delta t)_i} d\xi d\eta \equiv [\mathbf{u}_{en}^{\star}]^T \left[ \mathcal{F}_{\mathbf{OBF}}^{(t+\Delta t)_i \text{el}} \right] \end{aligned} \quad (5.46)$$

where  $\mathcal{W}_E^{\star(t+\Delta t)_i}$  contains the contribution of the body forces and boundary surface forces (both mechanical and flow terms), except the term associated to gravity volume force since the latter is considered to be involved in  $[\boldsymbol{\sigma}^{(t+\Delta t)_i}]$  (Equation 5.47) [Matsushima et al., 2002; Collin et al., 2006].

$$\begin{aligned} \left[ \boldsymbol{\sigma}^{(t+\Delta t)_i} \right] & = \left[ \begin{array}{cccccc} \sigma_{11}^{(t+\Delta t)_i} & -\lambda_{11}^{(t+\Delta t)_i} & \dots & \sigma_{22}^{(t+\Delta t)_i} & -\lambda_{22}^{(t+\Delta t)_i} & -\rho_m^{(t+\Delta t)_i} g_1 \\ -m_1^{(t+\Delta t)_i} & -m_2^{(t+\Delta t)_i} & \dot{S}^{(t+\Delta t)_i} & \Sigma_{111}^{(t+\Delta t)_i} & \dots & \Sigma_{222}^{(t+\Delta t)_i} \\ \lambda_{11}^{(t+\Delta t)_i} & \dots & \lambda_{22}^{(t+\Delta t)_i} & & & \end{array} \right] \\ & \quad - \left[ \begin{array}{cccc} \frac{\partial u_1^{(t+\Delta t)_i}}{\partial x_1^{(t+\Delta t)_i}} - v_{11}^{(t+\Delta t)_i} & \dots & \frac{\partial u_2^{(t+\Delta t)_i}}{\partial x_2^{(t+\Delta t)_i}} - v_{22}^{(t+\Delta t)_i} & \end{array} \right] \end{aligned} \quad (5.47)$$

#### Global resolution procedure in LAGAMINE:

The global out of balance force at the iteration  $i$  of the time step from  $t$  to  $t + \Delta t$ ,  $[\mathbf{F}_{\mathbf{OBF}}^{(t+\Delta t)_i}]$  is then obtained by assembling the element out of balance forces  $\left[ \mathcal{F}_{\mathbf{OBF}}^{(t+\Delta t)_i \text{el}} \right]$  (see Equation 5.46). Similarly, the global stiffness matrix  $[\mathbf{K}^{(t+\Delta t)_i}]$  is also obtained by assembling the element stiffness matrices  $[\mathcal{K}^{(t+\Delta t)_i \text{el}}]$  (see Equation 5.45). Hence, the corresponding global equation reads:

$$[\mathbf{K}^{(t+\Delta t)_i}] [\delta \mathbf{u}_{en}^{(t+\Delta t)_i}] = - [\mathbf{F}_{\mathbf{OBF}}^{(t+\Delta t)_i}] \quad (5.48)$$

where  $[\delta \mathbf{u}_{en}^{(t+\Delta t)_i}]$  is the global vector of correction that is acquired through solving of this auxiliary linear system. Then, it is applied to actualize the current configuration, after which the equilibrium is checked, and a new iteration may be necessarily started.

On the basis of the computation algorithm given in Section 3.2.7, and with regard to the developed numerical formulation in the framework of second gradient model explained in this Section, *an accomplished resolution algorithm in LAGAMINE is then summarized, for one time step, as follows:*

1. Consider a time step  $\Delta t$  from  $t$  to  $t + \Delta t$ , and the initial configuration at the beginning of the step; i.e.:  
Stress  $\boldsymbol{\sigma}^t$ , double stress  $\boldsymbol{\Sigma}^t$ , coordinates  $\mathbf{x}^t$ , pore water pressure  $p_w^t$ ;
2. The nodal coordinates are updated for the first iteration with an assumption on the final configuration and final pore pressure for the current step; thence, we have:  $\mathbf{x}^{(t+\Delta t)_i}$  for  $i = 1$ ;
3. The iterative procedure is launched for the iteration  $i$ ;
4. For each element:

- ✓ For each integration point:
    - The strain and rotation rates as well as the pore pressure rate and second gradient rate are computed;
    - Using the constitutive equations and flow model, the variation of effective stress  $\Delta\boldsymbol{\sigma}'^{(t+\Delta t)_i}$  and double stress  $\Delta\boldsymbol{\Sigma}^{(t+\Delta t)_i}$  as well as mass flow  $\mathbf{m}^{(t+\Delta t)_i}$  are computed;
    - The updated effective stress and double stress are obtained, such that:
 
$$\boldsymbol{\sigma}'^{(t+\Delta t)_i} = \boldsymbol{\sigma}'^t + \Delta\boldsymbol{\sigma}'^{(t+\Delta t)_i}$$

$$\boldsymbol{\Sigma}^{(t+\Delta t)_i} = \boldsymbol{\Sigma}^t + \Delta\boldsymbol{\Sigma}^{(t+\Delta t)_i};$$
    - The total stress is computed,  $\boldsymbol{\sigma}^{(t+\Delta t)_i} = \boldsymbol{\sigma}'^{(t+\Delta t)_i} - p_w^{(t+\Delta t)_i}$ ;
    - The compliance matrices are obtained with respect to the perturbation method [Charlier, 1987],  $\mathbf{C}_{(4 \times 4)}^{(t+\Delta t)_i}$  and  $\mathbf{D}_{(8 \times 8)}^{(t+\Delta t)_i}$ ;
  - ✓ The element out of balance forces  $\left[ \mathcal{F}_{\mathbf{OBF}}^{(t+\Delta t)_i, el} \right]$  are obtained;
  - ✓ The element stiffness matrix  $\left[ \mathcal{K}^{(t+\Delta t)_i, el} \right]$  is computed;
5. The global out of balance forces  $\left[ \mathbf{F}_{\mathbf{OBF}}^{(t+\Delta t)_i} \right]$  are computed;
  6. The global stiffness matrix  $\left[ \mathbf{K}^{(t+\Delta t)_i} \right]$  is assembled and inverted;
  7. The correction  $\left[ \delta \boldsymbol{\mathcal{U}}_{en}^{(t+\Delta t)_i} \right]$  is computed through solving the relation  $\left[ \mathbf{K}^{(t+\Delta t)_i} \right] \left[ \delta \boldsymbol{\mathcal{U}}_{en}^{(t+\Delta t)_i} \right] = - \left[ \mathbf{F}_{\mathbf{OBF}}^{(t+\Delta t)_i} \right]$ ;
  8. Convergence on a norm of out of balance forces and norm of generalized displacements - that actually contains the mechanical displacements, pore pressure variations and the change in second gradient terms - is checked with respect to a given precision which is prescribed by the user (see Appendix A):
    - ✓ If the convergence is reached: go to 9;
    - ✓ If no convergence: the correction is made and the final configuration and final pore pressure are then updated for a new iteration,  $i = i + 1$ , go to 3;
  9. End of the time step.

Finally, it must be noted that the constitutive equation for the second grade part can be defined through introducing the Jaumann double stress rate, similarly to classical media (Equation 3.11), such that:

$$\tilde{\Sigma}_{ijk} = \dot{\Sigma}_{ijk} + \Sigma_{ljk}\omega_{li} + \Sigma_{imk}\omega_{mj} + \Sigma_{ijn}\omega_{nk} \quad (5.49)$$

A simple linear elastic law, as a particular case of a more general isotropic linear relation deduced

by Mindlin [1964], is used to present the corresponding constitutive equation as follows:

$$\begin{bmatrix} \tilde{\Sigma}_{111} \\ \tilde{\Sigma}_{112} \\ \tilde{\Sigma}_{121} \\ \tilde{\Sigma}_{122} \\ \tilde{\Sigma}_{211} \\ \tilde{\Sigma}_{212} \\ \tilde{\Sigma}_{221} \\ \tilde{\Sigma}_{222} \end{bmatrix} = \begin{bmatrix} D & 0 & 0 & 0 & 0 & \frac{D}{2} & \frac{D}{2} & 0 \\ 0 & \frac{D}{2} & \frac{D}{2} & 0 & -\frac{D}{2} & 0 & 0 & \frac{D}{2} \\ 0 & \frac{D}{2} & \frac{D}{2} & 0 & -\frac{D}{2} & 0 & 0 & \frac{D}{2} \\ 0 & 0 & 0 & D & 0 & -\frac{D}{2} & -\frac{D}{2} & 0 \\ 0 & -\frac{D}{2} & -\frac{D}{2} & 0 & D & 0 & 0 & 0 \\ \frac{D}{2} & 0 & 0 & -\frac{D}{2} & 0 & \frac{D}{2} & \frac{D}{2} & 0 \\ \frac{D}{2} & 0 & 0 & -\frac{D}{2} & 0 & \frac{D}{2} & \frac{D}{2} & 0 \\ 0 & \frac{D}{2} & \frac{D}{2} & 0 & 0 & 0 & 0 & 0 \end{bmatrix} \begin{bmatrix} \frac{\partial \dot{v}_{11}}{\partial x_1} \\ \frac{\partial \dot{v}_{11}}{\partial x_2} \\ \frac{\partial \dot{v}_{12}}{\partial x_1} \\ \frac{\partial \dot{v}_{12}}{\partial x_2} \\ \frac{\partial \dot{v}_{21}}{\partial x_1} \\ \frac{\partial \dot{v}_{21}}{\partial x_2} \\ \frac{\partial \dot{v}_{22}}{\partial x_1} \\ \frac{\partial \dot{v}_{22}}{\partial x_2} \end{bmatrix} \quad (5.50)$$

where  $\dot{v}_{ij}$  is the material time derivative of microkinematic gradient field  $v_{ij}$ . Then, this relation depends only on one elastic parameter  $D$  to which the shear band width is proportional [Chambon et al., 1998; Matsushima et al., 2002].

## 5.4 Numerical examples: Definition of the corresponding parameters for modeling of strain localization and analysis of their impact

### 5.4.1 Simulation of biaxial compression test

This Section is assigned to the numerical modeling of a drained biaxial compression test in the plane strain state. It consists in the purely numerical simulations performed with a particular focus on the analysis of strain localization phenomenon regarding that there has been no available experimental results of biaxial compression test and a relative analysis of shear strain localization on Boom Clay sample. Thence, the main objective of this Section is to address some important features of modeling of strain localization using the second gradient method, such as mesh independency of the model, some principle parameters to affect the localization response, and the post-localization behavior. Then, it could be a primitive step to the following simulations of strain localization within the damaged zone around the underground galleries. Nevertheless, some qualitative comparisons could be still performed with regard to the experimental observations of strain localization through the biaxial tests on the other materials. In fact, modeling of biaxial compression test has been conducted here since the biaxial experiments are well-known to exhibit obviously the strain localization in the laboratory (see for instance [Desrues, 1998; Desrues and Viggiani, 2004]) and to study it numerically. It is usually preferred to the triaxial tests since in the latter, the localized bands could be somehow hidden, and some advanced techniques (similar to the ones explained in Section 5.2.2) may be then needed to see them in the laboratory and to analyze them.

### 5.4.1.1 General description

Figure 5.28 shows the mesh geometry and boundary condition of the biaxial model. It has a total number of 4141 nodes and 1100 elements of  $1 \times 1 \text{ mm}$ . The confining pressure of  $4.5 \text{ MPa}$  is applied which consists in an effective mean stress of  $2.3 \text{ MPa}$ , similar to the in-situ one, and pore water pressure of  $2.2 \text{ MPa}$ . The shearing is supposed to be performed through an ultimate vertical displacement of  $4 \text{ mm}$  imposed progressively (at a constant loading strain rate of  $7.7 \times 10^{-8} \text{ s}^{-1}$ ) on the upper surface of the model. The latter results in a total axial strain of 0.08 at the end of the test.

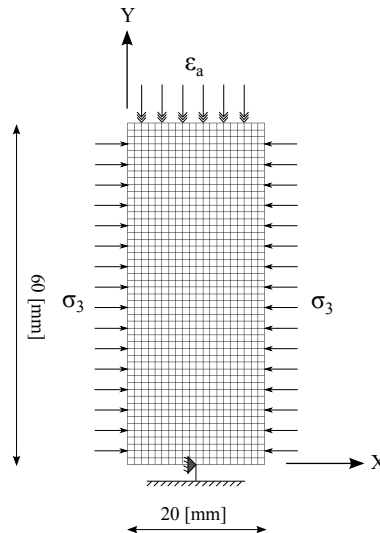


Figure 5.28: Biaxial numerical model; at the bottom, all the nodes are restricted in the vertical direction, and just one central node in the horizontal direction.

Moreover, there are some different approaches which can be applied to exhibit numerically strain localization. Among these approaches, there is the random initialization of the first guess of final configuration and nodal values  $[\delta \mathbf{u}_{en}^{(t+\Delta t)_i}]$  at the beginning of resolution iterative procedure (described at the end of Section 5.3.3) that allows to simulate the localized solution(s) [Chambon et al., 2001b; Chambon and Moullet, 2004]. In fact, this method consists in choosing randomly our first guess instead of following the standard choice of choosing the nodal values at the beginning of the iterative algorithm based on the ones obtained at the end of previous time step. Consequently to the first guess provided for the corresponding iteration, some finite number of solutions (possibly more than one) can be randomly produced [Chambon et al., 1998]. Furthermore, in a common, different way, we can define a geometrical defect or material imperfection [Matsushima et al., 2002] to ensure the occurrence of strain localization in our numerical modeling. It is then supposed that one solution can be obtained provided an initial imperfection, although, this solution could be changed (for instance through changing the defined imperfection) [Bésuelle et al., 2006a]. The latter procedure is used in the following modelings of biaxial test; an imperfection is defined in the bottom left side element of the model.

### 5.4.1.2 Analysis of the results

In the framework of the numerical modeling of strain localization, the results, in the following, are presented in four different points of view. First, the dependency of the shear bands thickness

Table 5.1: Mechanical parameters of the model; application of different values of  $D$ 

Parameter	Symbol	Value	Unit
Young elastic modulus	$E$	300	$MPa$
Poisson ratio	$\nu$	0.125	-
Specific mass of the grains	$\rho_s$	2700	$Kg/m^3$
Initial compression friction angle	$\varphi_{C0}$	8	$^\circ$
Final compression friction angle	$\varphi_{Cf}$	18	$^\circ$
Hardening coefficient	$B_\varphi$	0.001	-
Hardening coefficient	$D_\varphi$	0	-
Initial cohesion	$c_0$	300	$kPa$
Final cohesion	$c_f$	200	$kPa$
Softening coefficient	$B_c$	0.01	-
Softening coefficient	$D_c$	0	-
Dilatancy angle	$\Psi$	3	$^\circ$
Second gradient elastic modulus	$D$	<u>1</u> / <u>0.5</u> / <u>0.2</u> / <u>0.01</u>	$N$

to the choice of second gradient elastic modulus  $D$  is illustrated. Second, the mesh independent response of the model using the second gradient method is demonstrated in contrast with the pathological problem of mesh dependency occurred through application of the classical finite element. Third, the impact of softening parameters of the model in the post localization response of the material in the deviatoric plane is discussed. Forth, the strain localization evolution is shown during the simulation.

With regard to the second gradient elastic modulus  $D$ , four simulations have been performed to study how the width of the localized shear bands can be controlled by this constant parameter. Table 5.1 lists the (classical) mechanical parameters used for all these modelings in addition to four different values of the (new) introduced second gradient parameter  $D$ . As it is observed, the other main parameters have been chosen with respect to Section 3.5.2 (see Table 3.1). However, the dilatancy angle is chosen differently here; a low dilatancy angle equal to  $3^\circ$  is fixed in the defined properties considering that the material volumetric response is not aimed to be focused now, within the aforementioned framework of concentrating on basic concepts of strain localization phenomenon, besides that there is not any relative experimental data to be referred either. Moreover, the softening parameters of the model (i.e.  $c_f$ ,  $B_c$ , and  $D_c$ ) are also more particularly discussed and validated, in the following, with regard to the current simulations of biaxial test and the next example presented in Section 5.4.2, taking into account the important role of strain softening in initialization of strain localization. For the moment, a quite low softening of cohesion (final cohesion of  $200 kPa$ ) is considered in the first step.

Figure 5.29 shows the increment of deviatoric strain just after the appearance of strain localization and at the end of simulation for four simulations with different values of  $D$ . It is noteworthy that activity of localized shear band in each time step during the computation can be visualized through the contour of increment of deviatoric strain. With regard to four different values of  $D$ , which implicitly signifies four different material internal length, the obtained results demonstrate that the larger the internal length, i.e. higher value of  $D$ , the larger is the width of the bands. Furthermore, it has been recommended numerically [Bésuelle et al., 2006a] that the choice of  $D$  should be consistent with the mesh size so that there are at least about three elements in the band thickness. As a result, it could provide more numerical accuracy in the localization pattern of the solution and post-peak behavior. This sort of recommendation is not only addressed in the local second gradient model, but also in any non-local regularization technique. Within this framework,  $D = 0.2 N$  seems appropriate and it is then kept constant in the following simulations of biaxial test.

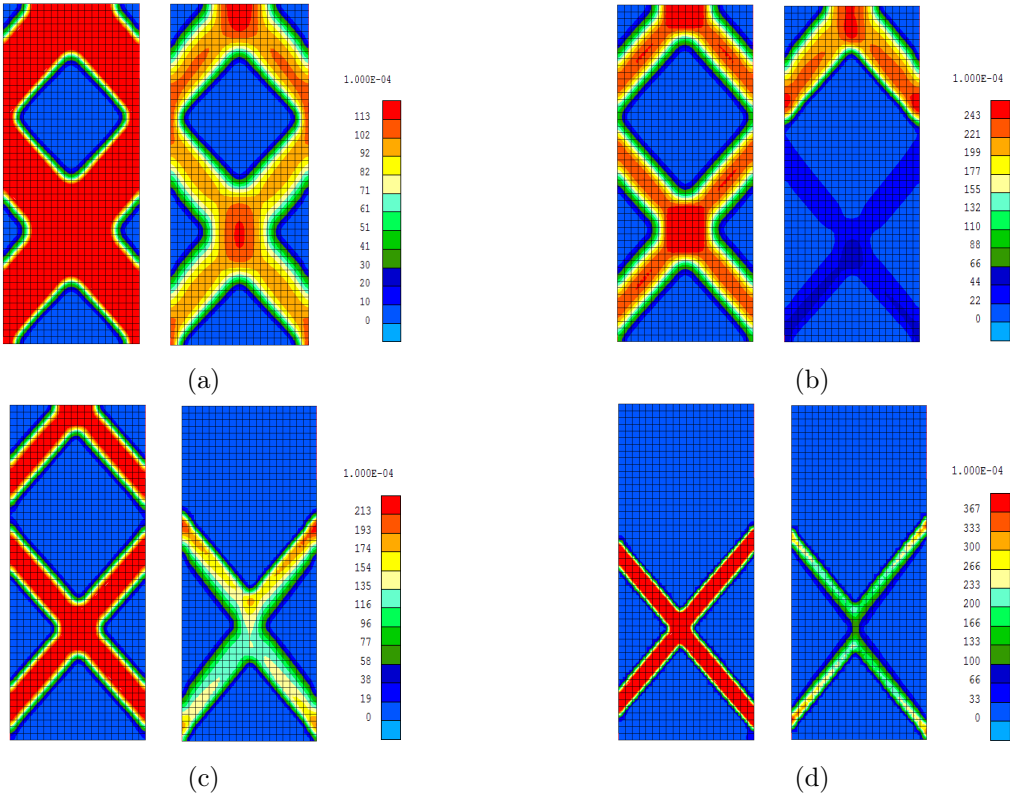


Figure 5.29: Increment of deviatoric strain during the localization process - just after the appearance of localized bands,  $\varepsilon_a \simeq 5\%$  (in the left side) and at the end of simulation,  $\varepsilon_a = 8\%$  (in the right side) - for the simulations with different values of  $D$ : (a)  $D = 1N$ . (b)  $D = 0.5N$ . (c)  $D = 0.2N$ . (d)  $D = 0.01N$ .

Next, it is aimed to visualize how dependent is the localization solution (bands' width) to the mesh size when using the classical finite element in contrast with the mesh independency provided in the framework of the used second grade enhanced model. Figure 5.30 shows the results of modelings, at  $\varepsilon_a = 8\%$ , with two different mesh ( $20 \times 50$  elements and  $40 \times 100$  elements) using the second gradient model, and also with application of classical finite element (i.e. the same simulation without using the second grade model). The parameters of the model is then the same for all the cases as listed in Table 5.1 while  $D = 0.2N$ . The results are shown in terms of increment of deviatoric strain and plastic loading index. The latter illustrates the immediate (i.e. at the current time step) response of the Gauss points in each element. When a Gauss point undergoes a plastic loading, then a small square is plotted, otherwise, for a Gauss point which undergoes either elastic unloading or reloading, nothing is drawn in the contour. As it is observed, the localization solution, the *width* and even pattern of shear bands, is perfectly the same for two simulations using the second gradient model, and the mesh size could not affect this solution. It is noteworthy that the aforesaid numerical requirement of having at least three elements in the band thickness is clarified here in another point of view since after the recommended limit, the finer the mesh is for a constant  $D$  (and the test condition), it is not supposed to be likely to change the localization pattern of solution. This solution is *a priori* mesh independent. On the other hand, it is demonstrated that the localization solution of the cases using the classical finite element is obviously dependent on the mesh size. The finer the mesh, the smaller is the width of the localized band. It could even change the direction of the band here, although, it might not be the case generally. Therefore, these simulations could confirm our need of the enhanced technique to regularize the trouble of mesh dependency occurred when using the classical finite elements.

Furthermore, several computations have been conducted to study the post localization response of the material. Table 5.2 lists the input parameters for different simulations where the focus is on the softening parameters. Their corresponding results in the deviatoric plane are then presented in Figure 5.31. The first simulation is the one that has previously been discussed for which the onset of localization has been shown to be at around  $\varepsilon_a = 5\%$  (see Figure 5.29c). This quite late localization appearance can be also understood from its deviatoric stress-axial strain curve which does not display a considerable effect of strain softening. As it has been already explained in this Chapter, the material softening can prompt the satisfaction of bifurcation conditions and onset of localization, which is then resulted in drop of resistance beyond stress peak (i.e. post localization regime). This material softening is achieved here through application of cohesion softening in the used strain-softening constitutive law. Within this framework, simulations 2-7 show the effect of three softening parameters,  $c_f$ ,  $B_c$ , and  $D_c$  (see Section 3.4.2.1), on the results.

A low value of  $D_c$  in *Num 2* has been defined to slightly postpone the softening procedure in the plastic state of the material (before the peak). It could subsequently help to initiate the localization of strain in the shear band mode. Thence, a pretty noticeable decrease of deviatoric stress is observed in the post localization regime (after axial strain of about 4%) in comparison with *Num 1*. Next, the decrease of final cohesion (i.e. more softening) - in *Num 3*, and then *Num 4* and *Num 5* - is demonstrated to induce more decrease of peak stress and drop of resistance indicating a sooner onset of localization (e.g. around 2% for *Num 5* as it can be also observed in Figure 5.34b). More decrease of  $c_f$  after about 50 *kPa* does not seem to make an important change in the obtained response (the corresponding curves of *Num 4* and *Num 5* are already comparable). Hence, keeping  $c_f = 30$  *kPa*, *Num 6* and *Num 7* illustrates the effect of  $B_c$  on the results. More  $B_c$  (increased to 10 times; *Num 6*) is being expected to decrease the softening rate and then, the obtained curve is above the one corresponds to *Num 5* (indicating the later onset of localized shear bands). On the contrary, there is some more decrease of stress peak for *Num 7* compared to *Num 5*. It must be noted that the strain localization is basically responsible for the

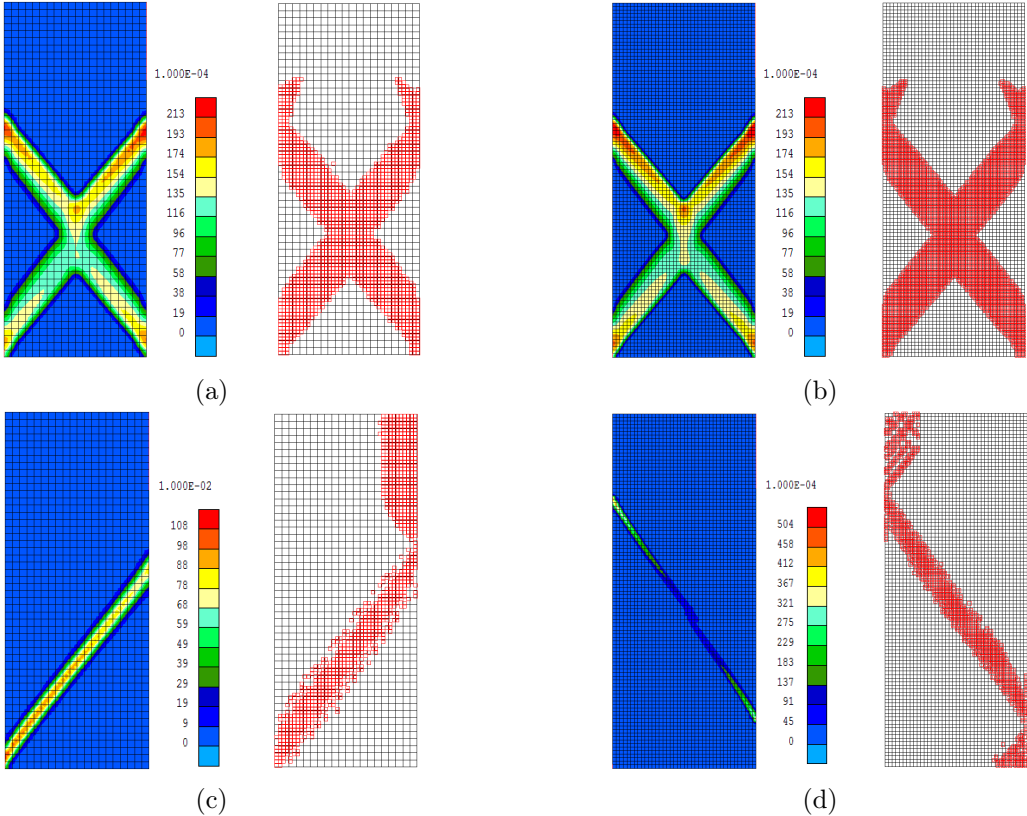


Figure 5.30: Comparison of the results of modeling (at  $\varepsilon_a = 8\%$ ) using the enhanced local second gradient model (top row) and in the framework of classical finite element (bottom row) in term of mesh dependency. Increment of deviatoric strain (in the left side) and plastic loading index (in the right side) are shown in each case of: (a) The model with  $20 \times 50$  elements. (b) The model with  $40 \times 100$  elements. (c) The model with  $20 \times 50$  elements. (d) The model with  $40 \times 100$  elements.

Table 5.2: Sets of mechanical parameters used for the modelings

Parameter	Symbol	Value							Unit
		<i>Num 1</i>	<i>Num 2</i>	<i>Num 3</i>	<i>Num 4</i>	<i>Num 5</i>	<i>Num 6</i>	<i>Num 7</i>	
Young elastic modulus	$E$	300	300	300	300	300	300	300	$MPa$
Poisson ratio	$\nu$	0.125	0.125	0.125	0.125	0.125	0.125	0.125	-
Specific mass of the grains	$\rho_s$	2700	2700	2700	2700	2700	2700	2700	$Kg/m^3$
Initial compression friction angle	$\varphi_{C0}$	8	8	8	8	8	8	8	$^\circ$
Final compression friction angle	$\varphi_{Cf}$	18	18	18	18	18	18	18	$^\circ$
Hardening coefficient	$B_\phi$	0.001	0.001	0.001	0.001	0.001	0.001	0.001	-
Hardening coefficient	$D_\phi$	0	0	0	0	0	0	0	-
Initial cohesion	$c_0$	300	300	300	300	300	300	300	$kPa$
Final cohesion	$c_f$	200	200	<u>100</u>	<u>50</u>	<u>30</u>	<u>30</u>	<u>30</u>	$kPa$
Softening coefficient	$B_c$	0.01	0.01	0.01	0.01	0.01	<u>0.1</u>	<u>0.007</u>	-
Softening coefficient	$D_c$	0	<u>0.005</u>	<u>0.005</u>	<u>0.005</u>	<u>0.005</u>	<u>0.005</u>	<u>0.005</u>	-
Dilatancy angle	$\Psi$	3	3	3	3	3	3	3	$^\circ$

drop of resistance beyond the stress peak while this localization of strain could be prompted by defined material softening. The same model with the same input parameters, including the softening parameters, as *Num 5* and with one element (i.e. homogeneous case) does not obviously show any localization and softening behavior; thence, reduction of shear stress with increase of plastic strain (see Figure 5.32).

All together, among the performed simulations of *Num 1-Num 7*, the obtained results of *Num 5* seems the most realistic in terms of simulation of localization behavior in the deviatoric stress-axial strain plane. Indeed, as previously discussed in the first part of this Chapter, a decrease of material's strength beyond the stress peak due to the occurrence of strain localization and material softening (as seen in *Num 5*) could be reasonably expected consistently with the experimental observations. In this sense, the development of the localized shear bands, relatively to the obtained stress-strain response, is illustrated in the following. Moreover, the response of the simulation *Num 5* could be somehow more respectful of the observed behavior (for instance the shearing resistance) of the studied material during the triaxial tests, discussed in Chapter 3.

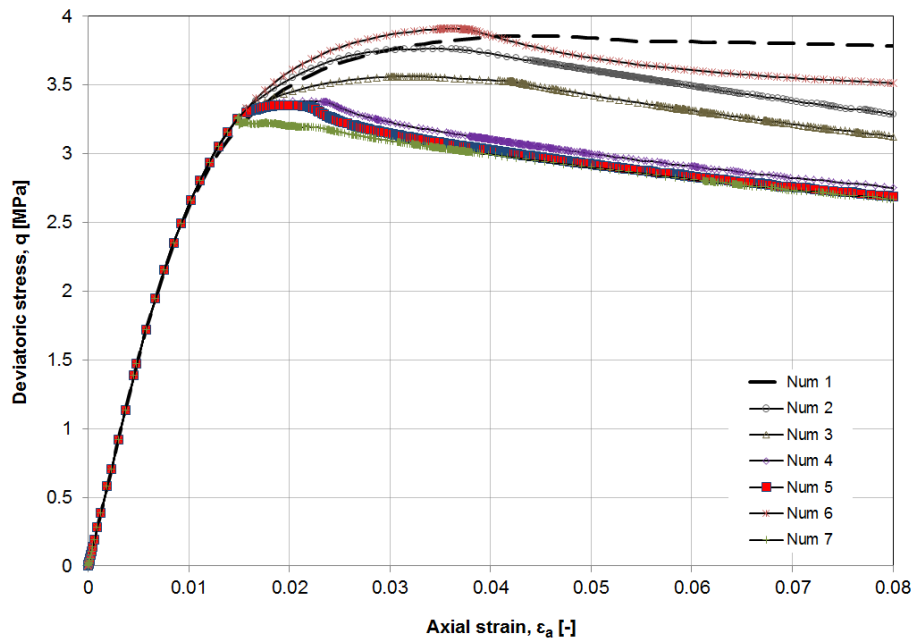


Figure 5.31: Deviatoric stress in function of axial strain.

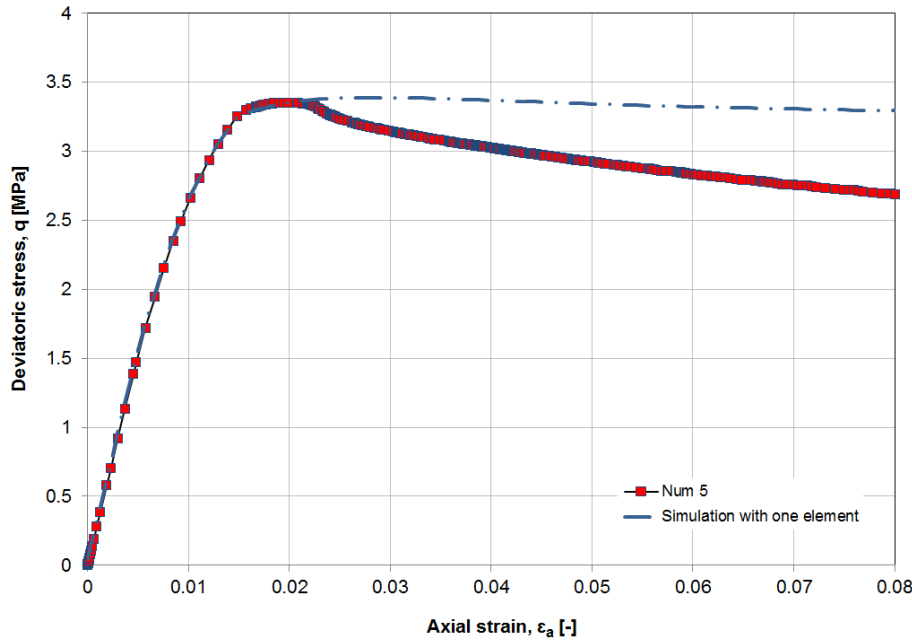


Figure 5.32: Deviatoric stress in function of axial strain for *Num 5* in comparison with the simulation with one element and homogeneous response.

Given the simulation *Num 5*, the evolution of localized shear band is demonstrated in Figure 5.34<sup>10</sup> through presentation of increment of deviatoric strain, plastic loading index, total deviatoric strain<sup>11</sup>, and nodal velocity norm in different analysis points (correspond to the numerical time steps as given in Figure 5.33). Besides the evolutionary localization response of the material in different steps of computation in terms of increment of deviatoric strain and plastic loading index, total deviatoric strain present, in each time step, the synthesis of the whole history of the shear band activity in the accumulated time. In addition, the nodal velocity norm indicates the norm of the nodal displacement rate, i.e.  $\|v\| = \sqrt{v_1^2 + v_2^2} = \sqrt{\dot{u}_1^2 + \dot{u}_2^2}$ , which is shown on the deformed state of the material during the simulation.

Roughly before the peak stress (see Figure 5.34a), some activity towards the creation of a shear band has been already initiated while the velocity norm tends a global downward sliding movement (see black arrows). However, the plasticity remains quite homogeneous and bifurcation has not yet reached (see Figure 5.35a). Next, strain localization in shear band mode rises at the peak stress (around  $\varepsilon_a = 2.1\%$ ) where the bifurcation has occurred. Figure 5.35b illustrates this bifurcation solution while the displayed green and red arrows estimate graphically two potential inclination of shear band. Subsequently, a more clear localized shear band can be identified just after the peak at  $\varepsilon_a = 2.8\%$  while elastic unloading occurs outside of the band giving birth to this fully formed shear band (see also Figure 5.35c). The evolutionary activity of the band can be then observed in the next steps (i.e. post localization regime). In the course of the shear strain localization and the band activity, its reflection can be also observed on the displacement throughout the specimen. It tends to be divided in two blocks while the top one (deforming downward) is sliding over the bottom one (which has been restricted at the bottom surface) along the created shear band.

<sup>10</sup>In order to be able to illustrate the evolution of strain localization in time, the legend scale of the presented numerical results, associated to localization phenomenon, all through this thesis, might be chosen differently for different time steps.

<sup>11</sup>Hereafter, the term total deviatoric strain in presentation of the strain localization evolution refers to the Von Mises equivalent strain.

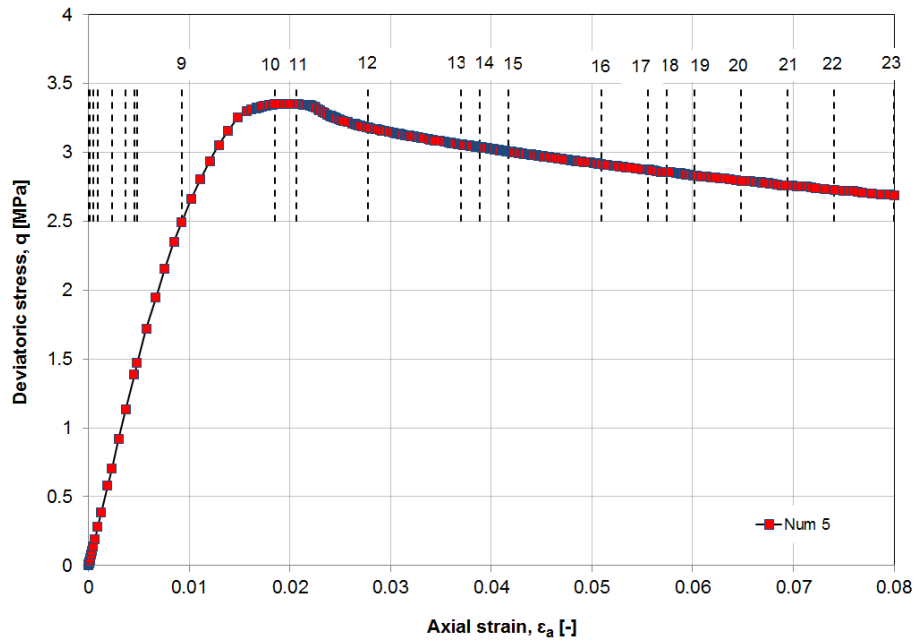


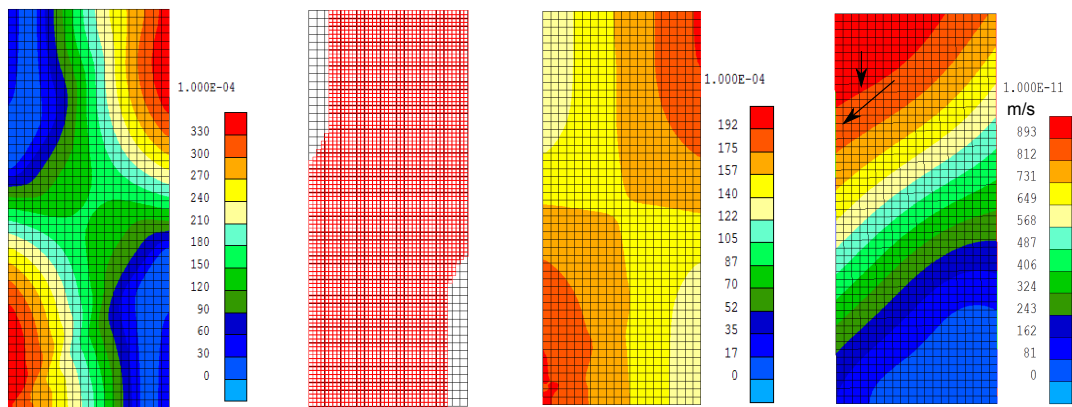
Figure 5.33: Deviatoric stress in function of axial strain for *Num 5*. Different numerical time steps are shown by the dash lines with regard to which the shear strain localization-post localization response is studied at different points.

Consistently, Figure 5.36 shows how the horizontal and vertical displacement is varied along a horizontal line, at the middle height of the biaxial model, passing through the created shear band.

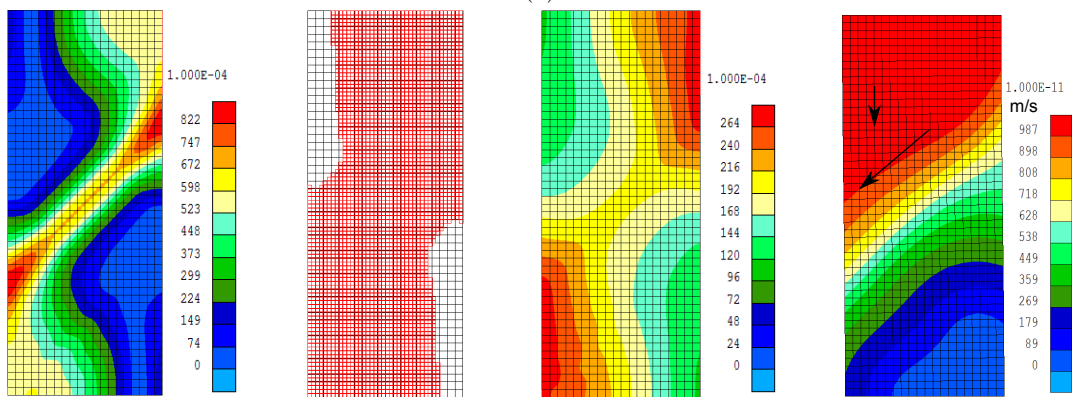
With respect to the experimental analysis of strain localization as described in Section 5.2.2, the similar pattern of shear strain localization relatively to the stress-strain behavior has been observed through different biaxial tests [Desrues, 1998; Mokni and Desrues, 1999; Desrues and Viggiani, 2004]. An initiation of the strain localization in shear band mode just before the stress peak, followed by a fully formed shear band state since the stress peak, has been evidenced experimentally (e.g. see Figures 5.5a and 5.8). Also, a similar relative movement of the sample's blocks along the shear band has been observed in the laboratory (e.g. see Figure 5.5b). Moreover, regarding the defined imperfection in our model, Desrues and Viggiani [2004] have performed an experimental study on the role of imperfection on shear banding and localization response. It has been then shown that an applied imperfection might impose the orientation and pattern of the resulted shear bands. As a result, instead of several localized solution in more than one location throughout the specimen which are in competition before that one could eventually takes over the others, one single localization solution is induced by defining an imperfection. This could be similarly observed in our modeling as well. Moreover, the authors have indicated that an introduced imperfection, be it weak or hard, has no impact on the obtained stress-strain response of the material, therefore, neither the stress peak nor the strain level where the localization occurs.

#### 5.4.2 Simulation of the excavation of Praclay gallery

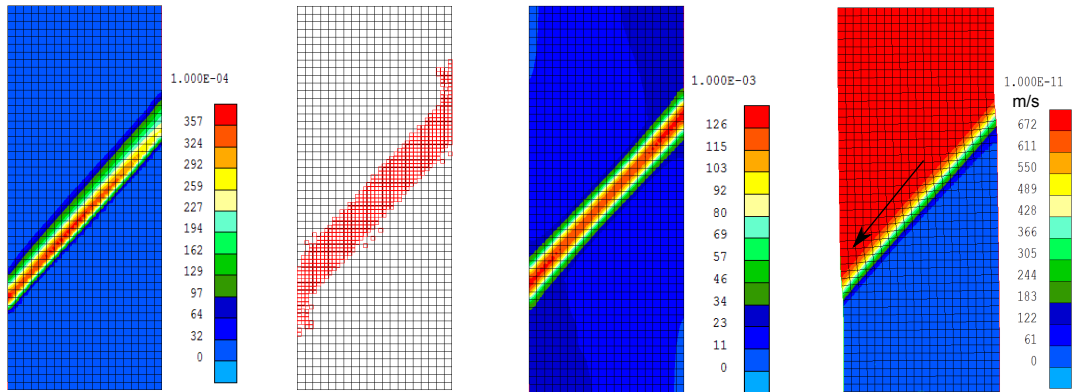
In the framework of studying the feasibility of high-level and high-lived nuclear waste disposal in deep Boom Clay formation in Belgium, the ONDRAF/NIRAS and SCK-CEN groups and the corresponding researchers have followed two principle goals in the HADES URL (Mol, Belgium)



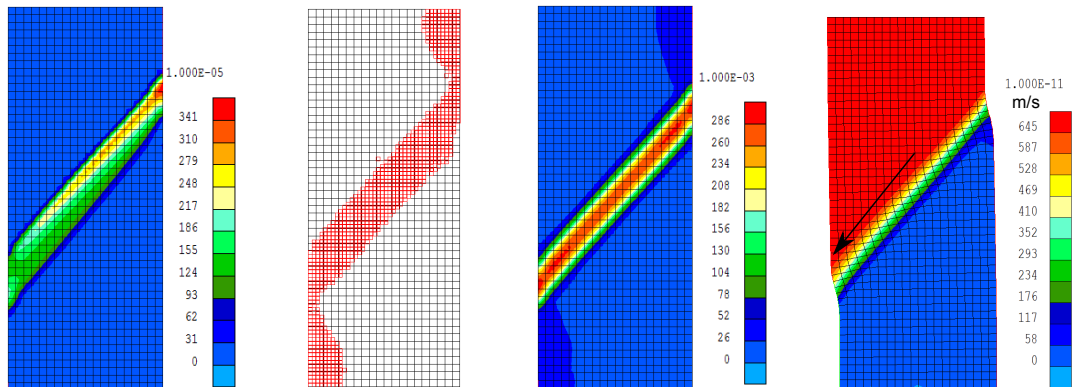
(a)



(b)



(c)



(d)

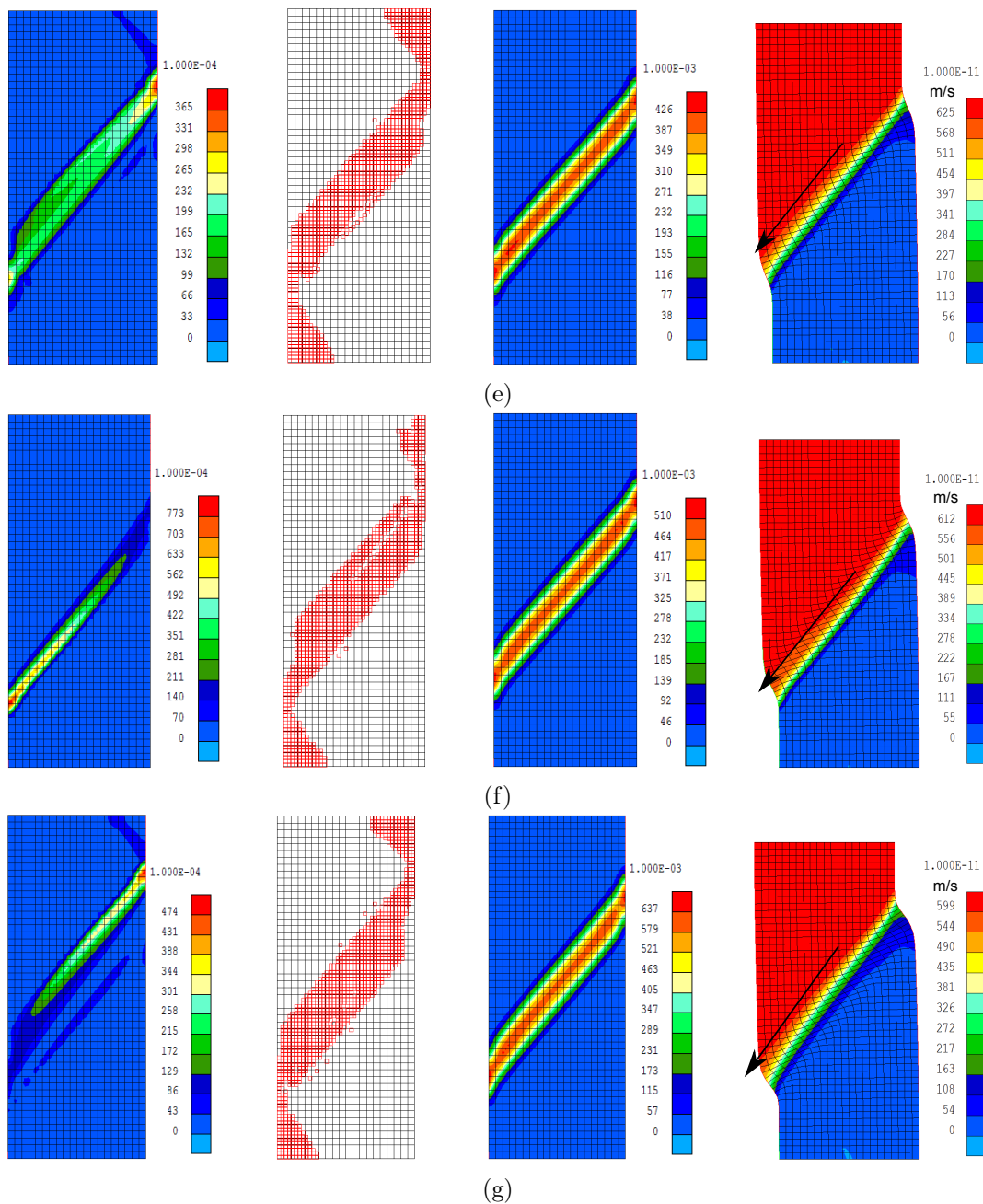


Figure 5.34: The results of *Num 5* in terms of increment of deviatoric strain (in the left side), plastic loading index (in the middle left), total deviatoric strain (in the middle right), and velocity norm on the deformed mesh (in the right side) for: (a) Time step 10;  $\varepsilon_a = 1.8\%$ . (b) Time step 11;  $\varepsilon_a = 2.1\%$ . (c) Time step 12;  $\varepsilon_a = 2.8\%$ . (d) Time step 15;  $\varepsilon_a = 4.1\%$ . (e) Time step 17;  $\varepsilon_a = 5.5\%$ . (f) Time step 20;  $\varepsilon_a = 6.5\%$ . (g) Time step 23;  $\varepsilon_a = 8\%$ .

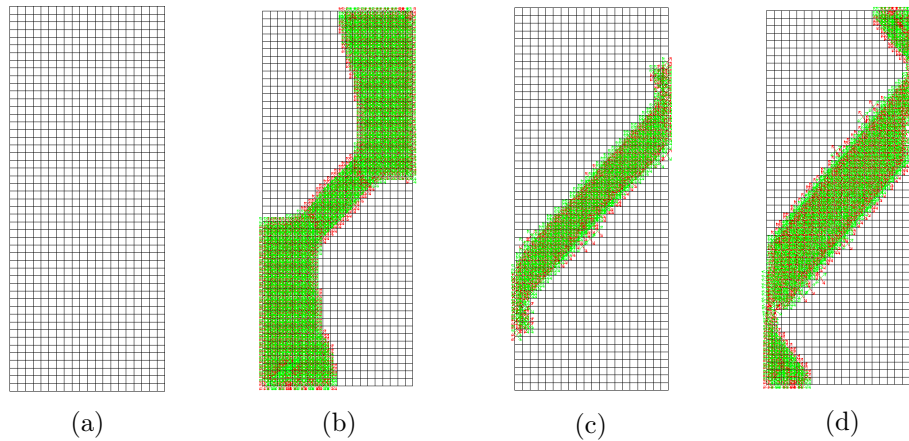


Figure 5.35: Bifurcation as the result of strain localization in shear band, for  $Num\ 5$ . (a) Time step 10,  $\varepsilon_a = 1.8\%$ , where bifurcation has not yet occurred. (b) Time step 11,  $\varepsilon_a = 2.1\%$ , which corresponds to the bifurcation point where the uniqueness of solution is lost; two possible orientations of shear band are then displayed. (c) Time step 12,  $\varepsilon_a = 2.8\%$ . (d) Time step 23,  $\varepsilon_a = 8\%$ .

since 1980. In the first place, studying the technical, scientific, economical and feasibility aspects of the construction of deep underground galleries in this host rock, using the industrial techniques, has been aimed. This has partly consisted in analysis of the subsequent effects of the construction of these galleries (which has been actually constructed similarly as inspected for (future) real disposal galleries) in the surrounding clay formation, and the relative conducted scientific researches - e.g. studying the evolution pattern and extension of resulted fracturing and damaged zone - during and long-term after the excavation process. In the second place, with regard to the fact that the high-level radioactive waste are supposed to emit some heat which can impose a temperature increase in the clay natural barrier, another objective has consisted in studying the effect of this heat on the clay mass at depth. The former goal could be quite accomplished through construction of the Connecting gallery. The excavation of Praclay gallery (see Figure 2.3) followed also this objective, though. But the more important scope of excavation of the Praclay gallery has been defined along the aforementioned second goal.

In the framework of the objectives defined by ONDRAF/NIRAS, in collaboration with EIG EURIDICE (European Underground Research Infrastructure for Disposal of nuclear waste in Clay Environment)<sup>12</sup>, for the conducted researches in this thesis, we were aimed to follow the first above goal. Thence, in the following, after a brief description of the whole Praclay experiment program, our focus is on the excavation procedure of this gallery and the resulted fractures development. Moreover, regardless of the heating effects following the defined scopes for this thesis, a consensus has held quite soon after the beginning of this work to divert our research focus on the Connecting gallery from the Praclay gallery. Therefore, the following simulations are presented as the preliminary simulations of a large-scale gallery excavation (with regard to Praclay gallery), while a more detailed discussions and analysis of different aspects of this sort of deep construction will be the objective of the next two Chapters (with regard to Connecting gallery). Within this sequence, we are aimed to analyze the effect of some main parameters in numerical modeling of strain localization in the large-scale, around a gallery defined by analogy with Praclay gallery, in the framework of a parametric study in this Section. Consequently, this study could accomplish our numerical preview of strain localization modeling which will be then

<sup>12</sup>It is a grouping between ONDRAF/NIRAS and SCK-CEN, in Mol, Belgium, with an economical interest basis.

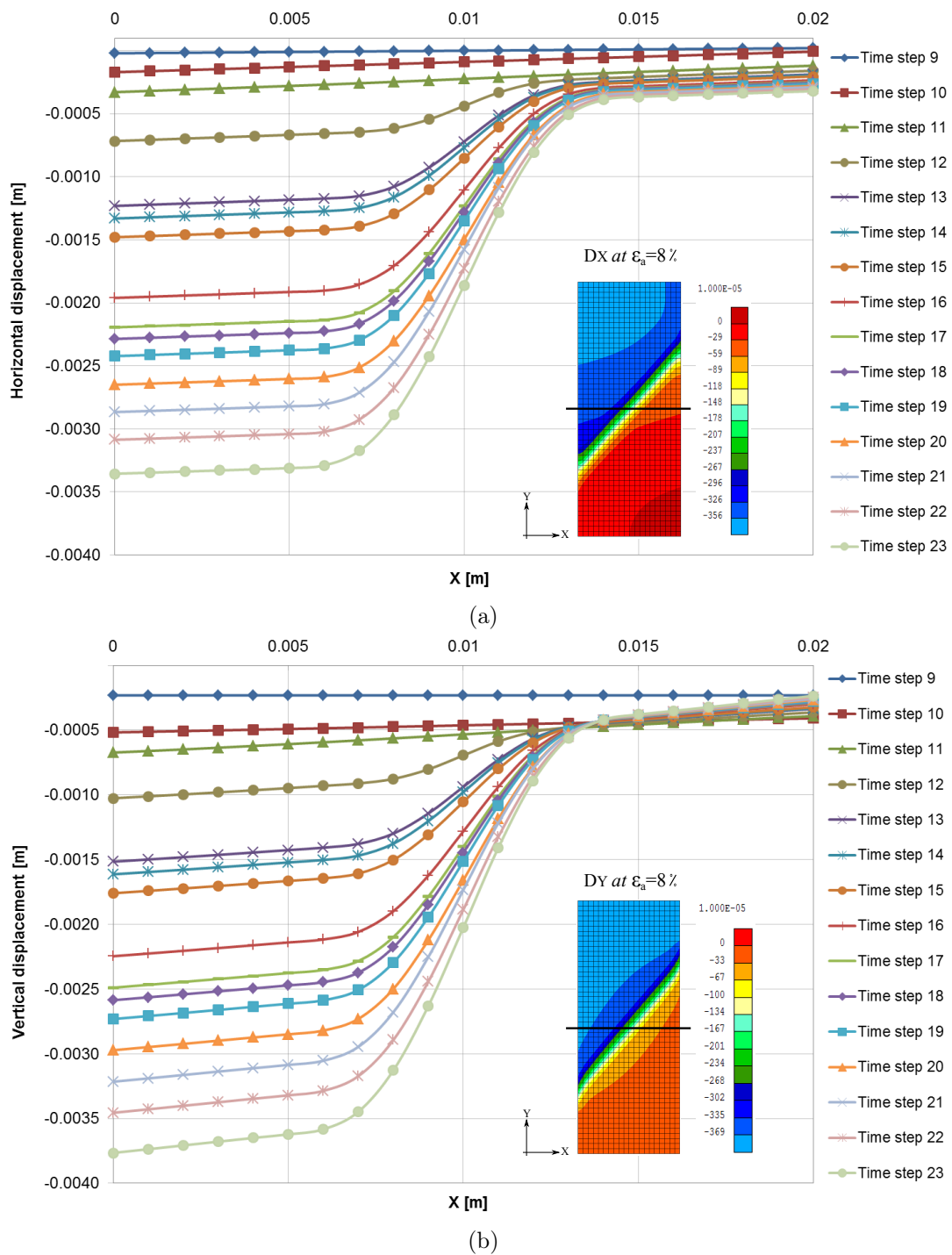


Figure 5.36: Variations of displacement along a horizontal line at the middle height of the biaxial model (see black line in the displayed contour) at different time steps for *Num 5*. (a) Horizontal displacement. (b) Vertical displacement. The contour of displacement at  $\epsilon_a = 8\%$ , corresponding to time step 23, is also shown in each case.

used in the next two Chapters' computations.

#### 5.4.2.1 Description of the Praclay experience

Praclay gallery, with 2.5 m diameter, was constructed in 2007, perpendicular to the Connecting gallery and between its rings 32 and 35. In order to prevent the probable collapse which could occur at the part of Connecting gallery where its lining had been removed for the excavation of (perpendicular) Praclay gallery, the steel reinforcement has been installed at that part of Connecting gallery (entrance of Praclay gallery). Figure 5.37 shows this reinforcement, which made possible the crossing of two galleries. In addition to this crossing practicality and excavation fulfillment, two other main tests have been being conducted by construction of Praclay gallery. These tests consists of the Seal test and Heater test [TIMODAZ, 2010a]. The former studied the feasibility of hydraulically sealing the heated part of the Praclay gallery from the non-heated part of the gallery. It was aimed to create an impermeable hydraulic boundary at these two parts' intersection to "close" the Praclay gallery and to maintain pore water pressure at the heated part. For this purpose, a steel structure as well as an annular ring of bentonite, placed against the clay, were installed (see Figure 5.37). The latter test (i.e. heater test) has been intended for imposing a constant temperature of 80° on the clay for which two heating sources, one close to the gallery intrados and the other inside its central line, have been installed. It is noteworthy that the heating experiment has been recently switched on - on November 3, 2014 - and it will normally provide lots of useful data, during the subsequent 10 years, for the future researches. In the following, as it has been already mentioned, the excavation phase of Praclay gallery and the subsequent damage evolution are simulated.

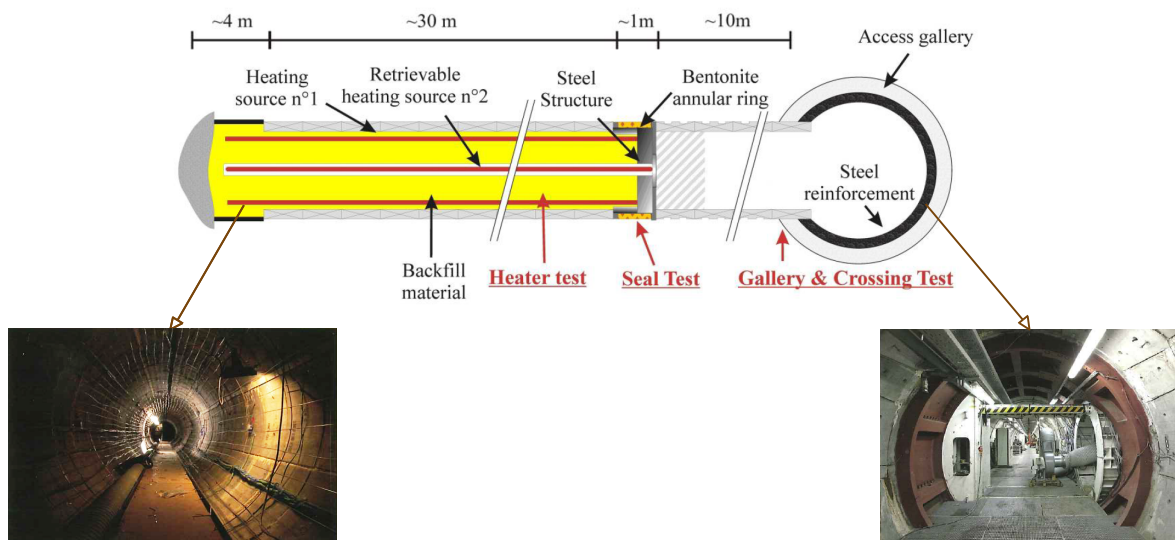


Figure 5.37: Praclay in-situ experiment. Heating system on the Praclay gallery wall is shown on the left side bottom, and the steel enforcement structure in the Connecting gallery at the entrance of the Praclay gallery is shown on the right side bottom; after [TIMODAZ, 2010a].

#### 5.4.2.2 Definition of the numerical model

A quarter of the gallery is modeled, assuming symmetry along x- and y-axes, in the plane strain state. Figure 5.38 shows the two-dimensional mesh geometry and boundary conditions of the

model. The gallery has a total excavated radius of  $1.25\text{ m}$ <sup>13</sup>, and a total number of 9455 nodes and 2370 elements which are become finer by getting closer to the gallery wall. In addition, the constrained normal derivatives are given to define the symmetry of the radial displacements ( $u_r$ ) around the symmetric boundaries (i.e.  $\partial u_x/\partial y = v_{12} = 0$  along the x axis and  $\partial u_y/\partial x = v_{21} = 0$  along the y axis). These kinematic boundary conditions are needed to establish correctly the symmetry (with regard to the second gradient part) along  $x$ - and  $y$ -axes, according to Zervos et al. [2001b]. Indeed, due to the existence of the gradient terms in the equilibrium conditions, the normal derivative of displacements are also prescribed besides the classical boundary conditions of displacements (see Equation 5.13).

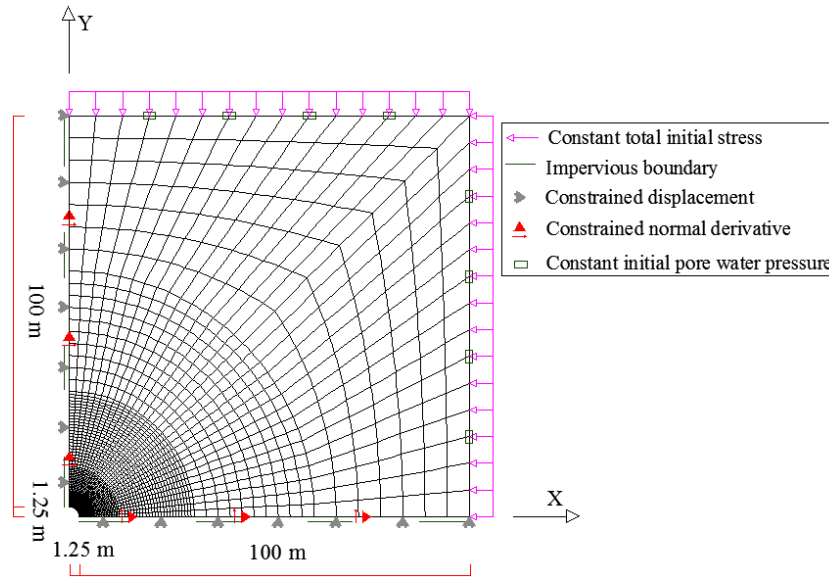


Figure 5.38: The mesh geometry and boundary conditions of the model.

Moreover, the initial stress anisotropy is accounted in our modelings, with regard to the in-situ stresses, as  $\sigma_{yy} = 4.5\text{ MPa}$  and  $\sigma_{xx} = 3.8475\text{ MPa}$  consisting in an earth pressure's coefficient at rest of  $K_0 = 0.855$ <sup>14</sup>. Also, the initial pore water pressure is defined as  $2.25\text{ MPa}$  while the clay is supposed to be fully saturated. To reproduce the excavation of the gallery in our coupled hydro-mechanical model, the both initial stresses and pore water pressure of the clay mass is considered to be decreased on the gallery wall during the excavation phase that is assumed to be one day. Then, they remain constant until the end of simulation which is 3.5 years (see Figure 5.39).

The hydro-mechanical parameters of the model are given here again in accordance with the main parameters defined for the triaxial tests' simulations and introduced to the biaxial model while the softening parameters and second gradient elastic modulus are initially introduced to be the same as the primary simulation of biaxial test *Num 1*; thence, see finally Tables 5.2 and 3.2. Consequently, Figure 5.40 shows the increment of deviatoric strain at different times during the simulation, in the radius of  $10\text{ m}$  from the gallery wall. As it is observed, the results do not show any appeared localized shear band after the end of excavation (i.e. one day) while the strain localization is mainly supposed to occur during the excavation phase. This late apparent and subsequently weak bands of localization has motivated us to perform a parametric study to analyze more precisely the impact of some likely influential mechanical parameters of the model on the obtained strain localization solution in our large-scale excavation problem.

<sup>13</sup>This includes  $30\text{ cm}$  of concrete lining.

<sup>14</sup>This is under the assumption of no influence of the pre-existing Connecting gallery (see Figure 2.3).

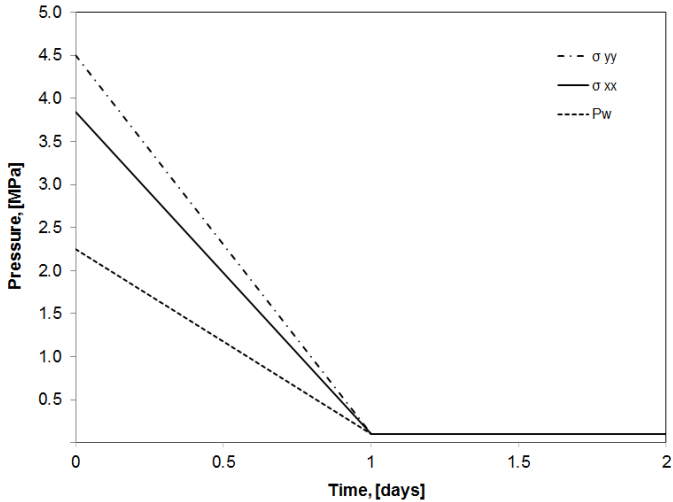


Figure 5.39: Imposed total stresses and pore water pressure on the gallery wall.

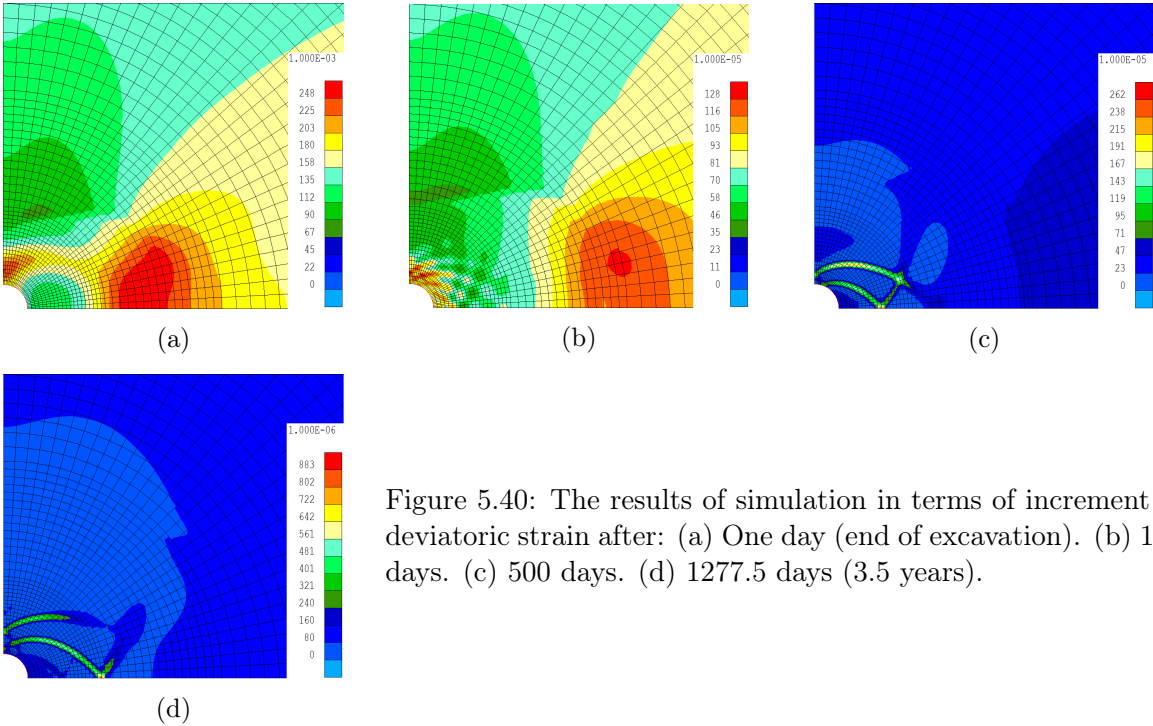


Figure 5.40: The results of simulation in terms of increment of deviatoric strain after: (a) One day (end of excavation). (b) 100 days. (c) 500 days. (d) 1277.5 days (3.5 years).

### 5.4.2.3 Parametric study

In the framework of a parametric study, the influence of changing the key parameters in the localization response's point of view, involving the elastic modulus of second gradient  $D$ , dilatancy angle, final cohesion  $c_f$  and the softening parameter  $B_c$ , is discussed. This study is performed *with reference to* the defined properties described for the preceding simulation except for the dilatancy angle which is now set to zero (instead of  $3^\circ$ )<sup>15</sup>. Then, in each case, one of the four aforementioned parameters is changed while all the other parameters of the model are kept constant. For instance, to analyze the impact of  $D$ , the results of four simulations with different introduced values of  $D = 2 \times 10^{-1} N$ ,  $D = 2 \times 10^1 N$ ,  $D = 2 \times 10^3 N$ , and  $D = 2 \times 10^5$  are presented while the values of the other parameters involved in our parametric study have been remained as:  $\Psi = 0^\circ$ ,  $c_f = 200 \text{ kPa}$ , and  $B_c = 0.01$  in these computations. Figures 5.41-5.44 show their corresponding results in terms of increment of deviatoric strain.

It must be underlined that the objective of this Section is not providing an uncertainty analysis neither an optimization analysis, but it is rather illustration of the impact of some leading input parameters in terms of computed numerical localization solution in order to better choose the corresponding parameters and to consequently achieve a more realistic prediction.

With regard to Figures 5.41-5.44, first, it is observed that all four simulations does not show any clear band of localization at one day (i.e. end of excavation). Second, in terms of the created localized shear bands, their appearance is quite thin and weak in Figures 5.41-5.42 (i.e.  $D = 2 \times 10^{-1} N$ ,  $D = 2 \times 10^1 N$ ). These bands are more well-constructed by application of  $D = 2 \times 10^3 N$ . Although, higher value of  $D$  could unrealistically postpone the appearance of localized shear bands; no created shear band and no activity is observed even after 3.5 years in the case with  $D = 2 \times 10^5 N$ . In fact, the higher the value of  $D$  (i.e. larger length scale), the smaller seems to be the apparent softening effect on initialization of strain localization, similarly to what has been also shown in [Matsushima et al., 2002]. These discussed features are also illustrated through a comparison of the bands activities in the four simulations after 100 days, as given in Figure 5.45 where the increment of deviatoric strain in the four cases is presented using the same legend scale. Consequently, the value of  $D = 2 \times 10^3 N$  seems the most appropriate one. To finalize this part of analysis, it must be ensured that this chosen value is consistent with our mesh size. In this sense, using this value, Figure 5.46 shows the increment of deviatoric strain, for instance after 100 days, for three simulations with three different mesh sizes; the mesh is finer (mostly around the gallery) in the case presented in Figure 5.46c, and quite larger in Figure 5.46a in reference to our spatial discretization so far (i.e. Figure 5.46b). As it is demonstrated, the localization solution have not been principally changed in three cases, and more precisely, it is the same for the cases with 2370 and 3360 elements (Figures 5.46b-5.46c) that this could confirm our consistent choice of  $D$  and mesh size so far. Thence, we can keep our reference spatial discretization (Figure 5.46b) in order to save the time consumed for our computations. Therefore, the value of second gradient modulus is kept constant from now on as  $D = 2 \times 10^3 N$ .

Furthermore, the impact of the dilatancy angle is studied while the other parameters are kept constant, i.e.  $D = 2 \times 10^3 N$  (as concluded in the previous part of analysis),  $c_f = 200 \text{ kPa}$ , and  $B_c = 0.01$ . Figure 5.47 shows the results of the simulation with  $\Psi = 5^\circ$  that can be compared with the same simulation with null dilatancy angle, i.e. Figure 5.43. It is immediately noticed that definition of a (moderate) constant dilatancy angle do strongly delay the appearance of strain localization. Indeed, considering a constant dilatancy angle in space and in time is not

<sup>15</sup>Since we want to study the influence of introducing a dilatancy angle separately during our parametric study, and to prevent that its initial introduction (with a non-zero value) into the model affect our interpretation of other parameters' impact.

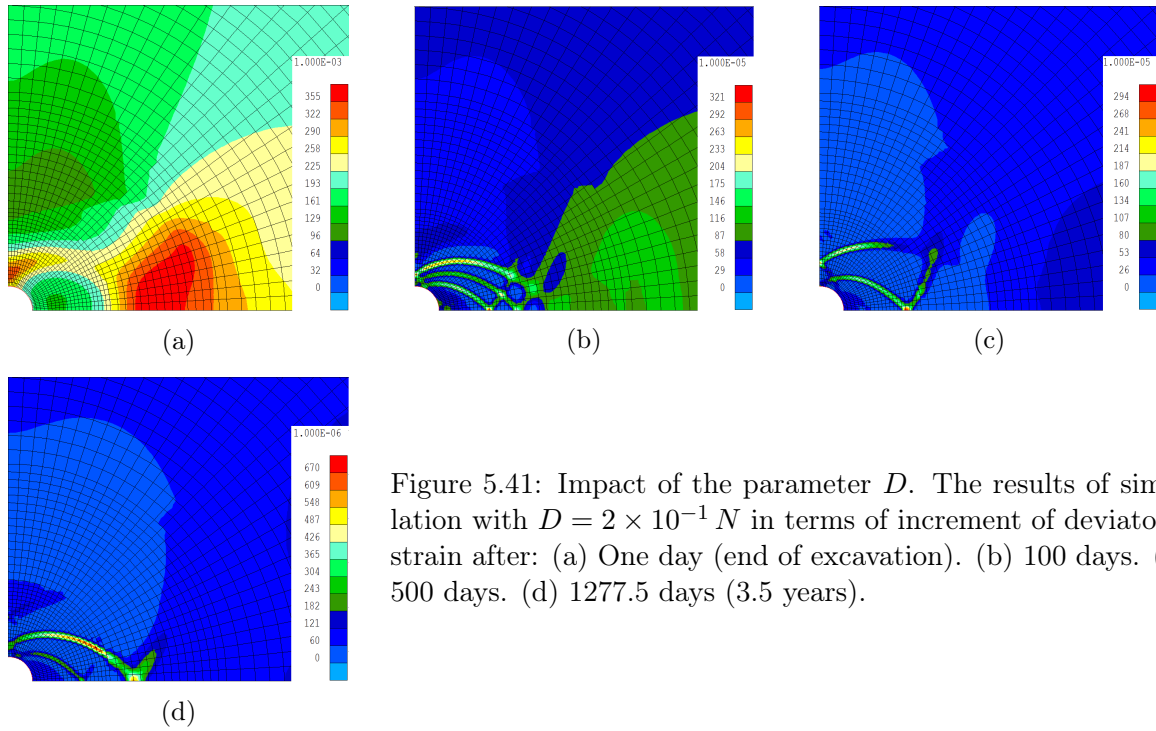


Figure 5.41: Impact of the parameter  $D$ . The results of simulation with  $D = 2 \times 10^{-1} N$  in terms of increment of deviatoric strain after: (a) One day (end of excavation). (b) 100 days. (c) 500 days. (d) 1277.5 days (3.5 years).

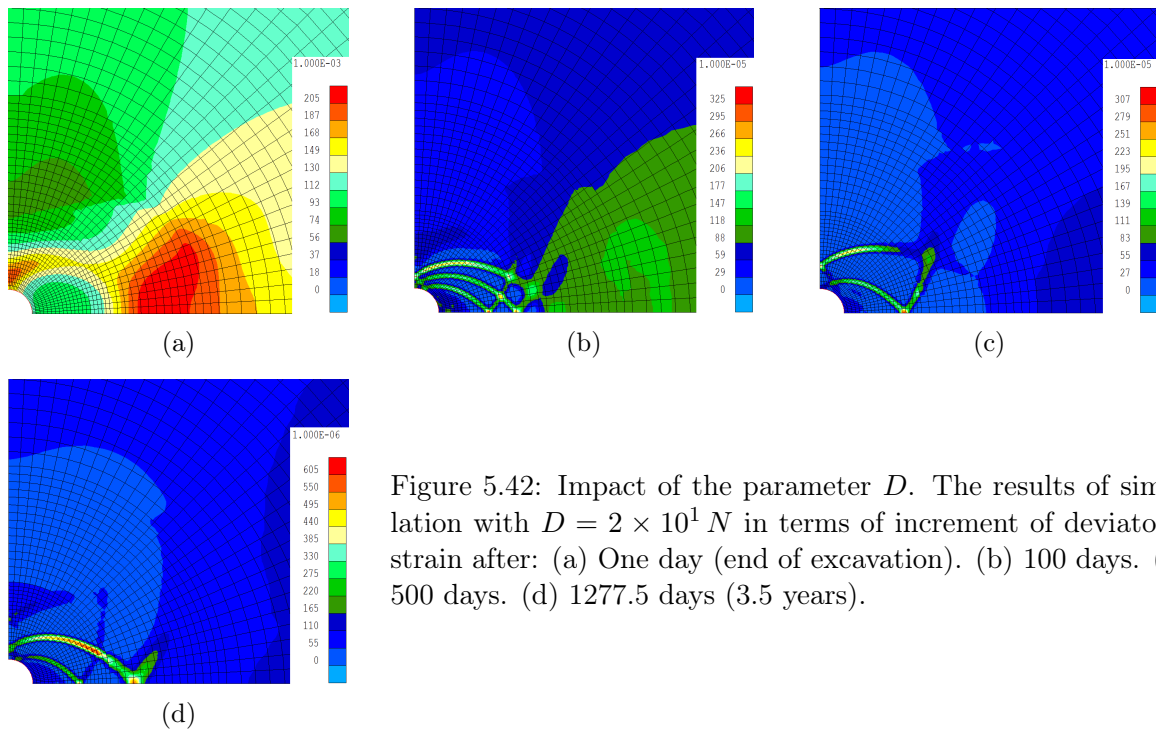


Figure 5.42: Impact of the parameter  $D$ . The results of simulation with  $D = 2 \times 10^1 N$  in terms of increment of deviatoric strain after: (a) One day (end of excavation). (b) 100 days. (c) 500 days. (d) 1277.5 days (3.5 years).

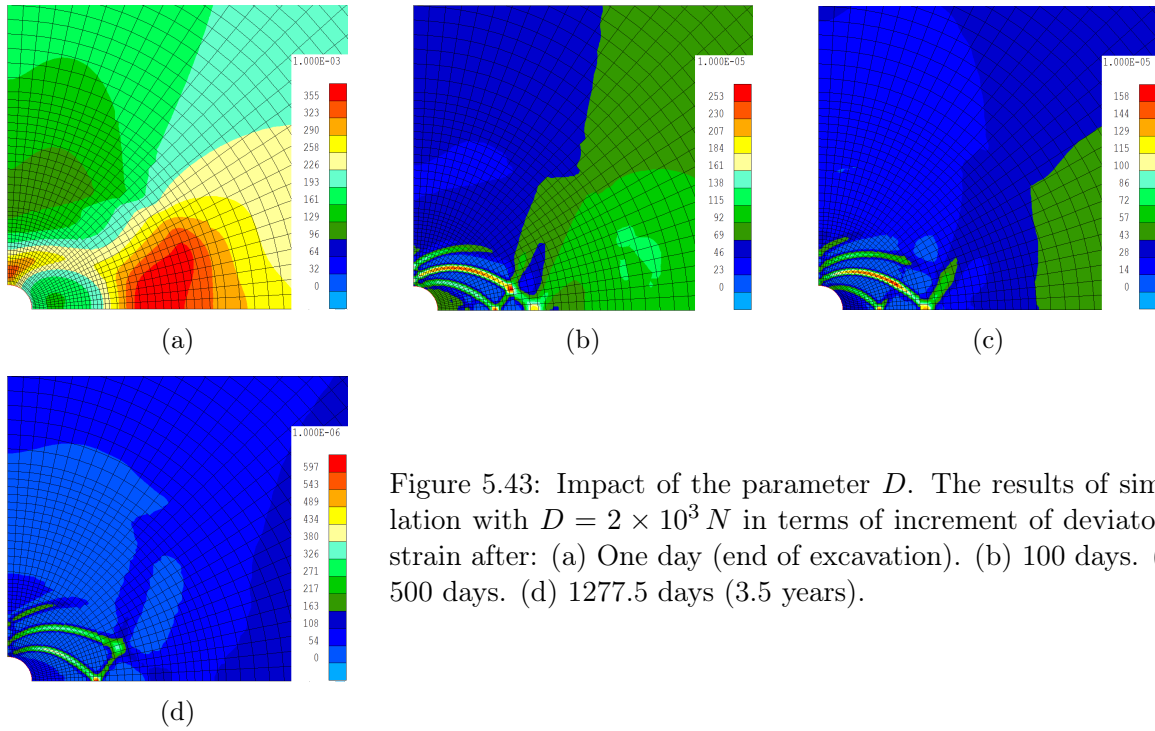


Figure 5.43: Impact of the parameter  $D$ . The results of simulation with  $D = 2 \times 10^3 N$  in terms of increment of deviatoric strain after: (a) One day (end of excavation). (b) 100 days. (c) 500 days. (d) 1277.5 days (3.5 years).

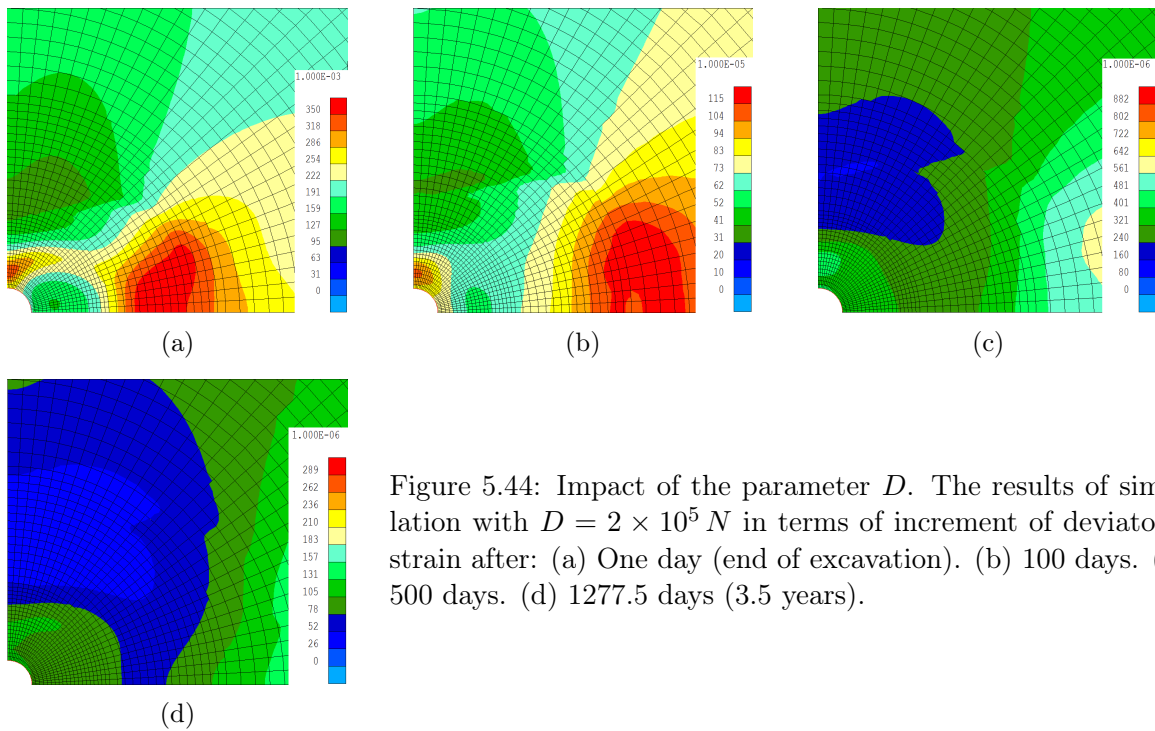


Figure 5.44: Impact of the parameter  $D$ . The results of simulation with  $D = 2 \times 10^5 N$  in terms of increment of deviatoric strain after: (a) One day (end of excavation). (b) 100 days. (c) 500 days. (d) 1277.5 days (3.5 years).

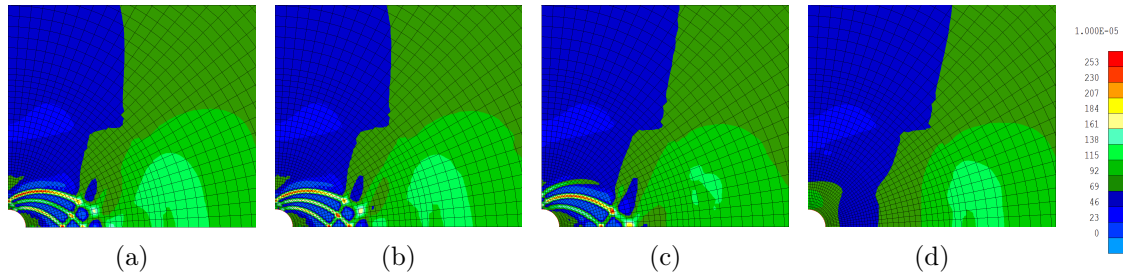


Figure 5.45: Impact of the parameter  $D$ . The results of simulation after 100 days in terms of increment of deviatoric strain for: (a)  $D = 2 \times 10^{-1} N$ . (b)  $D = 2 \times 10^1 N$ . (c)  $D = 2 \times 10^3 N$ . (d)  $D = 2 \times 10^5 N$ .

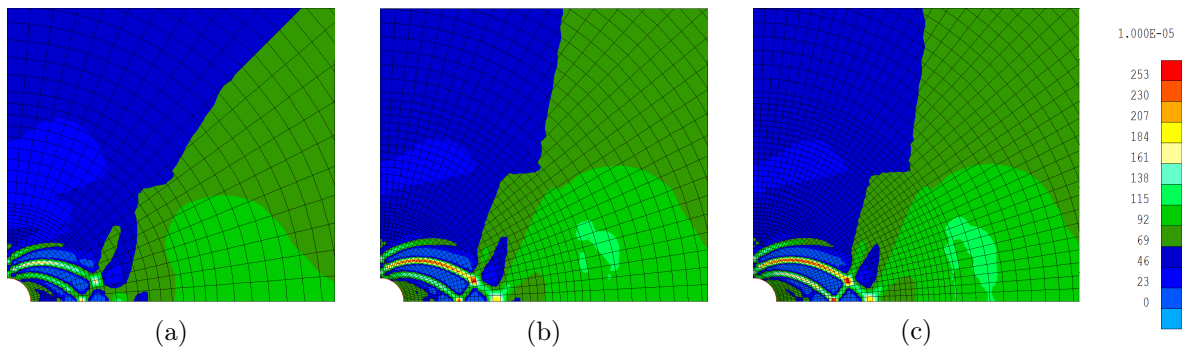


Figure 5.46: The results of simulation (using  $D = 2 \times 10^3 N$ ) after 100 days in terms of increment of deviatoric strain for the mesh with: (a) 1220 elements. (b) 2370 elements. (c) 3360 elements.

realistic during the localization process since *upon* the initiation of strain localization in the shear planes, a particular dilatancy tendency is supposed to be resulted in *that zone*. This zone in fact addresses the excavated gallery's proximity where the fractures opening might occur during a real excavation process. This dilatancy tendency is then supposed to decline, followed by a likely consolidation process in time. In this sense, the proposed method for application of variable dilatancy angle, in Chapter 4, could be useful (see Section 5.4.2.4). Moreover, introducing of a constant dilatancy angle into the latter modeling could be somehow interpreted as definition of a highly enough dilatant material, for which, Collin et al. [2013] have shown that the bifurcation criterion might be never met if the material remains saturated, and then localization could not even occur. In fact, this process lies in a resistance to plastic shearing and to the localization associated to the possible pore pressure drop in that dilatant material [Kirkebo, 1994; Bernier et al., 2007a]. In the similar manner, localization did only occur after more than 3 years in our case (Figure 5.47d). Therefore, the dilatancy angle is chosen to be still kept as zero for the rest of our parametric analysis.

Moreover, no appearance of localized shear bands during the excavation phase heretofore in our simulations (conclusively Figure 5.43) inspires the need for definition of more softening into the model. The influence of cohesion softening parameters is therefore addressed in simulating the appearance of strain localization during the excavation phase when it is *a priori* expected. Indeed, it has been already shown and discussed that how definition of strain softening could help to initiate the strain localization. In the particular case of gallery excavation, it can be said that our strain softening constitutive law - through which the softening of cohesion is being defined - is able to reproduce the progressive decrease of the material strength occurred during tunneling and appearance of strain localization. In this sense, in the numerical point of view, the material needs to be softened enough to simulate this process. Thence, in this step, the

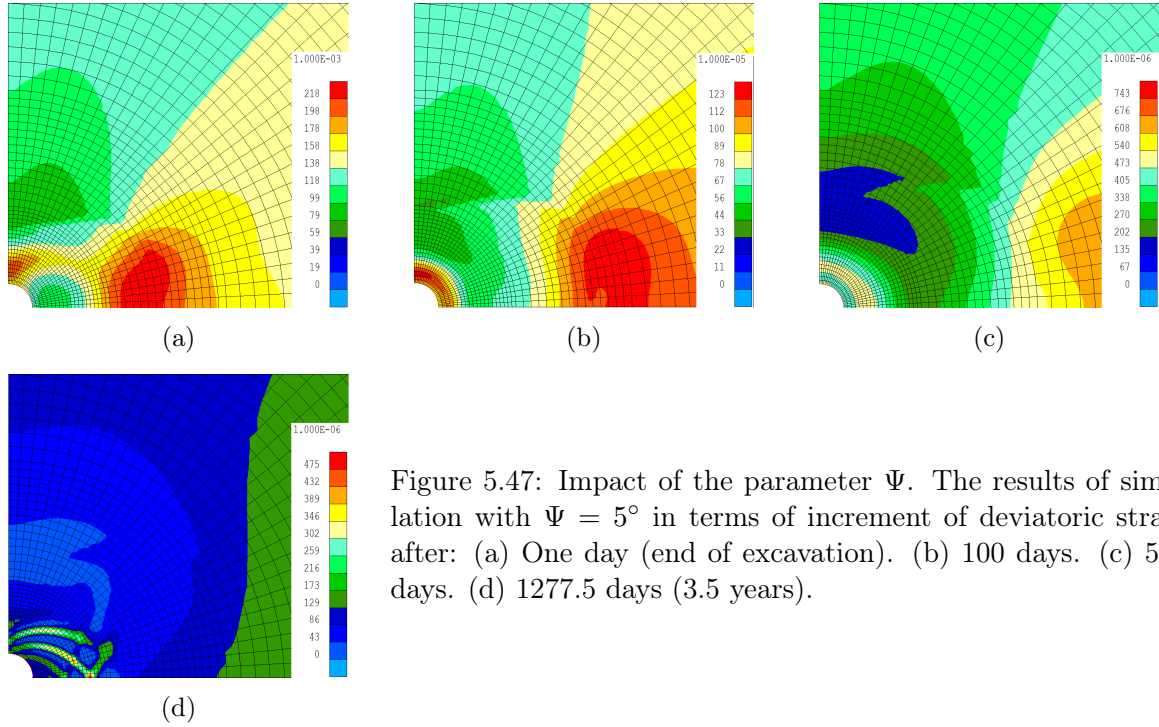


Figure 5.47: Impact of the parameter  $\Psi$ . The results of simulation with  $\Psi = 5^\circ$  in terms of increment of deviatoric strain after: (a) One day (end of excavation). (b) 100 days. (c) 500 days. (d) 1277.5 days (3.5 years).

influence of using four different final cohesion (i.e. different cohesion softening) is shown while the other parameters are kept constant in all these computations as :  $D = 2 \times 10^3 N$ ,  $\Psi = 0^\circ$ , and  $B_c = 0.01$ , with respect to the previous parts of our analysis. Figures 5.48-5.50 then present the results of three simulations (using  $c_f = 30 kPa$ ,  $c_f = 3 kPa$ , and  $c_f = 0.3 kPa$ ) in addition to  $c_f = 200 kPa$  (see Figure 5.43). With regard to Figures 5.43 and 5.48, it is illustrated that defining the final cohesion as  $c_f = 30 kPa$  (equal to the initial cohesion divided by factor 10) improves the numerical predictions - compared to the case with less softening (higher final cohesion) - in the sense that strain localization appear sooner, i.e. during the excavation phase (see the bands activity after one day in Figure 5.48a). Although, more softening does not actually change the localization pattern, with regard to Figures 5.49 and 5.50, except that the localized zone is fairly more extended in the latter simulations. Figure 5.51 presents the increment of deviatoric strain for four simulations at the end of excavation, and after 500 days. Therefore, the value of  $c_f = 30 kPa$  is considered to be appropriate to initiate realistically the strain localization in Boom Clay, similarly to what has been also concluded following our discussion on the biaxial test modeling.

Finally, with respect to  $D = 2 \times 10^3 N$ ,  $\Psi = 0^\circ$ ,  $c_f = 30 kPa$ , and  $B_c = 0.01$  (Figure 5.48), Figures 5.52-5.53 show the results of two other simulations with application of  $B_c = 0.05$  and  $B_c = 0.002$ , receptively. It is observed that using  $B_c = 0.05$  does not essentially change the localization solution in terms of the appearance and development of the shear bands (in comparison with  $B_c = 0.01$ ). On the contrary,  $B_c = 0.002$  creates more localized bands, at the beginning upon initiation of strain localization, with regard to the increased rate of softening that it imposes (compare for instance Figures 5.48b and 5.53b), besides that it made unexpectedly a delay in appearance of the localized bands. In all, we may keep  $B_c = 0.01$ , or equally  $B_c = 0.05$  in our next simulations.

On the whole, taking into account  $D = 2 \times 10^3 N$ ,  $\Psi = 0^\circ$ ,  $c_f = 30 kPa$ , and  $B_c = 0.01$ , Figure 5.54 shows the increment of deviatoric strain as well as the plastic loading index during the computation. Hence, the extension of the localized zone is finally estimated as about 13 m horizontally and 4.4 m vertically.

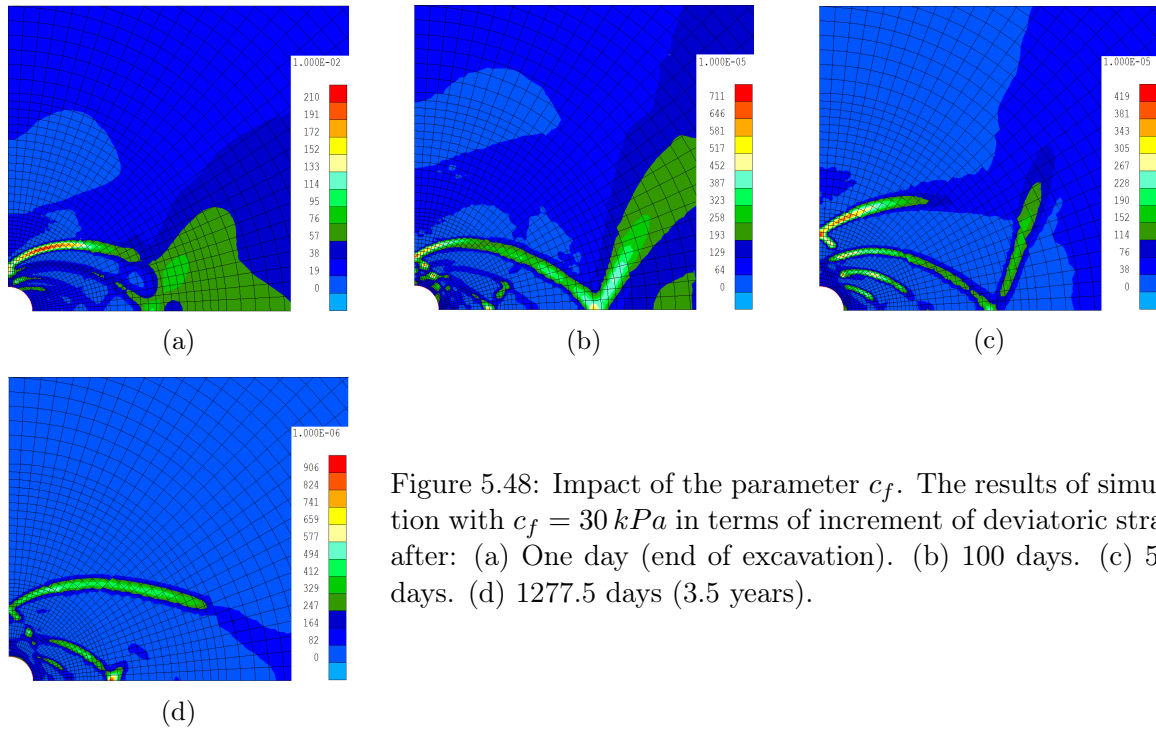


Figure 5.48: Impact of the parameter  $c_f$ . The results of simulation with  $c_f = 30 \text{ kPa}$  in terms of increment of deviatoric strain after: (a) One day (end of excavation). (b) 100 days. (c) 500 days. (d) 1277.5 days (3.5 years).

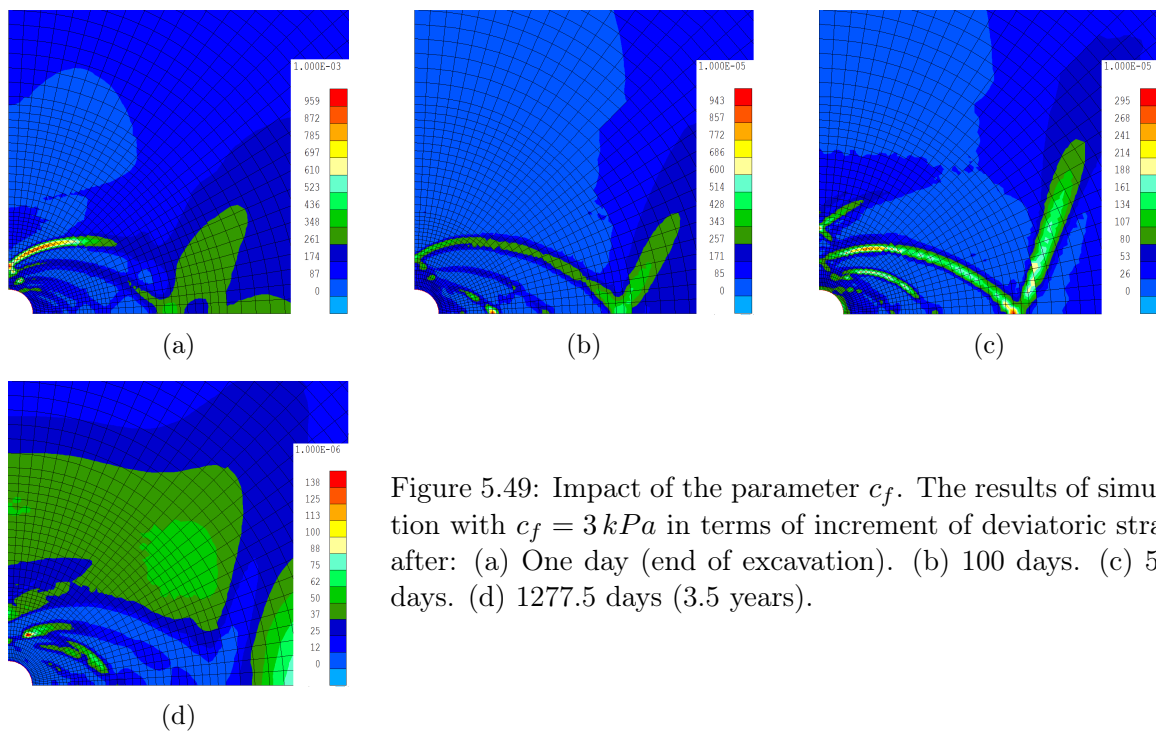


Figure 5.49: Impact of the parameter  $c_f$ . The results of simulation with  $c_f = 3 \text{ kPa}$  in terms of increment of deviatoric strain after: (a) One day (end of excavation). (b) 100 days. (c) 500 days. (d) 1277.5 days (3.5 years).

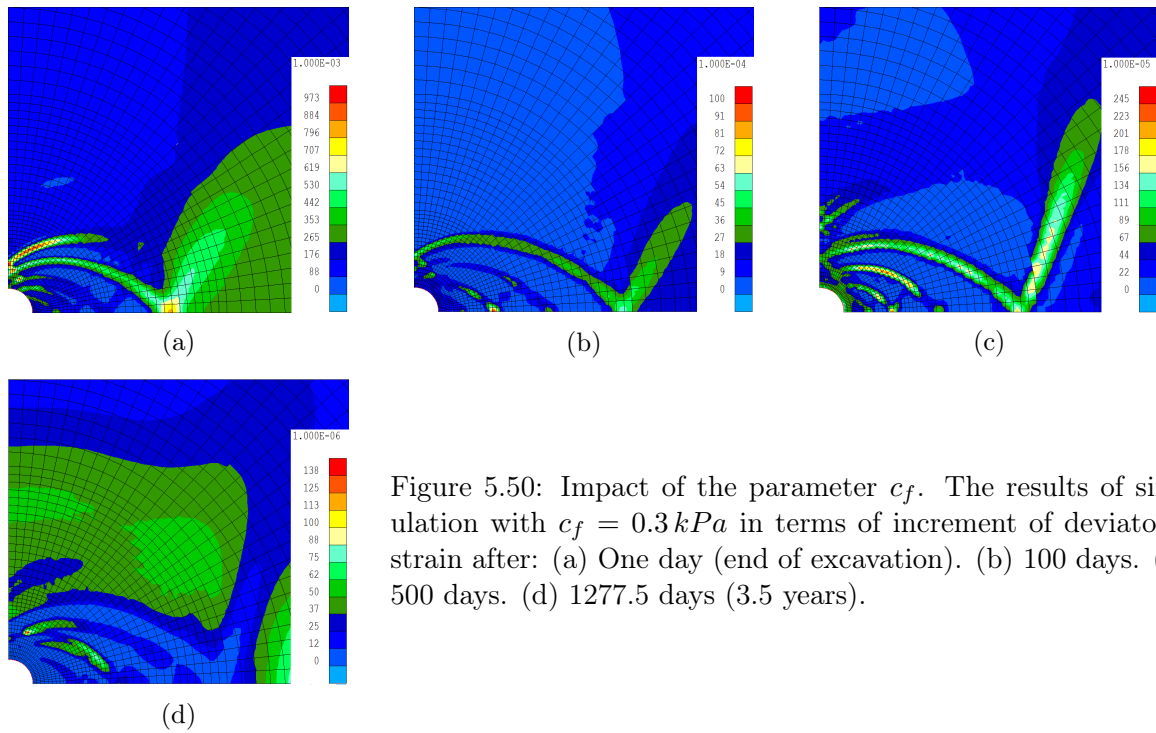


Figure 5.50: Impact of the parameter  $c_f$ . The results of simulation with  $c_f = 0.3 \text{ kPa}$  in terms of increment of deviatoric strain after: (a) One day (end of excavation). (b) 100 days. (c) 500 days. (d) 1277.5 days (3.5 years).

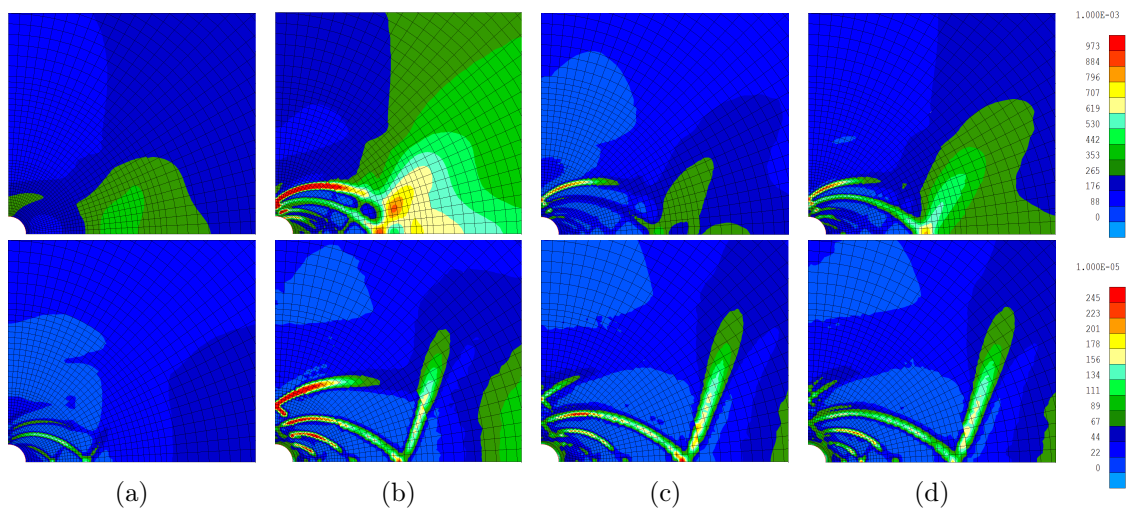


Figure 5.51: Impact of the parameter  $c_f$ . The results of simulation at the end of excavation (top row), and after 500 days (bottom row) in terms of increment of deviatoric strain for: (a)  $c_f = 200 \text{ kPa}$ . (b)  $c_f = 30 \text{ kPa}$ . (c)  $c_f = 3 \text{ kPa}$ . (d)  $c_f = 0.3 \text{ kPa}$ .

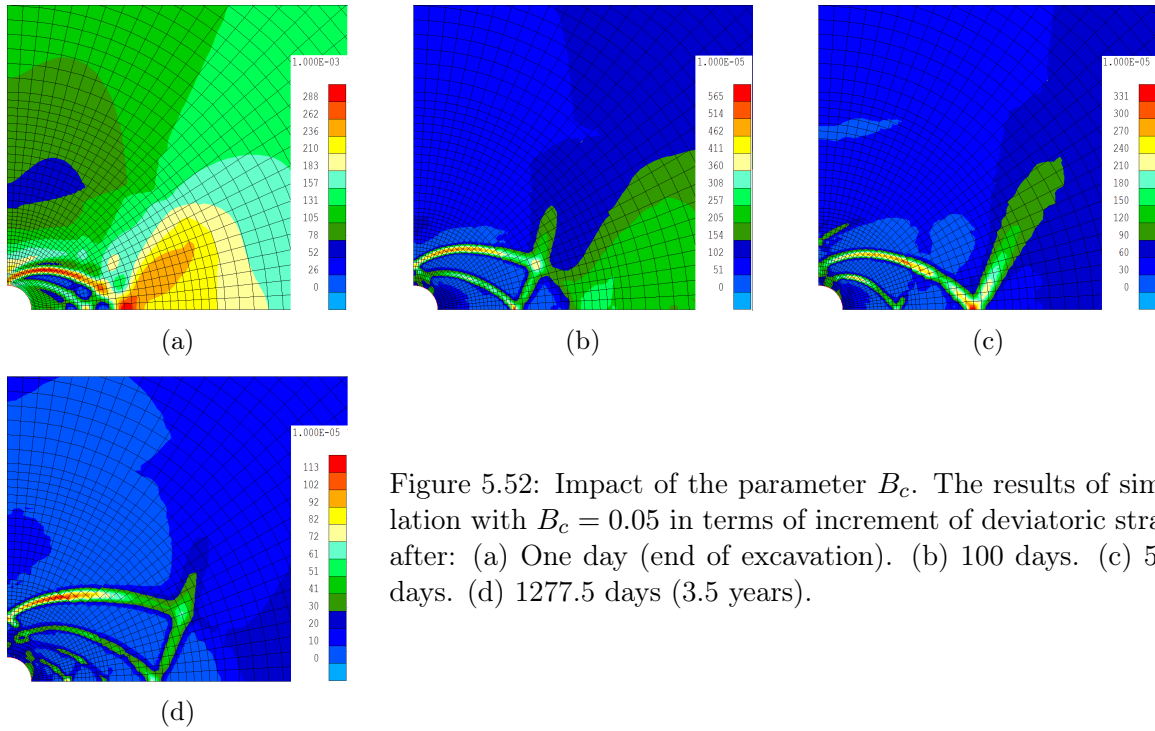


Figure 5.52: Impact of the parameter  $B_c$ . The results of simulation with  $B_c = 0.05$  in terms of increment of deviatoric strain after: (a) One day (end of excavation). (b) 100 days. (c) 500 days. (d) 1277.5 days (3.5 years).

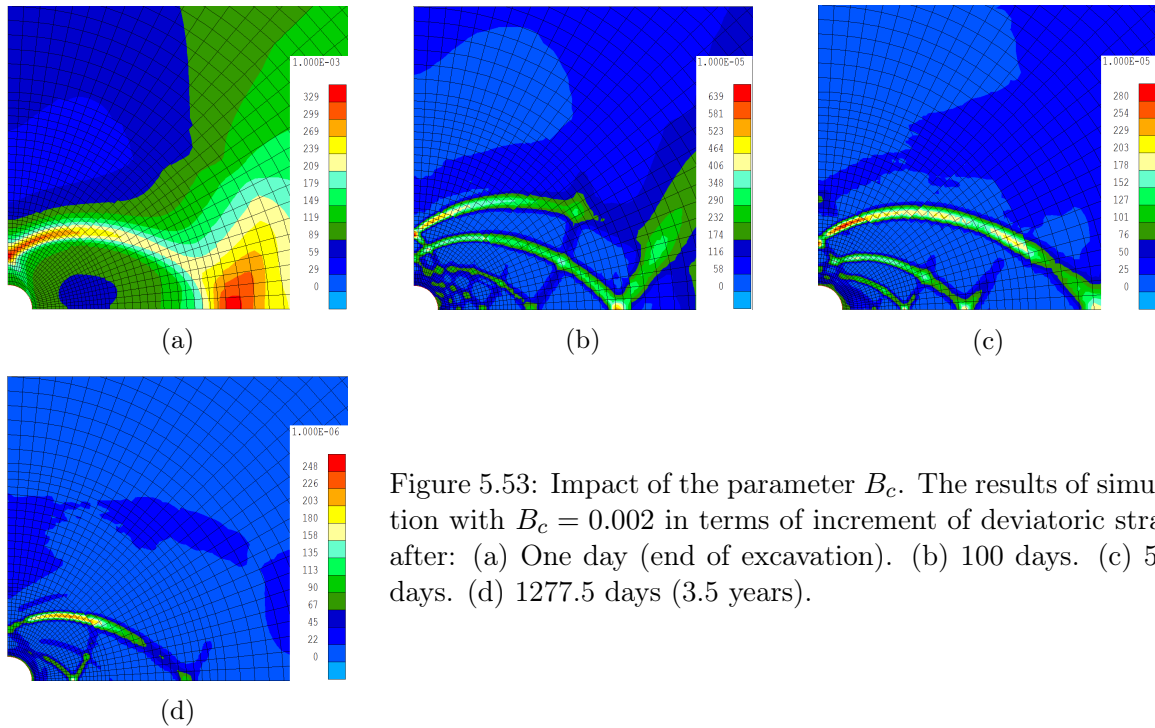


Figure 5.53: Impact of the parameter  $B_c$ . The results of simulation with  $B_c = 0.002$  in terms of increment of deviatoric strain after: (a) One day (end of excavation). (b) 100 days. (c) 500 days. (d) 1277.5 days (3.5 years).

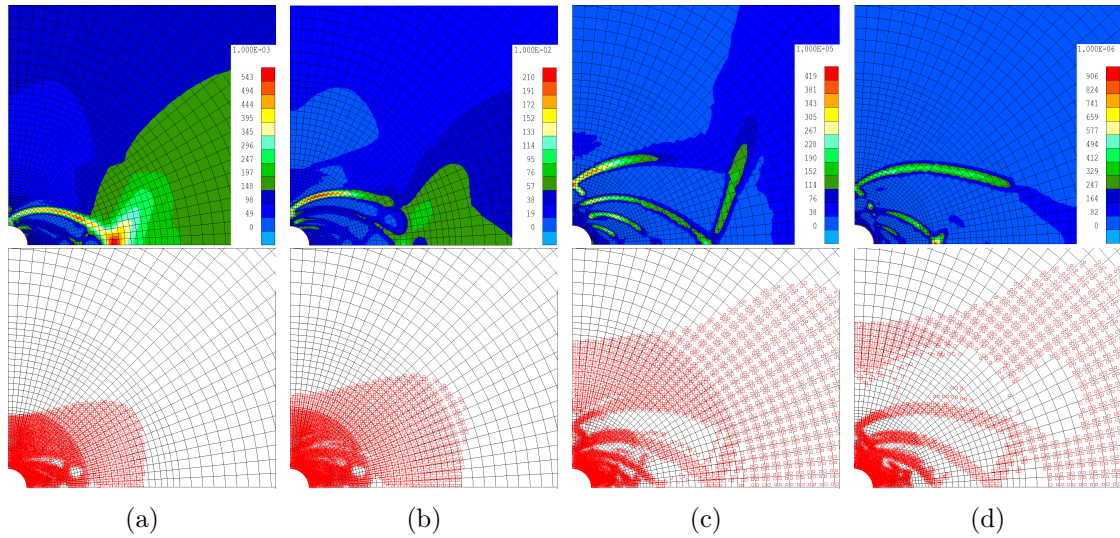


Figure 5.54: Increment of deviatoric strain (top row), and plastic loading index (bottom row) after: (a) 0.85 day. (b) One day (end of excavation). (c) 500 days. (d) 1277.5 days (3.5 years).

#### 5.4.2.4 On the application of variable dilatancy angle

Considering what has been seen with regard to using a constant dilatancy angle through our parametric study, this Section is aimed to illustrate the influence of application of variable dilatancy angle (see Chapter 4) in contrast with a constant value while dealing with the strain localization simulation in the course of a large-scale excavation. Therefore, the simulation with the parameters concluded at the end of our parametric study in the last Section, is compared to two other simulations with  $\Psi = 5^\circ$  and variable  $\Psi$  (see Table 5.3). For the latter simulation, the three main factors of dilatancy angle in the model of variable dilatancy (i.e.  $\Psi_{peak}$ ,  $\Psi_{res}$ , and  $Rat_\Psi$ ) are defined based on the values calibrated with regard to the test IRSM1 in Section 4.2.3.3, which has shown a more realistic stress-strain relationship and post-localization softening behavior. The purely numerical parameters  $B_\Psi$  and  $D_\Psi$  are slightly changed here. A lower value of  $B_\Psi$  is then defined so that it could accelerate the decline process of dilatancy angle after its peak. As a result, it could avoid the problem encountered for simulation of strain localization evolution with a high enough dilatancy angle throughout the excavation (a similar impact as consideration of a constant value, see Figure 5.47).

Given that the creation of the shear bands and the localization of strain is expected to mostly occur during the excavation phase of a gallery, Figures 5.55-5.56 compare how this process could be simulated using a moderate constant dilatancy angle ( $\Psi = 5^\circ$ ), null dilatancy angle and variable dilatancy angle, as defined in Table 5.3. In terms of increment of deviatoric strain<sup>16</sup> (Figure 5.55), it is firstly observed that considering constant dilatancy angle -  $\Psi = 5^\circ$  - did not allow the appearance of strain localization, as it has been already shown in the precedent parametric study. Then, the case with  $\Psi = 0^\circ$  (*Num 2*) could simulate the creation of the localized bands within the excavation period. However, these bands are better formed (and developed), and they are *physically* sooner regularized using the variable dilatancy angle (i.e. the case of *Num 3*). This conclusion can be more obviously perceived in Figure 5.56 where the total deviatoric strain<sup>16</sup> is demonstrated for our three computations. Apart from Figure 5.56a which does not show any created band (application of constant non zero  $\Psi$ ), the results of application of variable  $\Psi$  (i.e. Figure 5.56c) can be compared to the results of simulation with

<sup>16</sup>The results are presented in the same legend scale for the sake of a simpler comparison.

Table 5.3: Mechanical parameters used for the modelings; application of constant and variable dilatancy angle

Parameter	Symbol	Value			Unit
		<i>Num 1</i> - $\Psi = 5^\circ$	<i>Num 2</i> - $\Psi = 0^\circ$	<i>Num 3</i> - Variable $\Psi$	
Young elastic modulus	$E$	300	300	300	$MPa$
Poisson ratio	$\nu$	0.125	0.125	0.125	-
Specific mass of the grains	$\rho_s$	2700	2700	2700	$Kg/m^3$
Initial compression friction angle	$\varphi_{C0}$	8	8	8	$^\circ$
Final compression friction angle	$\varphi_{Cf}$	18	18	18	$^\circ$
Hardening coefficient	$B_\varphi$	0.001	0.001	0.001	-
Hardening coefficient	$D_\varphi$	0	0	0	-
Initial cohesion	$c_0$	300	300	300	$kPa$
Final cohesion	$c_f$	30	30	30	$kPa$
Softening coefficient	$B_c$	0.01	0.01	0.01	-
Softening coefficient	$D_c$	0	0	0	-
Dilatancy angle	$\Psi$	<u>5</u>	<u>0</u>		$^\circ$
Peak of dilatancy angle	$\Psi_{peak}$			<u>8</u>	$^\circ$
Limit of dilatancy angle	$\Psi_{lim}$			<u>-1.5</u>	$^\circ$
Dilatancy ratio	$Rat_\Psi$			<u>-0.06</u>	-
Dilatancy coefficient	$B_\Psi$			<u>0.001</u>	-
Dilatancy coefficient	$D_\Psi$			<u>0.017</u>	-

$\Psi = 0^\circ$  (i.e. Figure 5.56b). Thence, it is observed that using the model of variable dilatancy angle could obviously result in the properly formed localized shear bands while they are more well-constructed in the vicinity of the gallery wall. In fact, in the *Num 3*, close to the gallery wall, these bands could be individually appeared accompanied by an instantaneous dilatancy tendency imposed within them (with respect to the accumulated current plastic strain in the relative zone; see Equation 4.9) while the same process does not occur among these bands. The maximum dilatation tendency indeed lies within the *appearance/onset* of the localized shear bands (in our simulation) or the likely fractures *opening* in the course of a real excavation. The subsequent reduction tendency equally involves in the *physical* regularization of these created bands (see also the discussion thereafter). Consequently, well-formed shear bands are reproduced in the vicinity of the gallery (see also [Salehnia et al., forthcoming]).

Figure 5.57 shows the variation of dilatancy angle, in the simulation *Num 3*, for four random elements within the created localized bands. This variation is demonstrated in function of the time throughout the excavation (see Figure 5.57a), and also in function of the equivalent plastic strain (see Figure 5.57b). With respect to the evolutionary process of strain localization and the creation of the bands in time (see Figure 5.55c), dilatancy angle is varied in each element as observed in Figure 5.57a. The maximum dilatancy angle for each element then coincides with the *onset/appearance* of its corresponding band. With regard to a real gallery excavation, the latter may be interpreted as the maximum dilatation of the rock taken place simultaneously with the fractures opening. Although, this dilatant behavior is not supposed to remain constantly within the fractured zone afterwards. In addition, Figure 5.57b shows that  $\Psi$  is changed for all the elements after attaining the equivalent plastic strain equal to the defined  $D_\Psi$  (=0.017).

Furthermore, effective stress paths of the same elements are presented for three simulations *Num 1*, *Num 2*, and *Num 3*, during the excavation period of one day, in Figure 5.58. The localization solution is accompanied by a reduced shear stress and the material's resistance. This behavior consists in a dominant decrease of the first stress invariant with the decrease of second invariant of deviatoric stress beyond its maximal value along the stress path of the four studied elements, with regard to the simulation *Num 3*. On the contrary, the non-localized

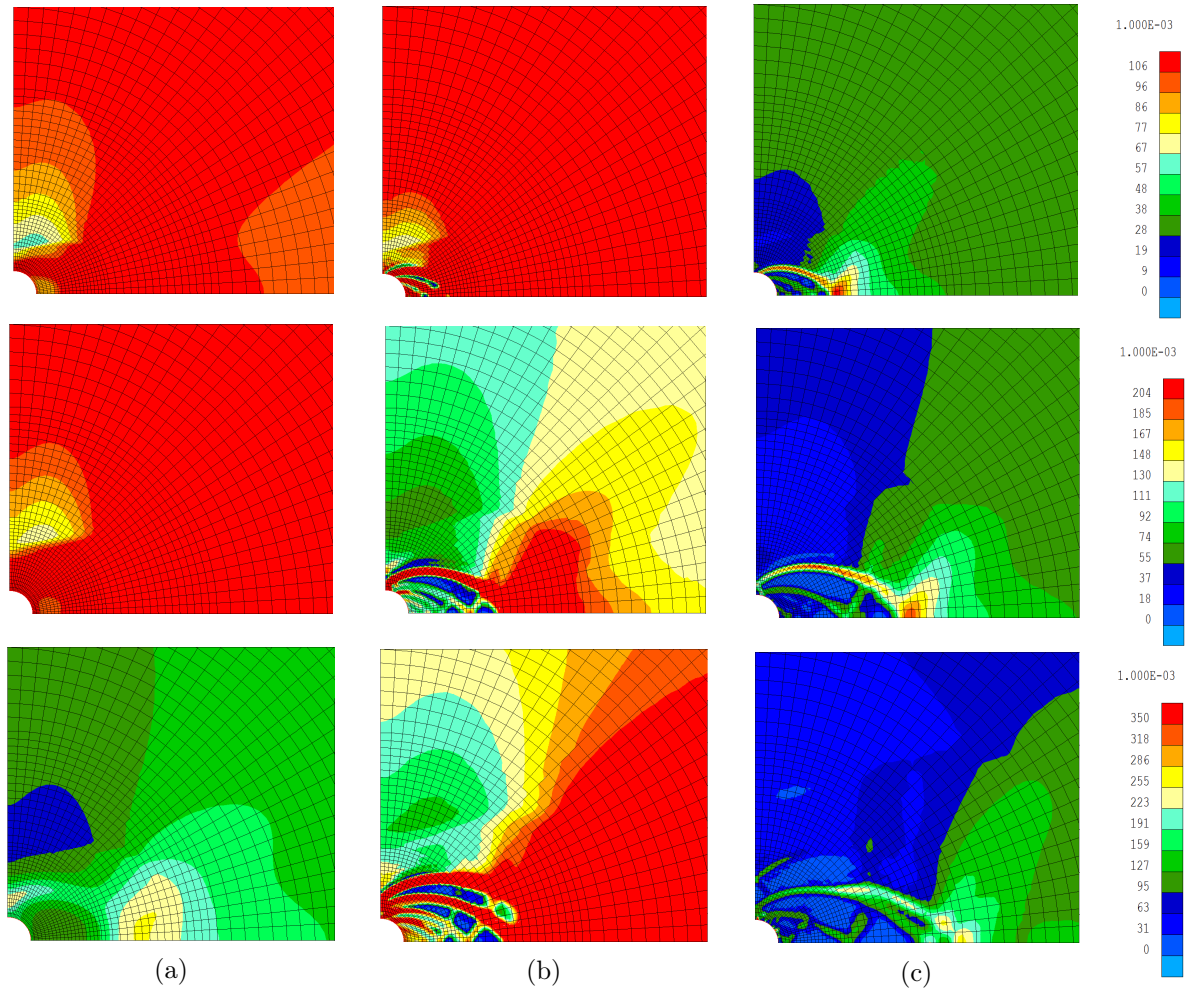


Figure 5.55: Increment of deviatoric strain after 0.65 day (top row), 0.85 day (middle row), and one day (bottom row) for the simulation with: (a) *Num 1* with  $\Psi = 5^\circ$ . (b) *Num 2* with  $\Psi = 0^\circ$ . (c) *Num 3* with variable  $\Psi$ .

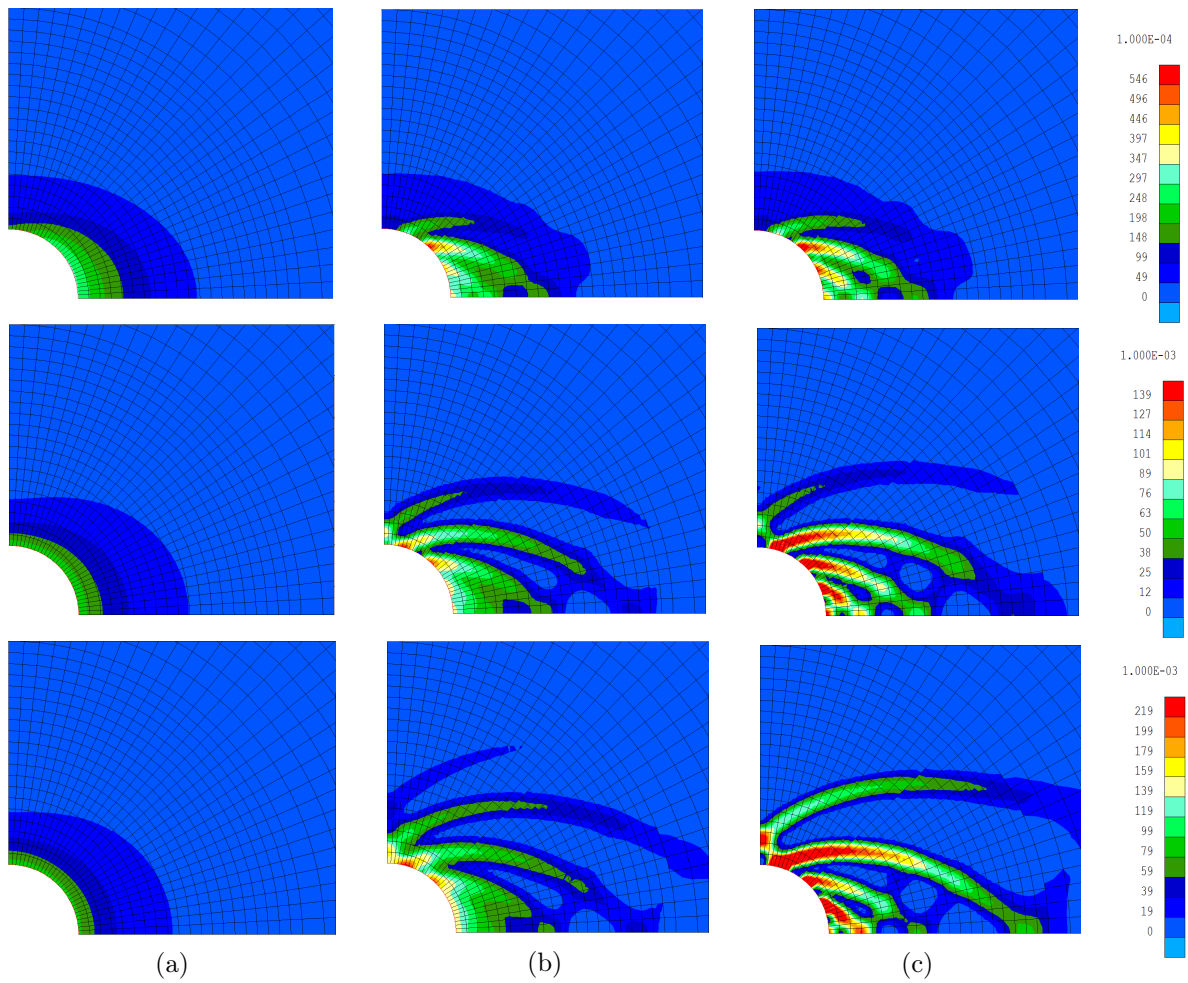


Figure 5.56: Total deviatoric strain after 0.65 day (top row), 0.85 day (middle row), and one day (bottom row) for the simulation: (a) *Num 1* with  $\Psi = 5^\circ$ . (b) *Num 2* with  $\Psi = 0^\circ$ . (c) *Num 3* with variable  $\Psi$ .

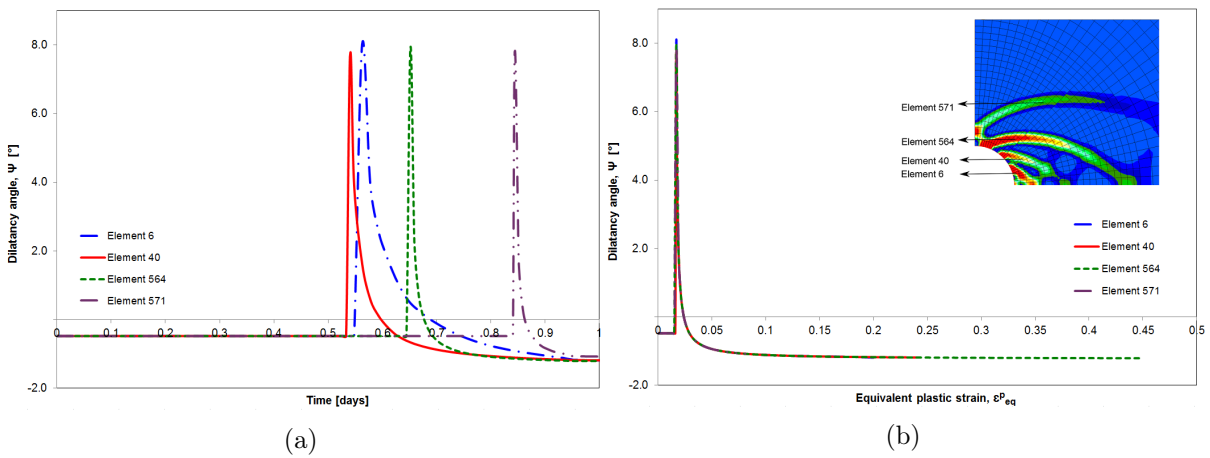


Figure 5.57: The change of dilatancy angles during the excavation phase for the elements 6, 40, 564, and 571 within the localized zone around the gallery. (a) Dilatancy angle in function of the time. (b) Dilatancy angle in function of the equivalent plastic strain.

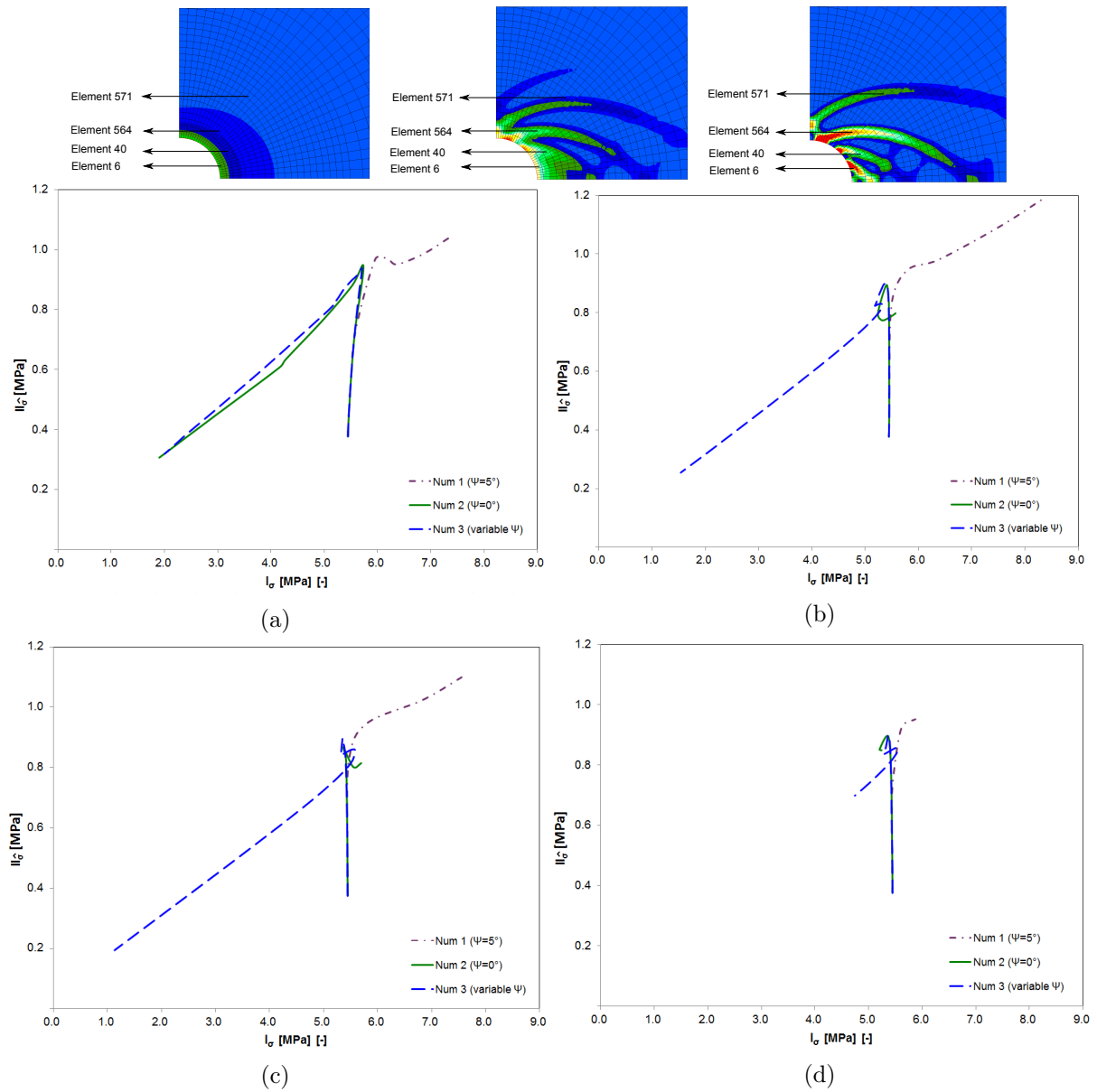


Figure 5.58: Effective stress paths in the  $(I_\sigma, II_\sigma)$  plane for the simulations *Num 1*, *Num 2*, and *Num 3* in: (a) Element 6. (b) Element 40. (c) Element 564. (d) Element 571. The elements position is demonstrated in the top image on the contour of total deviatoric strain in each case.

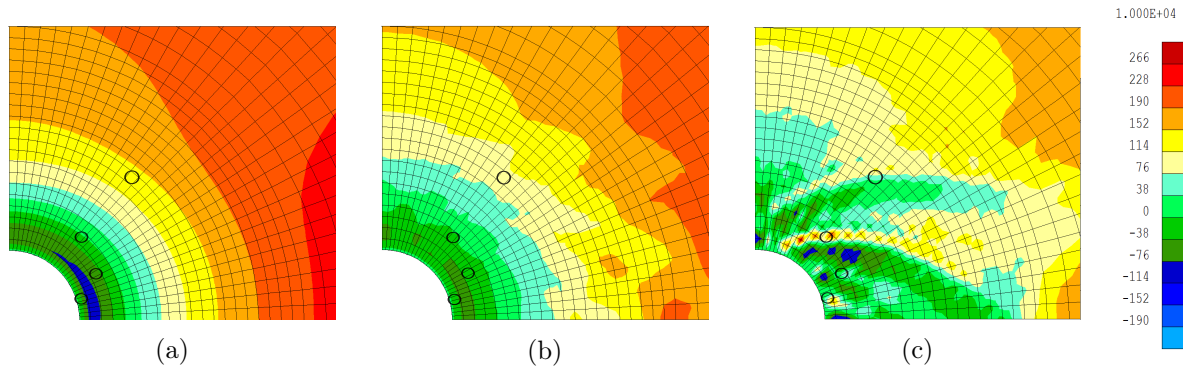


Figure 5.59: Contour of pore water pressure after one day for the simulation with: (a) *Num 1* with  $\Psi = 5^\circ$ . (b) *Num 2* with  $\Psi = 0^\circ$ . (c) *Num 3* with variable  $\Psi$ . The black circles represent the studied elements.

solution corresponding to the application of  $\Psi = 5^\circ$  is illustrated through its opposite-ward stress paths consisting in an increase of the deviatoric stress. In the hydraulic point of view, due to principally the existence of a constant (positive) dilatancy angle, besides the influence of the own excavation and decompression process, the pore water pressure is considerably decreased overall in the vicinity of the gallery (see Figure 5.59a) resulting in an increase of the effective stress. This coupled response is then reflected in the corresponding stress paths.

Keep looking at the whole problem in an hydraulic point of view, regarding the simulation *Num 2*, a decrease of the pore water pressure within a zone around the gallery is still expected due to the decompression, regardless of the defined null dilatancy angle parameter (see Figure 5.59b). It is noteworthy that this phenomenon would be limited if a support is considered on the gallery wall as the result of restriction that it would impose on the material's convergence (see Section 7.4.2). Although, in the current case (*Num 2*), the encountered decrease pattern (local drainage) of pore water pressure within the whole gallery's vicinity could mostly (in the stress path plane) consist in a slight increase of the first stress invariant towards the end of the excavation period. In fact, the coupled hydro-mechanical process seems to limit (or delay) a correct *physical* regularization of the localized shear bands, even though the localization has occurred; see also the relative obtained localization pattern in Figure 5.56 and the comparably less well-formed shear bands. A similar behavior is not demonstrated with regard to the relative stress path of the element 6 since it is located within the plastic zone besides the gallery wall (with an important plastic shear strain) in addition that the boundary condition restricts the pore water pressure on the wall, and the element might not therefore suffer a *relatively* considerable decrease of the pore pressure, i.e. suction tendency, (hence, increase of effective stress).

On the other hand, through application of a variable dilatancy angle, the peak of dilatation tendency, which results in the decrease of pore pressure in the course of excavation and by the onset of the bands, is followed by a diminishing trend (Figure 5.57). This non-constant decreasing  $\Psi$  thus controls the dilatation behavior of the rock. There is some immediate generation of the pore water pressure, and more importantly within the bands, while the redistribution of the pore pressure around the gallery throughout the decompression process is consistently spatially variable (see Figure 5.59c). This hydraulic behavior could then help the *physical* regularization of the shear bands with finite thickness [Thakur, 2011], in addition to the role of strain softening in initiation of the shear strain localization. The result of this response is then reflected on the relative stress paths as well as a better constructed localized shear bands during the excavation period of one day (see Figure 5.56).

## 5.5 Intermediate conclusions

This Chapter focused on the concept of strain localization, and development of the numerical framework for addressing a strain localization problem. At the first part, the concept of shear band and the phenomenon of strain localization were defined indicating that the onset of strain localization could be established by seeking a bifurcation point. Then, some experimental evidences of strain localization were described, with regard to the literature. Also, some well-known experimental techniques used in the laboratory for a better visualization of strain localization were summarized. In this way, some relevant experimental observations of strain localization in Boom Clay were represented as well. Moreover, some in-situ observations of fractures and localization of strain were shown, which have been evidenced through the underground deep excavations in the potential host rocks for geological disposal of high-level nuclear waste. The fracturing pattern observed during the construction of Connecting gallery in Boom Clay at the HADES URL was then described. Consequently, the importance of studying and simulation of development of strain localization in shear planes and analyzing the damaged zone have been illustrated as the inevitable phenomena occurred during the underground excavations in the clay rocks, namely Boom Clay, and they are essential in the framework of long-term safety of deep disposal of high-level radioactive waste.

In the second part of this Chapter, the bifurcation conditions were described. Additionally, our computational approach to treat the strain localization was introduced in the framework of microstructure continuum theory. Thence, the strain localization phenomenon is observed as the appearance of a discontinuity in strain rate (localized shear bands with finite thickness), which can be perceived by the loss of solution uniqueness (satisfaction of bifurcation conditions). Next, the need to use a regularization method in numerical analysis of strain localization was illustrated indicating that the classical finite element suffers from a pathological problem of mesh dependency in dealing with the strain localization problem. In this sense, the concept of continua with microstructures was described, and within this framework, the higher grade continuum theory consisting in the higher deformation gradients was then represented. Hence, it has been said that in this thesis, our material response in the presence of strain localization is being analyzed applying the strain softening constitutive law, which is then regularized in the framework of microstructure continuum theory, using a local second gradient continua. Furthermore, the classical numerical framework has been extended with regard to the coupled local second gradient formulation.

In the third part, two numerical examples were modeled focusing on the strain localization analysis. The drained biaxial compression test was firstly simulated. Through this simulation, the concept of the dependency of the shear bands thickness to the choice of second gradient elastic modulus, and the mesh independent response of the model using the second gradient method were demonstrated. In addition, the impact of the softening parameters in initiation of strain localization and the post-peak response of the material were illustrated through several simulations. The evolution of strain localization was finally visualized during the simulation. As the second example, a gallery excavation, defined by analogy with Praclay gallery, was modeled. A parametric study has been conducted to illustrate the impact of the key parameters in modeling of strain localization, and to eventually choose the appropriate parameters, which will be then used in the future simulation of strain localization. Based on the obtained results, the relevant parameters have been chosen to be added to the set of classical parameter concluded in Chapter 3. Finally, the influence of using the proposed model of variable dilatancy angle (in Chapter 4) in our simulation was demonstrated while the problem was analyzed in a coupled hydro-mechanical point of view. The latter could result in the better formed and well-constructed localized shear bands due to the excavation.

# Chapter 6

## Analysis of the hydro-mechanical behavior of Boom Clay associated with the construction of underground galleries: Application to the Connecting gallery

### Contents

---

<b>6.1</b>	<b>Introduction</b>	<b>186</b>
<b>6.2</b>	<b>Description of the Connecting gallery</b>	<b>186</b>
6.2.1	Construction objective and the applied technique	186
6.2.2	Relative projects	187
<b>6.3</b>	<b>Definition of the numerical model</b>	<b>189</b>
6.3.1	Geometry, initial and boundary conditions	189
6.3.2	Hydro-mechanical properties of the model	190
6.3.3	Simulation of the development of strain localization around the gallery	192
<b>6.4</b>	<b>An analysis of in-situ measurements and research programs</b>	<b>197</b>
6.4.1	Pore water pressure measurements	197
6.4.2	Permeability measurements	205
6.4.3	Strain measurements in the lining	205
6.4.4	Convergence measurements in the lining	207
<b>6.5</b>	<b>Comparison of the extended numerical predictions and in-situ measurements</b>	<b>210</b>
6.5.1	Development of the numerical simulation	210
6.5.2	Fracture characterization	224
6.5.3	Convergence of the rock	226
6.5.4	Numerical results of pore water pressure compared to the in-situ measurements: R55 and R13 boreholes	227
6.5.5	Numerical results of pore water pressure compared to the in-situ measurements: CLIPEX program	230
6.5.6	Numerical results of strain and convergence in the lining compared to the in-situ measurements	235
<b>6.6</b>	<b>Intermediate conclusions</b>	<b>236</b>

---

*Somewhere, something incredible is waiting  
to be known.*

Carl Sagan

## 6.1 Introduction

The argillaceous materials, namely Boom Clay, constitute the natural barrier aimed at confining the nuclear waste and protecting the biosphere from it. Therefore, analysis of their behavior is of significant importance in the framework of studying the feasibility of deep disposal of radioactive waste through them. However, *barrier behavior is highly complex and numerical analysis can be an effective way to bridge the gap between the theoretical and empirical understanding of the individual processes occurring and the resulting overall performance of the barrier*, stated by Gens et al. [1998]. In this sense, performing a large-scale numerical simulation under the conditions similar to those are encountered in the site provides a very useful complement to an analysis of the in-situ and field observations. This issue of paramount interest is aimed at being addressed in this Chapter.

In the framework of analysis of the coupled hydro-mechanical phenomena that take place in the Boom Clay formation during the excavation of Connecting gallery (HADES URL, Mol, Belgium) and afterwards, an introduction is firstly given to the construction scopes of this gallery, the used technique, and the relative research programs. Since around galleries excavated at depth in geological media, the creation of a damaged zone with significant irreversible deformation is generally unavoidable, predicting the extent of this so-called Excavation Damaged Zone (EDZ) and, the fractures' network remains a challenge. Hence, the numerical modeling then addresses the simulation of evolution of the localized shear zones around the gallery while some hydro-mechanical relative phenomena are also discussed. To model the realistic phenomena, a concrete lining is considered on the gallery similarly to the real case in HADES URL.

Besides all the numerical analyses given in the preceding Chapter and the ones which will be conducted in this Chapter and the next one, one other important task of this work has been analyzing an invaluable data library provided during and after the construction of Connecting gallery. This issue of particular importance is addressed in this Chapter as well. It has been then attempted to reproduce these in-situ data, to the best possible extent, through our numerical simulation.

Therefore, in the second part of this Chapter, an analysis of some in-situ measurements of pore water pressure in the clay as well as the strain and convergence in the gallery's lining is conducted. Then, these measurements are compared to the numerical results. To do this, the described model in the first part of this Chapter is developed to consider the material anisotropy and gravity effects. Next, the results of this extended modeling is presented in terms of strain localization evolution and extension of EDZ as well as the displacement and pore water pressure distribution around the gallery. These results are then analyzed in comparison with the in-situ data and observations, and the strengths and weaknesses of the model are discussed. However, some other main aspects of this analysis will be accomplished in Chapter 7 describing the contact mechanism between the clay mass and the lining, and also the phenomena occurred within the lining.

## 6.2 Description of the Connecting gallery

### 6.2.1 Construction objective and the applied technique

Since 1980, studying the feasibility of deep disposal of high-level radioactive waste in Boom Clay formation has been the fundamental scope of construction and development of HADES URL.

Within this framework, with regard to the necessity of using an industrial technique for constructing a real repository in geological media, the construction of 80 *m* long Connecting gallery (see Figures 2.3) was particularly aimed in demonstrating the feasibility of constructing the underground galleries using an industrial technique in poorly indurated Boom Clay [Bastiaens et al., 2003]. In addition to this goal that has been achieved by successful completion of the Connecting gallery project, this construction could supply an opportunity for some other studies. Thanks to the Connecting gallery, the fracturing mechanism due to excavation process could be observed, and many scientific researches have been conducted thereafter to study the characteristics of the fracturing and damaged zone (including this work as well; e.g. see also [Bastiaens et al., 2003; Mertens et al., 2004; Van Marcke and Bastiaens, 2010; Salehnia et al., 2015b]). In addition, many research programs and measurements (e.g. [Bastiaens et al., 2003; Bernier et al., 2007b,a]) have been conducted providing a rich data library with regard to the coupled phenomena occurred during and after the gallery construction, as it will be partly addressed in this Chapter.

The industrial excavation technique chosen for Connecting gallery to minimize the extension of the EDZ was using a tunneling machine consisted of a road header under the protection of a shield (Figure 6.1a). The process of construction of Connecting gallery - including the installation of the gallery's concrete lining which was done quite simultaneously with the gallery excavation - has principally consisted in [Bastiaens et al., 2003] firstly a forward movement of the shield, pushed by jacks resting on the already installed lining while the cutting head ensured a smooth excavation profile. Subsequently, the major surface irregularities were being filled, and the lining segments of the excavated profile behind the shield were being installed (see Figure 6.1c). A minimum construction rate of 2 meters per day (between 2-4 *m* per day) could be achieved in the steady state. The nominal external diameter of the lining is 4.8 *m* while the lining thickness is 40 *cm*. However, a total radial convergence of 9 *cm* has been estimated for the clay during the construction [Bastiaens et al., 2003]. This over-excavation is attributed to the convergence of the clay in the unsupported zone between the rear end of the shield and the installed lining (1 *cm*), at the level of the rear end of the shield (3.5 *cm*), and ahead of the excavation front (4.5 *cm*).

Furthermore, the wedge-block technique has been applied for the gallery's lining. The concrete segments were assembled to form the rings which were then expanded against the excavated clay massif through insertion of one or more key segments [Bastiaens et al., 2003]. The concrete rings of the Connecting gallery's lining includes 10 segments each, in addition to two key segments; see Figure 6.1d. While all the segments have a 40 *cm* thickness, the ten segments are one meter wide and the two key segments are 0.85 *m* wide.

## 6.2.2 Relative projects

Since the construction of Connecting gallery, and the extension of HADES URL, several research programs have been organized leading to a better comprehension of the coupled phenomena occurred in the clay surrounding the gallery, and in the lining. One important program is CLayer Instrumentation Program for the EXtension of an underground research laboratory (CLIPLEX) which has been launched during the construction period of Connecting gallery. This project provided an opportunity to measure the hydro-mechanical response of the clay both ahead of the excavation front of the advancing gallery (during the excavation) and around the gallery (during and partly after the excavation time) that was being excavated by an industrial technique [Bernier et al., 2007b]. One main experimental part of the CLIPLEX program - that will be addressed in this work - consists in acquiring and monitoring the pore water pressure through the relative instrumentation (see Section 6.4.1.1). Within this program, the strain could be also measured

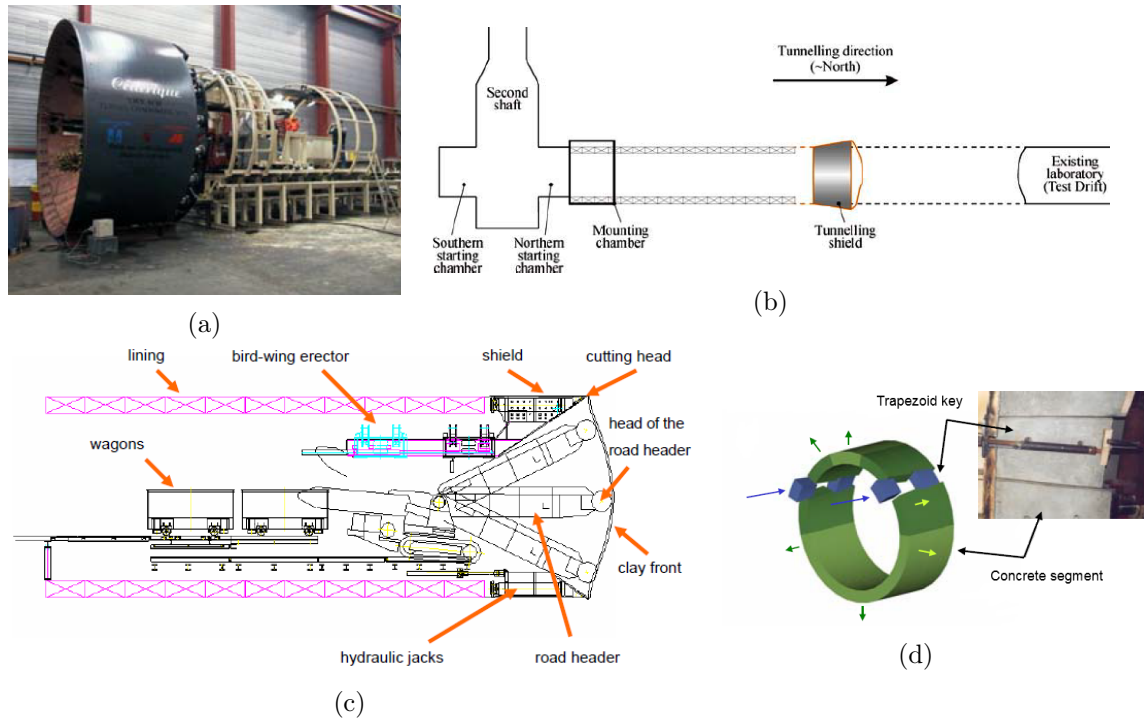


Figure 6.1: (a) The tunneling machine. (b) Tunneling direction of Connecting gallery linking Second shaft to the Test Drift. (c) Simplified sketch representing schematically the tunneling machine in practice. (d) The wedge-block technique [Bastiaens et al., 2003].

through the instrumented gauges in three rings of the gallery’s lining (see Section 6.4.3).

In the framework of the European Commission projects which aimed basically to characterize the EDZ around the underground galleries in clay host rocks, besides the CLIPEX program, the SELFRAC project (FRACtures and SELF-healing within the excavation disturbed zone in Clays) was another conducted program in the HADES URL. This project was mainly aimed to understand the fracturing and EDZ evolution in Boom Clay due to the excavation induced perturbation, and the sealing<sup>1</sup>/healing<sup>2</sup> processes subsequently to the possible important increase of permeability in the fractured zone [Bernier et al., 2007a]. With respect to the latter reference, there have been two multi-piezometers installed outward to the Connecting gallery which have provided the pore water pressure measurements, that are later addressed in this Chapter (see Section 6.4.1.2). Through these piezometers network, some permeability measurements could be performed as well (see Section 6.4.2).

In addition, thanks to some installed sensors in the lining segments of the Connecting gallery, the displacements could be measured in time, after the gallery’s excavation, since December 2004 (see Section 6.4.4).

Prior to the analysis of the aforesaid in-situ data, within the framework described in Section 6.1, the basic numerical modeling is firstly focused in the following.

<sup>1</sup>Sealing is defined as the reduction of fracture permeability by any of hydro-mechanical, hydro-chemical or hydro-biochemical process. It then considered as the closure of the newly formed/reactivated discontinuities while the stress transfer is possible across the discontinuities (no structural change) [Bernier et al., 2007a].

<sup>2</sup>Healing is defined as sealing with loss of memory of the pre-healing state. Thence, the healed fractures would not necessarily be the preferred site for new fracturing. On the contrary to sealing, the structural change occurs across the discontinuities [Bernier et al., 2007a].

## 6.3 Definition of the numerical model

### 6.3.1 Geometry, initial and boundary conditions

The two-dimensional mesh geometry and the boundary conditions of the model are shown in Figure 6.2. At this stage, a quarter of the gallery is modeled assuming symmetry along x- and y-axes, in the plane strain state. The gallery has a total excavated radius of 2.49 m taking into account 40 cm of the concrete lining and 9 cm of the gap between the clay mass and the lining. The latter is attributed to the over-excavation radius, as described in Section 6.2.1. In fact, this pre-introduced gap between two bodies in our two-dimensional model is supposed to take into account implicitly the evidenced clay convergence on the radius, during the construction, in the site. The concrete lining is one of the most significant feature about the Connecting gallery, excavated in the plastic Boom Clay layer. Thence, it is considered in our modeling to simulate the realistic phenomena while its impacts on the evolution of damaged zone around the gallery, and the contact phenomena<sup>3</sup> on the interface between the clay mass and the lining are illustrated later in this Chapter and more particularly in Chapter 7; see also [Salehnia et al., 2015a,b].

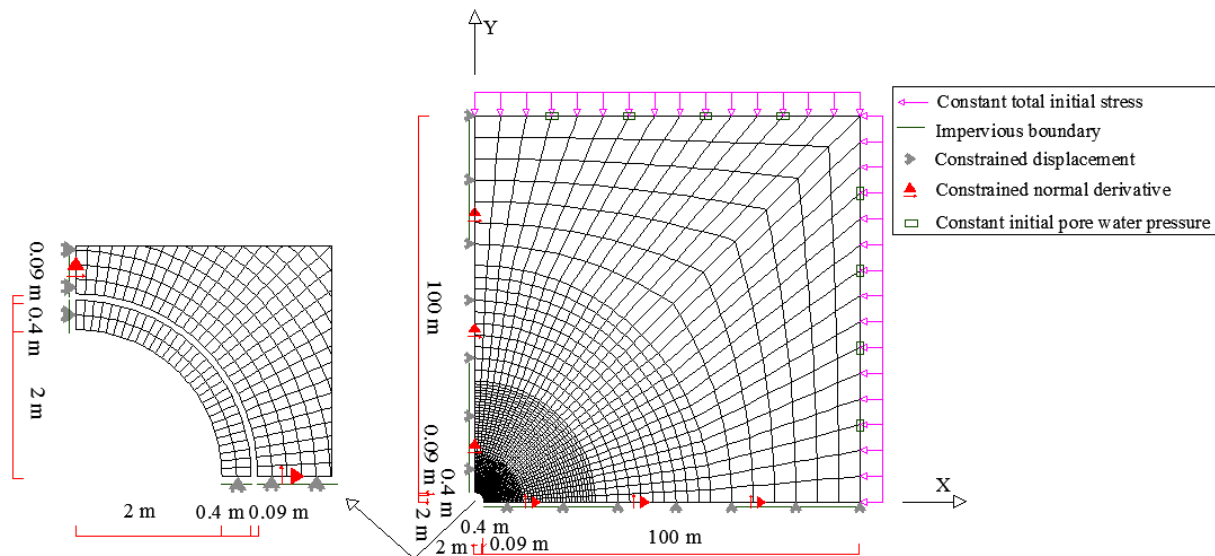


Figure 6.2: The mesh geometry and boundary conditions of the model. A close-up on the gallery's proximity is shown in the left-hand side.

The boundary conditions are defined similarly to the model of Praclay gallery, described in Section 5.4.2.2. In an alike manner, the initial stresses and pore water pressure of the clay mass are defined in the model based on the site measurements. The anisotropic total stresses are applied as  $\sigma_{yy} = 4.5 MPa$  and  $\sigma_{xx} = 3.8475 MPa$  - i.e. earth pressure's coefficient at rest equal to  $K_0 = 0.855$  - which are decreased to 100 kPa (atmospheric pressure) on the gallery wall during the excavation phase (6 days) and remain constant until the end of simulation (3.5 years) (see Figure 6.3). In addition, the initial pore water pressure is equal to 2.25 MPa followed by a decrease up to the atmospheric pressure on the gallery wall during the excavation phase. Since the convergence of the clay mass due to the excavation is mostly taken place during the excavation phase, it is supposed that the contact between clay and the lining occurs by there (illustrated in Section 7.4.3). From then on, the water pressure remains constant (equal to the atmospheric pressure) on the lining intrados. It must be noted that the progressive release of the

<sup>3</sup>In the numerical point of view, the lining is in fact inactive before this contact occurs.

initial stresses and pore water pressure on the gallery wall is introduced in our 2D plane strain model in order to account for 3D impact of the excavation front in its proximity.

Moreover, the excavation time interval (i.e. 6 days), during which the boundary forces and pore pressure are released, has been considered based on the reported excavation advance rate, and some measurements of pore water pressure in [Bastiaens et al., 2003]. In fact, assuming realistically that face effects on displacements extend up to a tunnel length of 3 diameters, the aforementioned excavation time interval (6 days) is consistent with the face advance rate of 2-4 *m* per day for Connecting gallery. Also, with regard to the in-situ pore water pressure recorded by some filters during the CLIPEX program (see for instance Figure 6.11a), the impact of excavation face on the measured pore pressures has mostly occurred since about 6 days before that the front of excavation crosses the position of each filter. Therefore, the choice of excavation period equal to 6 days in our 2D modeling seems realistic in order to account for the 3D effects ahead of the excavation front.

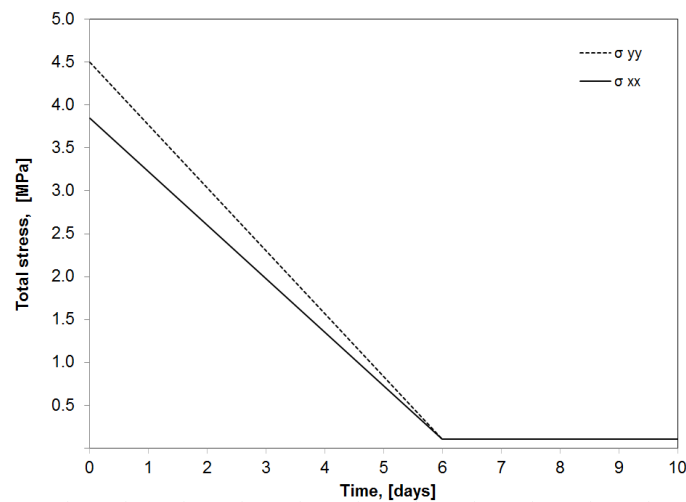


Figure 6.3: Imposed total stresses on the gallery wall.

## 6.3.2 Hydro-mechanical properties of the model

### 6.3.2.1 Mechanical part

Based on the parametric study described in Section 5.4.2.3, Table 6.1 lists the mechanical parameters used for the clay. Thence, they are once again consistent with the main parameters governing the behavior of Boom Clay in all previous modelings (i.e. triaxial test, biaxial test and the gallery excavation). In this sense, the isotropic properties are considered for the clay at this stage, and in Section 6.5.1, the model will be then developed to take into account the material anisotropy as well. In addition, Tables 6.2-6.3<sup>4</sup> introduce the mechanical parameters chosen for the concrete lining and the interface in our model. With regard to the lining, it must be noted that a simple elastic constitutive law using the total stresses is applied to model the concrete behavior.

<sup>4</sup>These parameters will be described in Chapter 7 focusing on the interfaces.

Table 6.1: Boom Clay mechanical parameters of the model

Parameter	Symbol	Value	Unit
Young elastic modulus	$E$	300	$MPa$
Poisson ratio	$\nu$	0.125	-
Specific mass of the grains	$\rho_s$	2700	$Kg/m^3$
Initial compression friction angle	$\varphi_{C0}$	8	$^\circ$
Final compression friction angle	$\varphi_{Cf}$	18	$^\circ$
Hardening coefficient	$B_\varphi$	0.001	-
Hardening coefficient	$D_\varphi$	0	-
Initial cohesion	$c_0$	300	$kPa$
Final cohesion	$c_f$	30	$kPa$
Softening coefficient	$B_c$	0.05	-
Softening coefficient	$D_c$	0	-
Dilatancy angle	$\Psi$	0	$^\circ$
Second gradient elastic modulus	$D$	2000	$N$

Table 6.2: Concrete mechanical parameters of the model

Parameter	Symbol	Value	Unit
Young elastic modulus	$E$	43305	$MPa$
Poisson ratio	$\nu$	0.25	-
Specific mass	$\rho$	2500	$Kg/m^3$

### 6.3.2.2 Hydraulic part

The hydraulic parameters governing the coupled hydro-mechanical behavior of the clay mass are presented in Table 6.4. In addition, Tables 6.5-6.6<sup>4</sup> list the hydraulic parameters of the model for the concrete lining and the interface. It has been already mentioned in Section 3.2.3.1 that Boom Clay remains in the saturated state in our modelings all through this thesis, although, there may be the case where the rock sustains some negative pore pressure. The latter case is linked to the definition of water retention curve and the corresponding air entry value in the modelings. That is to say that the air entry value of the (natural) Boom Clay is quite high so that it does not actually experience a real desaturation even in the state with some negative pore pressure (consisting in a suction less than the air entry value). This condition (i.e. existence of the negative pore pressure while the state is fully saturated) could be observed during the gallery excavation, as it will be demonstrated in this Chapter. In this sense, the air entry value and the parameters' values of the water retention curve<sup>5</sup>, with respect to the Van Genuchten approach [Van Genuchten, 1980] (see Equation 6.1 and Table 6.4), have been calibrated for Boom Clay in our simulations based on some former experimental works.

$$S_r = S_{r,res} + (S_{r,s} - S_{r,res}) \frac{1}{[1 + (\alpha s)^n]^m}, \quad (6.1)$$

Table 6.3: Interface mechanical parameters of the model

Parameter	Symbol	Value	Unit
Penalty coefficient on contact pressure	$K_N$	$3 \times 10^9$	$Pa.m^{-1}$
Penalty coefficient on contact friction	$K_T$	$3 \times 10^9$	$Pa.m^{-1}$
Coulomb friction coefficient	$\mu$	0.2	-

<sup>5</sup>That it could control the change in degree of saturation for the suctions beyond a defined air entry value (see Section 3.2.3.1).

where  $S_{r,res}$  is the residual value of degree of saturation,  $S_{r,s}$  is the saturated value of degree of saturation ( $=1$ ).  $\alpha$ ,  $m$ , and  $n$  are the model's parameters so that  $m = 1 - 1/n$ .

Table 6.4: Boom Clay hydraulic parameters of the model

Parameter	Symbol	Value	Unit
Water permeability	$k$	$3 \times 10^{-19}$	$m^2$
Specific mass of water	$\rho_w$	$1 \times 10^3$	$Kg/m^3$
Porosity	$n$	0.39	-
Water compressibility	$\frac{1}{\chi_w}$	$5 \times 10^{-10}$	$Pa^{-1}$
Water dynamic viscosity	$\mu$	$1 \times 10^{-3}$	$Pa.s$
Atmosphere pressure	$P_{atm}$	$1 \times 10^5$	$Pa$
Van Genuchten parameter	$m$	0.47	-
Van Genuchten parameter	$n$	1.887	-
Van Genuchten parameter	$\frac{1}{\alpha}$	7	$MPa$
Residual water degree of saturation	$S_{r,res}$	20	%

Table 6.5: Concrete hydraulic parameters of the model

Parameter	Symbol	Value	Unit
Water permeability	$k$	$4 \times 10^{-17}$	$m^2$
Porosity	$n$	0.15	-

Table 6.6: Interface hydraulic parameter of the model

Parameter	Symbol	Value	Unit
Transverse transmissivity	$T_w$	$1 \times 10^{-12}$	$m/Pa.s$

Figure 6.4 represents the referred experimental results while a synthesis of these results have been shown besides the corresponding calibrated numerical curve, in the *Suction* –  $S_r$  plane, in Figure 6.5. The results obtained at ENPC [Tinh, 2008] indicate that the samples subjected to the suction equal to 2.8-4.2  $MPa$  remained saturated estimating an air entry value of about 5  $MPa$ . In fact, a relatively high suction could be observed without inducing considerable desaturation of the material (i.e. large AEV). This aspect has been said to be a consequence of the shrinkage undergone by the material during drying so that despite loosing water, the material could undergo volume reduction as well. As the result, it could still have a relatively high degree of saturation. Nevertheless, the obtained curve shows a saturation degree of 90-100% for the suction less than 1  $MPa$  along the wetting path (see Figure 6.4a, or equally 6.5). This aspect has caused by a less precise used volume measurement technique based on the latter reference<sup>6</sup>. Moreover, with respect to the results obtained at UPC [Amorim, 2011], important changes in water content occurs when total suction is above 4  $MPa$  (indicating the AEV). In addition, the results obtained at EPFL during the TIMODAZ project [TIMODAZ, 2010b] estimated an air entry value of 3  $MPa$  for Boom Clay at the ambient temperature. With respect to all these results, the numerical calibration has been then performed as it can be observed in Figure 6.5.

### 6.3.3 Simulation of the development of strain localization around the gallery

Figure 6.6 presents the results of simulation, in terms of increment of deviatoric strain, plastic loading index and total deviatoric strain, during the excavation period (at 4, 5, and 6 days)

---

<sup>6</sup>Further information can be found in [Tinh, 2008] upon interest.

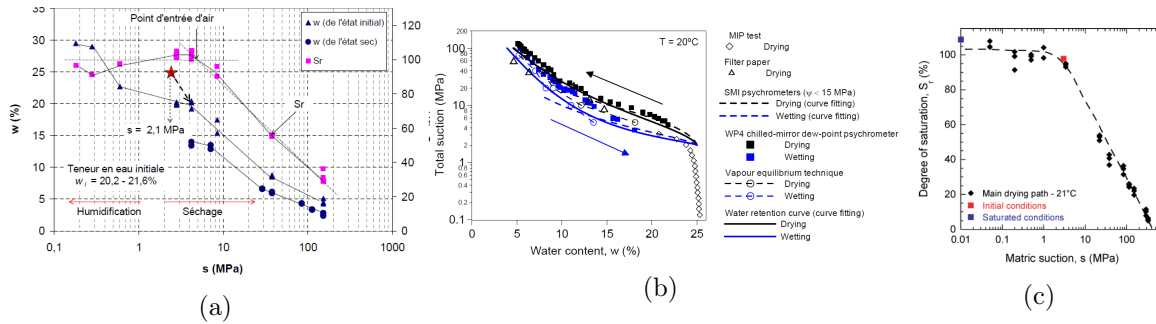


Figure 6.4: Experimental water retention curves for Boom Clay obtained at: (a) ENPC-CREMES [Tinh, 2008]. (b) UPC [Amorim, 2011]. (d) EPFL [TIMODAZ, 2010b].

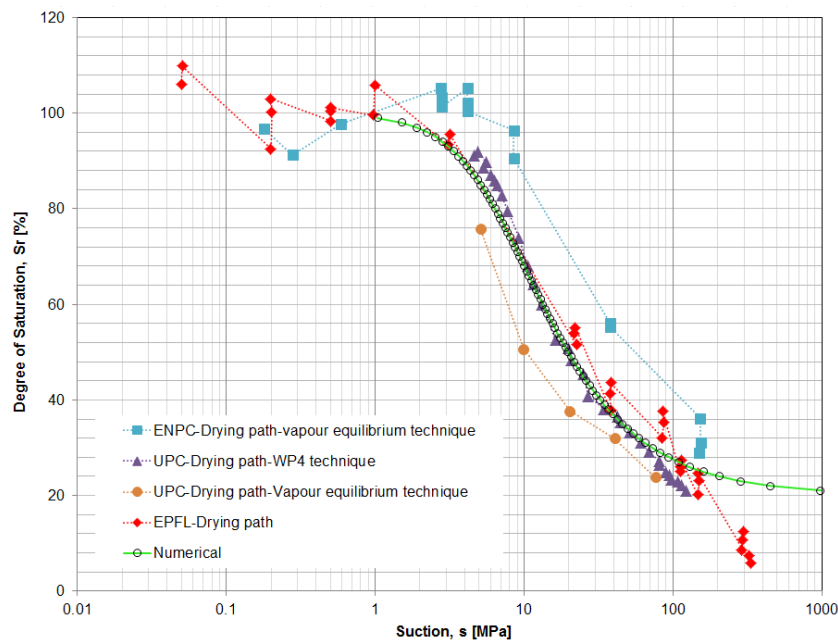


Figure 6.5: Synthesis of the experimental water retention curves, and the relative calibrated numerical curve.

and at the end of 3.5 years, in the radius of 10  $m$  from the gallery wall. The activity and the evolutionary appearance and disappearance (inactivity) of the localized bands in different time steps can be observed through the contours of increment of deviatoric strain. They show that the shear bands are created at about 4 days and since then, some of them are getting inactive or less active while some new ones are weakly created. In fact, this evolutionary process of the localized shear bands is almost limited to the excavation time since the increment of deviatoric strain does not show any remarkable activity of the shear bands after 6 days (see the contour of increment of deviatoric strain in Figure 6.6d). In addition, plasticity index indicates the appearance of plasticity at the excavation time which is followed by the elastic unloading at some Gauss points giving birth to the adjacent localized bands. The plastic loading index also corresponds to the computed response observed in the current time step. Hence, the current activity of the localized shear bands is quite reflected on the plastic points in each time step. Consequently to all this development process, total deviatoric strain which lies in the accumulation of the whole activity of the shear bands does not demonstrate any considerable change after the end of excavation (compare Figures 6.6c and 6.6d).

Moreover, the above behavior is also illustrated in Figure 6.7 where the bifurcation solution is

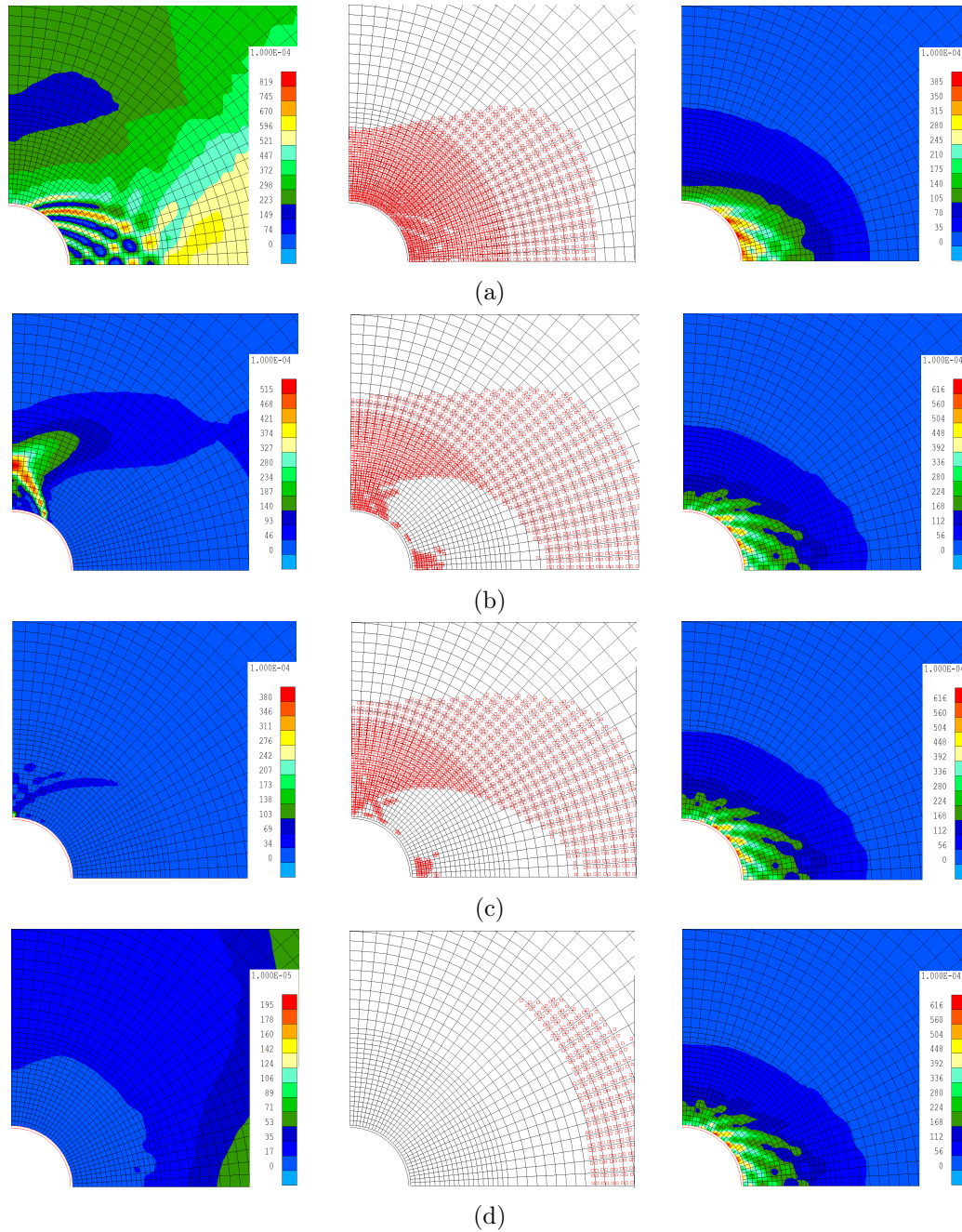


Figure 6.6: Increment of deviatoric strain (in the left side), plastic loading index (in the middle), and total deviatoric strain (in the right side) after: (a) 4 days. (b) 5 days. (c) 6 days (end of excavation). (d) 3.5 years.<sup>7</sup>

<sup>7</sup>The concrete lining is not shown in these contours (and in the similar results hereafter) for the sake of visibility, although, the red line below the gallery wall shows its boundary surface.

shown after 4 days (bifurcation has reached), 5 days, 6 days, and 3.5 years (with no bifurcated element); the displayed green and red arrows estimate graphically two potential inclinations of shear bands.

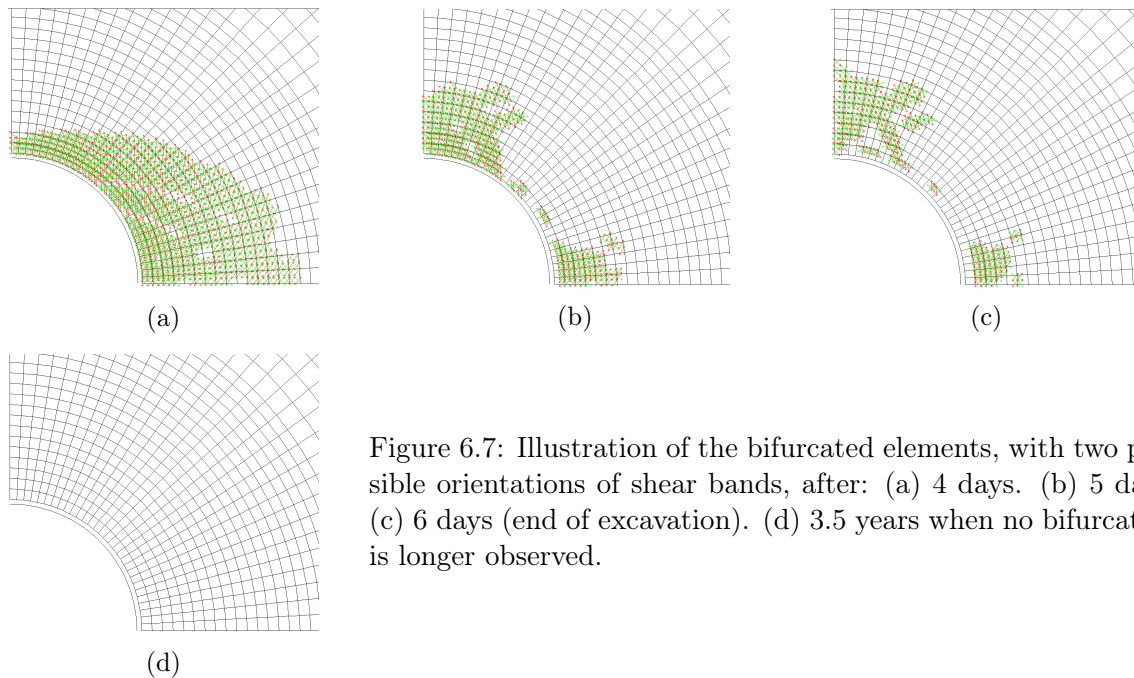
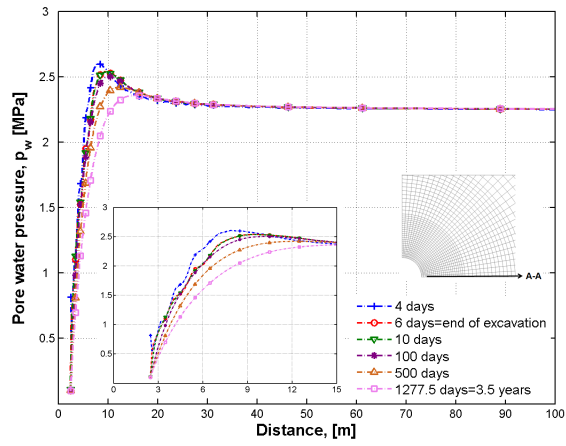


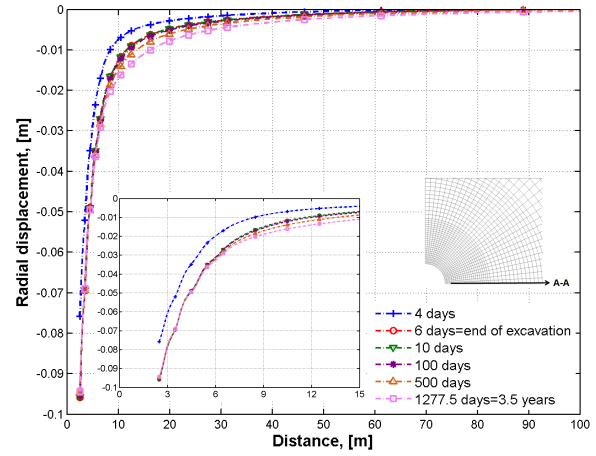
Figure 6.7: Illustration of the bifurcated elements, with two possible orientations of shear bands, after: (a) 4 days. (b) 5 days. (c) 6 days (end of excavation). (d) 3.5 years when no bifurcation is longer observed.

Furthermore, the obtained localization solution shows obviously the anisotropic response of the clay. This is associated to the introduced initial stress anisotropy and also the loss of symmetry that can be induced through the localization process. Finally, with regard to the total deviatoric strain after the end of excavation phase which can be the reference of the extension of localized zone (the shear bands do not have any distinguished activity afterwards), this extension is estimated about 3 *m* horizontally and 0.8 *m* vertically. The low extension of EDZ is of course associated to the existence of the lining which does not allow more development of the localized shear bands upon its contact with the clay; a detailed discussion on the influence of the lining will be given in Section 7.4.

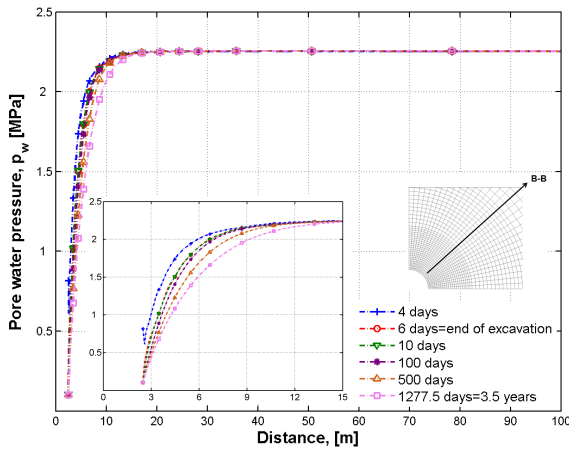
Moreover, the evolution of pore water pressure and radial displacement is shown in Figures 6.8 and 6.9 along three cross-sections - horizontal, inclined ( $45^\circ$ ) and vertical - in function of the distance from the gallery (axis), and at different times during the simulation. The results are presented for a total radius of 100 meters around the gallery, in addition to a close-up of the results in the vicinity of the gallery wall. First of all, the impact of localized bands could be observed through some fluctuations in the pore pressure variations pattern around the gallery wall where some localization has actually occurred. Thence, some ups and downs signify the appearance and the so-called disappearance (inactivity) of the localized bands. These fluctuations are mostly noticed along the horizontal direction with more development of localized bands (see Figure 6.8a). In terms of the pore pressure variations, an overall increase of the pressure approaching its initial value is observed by getting far from the gallery, along all three cross-section, because of the less influence of excavation process. Very close to the gallery wall, some decrease of pore water pressure is noticed during the excavation (see the curves of 4 and 6 days) with respect to the evolution pattern of localized bands in time (see Figure 6.6) and an immediate dilatancy tendency that it might impose (with regard to decompression of the clay). However, in a relatively more extended zone around the gallery wall, there is an increase of pore pressure along the horizontal direction simultaneously with a local decrease of pore



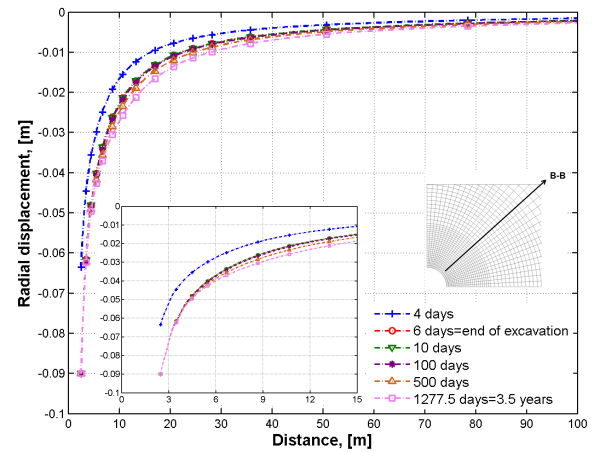
(a)



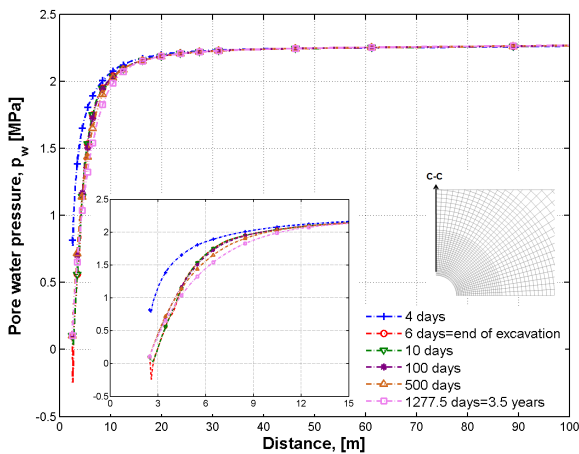
(a)



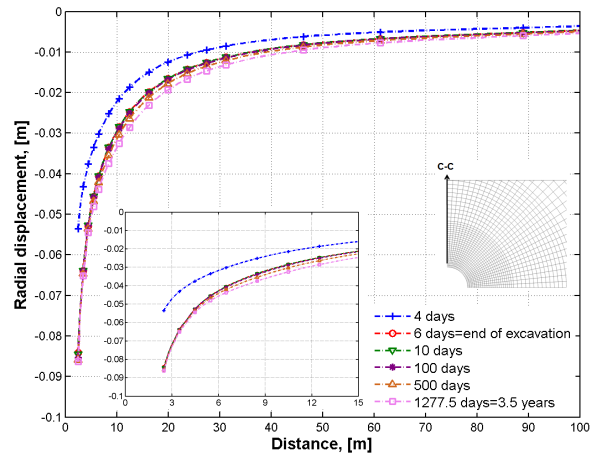
(b)



(b)



(c)



(c)

Figure 6.8: Pore water pressure evolution along (a) Horizontal cross-section A-A. (b) Inclined (45°) cross-section B-B. (c) Vertical cross-section C-C.

Figure 6.9: Radial displacement evolution along (a) Horizontal cross-section A-A. (b) Inclined (45°) cross-section B-B. (c) Vertical cross-section C-C.

pressure along the vertical cross-section. It must be noted that the material remains still in the saturated state even though some negative pore pressure is attained in the vertical proximity of the gallery (see Section 6.3.2.2). The response of the material in the hydraulic point of view (consisting in the obtained negative pore pressure or increase of the pore pressure from its initial value) is consistent with its mechanical behavior, i.e. hydro-mechanical coupling. In fact, due to the anisotropic response and convergence of the clay, it primarily comes into contact with the lining from the horizontal side<sup>8</sup> where the localized shear bands are firstly created (see the increment of deviatoric strain in Figure 6.6a). Then, the horizontal displacement of the rock is restricted and such global decrease of pore pressure in the gallery's proximity - which could be caused by excavation - is not observed. Since then, the localization process seems to be more accentuated along the vertical direction (compare the increment of deviatoric strain in Figure 6.6b to Figure 6.6a) where the clay is still supposed to be converged towards the lining, followed by some decrease of pore pressure (until a slight negative value). Eventually, a local drainage process towards the equilibrium, specially along the horizontal direction where a quite considerable increase of pore pressure has primarily occurred, can be interpreted through the decreasing pattern of the pressure in the long time.

In addition, considering Figure 6.9, it is observed that most of the displacement of the clay close to the gallery wall occurs during the excavation time. This radial displacement (or, half convergence under the assumption of the symmetric response) is more important along the horizontal axis than the vertical one indicating the anisotropic convergence of the massive (see also Section 6.5.3). This anisotropic convergence specifies the ovalization pattern of deformation of the clay during the excavation.

## 6.4 An analysis of in-situ measurements and research programs

It must be noted that all the in-situ data presented in this Section have been collected and provided to us by EIG EURIDICE. Interested readers may also see [Bastiaens et al., 2003; Bernier et al., 2007b,a; Bastiaens et al., 2007].

### 6.4.1 Pore water pressure measurements

#### 6.4.1.1 CLIPEX program

During the excavation time of Connecting gallery, pore water pressure has been monitored by the instrumentation installed both ahead of the excavation front of the advancing gallery and around the gallery. Figure 6.10a shows the location of the instrumented boreholes, in the y-z plane, for measuring the pore water pressure in the framework of CLIPEX program. These boreholes were principally installed out of the preceding excavated Test Drift (TD) in order to provide the data ahead of the excavation front and along the gallery axis, with respect to the excavation direction (towards the TD, see Figure 6.10a). However, given our two-dimensional numerical model of Connecting gallery in the plane strain conditions, the measurements provided by the filters of the boreholes A2 (aligned with the gallery axis) and B2 (almost parallel to the gallery axis), could not be addressed in comparison with the numerical predictions. On that accounts, the reference boreholes in our study have been the boreholes C2 and D2, which have a slight angle with the vertical y-axis and horizontal x-axis, respectively (see Figure 6.10b). In addition, with regard to the position of the boreholes A2 and B2 (i.e. aligned with/parallel to the gallery axis),

---

<sup>8</sup>This evolution of contact phenomenon will be illustrated in Chapter 7.

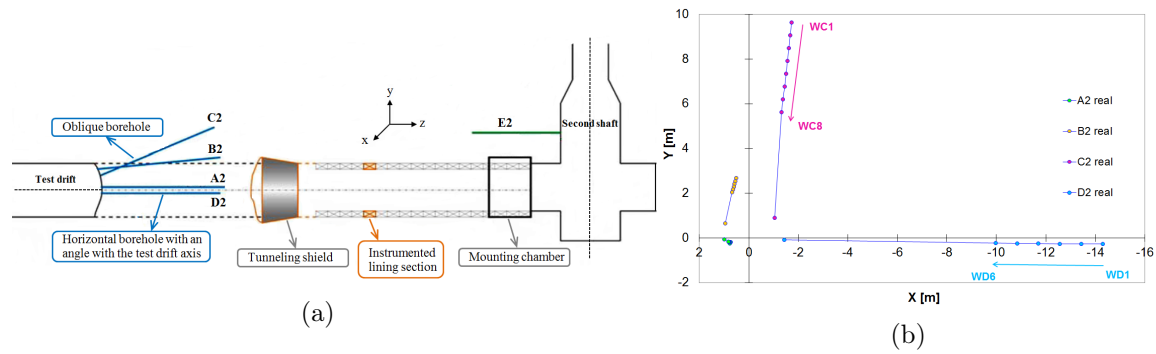


Figure 6.10: (a) Location of the CLIPLEX pore water pressure instrumentation. (b) Image of the boreholes' filters in the vertical plane ( $x, y$ ); after [Bernier et al., 2007b].

they were only usable during the excavation and before they have been crossed by the excavation front. On the contrary, the boreholes C2 and D2 could be restored after their casing was cut off by the tunneling machine and their data are available for a longer period. Figure 6.10b shows the image of these two boreholes' filters on the  $x$ - $y$  plane where the eight filters of the (quite) vertical borehole C2 and the six filters of the (quite) horizontal borehole D2 can be observed.

Figures 6.11 and 6.12 show the measured pore pressure by the filters of the boreholes C2 and D2, respectively, which have been corrected with respect to the gravity effects. These data are available since the excavation time in 2002 for a period of about 4.5 years. In the first place, it must be noted that some sudden ups and drops observed in the evolution process of pore water pressure after the end of excavation (Figures 6.11b and 6.12b) are linked to some local tests like the permeability test, and they are then being discarded in our analysis. Regarding the borehole C2, a sudden drop of pore water pressure (see Figure 6.11a) in all the filters is associated to the decompression of the clay mass. This drop occurs progressively for different filters (WC1-WC8) with respect to the relative position of the corresponding filter, and the relative time when the excavation front gets close to it. Thence, the pore pressure dropped down firstly in WC1 (i.e. closest filter to the excavation front), and ultimately in WC8. The latter drop seems to be the most considerable one that it is associated to the lowest distance of this filter with the gallery (see the image at the top of Figure 6.10b). Moreover, the drop of pressure is preceded by a quick increase to a peak. This increase of pore water pressure in some filters can be associated to the immediate undrained contracting response of the clay while the excavation front approaches that filter. Then, in the next level when this front gets very close to the filter, a pressure drop is recorded. It should be noticed that the aforementioned increase of pressure is also more accentuated in the closest filter to the gallery (i.e. WC8). In addition, it is now illustrated that the excavation time interval for release of pore pressure considered in our 2D model (i.e. 6 days) to account for 3D impact of the excavation front in its proximity is consistent with the in-situ measurements. Indeed, the explained variations of pore pressure measured in each filter principally occurs since about 6 days before that the excavation front crosses the position of each filter; see Figure 6.11a.

Besides, the pore pressure tends to be increased again in the longer time (see Figure 6.11b). This tendency may be related to the procedure of regaining the equilibrium after a strong drop of pore pressure. However, a contradictory process regarded to an internal local water flow and drainage process might be also expected.

Furthermore, regarding the filters of the borehole D2, the recorded decrease of pore pressure during the excavation is not noticeable in comparison with the borehole C1 (see Figure 6.12a). In the same line as the discussion given for Figure 6.8, such decrease of pore pressure is not observed

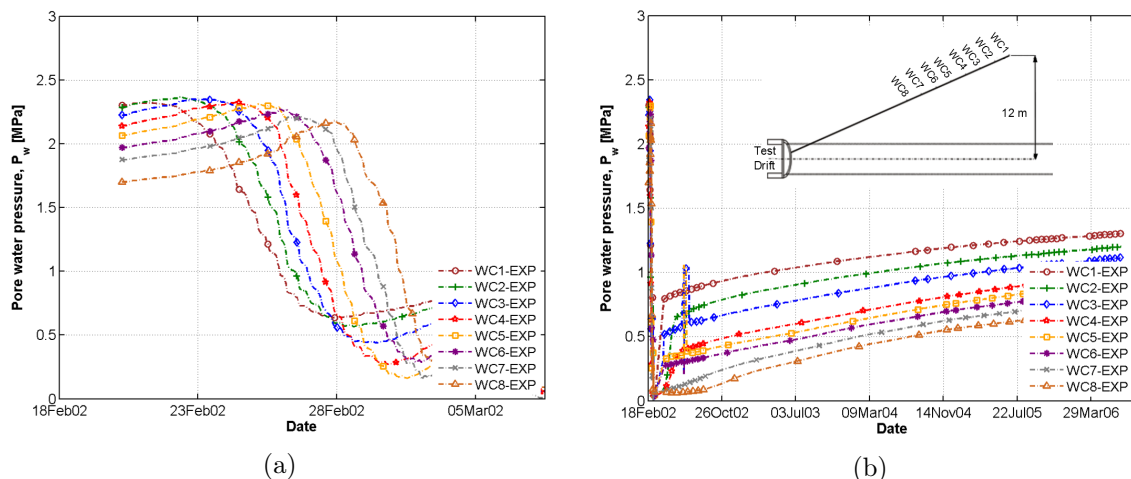


Figure 6.11: In-situ measured pore water pressure in function of the time: borehole C2. (a) During the excavation. (b) In the long-term.

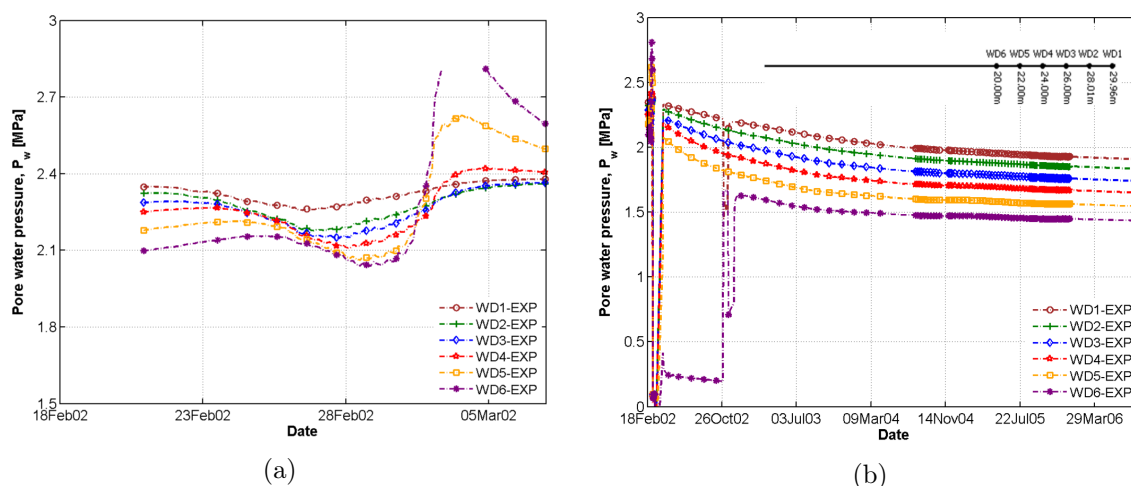


Figure 6.12: In-situ measured pore water pressure in function of the time: borehole D2. (a) During the excavation. (b) In the long-term.

in the horizontal direction (D2 is located almost horizontally in the perpendicular plane to the gallery). In fact, following the convergence of the clay (which is anisotropically higher along the horizontal direction) in the course of construction and its contact with the (immediately) installed lining, this contact does not allow more decrease of pore pressure, and it could impose the recompression of the clay and reincrease of pore pressure. This increase is more important in the closest filter to the gallery, i.e. WD6, as it is observed in Figure 6.12a. Subsequently in the longer time (see Figure 6.12b), the pore pressure decreases in all the filters as it could be expected with respect to a local flow and drainage process.

Considering Figures 6.11a and 6.12a, the initial pore water pressure at the beginning of the excavation is not consistent for all the filters of each borehole. In fact, the same pore pressure could be expected to be recorded by all the filters of the (almost) horizontal borehole D2 at the beginning of excavation. Also, the initial difference of the pore pressure taken from different filters of the borehole C2 could be expected to be limited to the gravity effects, which is indeed very low with regard to the position of those filters (see Figure 6.10b). This issue is supposed to be mostly due to the impact of the preceding excavated Test Drift. The influence of the TD is

stronger on the closest filters to TD (WC8 and WD6). This precedent influence of TD cannot be taken into account in our modeling. Therefore, for the sake of simplicity in our upcoming comparison between the in-situ measurements and numerical results, we have considered two options for representing the in-situ data. First, a reference pore water pressure is given to the filters of each borehole at the beginning of its excavation period (i.e. the point from which the impact of the gallery excavation on the corresponding filters measurements is supposed to occur), and the subsequent measured pressures at each filter are then altered with respect to the corresponding new reference pressure. Thence, we will have the same conditions at the beginning of excavation in the measurements and numerically. Second, the change in pore water pressure is presented in function of the days (change in time). In the following, the both options are discussed (a detailed analysis can be also found in [Salehnia, 2014]).

With regard to the borehole C2, a reference pore water pressure is considered for each filter which has basically consisted in the in-situ pressure at the gallery’s level (i.e.  $2.25 \text{ MPa}$ ) modified for the gravity effect taking into account the position of the corresponding filter. Then, considering a so-called excavation period of 6 days (i.e. the same as it has been given to our numerical model), the change in pore pressure of each filter during the excavation should occur from its relative reference value for a period of 6 days. Besides, with regard to the inclination of the borehole C2 (see Figure 6.10), the real time that the relative position of each filter has been crossed by the excavation front (which is assumed to be its so-called end of excavation phase) is not the same for all the filters. To clarify this point, the black points in Figure 6.13 show schematically this time for each filter. Hence, the relative excavation period corresponds to each filter can be supposed to be 6 days in advance to these black points. For instance, the brown and chocolate arrows show this period for the filters WC1 (between 20-26 February 2002) and WC8 (between 25 February-3 March 2002), respectively. Therefore, the reference pore pressure of the filter WC8 is for instance assumed to be constant until 25 February, i.e. beginning of its so-called excavation phase (see the chocolate box in Figure 6.13), and subsequently it changes. Then, all the pore pressures measured by each filter in time are altered with respect to its corresponding initial reference value. Within this framework, Figure 6.14 shows the pore pressure evolution for different filters of the borehole C2<sup>9</sup>.

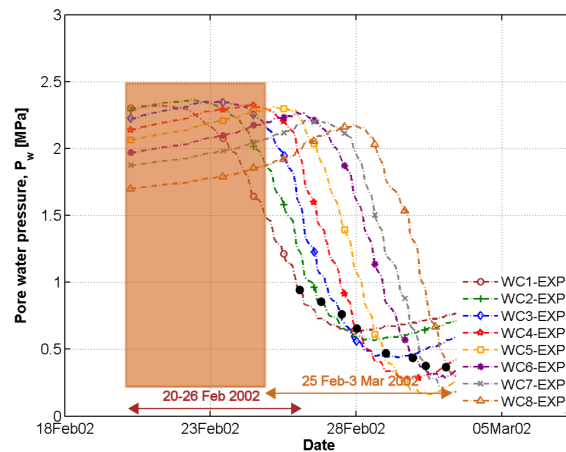


Figure 6.13: In-situ measured pore water pressure by the filters of the borehole C2 during the excavation. The black points correspond to the recorded time that front of excavation has crossed the position of each filter.

<sup>9</sup>It must be noted that some irregularities in the order of pore pressure of the last filters in long-term (Figure 6.14b) results from this modification and taking into account the primary low difference of pore pressure values recorded by the last filters at a constant time point in long-term (Figure 6.11b).

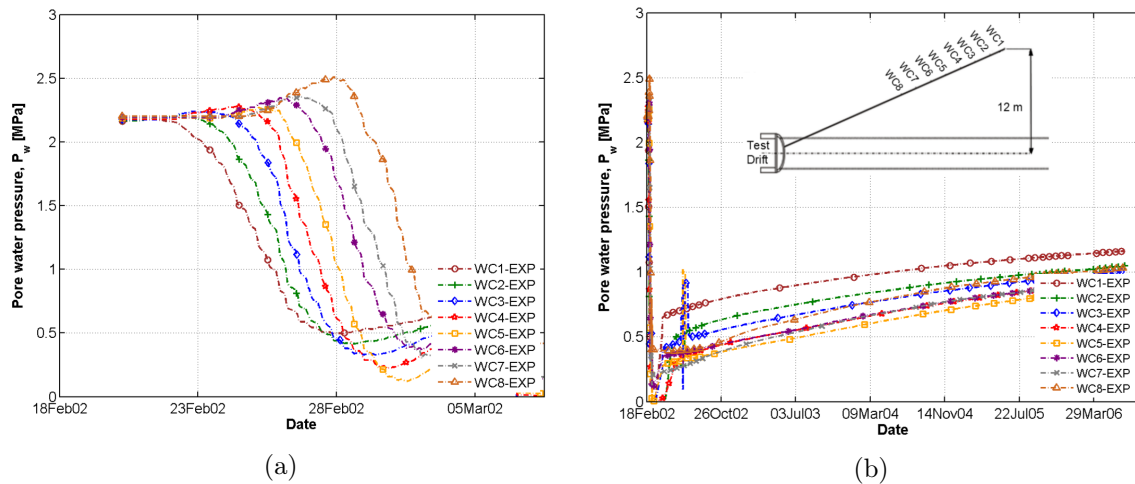


Figure 6.14: In-situ measured pore water pressure, altered for a considered reference initial value, in function of the time: borehole C2. (a) During the excavation. (b) In the long-term.

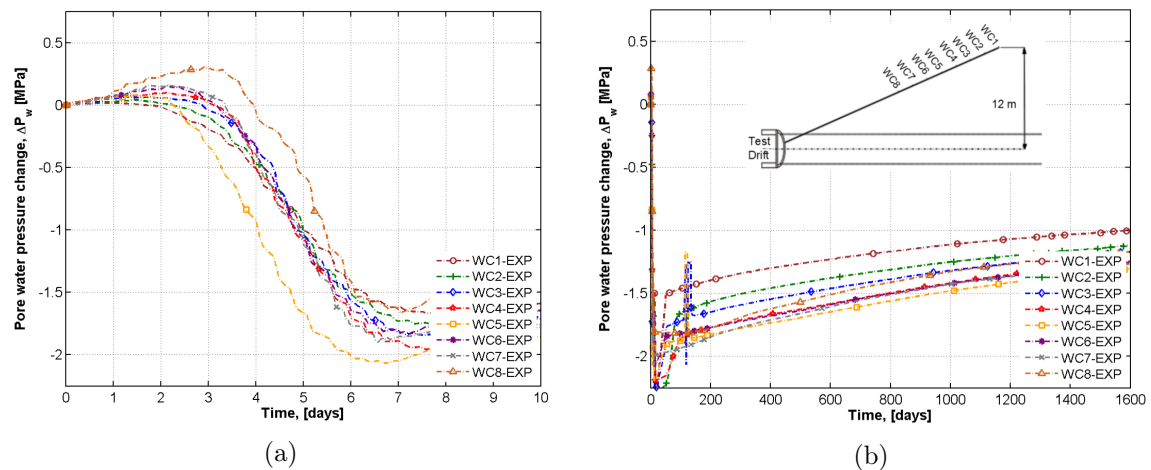


Figure 6.15: Change of the in-situ measured pore water pressure in function of the change in time (days): borehole C2. (a) During the excavation. (b) In the long-term.

Within the framework of the other perspective, Figure 6.15 represents the change of pore pressure, recorded by the filters of the borehole C2, in function of the days. Despite the different times that front of excavation crossed the position of different filters, this feature can not be illustrated when the data are presented in terms of the gradient since the excavation period is the same for all the filters (=6 days). As a result, the sequence of the increase and decrease process of pore pressure measured by different filters during the excavation can not be identified (Figure 6.15a). In fact, the measurements seem to be shifted in time here (see Figure 6.15a compared to Figure 6.14a). The evolution of pore water pressure in the long-term (see Figure 6.15b) can be interpreted in the similar manner to Figure 6.14b, though. Therefore, it is implied that the first option (i.e. giving an initial reference pore water pressure) can be more representative to be referred in our analysis.

Following a similar process explained for the borehole C2 to consider a reference pore pressure at the beginning of excavation time, Figure 6.16 shows the (altered) pore water pressure measured by the filters of the borehole D2. Given almost horizontal direction of the latter borehole, there is no gravity effect on the measured pore pressure. Consequently, the reference pore pressure is considered to be equal to the in-situ pressure at the gallery's level (i.e.  $2.25 \text{ MPa}$ ) for all the

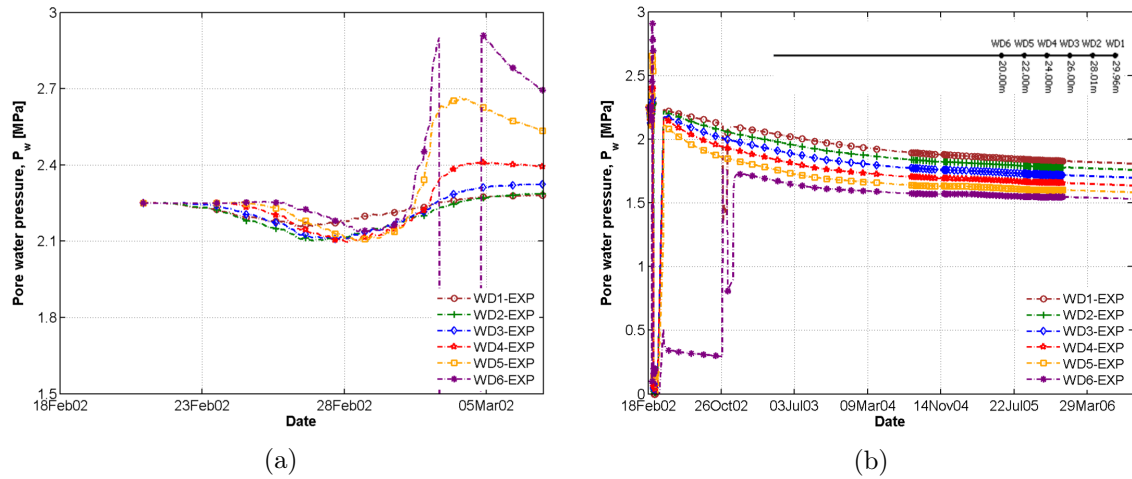


Figure 6.16: In-situ measured pore water pressure, altered for a considered reference initial value, in function of the time: borehole D2. (a) During the excavation. (b) In the long-term.

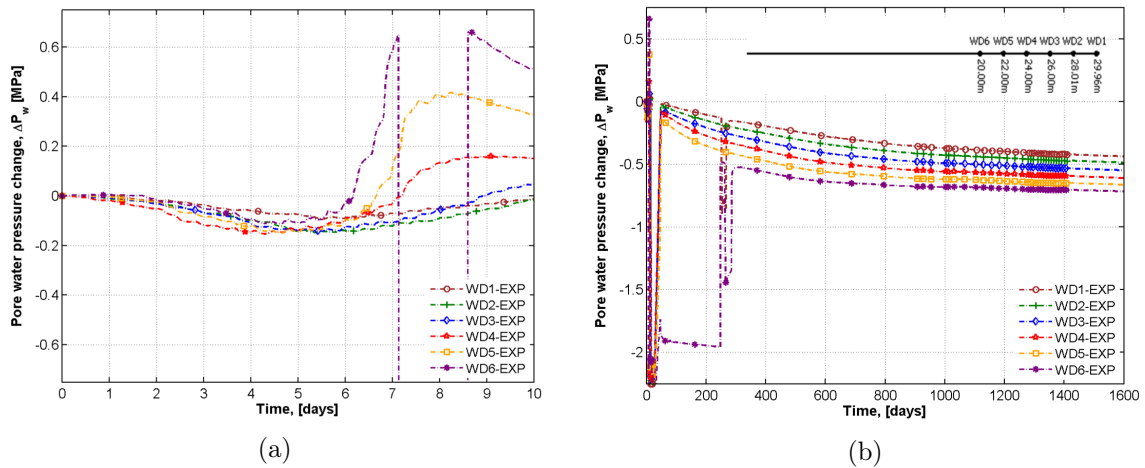


Figure 6.17: Change of the in-situ measured pore water pressure in function of the change in time (days): borehole D2. (a) During the excavation. (b) In the long-term.

six filters of this borehole. Moreover, within the second framework of representing the change of pore pressure in function of the change in time (days), Figure 6.17 shows the corresponding results for the borehole D2. In all, these results seem to be more regular in comparison with the corresponding results of the borehole C2 even though the sequence of the changing process of pore pressure in different filters remains undisclosed during the excavation period (Figure 6.17a).

#### 6.4.1.2 Boreholes R55 and R13

After the end of excavation of Connecting gallery, two multi-piezometers were installed outward to the gallery to measure the pore water pressure. Figure 6.18 shows schematically these piezometers consisting of R55 multi-piezometers - R55E (eastward), R55I (inclined) and R55D (downward) - and R13 multi-piezometers: R13D (downward) and R13U (upward).

Pore pressure recorded by the filters in different depths<sup>10</sup> of these piezometers are presented

<sup>10</sup>These depths indicate the distance from the gallery's intrados.

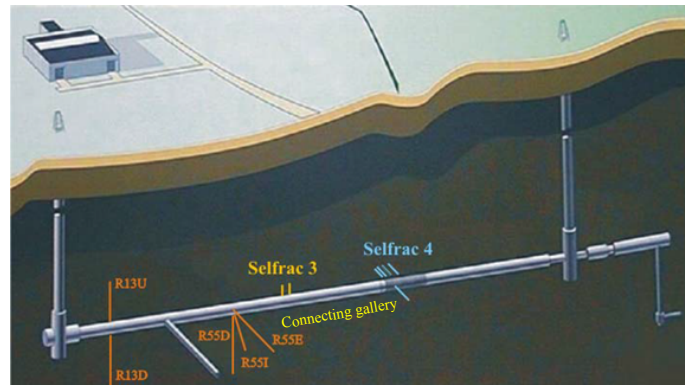
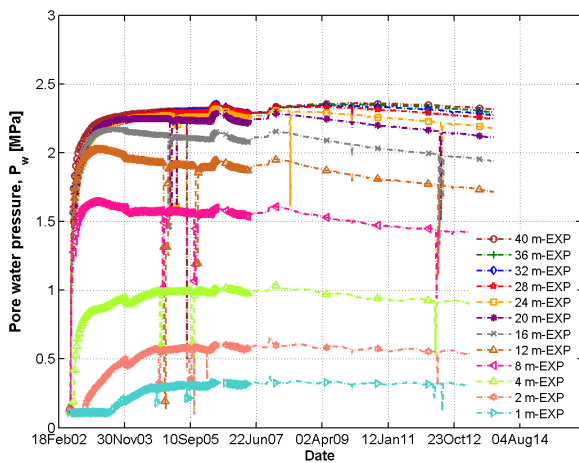
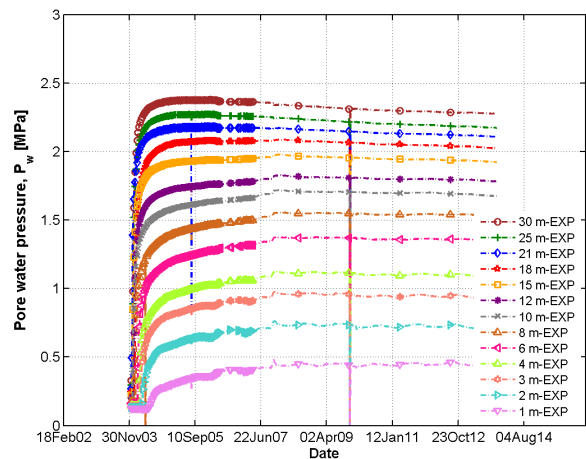


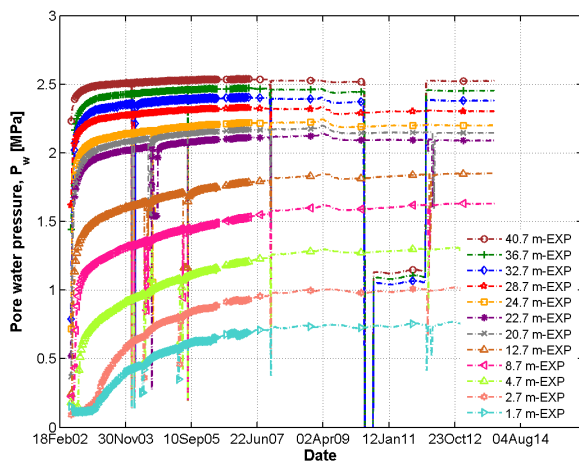
Figure 6.18: Layout of the location and orientation of the R55 and R13 boreholes outward to the Connecting gallery [Bernier et al., 2007a].



(a)



(b)



(c)

Figure 6.19: In-situ measured pore water pressure in function of the time for the piezometer: (a) R55E. (b) R55I. (c) R55D.

in Figures 6.19-6.20 for a long period of about 12 years after the gallery excavation. It must be noted that the primary increasing pattern of pore pressure at the beginning of all curves is linked to the necessary time for stabilization of the filters' record after the installation of the piezometers, and it should be then disregarded. Additionally, several sudden drops of the pressure afterwards in time are related to some local tests such as the hydraulic conductivity test, and they are also discarded in our analysis. With respect to Figure 6.19, a stationary or decreasing trend in pore pressure evolution (in time) measured at different filters of the horizontal piezometer R55E is observed (Figure 6.19a). The reduction tendency is mostly observed at the relatively higher depths (distance from the gallery's intrados), i.e. not very close to gallery, because of the local drainage process. This decreasing pattern is similar to what has been demonstrated for the (almost) horizontal borehole D2 (see Figure 6.12b) with some alike depth filters (see Figure 6.10b). Also, the measurements of the filters at the depth more than 20-24 m seem to be quite similar. In addition, the inclined piezometer R55I illustrates mostly a plateau state in the evolved pore water pressure at different depths (Figure 6.19b). Moreover, a stationary or a slight increasing trend is observed in pore pressure evolution (in time) measured at different depths of the vertical piezometer R55D (Figure 6.19c). The latter tendency occurs at the lower depths out of the gallery (relatively close filters to the gallery), similarly to the increasing trend shown for the borehole C2 (see Figure 6.11b). However, it is much more slighter and pretty negligible here. This difference may be partially interpreted with respect to various influential phenomena, during the construction process, that could affect the filters of the borehole C2 and their corresponding measurements in time, which is not the case of the borehole R55D (since it has been installed after the end of gallery construction).

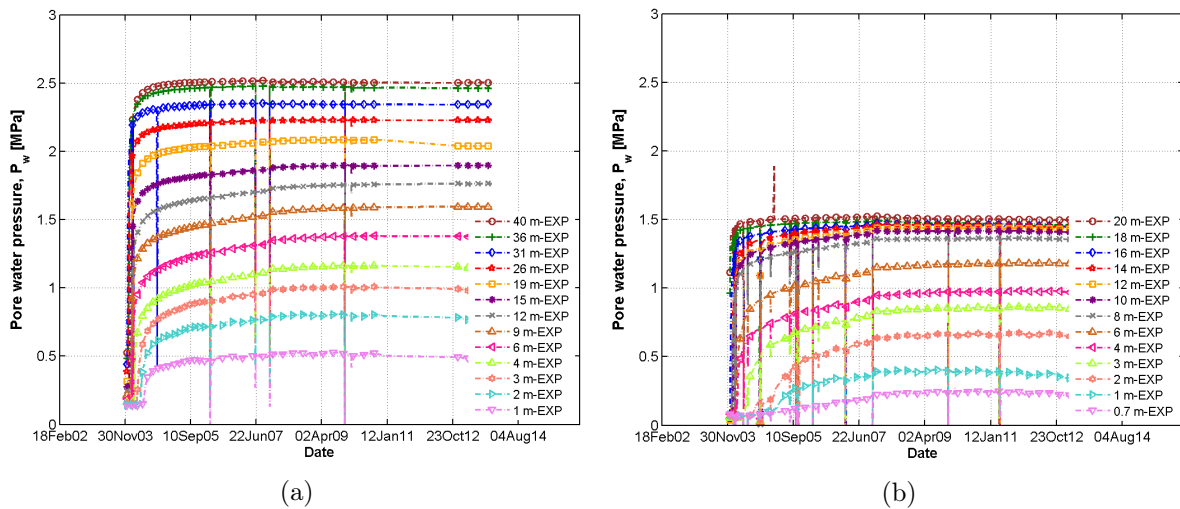


Figure 6.20: In-situ measured pore water pressure in function of the time for the piezometer: (a) R13D. (b) R13U.

With regard to Figure 6.20 which shows the pore pressure measured at different depths<sup>10</sup> in two vertical piezometers R13D and R13U, a dominant stationary trend is observed in the evolution of pressures in time. This is quite comparable with relative tendency observed in the measurements of the piezometer R55D, and it is in contrast to the recorded increasing pattern of pore pressures in the borehole C2. In fact, the measurements of the downward piezometers R13D can be said to be pretty undifferentiated - for most of the depths - with respect to the piezometer R55D despite the 42 m horizontal distance between them (see Figures 6.19c and 6.20a). In overall, the extent of the hydraulically influenced zone is illustrated to be higher vertically (about 40 m) than horizontally (about 20 m) [Bastiaens et al., 2007], as also noticed considering Figures 6.19 and 6.20.

Furthermore, comparing the measurements taken from the downward piezometer R13D (Figure 6.20a) and upward piezometer R13U (Figure 6.20b), the gravity effect is obvious in their relative measured pore pressures as the higher pressures have been recorded in the downward borehole.

### 6.4.2 Permeability measurements

The piezometers R55E and R55D have been used for the hydraulic conductivity measurements as well. These boreholes were equipped with pressure controllers and precision balances. A constant pressure could be imposed by the pressure controllers on a piezometer's filter, and the precision balance could then monitor the outflow into the clay host rock. As a result, the hydraulic conductivity have been derived using the Darcy's law; detailed information on the experiment can be found in [Yu et al., 2011]. Figure 6.21 shows the measured hydraulic conductivity (at three different time) through a few first filters of the two piezometers, in function of their relative distance with the gallery's intrados. The measurements on the vertical piezometer R55D correspond principally to the horizontal hydraulic conductivity  $K_h$ . In addition, the measurements on the horizontal piezometer R55E are supposed to be associated to the vertical hydraulic conductivity  $K_v$ . However, it must be noted that measuring on the horizontal piezometer could have some influence of  $K_h$  besides  $K_v$  as well [Yu et al., 2011].

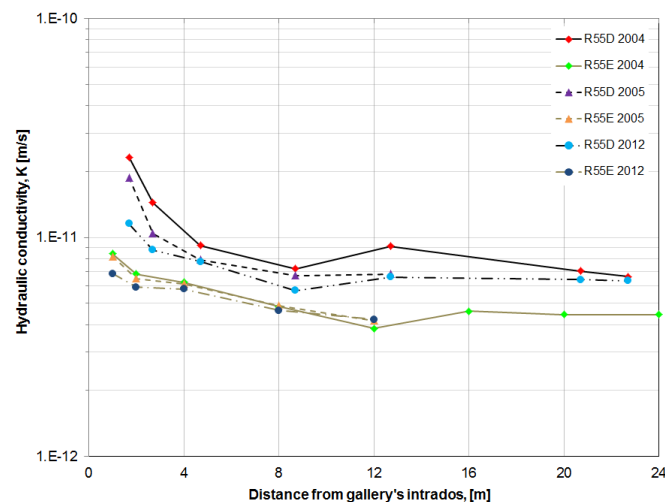


Figure 6.21: Hydraulic conductivity around the Connecting gallery measured on the piezometers R55E and R55D.

As it is observed, the hydraulic conductivities increased to maximum in a zone close to the gallery, corresponding to the EDZ. This increase has been concluded to be basically associated to the variation of effective stress in this zone. That is to say that the fractures have not played, themselves, a considerable role with regard to it, according to Bastiaens et al. [2007]; Bernier et al. [2007a]. In this sense, the self-sealing capacity of Boom Clay, and the time interval between the fracturing at the excavation period and the first given measurement in 2004 may worth to be taken into account as well. The hydraulic conductivity (perturbation) tends to lessen (mostly  $K_h$  measured on R55D) to some extent with time as seen in Figure 6.21.

### 6.4.3 Strain measurements in the lining

Thanks to the instrumentation in three rings (ring 15, ring 30 and ring 50) of the Connecting gallery's lining within the framework of the CLIPLEX program, the strain evolution could be monitored. The strain has been measured through two types of the segment instrumentation in these rings: 6 gauges and 12 gauges segments. Figure 6.22 illustrates the configuration of the both types of segments instrumentation as well as the plan of the instrumented ring 50. In this work, the data taken from the ring 50 are analyzed. In fact, this ring has been monitored more frequently, and particularly before and after the construction of the ring, according to Bernier et al. [2007b]. In addition, the convergence measurements are also available for the ring 50 (see Section 6.4.4). Hence, its measurements are focused in our analysis.

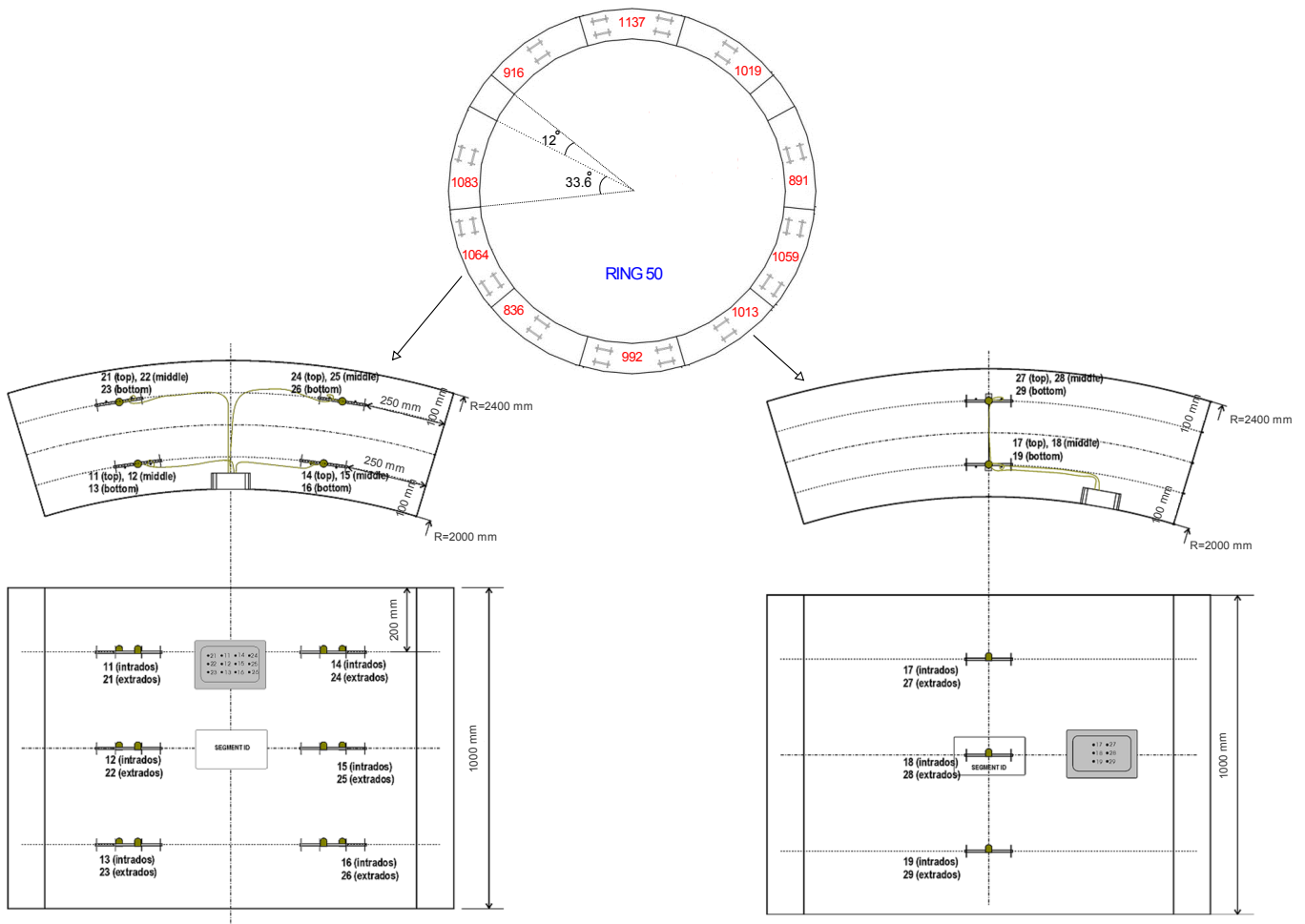


Figure 6.22: Instrumented ring 50 of the lining for the strain measurement (top row), and configuration of the 6 gauges (bottom right) and 12 gauges (bottom left) segments [Bernier et al., 2007b].

Figure 6.23 presents the strain measured by the internal and external sensors in all the segments of the ring 50 since the installation of the ring in February 2002. An average on the measurements of the internal /or/ external sensors is displayed during the time for each segment. The first point observed in the presented strain evolution is a similar strain trend, i.e. compressive deformation, recorded in the both internal and external sensors of each segment. The compression pattern of strain internally and externally in all the ring's segments (and similarly

in all the lining's rings), in spite of an anisotropic pattern of deformation of the clay mass in interaction with the lining, is associated to the joints between the segments. The latter does not allow the tension transition between the concrete blocks.

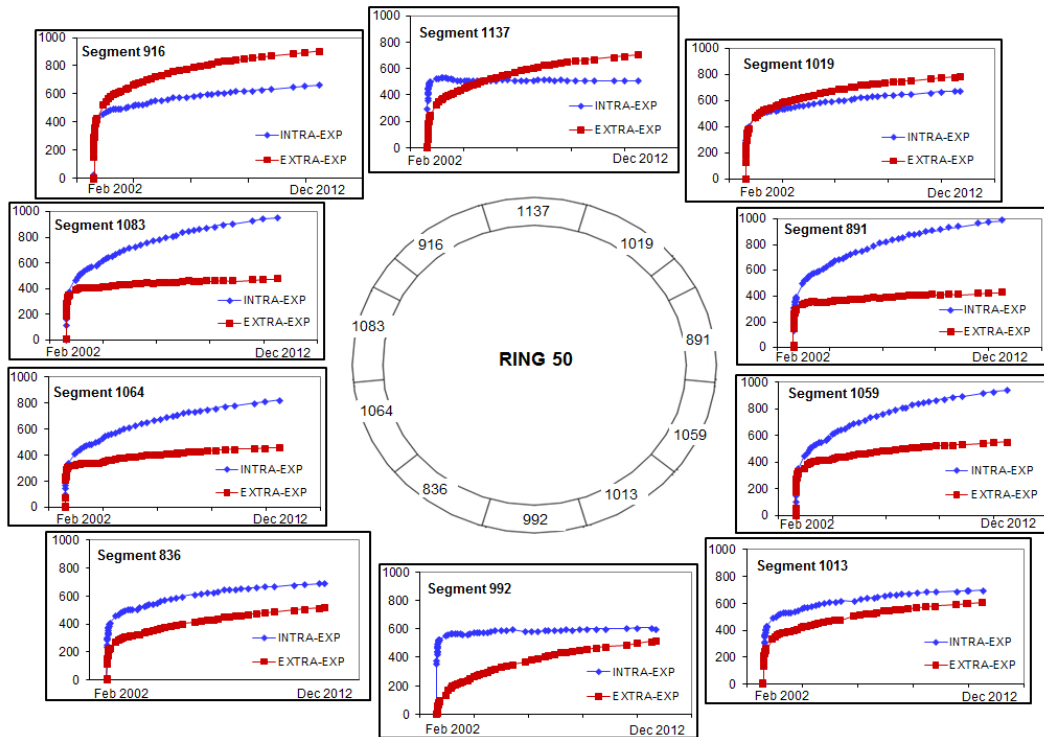


Figure 6.23: In-situ strain measurements ( $\times 10^{-6}$ , [-]) in the ring 50 of the lining in function of the time.

Moreover, it is noticed that in the right and left segments (i.e. segments 891, 1059, 1083, and 1064), there is more strain rate internally than externally. This pattern is quite contradictory in the top and bottom segments, specially in the segments 1137 and 992. In addition, with regard to the maximum strain reading in each segment, this value is almost higher for the aforesaid right and left segments, which are actually located around the horizontal axis. It indicates that these segments are under a relatively more compression in long-term. Indeed, all these patterns regarding the strain evolution in the lining in long-term are linked to the deformation of the clay during the time immediately after the excavation period (that is to say after the installation of the ring in February 2002). It must be noted that taking into account an oval deformation pattern of the clay during the excavation, it tends to an equilibrium and recompression after its contact with the lining (i.e. after the installation of the ring in February 2002 that since then, the strains have been read). Hence, the horizontal diameter of the ring is supposed to be increased in long-term - which lies in the higher (rate) compressive strain in the corresponding internal sensors - on the contrary to its vertical diameter. The latter issue will be illustrated once again in Section 6.4.4 by presenting the convergence evolution in the lining in long-term. Furthermore, a pretty symmetric pattern is generally observed with regard to the strain evolution of the segments in the whole ring. However, the top and bottom segments does not consist in a total symmetry of the strain readings.

### 6.4.4 Convergence measurements in the lining

This section focuses on the convergence measurements provided in the lining thanks to some instrumented rings for this purpose. With regard to the ring 50 (the same ring as discussed in Section 6.4.3), Figure 6.24 shows the position of installed sensors for monitoring the convergence. This set of measurements are available since 6/12/2004.

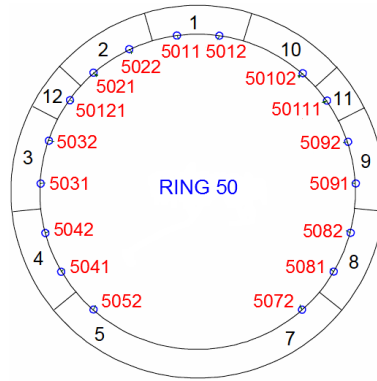


Figure 6.24: Instrumented ring 50 of the lining for the convergence measurement. The first two digits of the sensors' number correspond to the ring's number.

Figure 6.25 presents the convergence of different pairs of sensors (i.e. their diagonal reduction) in time relatively to the first data recorded on December 6, 2004. Despite lots of oscillations in the readings, it can be observed that the vertical chords consist in a positive convergence with an increasing pattern in time (see the chords of 5011-5072, 5012-5052, and 5022-5072). On the contrary, the horizontal chords show principally a negative convergence, i.e. diagonal increase, (see the chords 5032-5091, 5031-5092, 5082-50121, and roughly 5042-50111). Hence, the diameter is deduced to be increased horizontally, and to be decreased vertically in long-term based on these measurements. This pattern is consistent with our interpretation regarding the deformation of the clay mass after the excavation given the strain measurements in the lining, described in Section 6.4.3.

Moreover, considering four sensors in the top right quarter of the ring (corresponds to the segments 9, 11, 10, and 1), their absolute displacement during the time is plotted in Figure 6.26<sup>11</sup>. Since the high oscillations of the data makes their analysis quite difficult, an average linear evolution of the readings in time is also schematically displayed for each sensor. A quite considerable displacement is identified for these sensors still at more than 11 years after the construction time of the gallery, specially for the sensor 5012 located in the segment number 1. However, this difference in displacement of the latter sensor with the other ones' may not be concluded to be the case in all of the rings. Indeed, analysis of the in-situ convergence measurements in the lining have somehow illustrated a pretty non-uniform pattern of variation in different rings. In this sense, in order to better analyze the evolution of convergence in the lining, the measurements of one other ring, ring 8, are also presented in the following.

The convergence of different pairs of sensors of the ring 8, in time relatively to the first data recorded on December 6, 2004, is presented in Figure 6.27. A positive pattern of convergence is observed for the vertical chords 811-872, 812-852, and 822-872, similarly to the ring 50. The other chords, specially the horizontal chords 832-891, 831-892, 882-8121, consist in a negative convergence. In addition, the absolute displacement of the sensors 892, 8111, 8102, and 812,

<sup>11</sup>These displacements have been obtained based on the sensors' coordinates measured at different dates.

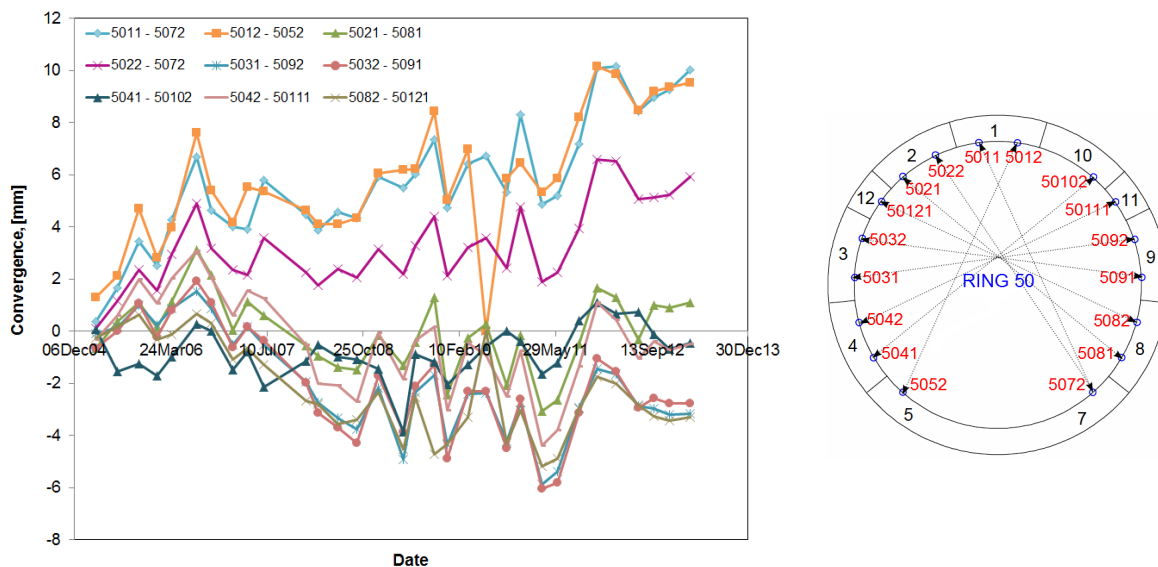


Figure 6.25: In-situ measured convergence (diagonal reduction) for the ring 50 in function of the time.

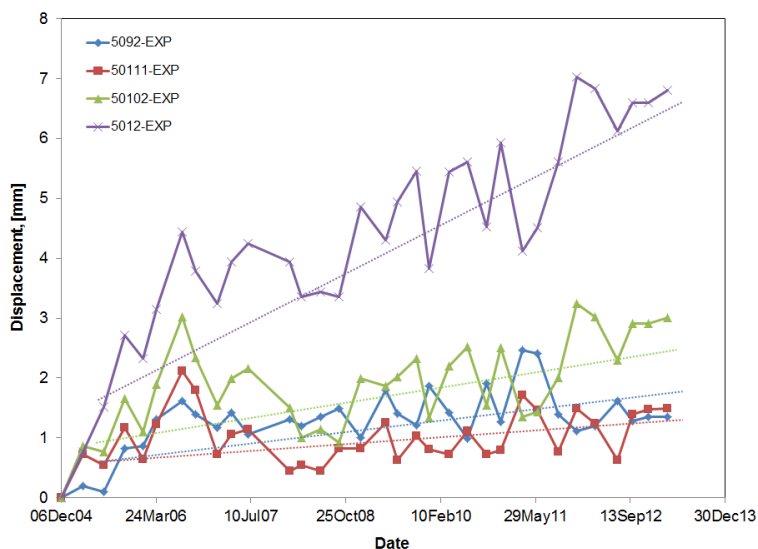


Figure 6.26: Displacement recorded for four sensors of the ring 50 in function of the time with reference to 6/12/2004. The dashed lines display schematically an average linear evolution of displacement readings of each sensor in time.

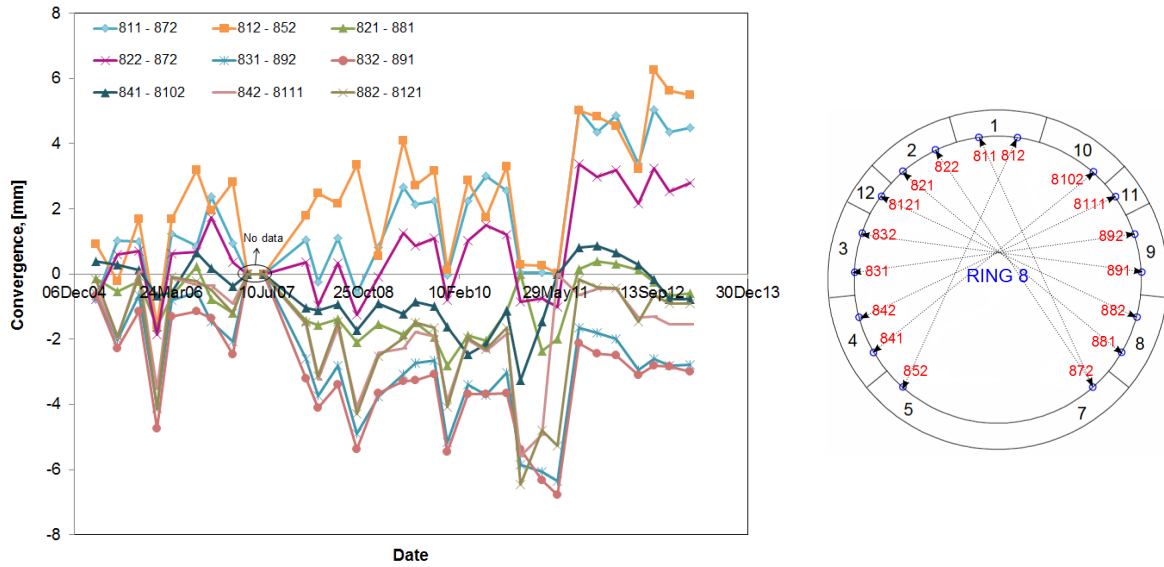


Figure 6.27: In-situ measured convergence (diagonal reduction) for the ring 8 in function of the time.

during the time is shown in Figure 6.28. In contrast to the ring 50, no important difference is noticed between the range of displacement evolution for the sensor 812, corresponding to the top segment, with the other three sensors. Therefore, the order of magnitude of the absolute displacement of the sensors, in different rings, may not be the same. Although, they follow an overall similar pattern of convergence in the lining consisting in a diagonal reduction tendency vertically and diagonal enlargement horizontally, in long-term.

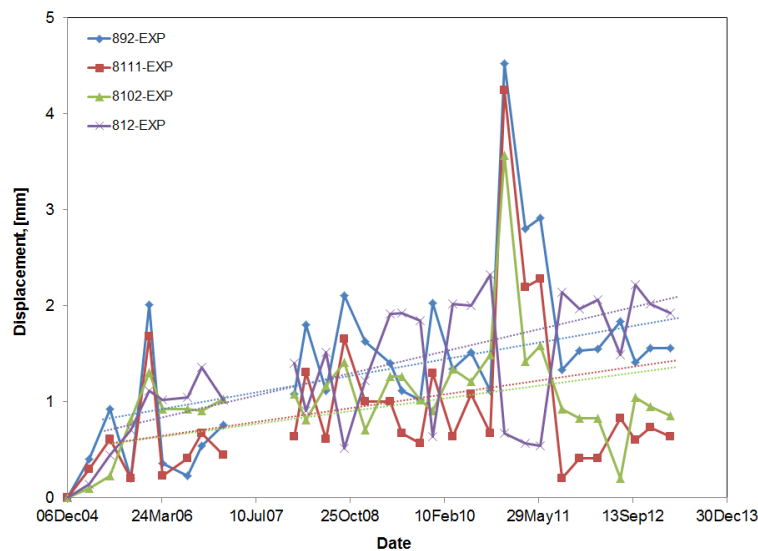


Figure 6.28: Displacement recorded for four sensors of the ring 8 in function of the time with reference to 6/12/2004. The dashed lines display schematically an average linear evolution of displacement readings of each sensor in time.

## 6.5 Comparison of the extended numerical predictions and in-situ measurements

### 6.5.1 Development of the numerical simulation

Strain localization by concept may possibly prompt a loss of symmetry in the system's behavior. Hence, our modeling is intended to be extended to a full gallery in this Section to address firstly the symmetrical aspects of the material response in the localization point of view, assumed through the primitive modeling of a quarter of the gallery. Moreover, the numerical results of this extended model, taking into account also the gravity effects, will be more realistic to be compared with the in-situ measurements taken from the both downward and upward piezometers.

In addition to the initial stress anisotropy and strain localization which could induce loss of symmetry in the system's response, the material inherent anisotropy can be another source that causes some directional dependency in the clay behavior. Therefore, our extension of numerical simulation consists also in considering the mechanical cross-anisotropy of the clay properties as well as the anisotropic hydraulic conductivity.

The numerical modeling is also extended in time and another phase of about 8 years with the same boundary conditions as the second phase (3.5 years since the excavation time, as defined in Section 6.3.1) is considered. Thus, the whole simulation is performed for a period of about 11.7 years, i.e. since the excavation time in 2002 until the end of 2013.

#### 6.5.1.1 Cross-anisotropy of the mechanical properties

Most of sedimentary rocks [Nova, 1980; Duveau et al., 1998] and slightly overconsolidated natural clays [Graham and Houlsby, 1983], exhibit an inherent anisotropy because of their mode of deposition so that their strength and deformation characteristics are directional dependent, with regard to the orientation of the bedding plane relatively to the principle stress direction. Such materials frequently possess a polar symmetry with respect to the axis normal to the bedding plane [Nova, 1980] so that their behavior is isotropic in the plane of bedding and the only direction of anisotropy is perpendicular to the bedding. In this case, they are called as cross-anisotropic or transversal isotropic materials [Lekhnitskii and Fern, 1963].

Our numerical simulation is therefore developed to take into account of the material cross-anisotropy as well in order to model more realistically the deformation response of clay mass to the excavation process accompanied by the onset of localized bands. To do this, an extension of the Drucker-Prager model (described in Section 3.4.2.1) is used integrated with the elastic [Lekhnitskii and Fern, 1963; Graham and Houlsby, 1983] and plastic cross-anisotropy with respect to the work of [François et al., 2012]. The cross-anisotropic elasticity of the material is taken into account through the compliance elastic matrix  $[\mathbb{C}_{ijkl}^e]^{-1}$  which relates the elastic component of the strain in our elasto-plastic law (see Section 3.3) to the stress, in the rate form, following the Hooke's law such that:

$$\dot{\epsilon}_{ij}^e = [\mathbb{C}_{ijkl}^e]^{-1} \dot{\sigma}_{kl} \quad (6.2)$$

Given the cross-anisotropy, the stress-strain relation 6.2 is generally expressed in the anisotropic axes  $(x'_1, x'_2, x'_3)$  (see Figure 6.29) associated to the bedding orientation with respect to which a change of the reference system may be then needed to obtain the strain in the global axes. Regarding our studied material, a horizontal bedding plane consists in the anisotropic axes to overlay the global basis, though ( $\alpha = 0$ ). Additionally, as a result of this cross-anisotropy (i.e. the isotropic behavior in the plane of bedding and anisotropic perpendicular to the bedding)

the material properties are independent of rotation around the axis  $x'_2$ , normal to the bedding plane. As a result, there are only five independent parameters which define the cross-anisotropic elasticity, which are integrated into the compliance matrix (Equation 6.3), namely:  $E_{\parallel}$ ,  $E_{\perp}$ ,  $\nu_{\perp\parallel}$ ,  $\nu_{\parallel\parallel}$ , and  $G_{\parallel\perp}$  [Lekhnitskii and Fern, 1963; Graham and Housby, 1983].

$$[\mathbb{C}_{ijkl}^e]^{-1} = \begin{bmatrix} \frac{1}{E_{\parallel}} & -\frac{\nu_{\parallel\parallel}}{E_{\parallel}} & -\frac{\nu_{\perp\parallel}}{E_{\perp}} & 0 & 0 & 0 \\ -\frac{\nu_{\parallel\parallel}}{E_{\parallel}} & \frac{1}{E_{\parallel}} & -\frac{\nu_{\perp\parallel}}{E_{\perp}} & 0 & 0 & 0 \\ -\frac{\nu_{\parallel\perp}}{E_{\parallel}} & -\frac{\nu_{\perp\perp}}{E_{\parallel}} & \frac{1}{E_{\perp}} & 0 & 0 & 0 \\ 0 & 0 & 0 & \frac{1}{2G_{\parallel\parallel}} & 0 & 0 \\ 0 & 0 & 0 & 0 & \frac{1}{2G_{\parallel\perp}} & 0 \\ 0 & 0 & 0 & 0 & 0 & \frac{1}{2G_{\perp\perp}} \end{bmatrix} \quad (6.3)$$

where the subscripts  $\parallel$  and  $\perp$  refer to the directions parallel and perpendicular to the bedding plane, respectively. Moreover, in order to ensure the symmetry of the compliance matrix,  $\nu_{\perp\parallel}/E_{\perp} = \nu_{\parallel\perp}/E_{\parallel}$ . Lastly, the shear modulus in the direction of bedding is obtained by:

$$G_{\parallel\parallel} = \frac{E_{\parallel}}{2(1 + \nu_{\parallel\parallel})} \quad (6.4)$$

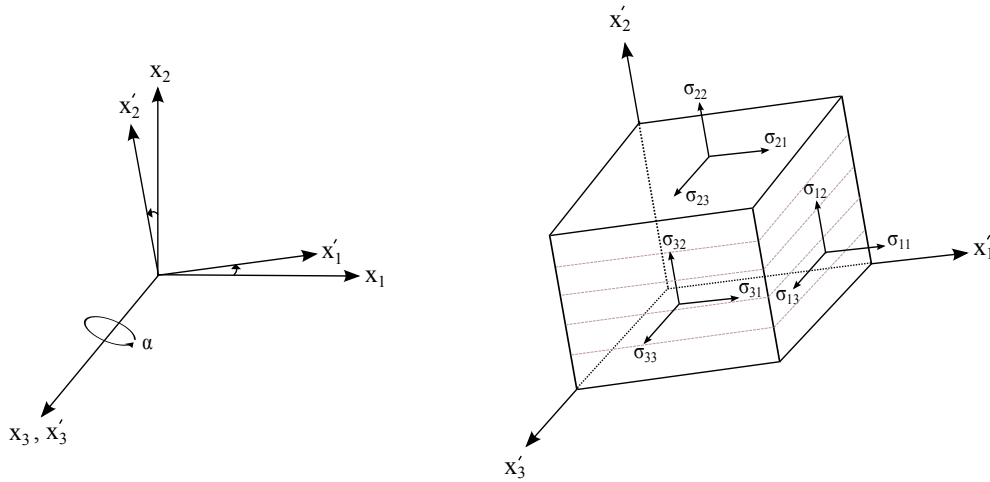


Figure 6.29: 3D representation of the global axes and anisotropic axes with a rotation around the axis  $x_3$  (left side), and the stress components for a representative elementary (right side); the brown dashed lines show the bedding direction.

Furthermore, regarding the elasto-plastic behavior of the material and anisotropy of the strength parameters, different failure criteria and numerical propositions have been developed; see [Duveau et al., 1998] for an assessment on some widely used ones. Donath [1972] and Nova [1980] have shown that the anisotropy of strength, and failure plane inclination of sedimentary rocks vary with respect to the angle between bedding plane and major principle stress. Through several triaxial compression tests, this dependency has been demonstrated by [Donath, 1972] indicating that the material cohesion has an essential impact on the mode of deformation and strength parameters of the material. Henceforth, with respect to consideration of cohesion softening in the Drucker-Prager model (see Equation 3.110), the plastic anisotropy is taken into account

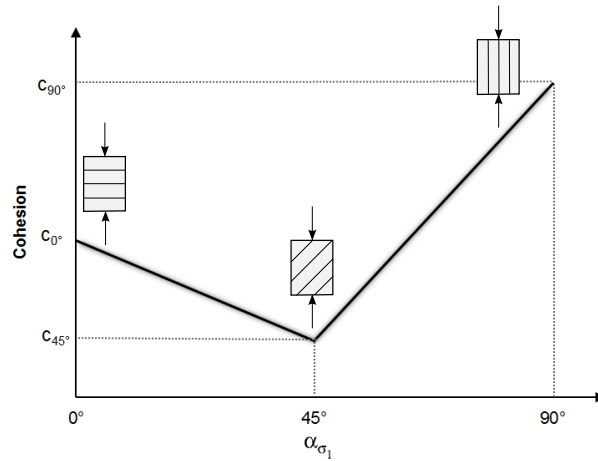


Figure 6.30: Schematic view of cohesion evolution as a function of the angle between major principle stress and the normal vector to the bedding plane; after [François et al., 2012].

through the material cohesion so that the initial and final cohesions are given by:

$$c_{0 \text{ or } f} = \max \left[ \left( \frac{c_{0 \text{ or } f}(45^\circ) - c_{0 \text{ or } f}(0^\circ)}{45^\circ} \right) \alpha_{\sigma_1} + c_{0 \text{ or } f}(0^\circ); \right. \\ \left. \left( \frac{c_{0 \text{ or } f}(90^\circ) - c_{0 \text{ or } f}(45^\circ)}{45^\circ} \right) (\alpha_{\sigma_1} - 45^\circ) + c_{0 \text{ or } f}(45^\circ) \right], \quad (6.5)$$

where the cohesion (initial/final) is defined depending on the angle between major principle stress and the normal vector to the bedding plane,  $\alpha_{\sigma_1}$  [François et al., 2012]. Then, the cohesion is assumed to be varied linearly in function of the angle  $\alpha_{\sigma_1}$ , between three cohesion values which are defined into the model for  $\alpha_{\sigma_1} = 0^\circ$ ,  $\alpha_{\sigma_1} = 45^\circ$ , and  $\alpha_{\sigma_1} = 90^\circ$  (see Figure 6.30).

Table 6.7 presents the extended mechanical properties defined for Boom Clay. The anisotropic degree of the initial cohesions and the elastic properties (Young's modulus and Poisson's ratio) are applied with respect to the study of François et al. [2012] where the calibrated anisotropic ratio of the latter elastic parameters have been obtained consistently with the back analysis performed by Chen et al. [2011]. The cohesion softening for  $\alpha_{\sigma_1} = 90^\circ$  is then defined similarly to our former modeling (based on our parametric study) while the ratio between the initial and final cohesions (i.e. softening level) for two other  $\alpha_{\sigma_1}$  ( $=0^\circ$  and  $45^\circ$ ) is kept the same as for  $\alpha_{\sigma_1} = 90^\circ$ .

### 6.5.1.2 Definition of the zones of anisotropic permeability

In the hydraulic point of view, the coupled numerical modeling is improved to consider the anisotropic permeability of the host rock as well. A literature review of the parameter of hydraulic conductivity of Boom Clay has been already given in Table 2.3. With reference to this Table, the horizontal and vertical permeabilities<sup>12</sup> of the material at the level of URL are defined in our simulation of the gallery's excavation to be equal to  $k_h = 5.06 \times 10^{-19}$  and  $k_v = 2.3 \times 10^{-19}$  with an anisotropic ratio of 2.2; see Table 6.8 for the extended hydraulic parameters. This choice is consistent with the previous works (see the relative references in Table 2.3, and a synthesis of

<sup>12</sup>The relation of permeability with hydraulic conductivity is given by Equation 3.25 taking into account  $\mu_w = 1 \times 10^{-3} \text{ Pa.s}$  and  $\rho_w = 1 \times 10^3 \text{ Kg/m}^3$ .

Table 6.7: Boom Clay mechanical parameters of the model considering material anisotropy

Parameter	Symbol	Value	Unit
Young elastic modulus	$E_{\parallel}$	400	$MPa$
Young elastic modulus	$E_{\perp}$	200	$MPa$
Poisson ratio	$\nu_{\parallel\parallel}$	0.125	-
Poisson ratio	$\nu_{\perp\parallel}$	0.0625	-
Shear modulus	$G_{\perp\parallel}$	178	$MPa$
Specific mass of the grains	$\rho_s$	2700	$Kg/m^3$
Initial compression friction angle	$\varphi_{C0}$	8	$^{\circ}$
Final compression friction angle	$\varphi_{Cf}$	18	$^{\circ}$
Hardening coefficient	$B_{\varphi}$	0.001	-
Hardening coefficient	$D_{\varphi}$	0	-
Initial cohesion	$c_0(0^{\circ})$	255	$kPa$
Initial cohesion	$c_0(45^{\circ})$	240	$kPa$
Initial cohesion	$c_0(90^{\circ})$	330	$kPa$
Final cohesion	$c_f(0^{\circ})$	23.18	$kPa$
Final cohesion	$c_f(45^{\circ})$	21.8	$kPa$
Final cohesion	$c_f(90^{\circ})$	30	$kPa$
Softening coefficient	$B_c$	0.05	-
Softening coefficient	$D_c$	0	-
Dilatancy angle	$\Psi$	0	$^{\circ}$
Second gradient elastic modulus	$D$	2000	$N$

Table 6.8: Boom Clay hydraulic parameters of the model considering the anisotropic permeability

Parameter	Symbol	Value	Unit
Horizontal water permeability*	$k_h$	$5.06 \times 10^{-19}$	$m^2$
Vertical water permeability*	$k_v$	$2.3 \times 10^{-19}$	$m^2$
Specific mass of water	$\rho_w$	$1 \times 10^3$	$Kg/m^3$
Porosity	$n$	0.39	-
Water compressibility	$\frac{1}{\chi_w}$	$5 \times 10^{-10}$	$Pa^{-1}$
Water dynamic viscosity	$\mu_w$	$1 \times 10^{-3}$	$Pa.s$
Atmosphere pressure	$P_{atm}$	$1 \times 10^5$	$Pa$
Van Genuchten parameter	$m$	0.47	-
Van Genuchten parameter	$n$	1.887	-
Van Genuchten parameter	$\frac{1}{\alpha}$	7	$MPa$
Residual water degree of saturation	$S_{r,res}$	0.2	%

\* They are the corresponding values applied for the excavation phase of 6 days. For the second and the third phases of simulation, see Figures 6.31a and 6.31b, respectively.

all the available relative former studies in [Yu et al., 2011]), and it is almost equal to the values reported in the recent study of Wemaere et al. [2008]. The latter study has stemmed from the hydraulic conductivities determined in the laboratory for the Boom Clay clay cores taken from the borehole Mol-1 (see Figure 2.7).

Subsequently to the excavation phase, hydraulic conductivity of the host rock is expected to be increased, specially within a zone around the gallery. This increase in the case of the excavation in Boom Clay is mostly related to the variation of effective stress in that zone, as mentioned in Section 6.4.2, rather than being associated to fracturing. Therefore, permeability is not considered to be varied in our simulation directly based on the evolution of strain localization. In fact, in order to take into account the actual process of variation of permeability around the real excavated gallery, we consider its increase through imposing the measured values, as presented in Section 6.4.2, in different times and spaces in our modeling. In this sense, after the first phase, i.e. excavation phase, throughout which the anisotropic permeabilities are defined in the whole model based on Table 6.8, two other phases in time are considered while the permeability is imposed differently for them: second phase for 3.5 years since the excavation time in February 2002, and third phase for the last 8.2 years until the end of simulation. Figure 6.31 shows the imposed permeabilities in these two phases. In fact, in each (time) phase, three zones are

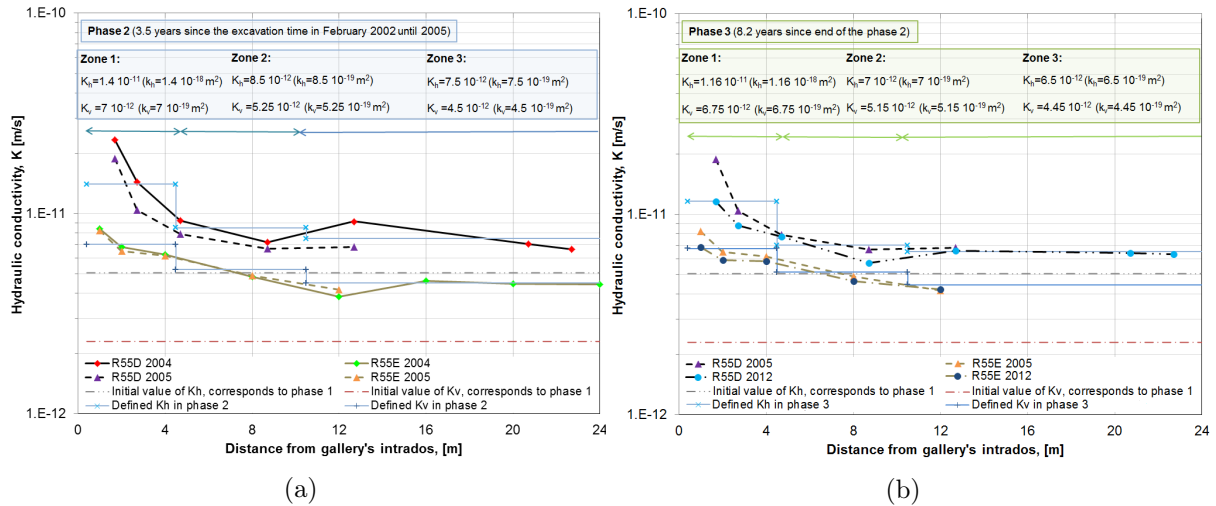


Figure 6.31: Defined spatial zones of anisotropic hydraulic conductivity/permeability with regard to the distance from the gallery's intrados (based on the measurements) for the (time) phase: (a) 2. (b) 3 of our simulation. The initial value of horizontal and vertical hydraulic conductivities corresponding to the phase 1 are also shown for a better comprehension.

considered in space as well, with regard to the distance from the gallery. Then, the vertical and horizontal hydraulic conductivity (or, permeability) is defined differently in each of these spatial zones and for each relative time phase (Figures 6.31a or 6.31b) based on an average of in-situ measurements in the corresponding time (with regard to the measurement year) and space (with regard to the filter's distance).

### 6.5.1.3 Gravity effects

With regard to the gravity effects, the initial stresses and pore pressure are noticeably varied by going far from the gallery (URL level). This effect could be for instance illustrated by the measurements of pore pressure taken from the upward and downward piezometers as shown in Figure 6.20. Therefore, in order to better simulate the site measurements, specially in the far field, the gravity effect is also considered in our extended modeling.

Figure 6.32 shows the geometry and boundary conditions of the extended model. The general boundary conditions are defined in the same manner as the previous modeling consisting in the constant initial stresses and pore pressure on the model's boundaries. However, given the consideration of the gravity, the initial stresses and pore pressure are varied along the model's height of 200 m with respect to the corresponding values at the URL level (i.e.  $\sigma_{yy} = 4.5 \text{ MPa}$ ,  $\sigma_{xx} = 3.8475 \text{ MPa}$  and  $p_w = 2.25 \text{ MPa}$ ), as it is shown in Figure 6.32. The release of the boundary forces and pore pressure on the gallery wall is defined in 6 days similarly to the model of a quarter of the gallery.

### 6.5.1.4 Results of the modeling

The increment of deviatoric strain, plastic loading index, and total deviatoric strain during the excavation period (at 4,5, and 6 days), after 3.5 years (end of second phase), and after 11.7 years (end of simulation) are presented in Figure 6.33 for a zone with the radius of 6.5 m from the gallery wall. The contours of increment of deviatoric strain show the initiation of the

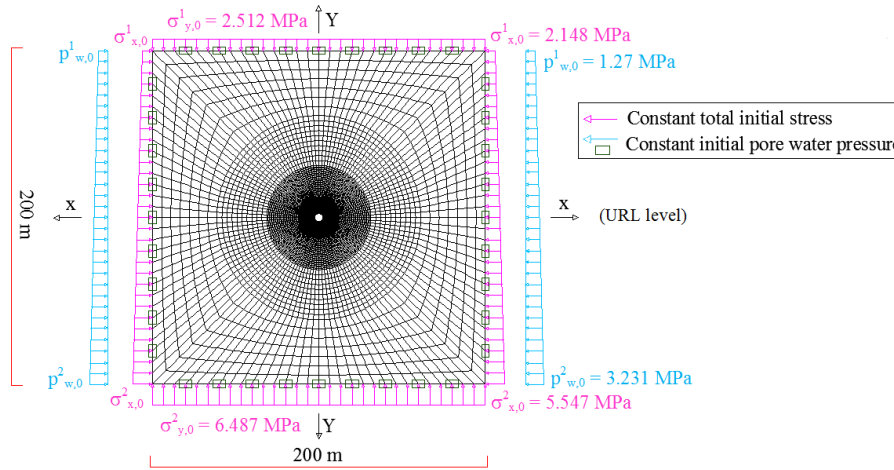


Figure 6.32: The mesh geometry and boundary conditions of the model of full gallery considering the gravity effect.

strain localization at about 4 days, in a symmetric pattern, around the gallery (mostly extended horizontally). Subsequently, the evolutionary activity of the bands - creation of the new bands and/or inactivity of some existed bands - are observed during the excavation (see Figures 6.33a-6.33c). The increment of deviatoric strain does show no noticeable activity of these bands in the later time steps after the excavation, and their evolutionary process is almost limited to the excavation period, similarly to what has been observed in the previous modeling (see Figure 6.6). In the similar manner, the plastic loading index, which also refers to the response of the material in the current time step as already described (see Section 6.3.3), consist in a dominant elastic behavior of the material around the gallery in long-term (see Figures 6.33d and 6.33e). As a result of such evolution pattern of the localized bands in time, total deviatoric strain that in fact correspond to the accumulation of the whole activity of the shear bands mostly evolves during the excavation phase. Hence, the latter is quite unchanged in Figures 6.33d and 6.33e compared to the corresponding contour at the end of excavation (6 days; see Figure 6.33c).

Moreover, the bifurcation solution as well as the nodal velocity norm on the deformed rock mesh, and the deformed configuration of the lining (deformation enlarged by a scale factor of 15) are presented in Figure 6.34 for the aforementioned analysis times. With respect to the bifurcation solution during the simulation - where the displayed green and red arrows estimate graphically two potential orientations of shear bands - the above explained evolutionary process of localization is consistently illustrated. It is demonstrated that bifurcation is reached in some elements around the gallery since 4 days resulting in the initiation of the strain localization. In the long-term (see Figures 6.34d and 6.34e), no bifurcation is longer observed inhering in no appearance of strain localization (see also Figures 6.33d and 6.33e).

Furthermore, the contours of the nodal velocity norm - where the black arrows show the global direction of the material movement (the velocities flow direction) - consist in a reflection of the the shear band activity and localization response within the clay. In fact, through the initiation of localization after about 4 days, and its extension along the horizontal direction, there is a global inward movement of the rock at the left and right sides of the gallery wall (see Figure 6.34a). Subsequently, an evolutionary activity of the bands during the excavation inheres in a dominant vertical (specially at the top of the gallery) movement of the rock. An anisotropic oval-shaped convergence of the clay is therefore illustrated (see Figure 6.34c). Consistently, the lining is deformed upon its contact with the clay during the rock's convergence evolution. Then, throughout a longer time, a recompression of the clay occurs while the lining tends to recover its

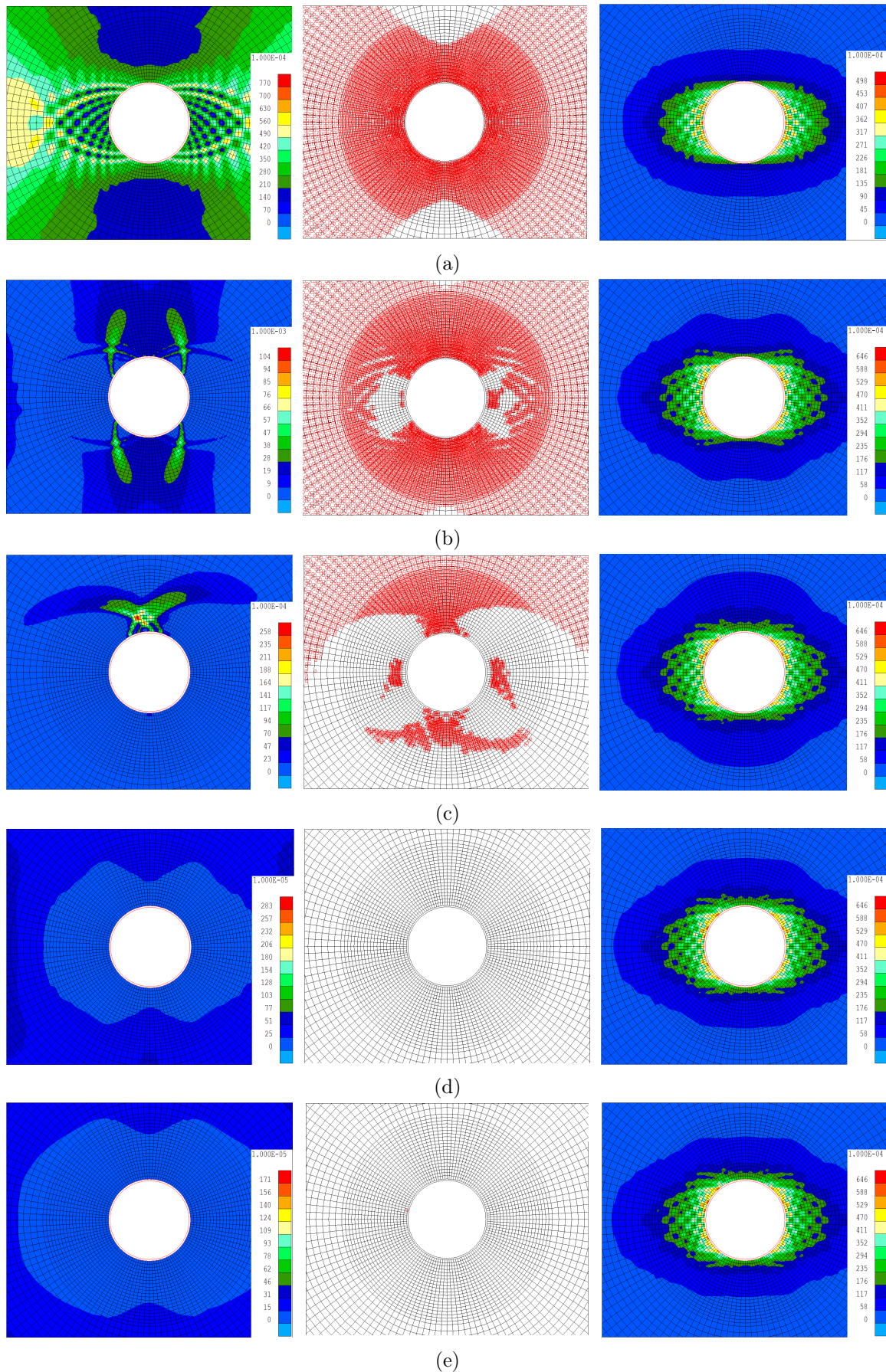


Figure 6.33: Increment of deviatoric strain (in the left side), plastic loading index (in the middle), and total deviatoric strain (in the right side) after: (a) 4 days. (b) 5 days. (c) 6 days (end of excavation). (d) 3.5 years. (e) 11.7 years.

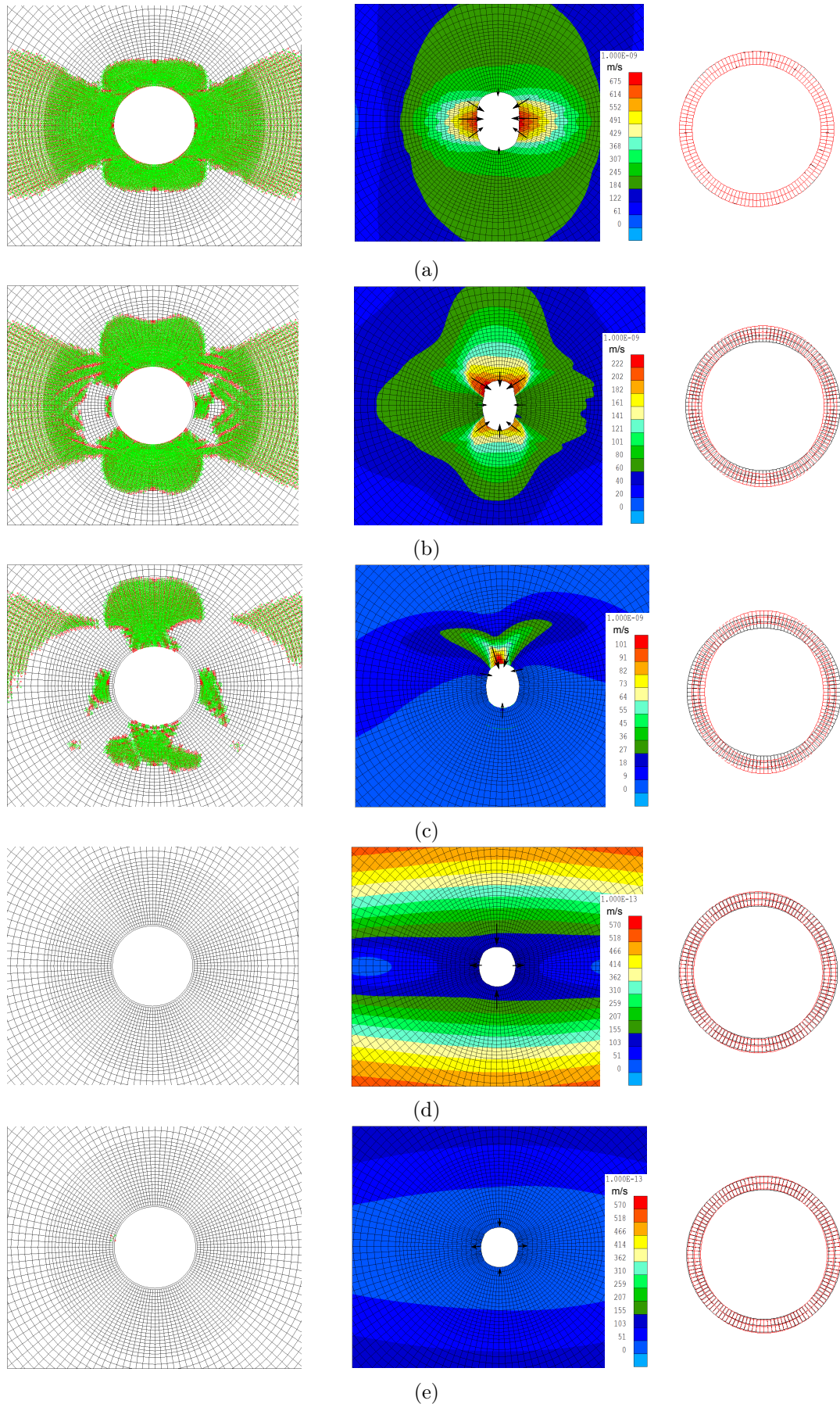


Figure 6.34: Illustration of the bifurcated elements (in the left side), velocity norm on the deformed rock mesh (in the middle), and deformed configuration of the lining (in the left side) after: (a) 4 days. (b) 5 days. (c) 6 days (end of excavation). (d) 3.5 years. (e) 11.7 years.

initial position. Ultimately, there is no more considerable nodal velocity norm within the rock in overall.

With regard to the evolutionary pattern of strain localization at once in Figure 6.33, a general quasi-symmetric response is observed around the gallery (compare also Figure 6.35a with the same simulation for a quarter of the gallery in Figure 6.35b). However, a totally full symmetrical response of the system is not necessarily expected when the strain localization plays an important role in the modeling [Sieffert et al., 2009]. Within this framework, a trivial loss of symmetry can be noticed in the pattern of localized shear bands within the surrounding clay, mostly in the vertical direction, at the end of excavation (Figure 6.33c). The latter may be also partially linked to the gravity effect. It may be noteworthy that this loss of symmetry within the surrounding rock, even insignificant, might have some impact on the behavior of the contacting lining, and the movement of its segments with regard to each other considering that the lining is made of the jointed segments in reality (see Section 7.5).

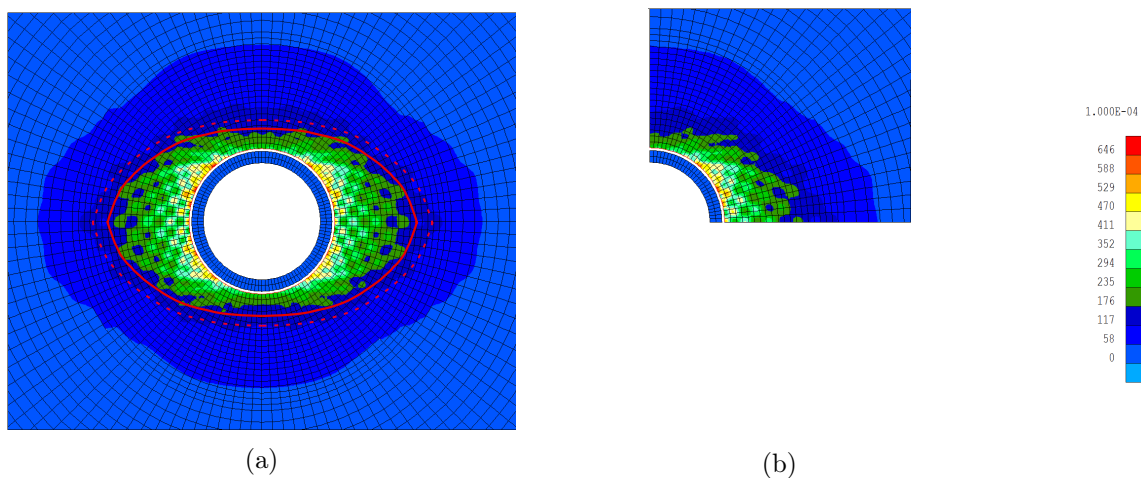


Figure 6.35: (a) Eye-shape extension of the EDZ around the gallery. The pink line shows schematically this eye-shape pattern of localization within the clay surrounding the gallery, with regard to the total deviatoric strain at the end of excavation. (b) The result of the similar modeling as the full gallery, for a quarter of the gallery, in terms of the total deviatoric strain at the end of excavation.

Furthermore, an eye-shape extension of the excavation damaged zone around the gallery is obtained numerically, as demonstrated in Figure 6.35a. This extension is estimated about  $2.8\text{ m}$  horizontally and  $0.6\text{ m}$  vertically, with reference to the total deviatoric strain at the end of excavation phase after which the shear bands do not have actually a noticeable activity as it has been already illustrated. This estimation lies in a quite low extension of the damaged zone around the gallery in the similar manner to the in-situ observations as it will be demonstrated in Section 6.5.2. In fact, this limited EDZ is linked to the used industrial tunneling technique that could importantly reduce the induced perturbation by the digging operations in the surrounding clay [Bernier et al., 2007c], and principally it is associated to the existence of the concrete lining. The latter does not allow more development of the localized shear bands immediately after its contact with the host rock (restraintment by tunnel lining); this significant role of the lining will be more precisely described in Section 7.4.

The anisotropic response of the clay to the excavation process inheres also in the eye-shape extension of the damaged zone around the gallery. This anisotropic feature is mainly associated to the applied initial anisotropic stresses. On the whole, the general coupled behavior of the host rock in the isotropic and symmetrical point of views should be analyzed with respect to

several definite aspects in our modeling: the anisotropic initial stresses, the material anisotropy - cohesion depending on the angle between major principle stress and the normal to the bedding orientation, cross-anisotropy of the elastic properties, and anisotropy of the hydraulic conductivity -, the gravity effects, and possible loss of symmetry induced by the strain localization process. With regard to the plastic anisotropy imposed through the anisotropic cohesion evolution, a primary higher displacement and development of the localized zone due to the excavation could be expected along the horizontal direction as well. In fact, the orthoradial stress is increased in the course of excavation while the radial stress is decreased (before contacting with the lining). Thence, the major loading direction tends to be vertical at the left and right side of the gallery (i.e. along the horizontal direction), and its angle with the normal to the bedding would be then zero. On the contrary, the orthoradial stress and the normal to the bedding are perpendicular at the top and bottom of the gallery (i.e. along the vertical direction). Consequently, a higher cohesion in the latter direction can be obtained (see Figure 6.30) consisting in a higher strength and less extension of the localized zone.

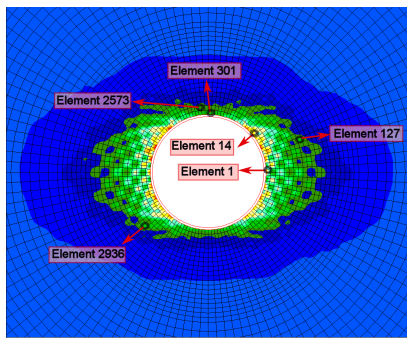
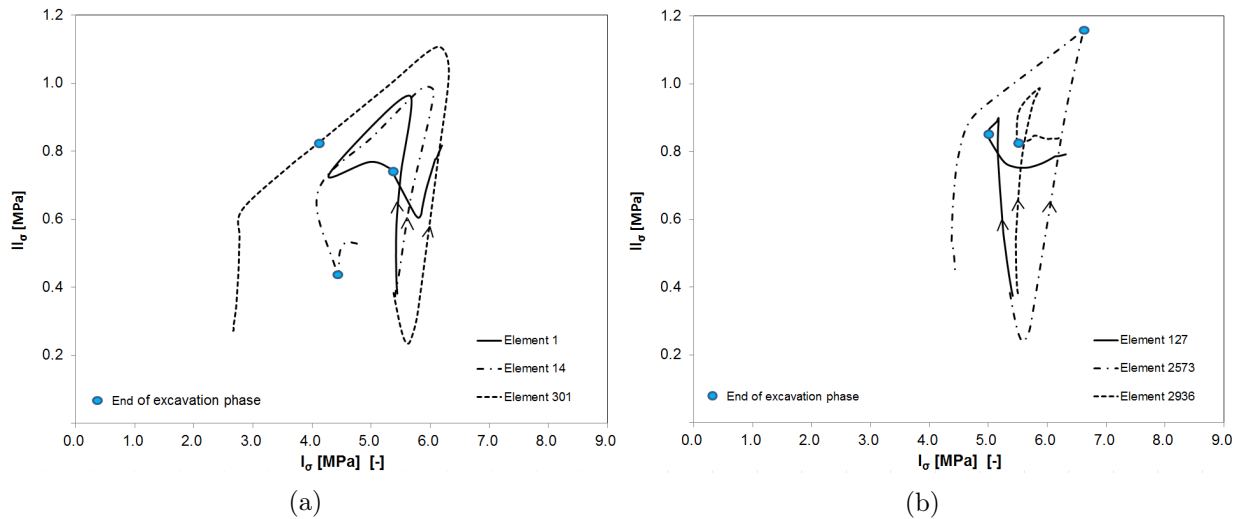


Figure 6.36: Effective stress paths in the  $(I_\sigma, II_\sigma)$  plane for the elements: (a) 1, 14, and 301 on the gallery wall. (b) 127, 2573, and 2936 around the gallery, as shown in the bottom image.

Moreover, Figure 6.36 shows the effective stress paths in the  $(I_\sigma, II_\sigma)$  plane for three elements lied on the gallery wall (elements 1, 14, and 301), and for three other elements within the localized zone around the gallery (elements 127, 2573, and 2936). With regard to the development process of strain localization around the gallery (see the evolution of increment of deviatoric strain in Figure 6.33), the material softening behavior and the initiation of strain localization are reflected on the stress path of these elements, located within different created localized shear bands, through a decrease in their first stress invariant with a decrease of second invariant of deviatoric stress after its maximum value. The localized shear bands are created firstly in a dominant direction of horizontal. As a result, given Figure 6.36a, the stress path in the element 1 turns left sooner in the course of excavation. Subsequently, since the (almost) horizontally directed

shear bands are getting mostly inactive (no more development of those bands) at the end of excavation phase while a new vertical band is created (see Figures 6.33b and 6.33c), the stress path of the element 1, and also the element 14 turns back to right some where before the end of excavation (shown by a blue point on the corresponding curves). Indeed, this process is linked to the contact phenomenon between the clay and the lining that seems to have been initiated from the horizontal direction consisting in the recompression of the clay (see Section 7.4.3 in the next Chapter). On the contrary, the localized shear band correspond to the vertical element 301, created towards the end of excavation phase, seems to be still active for a while after the end of excavation, based on its stress path. Moreover, some decrease of the second invariant of deviatoric stress is observed in the element 301 at the beginning of excavation phase. This decrease is *a priori* associated to consideration of the anisotropic initial stresses. In fact, since the vertical stress is higher than the horizontal one, their difference (that is supposed to imply the deviatoric component of stress) gets foremost (i.e. at the beginning of excavation phase, and therefore no contact with the lining yet) *lower* in the top and bottom of the gallery, due to the excavation resulting in the radial (vertical) stress to vanish and the orthoradial stress to be increased. Subsequently, there is an increase of the deviatoric stress until its peak initiating the strain localization.

The similar phenomena can be ascribed to the stress paths of the three other elements in Figure 6.36b. The stress path of the element 2573 then for instance shows primarily some decrease of the second invariant of deviatoric stress. Moreover, the first stress invariant seems to be decreased with the increase of the second invariant of deviatoric stress before its maximum value, in the element 127. Given the position of this element, this decrease is supposed to be linked to the local increase of the pore water pressure along the horizontal direction in the vicinity of the gallery (see Figure 6.38a) with respect to the coupled hydro-mechanical response of the clay.

Moreover, Figure 6.37 shows the contour of pore water pressure after 6 days for the whole model, and in a close-up around the gallery. First of all, the effect of gravity in our modeling is obvious in the hydraulic point of view through the different layers of pore water pressure along the model's height (see Figure 6.37a). Secondly, a local decrease of the pore pressure along the vertical direction, close to the gallery, and an increase of the pressure along the horizontal direction is observed (see Figure 6.37b), similarly to what has been shown with regard to the former modeling in Section 6.3.3.

This evolution of pore pressure is also demonstrated in Figure 6.38 which presents the pore pressure along the horizontal and vertical cross-sections in a distance of 100 meters from the gallery (axis), and at different times during the simulation. In fact, the overall variation pattern of pore pressure in the vicinity and far from the gallery, along the horizontal and vertical cross-sections follows the description given for the preceding model of a quarter of the gallery in Section 6.3.3 (see Figure 6.8 and its corresponding discussion). However, an interesting aspect illustrated here with respect to our current extended model of a full gallery is the clear effect of gravity in the obtained results. On the contrary to the symmetrical pattern of evolution of pore pressure along the horizontal cross-sections A-A and A'-A' (Figures 6.38a and 6.38b), the vertical cross-sections C-C and C'-C' demonstrate the considerable impact of gravity by getting quite far from the gallery until a distance of 100 m (Figures 6.38c and 6.38d). Hence, in the far field where the pore pressure tends to approach its initial value because of the less influence of excavation process, a decreasing or increasing pattern is observed by getting farther from the gallery wall along the upward cross-section C-C or downward cross-section C'-C', respectively. Furthermore, with regard to an increase of pore water pressure from its initial value during the excavation, along the horizontal cross-sections in a vicinity of the gallery, (see close-up plots in Figures 6.38a and 6.38b), this pore pressure tends to be considerably decreased (and locally drained) during the time after the excavation (from 6 days to 11.7 years) in order to recover its initial value.

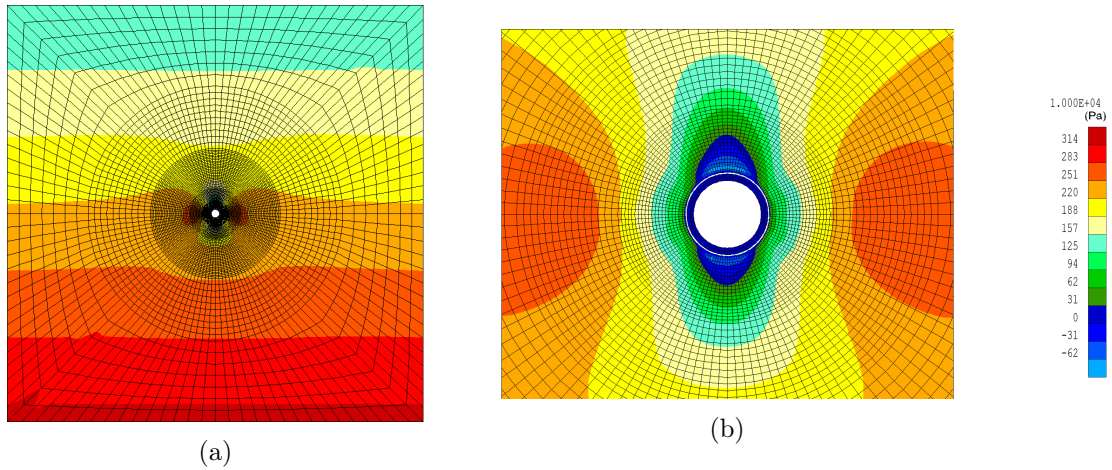


Figure 6.37: Contour of pore water pressure at the end of excavation phase (6 days) for the: (a) Entire model. (b) Zone around the gallery.

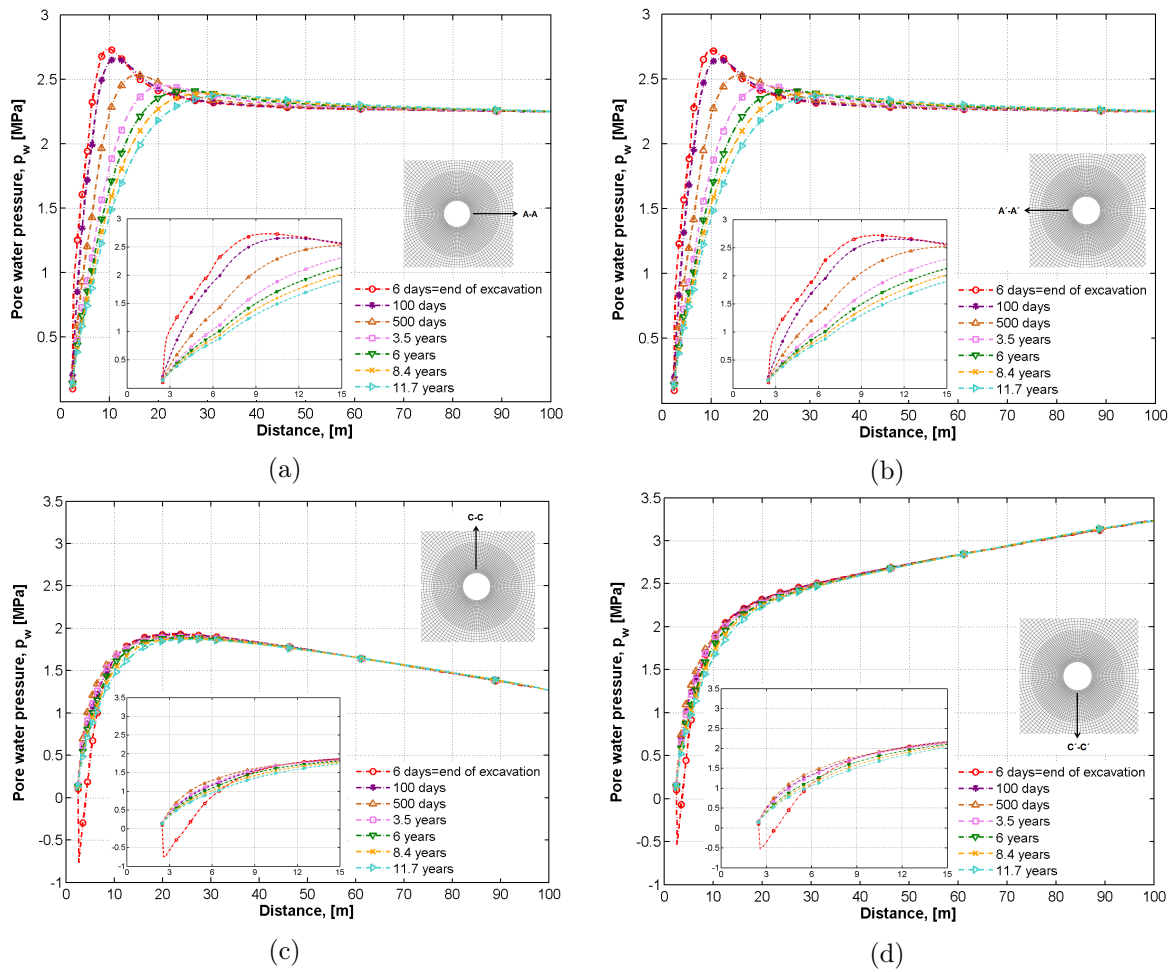


Figure 6.38: Pore water pressure evolution along (a) Horizontal cross section A-A. (b) Horizontal cross section A'-A'. (c) Vertical cross-section C-C. (d) Vertical cross-section C'-C'.

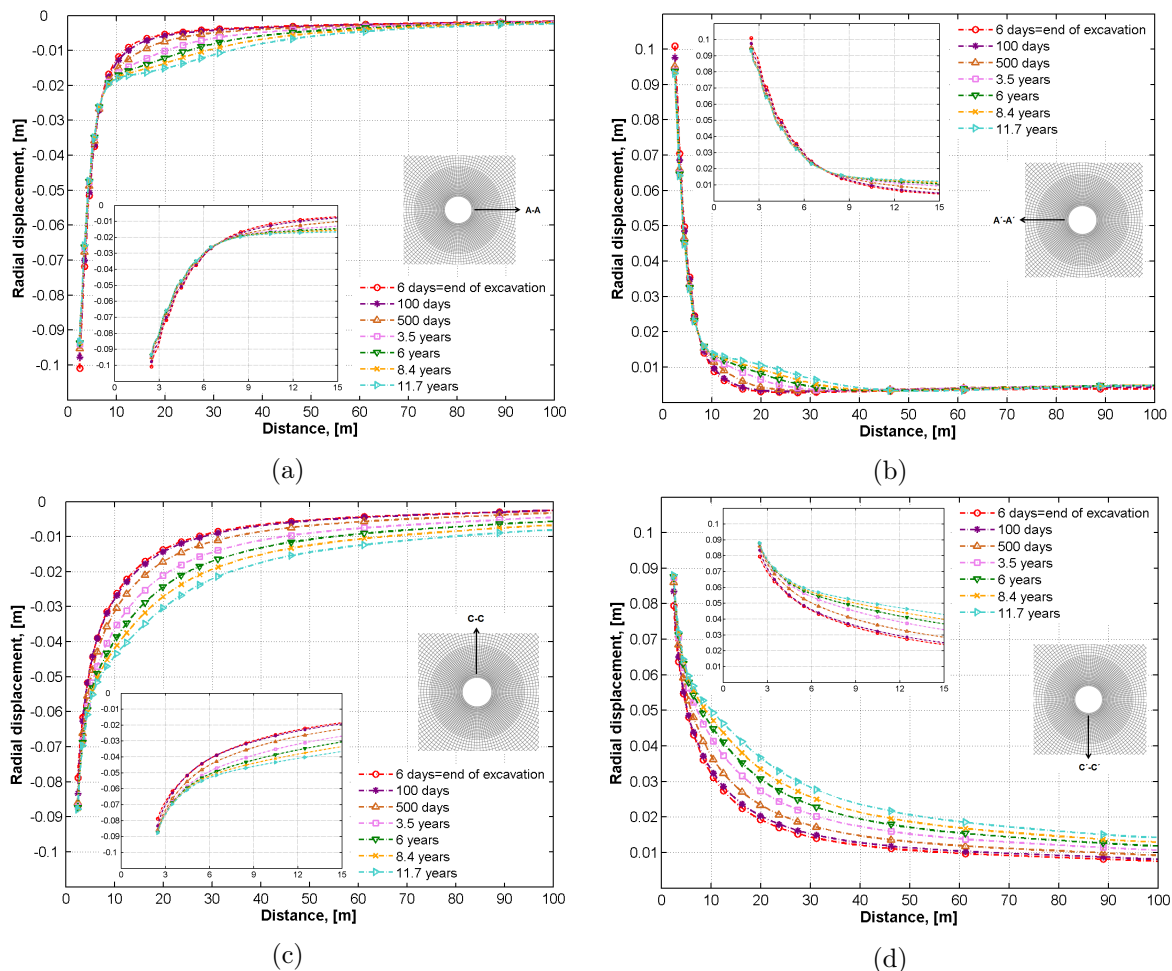


Figure 6.39: Radial displacement evolution along (a) Horizontal cross section A-A. (b) Horizontal cross section A'-A'. (c) Vertical cross-section C-C. (d) Vertical cross-section C'-C'.

Additionally, the evolution of radial displacement is presented in Figure 6.39 along the two horizontal and two vertical cross-sections in function of the distance from the gallery (axis). The displacement of the clay on the gallery wall at the end of the excavation (6 days) is higher for the horizontal cross-sections A-A and A'-A' (Figures 6.39a and 6.39b). This inheres in the anisotropic oval-shaped deformation of the clay (see Figure 6.34c) which could then result in a sooner contact of the clay with the lining from the horizontal side and hence, recompression of the clay during the time. Thus, an opposite pattern of clay deformation is tended in longer time and as a result, the obtained displacements in a very close horizontal distance to the gallery (see the close-ups in Figures 6.39a and 6.39b) show a very slight decreasing pattern during the time. With regard to the vertical cross-sections (Figures 6.39c and 6.39d), a gradual increase of the displacement is observed in time. This increase is more important getting pretty far from the gallery wall, and it is obviously more noticeable than the displacement evolution along the horizontal cross-sections in a relative distance from the gallery. The latter is mostly associated to the consideration of cross-anisotropy in the material's elastic properties in our modeling. In fact, the Young's modulus is defined to be higher parallel to the bedding (horizontal direction) than perpendicular to the bedding (see Table 6.7). Hence, getting some distance from the gallery where the material behaves elastically (specially in the higher time steps), the displacement is obtained more important along the vertical direction. The ultimate displacements in the last time steps, in the far field along the cross-sections C-C and C'-C' (until the distance of 100 m),

are therefore more considerable.

### 6.5.2 Fracture characterization

This Section is aimed to compare the obtained numerical predictions regarding the pattern of localized shear bands and their extension around the gallery with the fractures observed during the gallery construction. Figure 6.40 shows the extent of the fractured zone and its pattern in the gallery front and along the vertical (radial) direction around the Connecting gallery. The observed fracturing pattern has been already described in Section 5.2.3; it is recalled that "these fractures are curved at their intersection with the vertical and horizontal planes passing through the gallery axis, and this curve was found to be more accentuated vertically than horizontally" [Bastiaens et al., 2003]. Hence, the vertical extension of EDZ with respect to the gallery axis is less than the horizontal one. With regard to our presented computed results, the both features mentioned in the aforesaid in-situ evidence - i.e. the curved pattern of evolution and the higher horizontal extent compared to the vertical one - have been then predicted by our numerical simulation.

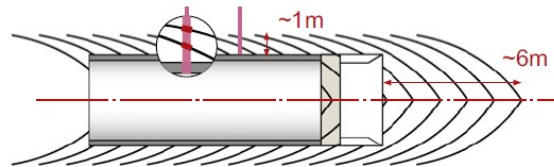


Figure 6.40: Fractures pattern and extent along a vertical cross-section parallel to the gallery axis [Bernier et al., 2007c].

The radial (in the vertical plane) extent of fracturing has been evidenced to be less than one meter with regard to Figure 6.40. Although, in a more precise point of view, while a downward core borehole (i.e. along vertical direction), performed after the execution of the gallery, identified a fractured zone up to  $0.6\text{ m}$  [Mertens et al., 2004], there have been some evidences of fractured zone in the horizontal direction to extend a few meters from the gallery [Van Marcke and Bastiaens, 2010], similarly to our numerical predictions (i.e.  $0.6\text{ m}$  vertically and  $2.8\text{ m}$  horizontally). The latter site evidences (regarding the horizontal extent) have been observed during the first few meters of construction of the Praclay gallery<sup>13</sup> where those fractures were crossed (see Figure 5.21).

On the other hand, with reference to the eastward core taken in the proximity of the gallery [Mertens et al., 2004], and the oxidation evidences [De Craen et al., 2008], the horizontal extent of (open) fractures around the gallery has been identified to be also about one meter. The oxidation evidences are based on the relation between the oxidation and fracturing: pore pressure chemistry and compositions would be affected by oxidation within the zone of open fractures (mode I), resulting in high concentration of sulphate and thiosulphate. Indeed, the reason for this difference in the observations of radial (refers to horizontal here) extent of fracturing around the Connecting gallery can be related to *existence* of some microfractures (beyond that one meter) which were not actually observed through the cores taken radially, and they were not in an opening mode to be in contact with air (oxidation). *But* they were likely to form the macrofractures (that have become observable), due to additional stress redistribution caused by excavation of Praclay gallery, and their extent could be then increased too [Van Marcke and Bastiaens, 2010]. As a result, they have been evidenced by then. All the above evidences together,

<sup>13</sup>Praclay gallery has been constructed perpendicular to the Connecting gallery; see Figure 2.3

an horizontal extension of one meter is deduced for the open fractures, due to excavation<sup>14</sup>, in the gallery's proximity while the total horizontal extension of (shear) fracturing is over this one meter, as predicted to be about 2.8 m ( $\sim 3$  m) based on our study. Figure 6.41 demonstrates conceptually the overall pattern of extension of the fractures and damaged zone around the gallery. Finally, it is worth to remind that the extension of fractured zone ahead of excavation front (i.e. about 6 m with regard to Figure 6.40) is not clearly possible to be modeled through our 2D numerical simulations.

Next, similarly to the numerical prediction of not having a noticeable extension of damaged zone after the excavation process is finished, the extent of oxidation (considering its relation with fracturing) around the Connecting gallery after its excavation and during ventilation is said to have been limited to the initial extension of open fractured zone [De Craen et al., 2008]. According to Van Marcke and Bastiaens [2010], an impact of ventilation of the gallery on the desaturation of the clay and the overall fractures extension around the gallery have not been observed.

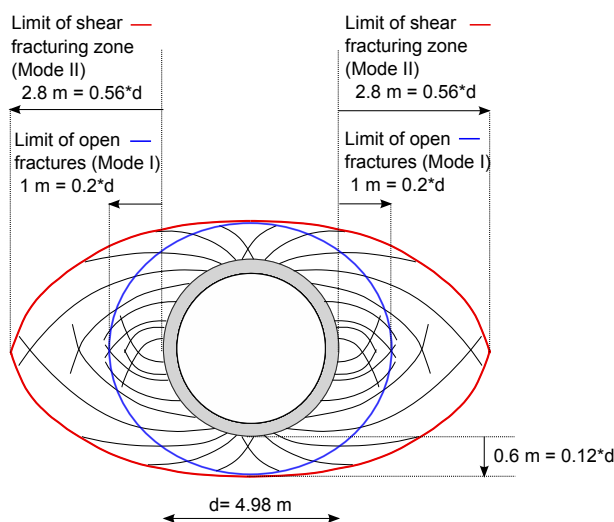


Figure 6.41: Conceptual representation of the fractured zones (in mode I and mode II) around the gallery due to the excavation.

Furthermore, an eye-shape EDZ pattern around the gallery (as could be also perceived in Figure 6.41) has been observed with regard to a cross-section perpendicular to the gallery axis, as schematically represented in Figure 6.42a. Our numerical simulation has been consistently lied in this eye-shape extension of damaged zone (see Figure 6.42b). In addition, the small-scale observations in the site and in the laboratory confirm this pattern of fracturing. Figure 6.43 shows the conjugated eye-shape shear induced fractures around a resin-immobilized borehole. Moreover, during the hollow cylinder test performed on the Boom Clay samples, an eye-shaped damaged zone around the central hole deduced from the displacement profiles - which were obtained by tracking the pyrite inclusions in the X-ray CT scans - could be identified (see Figure 5.13).

<sup>14</sup>With regard to the self-sealing capacity of Boom Clay, sealing of the open fractures occurs subsequently pretty fast while the oxidation products are trapped within this one meter in the gallery's proximity; see [De Craen et al., 2008] for further details on the re-distribution of the oxidation products since it is out of scope of this study.

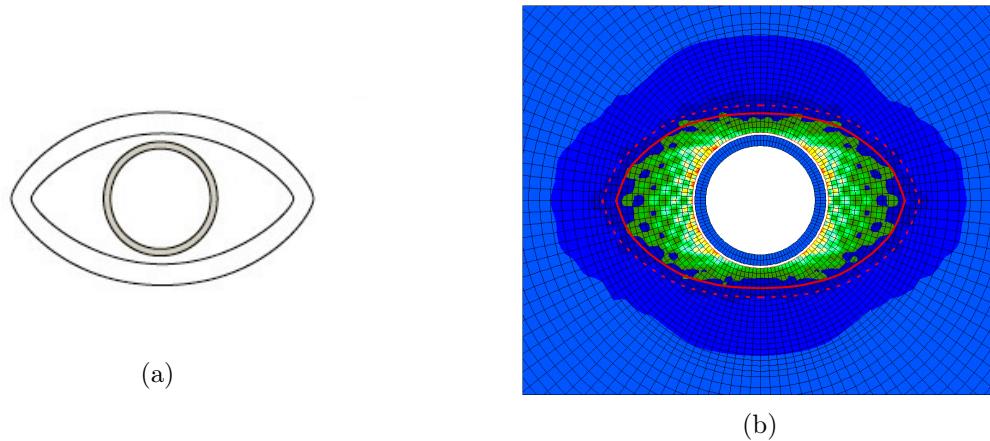


Figure 6.42: (a) Schematic representation of eye-shape fractures pattern around the gallery, in a cross-section perpendicular to the gallery axis [Bernier et al., 2007c]. (b) Numerical prediction of an eye-shape extension of the EDZ around the gallery.



Figure 6.43: Eye-shape fractures around a resin-immobilized borehole [Blümling et al., 2007].

### 6.5.3 Convergence of the rock

In terms of the clay convergence, during the excavation of the Connecting gallery, the radial convergence of the clay in the unsupported zone between the rear end of the shield and the installed lining (see Figure 6.1c) was observed to be higher in the horizontal direction (parallel to bedding) than the vertical one (perpendicular to bedding). In fact, the horizontal diameter seemed to be small to emplace the key segments of the lining, although, the vertical diameter was large enough. Consequently, a trimming of the clay sidewalls (10-20 *mm*) was even necessary over a portion of the gallery before placing the lining [Bastiaens et al., 2003; Mertens et al., 2004]. This anisotropic convergence of the clay sidewalls has been also predicted by our numerical simulations. Figure 6.44 presents the displacement (radial convergence<sup>15</sup>) of the clay in the course of the simulated excavation phase (i.e. 6 days) for two studied nodes (in the horizontal and vertical directions) on the gallery wall. As it is observed, the total horizontal displacement (about 10 *cm*) is more than the vertical one (about 8 *cm*). Moreover, considering this total horizontal displacement of about 10 *cm* of the clay side wall, a maximum displacement of about 1 *cm* is estimated for the lining in the horizontal direction - upon contact with the clay<sup>16</sup> - with respect to 9 *cm* of the initial gap considered between the clay and the lining in the numerical simulation (see Section 6.2.1). This 1 *cm* of the horizontal displacement over the considered over-excavation radius is identified in an equivalent manner as the trimming of the clay sidewall evidenced during

<sup>15</sup>The so-called radial (horizontal/vertical) convergence here may signify half convergence in its general definition (i.e. the reduction of distance between two given points of cavity boundary), under the assumption of a symmetric response

<sup>16</sup>See Section 7.4.3 for a particular discussion on the contact mechanism.

the gallery construction. On the contrary, in the similar sense as the in-situ observations, Figure 6.44 shows that the total vertical displacement is less than the over-excavation radius (9 cm).

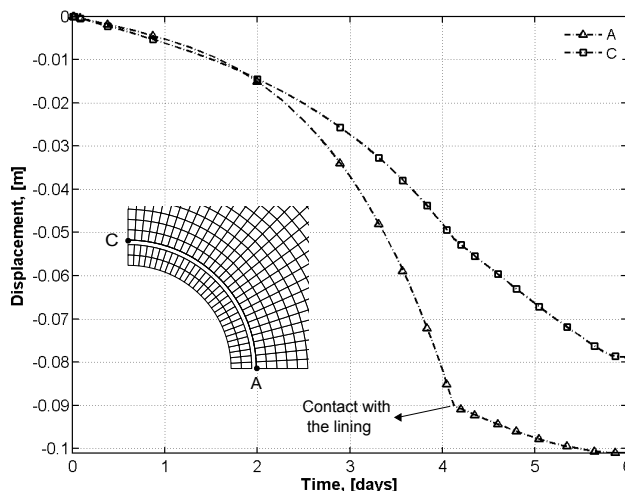


Figure 6.44: Horizontal and vertical displacement (radial convergence) of the clay sidewalls in the course of excavation phase.

This higher convergence in the horizontal direction compared to the vertical one in the observations and numerical results is linked to the anisotropic shape of fracturing and localization development around the gallery. In this sense, it is basically associated to the initial anisotropic stresses, and the subsequent stress redistribution (see also consistently stress paths in Figure 6.36a). In another point of view [Bastiaens et al., 2003; Van Marcke and Bastiaens, 2010], since the dip direction of the fractures are roughly parallel to the gallery axis (see Figure 6.40), vertical de-stressing is supposed to be quite affected by fracturing ahead of the excavation front. Thence, the vertical convergence is reduced thereafter. On the contrary, the clay converges along the horizontal direction such that no fracturing had occurred. Thus, the horizontal convergence is higher.

#### 6.5.4 Numerical results of pore water pressure compared to the in-situ measurements: R55 and R13 boreholes

In-situ measurements of pore water pressure presented in Section 6.4.1.2 are now compared to the numerical results. Figure 6.45 shows this comparison for the R55 multi-piezometers. With respect to the installation time of these piezometers (after the gallery's construction), there is not obviously any record of pore pressure during the excavation, although, a close-up of the computed results in the course of excavation is shown at the top of each piezometer's plot in Figure 6.45.

With regard to the horizontal piezometer R55E (see Figure 6.45a), it is observed that the numerical results are generally in a good agreement with the site measurements. A stationary or decreasing trend in pore pressure evolution is illustrated in time based on the computed results, similarly to what has been discussed with respect to the in-situ measurements represented in Section 6.4.1.2. In addition, the numerical predictions demonstrate an increase of pore pressure in a very close distance to the gallery, at the beginning of excavation, likely because of an immediate undrained response of the clay (see the curves correspond to 1-4 m). Contrarily, there could be also a considerable effect of decompression very close to the gallery; this distance in fact correspond to the horizontal extension of the damaged zone within the surrounding clay

around the gallery as well. Therefore, there is also a decrease of the pore pressure noticed with regard to the same aforementioned curves. Moreover, going relatively farther from the gallery, less influence of decompression is accompanied by the contact occurred between the clay and the lining in the course of excavation which do not allow such decrease of pore pressure.

A quite good agreement is also observed between the simulated results and the measurements with respect the two other piezometers, R55I and R55D. The pore pressures obtained along the inclined piezometer R55I (see Figure 6.45b) lie mostly within a pretty stabilized evolution in time. The corresponding numerical results in fact consist in an intermediate response with respect to the ones obtained for R55E and R55D. With regard to the vertical piezometer R55D (see Figure 6.45c), in a very close or quite farther depths from the gallery, a stationary trend is predicted numerically similarly to the measurements. Although, within some distance in the vicinity of the gallery (see the curves correspond to 4.7-12.7 m), numerical results show a fairly decreasing pattern (after a primary quick increase), on the contrary to a slight increasing tendency measured by the relative filters. Indeed, this fairly decreasing tendency obtained numerically may associate to the simultaneous influence of a local water flow and drainage in a longer time, in addition to the tendency to regain the equilibrium after a drop of pore pressure due to the excavation. This drop seems not to be that important for those (aforementioned) depths to become dominant to the local drainage impact in our simulation (see the close-up on the excavation phase in Figure 6.45c).

Moreover, the aforesaid increasing pattern of pore pressure measured through the piezometer R55D (i.e. mostly by the filters in the depth of 4.7-12.7 m) is not in fact observed with regard to the measurements of the other vertical piezometer, i.e. R13D (see Figure 6.46a), and the numerical and measured pore water pressures in the vicinity of the gallery match better, for the latter piezometer.

Furthermore, in the same line as the piezometer R13D, a quite good agreement is also observed between the simulated results and the measurements taken from the piezometer R13U, specially through the lower depths. Comparing Figures 6.46a and 6.46b, the gravity effect is noticeable with respect to the both simulated and measured pore pressures along the downward and upward piezometers. In this sense, the role of consideration of the gravity in our modeling is obvious in improving the numerical simulation in order to approach better the in-situ measurements. Figure 6.47 shows for instance the measurements of pore pressure through the piezometer R13U compared to our reference simulation so far, and another simulation without consideration of the gravity. It is then observed that the latter's results are further from the in-situ measurements, specially farther from the gallery.

In addition, some difference which still remained between our reference simulated results and the measurements at higher depths along the piezometer R13U (see Figure 6.46b/6.47a) - i.e. quite low measured pore pressures - might be associated to two main issues [Bastiaens et al., 2007; Yu et al., 2011]. First, there may be some influence of the preceding constructed Second Shaft (see Figure 2.3) on the corresponding in-situ measurements. Second, those filters located in the higher depths along R13U are situated in the top of the Boom Clay layer where more silty clay layers with a higher hydraulic conductivity are present.

Moreover, the in-situ pore pressures measured through the multi-piezometers R55 and R13 are compared to the numerical results, in function of the distance from the gallery (axis) and for three points in time. Thence, with regard to the results of our simulation presented in Figure 6.38, Figure 6.48 demonstrates their comparison with the measurements. In all, a good agreement is observed between the numerical and measured pore pressures for all the piezometers. Regarding the piezometer R13U (Figure 6.48e) - quite low measured pore pressure in relatively high distances - likely results from two causes explained beforehand.

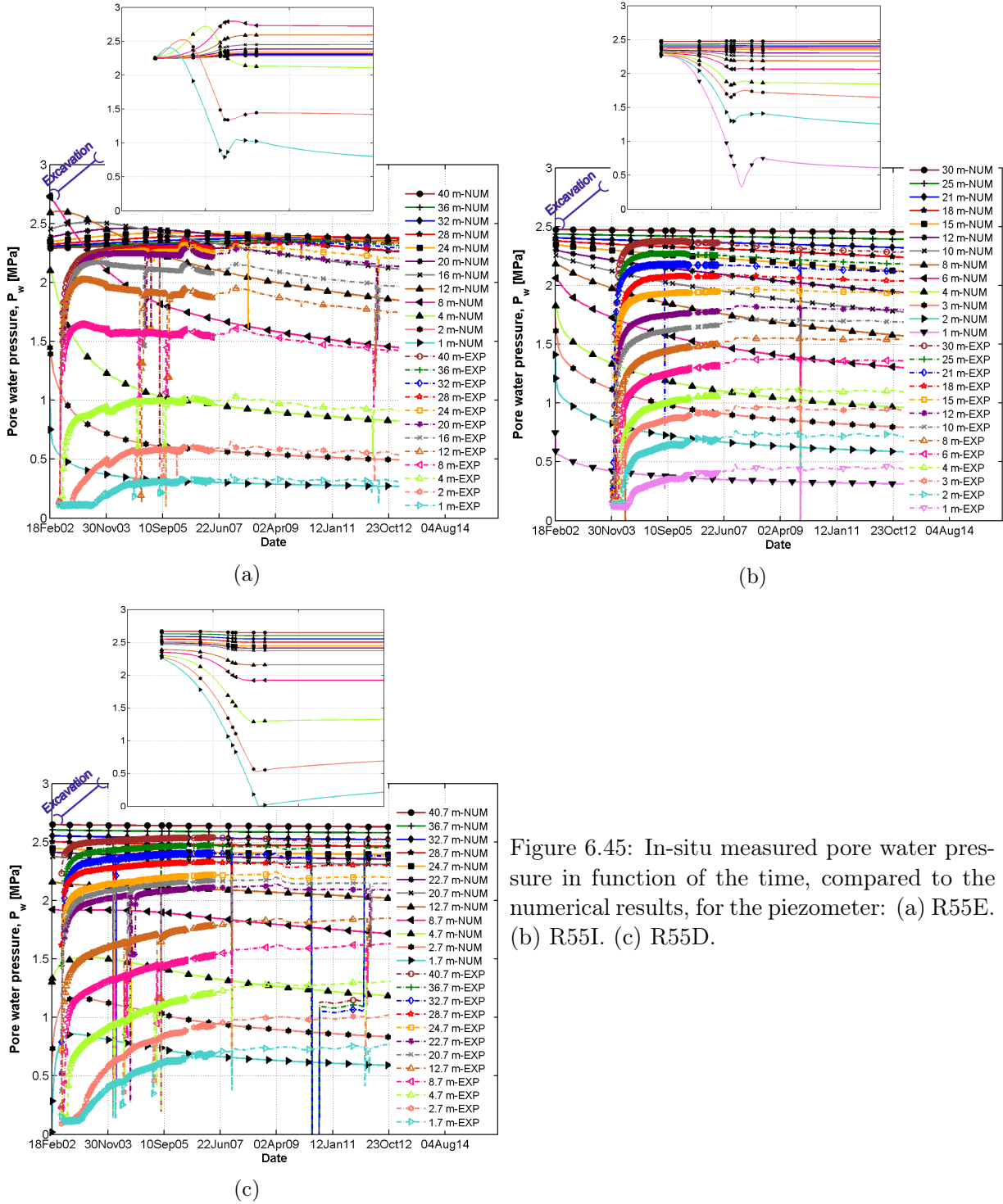


Figure 6.45: In-situ measured pore water pressure in function of the time, compared to the numerical results, for the piezometer: (a) R55E. (b) R55I. (c) R55D.

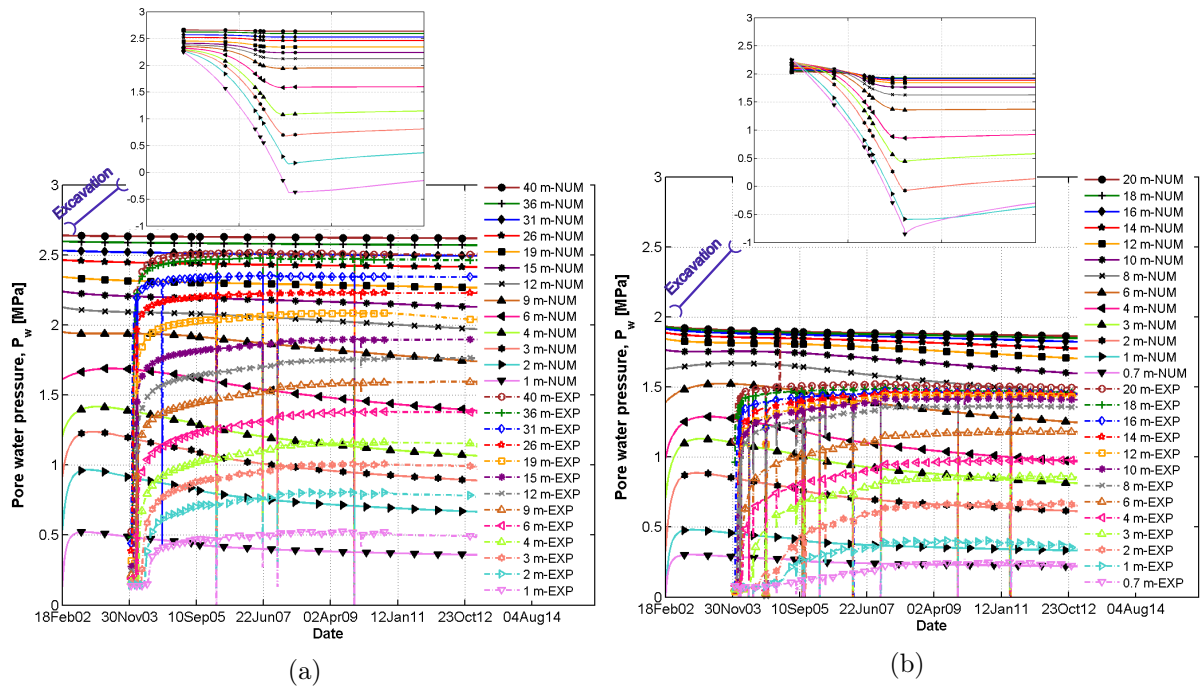


Figure 6.46: In-situ measured pore water pressure in function of the time, compared to the numerical results, for the piezometer: (a) R13D. (b) R13U.

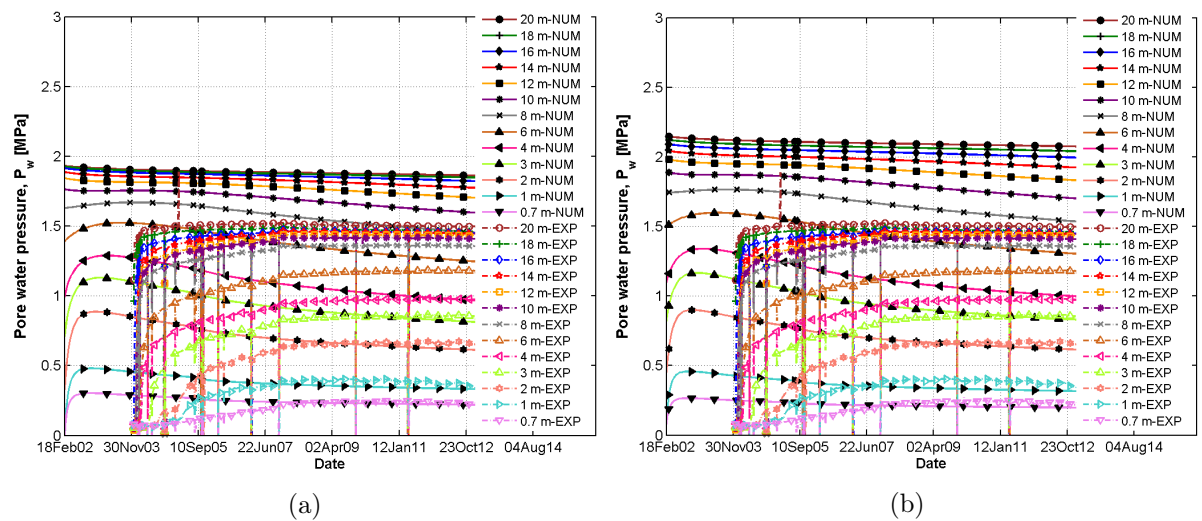
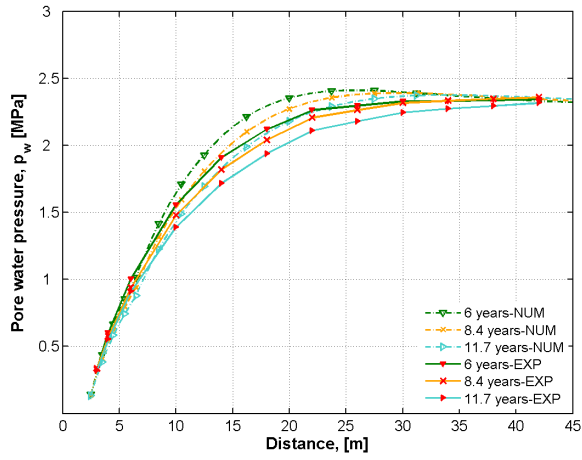
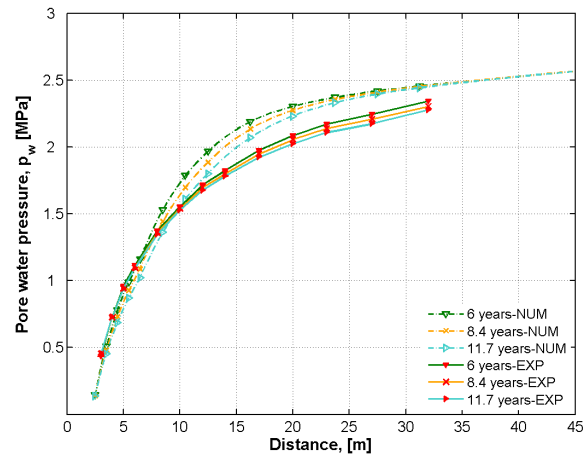


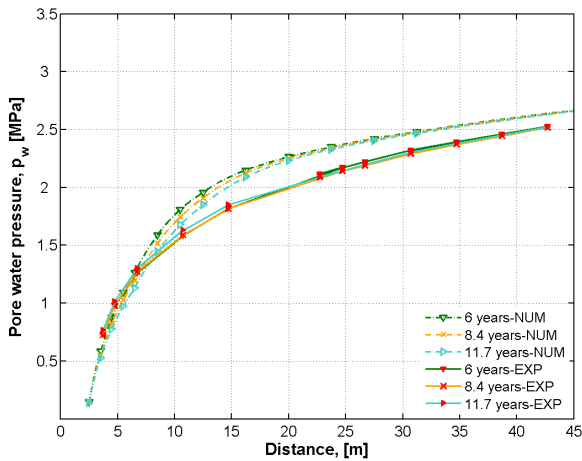
Figure 6.47: In-situ measured pore water pressure, along the piezometer R13U, in function of the time, compared to the numerical results, for: (a) Our current simulation (i.e. considering the gravity effect). (b) Without consideration of the gravity.



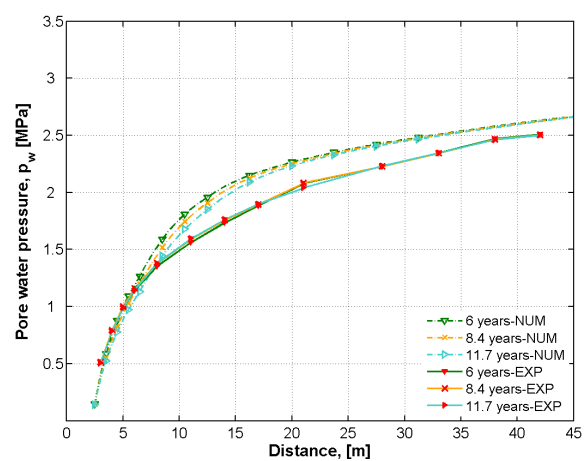
(a)



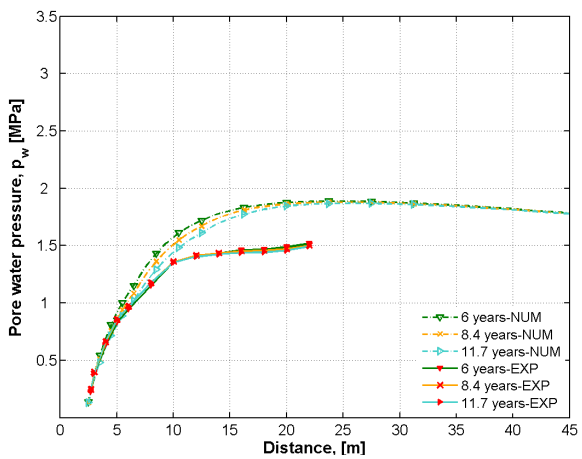
(b)



(c)



(d)



(e)

Figure 6.48: In-situ measured pore water pressure in different depths (distance from the gallery) compared to the numerical results, for the piezometer: (a) R55E. (b) R55I. (c) R55D. (d) R13D. (e) R13U.

### 6.5.5 Numerical results of pore water pressure compared to the in-situ measurements: CLIPEX program

With regard to the analysis performed in Section 6.4.1.1 on the in-situ pore water pressures measured in the framework of CLIPEX program, these data are compared to our numerical results in this Section. Figure 6.49 presents this comparison for the pore pressures measured by the filters of the borehole D2, taking into account a reference pore pressure at the beginning of the excavation phase, with respect to the discussion handled in Section 6.4.1.1. Given Figure 6.49a, it is observed that the computed results consist in a primary increase of pore pressure that might be interpreted in the similar manner as the increase of pressure recorded by the corresponding filters at the site. Although, the latter one (see the EXP curves) is preceded by a slight decrease of pore pressure (as already analyzed in Section 6.4.1.1). In fact, our computation seems to predict that increase ahead of time. This issue is linked to the fact that the lining has been considered in our simulation to be present from the beginning of excavation (even though inactive) while it has had an initial gap (of 90 mm) with the rock (see Section 6.2.1), and it could then come into contact with the host rock during the excavation phase and the convergence of the clay mass. Consequently to the oval convergence of the clay - which is anisotropically higher along the horizontal direction - and the contact with the lining in the course of excavation (inducing recompression of the clay), the simulated pore pressures at each filter could be increased before the end of 6 days considered for the excavation (and with respect to the relative position of that filter with regard to the excavation front). On the contrary, throughout the real excavation, the lining has been installed immediately after the excavation (quite simultaneously with the passage of excavation front along the gallery's axis). From then on, more convergence of the clay has been restricted and a rise of pore pressure could occur (see the experimental curves in Figure 6.49a). In all, the simulated increase of pore pressure is pretty shifted ahead in time, in comparison to the measurements. Moreover, the same comparison is also shown in Figure 6.50a in terms of the change in pore pressure in function of the days. As a result, the predicted increase of pore pressure is taken place for all the filters at the same time (after about 4-5 days corresponding to the contact time, see also Section 7.4.3). In addition, similarly to the measurements, the rise of pore pressure is more important in the closest filter to the gallery, i.e. WD6 (see Figure 6.10b). Furthermore, the borehole's casing was cut off on 7 March 2002 [Bernier et al., 2007b] (see the sudden drop at the beginning of the experimental plots in Figures 6.49b/6.50b) which has been then repaired, and the pore pressures measurements through this borehole are supposed to have been retrieved. Since then, with regard to Figures 6.49b/6.50b, the both simulated and measured pore pressures are consistent in a gradual decrease of pore water pressure in long-term. Additionally, the numerical curves tend to approach still more the experimental measurements if they would extend in time; this process could be better illustrated through the comparison given for the horizontal piezometer R55E in Figure 6.45a.

The simulated and measured pore water pressures through the borehole C2 are compared in Figure 6.51. The sudden drop of pore pressure in the course of excavation is reproduced, progressively for different filters and to the most for the closest filter to the gallery, similarly to the in-situ measurements (as analyzed in Section 6.4.1.1). Although, a precedent slight increase of pore pressure recorded by the relatively closer filters to the gallery is not predicted numerically. In addition, Figure 6.52a shows the same comparison in terms of the change in pore pressure versus the change in time (days). As a results, the drop of pore pressure occurs almost simultaneously for all the filters, numerically and experimentally, regardless of their relative position. In the long-term (see Figures 6.51b/6.52b), the simulated evolution of pore pressure consists in an initial increase and a subsequent slight decreasing or stationary pattern. The measured pore pressures tend to constantly increase in time, though. The computed decreasing tendency may be interpreted in the similar manner as the simulated pattern of pore pressure evolution observed

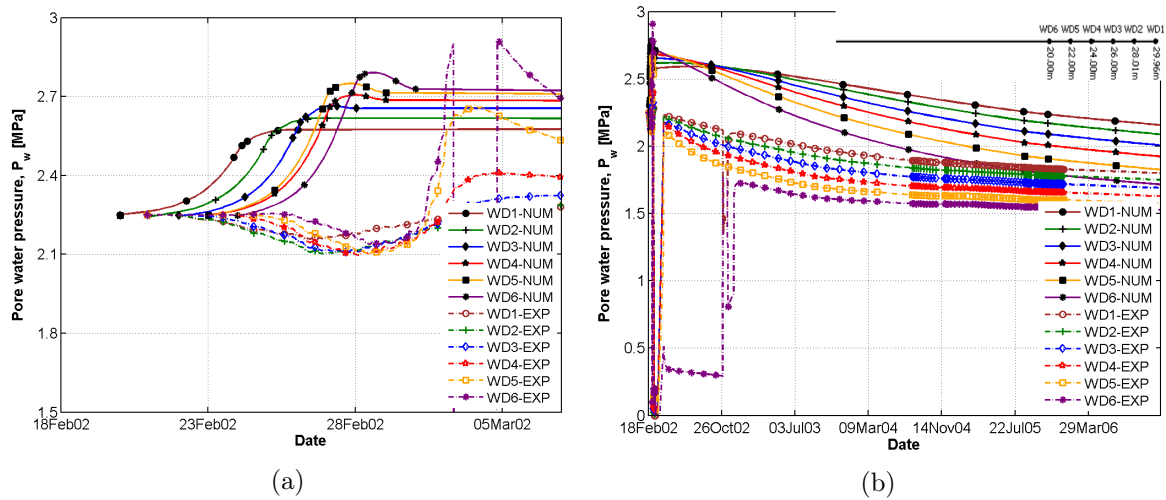


Figure 6.49: In-situ measured pore water pressure in function of the time, compared to the numerical results: borehole D2. (a) During the excavation. (b) In the long-term.

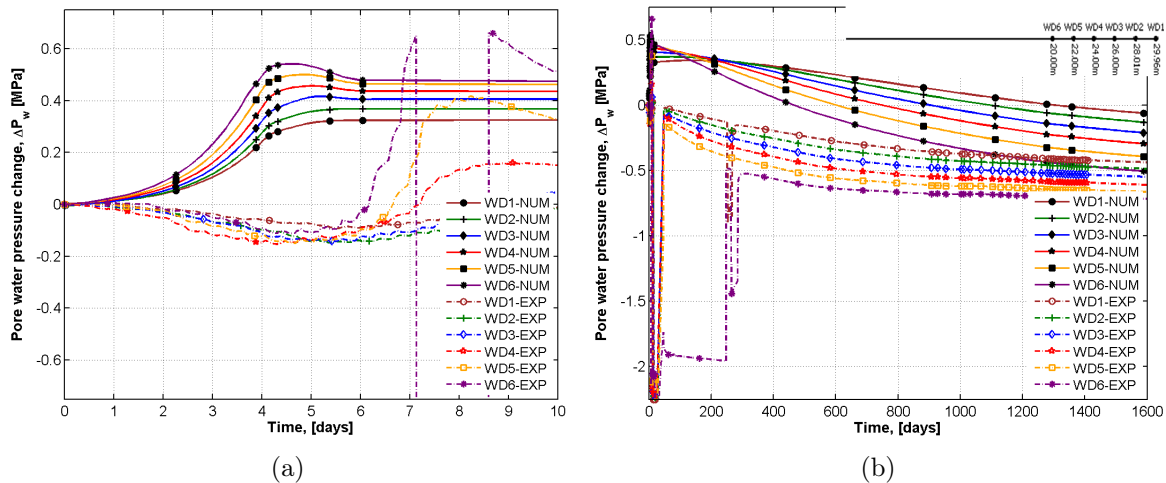


Figure 6.50: Change of the in-situ measured pore water pressure in function of the change in time (days), compared to the numerical results: borehole D2. (a) During the excavation. (b) In the long-term.

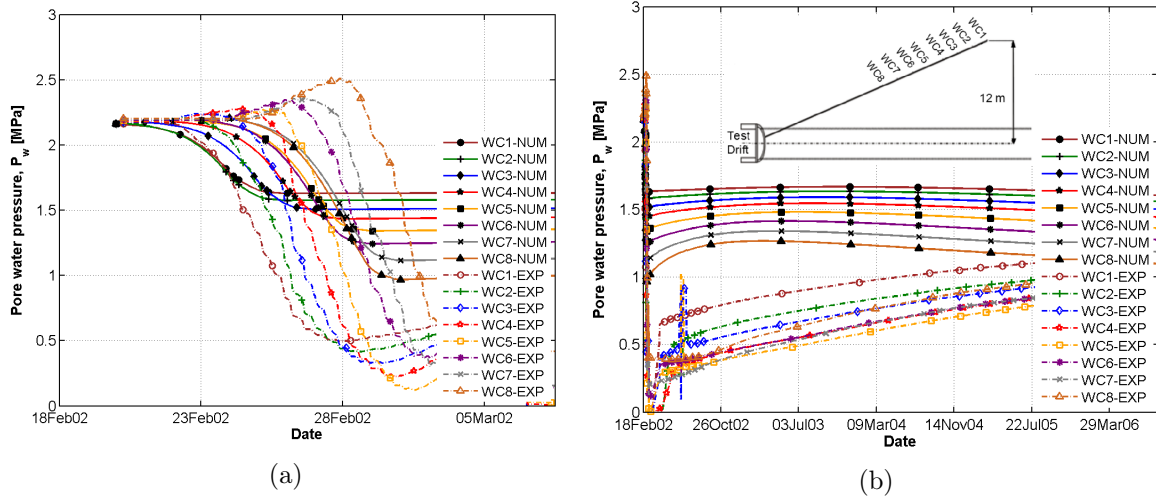


Figure 6.51: In-situ measured pore water pressure in function of the time, compared to the numerical results: borehole C2. (a) During the excavation. (b) In the long-term.

in several filters of the piezometer R55D which are situated in some relative depths with regard to WC1-WC8 (i.e. filters in the depth of 4.7-12.7 m; see Figure 6.45). However, the difference between the numerical and in-situ pore pressure seems to be more considerable here. In fact, the more important drop of pore pressures measured through the filters of the borehole C2 during the excavation, compared to the simulated ones (Figures 6.51a/6.52a), results in the primary less values of measured pressure in the second phase<sup>17</sup>, i.e. after the excavation (Figures 6.51b/6.52b). Hence, there is a subsequent noticeable increasing tendency to regain the equilibrium. In this sense, the less sudden drop of pore water pressure during the excavation based on our simulation (in comparison with the measurements) is likely to be somehow associated to some impacts of excavation front ahead of the front, the matter of a real three dimensional excavation case, and the pre-existing galleries, which cannot be perfectly modeled through a two-dimensional plane strain simulation. Besides, as any numerical modeling, the applied constitutive laws and the relative parameters might be in general influential to some limited extent.

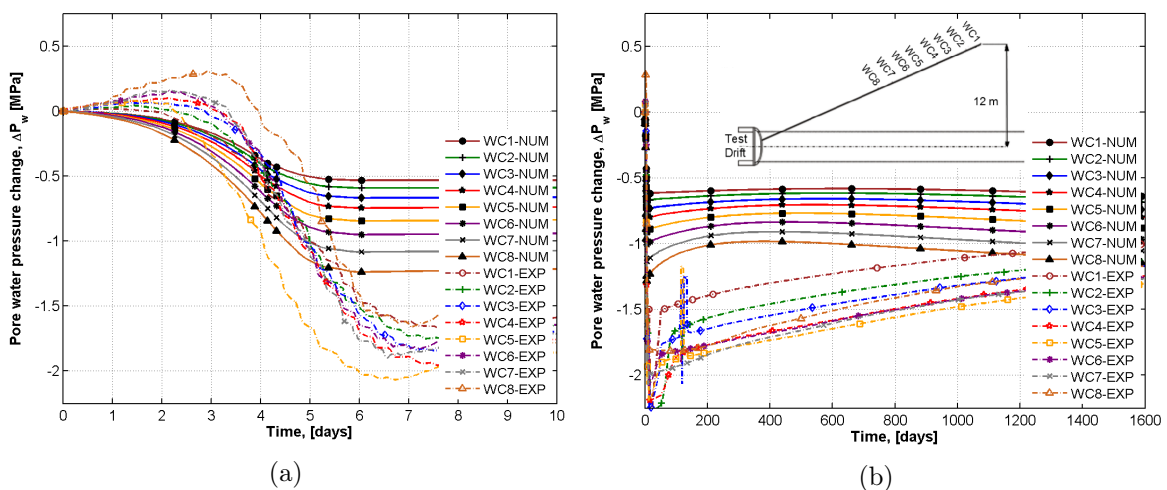


Figure 6.52: Change of the in-situ measured pore water pressure in function of the change in time (days), compared to the numerical results: borehole C2. (a) During the excavation. (b) In the long-term.

<sup>17</sup>The casing of the borehole C2 was cut off on 6 March 2002 [Bernier et al., 2007b].

Moreover, with regard to our numerical prediction of the pore pressure drop during the excavation and its subsequent evolution in time, it is noteworthy that taking into account the material cross-anisotropy (as described in Section 6.5.1.1) in the simulation could have a positive impact on the obtained results. Figure 6.53 illustrates this improvement where the results of the modeling considering the material cross-anisotropy (our reference simulation so far) is presented besides the results of another similar simulation taking into account the isotropic mechanical properties of the material, compared to the site measurements. The mechanical properties of the host rock in the latter simulation have been then defined based on the (isotropic) mechanical parameters given in Table 6.1. It is observed that a less drop of the pore pressure in the course of excavation is predicted by the simulation with isotropic material properties. As a result, there is less tendency in long-term to recover that experienced drop of pressure. Thus, the pore pressure evolution is mainly governed by the local drainage flow consisting in a more considerable decreasing pattern.

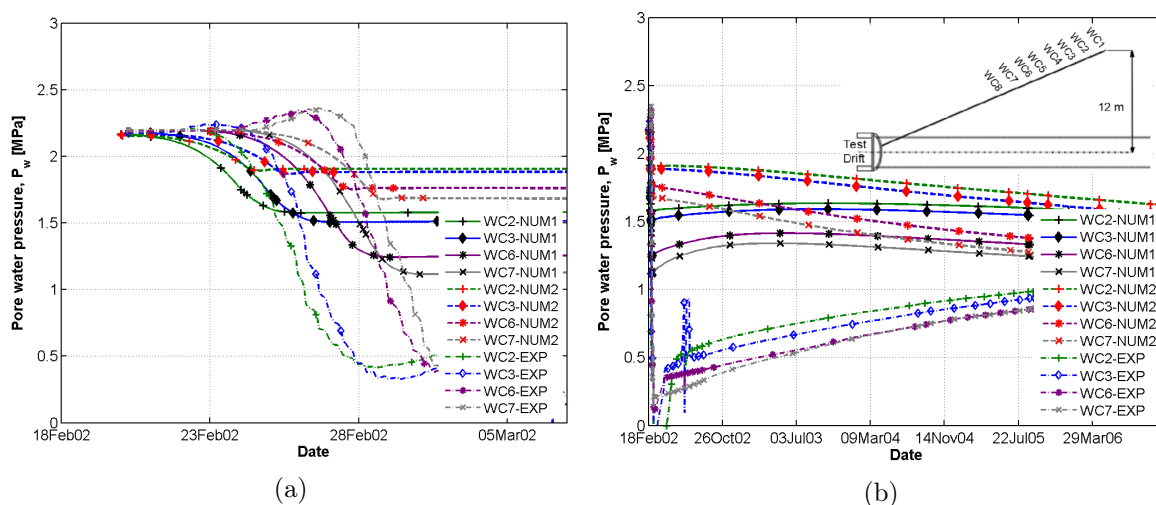


Figure 6.53: In-situ measured pore water pressure in function of the time, compared to the numerical results, for four filters of the borehole C2. (a) During the excavation. (b) In the long-term. The suffix "Num1" in the legend corresponds to the simulation considering the material cross-anisotropy (our reference case), and the suffix "Num2" corresponds to the simulation considering material isotropy.

### 6.5.6 Numerical results of strain and convergence in the lining compared to the in-situ measurements

With regard to the strain measurements in the ring 50 of the gallery's lining analyzed in Section 6.4.3, those data are now compared with the corresponding numerical results. Figure 6.54 shows this comparison for three segments in the top right quarter of the ring. First and foremost, the both compressive and tensile strains are predicted numerically, on the contrary to the measurements. This feature is linked to the fact that a continuous lining, without taking into account the jointed concrete blocks, has been considered in our modeling for the sake of simplicity. As a result, the tension could be transferred between the segments. Nevertheless, a compressive response for the internal sensor of the segment 891, and the external sensor of the segment 1137 is realistically predicted, with respect to the long-term deformation pattern of the lining and the rock, following its initial oval convergence (see Figure 6.34).

Therefore, one other originality of this work consists in another development of the numerical

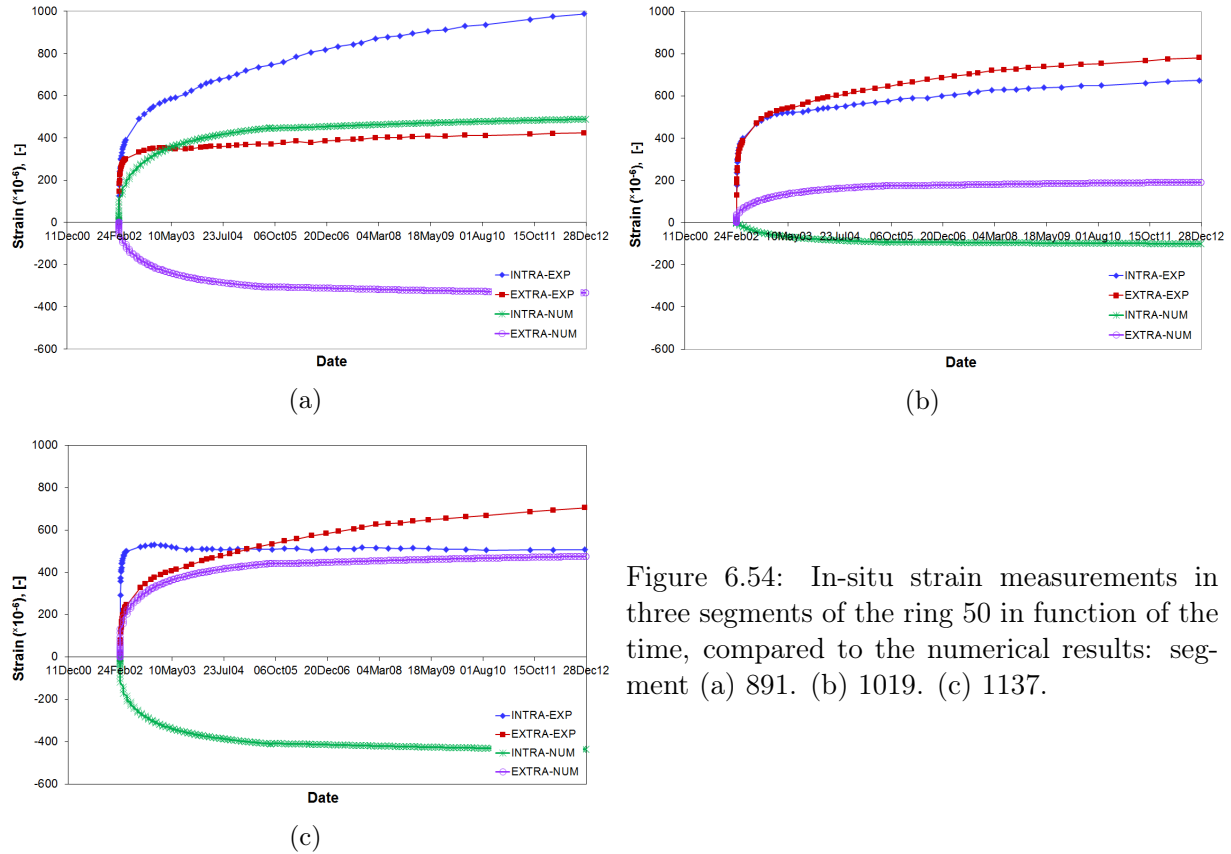


Figure 6.54: In-situ strain measurements in three segments of the ring 50 in function of the time, compared to the numerical results: segment (a) 891. (b) 1019. (c) 1137.

model to take into account of a discontinuous lining with the concrete segments in order to simulate more realistically the phenomena occurred in the lining. This development will be presented in Chapter 7 with a particular focus on the interfaces behavior.

Given the convergence measurements in the lining, as analyzed in Section 6.4.4, a comparison is performed with the corresponding numerical results in the following. The absolute displacement of four sensors in the top right quarter of the ring 50 (see Figure 6.26) and the ring 8 (see Figure 6.28) are represented in comparison with the corresponding numerical predictions in Figure 6.55. The both simulated and recorded displacements consist in an overall increasing trend of displacement in time. Additionally, the order of different plots corresponding different sensors of each ring (Figure 6.55a and 6.55b) is quite the same for the both predicted and recorded displacements consisting in a higher displacement of the sensor corresponds to the top segment in each ring (even though this difference is pretty insignificant with respect to numerical results). This fairly higher displacement is in accordance with the pattern of nodal velocity norm within the surrounding clay (converging towards the gallery) in time, as demonstrated in Figure 6.34, i.e. relatively higher velocities have been observed on the top of the gallery. However, the numerical simulation generally underestimates the long-term evolution of displacement measured in the lining. The latter aspect is more considerable with regard to the sensor 5012 located in the top segment of the ring 50 for which a more important displacement evolution has been recorded (see Section 6.4.4). It is noteworthy that the difference between the numerical predictions and the experimental measurements of the displacement can be partially related to the creep effects during the time, as this issue has not been taken into account in our numerical modeling. More importantly, consideration of a discontinuous lining, as it has been previously mentioned, can result in a more sophisticated modeling, and a more realistic simulation of the real phenomena taken place in the lining (see Section 7.5).

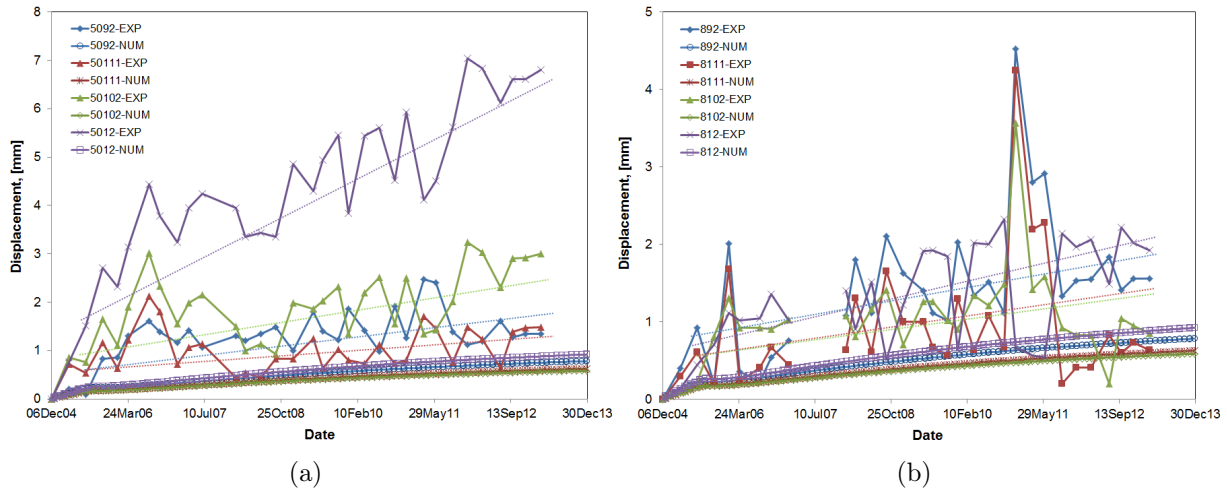


Figure 6.55: Displacement recorded for four sensors of the ring (a) 50. (b) 8, in function of the time with reference to 6/12/2004, compared to the numerical results. The dashed lines display schematically an average linear evolution of displacement readings of each sensor in time.

## 6.6 Intermediate conclusions

This Chapter focused on a coupled hydro-mechanical analysis of Boom Clay behavior around the Connecting gallery, during its excavation and afterwards, in the numerical and in-situ point of views. After giving a brief introduction on the construction's objective of this gallery, our numerical model (of a quarter of the gallery) and the relative defined properties were described. The simulated pattern of strain localization development, extension of the damaged zone, and the evolution of pore water pressure and displacement around the gallery were then discussed.

Moreover, a particular study has been conducted on analysis of some available in-situ measurements of pore water pressure in the host rock, and the strain and convergence measurements in the gallery's lining. These invaluable data library has been organized and analyzed in order to be compared to the computed results later on this Chapter. Within this framework, the numerical model was firstly extended to a full gallery considering the gravity effect, cross-anisotropy of the material mechanical properties and defining the zones of anisotropic permeability based on the in-situ measurements. The obtained pattern of development of strain localization around the gallery was then discussed illustrating an eye-shape extension of the damaged zone within the host-rock. Additionally, the predicted evolution of the displacement and pore water pressure within the clay were analyzed which the latter could highlight the influence of consideration of the gravity in the modeling.

The obtained results of the extended simulation were then compared to the in-situ observations and measurements. In terms of the pattern of fracturing and EDZ around the gallery, the site observations validated our simulated results while an eye-shape extension of the excavation damaged zone has been similarly evidenced at the site. Next, the convergence of the clay side walls was analyzed in comparison with the in-situ observations that the both consist in an anisotropic convergence of the rock.

Furthermore, the in-situ measurements of pore water pressure were compared to the corresponding computed results. It was shown that there is a quite good agreement between them in long-term while the strengths and weaknesses of the model in reproducing the rock behavior in the short-term, during the excavation, were also discussed. In addition, the strain and dis-

placement measurements in the lining were represented compared to the numerical predictions. This comparison has consisted in some similarities and differences in the pattern of strain and displacement obtained numerically with the corresponding in-situ measurements. In terms of the strain, the difference mainly addresses the numerical prediction of the tensile strain as well as the compressive strain within the lining's segments. In addition, the numerical results underestimate the displacement evolution in the lining, with respect to the measurements.

Therefore, the numerical model is aimed to be accomplished in the next Chapter to allow for consideration of a discontinuous lining with the concrete segments, introducing the interface elements between them. This development leads to a more realistic simulation of the lining behavior in interaction with the clay mass.

# Chapter 7

## Interface features

### Contents

---

<b>7.1</b>	<b>Introduction</b>	<b>240</b>
<b>7.2</b>	<b>General overview of the contact mechanism</b>	<b>242</b>
7.2.1	An introduction to the contact problem	242
7.2.2	Local kinematical relations of the contact	243
<b>7.3</b>	<b>Constitutive laws for interface element</b>	<b>247</b>
7.3.1	Mechanical part	247
7.3.2	Hydraulic part	249
7.3.3	Description of the interface finite element	250
7.3.4	Contact contribution to the global formulation	251
<b>7.4</b>	<b>Application of the interface element to the Connecting gallery</b>	<b>253</b>
7.4.1	Interface description	253
7.4.2	Role of the concrete lining	254
7.4.3	Contact phenomena between the lining and Boom Clay	257
<b>7.5</b>	<b>Application of the interface element to the gallery's lining</b>	<b>264</b>
7.5.1	Description of the numerical model	264
7.5.2	Analysis of the contact pressure on the interfaces	268
7.5.3	Comparison of the numerical predictions and in-situ measurements in the lining	271
<b>7.6</b>	<b>Intermediate conclusions</b>	<b>275</b>

---

*The important thing in science is not so much to obtain new facts as to discover new ways of thinking about them.*

William Lawrence Bragg

## 7.1 Introduction

The topic of interfaces and the contact mechanism may be said to have been launched in 1881 by the pioneering classic paper of Heinrich Hertz [Hertz, 1881]: *On the contact of elastic solids*. The Hertz theory has been limited to the frictionless contact and perfectly elastic solids. Later, it has been developed for slipping and frictional contact through a deeper insight to the friction phenomenon at the interfaces between two bodies in contact, and the advancement in theories of plasticity. Within this framework, the use of the computers and numerical techniques such as the finite element method could be highly influential in arising the new developments in the second half of the twentieth century (e.g. [Goodman et al., 1968; Beer, 1985; Charlier and Cescotto, 1988; Sharma and Desai, 1992; Laursen and Simo, 1993; Wriggers, 1995]).

In the conceptual point of view, through the finite element analysis of an engineering system, a discontinuous behavior may be encountered between the finite elements. Hence, the contact mechanism at their interface is of significant importance in a realistic analysis of the system's response. The examples of this phenomenon can be found in a wide range from the fractures within a material, interface between dissimilar materials, to the car crashes, metal forming process, etc., in many engineering fields such as mechanical and civil engineering, but also in the medical applications. Boundary value problems involving contact are equally of considerable importance in geomechanical applications and geotechnical engineering, such as soil-structure interaction, rock-concrete intermediate layer (e.g. in tunneling or arch dam analysis within the broad sense of civil engineering), rock joints, and geological faults. In this sense, for instance, numerical analysis of the shear band formation within the framework of stability behavior of a soil, or similarly the avalanches simulation in continuum mechanics could be also integrated with a contact formulation to compute the ultimate position of a part of the avalanche that has sheared off (see Figure 7.1).

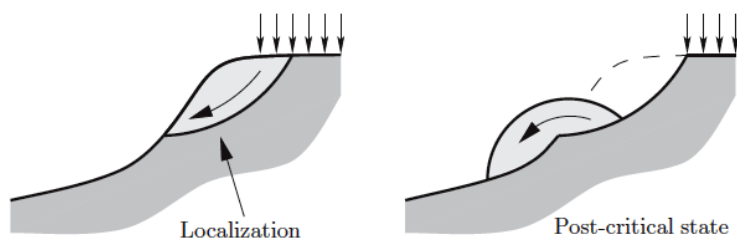


Figure 7.1: Conceptual representation of shear band formations and collapse in soils or avalanches [Wriggers, 2006].

With regard to our numerical simulation of the Connecting gallery excavation, presented in Chapter 6, a deeper insight is given to the interfaces features and the contact phenomena in this Chapter. These interfaces refer to the interface of the host rock and the concrete lining as well as the interfaces between the lining segments (see Figure 7.2). Interface element is a powerful tool in modeling of such geometrical discontinuities within a finite element analysis [Schellekens and De Borst, 1993]. Therefore, we propose modeling of the latter interfaces behavior through introducing of hydro-mechanical interface elements. Within this framework, the contact mechanism on the interface between the clay mass and the lining could be analyzed. In fact, during the excavation, the clay mass converges towards the lining, which is followed by the generation of some contact pressure on the interface between two bodies upon contact. Moreover, regarding the interfaces between the lining segments, our previous numerical modeling is still developed taking into consideration of a discontinuous lining (with the concrete segments). This

latter development in spite of the additional complexity that it imposes has been motivated by the difficulty encountered in a correct estimation of the strain and convergence evolution in the lining, with reference to the in-situ measurements (see Section 6.5.6). Hence, in order to a bit simplify the highly time-consuming simulation of the whole coupled phenomena occurred in the (finely discretized) model of full gallery in the course of clay convergence, localization and contact, we focus on a quarter of the gallery<sup>1</sup> (also with respect to the quasi-symmetric response observed in Section 6.5.1.4) in this Chapter while the gravity effect is neglected. The latter does not influence the aspects of analysis addressed hereafter since the focus is exclusively on the phenomena corresponding to the interfaces and occurred around the opening's level.

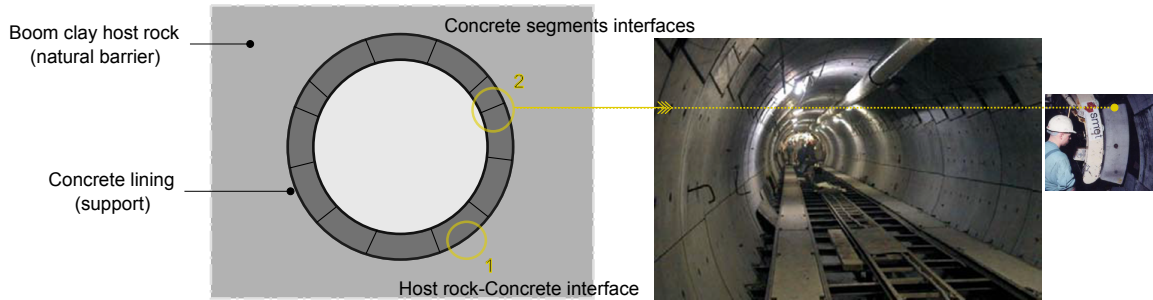


Figure 7.2: Schematic representation of the interfaces between the Boom Clay host rock and the gallery's lining, and between the lining's segments, in a perpendicular section to the gallery axis. The right image [Bastiaens et al., 2003] shows a general view of the Connecting gallery's lining besides a close-up on the emplacement of one segment of the lining demonstrating its two corresponding interfaces boundary with the adjacent segments.

Within the above framework, the first part of this Chapter describes the general concept of the contact mechanism, and the governing equations of the interface problem. The normal and tangential contact constraints are therefore discussed. Additionally, the relative constitutive laws for treatment of the contact problem are introduced, and the hydro-mechanical interface element is described.

Furthermore, the contact phenomena occurred between the clay mass and the lining are focused. In this sense, the significant role of the lining is firstly illustrated through a comparison between the numerical results obtained from the case with the lining and from another simulation of the gallery's excavation without consideration of the lining. Indeed, it is demonstrated that the lining could be highly influential in decreasing the extent of damaged zone and the rock's convergence around the gallery. Thence, studying its relative phenomena are of particular interest. The contact mechanism is analyzed simultaneously with the gallery excavation and onset of the localized shear bands, and in the long-term.

In the last part of this Chapter, a development of the modeling with the aim of consideration of a discontinuous lining is performed. The numerical steps followed for a correct simulation of the real phenomena related to the lining during the gallery construction are then described. The segments' behavior and the contact mechanism on their interfaces are described. In addition, the new obtained numerical results are presented in comparison with the in-situ measurements in the lining.

<sup>1</sup>With reference to the model presented in Section 6.5.1.

## 7.2 General overview of the contact mechanism

### 7.2.1 An introduction to the contact problem

In the conceptual point of view, the contact of two solids obviously results in generation of some restrictions on their displacements. This process then gives rise to the contact stresses on their interface, in the contact zone. In fact, the contact mechanics can be generally interpreted as a set of boundary conditions that vary throughout the analysis [Wriggers and Zavarise, 2004]. In this sense, upon contact of two bodies (i.e. gap closure), the contact constraints are activated which can be treated numerically based on two principle approaches [Zavarise et al., 1998], namely Lagrange multiplier method and penalty method:

- Lagrange multiplier method enforces exactly the normal contact constraint. That is to say that there is no penetration of two solids in contact, i.e. gap function  $g_N$  is null. Although, this null penetration may have a physical sense only in the case of contact between perfectly smooth surfaces. Through the use of this method, the total number of unknowns is increased since it adds the equations relative to the constraints to the global governing equations. Thence, a larger system of equations must be solved, and it can be unwieldy [Zavarise et al., 1998]. Figure 7.3 demonstrates the concept of the Lagrange multiplier approach on ensuring the normal contact constraint.

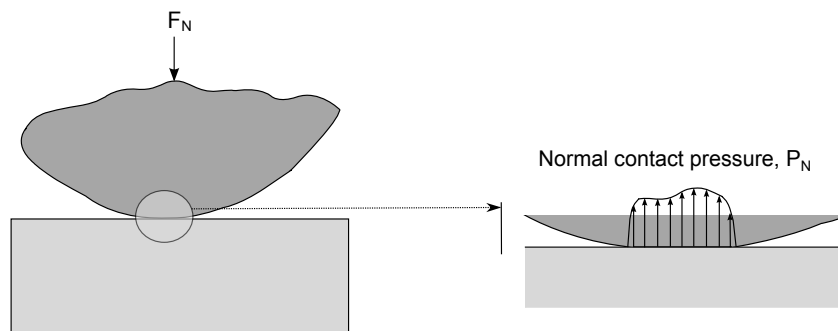


Figure 7.3: Conceptual representation of the Lagrange multiplier method on treatment of the normal contact constraint.

- Penalty method which is frequently applied in finite element analysis of contact problems [Wriggers, 2006] allows for some penetration of the bodies in contact (see Figure 7.4). This penetration depends on the penalty coefficient. Hence, this parameter must be chosen large enough in order not to induce a non-acceptable violation of the constraint conditions [Zavarise et al., 1998]. Indeed, the contact constraint is only fulfilled when an infinite penalty coefficient is defined. Nevertheless, increasing of this coefficient has some limitations since it may generally result in some numerical convergence<sup>2</sup> troubles and ill-conditioned system. Therefore, the penalty coefficient should be carefully introduced in the numerical model in order to prevent an ill-conditioned numerical problem while the penetration of two bodies in contact is also possibly minimized. This method, with regard to its simplicity to be implemented in the finite element software, has been incorporated into the LAGAMINE code [Charlier, 1987], and it is used in our study.

Given the framework of the classical solid mechanics, the solution of mechanical contact problem is attained through finding the displacement field  $\mathbf{u}$  for any  $\mathbf{x} \in \Omega$  so that Equations

<sup>2</sup>See Appendix A for the convergence criteria.

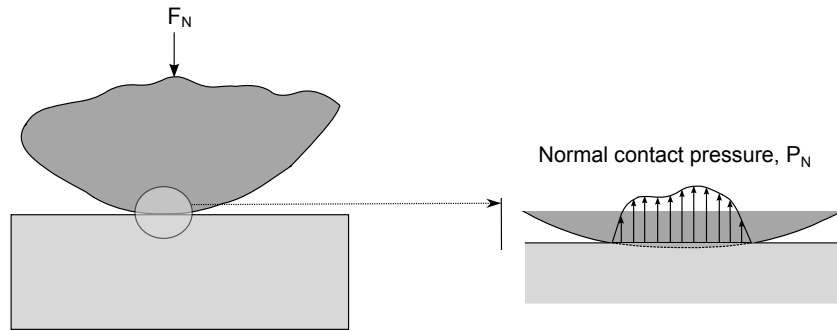


Figure 7.4: Conceptual representation of the penalty method on treatment of the normal contact constraint.

3.13-3.15 are satisfied taking into account of the contribution of both solids, in addition that the contact constraint must be also ensured in the contact area (upon contact). Therefore, given Equation 3.16, the weak form relation is represented by an inequality that the solution of the contact problem has to fulfill:

$$\sum_{n=1}^2 \int_{\Omega^n} \boldsymbol{\sigma} \cdot \boldsymbol{\varepsilon}^* d\Omega \geq \sum_{n=1}^2 \left[ \int_{\Omega^n} \mathbf{G} \cdot \mathbf{u}^* d\Omega + \int_{\Gamma_\sigma^n} \bar{\mathbf{t}} \cdot \mathbf{u}^* d\Gamma \right] \quad (7.1)$$

This inequality, arisen from the contact constraint inequality (see also Section 7.2.2.1), could be expressed as the equality 7.2 once the contact zone is known<sup>3</sup>. On the other words, assuming that contact between two bodies is active for a (known) contact interface  $\Gamma_c$ , the weak form relation on the interface is formulated as Equation 7.2.

$$\sum_{n=1}^2 \int_{\Omega^n} \boldsymbol{\sigma} \cdot \boldsymbol{\varepsilon}^* d\Omega = \sum_{n=1}^2 \left[ \int_{\Omega^n} \mathbf{G} \cdot \mathbf{u}^* d\Omega + \int_{\Gamma_\sigma^n} \bar{\mathbf{t}} \cdot \mathbf{u}^* d\Gamma \right] + \text{"Contact contribution"} \Big|_{\Gamma_c} \quad (7.2)$$

## 7.2.2 Local kinematical relations of the contact

Let us consider two deformable bodies  ${}^0\Omega_1$  and  ${}^0\Omega_2$  where the superscript  ${}^0$  refers to the reference configuration with the corresponding coordinates  $\mathbf{X}$ . To deal with the likely contact problem within the deformation process of two bodies, the contact conditions has to be formulated in the current configuration taking into account that two distinct points in the initial state of these bodies may have the same position in the current configuration [Wriggers and Zavarise, 2004]. Thus, given the current configuration with the corresponding coordinates  $\mathbf{x}$ , these bodies are assumed to come into contact at their boundary portions<sup>4</sup>  $\Gamma_c^1$  and  $\Gamma_c^2$ ; Figure 7.5 shows schematically the problem. A local referential system is then defined in the contact zone.

Therefore, assuming that the contact boundaries consist in a convex region, at least locally,

<sup>3</sup>The area along which the contact possibly occurs is *a priori* known in our application case, and this subject is not crucial anyway. Thus, going through the numerical approaches for searching this area is out of scope of this work. Although, the contact search algorithm can be generally of particular importance in computational contact mechanics, e.g. in the case of having variable contact area among different bodies in each load step of a large deformation problem. In this sense, a point on the surface of a body may contact with any portion of the surface of another body, or even come into contact with a part of the surface of its own body. Therefore, the contact search algorithm could be very time consuming, and it needs to be carefully treated [Wriggers, 2006].

<sup>4</sup>Part of the boundary ( $\Gamma_c^n$ ) of the body  $\Omega^n$  with  $n = 1, 2$ , besides the Neumann and Dirichlet boundary portions (see Section 3.2.2.1).

every point  $\mathbf{x}^2$  on the boundary  $\Gamma_c^2$  can be related to a point  $\bar{\mathbf{x}}^1$  on  $\Gamma_c^1$  through a minimum distance problem [Wriggers, 2006], such that:

$$d = \min_{\mathbf{x}^1 \in \Gamma_c^1} \|\mathbf{x}^2 - \mathbf{x}^1\| = \|\mathbf{x}^2 - \bar{\mathbf{x}}^1\| \quad (7.3)$$

In fact,  $\bar{\mathbf{x}}^1$  is the minimal distance point vector indicating the closest projection of a given *slave* point  $\mathbf{x}^2$  on the boundary  $\Gamma_c^2$  onto to the *master* boundary  $\Gamma_c^1$  [Wriggers and Zavarise, 2004]. In addition,  $\bar{\mathbf{e}}_1^1$  denotes the unit normal vector at the point  $\bar{\mathbf{x}}^1$ . This distance is subsequently applied to define the gap or penetration of one body into the other. It is noteworthy that the terms *slave* and *master* are respectively replaced by the *foundation* and *structure* in the LAGAMINE code. In addition, it is noticed that the both sides of contact are not treated in the similar manner, and one side is privileged. This distinction tends to physically vanish in the case of a perfect contact with no penetration [Zavarise et al., 1998; Wriggers and Zavarise, 2004].

It must be noted that the theoretical formulation that is being given in this Section is principally with respect to Wriggers and Zavarise [2004]; Wriggers [2006], described in the framework of this thesis. Detailed approaches and further insight into the contact problem can be then attained in those references as well as other relative numerous literature upon interest (e.g. see also [Johnson, 1987; Charlier and Cescotto, 1988; Laursen and Simo, 1993; Wriggers, 1995; Zavarise et al., 1998]).

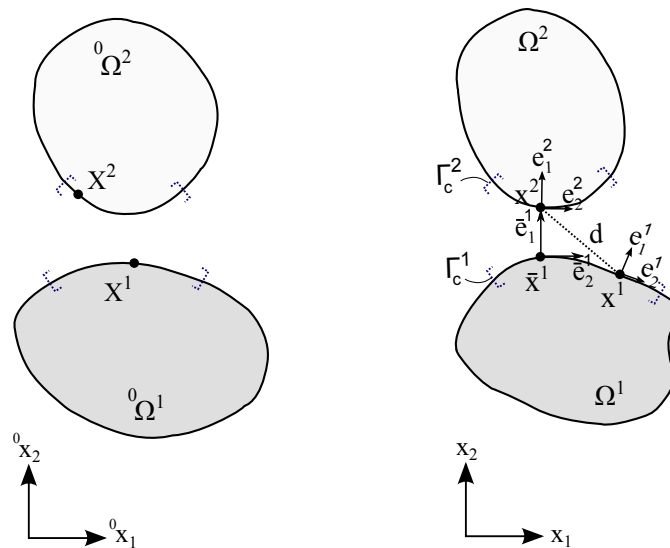


Figure 7.5: Schematic representation of the two bodies in their reference configuration ( ${}^0$  superscript) and their deformed state in the current configuration where the contact is assumed to occur along the boundary portions  $\Gamma_c^1$  and  $\Gamma_c^2$ .  $(e_1, e_2)$  stands for the local referential basis.<sup>5</sup>

<sup>5</sup>Inspired by [Wriggers, 2006].

### 7.2.2.1 Normal contact

With respect to the relation 7.3, once the point  $\bar{\mathbf{x}}^1$  is known, the gap function  $g_N$  is defined consisting in the constraint 7.4 in the case of no penetration [Wriggers, 2006].

$$g_N = (\mathbf{x}^2 - \bar{\mathbf{x}}^1) \cdot \bar{\mathbf{e}}_1^1 \geq 0 \quad (7.4)$$

Alternatively, integrating with the use of penalty method, the penetration function - consisting in the magnitude of penetration of one body into another - is given by:

$$g_N = \begin{cases} (\mathbf{x}^2 - \bar{\mathbf{x}}^1) \cdot \bar{\mathbf{e}}_1^1 & \text{if } (\mathbf{x}^2 - \bar{\mathbf{x}}^1) \cdot \bar{\mathbf{e}}_1^1 < 0 \\ 0 & \text{otherwise} \end{cases} \quad (7.5)$$

Consequently to the contact between two bodies, the contact stress vector on their interface boundary,  $\boldsymbol{\sigma}_c^1$ , overall yields:

$$\boldsymbol{\sigma}_c^1 = p_N \bar{\mathbf{e}}_1^1 + \tau_T \bar{\mathbf{e}}_2^1 \quad (7.6)$$

where  $p_N$  and  $\tau_T$  are the normal and tangential components of the stress vector. The above representation of the stress corresponds to a 2D contact problem within the framework of this thesis. In a 3D case, both components of tangential stress in the plane of interface (between two bodies) are integrated in the stress vector (i.e. tangential stress is not a scalar). Moreover, given the action-reaction principle,  $\boldsymbol{\sigma}_c^1 = -\boldsymbol{\sigma}_c^2$  is concluded (Figure 7.6).

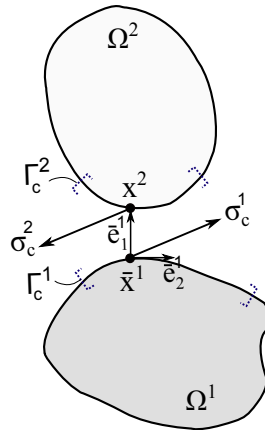


Figure 7.6: Schematic representation of the stresses on the contact interfaces.

Let us consider the treatment of the normal contact constraint as an uni-lateral constraint problem for which the most important is correctly ensuring the geometrical constraints. That is to say that no penetration condition between the two bodies in contact (Equation 7.4) is satisfied. As a result, the contact stress can be computed as the reaction force in the contact zone rather than using a specific constitutive law. This approach has been addressed by some former researchers (e.g. [Johnson, 1987; Kikuchi and Oden, 1988]). However, this no penetration condition corresponds to a perfect contact and it may be violated in reality.

Within this framework (i.e.  $g_N \geq 0$ ), contact between two solids occurs when the gap function  $g_N$  is equal to zero. This contact gives consequently rise to a non-zero normal contact pressure  $p_N$  in the stress vector  $\boldsymbol{\sigma}_c^1$  (Equation 7.6). Additionally, it is noted that the tangential stress component  $\tau_T$  is zero in the case of frictionless contact. With respect to this latter contact state, the so-called Hertz-Signorini-Moreau conditions<sup>5</sup> is then verified for an ideal (perfect) contact

<sup>5</sup>This condition is sometimes known as Kuhn-Trucker-Karush condition in optimization theory [Wriggers,

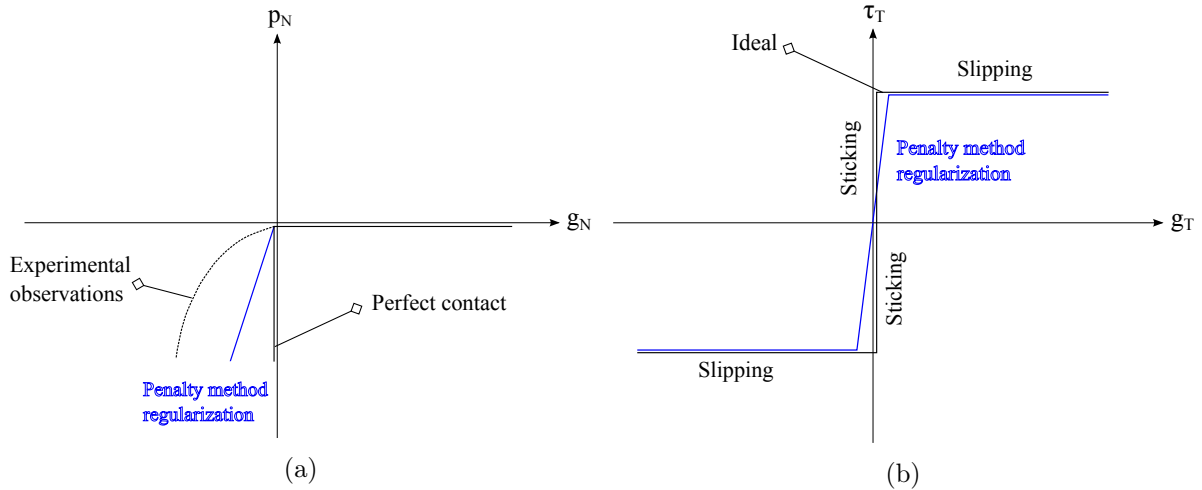


Figure 7.7: Conceptual representation of a perfect and regularized contact through the use of penalty method: (a) Normal contact. (b) Tangential contact.

[Wriggers, 2006]:

$$g_N \geq 0, \quad p_N \leq 0, \quad p_N g_N = 0 \quad (7.7)$$

This relation consists in a null normal contact pressure in the case of a gap between two bodies (i.e.  $g_N > 0$ ), and a compressive contact pressure in the case of contact, i.e.  $g_N = 0$ .

It is once again underlined that the above statement - consisting in a non negative normal gap function - is *only* verified in the case of a perfect contact. It is then violated upon using the penalty method and the penetration of two bodies in contact. This latter case, i.e. existence of some penetration upon contact through application of the penalty method (see relation 7.5), as addressed in this work, is illustrated in Figure 7.7a besides the perfect contact state. The relation between the established contact pressure and the gap function/penetration within the latter condition will be subsequently described in Section 7.3.1.

### 7.2.2.2 Tangential contact

In the case of contact between two bodies, the ideal tangential response at their interface is split into two states: so-called *stick* and *slip* phases. The first one consists in no tangential relative movement in the plane of contact interface. The latter lies in the allowance of the two bodies in contact to be slipped over each other ( $g_T^{sl} \neq 0$ ). Hence, there is some relative tangential displacement at their contact interface. These two states are then distinguished by a slip yield function  $f_{sl}$  within the framework of a defined constitutive law (as will be described in Section 7.3.1). Consequently, the so-called Kuhn-Trucker-Karush condition is verified, in the similar manner as the statement 7.7, such that [Laursen and Simo, 1993; Wriggers and Zavarise, 2004]:

$$\dot{g}_T^{sl} \geq 0, \quad f_{sl} \leq 0, \quad \dot{g}_T^{sl} f_{sl} = 0 \quad (7.8)$$

This relation consists in a positive value of  $\dot{g}_T^{sl}$  when the slip yield function  $f_{sl}$  is equal to zero. The variational form of this statement originates in the fact that the definition of the absolute relative tangential displacement between two points in contact may be unintelligible while dealing with large deformation regarding the two contacting bodies. Thence, working in the variational state is more appropriate with respect to which a rate form constitutive relation can be expressed (see 2006].

Section 7.3.1). In this sense,  $\dot{g}_T^{sl}$ <sup>6</sup> is the magnitude of variation of relative slipping (tangential) displacement, equal to relative tangential velocity  $\dot{g}_T$  taking into account an ideal tangential response and perfect sticking condition.

In addition, the total velocity vector  $\dot{\mathbf{g}}$  can be defined through the contribution of both normal and tangential velocities, such that:

$$\dot{\mathbf{g}} = \dot{g}_N \bar{\mathbf{e}}_1^1 + \dot{g}_T \bar{\mathbf{e}}_2^1 \quad (7.9)$$

However, through the use of penalty method, the perfect sticking contact condition, i.e.  $\dot{g}_T = 0$ , is regularized allowing a (reversible) slight tangential relative micro displacement between the contacting bodies. Figure 7.7b shows the concept of this regularized approach. Thence,  $\dot{g}_T$  has a sticking part,  $\dot{g}_T^{st}$ , which is then additional to the slipping irreversible part  $\dot{g}_T^{sl}$  in the case of slip between the contacting bodies, such that:

$$\dot{g}_T = \dot{g}_T^{st} + \dot{g}_T^{sl} \quad (7.10)$$

## 7.3 Constitutive laws for interface element

### 7.3.1 Mechanical part

The frictional contact problem are usually treated by mean of elasto-plasticity analogy [Curnier, 1984]. Within this framework, the sticking phase is compared to the elastic state of contact behavior. Then, when the interface behavior in the course of an evolutionary contact verifies the slipping condition, it is equivalent to an elasto-plastic state.

As a result of this idea, the relative tangential velocities could be split into the stick and slip parts, as given in Equation 7.10. This decomposition can be seen as a regularization of the frictional behavior [Wriggers and Zavarise, 2004] through which an elastic tangential micro displacement is considered given that this deformation vanishes once the loading is removed from the system.

The stick and slip states of the contact interface behavior are then distinguished via the Coulomb yield criterion (Equation 7.11) as it is widely used in soil and rock mechanics to deal with the contact problems [Charlier and Cescotto, 1988; Laursen and Simo, 1993; Wriggers and Zavarise, 2004].

$$f_{sl}(\boldsymbol{\sigma}_c, \mu) = |\tau_T| + \mu p_N \quad (7.11)$$

where<sup>7</sup>  $\mu$  is the Coulomb friction coefficient. Thence, assuming two contacting bodies, if the interface's stress state lies below the yield criterion (i.e.  $f_{sl} < 0$ ; see Figure 7.8), this elastic domain corresponds to the sticking behavior. Then, when the threshold value in the modulus of the tangential stress is reached, i.e. the stress state hits the the yield criterion and  $f_{sl} = 0$ , the slip condition is verified.

A linear elastic relation is considered between the variation of stresses and the variation of gap function in the sticking state, which yields:

$$\dot{\boldsymbol{\sigma}}_c = \mathbb{C}^e \cdot \dot{\mathbf{g}} \quad (7.12)$$

where  $\mathbb{C}^e$  is the elastic constitutive tensor. Given the regularization of the problem using the

<sup>6</sup>Equivalent to  $\dot{\lambda}$  in Equation 7.17.

<sup>7</sup>Note that on this convention, the compressive contact pressure is a negative quantity.

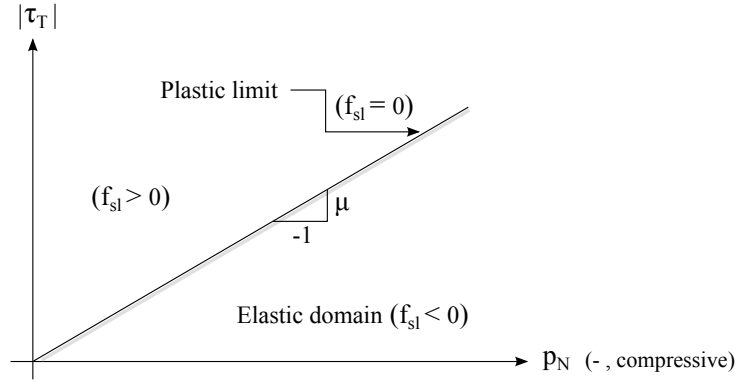


Figure 7.8: Representation of the Coulomb yield criterion.

penalty method, the stick state relation can be then rewritten as:

$$\begin{bmatrix} \dot{p}_N \\ \dot{\tau}_T \end{bmatrix} = \begin{bmatrix} K_N & 0 \\ 0 & K_T \end{bmatrix} \begin{bmatrix} \dot{g}_N \\ \dot{g}_T \end{bmatrix} \quad (7.13)$$

where  $K_N (> 0)$  and  $K_T (> 0)$  are the penalty coefficients which control the tolerated penetration of the contacting bodies and their relative tangential micro displacement, respectively.

In fact, following this incremental relation, the normal effective stress at the end of a considered time step  $\Delta t$  during our numerical analysis, called  $p_N^{t+\Delta t}$ , is obtained by Eq. 7.14 while  $p_N^t$  is the corresponding value at the beginning of the time-step.

$$p_N^{t+\Delta t} = p_N^t + \dot{p}_N \cdot \Delta t \quad (7.14)$$

where,

$$p_N^{t+\Delta t} = \begin{cases} p_N^{t+\Delta t} & \text{if } p_N^{t+\Delta t} \leq 0 \\ 0 & \text{if } p_N^{t+\Delta t} > 0 \end{cases} \quad (7.15)$$

Indeed, in the case of loss of contact, the tensile stress is not admissible. Instead, the normal component of effective stress is set equal to zero.

It is noteworthy that in a more complex contact problem, a so-called *initial contact pressure* can be defined upon necessity<sup>8</sup>, with respect to which the variations in the contact stress tensor is established. This condition will be addressed in our application case in Section 7.5.

Furthermore, reaching to the threshold value in the modulus of the tangential stress, relation 7.12 reads:

$$\dot{\sigma}_c = \mathbf{C}^e \cdot (\dot{\mathbf{g}} - \dot{\mathbf{g}}^{sl}) \quad (7.16)$$

The slipping velocity is then controlled by the flow rule, such that:

$$\dot{\mathbf{g}}^{sl} = \dot{\lambda} \frac{\partial \mathbf{g}}{\partial \sigma_c} \quad (7.17)$$

where the plastic multiplier,  $\dot{\lambda}$ , describes the magnitude of the plastic slip. The plastic potential  $\mathbf{g}$  is defined by Equation 7.18 in the framework of a non-associated plastic flow.

$$\mathbf{g} = |\tau_T| + M p_N \quad (7.18)$$

<sup>8</sup>For instance for the sake of initial stability.

where the coefficient  $M$  (generally  $M \neq \mu$ ) is assumed to be zero; a non-zero value is basically appropriate for the rock joints interfaces behavior [Charlier, 1987]. In addition, the consistency condition (see Section 3.3.4) yields:

$$\dot{f}_{sl} = \frac{\partial f_{sl}}{\partial \sigma_c} \cdot \dot{\sigma}_c + \frac{\partial f_{sl}}{\partial \mu} \cdot \dot{\mu} = 0 \quad (7.19)$$

where  $\dot{\mu}$  is assumed to be zero consisting in a frictional behavior without hardening. We are not essentially dealing with the slipping phase with regard to the interfaces behavior in this work and this assumption remains reasonable. Then, combining the relation 7.19 with Equations 7.16 and 7.17 gives the plastic multiplier expression as:

$$\dot{\lambda} = \frac{\frac{\partial f_{sl}}{\partial \sigma_c} \cdot \mathbf{C}^e \cdot \dot{\mathbf{g}}}{\frac{\partial f_{sl}}{\partial \sigma_c} \cdot \mathbf{C}^e \cdot \frac{\partial \mathbf{g}}{\partial \sigma_c}} \quad (7.20)$$

Thence, incorporating this relation into Equation 7.17 and then introducing in Equation 7.16 reads:

$$\sigma_c = \mathbf{C}^e \cdot \dot{\mathbf{g}} - \frac{\frac{\partial f_{sl}}{\partial \sigma_c} \cdot \mathbf{C}^e \cdot \dot{\mathbf{g}}}{\frac{\partial f_{sl}}{\partial \sigma_c} \cdot \mathbf{C}^e \cdot \frac{\partial \mathbf{g}}{\partial \sigma_c}} \mathbf{C}^e \cdot \frac{\partial \mathbf{g}}{\partial \sigma_c} \quad (7.21)$$

which lies in:

$$\sigma_c = (\mathbf{C}^e - \mathbf{C}^p) \cdot \dot{\mathbf{g}} = \mathbf{C}^{ep} \cdot \dot{\mathbf{g}} \quad (7.22)$$

Consequently, in the case of slipping, the elasto-plastic relation is given by:

$$\begin{bmatrix} \dot{p}_N \\ \dot{\tau}_T \end{bmatrix} = \begin{bmatrix} K_N & 0 \\ \mu K_N \frac{\tau_T}{|\tau_T|} & 0 \end{bmatrix} \begin{bmatrix} \dot{g}_N \\ \dot{g}_T \end{bmatrix}, \quad (7.23)$$

### 7.3.2 Hydraulic part

Concerning the hydraulic constitutive law, the fluid flux within the interface of two contacting bodies results from the transversal pore water pressure exchange between two sides of interface, such that:

$$f_{w,t} = \rho_w T_w \Delta p_w \quad (7.24)$$

where  $T_w$  is the transverse transmissivity to which the fluid flux is proportional. Additionally,  $\Delta p_w$  is the local gradient of pore water pressure between two bodies in contact, i.e. pressure difference of foundation side with the structure side (see Figure 7.9a).

It is noteworthy that in a more general point of view, a longitudinal flux may be considered as well (see Appendix C) which can be influential for instance in the case of simulation of interface behavior of the faults and fractures and the corresponding preferential paths for the fluid flow along the interface. Additionally, in simulation of the opening/closing of the faults, rough surfaces interface and the similar cases, a fluid storage through the interface may be also considered. However, these phenomena are not the concern of this Chapter (e.g. see [Guiducci et al., 2002; Cerfontaine, 2014] for some relative applications), and the latter fluxes are negligible in our application cases. Indeed, with regard to the loading procedure and boundary conditions in our subsequent interface modelings (see Section 7.4 and 7.5), the dominant phenomena on the interfaces are mechanical overall, although, the computation is in fact hydro-mechanical.

### 7.3.3 Description of the interface finite element

The contact interface is discretized by definition of 2D (zero-thickness) isoparametric finite elements with three nodes. These elements on  $\Gamma_c^1$  are compatible (in nodes) with the solid finite element used to discretize the corresponding body (i.e. structure side), as shown in Figure 7.9. With respect to a segment-to-segment contacting approach, there are three-nodes segments on the foundation side ( $\Gamma_c^2$ ) compatibly with the corresponding solid finite element. Thence, the nodal unknowns on each side of the interface unify with the ones on the corresponding body's contacting surface. Therefore, in an overall point of view, six nodes could be said to represent the interface behavior while each has three degrees of freedom (see Figure 7.9). As a result, the discontinuity of displacement and pore water pressure is generally allowed through the use of interface elements.

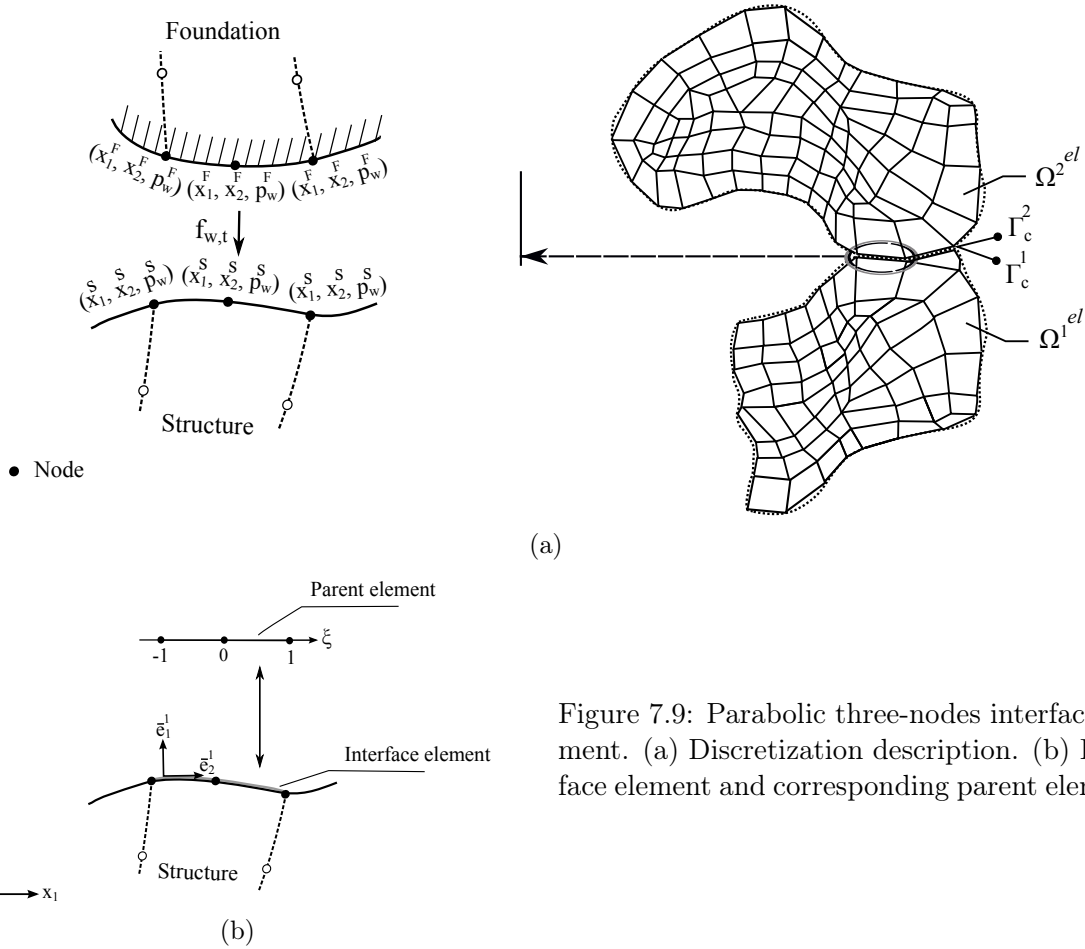


Figure 7.9: Parabolic three-nodes interface element. (a) Discretization description. (b) Interface element and corresponding parent element.

The quadratic interpolation (shape) functions  $N$  [Zienkiewicz and Taylor, 2000] are used to interpolate hydraulic pore water pressure, mechanical coordinates and relative displacements over the interface elements<sup>9</sup> in the approximate form of:

$$\mathbf{x}^{el} \approx \hat{\mathbf{x}} = \sum_{en=1}^{nen} N_{en}(\xi) \mathbf{x}_{en} \quad \text{and} \quad \mathbf{u}^{el} \approx \hat{\mathbf{u}} = \sum_{en=1}^{nen} N_{en}(\xi) \mathbf{U}_{en} \quad (7.25)$$

<sup>9</sup>Interface discretized finite elements on the (reference) structure side.

$$p_w^{el} \approx \hat{p}_w = \sum_{en=1}^{n_{en}} N_{en}(\xi) P_{w,en} \quad \text{and} \quad \Delta p_w^{el} \approx \Delta \hat{p}_w = \sum_{en=1}^{n_{en}} N_{en}(\xi) \Delta P_{w,en} \quad (7.26)$$

where the subscript  $_{en}$  refers to the corresponding variable at the  $en^{th}$  node of the interface element  $^{el}$ .

Furthermore, the Jacobian matrix  $\mathbf{J}$  for mapping from the isoparametric local basis to the global coordinates  $(x_1, x_2)$  reads:

$$\mathbf{J} = \begin{bmatrix} \frac{\partial x_1}{\partial \xi} \\ \frac{\partial x_2}{\partial \xi} \end{bmatrix} \quad (7.27)$$

The tangential component of the local referential system,  $\bar{\mathbf{e}}_2^1$ , (see Figure 7.9) then yields:

$$\bar{\mathbf{e}}_2^1 = \frac{1}{\det \mathbf{J}} \begin{bmatrix} \frac{\partial x_1}{\partial \xi} \\ \frac{\partial x_2}{\partial \xi} \end{bmatrix} = \frac{1}{\sqrt{\left(\frac{\partial x_1}{\partial \xi}\right)^2 + \left(\frac{\partial x_2}{\partial \xi}\right)^2}} \begin{bmatrix} \frac{\partial x_1}{\partial \xi} \\ \frac{\partial x_2}{\partial \xi} \end{bmatrix} \quad (7.28)$$

Thence, the other orthonormal component  $\bar{\mathbf{e}}_1^1$  can be simply given by:

$$\bar{\mathbf{e}}_1^1 = \frac{1}{\det \mathbf{J}} \begin{bmatrix} -\frac{\partial x_2}{\partial \xi} \\ \frac{\partial x_1}{\partial \xi} \end{bmatrix} = \frac{1}{\sqrt{\left(\frac{\partial x_1}{\partial \xi}\right)^2 + \left(\frac{\partial x_2}{\partial \xi}\right)^2}} \begin{bmatrix} -\frac{\partial x_2}{\partial \xi} \\ \frac{\partial x_1}{\partial \xi} \end{bmatrix} \quad (7.29)$$

Therefore, the rotation matrix is built by collecting these two vectors, such that:

$$\mathbf{R} = [\bar{\mathbf{e}}_1^1 \quad \bar{\mathbf{e}}_2^1] \quad (7.30)$$

Consequently, this rotation matrix can be used to give the  $\mathbf{g}$  expression as Equation 7.31, with respect to the relation 7.5. In the physical point of view, this relation declares that  $\mathbf{g}$  is an objective statement of the distance vector of two solids (i.e. structure and foundation). In this sense, following a rigid displacement of the whole system, the both solids and their interface are affected by this transition/rotation, although, their relative position would not be affected. Hence,  $\mathbf{g}$  does not vary considering that it is expressed in the local axes, and it is linked to the solids and rotates with them in the case of that rigid movement.

$$\mathbf{g} = \mathbf{R}^T \cdot (\mathbf{x}^2 - \bar{\mathbf{x}}^1) = \mathbf{R}^T \cdot (\mathbf{x}^f - \mathbf{x}^s) = \mathbf{R}^T \cdot \Delta \mathbf{x} = \mathbf{R}^T \cdot \mathbf{u} \quad (7.31)$$

where  $^f$  and  $^s$  refer to the foundation and structure.

### 7.3.4 Contact contribution to the global formulation

To formulate our global boundary value problem, the contact contribution must be considered as the additional term to the equations describing the behavior of two bodies in contact. In this sense, with regard to the mechanical weak formulation, Equation 7.2, this contribution on the external virtual work, for an interface element, can be expressed by:

$$\mathcal{W}_{c,E}^{\star el} = \int_{\Gamma_c^{1,el}} (p_N \delta g_N + \tau_T \delta g_T) d\Gamma \quad (7.32)$$

Thence, considering the relation 7.31, projection of Equation 7.32 in the global coordinates yields:

$$\mathcal{W}_{c,E}^{\star el} = \int_{\Gamma_c^{1,el}} \boldsymbol{\sigma}_c^T \cdot \mathbf{R}^T \cdot \mathbf{u}^{\star} d\Gamma \quad (7.33)$$

This relation can be then expressed in terms of the so-called energetically equivalent nodal force so that the corresponding contribution of the  $en^{th}$  node of the element consists in:  $\left[ \mathcal{F}_{c,E,en}^{el} \right]^T \cdot \mathbf{U}_{en}^{\star}$  where  $\mathbf{U}_{en}^{\star}$  is the nodal virtual displacement vector, and  $en$  varies between 1 and  $n_{en}$ . The energetically external equivalent nodal force  $\mathcal{F}_{c,E,en}^{el}$  (associated to the node  $en$ ) using the Gauss scheme to integrate over the element thence reads:

$$\mathcal{F}_{c,E,en}^{el} = \sum_{IP=1}^{n_{IP}} [\mathbf{R} \cdot \boldsymbol{\sigma}_c N_{en} \det \mathbf{J} W_{IP}] \quad (7.34)$$

where  $n_{IP}$  is the number of integration points,  $N_{en}$  is the shape function associated to the node  $en$ ,  $W_{IP}$  is the Gauss weight corresponding to the integration point  $IP$ , and  $\det \mathbf{J}$  stands for the determinant of the Jacobian matrix (which is computed with respect to the structure side). Therefore, the force vector for three nodes of the interface on the structure side, i.e.  $en = 1, 2, 3$ , is computed.

It is noteworthy that subsequently to a local searching process for the nodes on the foundation side which are in front of (in contact with) the three nodes on the structure side, the reaction forces acting on the foundation (i.e.  $en = 4, 5, 6$ ) can be obtained by:

$$\mathcal{F}_{c,E,en}^{el} = - \sum_{IP=1}^{n_{IP}} [\mathbf{R} \cdot \boldsymbol{\sigma}_c N_{en} \det \mathbf{J} W_{IP}] \quad (7.35)$$

Similarly to the mechanical part, the contact contribution is involved in the hydraulic weak form formulation as well. Hence, upon the contact of two bodies, the classical mass balance equation (described in Section 3.2.5) of the system consists in an inequality, such that:

$$\sum_{n=1}^2 \left[ \int_{\Omega^n} \left( \dot{S} p_w^{\star} - \mathbf{m} \cdot \nabla p_w^{\star} \right) d\Omega \right] \leq \sum_{n=1}^2 \left[ \int_{\Omega^n} Q p_w^{\star} d\Omega - \int_{\Gamma_q^n} \bar{q} p_w^{\star} d\Gamma \right] \quad (7.36)$$

Therefore, the contribution of the interface is needed to fulfill the equilibrium condition. In this sense, transversal fluid flow between two bodies in contact produces the external virtual work associated to the interface (see Equation 7.37) while the source term inside the interface is null. It is noteworthy that in the case of considering the fluid flow along an interface, its contribution is involved in the internal virtual work (left-hand side of Equation 7.36; see Appendix C) while the storage inside the interface is assumed to be negligible.

$$\mathcal{W}_{c,E}^{\star el} = \int_{\Gamma_c^{1,el}} f_{w,t} p_w^{\star} d\Gamma \quad (7.37)$$

which gives:

$$\mathcal{W}_{c,E}^{\star el} = \int_{\Gamma_c^{1,el}} \rho_w T_w \Delta p_w p_w^{\star} d\Gamma = \int_{\Gamma_c^{1,el}} \rho_w T_w \left( p_w^f - p_w^s \right) p_w^{\star} d\Gamma \quad (7.38)$$

In the same manner as the mechanical part, the contribution of  $en^{th}$  node of the interface element within the above weak form relation consists in  $\mathcal{F}_{c,E,en}^{el} \cdot P_{w,en}^{\star}$  where  $P_{w,en}^{\star}$  is the nodal virtual pore water pressure, and  $\mathcal{F}_{c,E,en}^{el}$  is the energetically equivalent

external nodal force (associated to the node  $en$ ;  $en = 1, 2, 3$ ) which reads:

$$\mathcal{F}_{c,E,en}^{el} = \sum_{IP=1}^{n_{IP}} \left[ \rho_w T_w \left( p_w^f - p_w^s \right) N_{en} \det \mathbf{J} W_{IP} \right] \quad (7.39)$$

Accordingly, the reaction forces acting on the foundation side (i.e.  $en = 1, 2, 3$ ) can be computed, such that:

$$\mathcal{F}_{c,E,en}^{el} = - \sum_{IP=1}^{n_{IP}} \left[ \rho_w T_w \left( p_w^f - p_w^s \right) N_{en} \det \mathbf{J} W_{IP} \right] \quad (7.40)$$

The hydraulic and mechanical energetically equivalent forces are gathered together for six nodes to make a generalized nodal force vector of the element. It should be noticed that this is just the contribution of the contact interface, and it needs to be incorporated into the global force vector. The global out of balance force vector  $\mathbf{F}_{\mathbf{OBF}}$  can be then computed as described in Section 3.2.7.

Moreover, the global stiffness matrix  $\mathbf{K}$  is assembled by the element stiffness matrices while the contribution of an interface element,  $\mathcal{K}_c^{el}$  is structured as a  $18 \times 18$  matrix, such that:

$$\left[ \mathcal{K}_c^{el} \right]_{(18 \times 18)} = \begin{bmatrix} \left[ \mathcal{K}_c^{el} \right]_{(9 \times 9)}^{SS} & \left[ \mathcal{K}_c^{el} \right]_{(9 \times 9)}^{SF} \\ \left[ \mathcal{K}_c^{el} \right]_{(9 \times 9)}^{FS} & \left[ \mathcal{K}_c^{el} \right]_{(9 \times 9)}^{FF} \end{bmatrix} \quad (7.41)$$

This matrix is then made of the contribution of 6 nodes with a total of 18 degrees of freedom (see Figure 7.9a)<sup>10</sup>. This matrix is in fact constructed in terms of the derivation of the nodal forces with respect to the generalized coordinates (i.e. displacements and pore pressure). In this sense, the first subscript on the above submatrices specifies the side to which the nodal force vector is associated, and the second subscript indicates the derivative basis.

## 7.4 Application of the interface element to the Connecting gallery

### 7.4.1 Interface description

Regarding the concrete lining of the Connecting gallery, which has been emplaced almost simultaneously with the gallery excavation, the contact mechanism between Boom Clay and the lining is an essential issue which needs to be analyzed. The contact is supposed to occur during the gallery excavation while the clay converges towards the lining producing some contact pressure on the interface between two bodies. Analyzing this contact process between the clay mass and the lining concurrently with the gallery construction, and onset of the localized shear bands, and in the long-term as an open crucial topic is our focus in Section 7.4. To analyze these phenomena, the interface elements (introduced in Section 7.3.3), have been applied between the clay and the concrete lining (see Tables 6.3 and 6.6 for the relative properties).

With respect to the model of Connecting gallery described in Chapter 6, Figure 7.10 demonstrates a close up on the interface between the clay and the lining. The interface elements have been defined on the rock's boundary surface, as to be our *structure* while the concrete has been considered as the *foundation* so far.

<sup>10</sup>A detailed procedure can be found in [Charlier et al., 2009; Cerfontaine, 2014] upon interest.

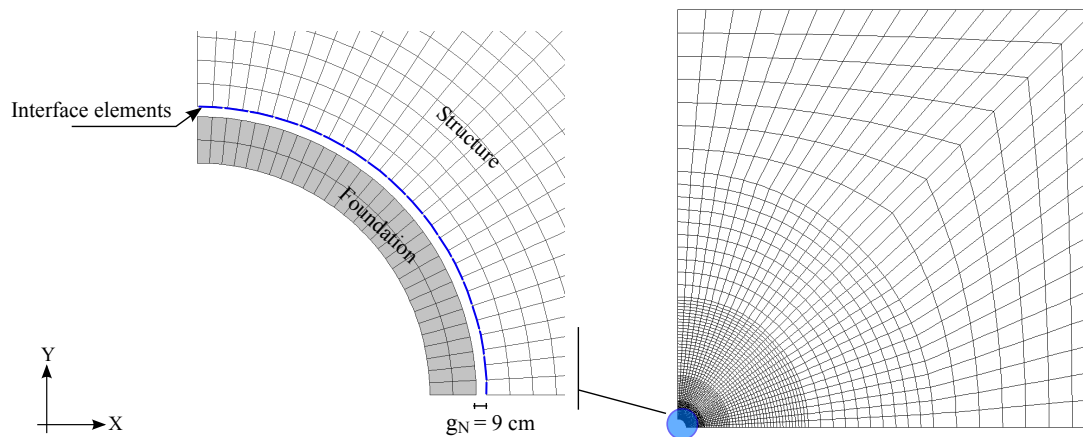


Figure 7.10: Representation of the interface model. Structure (clay mass) and foundation (concrete lining) are in their no-contact state.

Although, in the fundamental point of view, giving a particular attention to the interface behavior of the host rock with another body as its foundation without understanding the necessity of existence of this foundation (i.e. gallery's lining) is debatable. In this sense, an analysis of the impact of the lining on the coupled response of the clay (around the gallery) can be of particular interest within the framework of deep underground excavations in Boom Clay host rock [Salehnia et al., 2015b]. The latter is then firstly focused in the following before going through the interface relative phenomena.

#### 7.4.2 Role of the concrete lining

The gallery excavation in Boom Clay as a plastic clay can result in a relatively high convergence [Van Marcke and Bastiaens, 2010]. Thence, the concrete lining of the Connecting gallery, excavated through this host rock, is one of the significant feature about this gallery since it could play an essential role in decreasing the convergence of the rock around the gallery wall [Salehnia et al., 2013b; Salehnia, 2013]. Consistently, thanks to the lining, the extension of the damaged zone around the gallery is also effectively reduced.

To better clarify the significant influence of the lining, the simulation of the excavation of the Connecting gallery and the resulting extension of the localized zone in the course of excavation and afterwards are represented here, without considering the gallery's lining. The similar initial boundary conditions as the real gallery case (i.e. with the lining) has been applied to the model (Figure 7.11, see Section 6.3.1) besides that subsequently to the release of the boundary forces and pore pressure on the gallery wall during the excavation (i.e. 6 days), the pore pressure is kept constant as the atmospheric pressure on the wall until the end of simulation.

Figure 7.12 shows the evolution of localized shear bands within a radius of  $20m$  in the clay around the gallery (without the lining), in terms of the increment of deviatoric strain, plastic loading index and total deviatoric strain, during the excavation period (at 4, 5, and 6 days), and after 3.5 years. With reference to our former modeling with the lining (see Section 6.5.1.4), a noticeably more activity and extension of the localized shear bands is observed. The bands are in fact still active even some years after the end of excavation (see the increment of deviatoric strain in Figure 7.12d). Thence, the evolution of the total deviatoric strain and the extension of the damaged zone are important at the end of simulation compared to the end of excavation. (compare Figures 7.12d and 7.12c). The anisotropic extension of the localized shear bands around

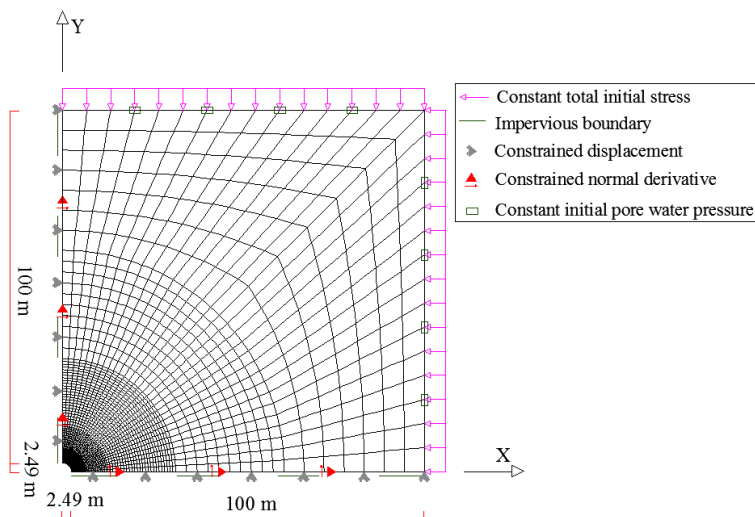


Figure 7.11: The mesh geometry and boundary conditions of the model without the lining.

the gallery without the lining is hence estimated as about  $16m$  horizontally and  $4.4m$  vertically. This is averagely more than 6.5 times of the EDZ predicted around the gallery with the concrete lining (Section 6.5.1.4), which has been consistent with the in-situ observation (see Section 6.5.2). Indeed, once the lining is emplaced, the convergence of the clay is confined resulting in an increase of pressure exerted by the rock on its interface with the lining (see Section 7.4.3). As a result, the activity and extension of the shear bands are restricted.

In terms of the evolution of pore water pressure and radial displacement along the horizontal and vertical cross-sections from the gallery wall, Figures 7.13-7.14 compare the results of the current simulation without the lining with the case taking into account of the lining (i.e. with reference to a quarter of the model presented in Section 6.5.1, neglecting the gravity effect). The results of both cases are shown in a similar scale and for a total radius of 100 meters around the gallery besides a close-up of the corresponding result in the vicinity of the gallery wall. First and foremost, the impact of the localized shear bands development through some fluctuations in the pore pressure and displacement evolution around the gallery is obviously more considerable for the case without the lining for which more shear banding with localization of strain occurs.

Furthermore, regarding the pore pressure distribution close to the gallery wall, a higher decrease of the pore water pressure towards the negative values (following the decompression of the clay) is observed both horizontally and vertically in the simulation without the lining. This is linked to the free convergence of the clay and its dilatant deformation in the gallery's proximity during and after the excavation, as the result of non-existence of any support (lining). On the contrary, the contact phenomenon for the case with the lining could primarily restrict the horizontal convergence of the rock and such decrease of pore pressure in the gallery's proximity (as described in Sections 6.3.3 and 6.5.1.4). Moreover, in an extended radius in the vicinity of the gallery, with regard to the top image in Figure 7.13b, a drainage equilibrium process in longer time tends to decrease the increased pore pressure along the horizontal direction. This process in Figure 7.13a (i.e. case without the lining) seems to be accompanied by the contradictory influence of an internal flow conducted from the vertical side towards the horizontal axis with a more important extended localized bands. As a result, more decrease of the pore pressure in time is consistently observed within the clay along the vertical cross-section from the gallery wall (see bottom image in Figure 7.13a).

In terms of the radial displacement evolution as demonstrated in Figure 7.14, a very higher

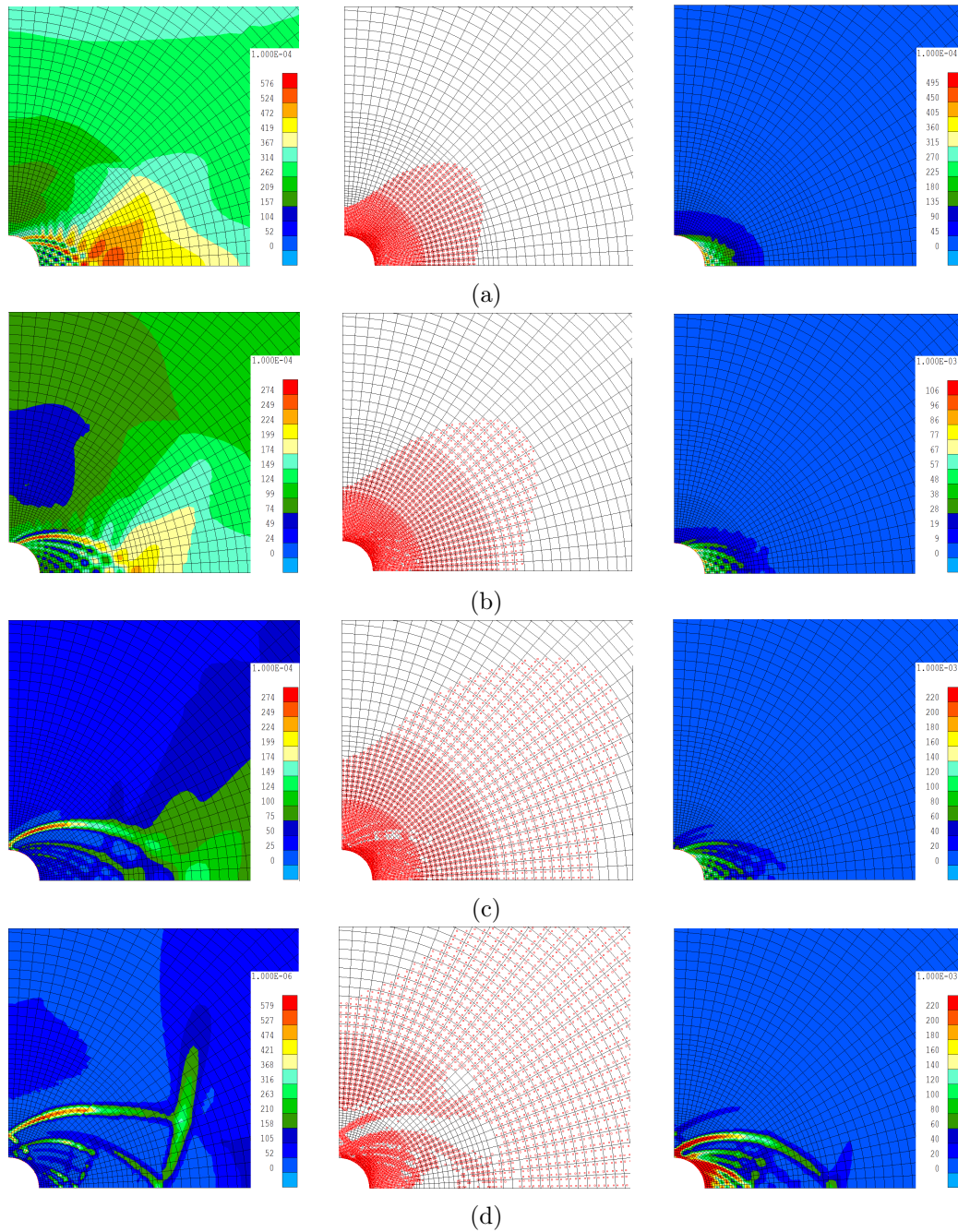


Figure 7.12: Increment of deviatoric strain (in the left side), plastic loading index (in the middle), and total deviatoric strain (in the right side) around the gallery without the lining after: (a) 4 days. (b) 5 days. (c) 6 days (end of excavation). (d) 3.5 years.

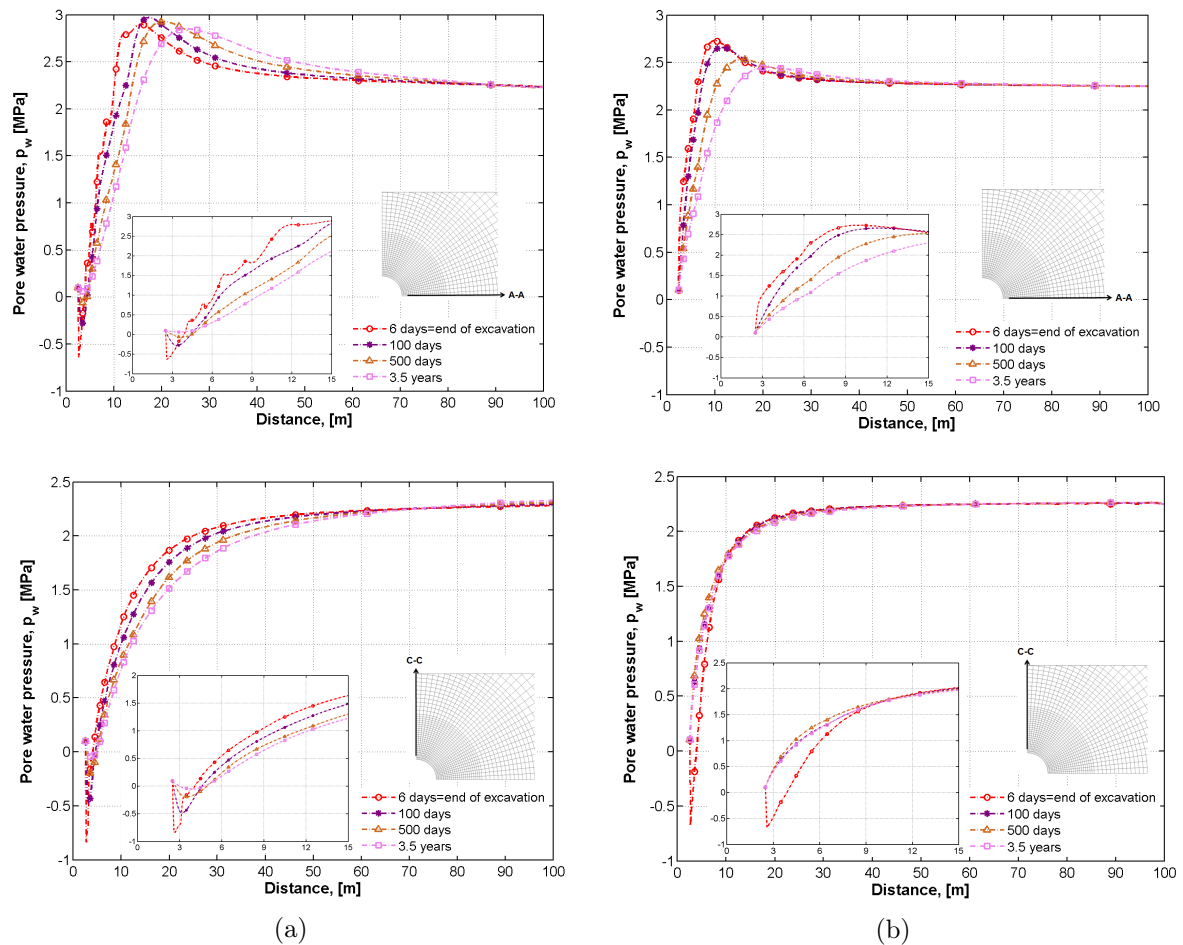


Figure 7.13: Pore water pressure evolution along the horizontal cross section A-A (top row) and the vertical cross-section C-C (bottom row) for the simulation: (a) Without the lining. (b) With the lining.

displacement (or, half convergence considering a symmetric response) of the clay sidewalls (about  $0.9m$  horizontally and  $0.6m$  vertically at the end of simulation) is computed for the case without the lining. The both horizontal and vertical displacements in the vicinity of the gallery tend indeed to be increased in a longer time, throughout some years after the end of excavation, since there is no support to restrict the high convergence of the clay and the development of the damaged zone.

All together, the existence of the concrete lining is elucidated to have an essential role while excavating in the plastic Boom Clay layer. In this sense, analysis of its relative phenomena, consisting in the contact mechanism on its interface with the host rock besides the previously discussed aspects of the clay behavior, and among the lining segments are of a unique interest. Hereinafter, another originality of this work lies in a particular analysis of these phenomena.

### 7.4.3 Contact phenomena between the lining and Boom Clay

The contact process between the gallery's lining and the clay mass induces some contact pressure on the interface between two bodies. From then on, it does not allow important evolution of shear bands around the gallery within the clay mass, nor does it permit more convergence of the rock. Figure 7.15 presents the diagram of the normal contact pressure on the interface between

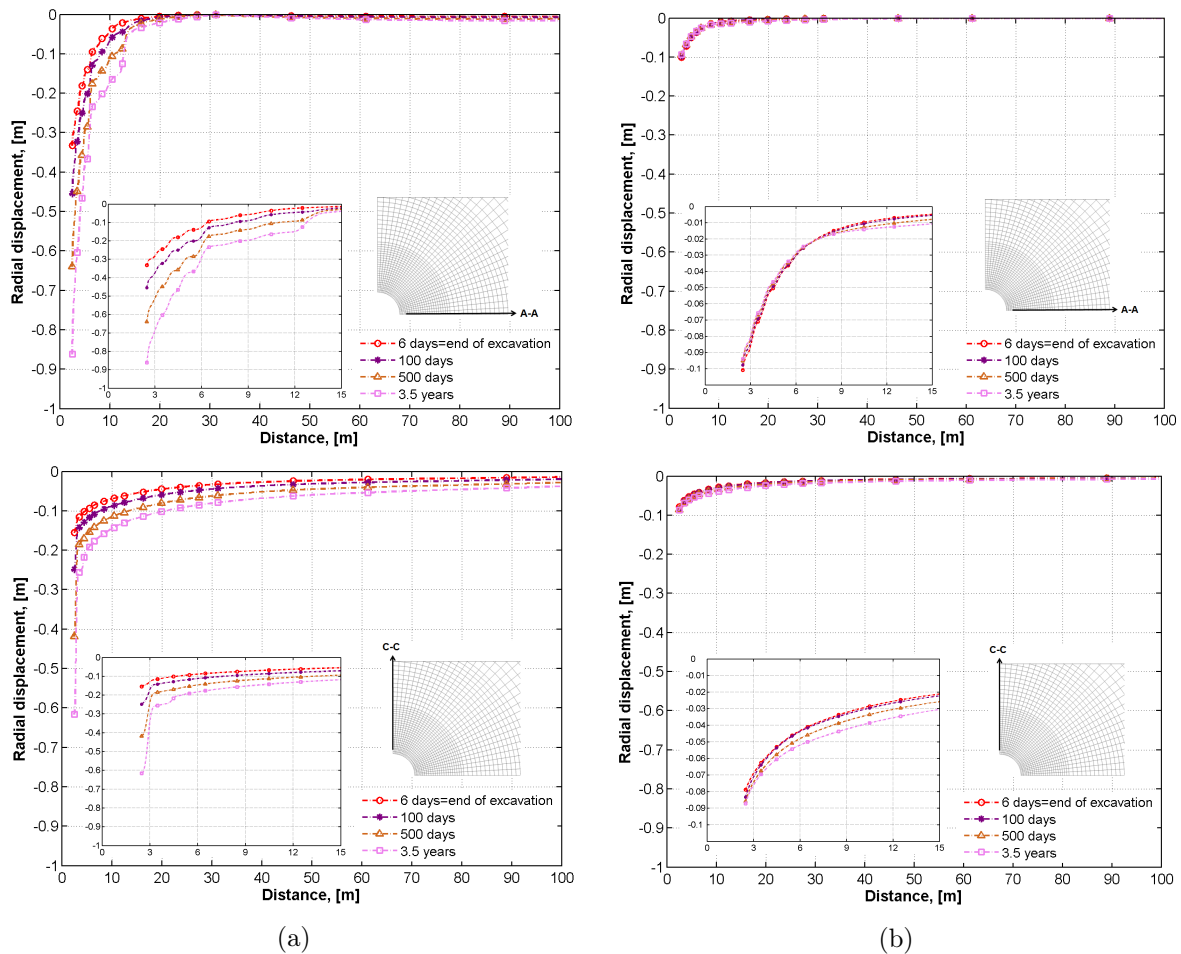


Figure 7.14: Radial displacement evolution along the horizontal cross section A-A (top row) and the vertical cross-section C-C (bottom row) for the simulation: (a) Without the lining. (b) With the lining.

the concrete lining and Boom Clay mass after 5 days and 6 days (i.e end of excavation). As it is observed, the contact is initiated on the horizontal side and then, it is developed on the whole interface till the end of excavation phase. This phenomenon confirms the anisotropic response of the clay during the excavation as it was discussed in Section 6.5.3. In fact, due to the ovalization pattern in deformation of the clay mass during the excavation (see Figure 6.34c), the bottom elements firstly come into contact with the lining and normal contact pressure is established on the interface.

The normal contact pressure on the interface (on the first integration point of interface elements; there are two integration points per element), in function of the angle from the bottom surface, throughout the excavation phase and afterwards is presented in Figure 7.16 to better clarify the pressure's time-dependent evolution process. The maximum of contact pressure is primarily taken place on the interface bottom side during the excavation following the clay convergence. Accordingly, a slight inward horizontal movement of the lining and consequently, an upward vertical movement of the lining could be induced as well (see also Figure 6.34). The clay mass and lining are tended to behave oppositely in long-term, consisting in a downward movement of the rock at top of the gallery (see the velocity norm in Figure 6.34d), which prompts the increase of contact pressure on the top elements of interface throughout the time after the end of excavation.

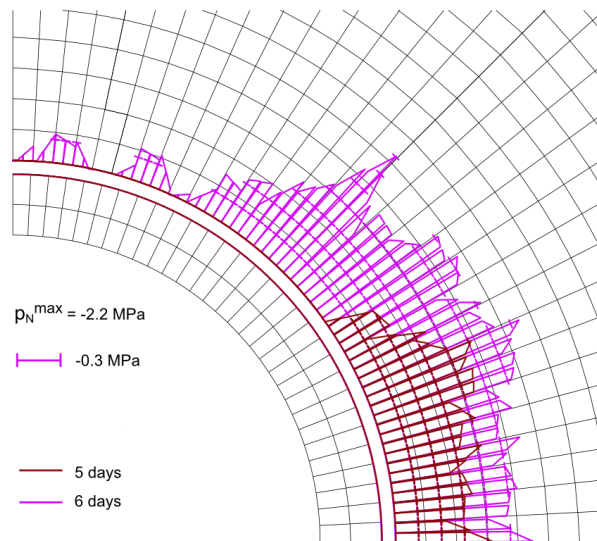


Figure 7.15: Diagram of the normal contact pressure on the interface.

#### 7.4.3.1 Analysis of the oscillations

With regard to Figure 7.16, some oscillations could be observed in the development pattern of normal contact pressure on the interface. The oscillatory type of response has been studied to find out any possible numerical or physical origin. Our theory is that the physical aspects give birth to these oscillations. Although, several numerical characteristics may be said to also induce this kind of oscillations, based on the literature. In this sense, the problem is firstly analyzed in the numerical point of view.

There are several main numerical factors which might have some role in producing this sort of oscillations, consisting of the applied numerical integration scheme and the number of sampling points considered for integration over the interface elements, the chosen penalty coefficients, and the mesh size. These numerical factors are analyzed through several computations. With regard to the numerical integration scheme, Schellekens and De Borst [1993] have analyzed the impact of using the Gauss integration method in contrast to the Newton-Cotes and Lobatto schemes indicating that the former one may cause some oscillations when dealing with the interface elements with definition of relatively high stiffness value (i.e. penalty coefficient). In fact, approaching a more fulfilled contact constraint needs the definition of a large enough penalty coefficient. The combination of this large value of penalty coefficient with application of the Gauss integration scheme might be then a candidate for imposing an oscillatory response, with respect to the latter reference. However, the authors indicate that this defined large value is not the cause of the problem, but rather is the resulting large pressure gradient over an interface element while there is a coupling between the degrees of freedom of the individual nodes of the element<sup>11</sup>. In this sense, it has been shown that application of Newton-Cotes/Lobatto<sup>12</sup> integration schemes (with less than four integration points) might improve the oscillatory results consisting in a no coupling of the degrees of freedom of the interface elements and a more smooth pressure profile over the element [Gens et al., 1989; Schellekens and De Borst, 1993].

Within this point of view, several simulations performed with application of different nu-

<sup>11</sup>Detailed information on this issue can be found in [Gens et al., 1989; Schellekens and De Borst, 1993] upon interest.

<sup>12</sup>The Newton-Cotes and Lobatto integration schemes are numerically identical for two and three integration points [Schellekens and De Borst, 1993].

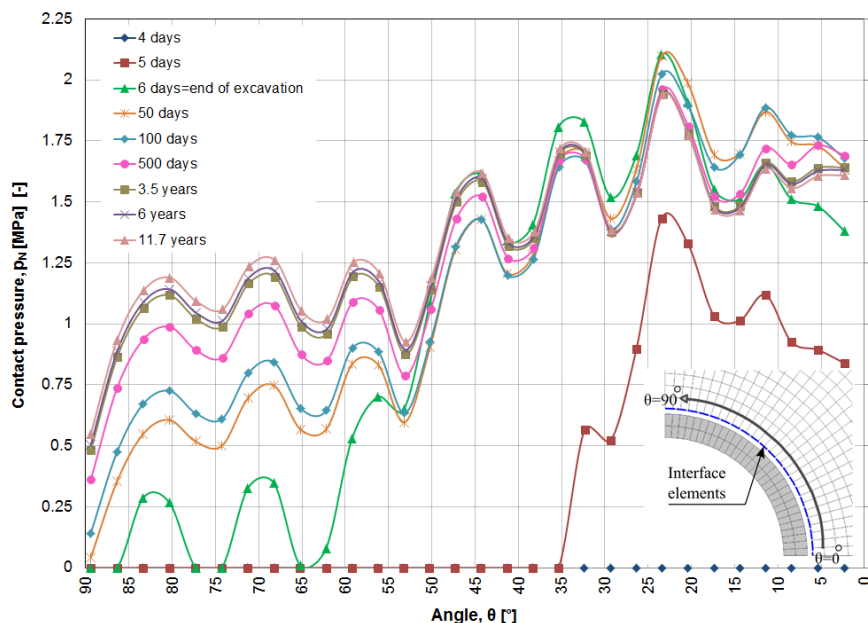


Figure 7.16: Evolution of the normal contact pressure on the interface.

merical approaches including the Gauss integration scheme (our reference scheme so far with two integration points) with two or three integration points as well as the Newton-Cotes and Lobatto schemes. Since the Newton-Cotes/Lobatto approaches are generally less precise than the Gauss scheme, three integration points have been considered for the corresponding computation. Figure 7.17 compares the obtained results of the contact pressure on the interface at the end of excavation (6 days) using these different approaches; all the integration points are considered in each case for a better illustration. It is then observed that neither the applied numerical integration scheme nor the number of integration points could really modify the obtained oscillatory response in our numerical interface problem. In the case of using the Gauss scheme, over-integration does not improve the result, as similarly demonstrated by [Schellekens and De Borst, 1993]. The use of the Newton-Cotes/Lobatto integration schemes seems to even induce more pronounced oscillations, and it is not then an appropriate solution to those oscillations.

Moreover, focusing on the introduced penalty coefficient into the model, its own influence on the obtained results is studied. Practically, the value of this parameter should be defined large enough in order to minimize the penetration of the two bodies in contact and violation of the contact constraint, as it has been explained at the beginning of this Chapter. Nevertheless, the corresponding limitations concerning the likely resulting numerical convergence<sup>13</sup> troubles and an ill-conditioned system (physically a resulting large pressure gradient over an interface element) must be also taken into account for a careful choice of this parameter. Figure 7.18 compares the development of contact pressure on the interface at the end of excavation (6 days) using three values of the penalty coefficients ( $3 \times 10^9 \text{ Pa}\cdot\text{m}^{-1}$  has been basically defined in our modelings as it was given in Table 6.3). It is observed that decreasing the penalty coefficient by one order of magnitude (to our reference value) could importantly reduce the *amplitude* of the pressure's oscillation produced on the interface, and *not basically the own oscillations*. On the other words, by increasing the penalty coefficient after a limit (around  $3 \times 10^9 \text{ Pa}\cdot\text{m}^{-1}$  in our case), there is a considerable negative influence on the amplitude and period of pressures' oscillations produced on the interface; besides, there has been sort of numerical convergence problems as well. Although, more reduction (from our chosen value to  $8 \times 10^8 \text{ Pa}\cdot\text{m}^{-1}$ ) could not make an important

<sup>13</sup>See Appendix A for the convergence criteria.

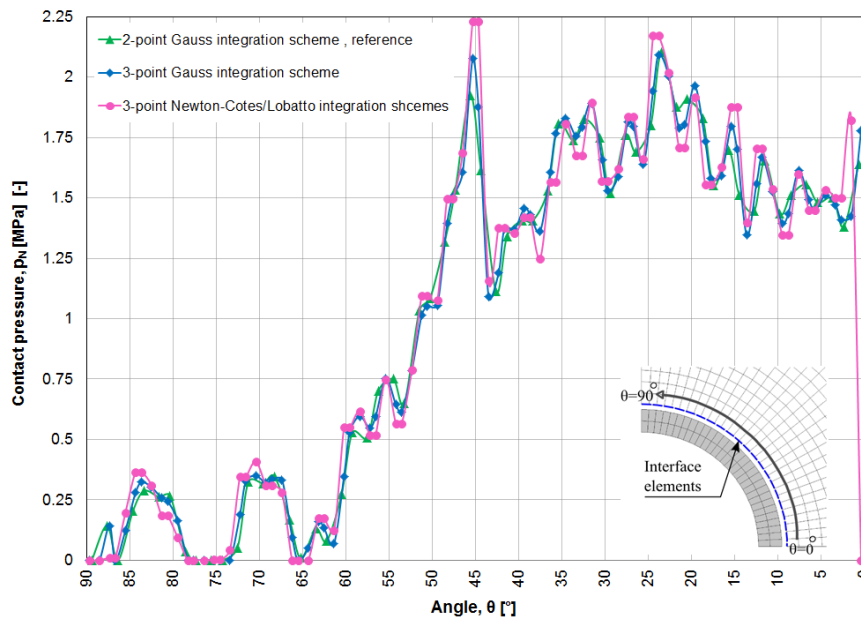


Figure 7.17: Development of the normal contact pressure on the interface after 6 days with application of different numerical integration schemes.

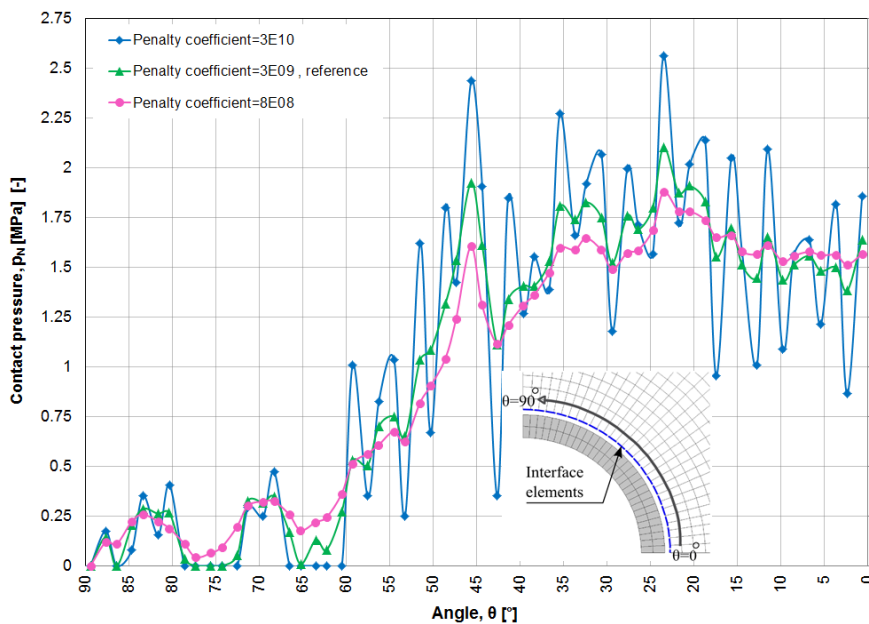


Figure 7.18: Development of the normal contact pressure on the interface after 6 days using three values of penalty coefficient.

change in the observed oscillations, and it can rather increase the penetration of two bodies in contact. On the whole, the value given to the penalty coefficient so far seems convenient and as yet, it has partially reduced the oscillations' amplitude. However, from a fundamental point of view, these oscillations still exist even though with a limited amplitude.

Finally, numerical discretization of the interface into the finer elements is also studied in the sense that it may improve the performance of each element as the computed pressure gradient over that single element gets decreased. In another point of view, it is noteworthy that a relatively large element size may cause a half sticking state over an interface element while the other half is in no-contact state. In this case, the interpolation over that element may result in a very non-smooth displacement field and consistently, an oscillated computed pressure. Hence, considering a mesh refinement, the development of contact pressure on the interface, with 40 elements, at the end of excavation (6 days) is compared to the results of our reference simulation with a 30 elements interface discretization in Figure 7.19. As it is observed, no improvement appears to be attained on the elements' response. The element size does not seem to be therefore responsible in our case for the obtained oscillatory type of response on the interface either.

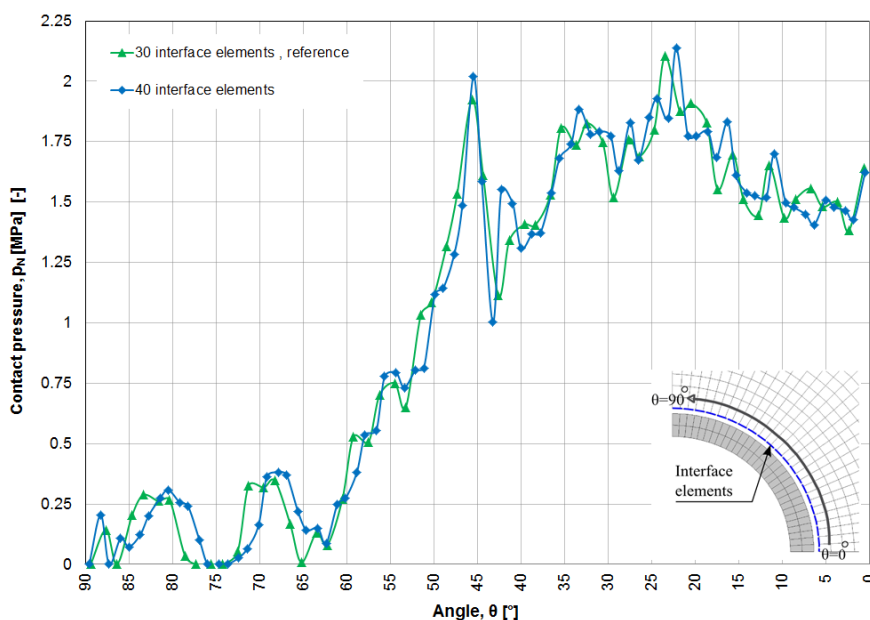


Figure 7.19: Development of the normal contact pressure on the interface after 6 days using finer mesh with 40 interface elements in comparison to the case with 30 interface elements.

Consequently to the above overall study, the obtained oscillations in development pattern of normal contact pressure on the interface do not *fundamentally* originate in the numerical aspects, even though their amplitude could be some how limited through a careful choice of the penalty coefficient.

#### 7.4.3.2 The oscillations: Relation between the contact pressure and strain localization

Indeed, a physical origin has been believed to give birth to those oscillations. That is to say the development pattern of the localized shear bands within the clay around the gallery (see Section 6.5.1.4). In fact, the oscillations of normal contact pressure on the interface are comparatively related to the shear bands created in the gallery's proximity due to the excavation. Figure 7.20

presents superposition of the normal contact pressure on the interface (see Figure 7.15) and the total deviatoric strain in Boom Clay mass around the gallery (see the relative contours in Figures 6.33b-6.33c) during the excavation. A fundamental accordance is noticed between the corresponding two phenomena. Indeed, the larger shear bands are reasonably compared with the peaks of the contact pressure produced on the interface. Furthermore, the both features affirm the anisotropic pattern of the clay response.

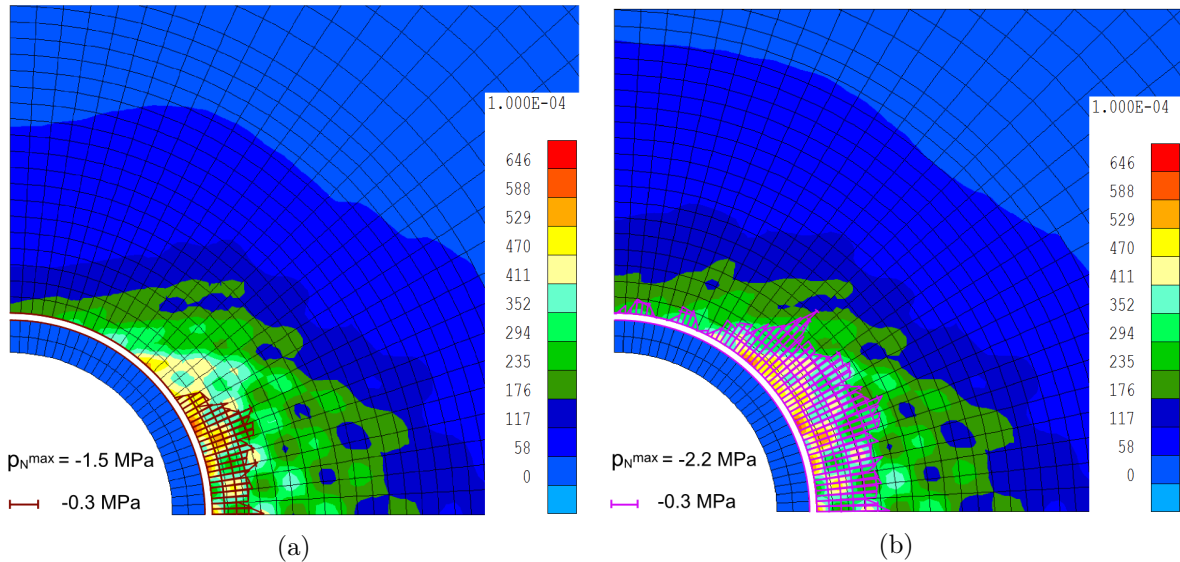


Figure 7.20: Superposition of the localized shear bands and normal contact pressure on the interface after: (a) 5 days. (b) 6 days.

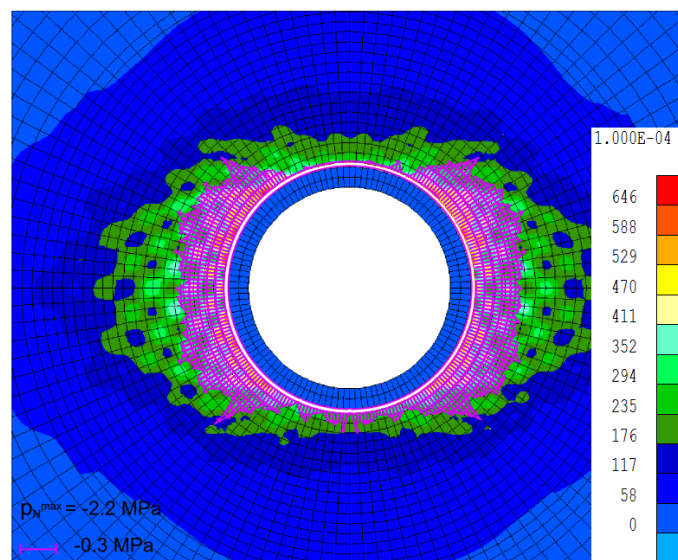


Figure 7.21: Superposition of the localized shear bands and normal contact pressure on the interface after 6 days for the model of full gallery.

On the whole, from a fundamental point of view, these oscillations are identified to *originate* in the development pattern of the localized shear bands in the gallery's proximity independent of the applied numerical approach. Similarly to the model of a quarter of the gallery, Figure 7.21 demonstrates the relation between the contact pressure and shear strain localization for the

model of a full gallery [Salehnia et al., 2015b].

## 7.5 Application of the interface element to the gallery's lining

### 7.5.1 Description of the numerical model

The accomplishment of our numerical analysis of the coupled behavior of Boom Clay around the Connecting gallery, and in interaction with the gallery's lining (presented in this Chapter and the previous one) is aimed at this stage through a particular focus on the lining response. Numerical modeling of the long-term behavior of discontinuous lining of the gallery composed of the concrete segments, like the real case (see Figure 7.2), and the relative phenomena associated to their interfaces are being our main focus. As a result of this development, the inconveniences encountered in reproducing the in-situ measurements in the gallery's lining, as described in Section 6.5.6, are expected to be basically overcome.

To simulate the response of this discontinuous lining and the contact phenomenon occurred between the corresponding segments, we propose the application of the interface elements (see Section 7.3.3) as shown in Figure 7.22. The overall model follows the initial and boundary conditions thus far. Besides, new conditions are needed for the three interfaces defined within the lining, as described in the following through *two* main steps.

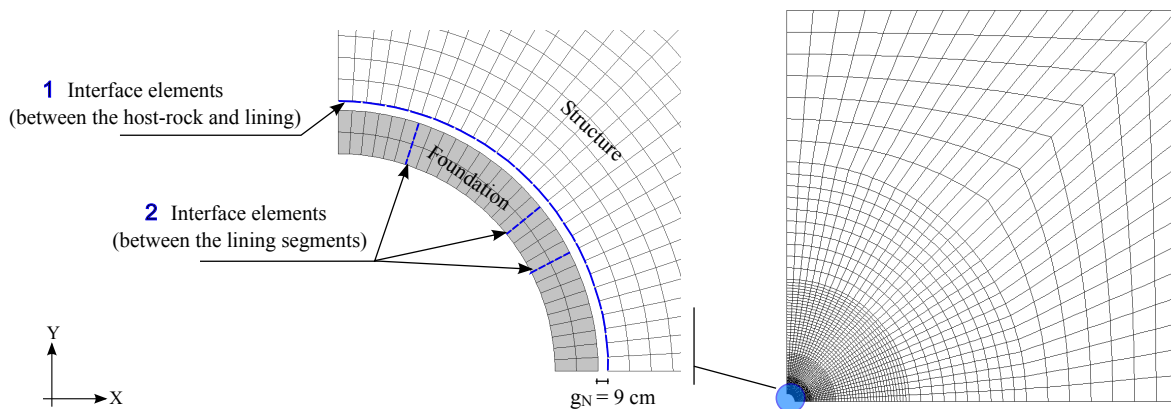


Figure 7.22: Representation of the interfaces model considering a discontinuous lining. Structure (clay mass) and foundation (concrete lining) are in their no-contact state.

#### First step:

In the *numerical* point of view, an *initial* stability of these discontinuous segments neighboring each other (i.e. in contact; stuck) needs the definition of an initial pressure on their contact interfaces, which restricts their *initial* (at just starting point of the numerical simulation) movement apart from other. It must be noted that there is no contact yet with the rock. Consistently, assuming that the lining behaves as a cylinder, the equilibrium condition consists in an external pressure  $p_e$  (see Figure 7.23) which is related to the defined initial pressure between the neighboring segments - equivalent to the circumferential (Hoop) stress  $\sigma^H$  - through:

$$\sigma^H = \frac{p_i r_i^2 - p_e r_e^2}{r_e^2 - r_i^2} - \frac{r_i^2 r_e^2 (p_e - p_i)}{r^2 (r_e^2 - r_i^2)} \quad (7.42)$$

where  $r_i$  and  $r_e$  are the internal and external radii which are respectively equal to 2 m and 2.4 m.  $r$  is the radius at a point in the cylinder (i.e. lining) where the circumferential stress (i.e.

initial pressure between the neighboring segments) is addressed, which is considered as  $2.2\text{ m}$  (i.e. mean radius).  $p_i$  is the internal pressure that is equal to zero.

The initial pressure between each of two neighboring segments could be numerically attained

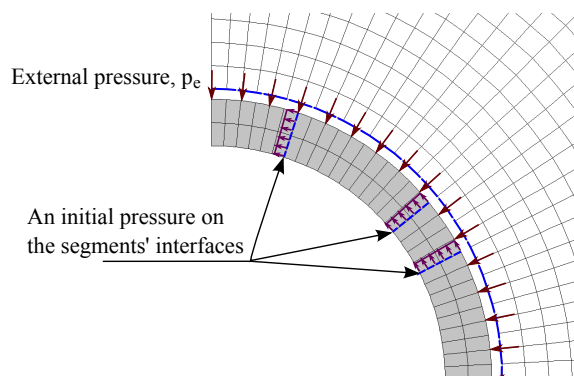


Figure 7.23: Schematic representation of the initial pressure on three contact interfaces, and the external pressure on the lining.

in two manners:

- An initial penetration ( $g_N < 0$ ) of two neighboring segments with regard to each of three interfaces can be defined. As a result, an initial pressure on these interface is obtained through the constitutive relation  $p_N = K_N g_N$ . The significant deficiency of this method can be said to be the dependency of this initial pressure to the penalty coefficient introduced into the model. In this sense, a larger penalty coefficient may be for instance desirable (carefully with respect to the numerical limitations as already explained), although, it inevitably results in a higher initial pressure applied on the interfaces too. Besides, it is noteworthy that the obtained result through this approach is very sensitive to the defined geometry of those initial penetrations, as our study has shown. That is to say that these geometries (i.e. the relative coordinates) need to be precisely defined. For instance, the actualized configuration of an exclusive model of the lining (without the rock) is shown after a so-called white numerical step (without any loading) in Figures 7.24a-7.24b for a very precise and a less precise definition of the coordinates correspond to a considered penetration of each two segments in contact. This penetration has been considered to be  $-0.5\text{ mm}$  in this test while the penalty coefficient is equal to  $4 \times 10^9\text{ Pa.m}^{-1}$  consisting in an initial pressure between the segments equal to  $-2 \times 10^6\text{ Pa}$ . With regard to Equation 7.42, the external pressure on the lining is then equal to  $3.345 \times 10^5\text{ Pa}$ . Considering Figure 7.24b, besides the desired initial stability of the lining's segments, it is then observed that the computed very slight movement of the segments occur in a quite symmetrical manner, on the contrary to Figure 7.24a.

Nevertheless, it may be noteworthy that an insignificant unsymmetrical behavior is generally realistic since the (four) segments are not identical, nor in symmetry with regard to Figure 7.22. In this sense, the comparison of Figure 7.24b with a similar case taking into account of three identical segments (instead of four dissimilar ones; see Figure 7.22) in the lining (Figure 7.24c) is interesting, although, the corresponding difference is pretty negligible in this small test.

- A so-called *initial contact pressure* is defined for the interface elements corresponding to each of two neighboring segments (i.e.  $p_N^0 < 0$ ). Thus, the initial pressure is ideally independent from the introduced penalty coefficient. Henceforth, this approach is applied in our modeling within a more sophisticated numerical point of view.

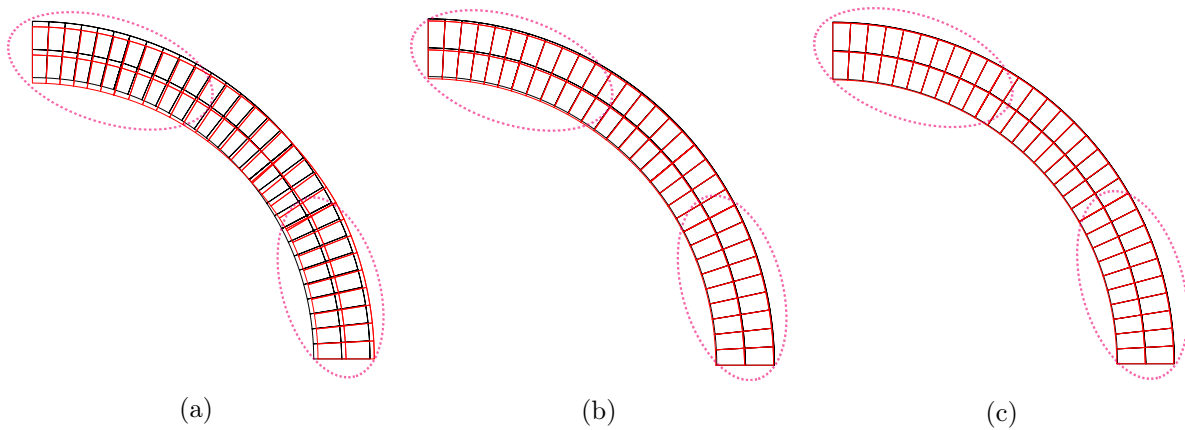


Figure 7.24: Representation of the lining's actualized configuration (deformation enlarged by a scale factor of 50) after a numerical white step (without any loading) with: (a) Less precise definition of geometry of the neighboring segments' penetration. (b) Very precise definition of geometry of the neighboring segments' penetration. (c) Three identical segments with definition of a very precise geometry of their penetration. The pink dashed ellipses highlight the symmetrical/unsymmetrical aspect of the model's response.

Let us assume an initial contact pressure of  $-2 \times 10^6 Pa$  which lies in an external pressure on the lining as  $p_e = 3.345 \times 10^5 Pa$  (see Figure 7.23). The hydro-mechanical parameters of the interfaces embedded within the lining are given in Tables 7.1 and 7.2 while a larger value of penalty coefficient could be introduced independently from the aforesaid applied pre-pressure. It is recalled that increasing this value is although limited due to the numerical convergence and likely oscillations troubles. The response of the lining at the starting point of simulation, and in the contact state with the rock at the end of excavation is now analyzed in order to assess the performance of the assumed pre-pressure.

Table 7.1: Mechanical parameters for the interfaces between lining's segments in the modeling

Parameter	Symbol	Value	Unit
Penalty coefficient on contact pressure	$K_N$	$1.8 \times 10^{10}$	$Pa.m^{-1}$
Penalty coefficient on contact friction	$K_T$	$1.8 \times 10^{10}$	$Pa.m^{-1}$
Coulomb friction coefficient	$\mu$	0.3	-

Table 7.2: Hydraulic parameter for the interfaces between lining's segments in the modeling

Parameter	Symbol	Value	Unit
Transverse transmissivity	$T_w$	$1 \times 10^{-14}$	$m/Pa.s$

Figure 7.25a shows the resulting lining's deformation pattern at the beginning and end of our excavation phase (6 days; when it has come into contact with the rock). Indeed, with regard to the quite simultaneous installation of the lining with the gallery's construction (in reality) [Bastiaens et al., 2003], it is realistically supposed that the segments do not slide apart during the excavation phase, dissimilar to what is observed in Figure 7.25a (specially regarding the bottom block). Thence, even though the segments' stability at the beginning of computation is satisfied in this case, it is unrealistically violated during the excavation period. In this sense, a higher initial contact pressure may be required, in the numerical point of view. This pre-pressure is defined as  $p_N^0 = -4 \times 10^7 Pa$  (based on our study) consisting in an external pressure

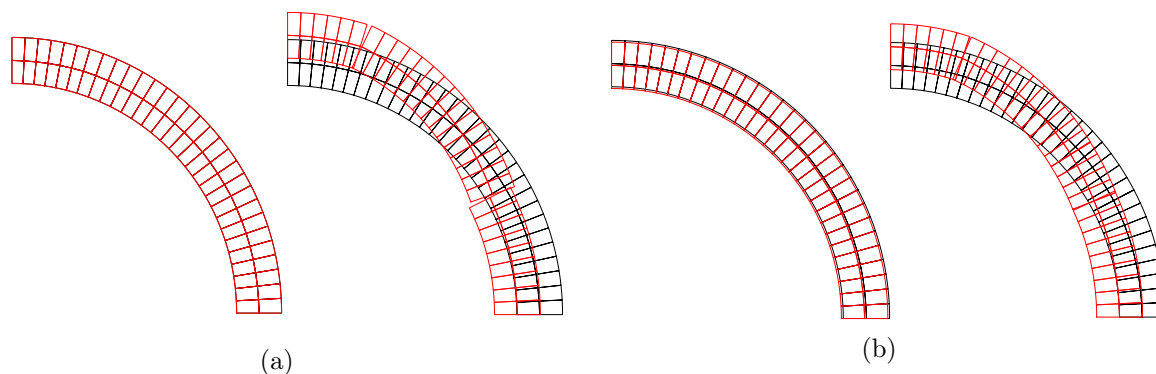


Figure 7.25: Representation of the lining's deformation pattern (deformation enlarged by a scale factor of 10) at the beginning of computation (after one second; left side), and at the end of excavation phase (right side) for the simulation considering: (a)  $p_N^0 = -2 \times 10^6 Pa$ . (b)  $p_N^0 = -4 \times 10^7 Pa$ .

of  $p_e = 6.69 \times 10^6 Pa$ . Consequently, it results in a more realistic prediction of the lining behavior in the course of excavation while it satisfies the segments' stability condition at the starting point of the simulation as well (see Figure 7.25b).

### Second step:

Given the installation process of the 12 segments in each ring of the lining (Figure 7.26), the performed procedure is mainly summarized as follows (more information can be found in [Bastiaens et al., 2003]):

1. Placement of the segment 6 on the bottom of the gallery while it has been held in place against the corresponding segment "6" of the previous ring (along the gallery axis) by the thrust pressure of the jacks.
2. Placement of the segments 7, 5, 4, and 8, in the similar manner as the segment 6.
3. Placement of the two segments 3 (corresponds to the right image in Figure 7.2) and 9.
4. *Partial* insertion of the key segments 11 and 12.
5. Placement of the segments 10, 1, and 2 while an anti-fall system has been subsequently emplaced for each of these three segments.
6. *Full insertion of the two key segments to their final position, with an expansion of the ring.*

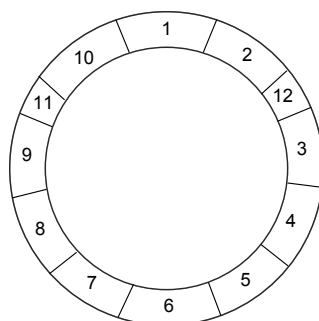


Figure 7.26: Segments numbering<sup>14</sup>; after [Bastiaens et al., 2003].

The first five stages of the above procedure - which lie in the overall process of the segments placement besides each other while some pressure could be considered to be produced among

<sup>14</sup>looking towards Test Drift (see Figure 2.3).

them and that they are in an equilibrium with no important violation of their stability - is supposed to have been integrated within the described "first step" of our numerical approach hitherto. Lastly, the *full insertion of the key segments* is considered to produce an *extra* pressure among the segments which could also result in the aforesaid expansion of the lining's ring. The lining's installation has been performed quite simultaneously with the gallery's construction (almost immediately after the passage of the excavation front, as already mentioned [Bastiaens et al., 2003]). Hence, this last step (extra) pressure (linked to the keys insertion) is regarded, in the numerical point of view, as the pressure exerted between the segments at the end of our so-called excavation phase.

Therefore, our numerical modeling is aimed to take into account of an increase of the pressure on the segments interfaces at the beginning of second numerical phase (i.e. since end of the sixth day) in order to simulate the pressure imposed by the keys full insertion between the segments.

Indeed, we do not have any direct in-situ measurements of the pressure between the segments to be referred in our numerical simulation. Although, the strain measurements within the lining's segments (see Section 6.4.3), which are exactly available since the full insertion of the key segments, may be the best tool to calibrate our assumption of the pressure produced between the segments through the keys insertion. In this sense, the numerical results of the strain evolution could be checked against the corresponding measurements, and as a result, the appropriateness of our assumption of that pressure considered between the segments could be also verified.

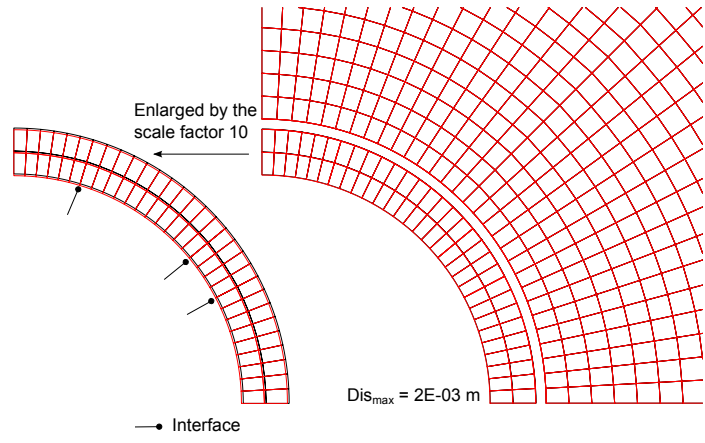
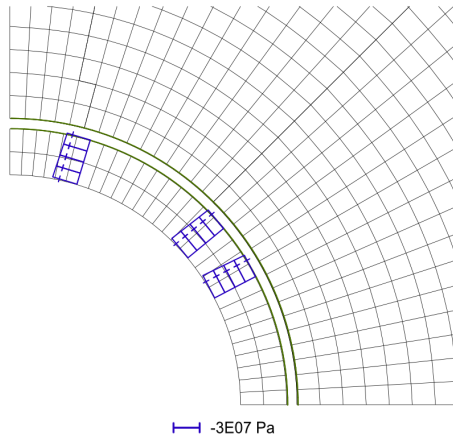
Within this framework and through several simulations (with different assumptions), the produced (extra) compressive pressure on the segments' interfaces has been estimated as  $-1.5 \times 10^7 Pa$ , consisting in a 37.5% increase of the aforesaid defined pre-pressure  $p_N^0$ . Consequently (with respect to Equation 7.42), the corresponding external pressure on the lining is equal to  $2.51 \times 10^6 Pa$ .

This assumption of pressure increase (extra pressure) on the segments interfaces in our simulation, which is considered to be appropriate for reproducing the in-situ measurements, is then later validated based on the strain measurements in the lining in Section 7.5.3.1.

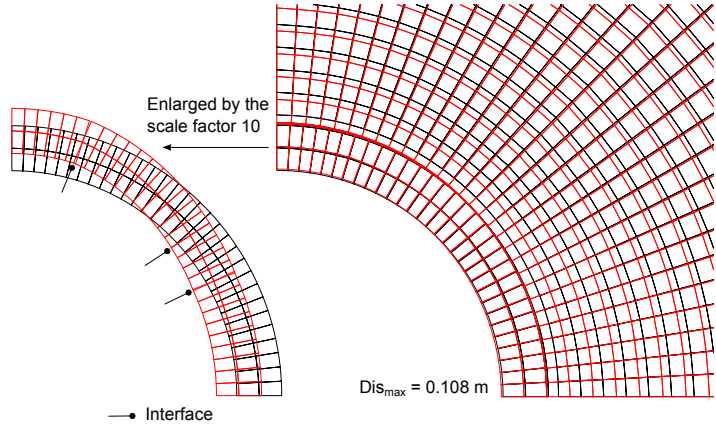
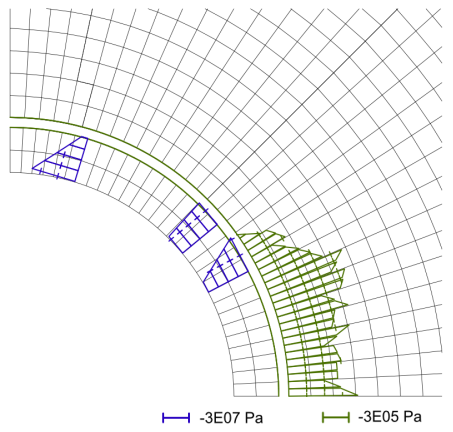
## 7.5.2 Analysis of the contact pressure on the interfaces

Figure 7.27 presents the evolution of the normal contact pressure on the three interfaces between the concrete segments as well as the interface between the lining and the clay. The deformation pattern of the rock mesh, in the vicinity of the gallery, in interaction with the (deformed) lining is also demonstrated. At the beginning of the simulation (Figure 7.27a), no deformation is obviously observed while the lining's segments are in the desirable stability thanks to the defined  $p_N^0$  (see the relative diagram of the contact pressure on the segments' interfaces). Next, in the course of convergence of the clay towards the lining during the excavation, which results in its primary contact with the lining from the horizontal side<sup>15</sup>, the lining is marginally deformed while the segments' movement allows a very slight penetration of the neighboring segments (Figure 7.27b). Consistently to the movement manner of the segments, it is observed that the contact pressure on their interfaces evolves more importantly on the right side of the first interface from the bottom, and on the left side of the first interface from the top. This pattern is followed until the end of excavation phase (Figure 7.27c) while the contact pressure is developed on the whole interface between the lining and the rock due to the full contact between two bodies (see also Section 7.4.3). In a longer time (Figure 7.27d), a recompression of the clay and an opposite-ward movement of the lining is tended while contact pressure evolves on all the interfaces; there

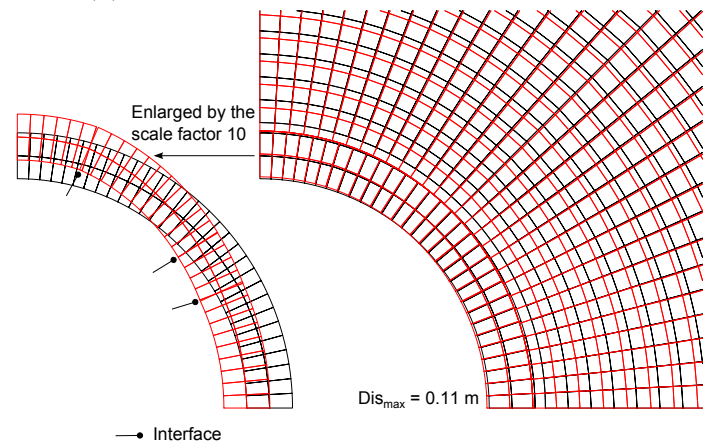
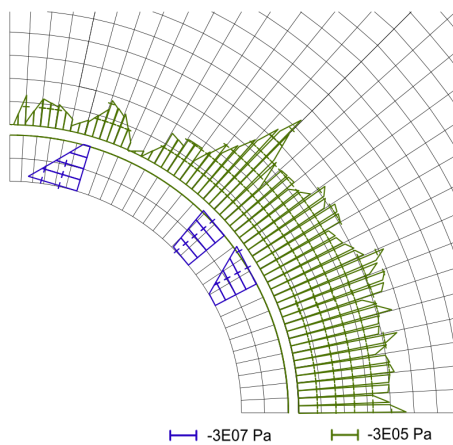
<sup>15</sup>It is noteworthy that the general behavior of the rock and its overall contact mechanism with the lining remain quite the same in the both cases considering a discontinuous or continuous lining. The difference in fact addresses mainly the lining behavior, i.e. its segments response in interaction with each other.



(a)



(b)



(c)

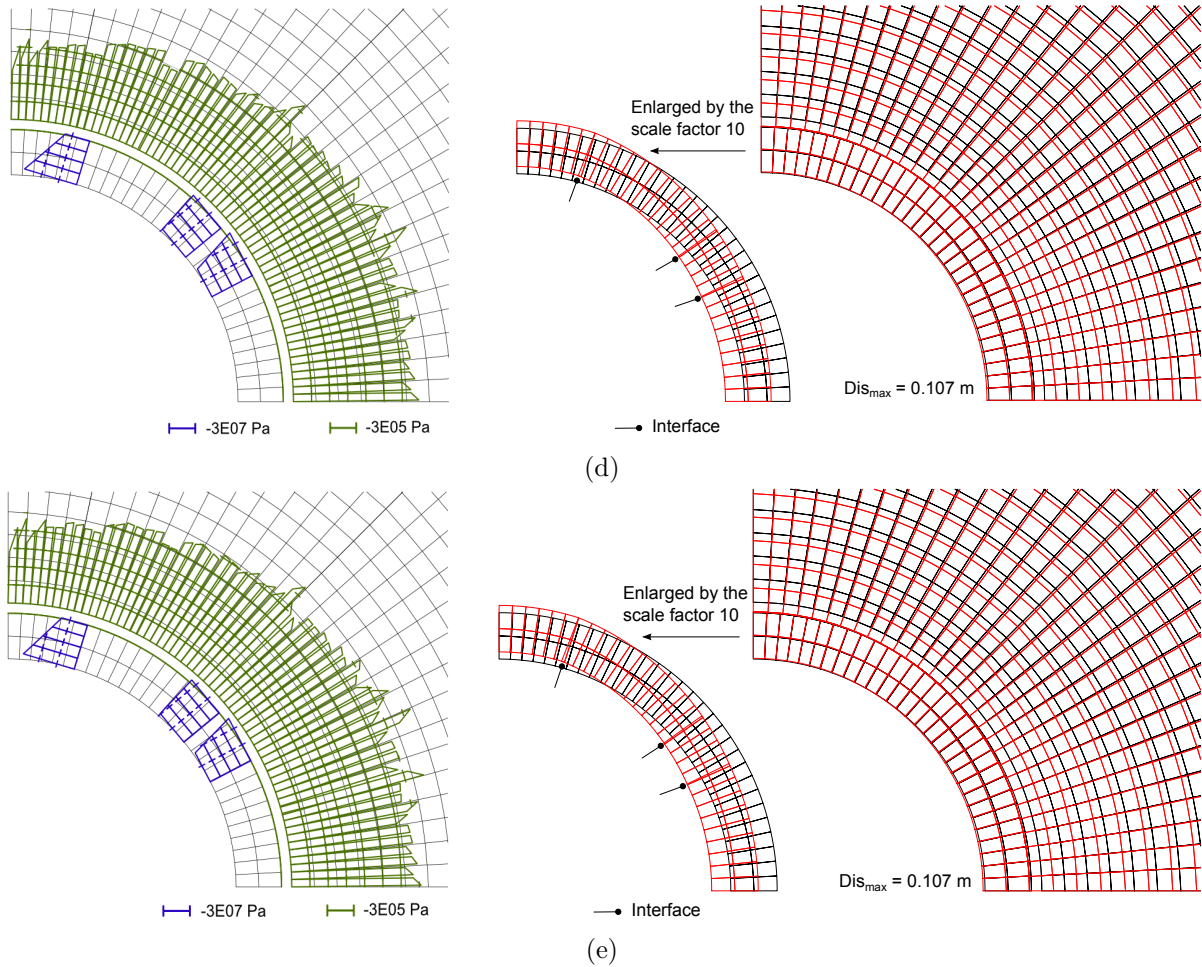


Figure 7.27: Diagram of the normal contact pressure on the interfaces (left side) and the model's deformation pattern (right side) after: (a) One second (beginning of the simulation). (b) 5 days. (c) 6 days (end of excavation). (d) 3.5 years. (e) 11.7 years.

is obviously more pressure developed on the whole interface between the clay and the lining. Additionally, the evolution of the contact pressure on the segments' interfaces takes into account of the extra pressure imposed at the beginning of second phase of our simulation (i.e. end of the sixth day) with respect to the impact of full insertion of the key segment (see Section 7.5.1) while the manner of segments' movement (and relative penetration) in time is also regarded. The model's behavior is almost unchanged after some more years of simulation (see Figure 7.27e).

### 7.5.3 Comparison of the numerical predictions and in-situ measurements in the lining

This Section is aimed to compare the results of the developed modeling with the in-situ measurements in the lining, in contrast to the previous analysis performed in Section 6.5.6 considering a continuous lining.

#### 7.5.3.1 Analysis of strain

The strain measurements, as described in Section 6.4.3 (with regard to the ring 50 of the lining), are available since the installation of the ring in February 2002. In a more precise point of view, the first data of the both internal and external sensors of each segment have been recorded at the day *before key* and *after key* full insertion that thereafter the measurements have been persisted in time.

In the numerical point of view, the above procedure is considered through presenting the predicted strain evolution with reference to *one day before* imposing of the extra pressure induced by the key segment (as described in Section 7.5.1), i.e. end of fifth day of computation, compared to the in-situ data. On the whole, two main features are therefore regarded in the following comparison, summarized as:

- *An extra pressure, related to the full insertion of the key segment in the last step of the ring's installation, is considered on the segments' interfaces.*
- *The comparison is performed since one day before the key insertion - reproduced through the above imposed contact extra pressure - relatively to the reference in-situ data.*

Figure 7.28 presents the obtained numerical results compared to the in-situ measurements, in three segments of the ring 50 (see Figure 6.22). This comparison can be then contrasted with the one given in Figure 6.54 based on the assumption of a continuous lining. First and foremost, it is observed that the numerical predictions are principally improved here taking into account of the discontinuous lining with application of interface elements between the segments. As a result, no tension is permitted to be transferred between the segments. Additionally, the immediate increase of the strain at the beginning of the experimental curves, associated to the quick response of the blocks after the key insertion (considering some produced pressure among the segments), is quite well reproduced by the numerical simulation. This latter could also validate the relevancy of our applied assumption of the extra contact pressure on the segments interfaces correspondingly to the keys full insertion (see the described approach in Section 7.5.1). Moreover, the predicted evolution pattern of strain is overall in a pretty good agreement with the measurements, specially with respect to the top and bottom segment. Nevertheless, the compressive behavior recorded through the internal sensor of the segments 891 and 1019, and the external sensor of the segments 1137 and 1019 - linked to the deformation pattern of the

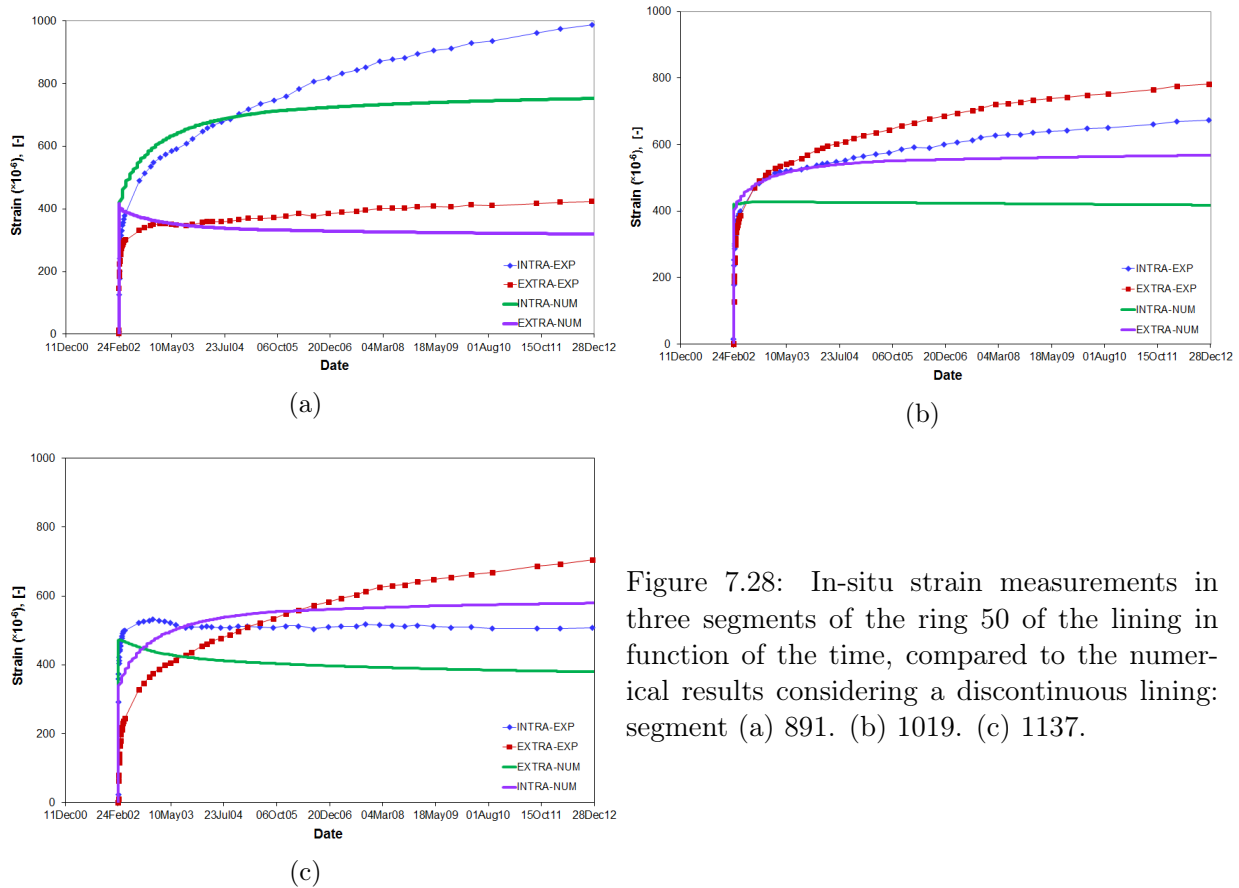


Figure 7.28: In-situ strain measurements in three segments of the ring 50 of the lining in function of the time, compared to the numerical results considering a discontinuous lining: segment (a) 891. (b) 1019. (c) 1137.

lining's segments in interaction with the rock - seems to be fairly underestimated in a very long time. This underestimation may be reasonably associated to the creep of concrete which has not been inhaled in our modeling.

The creep of concrete is supposed to be integrated through the diminution of its Young's modulus in time. The effect of this issue on the obtained results has been inquisitively studied simply through several performed numerical simulations with modification of the concrete Young's modulus in time so that the long-term in-situ strain measurements could be better reproduced. Thence, an estimation of the creep behavior is considered as follows: the defined initial value of the Young's modulus, i.e.  $43305 \text{ MPa}$  (see Table 6.2), is assumed to be diminished to one third after 2 years (of our analysis) while this latter value is imposed until the end of 3.5 years (i.e. our second phase of computation). Subsequently, the creep behavior of concrete in a longer time (since 3.5 years until 11.7 years which is end of our analysis) is assumed to consist in an (initial) Young's modulus decreased to one sixth.

Consequently, Figure 7.29 represents the numerical results of the strain evolution in the studied segments, compared to the relative in-situ measurements. It is observed that the long-term behavior of concrete is still upgraded here (see also Figure 7.28) while the corresponding numerical curves, in the longer time, approach overall better the experimental ones (see also [Salehnia et al., forthcoming]).

All together, with regard to the strain evolution in the lining segments, the described significant improvement obtained *basically* through the development of the model to consider discontinuous lining segments, introducing the interface elements between them, is illustrated in Figure 7.30. It brings together the final numerical results of strain evolution in three segments of the lining besides the former ones (assuming a continuous lining; Figure 6.54), compared to

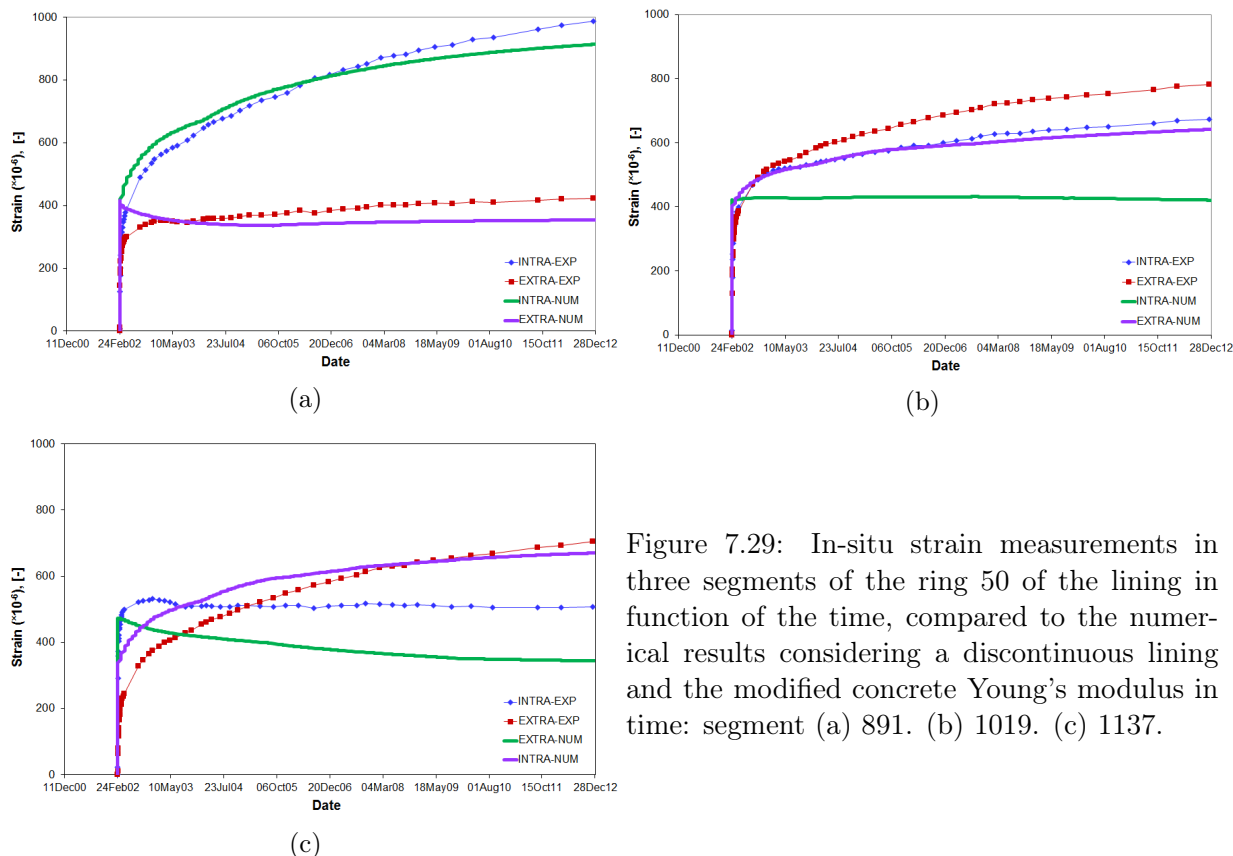


Figure 7.29: In-situ strain measurements in three segments of the ring 50 of the lining in function of the time, compared to the numerical results considering a discontinuous lining and the modified concrete Young's modulus in time: segment (a) 891. (b) 1019. (c) 1137.

the in-situ measurements.

### 7.5.3.2 Analysis of convergence

With regard to the convergence measurements described in Section 6.4.4, the absolute displacement of four sensors of the rings 50 and 8 has been analyzed in Section 6.5.6 compared to the result of the numerical modeling taking into account of a continuous lining. This study is represented in this Section, in contrast to a similar comparison presenting the final results<sup>16</sup> obtained through our developed model of the lining made of the segments.

Thence, Figure 7.31 demonstrates the numerical predictions of the lining response, in the rings 50 and 8, for the both latter cases compared to the in-situ data. First of all, an important improvement is noticed with respect to the current simulation considering the discontinuous lining than the former modeling. The increasing pattern of displacement in a longer time is notably better reproduced here (i.e. left side graphs; notice also the average linear evolution of the readings in time shown schematically by the dashed lines). Nevertheless, the long-term important displacement evolution corresponding to the sensor 5012 in the top segment of the ring 50 (see Figure 6.26) is still underestimated. However, this high difference of displacement recorded through the top sensor with the other ones is not the case of all the rings, as already mentioned in Section 6.4.4. It is observed that the numerical results of the displacement evolution regarding all the four sensors of the ring 8 are in a very good agreement with the corresponding in-situ data (see

<sup>16</sup>The presented results correspond to the case with the discontinuous lining while an estimation of the concrete creep behavior is applied through the aforesaid modifications of the Young's modulus in time. Although, similarly to the strain measurements, the obtained improvement demonstrated in Figure 7.31 *basically* corresponds to development of the model to consider the discontinuous lining segments and the applied approach on their interfaces, rather than the secondary impact of the concrete Young's modulus modifications.

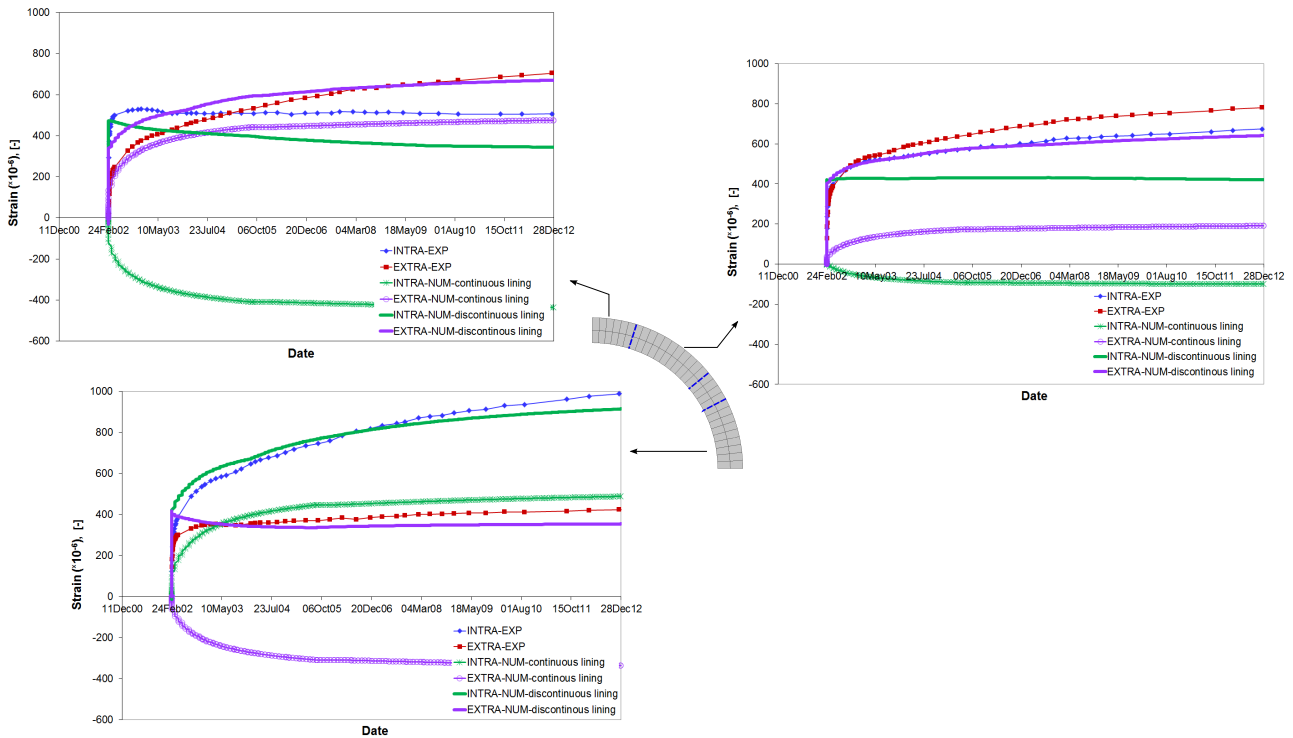


Figure 7.30: In-situ strain measurements in three segments of the ring 50 of the lining in function of the time, compared to the numerical predictions with two different approaches: considering a continuous or discontinuous lining.

the left side graph in Figure 7.31b).

Moreover, the both simulated and recorded displacements in the two rings consist in, by any means, an overall higher displacement of the sensor corresponding to the top segment (i.e. 5012 and 812) than the other three studied sensors of the relative ring. With regard to the numerical results, this aspect is more noticeable with respect to the current simulation taking into account of a discontinuous lining (i.e. left side graphs). Indeed, the long-term movement of the top segment is more important than the other ones; see the gradual deformation of the lining in Figures 7.27c-7.27e. Following a relatively higher velocity norm within the clay on the top of the gallery (similarly to Figure 6.34), the lining segments could be in fact moved relatively to each other (in an anti-symmetrical pattern) in the current modeling in contrast to the model of a continuous lining. Figure 7.32 shows the nodal velocity norm in the lining, for the two studied cases (with continuous and discontinuous lining) in long-term: after 3.5 years (since the excavation time) and 11.7 years (end of simulation). A more important difference of the nodal velocity norm within the top and bottom parts of the lining is observed for the current simulation where the relative displacements of the segments occurs. The middle segments show the least nodal velocities resulting in a less displacement evolution of the sensors 50111, 8111, 50102, and 8102, which it is in a quite good agreement with the in-situ measurements (Figure 7.31).

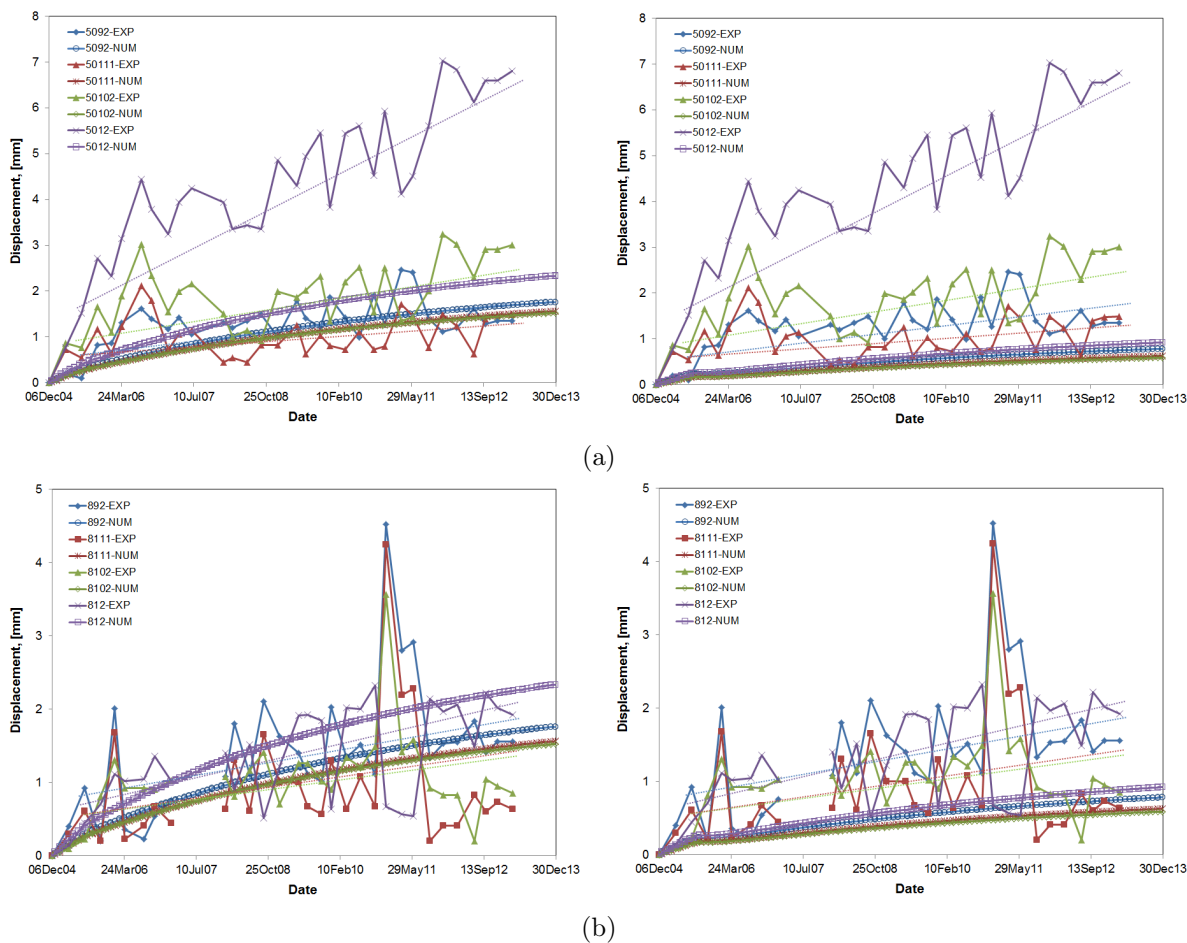


Figure 7.31: Displacement recorded for four sensors of the ring (a) 50. (b) 8, in function of the time with reference to 6/12/2004, compared to the numerical results considering a discontinuous lining (left side) or continuous lining (right side). The dashed lines display schematically an average linear evolution of displacement readings of each sensor in time.

## 7.6 Intermediate conclusions

This Chapter focused on the the contact problem, and it was more particularly aimed to address the contact phenomena integrated through the large-scale excavation (of Connecting gallery) in Boom Clay host-rock in order to accomplish our relative hydro-mechanical analysis in the last two Chapters.

Within this framework, the general concept of the contact mechanism was firstly described. The contact constraints were discussed and the governing equations of the contact problem were represented. The constitutive laws for treatment of the contact problem have been introduced indicating that the sticking and slipping phases of the mechanical contact are distinguished via the Coulomb yield criterion under the concept of an elasto-plasticity analogy. The interface element, in the LAGAMINE code, was then described.

In the second part of this Chapter, an analysis of the contact phenomena between the clay mass and the gallery's concrete lining, with application of the interface elements between two bodies, was aimed. In this sense, the essential role of the lining in diminishing the extent of

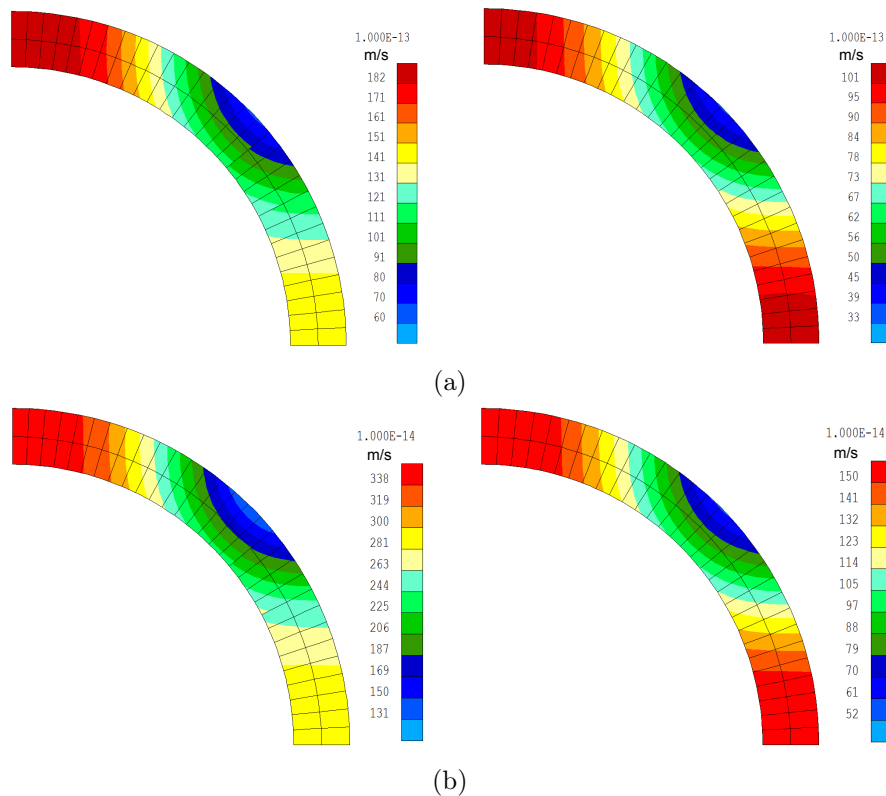


Figure 7.32: Velocity norm in the discontinuous lining (left side) and continuous lining (right side) after: (a) 3.5 years. (b) 11.7 years.

the strain localization and EDZ as well as the convergence of the clay around the gallery has been primarily highlighted. Given the need to the lining while excavating in the plastic Boom Clay, the relative contact phenomenon of the rock with the lining was analyzed demonstrating a fundamental relation between the pattern of the produced contact pressure on the interface between two bodies and the strain localization evolution within the clay in the gallery's proximity.

Lastly, the application of the interface elements within a discontinuous concrete lining of the gallery, as a topic of unique interest, has been focused. Indeed, considering that the gallery's lining is in fact made of the jointed segments, the simulation of its behavior has been aimed to be improved - with respect to the assumption of a continuous lining - through a developed model of the discontinuous lining with application of the interface elements between the neighboring segments. The followed numerical steps for a realistic modeling of the lining behavior were then described. The relative behavior of the segments within this discontinuous lining and also in interaction with the rock were demonstrated during and after the (so-called) excavation phase. Moreover, the numerical results of the long-term strain and convergence evolution in the lining were analyzed in comparison with the in-situ measurements. This study has shown an important improvement of the numerical prediction of the lining response as a result of the new developed model of the lining, compared to consideration of a continuous body for the lining. Although, it is noteworthy that the main hydro-mechanical features of the rock behavior remain principally the same in the both cases, and the difference addresses mainly the lining behavior, i.e. its segments response in interaction with each other.

# Chapter 8

## Conclusions and perspectives

### Contents

---

8.1	General conclusions . . . . .	278
8.2	Perspectives . . . . .	282

---

*Without ambition one starts nothing.  
Without work one finishes nothing. The prize  
will not be sent to you. You have to win it.*

Ralph Waldo Emerson

*Science never solves a problem without  
creating ten more.*

George Bernard Shaw

## 8.1 General conclusions

The present thesis has been basically aimed for a more clarified and better understanding of the coupled hydro-mechanical behavior of Boom Clay host rock, and more particularly in the presence of strain localization. Boom Clay is considered as the reference host formation in Belgium to be suitable for deep disposal of high-level radioactive waste, within an international consensus on feasibility of the deep storage solution for the long-term management of these wastes. Some large-scale experiments and relevant research projects have been conducted (in the HADES URL) to collect some in-situ measurements in the host rock subsequently to an underground excavation, and to better understand its behavior. However, with regard to the large-scale and complexity of the problem as well as the interaction between different phenomena occurred due to the excavation and afterwards, the role of the numerical modeling is significant. It could help in better understanding of the obtained field data, and to address some aspects which could not be understood, or at least to the desirable extent, through the site observations and measurements (notably the evolution of the fracturing and localization of deformation in rock during the time). Additionally, considering the paramount interest in understanding and characterization of damaged zone, development of strain localization, and the relative coupled hydro-mechanical phenomenon within the clay due to a large-scale excavation - in the framework of studying the performance of future nuclear waste disposal system confined by the Boom Clay natural barrier - this task has hence been the foundation of the main numerical analyses presented in this thesis.

In a progressive manner, the concept of deep disposal of high-level radioactive waste in deep geological formations, and the role of Boom Clay within this framework was firstly discussed. Next, a literature review on some principle factors of behavior and deformation mechanism of Boom Clay, and its mineralogical compositions were given. Moreover, a bibliographical analysis was performed on the main mechanical and hydraulic properties of natural Boom Clay, as an introduction to the subsequent studies in this work.

The numerical analysis of a complex large-scale problem requires certainly an appropriate numerical framework, a well chosen constitutive law, and a proper definition of the relative parameters of the model. In this sense, the theoretical formulation was primarily described. An internal frictional elasto-plastic constitutive law with the Drucker-Prager yield surface has been introduced as our applied model in this work. The corresponding hydro-mechanical parameters of the model were then aimed to be validated, for a realistic modeling of our material behavior, based on some available experimental results in the laboratory. Four series of the published results of undrained and drained triaxial compression tests, performed on Boom Clay samples, have been referred. The corresponding parameters were then calibrated while a particular focus has been done on the least regarded parameter in the literature, i.e. dilatancy angle. Our study declared the deficiency of considering a constant value of dilatancy angle in the modeling for correctly reproducing the experimental results of the material volumetric behavior; and in a general point of view, in fact in many applications in rock engineering.

Therefore, one originality of this work has consisted in developing a new formula for consideration of variable dilatancy angle, incorporated into the framework of the applied elasto-plastic hardening/softening model. The developed formula has been overall implemented into the PLASOL and ORTHOPLA laws in LAGAMINE finite element code's library, which use the frictional elasto-plastic models (with Drucker-Prager/Van Eekelen yield surfaces) considering the material's isotropy and anisotropy, respectively. This proposition consists in definition of three main factors of dilatancy angle providing the possibility of reproducing a dilatant or contracting volumetric behavior of a rock as well as a dilatant/contracting transitional response. Through the

latter capability, for instance a primary contracting behavior and subsequent dilatancy tendency of a material (e.g. as a result of a drained compression test and the ultimate creation of localized fractures) could be reproducible. The model has been basically developed in a semi-empirical manner with respect to the aforesaid experimental results of triaxial tests performed on Boom Clay sample. Although, it can be *a priori* appropriate to be applied to other rocks and even (non-granular) soils. The capability of the model to address different observed volumetric behaviors in the laboratory was illustrated through some numerical simulations, and the new parameters of the model were also better described. Some precedent numerical simulations of (drained and undrained) triaxial tests were thence re-performed using the new model, following by a discussion on the achieved improvement in reproducing the corresponding experimental results.

Subsequently to concluding the basic numerical framework and the model's parameters, analysis of strain localization has been focused. The concept of strain localization and shear banding were therefore primarily defined. It has been said that localization condition can be analyzed with respect to the onset of instability while the latter is frequently sought through the bifurcation theory. The bifurcation conditions, which in fact consist in a loss of solution uniqueness, were described. Furthermore, the importance of analyzing the strain localization was illustrated through representing some experimental and in-situ evidences of strain localization in different geomaterials, namely Boom Clay, as a frequent source of failure. In fact, in a progressive failure, the shear zones with localized plastic strain are realistically giving rise to the discontinuities, the rupture zones. Thence, to better understand the mechanisms leading to this fractures' network, we have proposed to analyze the EDZ and its extension around an underground gallery, during its construction and in the long-term, by numerical modeling, in the framework of a strain localization approach in shear band mode. To do this, the theoretical formulation was developed to be integrated with the coupled local second gradient (regularization) method. The latter has aimed to overcome the mesh dependency problem encountered using the classical finite element, for a correct simulation of the localization and post-localization response.

Next, as an introductory numerical example of strain localization simulation, a biaxial compression test was modeled. This simulation could highlight the mesh independent response obtained through the application of the second gradient model. Additionally, the dependency of the shear bands thickness to the elastic modulus of second gradient was illustrated. Moreover, it has been demonstrated that the material softening, accounted through the cohesion softening in our constitutive law, has an essential impact in initiation of strain localization. The significant parameters in terms of the strain localization analysis were aimed to be focused through a large-scale application as well. Hence, a gallery excavation, defined by analogy with Praclay gallery, was modeled through which a parametric study has been conducted. As a result of this study, the key numerical parameters for a realistic modeling of strain localization, resulted from an underground excavation - consisting in the softening parameters and modulus of second gradient - have been concluded to be used in the rest of numerical analyses through this thesis.

Furthermore, our developed model of variable dilatancy angle has been applied into the aforesaid large-scale modeling. As a result, the capability of this model for a better reproducing the coupled hydro-mechanical response of the host rock within the damaged zone around the gallery - the development of localized shear bands and the distribution of pore water pressure within this zone<sup>1</sup> - in contrast with application of a constant (zero/non-zero) value of dilatancy angle was demonstrated. Indeed, a dilatancy tendency of the rock is supposed to occur due to the excavation, with a peak of this tendency within the zone with localization of deformation, and coinciding with the onset/appearance of the localized shear bands. This could indicate the shear dilatation behavior. With regard to a real gallery excavation, this response may be interpreted as

---

<sup>1</sup>Specially considering the fact that the studied galley has had no support, resulting in a large localized zone and a considerable redistribution of pore pressure in the gallery's proximity.

the maximum dilatation of the rock taken place simultaneously with the fractures opening. This tendency is then expected to vanish afterwards following a possible closure or no more opening mode of the fractures/no more activity of the shear bands.

The last two Chapters have focused on our main application case, i.e. the Connecting gallery. Its excavation and the following coupled hydro-mechanical phenomena occurred within the surrounding clay and the gallery's lining in time have been analyzed numerically and also in the in-situ point of view. The corresponding phenomena have not been partially regarded in the past relevant studies (specially in the numerical point of view), or some might have suffered of a lack of their coupled analysis and in interaction with each other, in the case that they have been considered (mostly in the in-situ point of view). In this sense, through the competence provided by numerical simulations, the development of localized shear bands and damaged zone around the gallery during the excavation and afterwards, and relatively, the phenomenon of contact between the clay and the gallery's concrete lining, the redistribution of stress, pore water pressure, and displacement within the host rock, the gallery's convergence, in addition to the lining behavior have been principally analyzed in a coupled original point of view, and in the both numerical and field point of views.

The numerical modeling has firstly concerned a quarter of the gallery, given initial anisotropic stresses while the lining of the gallery has been taken into consideration (with a continuous body). This modeling was later extended to a full gallery. The latter extension was basically linked to the consideration of a possible loss of symmetry in the system's behavior which might be prompted by strain localization, as well as the gravity effect. Through this extension, material inherent anisotropy was also taken into account given that it might equally cause some directional dependency in the clay behavior. The cross-anisotropy of the mechanical properties were hence considered consisting in the elastic (through the compliance matrix) and plastic cross-anisotropy (through the material cohesion expression). In addition, the zones of anisotropic permeability were defined spatially in the whole model, and throughout the three (time) phases of simulation (for a total of 11.7 years), based on the relative in-situ measurements.

The results of the modeling have demonstrated the development pattern of localized shear bands in the course of excavation phase (of 6 days) and afterwards. The extension of the localized zone and EDZ in Boom Clay is in fact mainly limited to the excavation period since no important evolution of the bands have been observed after the end of excavation. An eye-shape extension of the damaged zone accompanied by an anisotropic oval-shaped pattern of rock deformation around the opening (clay convergence) due to the excavation were predicted numerically. These aspects have been discussed in comparison with the in-situ observations demonstrating a very good agreement between them. Moreover, in a coupled hydro-mechanical point of view, the pore water pressure distribution within the clay during and after the excavation phase has been analyzed, with respect to all the aforesaid phenomena.

There is an invaluable data library provided during and after the gallery's construction through some conducted large-scale experiments. These data could be a powerful source to be integrated with our numerical analysis in the sense that they could in one hand validate the numerical predictions. On the other hand, our numerical perception of the whole coupled problem could help to a better comprehension of those data, and to also make a bridge on some remained aspects which could not be clarified (or addressed) through the in-situ experiments. A precise coupled analysis of the in-situ data have been therefore performed to give those invaluable data firstly a practical sense. They have been then analyzed in comparison with the obtained numerical results. This study, in an extensive sense, consisted in the pore pressure measurements in time along the different piezometers installed out of the gallery during and after the gallery's construction, in addition to the strain and convergence measurements in the lining in long-term.

Comparison of the pore pressure measurements with the corresponding numerical results have shown a quite good agreement between them, specially in the long-term. It must be noted that with regard to the excavation process, a full representation of the whole phenomena integrated through the 3D complex excavation problem (and so the relative field data), and specially with regard to the impacts of the other preexisting galleries, would not be perfectly possible with respect to the 2D plane strain simulation. Although, a very important progress has been achieved in understanding the governing coupled phenomena.

The analysis of the strain and convergence measurements in the lining has demonstrated the deficiency of the model, considering a continuous lining, in reproducing the field data. With regard to the unique interest in studying the behavior of the lining's segments (considering a discontinuous lining) and their contact behavior, and the interaction of the whole lining with the rock, another originality of this thesis has consisted in analysis of these contact phenomena, integrated within the overall problem. The concept of contact mechanism and its governing equations were then firstly introduced. Application of the interface finite elements have been proposed to treat the aforesaid contact phenomena; these elements in the LAGAMINE code were then introduced.

In the first place, the gallery's lining has an essential role while excavating in the plastic Boom Clay formation, which it is in fact a powerful motivation providing a paramount interest to focus on its behavior and the relative phenomena. This role has been then primarily illustrated through performing another simulation without considering the lining, which resulted in a much more extended damaged zone and the clay convergence. Moreover, given the need to the lining, its progressive contact mechanism with the rock was analyzed with application of the interface elements. As a result of the anisotropic convergence of the clay due to the excavation, it comes into contact with the lining firstly from the horizontal side producing some contact pressure on their interface. This pressure is then developed on the whole interface. The pattern of development of contact pressure on the interface has been then demonstrated to be fundamentally related to the strain localization evolution within the clay in the gallery's proximity. The latter has been illustrated to be the basic origin of some oscillations in the evolution pattern of contact pressure along the interface.

With regard to the phenomena occurred within the lining, the unique interest addresses the segmentation and developing a numerical model which could simulate realistically the behavior of these segments and their contact mechanism. Hence, the interface elements has been defined between each of two neighboring segments (four segments considering a quarter of the galley). A realistic modeling of the real phenomena occurred among the segments of this discontinuous lining, in the numerical point of view, has needed some special attentions. Definition of an initial contact pressure between the neighboring segments could provide an initial stability of the segments in place. Moreover, with regard to the real procedure of installation of the segments (of each ring of the lining), the full insertion of the key segments has been supposed to induce an extra pressure among the segments which was simulated numerically through an increase of the aforesaid initial contact pressure. The obtained behavior of the segments within this discontinuous lining, following the aforesaid numerical steps, was the analyzed. The numerical results of the long-term strain and convergence evolution in the lining were compared to the corresponding in-situ measurements. This study has demonstrated a very important improvement of the numerical prediction of the lining response as a result of the new developed model of the lining, compared to consideration of a continuous body of the lining. Besides, it could consistently validate the relevancy of our applied approach for simulating the phenomena occurred within the lining following the (real) installation process and notably the keys' insertion.

## 8.2 Perspectives

The aim of each PhD thesis is pushing the boundary of science in a well-organized direction to make a little of enlargement. Although, the science's boundary is never limited to the enlargement provided as the conclusion of each thesis since it equally imposes the new questions to motivate the new violations of the science's boundary!

This thesis could fulfill a series of gaps in understanding the coupled HM behavior of Boom Clay - as a potential natural barrier for hosting the deep excavated galleries for disposal of nuclear waste - in the presence of strain localization, and its response in interaction with the gallery's lining, in addition to the own lining behavior. Nevertheless, within the above concept, some perspectives subsequently to this work could be equally revealed as summarized in the following.

In terms of the particular interest in concerning more realistically the volumetric behavior of a rock in the course of a loading procedure, the developed model in this thesis has pioneered a new method for consideration of the variable dilatancy angle. This proposition has been checked against some available experimental works on Boom Clay. Although, conducting some particular experiments for a more organized perception of the volumetric behavior of a material in the course of different loading-unloading procedures is advantageous for providing a more critical point of view, and ultimately even attaining a more sophisticated numerical model. In this sense, the excavation paths could be also attentively addressed in the laboratory. Additionally, for instance through a shear testing set-up, some useful information on the shear dilatation behavior of a material could be attained. The latter concerns the creation of a fracture while it slips by shear and dilate. This behavior could be then accompanied by large deformation and a variable dilatancy tendency within the shear band. The basics of our model could desirably address this sort of volumetric behavior. Although, a more organized laboratory study could help to complement this approach through a better experimental perception. These experiments are advisable to address the behavior of different geomaterials based on which a more accomplished empirical view would be achieved, and the model's parameters could be desirably calibrated for each material.

Furthermore, combining the dilatation response of the material with the concept of a likely variation of its permeability, this relation could be particularly studied. This aspect may be then focused concerning the simulation of a gallery excavation through it, and the dilatancy tendency around the opening and within the created fractures.

With regard to the large-scale numerical modeling of an underground excavation, and our particular focus on strain localization development within the surrounding host rock, a general interest addresses a 3D simulation. This needs, in the first stage, a development of coupled second gradient method in the LAGAMINE finite element code for a 3D computation. As a result, the strain localization modeling could be performed integrated with a 3D analysis of the other coupled phenomena occurred within the rock. The latter for instance could address a likely more realistic evolution of pore water pressure around an excavated gallery as well as along the gallery axis (in the course of excavation), simultaneously with the strain localization development in the front of advancing gallery and around the gallery. Although, 3D development of second gradient method may not be a straightforward job concerning a correct treatment of the localization phenomenon. In this sense, one likely difficulty for instance may be the high number of degrees of freedom over a 3D coupled second gradient element, which is already 44 over a 2D coupled (hydro-mechanical) second gradient element.

Moreover, integrating the thermal phase within the whole analysis - either in 2D or in 3D (hopefully in the future) - would be another interesting aspect for the future researches. In this sense, the second gradient formulation needs still another development to be integrated with a

third phase, i.e. thermal, in order to provide the possibility of a coupled THM analysis in the presence of strain localization. In that case, besides the anisotropy of mechanical and hydraulic properties as considered in this thesis, the anisotropic thermal properties would be advantageous to be considered for a more realistic THM analysis. In addition, in terms of anisotropy, analysis of the anisotropy induced inside the shear bands could be another concern.

With regard to the in-situ data in Boom Clay host rock (as analyzed in the HM point of view in the present thesis), a sophisticated series of thermal measurements will be available to be analyzed - considering the general interest of thermal aspects, concerning the thermal impact of a repository [Sillen, 2008] in the framework of long-term management of high-level nuclear waste disposal - throughout the coming years. In fact, the Praclay heater test [TIMODAZ, 2010a] has been recently switched on; on November 3, 2014. This large-scale experiment will normally provide lots of useful data, during the subsequent 10 years, for the future researches. Therefore, analyzing of these data and integrating the obtained field perception with a THM numerical modeling, in the presence of strain localization, will be useful to assess the long-term performance of the future nuclear waste disposal system confined by the Boom Clay natural barrier.

Furthermore, with regard to the demonstrated impact of the (lining) segments' symmetry and geometry on their relative response (in Section 7.5.1), and likely influence of this behavior on the response of the rock in interaction with the lining, this aspect needs to be considered in the preliminary design of the real repositories, and their performance assessment.

In addition, with respect to some effect of the creep of concrete on better reproducing of its time-dependent behavior (demonstrated in Section 7.5.3.1), application of a relative viscous constitutive law could be interesting.



# Bibliography

- Aertsens, M., Wemaere, I., and Wouters, L. Spatial variability of transport parameters in the boom clay. *Applied Clay Science*, 26(1):37–45, 2004.
- Aifantis, E. On the microstructural origin of certain inelastic models. *Journal of Engineering Materials and technology*, 106(4):326–330, 1984.
- Alejano, L. and Alonso, E. Considerations of the dilatancy angle in rocks and rock masses. *International Journal of Rock Mechanics and Mining Sciences*, 42(4):481–507, 2005.
- Alonso, E. E., Gens, A., and Josa, A. A constitutive model for partially saturated soils. *Géotechnique*, 40(3):405–430, 1990.
- Amorim, A. F. L. *Thermo-Hydro-Mmechanical behavior of two deep Belgian clay formations: Boom and Ypresian clay*. PhD thesis, Technical University of Catalonia, July 2011.
- Armero, F. and Garikipati, K. An analysis of strong discontinuities in multiplicative finite strain plasticity and their relation with the numerical simulation of strain localization in solids. *International Journal of Solids and Structures*, 33(20):2863–2885, 1996.
- Baldi, G., Hueckel, T., Peano, A., and Pellegrini, R. *Developments in Modelling of Thermo-hydro-geomechanical Behaviour of Boom Clay and Clay-based Buffer Materials*. EUR 13365/1 and EUR 13365/2. Commission of the European Communities, Nuclear Science and Technology, 1991.
- Barnichon, J.-D. *Finite element modelling in structural and petroleum geology*. PhD thesis, Université de Liège, 1998.
- Barnichon, J.-D. and Volckaert, G. Hydro-mechanical coupling in the boom clay (mol url, belgium): recent in situ observations, predictions and perspectives. In *International Workshop on Geomechanics: HM and THM behaviour of deep argillaceous rocks: Theory and Experiments, Paris, Ecole des Mines*, 2000.
- Bastiaens, W., Bernier, F., and Li, X. L. An overview of long-term HM measurements around HADES URF. In *Proceedings of International Symposium on multiphysics coupling and long-term behaviour in rock mechanics, Liège*, pages 15–26, 1991.
- Bastiaens, W., Bernier, F., Buyens, M., Demarche, M., Li, X. L., Linotte, J. M., and Verstricht, J. The Connecting gallery. Technical report, EURIDICE, 2003. Report to European Commission.
- Bastiaens, W., Bernier, F., and Li, X. L. Selfrac: experiments and conclusions on fracturing, self-healing and self-sealing processes in clays. *Physics and Chemistry of the Earth, Parts A/B/C*, 32(8):600–615, 2007.
- Bathe, K.-J. *Finite element procedures*. Klaus-Jurgen Bathe, 1996.
- Beer, G. An isoparametric joint/interface element for finite element analysis. *International journal for numerical methods in engineering*, 21(4):585–600, 1985.

- Belgium Profile. Radioactive waste management programmes in OECD/NEA member countries. Technical report, Nuclear energy agency, 2013.
- Bernier, F., Volckaert, G., Alonso, E., and Villar, M. Suction-controlled experiments on Boom clay. *Engineering Geology*, 47(4):325–338, 1997.
- Bernier, F., Li, X., Bastiaens, W., Ortiz, L., Van Geet, M., Wouters, L., Frieg, B., Blümling, P., Desrues, J., Viaggiani, G., et al. Fractures and self-healing within the excavation disturbed zone in clays (selfrac). *Final report to EC (Project FIKW-CT2001-00182)*. EUR, 22585, 2007a.
- Bernier, F., Li, X., Verstricht, J., Barnichon, J., Labiouse, V., Bastiaens, W., Palut, J., Slimane, J. B., Ghoreychi, M., Gaombalet, J., Huertas, F., Galera, J., and Elorza, K. M. F. CLIPLEX: Clay instrumentation programme for the extension of an underground research laboratory. Technical report, EURIDICE, 2007b. Report EUR 20619 EN to European Commission.
- Bernier, F., Li, X. L., and Bastiaens, W. Twenty-five years' geotechnical observation and testing in the tertiary Boom clay formation. *Géotechnique*, 57(2):229–237, 2007c.
- Besuelle, P. and Rudnicki, J. W. Localization: shear bands and compaction bands. *International Geophysics*, 89:219–321, 2003.
- Bésuelle, P., Desrues, J., and Raynaud, S. Experimental characterisation of the localisation phenomenon inside a vosges sandstone in a triaxial cell. *International Journal of Rock Mechanics and Mining Sciences*, 37(8):1223–1237, 2000.
- Bésuelle, P., Chambon, R., and Collin, F. Switching deformation modes in post-localization solutions with a quasibrittle material. *Journal of Mechanics of materials and structures*, 1(7): 1115–1134, 2006a.
- Bésuelle, P., Viggiani, G., Lenoir, N., Desrues, J., and Bornert, M. X-ray micro ct for studying strain localization in clay rocks under triaxial compression. *Advances in X-ray Tomography for Geomaterials*, 118:35–52, 2006b.
- Bésuelle, P., Viggiani, G., Desrues, J., Coll, C., and Charrier, P. A laboratory experimental study of the hydromechanical behavior of Boom clay. *Rock Mechanics and Rock Engineering*, 47(1):143–155, 2014.
- Biot, M. A. Nonlinear and semilinear rheology of porous solids. *Journal of Geophysical Research*, 78(23):4924–4937, 1973.
- Bishop, A., Webb, D., and Lewin, P. Undisturbed samples of london clay from the ashford common shaft: strength–effective stress relationships. *Geotechnique*, 15(1):1–31, 1965.
- Blümling, P., Bernier, F., Lebon, P., and Martin, C. D. The excavation damaged zone in clay formations time-dependent behaviour and influence on performance assessment. *Physics and Chemistry of the Earth, Parts A/B/C*, 32(8):588–599, 2007.
- Borja, R. I. *Plasticity*. Springer, 2013.
- Burland, J. and Yu, H.-S. *Plasticity and geotechnics*, volume 13. Springer, 2007.
- Callari, C., Armero, F., and Abati, A. Strong discontinuities in partially saturated poroplastic solids. *Computer Methods in Applied Mechanics and Engineering*, 199(23):1513–1535, 2010.
- Cerfontaine, B. *The cyclic behaviour of sand, from the Prevost modl to offshore geotechnics*. PhD thesis, University of Liège, 2014.

- Chambon, R. and Moullet, J.-C. Uniqueness studies in boundary value problems involving some second gradient models. *Computer methods in applied mechanics and engineering*, 193(27): 2771–2796, 2004.
- Chambon, R., Caillerie, D., and El Hassan, N. One-dimensional localisation studied with a second grade model. *European Journal of Mechanics-A/Solids*, 17(4):637–656, 1998.
- Chambon, R., Caillerie, D., and Matsushima, T. Plastic continuum with microstructure, local second gradient theories for geomaterials: localization studies. *International Journal of Solids and Structures*, 38(46):8503–8527, 2001a.
- Chambon, R., Crochepeyre, S., and Charlier, R. An algorithm and a method to search bifurcation points in non-linear problems. *International Journal for Numerical Methods in Engineering*, 51(3):315–332, 2001b.
- Charlier, R. *Approche unifiée de quelques problèmes non linéaires de mécanique des milieux continus par la méthode des éléments fini*. PhD thesis, Université de Liège, 1987.
- Charlier, R. and Cescotto, S. Modélisation du phénomène de contact unilatéral avec frottement dans un contexte de grandes déformations. *Journal de Mécanique Théorique et Appliquée*, 7 (Suppl. 1), 1988.
- Charlier, R., Collin, F., Gerard, P., and Radu, J. P. Développement d'un modèle (élément fini et loi de comportement) de fracture couple mécanique – écoulement en saturation partielle. Technical report, Université de Liège, 2009.
- Chen, G., Sillen, X., Verstricht, J., and Li, X. ATLAS III in situ heating test in boom clay: Field data, observation and interpretation. *Computers and Geotechnics*, 38(5):683–696, 2011.
- Chen, W. Z. and Li, X. L. Research on long-term hydro-mechanical coupling behavior of Boom clay. Presentation by IRSM, CAS, 2011.
- Coll, C. *Endommagement des roches argileuses et perméabilité induite au voisinage d'ouvrages souterrains*. PhD thesis, Université Joseph-Fourier-Grenoble I, 2005.
- Collin, F. *Couplages thermo-hydro-mécaniques dans les sols et les roches tendres partiellement saturés*. PhD thesis, Université de Liège, 2003.
- Collin, F., Chambon, R., and Charlier, R. A finite element method for poro mechanical modelling of geotechnical problems using local second gradient models. *International journal for numerical methods in engineering*, 65(11):1749–1772, 2006.
- Collin, F., Sieffert, Y., Chambon, R., and Laloui, L. Strain localization modeling in coupled transient phenomena. *Mechanics of Unsaturated Geomaterials*, pages 209–232, 2013.
- Coop, M. R., Atkinson, J. H., and Taylor, R. N. Strength and stiffness of structured and unstructured soils. In *Proceedings of the 11th European Conference on Soil Mechanics and Foundation Engineering, Danish Geotechnical Society, Bulletin*, volume 11, pages 55–62, 1995.
- Cornet, F. H. In situ stress measurement campaign, SCK-CEN underground laboratory Boerentang-Mol. Technical report, Institut de Physique du Globe de Strasbourg, 2009.
- Cosserat, E. and Cosserat, F. *Théorie des corps déformables*. Paris, 1909.
- Coussy, O. and Ulm, F. *Mechanics of porous continua*, volume 1016. Wiley Chichester, 1995.

- Craeye, B., Schutter, G. D., Humbeeck, H. V., and Cotthem, A. V. Early age behaviour of concrete supercontainers for radioactive waste disposal. *Nuclear Engineering and Design*, 239 (1):23 – 35, 2009.
- Curnier, A. A theory of friction. *International Journal of Solids and Structures*, 20(7):637–647, 1984.
- De Borst, R. and Mühlhaus, H.-B. Gradient-dependent plasticity: Formulation and algorithmic aspects. *International Journal for Numerical Methods in Engineering*, 35(3):521–539, 1992.
- De Borst, R. and Sluys, L. Localisation in a cosserat continuum under static and dynamic loading conditions. *Computer Methods in Applied Mechanics and Engineering*, 90(1):805–827, 1991.
- De Craen, M., Van Geet, M., Honty, M., Weetjens, E., and Sillen, X. Extent of oxidation in boom clay as a result of excavation and ventilation of the hades urf: Experimental and modelling assessments. *Physics and Chemistry of the Earth, Parts A/B/C*, 33:S350–S362, 2008.
- Decler, J., Viaene, W., and Vandenberghe, N. Relationship between chemical, physical and mineralogical characteristics of the rupelian Boom clay, Belgium. *Clay minerals*, 18:1–10, 1983.
- Dehandschutter, B., Sintubin, M., Vandenberghe, N., Vandycke, S., Gaviglio, P., and Wouters, L. Fracture analysis in the Boom clay (URF, Mol, Belgium). *Aardkundige Mededelingen*, 12: 245–248, 2002.
- Dehandschutter, B., Vandycke, S., Sintubin, M., Vandenberghe, N., Gaviglio, P., Sizun, J.-P., and Wouters, L. Microfabric of fractured Boom clay at depth: a case study of brittle–ductile transitional clay behaviour. *Applied Clay Science*, 26(1):389–401, 2004.
- Dehandschutter, B., Vandycke, S., Sintubin, M., Vandenberghe, N., and Wouters, L. Brittle fractures and ductile shear bands in argillaceous sediments: inferences from oligocene boom clay (Belgium). *Journal of Structural Geology*, 27(6):1095–1112, 2005.
- Delage, P., Sultan, N., and Cui, Y. J. On the thermal consolidation of boom clay. *Canadian Geotechnical Journal*, 37(2):343–354, 2000.
- Delage, P., Le, T. T., Tang, A.-M., Cui, Y.-J., and Li, X.-L. Suction effects in deep boom clay block samples. *arXiv preprint arXiv:0801.2105*, 2008.
- Desai, C. S. and Siriwardane, H. J. *Constitutive laws for engineering materials with emphasis on geologic materials*. Prentice-Hall, 1984.
- Desrues, J. Localization patterns in ductile and brittle geomaterials. *Material instabilities in solids*, pages 137–158, 1998.
- Desrues, J. and Viggiani, G. Strain localization in sand: an overview of the experimental results obtained in grenoble using stereophotogrammetry. *International Journal for Numerical and Analytical Methods in Geomechanics*, 28(4):279–321, 2004.
- Detournay, E. Elastoplastic model of a deep tunnel for a rock with variable dilatancy. *Rock Mechanics and Rock Engineering*, 19(2):99–108, 1986.
- Di Maio, C. *Consolidation, swelling and swelling pressure induced by exposure of clay soils to fluids different from the pore fluid*. Springer, 2004.

- Dizier, A. *Caractérisation des effets de températures dans la zone endommagée autour de tunnel de stockage de déchets nucléaires dans des roches argileuses*. PhD thesis, Université de Liège, 2011.
- Donath, F. A. Effects of cohesion and granularity on deformational behavior of anisotropic rock. *Geological Society of America Memoirs*, 135:95–128, 1972.
- Drucker, D. C. and Prager, W. Soil mechanics and plastic analysis or limit design. *Quarterly of applied mathematics*, 10, 1952.
- Duveau, G., Shao, J., and Henry, J. Assessment of some failure criteria for strongly anisotropic geomaterials. *Mechanics of Cohesive-frictional Materials*, 3(1):1–26, 1998.
- El Moustapha, K. *Identification of an enriched constitutive law for geomaterials in the presence of a strain localisation*. PhD thesis, Université de Grenoble, 2014.
- Ewy, R. Yield and closure of directional and horizontal wells. In *International journal of rock mechanics and mining sciences & geomechanics abstracts*, volume 30, pages 1061–1067. Elsevier, 1993.
- François, B. *Thermo-plasticity of fine-grained soils at various saturation states: Application to nuclear waste disposal*. PhD thesis, Ecole Polytechnique Fédérale de Lausanne, 2008.
- François, B., Labiouse, V., Dizier, A., Marinelli, F., Charlier, R., and Collin, F. Hollow cylinder tests on boom clay: Modelling of strain localization in the anisotropic excavation damaged zone. *Rock Mechanics and Rock Engineering*, pages 1–16, 2012.
- Fredlund, D., Morgenstern, N., and Widger, R. The shear strength of unsaturated soils. *Canadian Geotechnical Journal*, 15(3):313–321, 1978.
- Fredlund, D. G. and Rahardjo, H. *Soil mechanics for unsaturated soils*. John Wiley & Sons, 1993.
- Gaombalet, J. *Le gonflement des argiles et ses effets sur les ouvrages souterrains de stockage*. PhD thesis, Palaiseau, Ecole polytechnique, 2004.
- Gatmiri, B. and Arson, C.  $\theta$ -stock, a powerful tool of thermohydromechanical behaviour and damage modelling of unsaturated porous media. *Computers and Geotechnics*, 35(6):890–915, 2008.
- Gens, A., Carol, I., and Alonso, E. An interface element formulation for the analysis of soil-reinforcement interaction. *Computers and Geotechnics*, 7(1):133–151, 1989.
- Gens, A., Garcia-Molina, A., Olivella, S., Alonso, E., and Huertas, F. Analysis of a full scale in situ test simulating repository conditions. *International Journal for Numerical and Analytical Methods in Geomechanics*, 22(7):515–548, 1998.
- Germain, P. The method of virtual power in continuum mechanics. part 2: Microstructure. *SIAM Journal on Applied Mathematics*, 25(3):556–575, 1973a.
- Germain, P. La méthode des puissances virtuelles en mécanique des milieux continus. *J. Mécanique*, 12:236–274, 1973b.
- Goodman, R. E., Taylor, R. L., and Brekke, T. L. A model for the mechanics of jointed rock. *Journal of Soil Mechanics & Foundations Div*, 1968.
- Goriely, A. *Solid mechanics*. Lecture Notes, University of Oxford, 2013.

- Graham, J. and Houlsby, G. Anisotropic elasticity of a natural clay. *Géotechnique*, 33(2):165–180, 1983.
- Grossetie, J. C. Puissances virtuelles et travaux virtuels en mécanique des milieux continus micropolaires. Technical report, Commission of the European Communities, Luxembourg, 1981.
- Guiducci, C., Pellegrino, A., Radu, J.-P., Collin, F., and Charlier, R. Numerical modeling of hydro-mechanical fracture behavior. In *NUMOG VIII*, pages 293–299. Balkema, 2002.
- Habraken, A.-M. *Contribution à la modélisation du formage des métaux par la méthode des éléments finis*. PhD thesis, Universtie de Liège, 1989.
- Haied, A. *Etude expérimentale de la rupture en mode localisé dans un grès*. PhD thesis, 1995.
- Hall, S. A., Wood, D. M., Ibraim, E., and Viggiani, G. Localised deformation patterning in 2d granular materials revealed by digital image correlation. *Granular matter*, 12(1):1–14, 2010.
- Hertz, H. On the contact of elastic solids. *J. reine angew. Math*, 92(156-171):110, 1881.
- Hill, R. Acceleration waves in solids. *Journal of the Mechanics and Physics of Solids*, 10(1):1–16, 1962.
- Hoek, E. and Brown, E. Practical estimates of rock mass strength. *International Journal of Rock Mechanics and Mining Sciences*, 34(8):1165–1186, 1997.
- Horseman, S. T., Winter, M. G., and Enwistle, D. C. Geotechnical characterization of Boom clay in relation to the disposal of radioactive waste. Technical report, Commission of the European Communities, Luxembourg, 1987.
- Houlsby, G. *How the dilatancy of soils affects their behaviour*. University of Oxford, Department of Engineering Science, 1991.
- Hughes, T. J. The finite element method. *Englewood Cliffs, NJ*, 1987.
- IAEA. The world nuclear industry status report 2015, 2015. URL <http://www.worldnuclearreport.org/-2015-.html>. Source: IAEA-PRIS, MSC, 2015.
- JAEA. Multibarrier concept for HLW disposal, 1995. URL <http://jolisfukyu.tokai-sc.jaea.go.jp/fukyu/tayu/ACT95E/04/0408.htm>. Visited on 12/2014.
- Johnson, K. L. *Contact mechanics*. Cambridge university press, 1987.
- Kikuchi, N. and Oden, J. T. *Contact problems in elasticity: a study of variational inequalities and finite element methods*, volume 8. siam, 1988.
- Kirkebø, S. *A numerical study of excavations in low permeable soils*. PhD thesis, Norwegian Institute of Technology, University of Trondheim, 1994.
- Kolymbas, D. An outline of hypoplasticity. *Archive of applied mechanics*, 61(3):143–151, 1991.
- Kuhn, H. W. and Tucker, A. W. Nonlinear programming. In *Proceedings of the Second Berkeley Symposium on Mathematical Statistics and Probability*, pages 481–492. University of California Press, 1951.
- Kunin, I. A. Elastic media with microstructure. i-one-dimensional models. *Springer Verlag Springer Series on Solid State Sciences*, 26, 1982.

- Labouse, V., Sauthier, C., and You, S. Hollow cylinder simulation experiments of galleries in boom clay formation. *Rock mechanics and rock engineering*, 47(1):43–55, 2014.
- Laenen, B. The geochemical signature of relative sea-level cycles recognised in the boom clay. *Aardkundige Mededelingen*, 9:61–82, 1998.
- Larsson, R., Steinmann, P., and Runesson, K. Finite element embedded localization band for finite strain plasticity based on a regularized strong discontinuity. *Mechanics of Cohesive-frictional Materials*, 4(2):171–194, 1999.
- Laursen, T. and Simo, J. A continuum-based finite element formulation for the implicit solution of multibody, large deformation-frictional contact problems. *International Journal for numerical methods in engineering*, 36(20):3451–3485, 1993.
- Lekhnitskii, S. G. and Fern, P. *Theory of elasticity of an anisotropic elastic body*. Holden-Day, 1963.
- Lemaitre, J., Chaboche, J.-L., Benallal, A., and Desmorat, R. *Mécanique des matériaux solides-3eme édition*. Dunod, 2009.
- Lenoir, N., Bornert, M., Desrues, J., Bésuelle, P., and Viggiani, G. Volumetric digital image correlation applied to x-ray microtomography images from triaxial compression tests on argillaceous rock. *Strain*, 43(3):193–205, 2007.
- Lenoir, N., Artale, B., Bésuelle, P., Charrier, P., Desrues, J., and Viggiani, G. Progress at UJF for WP 3.1 (THM characterization). TIMODAZ meeting, Lausanne, July 2008.
- Leroy, Y. and Ortiz, M. Finite element analysis of strain localization in frictional materials. *International Journal for Numerical and Analytical Methods in Geomechanics*, 13(1):53–74, 1989.
- Lewis, R. W. and Schrefler, B. A. *The finite element method in the static and dynamic deformation and consolidation of porous media*. John Wiley, 1998.
- Li, X. L. *Comportement Hydromécanique des Sols Fins: de l'état saturé à l'état non saturé*. PhD thesis, Université de Liège, 2000.
- Li, X. L., Areias, L., Cornet, F. H., Célérier, B., Whittle, R. W., Chen, G. J., and Bastiaens, W. Test program for in situ stress determination/estimation in the Boom clay at the HADES underground research laboratory in Mol, Belgium. Presentation in 4th International Meeting of Clays in Natural and Engineered Barriers for Radioactive Waste Confinement, 2010.
- Lu, N. and Likos, W. J. *Unsaturated soil mechanics*. Wiley, 2004.
- Lyapunov, A. M. The general problem of the stability of motion. *International Journal of Control*, 55(3):531–534, 1992.
- Matsushima, T., Chambon, R., and Caillerie, D. Large strain finite element analysis of a local second gradient model: application to localization. *International journal for numerical methods in engineering*, 54(4):499–521, 2002.
- Mertens, J. correlation between FMI log of Mol-1 borehole and the “clayey/silty beds” sequence of the Boom clay described in the outcrop area. Personal communication, 2002.
- Mertens, J., Vandenberghe, N., Wouters, L., and Sintubin, M. The origin and development of joints in the boom clay formation (rupelian) in belgium. *Geological Society, London, Special Publications*, 216(1):309–321, 2003.

- Mertens, J., Bastiaens, W., and Dehandschutter, B. Characterisation of induced discontinuities in the boom clay around the underground excavations (URF, Mol, Belgium). *Applied Clay Science*, 26(1):413–428, 2004.
- Mindlin, R. Influence of couple-stresses on stress concentrations. *Experimental mechanics*, 3(1): 1–7, 1963.
- Mindlin, R. Micro-structure in linear elasticity. *Archive for Rational Mechanics and Analysis*, 16(1):51–78, 1964.
- Mokni, M. and Desrues, J. Strain localization measurements in undrained plane-strain biaxial tests on hostun rf sand. *Mechanics of Cohesive-frictional Materials*, 4(4):419–441, 1999.
- Mühlhaus, H. and Vardoulakis, I. The thickness of shear bands in granular materials. *Geotechnique*, 37(3):271–283, 1987.
- Mühlhaus, H.-B. and Alfantis, E. A variational principle for gradient plasticity. *International Journal of Solids and Structures*, 28(7):845–857, 1991.
- Nguyen, T. L., Hall, S. A., Vacher, P., and Viggiani, G. Fracture mechanisms in soft rock: identification and quantification of evolving displacement discontinuities by extended digital image correlation. *Tectonophysics*, 503(1):117–128, 2011.
- Nova, R. The failure of transversely isotropic rocks in triaxial compression. *International Journal of Rock Mechanics and Mining Sciences & Geomechanics Abstracts*, 17(6):325–332, 1980.
- Oden, J. T. and Ripperger, E. A. *Mechanics of elastic structures*. McGraw-Hill New York, 1967.
- OECD/NEA, editor. *Field tracer experiments: Role in the prediction of radionuclides migration*, 1996. OECD document, Disposal of radioactive waste. Synthesis and Proceedings of an NEA/EC GEOTRAP Workshop.
- ONDRAF/NIRAS. Technical overview of the safir 2 report: Safety assessment and feasibility interim report 2. Technical Report NIROND 2001–05 E, December 2001.
- Pamin, J. K. *Gradient-dependent plasticity in numerical simulation of localization phenomena*. TU Delft, Delft University of Technology, 1994.
- Papamichos, E. Continua with microstructure: Cosserat theory. *European Journal of Environmental and Civil Engineering*, 14(8-9):1011–1029, 2010.
- Pardoen, B., Seyedi, D., and Collin, F. Shear banding modelling in cross-anisotropic rocks. *International Journal of Solids and Structures*, 2015. doi: 10.1016/j.ijsolstr.2015.07.012.
- Paterson, M. S. and Wong, T.-f. *Experimental rock deformation-the brittle field*. Springer Science & Business Media, 2005.
- Pijaudier-Cabot, G. and Bazant, Z. P. Nonlocal damage theory. *Journal of Engineering Mechanics*, 113(10):1512–1533, 1987.
- Prager, W. Recent developments in the mathematical theory of plasticity. *Journal of Applied Physics*, 20(3):235–241, 1949.
- Quek, S. and Liu, G. *Finite element method: a practical course*. Butterworth-Heinemann, 2003.
- Rice, J. and Rudnicki, J. A note on some features of the theory of localization of deformation. *International Journal of solids and structures*, 16(7):597–605, 1980.

- Rice, J. R. *The localization of plastic deformation*. Division of Engineering, Brown University, 1976.
- Romero, E., Gens, A., and Lloret, A. Water permeability, water retention and microstructure of unsaturated compacted boom clay. *Engineering Geology*, 54(1):117–127, 1999.
- Romero, E., Vaunat, J., and Merch, V. Suction effects on the residual shear strength of clays. 2:17–37, 2014. doi: 10.3233/JGS-141320.
- Romero Morales, E. *Characterization and thermo-hydro-mechanical behavior of unsaturated Boom clay: An eperimental study*. PhD thesis, Universitat Politècnica de Catalunya, 1999.
- Roscoe, K. and Burland, J. On the generalized stress-strain behaviour of wet clay. 1968.
- Roscoe, K. H., Schofield, A., and Wroth, C. On the yielding of soils. *Geotechnique*, 8(1):22–53, 1958.
- Rudnicki, J. W. and Rice, J. Conditions for the localization of deformation in pressure-sensitive dilatant materials. *Journal of the Mechanics and Physics of Solids*, 23(6):371–394, 1975.
- Salehnia, F. Analysis of the soil media using the theory of unsaturated soils with nonlinear behaviour. Master’s thesis, Tehran University, 2010.
- Salehnia, F. Numerical analysis of in-situ hydro-mechanical behavior of Boom clay around the Connecting gallery. Technical report, Université de Liège, 2013. Annual report to ON-DRAF/NIRAS.
- Salehnia, F. Hydro-mechanical behavior of Boom clay around the Connecting gallery. Technical report, Université de Liège, 2014. Annual report to ONDRAF/NIRAS.
- Salehnia, F. and Gatmiri, B. Comparison of the nonlinear elastic and elastoplastic models in thm response of unsaturated soils. In *Proceedings of the fifth international conference on unsaturated soils*, pages 1067–1073. Taylor and Francis Group, London, 2011.
- Salehnia, F., Charlier, R., and Levasseur, S. Modeling of strain localization around the radioactive waste disposal galleries. In *Coupled Phenomena in Environmental Geotechnics, CPEG 2013*, pages 443–450. CRC Press, 2013a.
- Salehnia, F., Charlier, R., and Levasseur, S. Numerical modelling of the excavated damaged zone in boom clay. In *International EAGE Workshop on Geomechanics and Energy*, 2013b.
- Salehnia, F., Charlier, R., Sillen, X., and Dizier, A. Modeling of excavation damaged zone through the strain localization approach in boom clay. In *Proceedings of the 14th Int. Conference of International Association for Computer Methods and Recent Advances in Geomechanics, IACMAG 2014*, pages 335–340. CRC Press, 2015a.
- Salehnia, F., Collin, F., Li, X. L., Dizier, A., Sillen, X., and Charlier, R. Coupled modeling of excavation damaged zone in boom clay: Strain localization in rock and distribution of contact pressure on the gallery’s lining. *Computers and Geotechnics*, 69:396–410, 2015b. doi: 10.1016/j.compgeo.2015.06.003.
- Salehnia, F., Collin, F., and Charlier, R. On the variable dilatancy angle in rocks around the underground galleries. Manuscript in preparation for publication, forthcominga.
- Salehnia, F., Sillen, X., Li, X. L., Collin, F., and Charlier, R. Numerical modeling of a discontinuous lining behavior, and its interaction with the rock. Manuscript in preparation for publication, forthcomingb.

- Schellekens, J.-C.-J. and De Borst, R. On the numerical integration of interface elements. *International Journal for Numerical Methods in Engineering*, 36(1):43–66, 1993.
- Schittekat, J., Henriët, J. P., and Vandenberghe, N. Geology and geotechnique of the scheldt surge barrier. characteristics of an overconsolidated clay. In *8th International Harbour Congress*, volume 2, pages 121–135, 1983.
- Schofield, A. and Wroth, P. Critical state soil mechanics. 1968.
- SCK-CEN. HADES TOUR GUIDE. Notebook, fifth ed. 1997.
- SCK-CEN. R and D for the geological disposal of medium and high level waste in the Boom clay, 2009. URL [http://science.sckcen.be/en/Projects/Project/RD\\_waste\\_disposal/Geological\\_disposal](http://science.sckcen.be/en/Projects/Project/RD_waste_disposal/Geological_disposal). Visited on 12/2014.
- SCK-CEN. Repository concept: the supercontainer, 2014. URL [http://science.sckcen.be/en/Disposal\\_radioactive\\_waste/Safety\\_assessment\\_geological\\_disposal](http://science.sckcen.be/en/Disposal_radioactive_waste/Safety_assessment_geological_disposal).
- Sharma, K. and Desai, C. Analysis and implementation of thin-layer element for interfaces and joints. *Journal of engineering mechanics*, 118(12):2442–2462, 1992.
- Sieffert, Y., A-l Holo, S., and Chambon, R. Loss of uniqueness of numerical solutions of the bore-hole problem modelled with enhanced media. *International Journal of Solids and Structures*, 46(17):3173–3197, 2009.
- Sillen, X. Modelling the thermal impact of a repository for high-level radioactive waste in a clay host formation. In *Proceedings of of the COMSOL Conference, Hannover*, 2008.
- Simo, J. and Hughes, T. Computational inelasticity. *Springer-Verlag New York*, 1998.
- Simo, J. C. and Taylor, R. L. Consistent tangent operators for rate-independent elastoplasticity. *Computer methods in applied mechanics and engineering*, 48(1):101–118, 1985.
- Sulem, J. Bifurcation theory and localization phenomena. *European Journal of Environmental and Civil Engineering*, 14(8-9):989–1009, 2010.
- Sultan, N. *Etude du comportement thermo-mécanique de l'argile de Boom: expériences et modélisation*. PhD thesis, Ecole Nationale des Ponts et Chaussées, 1997.
- Taylor, D. W. Fundamentals of soil mechanics. *Soil Science*, 66(2):161, 1948.
- Thakur, V. Numerically observed shear bands in soft sensitive clays. *Geomechanics and Geo-engineering: An International Journal*, 6(2):131–146, 2011.
- TIMODAZ. Large scale excavation and heater in-situ experiment: the PRACLAY experiment modelling. Technical Report WP 5.2, D13, Commission of the European Communities, September 2010a. Editor: Charlier, R.
- TIMODAZ. THM characterisation and input for simulation. Technical Report WP 3.1, D5, Commission of the European Communities, July 2010b. Editor: Delage, P.
- Tinh, L. T. *Comportement thermo-hydro-mécanique de l'argile de Boom*. PhD thesis, Ecole Nationale des Ponts et Chaussées, January 2008.
- Toupin, R. A. Elastic materials with couple-stresses. *Archive for Rational Mechanics and Analysis*, 11(1):385–414, 1962.

- Tvergaard, V. and Needleman, A. Effects of nonlocal damage in porous plastic solids. *International Journal of Solids and Structures*, 32(8):1063–1077, 1995.
- Valès, F. *Modes de déformation et d'endommagement de roches argileuses profondes sous sollicitations hydro-mécaniques*. PhD thesis, Ecole Polytechnique X, 2008.
- Van Eekelen, H. Isotropic yield surfaces in three dimensions for use in soil mechanics. *International Journal for Numerical and Analytical Methods in Geomechanics*, 4(1):89–101, 1980.
- Van Genuchten, M. T. A closed-form equation for predicting the hydraulic conductivity of unsaturated soils. *Soil Science Society of America Journal*, 44(5):892–898, 1980.
- Van Marcke, P. and Bastiaens, W. Excavation induced fractures in a plastic clay formation: Observations at the hades urf. *Journal of Structural Geology*, 32(11):1677–1684, 2010.
- Vardoulakis, I. Equilibrium theory of shear bands in plastic bodies. *Mechanics Research Communications*, 3(3):209–214, 1976.
- Vardoulakis, I. and Aifantis, E. A gradient flow theory of plasticity for granular materials. *Acta Mechanica*, 87(3-4):197–217, 1991.
- Vardoulakis, I. I. Shear-banding and liquefaction in granular materials on the basis of a cosserat continuum theory. *Ingenieur-Archiv*, 59(2):106–113, 1989.
- Vermeer, P. A. and De Borst, R. Non-associated plasticity for soils, concrete and rock. *HERON*, 29(3), 1984.
- Viggiani, G. and Hall, S. A. Full-field measurements in experimental geomechanics: historical perspective, current trends and recent results. *Advanced experimental techniques in geomechanics*, pages 3–67, 2012.
- Volckaert, G., Ortiz, L., De Cannière, P., Put, M., Horseman, S., Harrington, J., Fioravante, V., and Impey, M. Megas: modelling and experiments on gas migration in repository host rocks. Technical report, Office for official publications of the European Communities, 1994. Final report EUR 16325. European Commission, Luxembourg.
- Wang, X. Modélisation numérique des problèmes avec localisation de la déformation en bandes de cisaillement. *Thèse de doctorat, Université de Liege, Belgique*, 1993.
- Wells, G. N. *Discontinuous modelling of strain localisation and failure*. Delft University of Technology, 2001.
- Wemaere, I., Marivoet, J., and Labat, S. Hydraulic conductivity variability of the Boom clay in north-east Belgium based on four core drilled boreholes. *Physics and Chemistry of the Earth, Parts A/B/C*, 33:S24–S36, 2008.
- Wileveau, Y. and Bernier, F. Similarities in the hydromechanical response of callovo-oxfordian clay and boom clay during gallery excavation. *Physics and Chemistry of the Earth, Parts A/B/C*, 33:S343–S349, 2008.
- Wilkins, M. L. Calculation of elastic-plastic flow. Technical report, DTIC Document, 1963.
- WNA. Storage and disposal options, 2013. URL <http://www.world-nuclear.org/info/Nuclear-Fuel-Cycle/Nuclear-Wastes/Appendices/Radioactive-Waste-Management-Appendix-2--Storage-and-Disposal-Options/>. Visited on 12/2014.

- Wriggers, P. Finite element algorithms for contact problems. *Archives of Computational Methods in Engineering*, 2(4):1–49, 1995.
- Wriggers, P. *Computational contact mechanics*, volume 30167. Springer, 2006.
- Wriggers, P. and Zavarise, G. Computational contact mechanics. *Encyclopedia of computational mechanics*, 2004.
- Yu, H.-D., Chen, W.-Z., Jia, S.-P., Cao, J.-J., and Li, X.-L. Experimental study on the hydro-mechanical behavior of boom clay. *International Journal of Rock Mechanics and Mining Sciences*, 53:159–165, 2012.
- Yu, L., Gedeon, M., Wemaere, I., Marivoet, J., and De Craen, M. Boom clay hydraulic conductivity—a synthesis of 30 years of research. Technical report, External report of Belgian Nuclear Research Centre, SCK•CEN-ER-122, 2011.
- Yu, L., Rogiers, B., Gedeon, M., Marivoet, J., De Craen, M., and Mallants, D. A critical review of laboratory and in-situ hydraulic conductivity measurements for the boom clay in Belgium. *Applied Clay Science*, 75:1–12, 2013.
- Zavarise, G., Wriggers, P., and Schrefler, B. A method for solving contact problems. *International Journal for Numerical Methods in Engineering*, 42(3):473–498, 1998.
- Zervos, A., Papanastasiou, P., and Vardoulakis, I. A finite element displacement formulation for gradient elastoplasticity. *International Journal for Numerical Methods in Engineering*, 50(6):1369–1388, 2001a.
- Zervos, A., Papanastasiou, P., and Vardoulakis, I. Modelling of localisation and scale effect in thick-walled cylinders with gradient elastoplasticity. *International Journal of Solids and Structures*, 38(30):5081–5095, 2001b.
- Zienkiewicz, O. C. and Taylor, R. L. *The finite element method: Solid mechanics*, volume 2. Butterworth-Heinemann, 2000.

# Appendix A

## Convergence criteria

### A.1 Convergence criterion for the displacement

During the time step resolution algorithm, the convergence for the displacement in our analyses is governed by:

$$\mathbf{Conve}_D = \begin{cases} \sqrt{\frac{1}{N_{Anal}} \sum_1^{N_{Anal}} \left( \frac{\sum_{N_{Dof}} [\delta \mathbf{u}_{en}]^2}{\max \left\{ \sum_{N_{Dof}} [\Delta \mathbf{u}_{en}]^2, [\mathbf{COMP}A]^2 \right\}} \right)} \leq \mathfrak{Tol}_D, & \text{if } \mathbf{COMP}A \leq 0 \\ \sqrt{\frac{1}{N_{Anal}} \sum_1^{N_{Anal}} \left( \frac{\sum_{N_{Dof}} [\delta \mathbf{u}_{en}]^2}{\mathbf{COMP}A^2} \right)} \leq \mathfrak{Tol}_D, & \text{if } \mathbf{COMP}A > 0 \end{cases} \quad (\text{A.1})$$

where  $N_{Anal}$  is the number of facet types involved in our analysis; e.g. three if second gradient model is also involved in the analysis: mechanical (displacements), hydraulic (pore pressure), and second gradient terms.  $N_{Dof}$  is the number of degrees of freedom.  $\delta \mathbf{u}_{en}$  is the increment (correction) of generalized coordinates corresponding the nodal degree of freedom - which refers to the mechanical displacements, pore pressure variations and the change in second gradient terms (if the second grade model is also involved) - between the current and previous iterations.  $\Delta \mathbf{u}_{en}$  is the generalized displacement occurred between the current iteration and the end of previous step.  $\mathbf{COMP}A$  consists in the absolute values of reference displacements -  $N_{Anal}$  (individual) values for all the facet types involved in our analysis - that can be defined to manage the convergence on displacements if necessary (in the complex computations).  $\mathfrak{Tol}_D$  is the input tolerance parameter; it is defined as  $1 \times 10^{-3}$  in our modelings.

## A.2 Convergence criterion for the force

The convergence for the forces is governed by:

$$\mathbf{Conve}_F = \left\{ \begin{array}{l} \left( \frac{1}{N_{Anal}} \sum_1^{N_{Anal}} \left( \frac{\sum_{N_{Dof}} \mathbf{F}_{OBF}^2}{\sum_{N_{Dof}} N_{OBF}} \right) \right) \leq \mathfrak{tol}_F, \quad \text{if } \mathcal{COMPA} \leq 0 \\ \max \left\{ \frac{\sum_{N_{Dof}} \mathbf{F}_{REA}^2}{\sum_{N_{Dof}} N_{REA}}, \frac{[\mathcal{COMPA}]^2}{\sum_{N_{Dof}} N_{REA}} \right\} \\ \left( \frac{1}{N_{Anal}} \sum_1^{N_{Anal}} \left( \frac{\sum_{N_{Dof}} \mathbf{F}_{OBF}^2}{\sum_{N_{Dof}} N_{OBF}} \right) \right) \leq \mathfrak{tol}_F, \quad \text{if } \mathcal{COMPA} > 0 \end{array} \right. \quad (\text{A.2})$$

where  $\mathbf{F}_{OBF}$  is the out of balance force,  $\mathbf{F}_{REA}$  is the reaction force,  $N_{OBF}$  and  $N_{REA}$  are the number of out of balance forces and reactions corresponding to each degree of freedom. Similarly to displacement,  $\mathcal{COMPA}$  consists in  $N_{Anal}$  (individual) values of the absolute reference forces that can be defined to manage the convergence on out of balance forces, and  $\mathfrak{tol}_F$  is the input tolerance parameter which is defined as  $1 \times 10^{-3}$  in our modelings.

The time step convergence can be managed by the user of LAGAMINE so that it is achieved if  $\mathbf{Conve}_D$  or/and  $\mathbf{Conve}_F$  are satisfied. In our analyses, the step converges if the both criteria are met.

## Appendix B

### Accomplishment to the coupled second gradient formulation

The matrix  $\left[\mathbf{E}_{(25 \times 25)}^{(t+\Delta t)_i}\right]$  contains the terms corresponding to the local second gradient model for monophasic medium [Matsushima et al., 2002; Chambon and Moullet, 2004], i.e. matrices  $\left[\mathbf{E}_{1(4 \times 4)}^{(t+\Delta t)_i}\right]$ ,  $\left[\mathbf{E}_{2(8 \times 4)}^{(t+\Delta t)_i}\right]$ ,  $\left[\mathbf{E}_{3(4 \times 4)}^{(t+\Delta t)_i}\right]$ ,  $\left[\mathbf{E}_{4(4 \times 4)}^{(t+\Delta t)_i}\right]$ , as defined in Equations B.2-B.5, and  $\left[\mathbf{D}_{(8 \times 8)}^{(t+\Delta t)_i}\right]$ . In addition, there are all the coupling terms between the mechanical and hydraulic part of the problem, i.e.  $\left[\mathbf{K}_{\mathbf{WM}_{(4 \times 3)}}^{(t+\Delta t)_i}\right]$  (Equation B.7) and  $\left[\mathbf{K}_{\mathbf{MW}_{(3 \times 4)}}^{(t+\Delta t)_i}\right]$  (Equation B.8), in addition to the classical stiffness matrix for a flow problem, i.e.  $\left[\mathbf{K}_{\mathbf{WW}_{(3 \times 3)}}^{(t+\Delta t)_i}\right]$  (Equation B.6), following the development of the second gradient theory for multiphasic medium [Collin et al., 2006]. With regard to the numerical modelings presented in Chapters 6-7, these latter equations are extended here for an anisotropic porous medium where a second rank tensor of intrinsic permeability is applied ( $k_{ij}$ ; see Equation 3.27). Moreover, the contribution of gravity volume force is involved in the matrix  $\left[\mathbf{E}_{(25 \times 25)}^{(t+\Delta t)_i}\right]$  by the terms  $\left[\mathbf{G}_{1(2 \times 4)}^{(t+\Delta t)_i}\right]$  and  $\left[\mathbf{G}_{2(2 \times 3)}^{(t+\Delta t)_i}\right]$  (Equations B.9-B.10). The latter are then null if one ignores the gravity effect in a numerical analysis.

$$\left[\mathbf{E}_{(25 \times 25)}^{(t+\Delta t)_i}\right] = \begin{bmatrix} \mathbf{E}_{1(4 \times 4)}^{(t+\Delta t)_i} & 0_{(4 \times 2)} & \mathbf{K}_{\mathbf{WM}_{(4 \times 3)}}^{(t+\Delta t)_i} & 0_{(4 \times 8)} & 0_{(4 \times 4)} & -\mathbf{I}_{(4 \times 4)} \\ \mathbf{G}_{1(2 \times 4)}^{(t+\Delta t)_i} & 0_{(2 \times 2)} & \mathbf{G}_{2(2 \times 3)}^{(t+\Delta t)_i} & 0_{(2 \times 8)} & 0_{(2 \times 4)} & 0_{(2 \times 4)} \\ \mathbf{K}_{\mathbf{MW}_{(3 \times 4)}}^{(t+\Delta t)_i} & 0_{(3 \times 2)} & \mathbf{K}_{\mathbf{WW}_{(3 \times 3)}}^{(t+\Delta t)_i} & 0_{(3 \times 8)} & 0_{(3 \times 4)} & 0_{(3 \times 4)} \\ \mathbf{E}_{2(8 \times 4)}^{(t+\Delta t)_i} & 0_{(8 \times 2)} & 0_{(8 \times 3)} & \mathbf{D}_{(8 \times 8)}^{(t+\Delta t)_i} & 0_{(8 \times 4)} & 0_{(8 \times 4)} \\ \mathbf{E}_{3(4 \times 4)}^{(t+\Delta t)_i} & 0_{(4 \times 2)} & 0_{(4 \times 3)} & 0_{(4 \times 8)} & 0_{(4 \times 4)} & \mathbf{I}_{(4 \times 4)} \\ \mathbf{E}_{4(4 \times 4)}^{(t+\Delta t)_i} & 0_{(4 \times 2)} & 0_{(4 \times 3)} & 0_{(4 \times 8)} & -\mathbf{I}_{(4 \times 4)} & 0_{(4 \times 4)} \end{bmatrix} \quad (\text{B.1})$$

$$\begin{aligned}
\left[ \mathbf{E}_1^{(t+\Delta t)_i} \right] &= \left[ \mathbf{C}_{(4 \times 4)}^{(t+\Delta t)_i} \right] \\
+ \begin{bmatrix} 0 & -\sigma_{12}^{(t+\Delta t)_i} + \lambda_{12}^{(t+\Delta t)_i} & 0 & \sigma_{11}^{(t+\Delta t)_i} - \lambda_{11}^{(t+\Delta t)_i} \\ \sigma_{12}^{(t+\Delta t)_i} - \lambda_{12}^{(t+\Delta t)_i} & 0 & -\sigma_{11}^{(t+\Delta t)_i} + \lambda_{11}^{(t+\Delta t)_i} & 0 \\ 0 & -\sigma_{22}^{(t+\Delta t)_i} + \lambda_{22}^{(t+\Delta t)_i} & 0 & \sigma_{21}^{(t+\Delta t)_i} - \lambda_{21}^{(t+\Delta t)_i} \\ \sigma_{22}^{(t+\Delta t)_i} - \lambda_{22}^{(t+\Delta t)_i} & 0 & -\sigma_{21}^{(t+\Delta t)_i} + \lambda_{21}^{(t+\Delta t)_i} & 0 \end{bmatrix}
\end{aligned} \tag{B.2}$$

$$\left[ \mathbf{E}_2^{(t+\Delta t)_i} \right] = \begin{bmatrix} 0 & -\Sigma_{112}^{(t+\Delta t)_i} & 0 & \Sigma_{111}^{(t+\Delta t)_i} \\ \Sigma_{112}^{(t+\Delta t)_i} & 0 & -\Sigma_{111}^{(t+\Delta t)_i} & 0 \\ 0 & -\Sigma_{122}^{(t+\Delta t)_i} & 0 & \Sigma_{121}^{(t+\Delta t)_i} \\ \Sigma_{122}^{(t+\Delta t)_i} & 0 & -\Sigma_{121}^{(t+\Delta t)_i} & 0 \\ 0 & -\Sigma_{212}^{(t+\Delta t)_i} & 0 & \Sigma_{211}^{(t+\Delta t)_i} \\ \Sigma_{212}^{(t+\Delta t)_i} & 0 & -\Sigma_{211}^{(t+\Delta t)_i} & 0 \\ 0 & -\Sigma_{222}^{(t+\Delta t)_i} & 0 & \Sigma_{221}^{(t+\Delta t)_i} \\ \Sigma_{222}^{(t+\Delta t)_i} & 0 & -\Sigma_{221}^{(t+\Delta t)_i} & 0 \end{bmatrix} \tag{B.3}$$

$$\left[ \mathbf{E}_3^{(t+\Delta t)_i} \right] = \begin{bmatrix} \lambda_{11}^{(t+\Delta t)_i} & 0 & 0 & \lambda_{11}^{(t+\Delta t)_i} \\ \lambda_{12}^{(t+\Delta t)_i} & 0 & 0 & \lambda_{12}^{(t+\Delta t)_i} \\ \lambda_{21}^{(t+\Delta t)_i} & 0 & 0 & \lambda_{21}^{(t+\Delta t)_i} \\ \lambda_{22}^{(t+\Delta t)_i} & 0 & 0 & \lambda_{22}^{(t+\Delta t)_i} \end{bmatrix} \tag{B.4}$$

$$\left[ \mathbf{E}_4^{(t+\Delta t)_i} \right] = \begin{bmatrix} 1 - v_{11}^{(t+\Delta t)_i} & 0 & -\frac{\partial u_1^{(t+\Delta t)_i}}{\partial x_2^{(t+\Delta t)_i}} & \frac{\partial u_1^{(t+\Delta t)_i}}{\partial x_1^{(t+\Delta t)_i}} - v_{11}^{(t+\Delta t)_i} \\ \frac{\partial u_1^{(t+\Delta t)_i}}{\partial x_2^{(t+\Delta t)_i}} - v_{12}^{(t+\Delta t)_i} & 1 - \frac{\partial u_1^{(t+\Delta t)_i}}{\partial x_1^{(t+\Delta t)_i}} & 0 & -v_{12}^{(t+\Delta t)_i} \\ -v_{21}^{(t+\Delta t)_i} & 0 & 1 - \frac{\partial u_2^{(t+\Delta t)_i}}{\partial x_2^{(t+\Delta t)_i}} & \frac{\partial u_2^{(t+\Delta t)_i}}{\partial x_1^{(t+\Delta t)_i}} - v_{21}^{(t+\Delta t)_i} \\ \frac{\partial u_2^{(t+\Delta t)_i}}{\partial x_2^{(t+\Delta t)_i}} - v_{22}^{(t+\Delta t)_i} & -\frac{\partial u_2^{(t+\Delta t)_i}}{\partial x_1^{(t+\Delta t)_i}} & 0 & 1 - v_{22}^{(t+\Delta t)_i} \end{bmatrix} \tag{B.5}$$

$$\left[ \mathbf{K}_{\mathbf{w}\mathbf{w}\mathbf{w}}^{(t+\Delta t)_i} \right] = \begin{bmatrix} \rho_w^{(t+\Delta t)_i} \frac{k_{11}}{\mu_w} & \rho_w^{(t+\Delta t)_i} \frac{k_{12}}{\mu_w} & \mathcal{A} \\ \rho_w^{(t+\Delta t)_i} \frac{k_{21}}{\mu_w} & \rho_w^{(t+\Delta t)_i} \frac{k_{22}}{\mu_w} & \mathcal{B} \\ 0 & 0 & \mathcal{C} \end{bmatrix} \tag{B.6}$$

where

$$\begin{aligned}
\mathcal{A} &= \frac{\rho_w^{(t+\Delta t)_i}}{\mu_w \chi_w} \left( k_{11} \left( \frac{\partial p_w^{(t+\Delta t)_i}}{\partial x_1^{(t+\Delta t)_i}} + \rho_w^{(t+\Delta t)_i} g_1 \right) + k_{12} \left( \frac{\partial p_w^{(t+\Delta t)_i}}{\partial x_2^{(t+\Delta t)_i}} + \rho_w^{(t+\Delta t)_i} g_2 \right) \right) \\
&\quad + \rho_w^{(t+\Delta t)_i} \frac{k_{11} \rho_w^{(t+\Delta t)_i} g_1}{\mu_w \chi_w} + \rho_w^{(t+\Delta t)_i} \frac{k_{12} \rho_w^{(t+\Delta t)_i} g_2}{\mu_w \chi_w} \\
\mathcal{B} &= \frac{\rho_w^{(t+\Delta t)_i}}{\mu_w \chi_w} \left( k_{21} \left( \frac{\partial p_w^{(t+\Delta t)_i}}{\partial x_1^{(t+\Delta t)_i}} + \rho_w^{(t+\Delta t)_i} g_1 \right) + k_{22} \left( \frac{\partial p_w^{(t+\Delta t)_i}}{\partial x_2^{(t+\Delta t)_i}} + \rho_w^{(t+\Delta t)_i} g_2 \right) \right) \\
&\quad + \rho_w^{(t+\Delta t)_i} \frac{k_{21} \rho_w^{(t+\Delta t)_i} g_1}{\mu_w \chi_w} + \rho_w^{(t+\Delta t)_i} \frac{k_{22} \rho_w^{(t+\Delta t)_i} g_2}{\mu_w \chi_w} \\
\mathcal{C} &= \rho_w^{(t+\Delta t)_i} \frac{\dot{p}_w^{(t+\Delta t)_i}}{\chi_w} n^{(t+\Delta t)_i} + \frac{\rho_w^{(t+\Delta t)_i} n^{(t+\Delta t)_i}}{\chi_w} \frac{1}{\Delta t} + \frac{\rho_w^{(t+\Delta t)_i}}{\chi_w} \frac{\dot{\Omega}^{(t+\Delta t)_i}}{\Omega^{(t+\Delta t)_i}}
\end{aligned}$$

$$\left[ \mathbf{K}_{\mathbf{WM}_{(4 \times 3)}}^{(t+\Delta t)_i} \right] = \begin{bmatrix} 0 & 0 & -1 \\ 0 & 0 & 0 \\ 0 & 0 & 0 \\ 0 & 0 & -1 \end{bmatrix} \quad (\text{B.7})$$

$$\left[ \mathbf{K}_{\mathbf{MW}_{(3 \times 4)}}^{(t+\Delta t)_i} \right] = \begin{bmatrix} \mathcal{D} & \mathcal{E} & \mathcal{F} & \mathcal{G} \\ \mathcal{H} & \mathcal{J} & \mathcal{I} & \mathcal{K} \\ \mathcal{L} & 0 & 0 & \mathcal{L} \end{bmatrix} \quad (\text{B.8})$$

where

$$\begin{aligned}
\mathcal{D} &= -\rho_w^{(t+\Delta t)_i} \frac{k_{11}}{\mu_w} \frac{\partial p_w^{(t+\Delta t)_i}}{\partial x_1^{(t+\Delta t)_i}} \\
\mathcal{E} &= m_2^{(t+\Delta t)_i} - \rho_w^{(t+\Delta t)_i} \frac{k_{12}}{\mu_w} \frac{\partial p_w^{(t+\Delta t)_i}}{\partial x_1^{(t+\Delta t)_i}} \\
\mathcal{F} &= -\rho_w^{(t+\Delta t)_i} \frac{k_{11}}{\mu_w} \frac{\partial p_w^{(t+\Delta t)_i}}{\partial x_2^{(t+\Delta t)_i}} \\
\mathcal{G} &= -m_1^{(t+\Delta t)_i} \\
\mathcal{H} &= -m_2^{(t+\Delta t)_i} \\
\mathcal{J} &= -\rho_w^{(t+\Delta t)_i} \frac{k_{22}}{\mu_w} \frac{\partial p_w^{(t+\Delta t)_i}}{\partial x_1^{(t+\Delta t)_i}} \\
\mathcal{I} &= m_1^{(t+\Delta t)_i} - \rho_w^{(t+\Delta t)_i} \frac{k_{12}}{\mu_w} \frac{\partial p_w^{(t+\Delta t)_i}}{\partial x_2^{(t+\Delta t)_i}} \\
\mathcal{K} &= -\rho_w^{(t+\Delta t)_i} \frac{k_{22}}{\mu_w} \frac{\partial p_w^{(t+\Delta t)_i}}{\partial x_2^{(t+\Delta t)_i}}
\end{aligned}$$

$$\mathcal{L} = \left( \rho_w^{(t+\Delta t)_i} \frac{\dot{p}_w^{(t+\Delta t)_i}}{\chi_w} \left( 1 - n^{(t+\Delta t)_i} \right) + \rho_w \frac{1}{\Delta t} - \rho_w \left( \frac{\dot{\Omega}^{(t+\Delta t)_i}}{\Omega^{(t+\Delta t)_i}} \right) \right) + \dot{S}^{(t+\Delta t)_i}$$

$$\left[ \mathbf{G}_{\mathbf{1}(2 \times 4)}^{(t+\Delta t)_i} \right] = \begin{bmatrix} \mathcal{M} & 0 & 0 & \mathcal{M} \\ \mathcal{M} & 0 & 0 & \mathcal{M} \end{bmatrix} \quad (\text{B.9})$$

where

$$\mathcal{M} = \left( 1 - n^{(t+\Delta t)_i} \right) \left( \rho_s^{(t+\Delta t)_i} - \rho_w^{(t+\Delta t)_i} \right) - \rho_m^{(t+\Delta t)_i}$$

$$\left[ \mathbf{G}_{\mathbf{2}(2 \times 3)}^{(t+\Delta t)_i} \right] = \begin{bmatrix} 0 & 0 & -\rho_w^{(t+\Delta t)_i} \frac{g_1}{\chi_w} n^{(t+\Delta t)_i} \\ 0 & 0 & -\rho_w^{(t+\Delta t)_i} \frac{g_2}{\chi_w} n^{(t+\Delta t)_i} \end{bmatrix} \quad (\text{B.10})$$

## Appendix C

### On the fluid flow along the interface

Upon considering fluid flux along the interface - i.e. in the local tangential direction  $\bar{\mathbf{e}}_2^1$  (see Figure 7.5) - it is assumed to be governed by the generalized Darcy's law, such that:

$$f_{w,l} = -\rho_w \frac{k_l}{\mu_w} \cdot \left( \nabla_{\bar{\mathbf{e}}_2^1} p_w + \rho_w g \nabla_{\bar{\mathbf{e}}_2^1} x_2 \right) \quad (\text{C.1})$$

where  $k_l$  is the longitudinal permeability.  $\nabla_{\bar{\mathbf{e}}_2^1}$  is the gradient in the direction  $\bar{\mathbf{e}}_2^1$  with respect to which  $\nabla_{\bar{\mathbf{e}}_2^1} p_w$  and  $\nabla_{\bar{\mathbf{e}}_2^1} x_2$  are described in the following.

$$\nabla_{\bar{\mathbf{e}}_2^1} p_w = \nabla^T p_w \cdot \bar{\mathbf{e}}_2^1 \quad (\text{C.2})$$

With regard to Equation 7.28, it yields:

$$\begin{aligned} \nabla_{\bar{\mathbf{e}}_2^1} p_w &= \begin{bmatrix} \frac{\partial p_w}{\partial x_1} & \frac{\partial p_w}{\partial x_2} \end{bmatrix} \cdot \frac{1}{\det \mathbf{J}} \begin{bmatrix} \frac{\partial x_1}{\partial \xi} \\ \frac{\partial x_2}{\partial \xi} \end{bmatrix} = \frac{1}{\det \mathbf{J}} \left[ \frac{\partial p_w}{\partial x_1} \frac{\partial x_1}{\partial \xi} + \frac{\partial p_w}{\partial x_2} \frac{\partial x_2}{\partial \xi} \right] \\ &= \frac{1}{\det \mathbf{J}} \frac{\partial p_w}{\partial \xi} \cdot \left[ \frac{\partial \xi}{\partial x_1} \frac{\partial x_1}{\partial \xi} + \frac{\partial \xi}{\partial x_2} \frac{\partial x_2}{\partial \xi} \right] = \frac{1}{\det \mathbf{J}} \frac{\partial p_w}{\partial \xi} \cdot \mathbf{J}^{-1} \cdot \mathbf{J} = \frac{1}{\det \mathbf{J}} \frac{\partial N_{en}}{\partial \xi} P_{w,en} \end{aligned} \quad (\text{C.3})$$

where  $N_{en}$  is the shape function associated to the node  $en$ ,  $P_{w,en}$  is the nodal pore water pressure, and  $\mathbf{J}^{-1}$  is the inverse of the Jacobian matrix. Similarly,  $\nabla_{\bar{\mathbf{e}}_2^1} x_2$  reads:

$$\nabla_{\bar{\mathbf{e}}_2^1} x_2 = \frac{1}{\det \mathbf{J}} \frac{\partial N_{en}}{\partial \xi} x_{2,en} \quad (\text{C.4})$$

Furthermore, with respect to the description given in Section 7.3.4, the contribution of the interface in Equation 7.36 includes another additional term. It concerns the fluid flux  $f_{w,l}$ , which is involved in the internal virtual work expression on the left-hand side of the weak form equation. This contribution for an interface element can be given by Equation C.5 assuming that the inner pressure is constant over the gap  $g_N$ , and the integral over the gap volume is therefore transferred into a surface integral over  $\Gamma_c^1$  (as our reference interface so far).

$$\mathcal{W}_{c,I}^{*el} = \int_{\Gamma_c^{1,el}} \left( -f_{w,l} \cdot \nabla_{\bar{\mathbf{e}}_2^1} p_w^* \right) g_N d\Gamma \quad (\text{C.5})$$

within which the contribution of  $en^{th}$  node of the interface element, in terms of energetically equivalent nodal force, consists in  $\mathcal{F}_{c,I,en}^{el} \cdot P_{w,en}^*$

where the energetically internal equivalent nodal force (associated to the node  $en$ ),  $\mathcal{F}_{c,I,en}^{el}$ , is given by:

$$\mathcal{F}_{c,I,en}^{el} = \sum_{IP=1}^{n_{IP}} \left[ \left( -f_{w,l} \cdot \nabla_{\bar{\mathbf{e}}_2^1} N_{en} \right) \det \mathbf{J} g_N W_{IP} \right] \quad (\text{C.6})$$

where, with respect to Equation C.3,  $\nabla_{\bar{\mathbf{e}}_2^1} N_{en}$  can be given by:

$$\nabla_{\bar{\mathbf{e}}_2^1} N_{en} = \frac{1}{\det \mathbf{J}} \frac{\partial N_{en}}{\partial \xi} N_{en} \quad (\text{C.7})$$